MULTIFUNCTIONAL POLYMERIC MATERIALS FOR DRUG AND GENE DELIVERY

EDITED BY: Yakai Feng, Abraham Jacob Domb, Bin He and Wenzhong Li
PUBLISHED IN: Frontiers in Bioengineering and Biotechnology

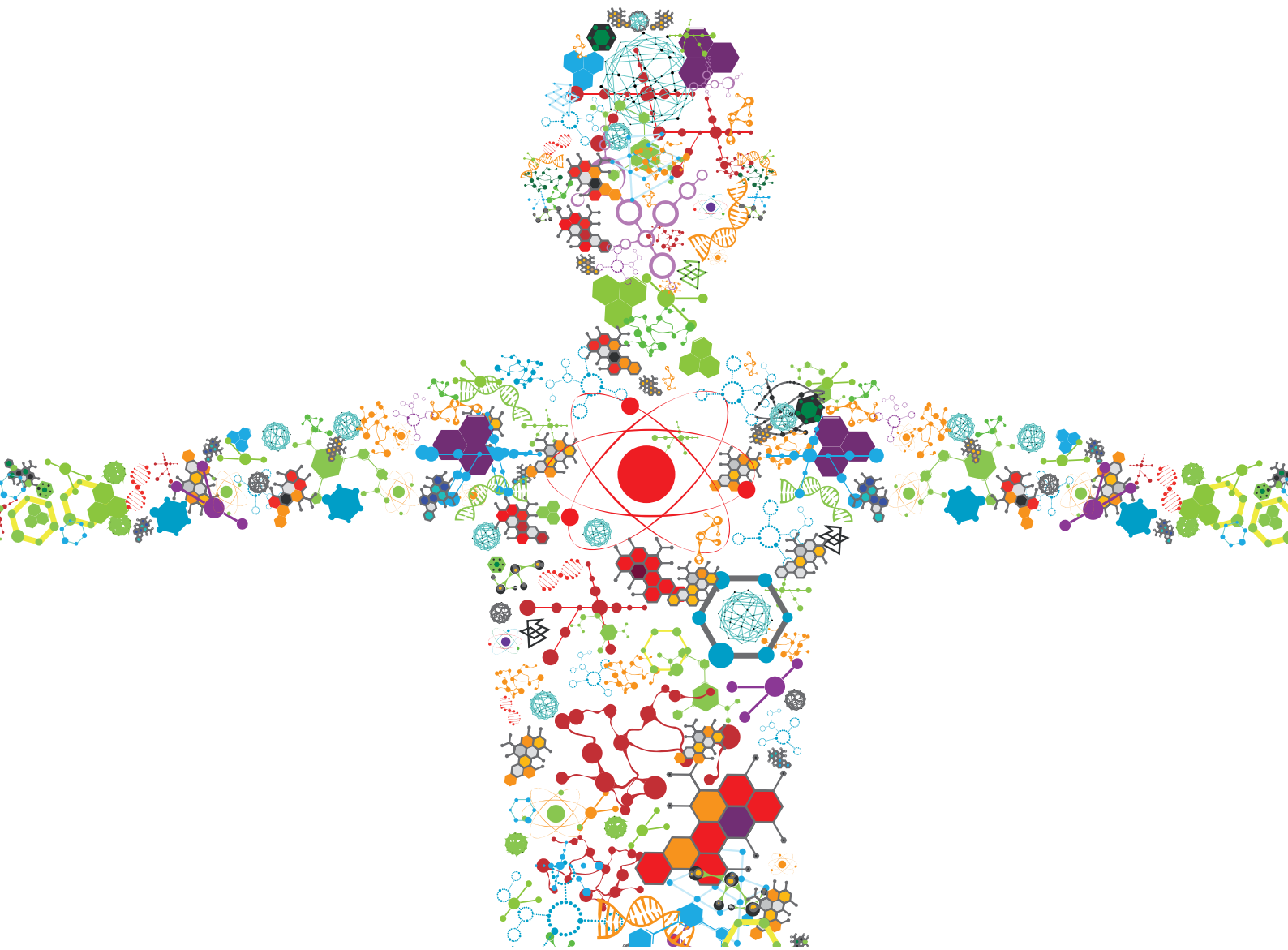

frontiers Research Topics

ISSN 1664-8714
ISBN 978-2-88976-274-3
DOI 10.3389/978-2-88976-274-3

About Frontiers

Frontiers is more than just an open-access publisher of scholarly articles: it is a pioneering approach to the world of academia, radically improving the way scholarly research is managed. The grand vision of Frontiers is a world where all people have an equal opportunity to seek, share and generate knowledge. Frontiers provides immediate and permanent online open access to all its publications, but this alone is not enough to realize our grand goals.

Frontiers Journal Series

The Frontiers Journal Series is a multi-tier and interdisciplinary set of open-access, online journals, promising a paradigm shift from the current review, selection and dissemination processes in academic publishing. All Frontiers journals are driven by researchers for researchers; therefore, they constitute a service to the scholarly community. At the same time, the Frontiers Journal Series operates on a revolutionary invention, the tiered publishing system, initially addressing specific communities of scholars, and gradually climbing up to broader public understanding, thus serving the interests of the lay society, too.

Dedication to Quality

Each Frontiers article is a landmark of the highest quality, thanks to genuinely collaborative interactions between authors and review editors, who include some of the world's best academicians. Research must be certified by peers before entering a stream of knowledge that may eventually reach the public - and shape society; therefore, Frontiers only applies the most rigorous and unbiased reviews.
Frontiers revolutionizes research publishing by freely delivering the most outstanding research, evaluated with no bias from both the academic and social point of view. By applying the most advanced information technologies, Frontiers is catapulting scholarly publishing into a new generation.

What are Frontiers Research Topics?

Frontiers Research Topics are very popular trademarks of the Frontiers Journals Series: they are collections of at least ten articles, all centered on a particular subject. With their unique mix of varied contributions from Original Research to Review Articles, Frontiers Research Topics unify the most influential researchers, the latest key findings and historical advances in a hot research area! Find out more on how to host your own Frontiers Research Topic or contribute to one as an author by contacting the Frontiers Editorial Office: frontiersin.org/about/contact

MULTIFUNCTIONAL POLYMERIC MATERIALS FOR DRUG AND GENE DELIVERY

Topic Editors:
Yakai Feng, Tianjin University, China
Abraham Jacob Domb, Hebrew University of Jerusalem, Israel
Bin He, Sichuan University, China
Wenzhong Li, Freie Universität Berlin, Germany

Citation: Feng, Y., Domb, A. J., He, B., Li, W., eds. (2022). Multifunctional Polymeric Materials for Drug and Gene Delivery. Lausanne: Frontiers Media SA. doi: 10.3389/978-2-88976-274-3

Table of Contents

04 ***Editorial: Multifunctional Polymeric Materials for Drug and Gene Delivery***
Yakai Feng, Bin He, Wenzhong Li and Abraham Jacob Domb

06 ***Micelles Based on Lysine, Histidine, or Arginine: Designing Structures for Enhanced Drug Delivery***
Li Xie, Rong Liu, Xin Chen, Mei He, Yi Zhang and Shuyi Chen

26 ***An NIR-II Responsive Nanoplatform for Cancer Photothermal and Oxidative Stress Therapy***
Bin Huang, Yuanpeng Huang, Han Han, Qiuyue Ge, Dongliang Yang, Yanling Hu, Meng Ding, Yanqing Su, Yanbin He, Jinjun Shao and Jianfeng Chu

36 ***Design and Applications of Tumor Microenvironment-Responsive Nanogels as Drug Carriers***
Xinjing Du, Yuting Gao, Qi Kang and Jinfeng Xing

53 ***Ocular Wnt/β-Catenin Pathway Inhibitor XAV939-Loaded Liposomes for Treating Alkali-Burned Corneal Wound and Neovascularization***
Yueyang Zhong, Kai Wang, Yin Zhang, Qichuan Yin, Su Li, Jiaming Wang, Xiaobo Zhang, Haijie Han and Ke Yao

66 ***Smart Polymeric Delivery System for Antitumor and Antimicrobial Photodynamic Therapy***
Zhijia Wang, Fu-Jian Xu and Bingran Yu

89 ***Mitochondrial Targeting and pH-Responsive Nanogels for Co-Delivery of Lonidamine and Paclitaxel to Conquer Drug Resistance***
Enping Chen, Ting Wang, Junmei Zhang, Xiang Zhou, Yafan Niu, Fu Liu, Yinan Zhong, Dechun Huang and Wei Chen

101 ***Nitrate-Functionalized poly(ε-Caprolactone) Small-Diameter Vascular Grafts Enhance Vascular Regeneration* via *Sustained Release of Nitric Oxide***
Sen Yang, Xueni Zheng, Meng Qian, He Wang, Fei Wang, Yongzhen Wei, Adam C. Midgley, Ju He, Hongyan Tian and Qiang Zhao

114 ***Inhibition of Neovascularization and Inflammation in a Mouse Model of Corneal Alkali Burns Using Cationic Liposomal Tacrolimus***
Xueqi Lin, Xuewen Yu, Xiang Chen, Siting Sheng, Jingwen Wang, Ben Wang and Wen Xu

128 ***Efficient Transient Expression of Plasmid DNA Using Poly (2-(*N,N*-Dimethylamino) Ethyl Methacrylate) in Plant Cells***
Zishuai An, Bing Cao, Junzhe Zhang, Baihong Zhang, Chengqian Zhou, Xianglong Hu and Wenli Chen

frontiers | Frontiers in Bioengineering and Biotechnology

EDITORIAL
published: 13 May 2022
doi: 10.3389/fbioe.2022.917690

Editorial: Multifunctional Polymeric Materials for Drug and Gene Delivery

Yakai Feng[1]*, *Bin He*[2], *Wenzhong Li*[3] and *Abraham Jacob Domb*[4]*

[1]School of Chemical Engineering and Technology, Tianjin University, Tianjin, China, [2]National Engineering Research Center for Biomaterials, Sichuan University, Chengdu, China, [3]Institute of Chemistry and Biochemistry, Freie Universität Berlin, Berlin, Germany, [4]School of Pharmacy, Faculty of Medicine, Hebrew University of Jerusalem, Jerusalem, Israel

Keywords: multifunctional polymer, drug delivery, gene delivery, cancer treatment, targeting

Editorial on the Research Topic

Multifunctional Polymeric Materials for Drug and Gene Delivery

In recent years, various multifunctional polymers have been vastly explored as drug/gene carriers intended to deliver therapeutic reagents (Guo et al., 2019; Duo et al., 2020; Zhang et al., 2020). Their unique physical and biochemical properties render them new functions and possibilities such as targeting, bio-responsiveness, biointeractivity and adaptivity. This Research Topic focuses on recent advances of multifunctional polymers for drug and gene delivery, especially for tissue engineering and regeneration, cancer treatment. There are nine articles, including three review articles and six original research articles. The three review articles summarized the photodynamic therapy, nanogels and polypeptide micelles with tumor microenvironment-responsive drug release, enhanced membrane penetration and gas therapy by generating metabolites of nitric oxide (NO). Wang et al. introduced the smart polymeric delivery systems for the photodynamic therapy of tumor and bacterial infections, mainly discussed the strategies that could be tumor/bacteria targeted or activatable by their microenvironment such as enzyme/pH/reactive oxygen species (ROS). The activation of photodynamic therapy mainly involves following strategies: self-quenching and dequenching of photosensitizers, quenching the triplet state of photosensitizer via using another quencher and dequenching upon cleavage of sensitive bonds, and the responsive change of size and surface charge to enhance the internalization and penetration of tumor cells/bacterial cells. Du et al. summarized tumor microenvironment-responsive nanogels especially their preparation and applications. Nanogels are commonly prepared by free radical polymerization, covalent cross-linking, and physical self-assembly technologies. The drugs can be loaded in nanogels by physical encapsulation and chemical coupling methods. Nanogels endow with unique and useful properties with great potential in chemotherapy owing to their stable size, superior hydrophilicity, excellent biocompatibility, and microenvironment-responsively controlled drug release behaviors (Pinelli et al., 2020). Meanwhile, the authors briefly described the challenges and perspectives of nanogels. Xie et al. introduced the functional polymeric micelles based on basic amino acids i.e., lysine, histidine and arginine, and highlighted their applications as drug carriers for cancer therapy. Polylysine-based polymers with abundant active groups can be used as chemical attachment sites facilitating the construction of drug carriers. Polyhistidine-based polymers having imidazolyl functional groups possess the protonation and deprotonation under different pH-environments, thus enabling pH-responsive drug release. Polyarginine can enhance membrane penetration and gas therapy by generating metabolites of NO (Kudo and Nagasaki, 2015).

The original research articles involved drug/gene delivery for vascular regeneration by sustained release of NO, cancer photothermal and oxidative stress therapy by an NIR-II responsive nanoplatform, nanogel-mediated drug resistance alleviation, ameliorating corneal wound and suppressing neovascularization by Wnt/β-catenin pathway inhibitor and tacrolimus, as well as

OPEN ACCESS

Edited and reviewed by:
Hasan Uludag,
University of Alberta, Canada

***Correspondence:**
Yakai Feng
yakaifeng@tju.edu.cn
Abraham Jacob Domb
avid@ekmd.huji.ac.il

Specialty section:
This article was submitted to Biomaterials, a section of the journal Frontiers in Bioengineering and Biotechnology

Received: *11 April 2022*
Accepted: *27 April 2022*
Published: *13 May 2022*

Citation:
Feng Y, He B, Li W and Domb AJ (2022) Editorial: Multifunctional Polymeric Materials for Drug and Gene Delivery. Front. Bioeng. Biotechnol. 10:917690. doi: 10.3389/fbioe.2022.917690

genetic transformation of plants. These delivery strategies were rationally designed, and demonstrated improvement effects compared with traditional therapeutic methods. Yang et al. developed a nitrate-functionalized vascular graft by electrospinning technology, which could release NO via stepwise biotransformation *in vivo*. This localized delivery of NO demonstrated enhanced cell in growth, endothelial cell monolayer formation, long-termpatency, and vascular smooth muscle cell layer regeneration, whilst inhibiting calcified plaque formation. Thus, the NO release graft could serve as a promising candidate for artificial small-diameter vascular graft replacement and bypass surgery.

ROS can be counteracted by the exorbitant glutathione (GSH) produced by the tumor cells before exerting the antitumor effect of chemodynamic therapy (Liu et al., 2020). Therefore, Huang et al. prepared a thermo-responsive vehicle (NB/CuS@PCM NPs) from borneol (NB) serving as a monoterpenoid sensitizer, and copper sulfide nanoparticles (CuS NPs) as an NIR-II photothermal agent. In the acidic microenvironment, CuS NPs released from vehicle could degrade to Cu^{2+} with the ability of the depletion of GSH. Besides, the copper ion could also convert hydrogen peroxide into hydroxyl radicals for chemodynamic therapy. The combination of oxidative stress–induced damage and photothermal therapy is a potential therapeutic strategy for cancer treatment. To overcome multidrug resistance, Chen et al. developed a mitochondrial-targeting and pH-sensitive nanogel *via* incorporating the hexokinase inhibitor lonidamine and paclitaxel (PTX). The mitochondrial targeting was beneficial for the accumulation and pH-triggered PTX release in the mitochondria. Lonidamine can destroy the mitochondria by exhausting the mitochondrial membrane potential, generating ROS and restraining the energy supply, leading to apoptosis and susceptibility of the cancer cells to PTX. This work provides us a promising and synergistic strategy to conquer tumor multidrug resistance.

Zhong et al. and Lin et al. investigated the Wnt/β-catenin pathway inhibitor XAV939-loaded liposome and tacrolimus-loaded liposome for corneal wound treatment, respectively. These liposomes possessed excellent biological compatibility in human corneal epithelial cells, mouse corneas and eyeballs. The XAV939-loaded liposome demonstrated the antiangiogenic effect, and significantly suppressed the LPS-induced expressions of pro-inflammatory genes. The *in vivo* results also showed that XAV939-loaded liposome ameliorated alkali-burned corneas with slight corneal opacity, reduced neovascularization, and enhanced recovery. The tacrolimus-loaded liposome enhanced corneal epithelial recovery, inhibited corneal neovascularization, and reduced corneal inflammation.

In summary, the current Research Topic reports the recent significant advances in drug and gene delivery with the help of functional polymers. The designing and developing multifunctional polymers will provide new chances for smart drug delivery towards clinical application. These articles in this Research Topic will be a helpful reference for drug/gene delivery.

AUTHOR CONTRIBUTIONS

All authors listed have made a substantial, direct, and intellectual contribution to the work and approved it for publication.

FUNDING

This work was supported by the National Natural Science Foundation of China (Grant No. 51873149).

REFERENCES

Duo, X., Bai, L., Wang, J., Guo, J., Ren, X., Xia, S., et al. (2020). Multifunctional Peptide Conjugated Amphiphilic Cationic Copolymer for Enhancing ECs Targeting, Penetrating and Nuclear Accumulation. *Front. Chem. Sci. Eng.* 14, 889–901. doi:10.1007/s11705-020-1919-8

Guo, K., Zhao, X., Dai, X. G., Zhao, N., and Xu, F. J. (2019). Organic/inorganic Nanohybrids as Multifunctional Gene Delivery Systems. *J. Gene Med.* 21 (5), e3084. doi:10.1002/jgm.3084

Kudo, S., and Nagasaki, Y. (2015). A Novel Nitric Oxide-Based Anticancer Therapeutics by Macrophage-Targeted Poly(L-Arginine)-Based Nanoparticles. *J. Control. Release* 217, 256–262. doi:10.1016/j.jconrel.2015.09.019

Liu, M. D., Guo, D. K., Zeng, R. Y., Ye, J. J., Wang, S. B., Li, C. X., et al. (2020). Yolk-Shell Structured Nanoflowers Induced Intracellular Oxidative/Thermal Stress Damage for Cancer Treatment. *Adv. Funct. Mat.* 30, 2006098. doi:10.1002/adfm.202006098

Pinelli, F., Ortolà, Ó. F., Makvandi, P., Perale, G., and Rossi, F. (2020). *In Vivo* Drug Delivery Applications of Nanogels: A Review. *Nanomedicine* 15, 2707–2727. doi:10.2217/nnm-2020-0274

Zhang, L., Pu, Y., Li, J., Yan, J., Gu, Z., Gao, W., et al. (2020). pH Responsive Coumarin and Imidazole Grafted Polymeric Micelles for Cancer Therapy. *J. Drug Deliv. Sci. Technol.* 58, 101789. doi:10.1016/j.jddst.2020.101789

Conflict of Interest: The authors declare that the research was conducted in the absence of any commercial or financial relationships that could be construed as a potential conflict of interest.

Publisher's Note: All claims expressed in this article are solely those of the authors and do not necessarily represent those of their affiliated organizations, or those of the publisher, the editors and the reviewers. Any product that may be evaluated in this article, or claim that may be made by its manufacturer, is not guaranteed or endorsed by the publisher.

frontiers in Bioengineering and Biotechnology

SYSTEMATIC REVIEW
published: 27 September 2021
doi: 10.3389/fbioe.2021.744657

Micelles Based on Lysine, Histidine, or Arginine: Designing Structures for Enhanced Drug Delivery

Li Xie, Rong Liu, Xin Chen, Mei He, Yi Zhang and Shuyi Chen*

School of Medicine and Nursing, Chengdu University, Chengdu, China

Natural amino acids and their derivatives are excellent building blocks of polymers for various biomedical applications owing to the non-toxicity, biocompatibility, and ease of multifunctionalization. In the present review, we summarized the common approaches to designing and constructing functional polymeric micelles based on basic amino acids including lysine, histidine, and arginine and highlighted their applications as drug carriers for cancer therapy. Different polypeptide architectures including linear polypeptides and dendrimers were developed for efficient drug loading and delivery. Besides, polylysine- and polyhistidine-based micelles could enable pH-responsive drug release, and polyarginine can realize enhanced membrane penetration and gas therapy by generating metabolites of nitric oxide (NO). It is worth mentioning that according to the structural or functional characteristics of basic amino acids and their derivatives, key points for designing functional micelles with excellent drug delivery efficiency are importantly elaborated in order to pave the way for exploring micelles based on basic amino acids.

Keywords: micelles, lysine, histidine, arginine, basic amino acids, drug delivery

OPEN ACCESS

Edited by:
Bin He,
Sichuan University, China

Reviewed by:
Xianglong Hu,
South China Normal University, China
Aristeidis Papagiannopoulos,
Theoretical and Physical Chemistry Institute, National Hellenic Research Foundation, Greece

****Correspondence:***
Rong Liu
liurongscu@126.com

Specialty section:
This article was submitted to Biomaterials, a section of the journal Frontiers in Bioengineering and Biotechnology

Received: *20 July 2021*
Accepted: *30 August 2021*
Published: *27 September 2021*

Citation:
Xie L, Liu R, Chen X, He M, Zhang Y and Chen S (2021) Micelles Based on Lysine, Histidine, or Arginine: Designing Structures for Enhanced Drug Delivery. Front. Bioeng. Biotechnol. 9:744657. doi: 10.3389/fbioe.2021.744657

INTRODUCTION

In the past few decades, micelles, as an effective drug delivery system, have considerably attracted worldwide attention for the treatment of tumors. As drug carriers, micelles have many advantages, such as easily synthesizing and modifying chemical structures, nanoparticulate size, enhanced water solubility of drug, prolonged circulation time, increased accumulation in tumor sites, reduced side effects of drugs, as well as improved drug bioavailability and efficiency (Kim et al., 2008; Sun et al., 2009; Aw et al., 2011; Wang et al., 2011). However, up to now, only a few micellar products have been approved by the Food and Drug Administration (FDA) (Cabral and Kataoka, 2014; Deshmukh et al., 2017; Adityan et al., 2020). One possible reason is their potential toxicity (Gupta et al., 2015; Knudsen et al., 2015; Deshmukh et al., 2017). Thus, natural or synthetic biodegradable materials are utilized for constructing micelles to solve the problem (Deng et al., 2012; Grossen et al., 2017; George et al., 2019).

Amino acids are a class of small-molecule compounds that are widespread in nature. More than 300 natural amino acids have been found, but only 20 amino acids take part in the human protein synthesis (Canfield and Bradshaw, 2019; Kelly and Pearce, 2020). Most of the 20 amino acids are good raw materials for fabricating micelles, for example, lysine (Itaka et al., 2003; Cheng et al., 2021; Kanto et al., 2021), arginine (Yao et al., 2016; Jiao et al., 2019), histidine (Guan et al., 2019; Wang Z. et al., 2019), glutamic acid (Krivitsky et al., 2018; Ma et al., 2020; Brunato et al., 2021), aspartic acid (Yeh et al., 2013; Teng et al., 2017), cysteine (Xu W. et al., 2015). Among them, there are three basic amino acids namely, lysine, histidine, and arginine, whose side chains contain amino, imidazolyl, and guanidine groups, respectively. The three basic groups can be protonated in acidic condition to play

some special roles in the construction of micelles. For example, amino groups in the lysine side chain can be applied as a chemical attachment site, which facilitates the construction of micelles (Liu et al., 2015). The imidazolyl group of histidine has the characteristics of protonation and deprotonation, making histidine-based micelles pH-responsive (Augustine et al., 2020a). Guanidine group of arginine is positively charged after protonation and contributes to the membrane-penetration ability of micelles (Geihe et al., 2012; Hu et al., 2015). In addition, poly(amino acids) synthesized by the above three basic amino acids have good biocompatibility and biodegradability. Moreover, poly(amino acids) contain many chemically modifiable side groups, providing abundant active groups for constructing functional micelles (Xu H. et al., 2015; Augustine et al., 2020b). Therefore, basic amino acids have a broad application in the field of drug delivery.

This review describes the design and construction of drug-loaded micelles based on the three basic amino acids or their derivatives from the following perspectives: 1) Design of micelles based on the position and role of lysine in the micelle skeleton. 2) Construction of micelles based on the pH-sensitive properties of histidine. 3) Introduction of micelles using arginine's cell-membrane-penetrating activity, and antitumor ability to convert to NO.

LYSINE-BASED MICELLES

Lysine-Based Linkers

Lysine, lysine-based dendrimer, or polylysine may serve as a linker in micelles. Compared with a single lysine molecule as a linker, the lysine-based dendrimer and polylysine possess more abundant active groups.

A Single Lysine Molecule as Linker

Lysine contains two amino groups and one carboxylic group. Therefore, when lysine is adopted as a linker during the construction of micelles, it can react with drugs, compounds, or polymeric materials containing active groups.

There are two methods of linking lysine and the above materials: 1) two amino groups of lysine are utilized to connect materials with carboxylic groups. For example, two amino groups of lysine are separately connected with carboxyl group of hydrophobic stearic acid and the terminal carboxyl group of hydrophilic polyglutamic acid to obtain amphiphilic diblock micelle skeleton (Chang et al., 2017); 2) amino group and carboxyl group of lysine are linked to hydrophilic or hydrophobic materials with carboxyl group or amino group. For example, Wang et al. (2012) connected carboxyl group of lysine with hydroxyl group of hydrophilic polyethylene glycol by an ester bond and connected two amino groups of lysine with two vitamin E succinate molecules as hydrophobic anticancer drug to construct a drug-loaded micelle skeleton.

Lysine-Based Dendrimer as Linker

Compared with lysine, lysine-based dendrimer as linker contains more active functional groups, which can provide more conjugation sites for micelles construction (Xiao et al., 2009; Li et al., 2011; Guo et al., 2020). For example, the third-generation lysine dendrimer has one carboxyl group and eight amino groups. In **Figure 1A** (Xiao et al., 2009), Kit S Lam group built the hydrophilic part of micelles by condensation of carboxyl group of generation 3 (G3) lysine dendrimer and amino groups of monomethyl-terminated polyethylene glycol monoamine with a molecular weight of 5,000 Da (PEG^{5k}). Subsequently, eight cholic acid molecules (CA) were connected to the terminal amino groups of G3 lysine dendrimer through an ester bond to construct amphiphilic block polymer (PEG^{5k}-CA_8). Finally, PEG^{5k}-CA_8 was self-assembled into micelles, which significantly increased the paclitaxel loading capacity and fulfilled enhanced *in vivo* drug delivery. Three years later, the same research group made a cross-linked micelle based on PEG^{5k}-CA_8 (**Figure 1B**; Li et al., 2011). Unlike PEG^{5k}-CA_8, four amino groups of the G3 lysine dendrimer were firstly connected with cysteine (Cys), and then, eight cholic acid molecules were introduced to construct PEG^{5k}-Cys_4-L_8-CA_8 micelle. Finally, thiol groups in the cysteine were oxidated to form cross-linked micelles, resulting in the improvement of micellar stability.

Poly(L-lysine) as Linker

Poly(L-lysine) has abundant side chain amino groups (Li et al., 2020), which provides many chemical active sites to connect hydrophilic and hydrophobic segments. Therefore, poly(L-lysine) as linker has several advantages over constructing drug or gene delivery vehicle.

Firstly, the side chain amino groups located in poly(L-lysine) interact with drugs, siRNA, or other substances through physical interactions to achieve desired loading of micelle, including electrostatic interactions and hydrophobic interactions. For example, Lintao Cai group designed an amphiphilic triblock copolymer poly(ethylene glycol)-*b*-poly(L-lysine)-*b*-poly(L-leucine) (PEG-PLL-PLLeu) to load ovalbumin (OVA) by electrostatic interactions between the side chain amino groups of polylysine and ovalbumin vaccine (**Figure 2A**; Luo et al., 2013). Using the same triblock polymer, the research team also used the polyleucine block as the hydrophobic core to incorporate docetaxel by the hydrophobic interactions, while the side chain amino groups of polylysine were used to load siRNA by electrostatic interaction to achieve co-loading of anticancer drug and gene (**Figure 2B**; Zheng et al., 2013).

Secondly, covalently cross-linked polylysine linker could be constructed by the addition of disulfide cross-linker to realize the improvement of micellar stability. To take an example, Koo et al. prepared a triblock polymer, poly (ethylene glycol)-b-poly(L-lysine)-b-poly(L-phenylalanine) (PEG-PLys-PPhe) (Koo et al., 2008; Koo et al., 2012), which self-assembled into micelles. Then, the side chain amino groups of polylysine linker were reacted with 3,3′-dithiobis (sulfosuccinimidylpropionate) cross-linkers to realize micellar cross-linking (**Figure 3**; Koo et al., 2012). For the cross-linked micelles, there was no change in the particle size and spherical morphology. The stability of micelles in solution was investigated by detecting the scattering light intensity. The non-cross-linked and cross-linked micelles were

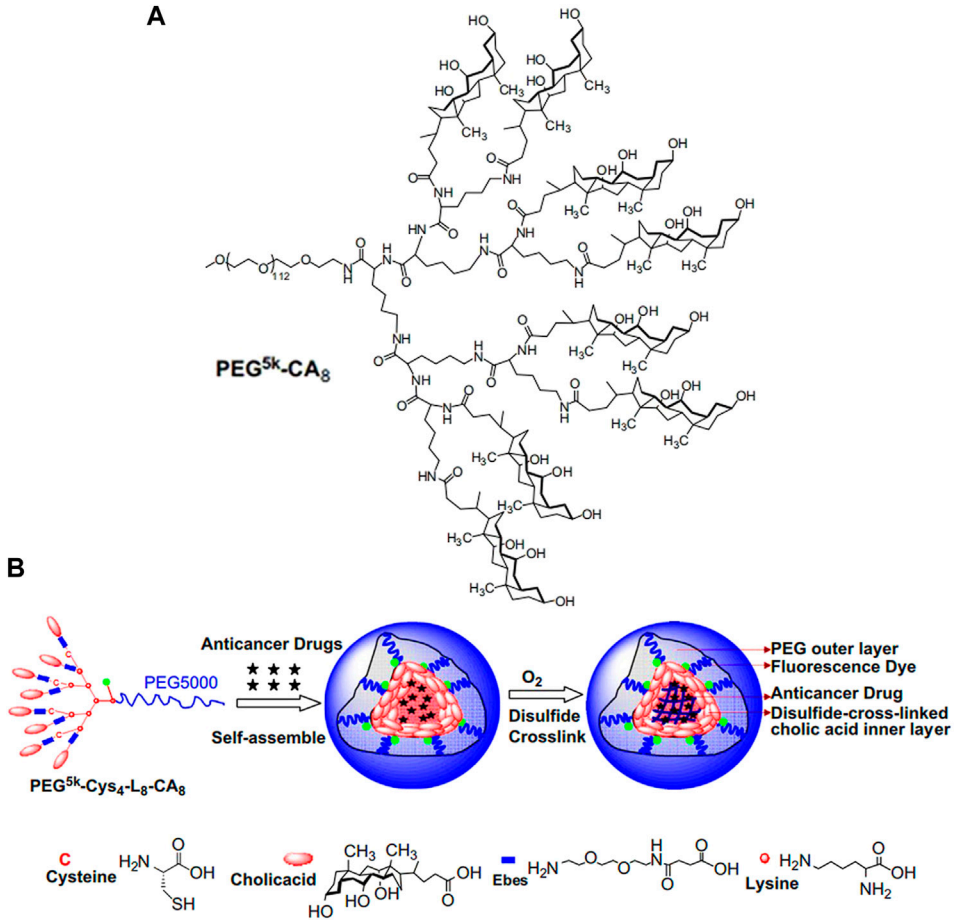

FIGURE 1 | (A) The chemical structure of PEG^{5k}-CA_8 G3 lysine dendrimer (Xiao et al., 2009). **(B)** Schematic representation of the disulfide cross-linked micelles formed by the oxidization of thiolated PEG^{5k}-Cys_4-L_8-CA_8 after self-assemble (Li et al., 2011). Abbreviation: PEG, polyethylene glycol; CA, cholic acid; Cys, cysteine; L, lysine.

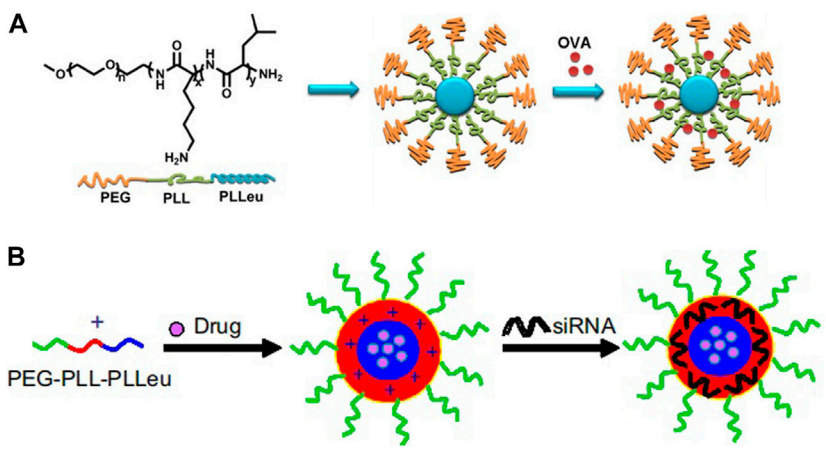

FIGURE 2 | Schematic illustration of PEG-PLL-PLLeu micelles loaded with OVA **(A)** (Luo et al., 2013) or siRNA and drug **(B)** (Zheng et al., 2013). Abbreviation: PEG, poly(ethylene glycol); PLL, poly(L-lysine); PLLeu, poly(L-leucine); OVA, ovalbumin.

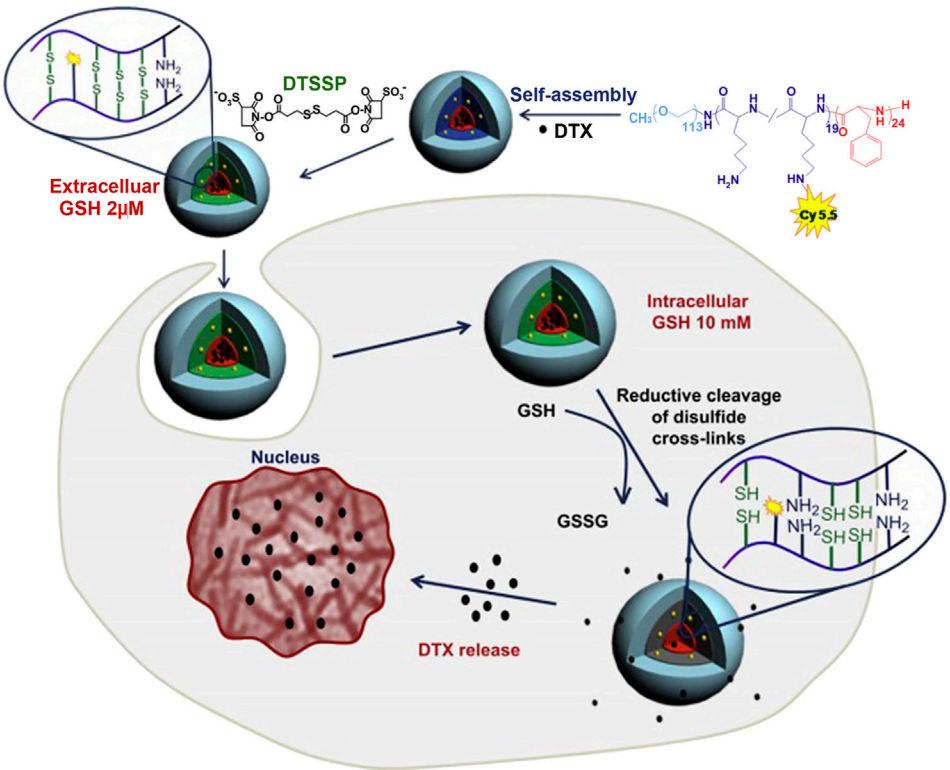

FIGURE 3 | Illustration of shell cross-linking of DTX-loaded micelles with redox-labile disulfide cross-links and triggered release of DTX by intracellular GSH (Koo et al., 2012). Abbreviation: GSH, glutathione; DTSSP, 3,3′-Dithiobis (sulfosuccinimidylpropionate); DTX, docetaxel.

separately incubated in PBS with 50% serum for 30 min, and the scattered light intensity of the former decreased to 49% of the initial intensity, while that of the latter dropped about 5%. Even if the incubation time of the latter was prolonged to 2 h, 85% of the initial intensity was still maintained. In addition, the non-cross-linked and cross-linked micelles were also incubated with a 2.5 g/L SDS solution. At 2 h, the scattering light intensity of the non-cross-linked micelles decreased to 50%, while that of the cross-linked micelles still reached more than 90% of the initial scattering intensity. The above results suggested that micellar stability was improved by cross-linking of polylysine linker. More importantly, disulfide bonds in cross-linked micelles are redox-sensitive, which can be cleaved by glutathione (GSH) (Zhang et al., 2016; Kang et al., 2018). In the blood circulation and cells, there are different concentrations of GSH (Jones et al., 1998; Kang et al., 2018), which directly affected the degree of disulfide bond cleavage in polylysine linker. For example, in the blood circulation, GSH concentration is low (~2 μM) (Jones et al., 1998), and the degree of disulfide bond breakage is low, resulting in slow drug release in blood. Conversely, the concentration of GSH in most cancer cells is high (~10 mM) (Kim et al., 2021), the disulfide bond in polylysine linker is broken to a high degree, and the barrier for drug release is caused by the layer of polylysine linker is removed, resulting in faster drug release. Therefore, cross-linked micelles by 3,3′-dithiobis (sulfosuccinimidylpropionate) cross-linkers were beneficial to reduce the loss of encapsulated drugs in the blood circulation and achieve responsive drug release in the target cells.

Poly(L-lysine) as the Core of Micelles

Poly(L-lysine) is positively charged and water-soluble, containing a lot of amino groups. Theoretically, poly(L-lysine) is difficult to form the core of micelles because of the poor hydrophobicity. However, there are several ways to assist polylysine in constructing the micellar core. First of all, based on electrostatic interaction, polylysine reacts with oppositely charged polyelectrolytes or molecules to significantly reduce its water solubility, so that polylysine can be used to construct the core of micelles (Boudier et al., 2009; Mebarek et al., 2013). In the next place, amino groups of polylysine are chemically modified to enhance the nucleation force of micellar core. In the following sections, the above two ways will be presented separately.

Construction of Micellar Core Through Electrostatic Interaction

The positively charged polylysine and negatively charged polymers can facilely form micellar core by electrostatic interaction. Taking polylysine and polymethacrylic acid-*b*-polyethylene oxide as an example, amino group of polylysine and carboxyl group of polymethacrylic acid block were combined by electrostatic interaction, and then, peptide drugs were wrapped to give a stable ternary composite micelle with a particle size of

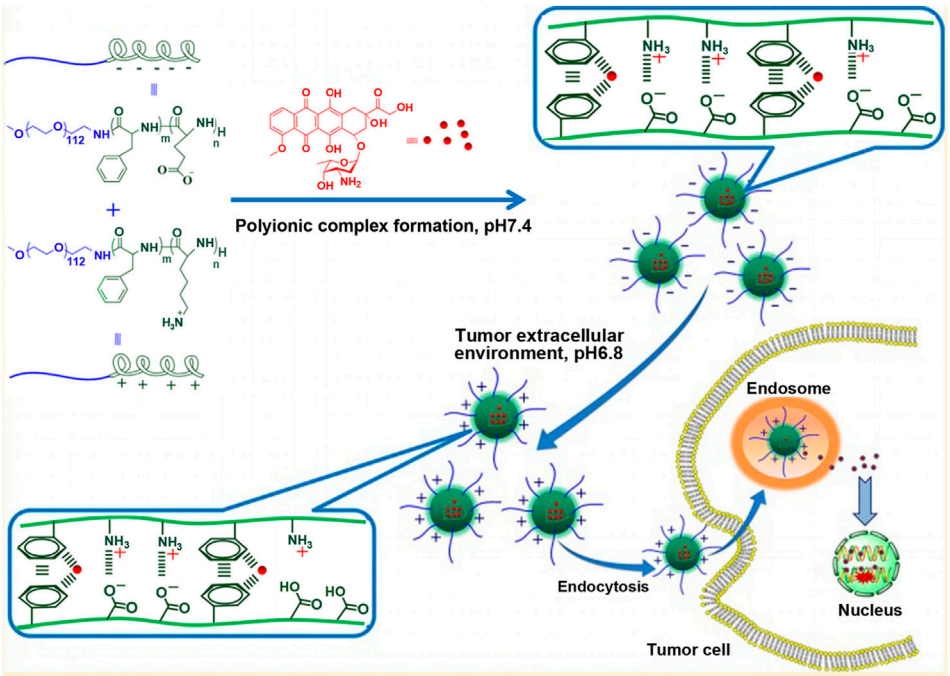

FIGURE 4 | Schematic illustration of charge-conversional behavior and endocytosis performance of polyion complex micelles (Lv et al., 2014).

82 nm (Boudier et al., 2011). The micelle not only kept stable under physiological pH conditions (pH = 7.4) but also facilitated the delivery of peptide drugs. After being endocytosed, the side chain amino group of polylysine was protonated under the acidic condition of cell endosomes (pH = 5), which would disintegrate the micellar core and release peptide drugs.

Alternatively, the terminal group of polylysine is connected with a hydrophilic chain segment, such as polyethylene glycol to form hydrophilic block polymer, which is chosen as positively charged polymer to build the core of the micelle through electrostatic interaction with other hydrophilic block polymers with opposite charge (Xu H. et al., 2015). It has been reported that the influence of the length of positively charged chain of pol(ethylene glycol)-b-poly(L-lysine) and negatively charged chain of poly(ethylene glycol)-b-poly(α, β-aspartic acid) on the self assembly of polyion complex micelles. When the lengths of poly(L-lysine) and poly(α, β-aspartic acid) segments with opposite charge differed greatly, the complex formed by poly (ethylene glycol)-*b*-poly(L-lysine) and poly(ethylene glycol)-*b*-poly(α, β-aspartic acid) was unstable and micelles could not form. For example, there were 18 repeating units of polylysine segment and 78 repeating units of polyaspartic acid segment, or 78 repeating units of polylysine segment and 18 repeating units of polyaspartic acid segment. On the contrary, if there was a small difference in the chain length of poly(L-lysine) and poly(α, β-aspartic acid) segments, micelles with charge would be constructed. While the dissociation degree of carboxyl group and amino group in polymer was easily affected by environmental acidity, resulting pH-dependent charge-reversal micelle was fabricated (Lv et al., 2014). Lv et al. (2014) employed MPEG-NH_2 as initiator and prepared cationic block copolymer containing lysine and phenylalanine, methoxy poly (ethylene glycol)-b-poly(L-lysine-*co*-L-phenylalanine), by NCA ring-opening polymerization. In the same way, they also prepared anionic block polymer containing glutamic acid and phenylalanine, methoxy poly(ethylene glycol)-*b*-poly(L-glutamic acid-*co*-L-phenylalanine). In two block copolymers, the molar ratio of lysine and L-glutamic acid residues was 1:1.1, that is, lysine repeating unit in cationic block polymer was one less than glutamic acid repeating unit in the anionic block polymer. When methoxy poly(ethylene glycol)-*b*-poly(L-lysine-*co*-L-phenylalanine) and methoxy poly(ethylene glycol)-*b*-poly(L-glutamic acid-*co*-L-phenylalanine) were electrostatically combined to form micelle, due to the presence of free carboxyl residue of glutamic acid, the surface of micelle was negatively charged at physiological pH (pH 7.4). However, in acidic tumor microenvironment, the dissociation degree of carboxyl group decreased, while that of amino group increased. Consequently, the surface charge of micelles reversed from negative to positive, which was not only beneficial for micellar stability under physiological pH but also for their endocytosis after reaching cancer cells, as shown in **Figure 4**.

Besides adding hydrophilic block polymers with negative charge, some negatively charged photosensitizers, drugs, or genes can also interact with hydrophilic block polymer containing polylysine to form micellar core through electrostatic interactions (Jang et al., 2006; Osada et al., 2010; Dirisala et al., 2014; Lu et al., 2020; Zheng et al., 2020). Positively charged polylysine segments were complexed with negatively

charged photosensitizers, genes, or drugs to make them become a part of the micellar core. The encapsulated photosensitizers, genes, or drugs could avoid enzyme degradation or removal by the reticuloendothelial system (Beyermann and Kukula, 2000; Harada-Shiba et al., 2002; Osada et al., 2012), thereby improving the therapeutic effect (Sugisaki et al., 2008; Nishiyama et al., 2009). For example, when poly(ethylene glycol)-*block*-poly(L-lysine) (PEG-PLys) was electrostatically compounded with plasmid DNA (pDNA), pDNA was folded by PEG-PLys to form a hydrophobic rod-like core (Osada et al., 2010). The length of the rod-like core was affected by the length of polylysine segment. The longer the polylysine segment was, the more conducive the DNA was compressed. Moreover, with increasing the length of polylysine, the length distribution of the formed micellar core became narrower, which was favorable for endocytosis (Dirisala et al., 2014).

Enhancing the Nucleation Force of Micelles Through Chemically Modifying Amino Groups of Polylysine to Construct Micellar Core

Sulfhydryl groups, carboxyl groups, or hydrophobic molecules are introduced to the side chain amino groups of polylysine segment by chemical method, which improves the nucleation force of micelles containing polylysine segment.

Cross-Linking the Micellar Core by Introducing Sulfhydryl Groups

When sulfhydryl groups are introduced into hydrophilic block polymer with polylysine segment, under oxidation condition, sulfhydryl groups are oxidized to form disulfide bond, thereby cross-linking polylysine segment and forming core cross-linked micelle (Miyata et al., 2004; Vachutinsky et al., 2011; Oe et al., 2014; Takeda et al., 2017). Core cross-linked micelles show enhanced resistance to the shear stress of blood circulation. Takeda et al. (2017) integrated 1-imino-4-mercaptobutyl (IM) groups as cross-linking agent into the side chain amino groups of polylysine segment in poly (ethylene glycol)-*b*-poly(L-lysine) (PEG-PLys). Introduction rate of IM accounted for 49% of lysine residues of polylysine segment. Under oxidation condition, PEG-PLys (IM) and pDNA were compounded to form core cross-linked polyplex micelle at the N/P ratio of 2:0, which was defined as a residual molar ratio of amino groups in PEG-PLys to phosphate groups in pDNA. In this process, it was accompanied by disulfide bond cross-linking and a combination of positive and negative charges. When core cross-linked micelles were exposed to venular blood flow (30 dyne/cm^2 shear stress) for 30 min, they could remain stable, and the size of the rod-shaped core was not affected. In contrast, non-cross-linked micelles showed a size increase, from 194 to 242 nm, and pDNA degradation up to 50% under the same condition. Even if shear stress reached 100 dyne/cm^2, the particle size of core cross-linked micelles was still maintained unchanged. Maintenance of the particle size was not only beneficial for micelles to enter cells and protect pDNA from degradation by DNaseI but also significantly prolonged residence time of pDNA in mice and improved gene transfection efficiency *in vivo*.

Charge Reversal of Polylysine by Introducing Carboxyl Groups

If carboxyl groups are introduced into polylysine, its electrical property will vary from positive to negative charge. Thus, polylysine with negative charge can be combined with drugs with positive charge, such as doxorubicin with one amino group, to realize the load of positively charged drugs. For example, the ring-opening polymerization of cis-cyclohexene-1,2-dicarboxylic anhydride (CDA) was initiated from the side chain amino groups of methoxy poly(ethylene glycol)-*block*-poly(L-lysine) (mPEG-*b*-PLL) to get anionic methoxy poly(ethylene glycol)-*block*-poly(N(ε)-((1-carboxyl-cis-cyclohexene)-2-carbonyl)-L-lysine (mPEG-*b*-PCLL) with acid-degradable side amide bond, which was shown in **Figure 5** (Wang J. et al., 2015). The carboxyl-functionalized polylysine segment of mPEG-b-PCLL interacted with doxorubicin to form micellar core. In acidic extracellular microenvironment of tumor cells (pH = 6.8), the volume of micelles expanded, resulting in rapid release of drug. When micelles entered more acidic endo/lysosomes (pH = 5.5), the cumulative release rate of drug was over 75% at 72 h. This might be related to the cleavage of the side amide bond of mPEGpolypeptide copolymer, leading to the disassembly of the micellar core (Chen et al., 2015).

Hydrophobic Modification of Polylysine by Introducing Hydrophobic Molecules

After introducing hydrophobic molecules into the side chain amino groups of polylysine, the solubility of polylysine was changed from hydrophilic to hydrophobic. The modified hydrophobic polylysine could directly construct the core of micelles and wrap hydrophobic drugs (Wen et al., 2011; Ding et al., 2013; Lin et al., 2014). For instance, ε-carbobenzyloxy-L-lysine N-carboxyanhydride (Lys(Z)-NCA) was first synthesized by using N-ε-carbobenzyloxy-L-lysine as starting material. Then, it was reacted with propargylamine through ring-opening polymerization to produce hydrophobic α-alkyne-poly-(N-ε-carbobenzyloxy-L-lysine) (α-alkyne-PZLL). Next, α-alkyne-PZLL was added to further link with dendritic polyamidoamine (PAMAM) block copolymer (N_3-D3) to synthesize amphiphilic PZLL-block-dendritic PAMAM copolymers (PZLL-D3) by copper-catalyzed azidealkyne cyclization (Lin et al., 2014). PZLL-D3 micelles enabled co-loading of doxorubicin and gene, where the PZLL core loaded doxorubicin through hydrophobic interactions, and the PAMAM shell carried gene through electrostatic interactions.

If nitro group was also introduced into the para-position of benzene ring of poly-(N-ε-carbobenzyloxy-L-lysine) segment of micelle, it would make micelle sensitive to hypoxia, which was more conducive to the rapid drug release of micelle in the hypoxic tumor tissue (Thambi et al., 2016). The case in point was the two-layered biodegradable micelle prepared by self-assembly of poly(ethylene glycol)-*b*-poly(ε-(4-nitro)benzyloxycarbonyl-L-lysine) (PEG-*b*-PLys-*g*-NBCF) diblock copolymers (**Figure 6A**). Under the hypoxic environment, the nitro groups on NBCF were easily reduced to produce amine groups by a series of six electron-transfer reactions in the

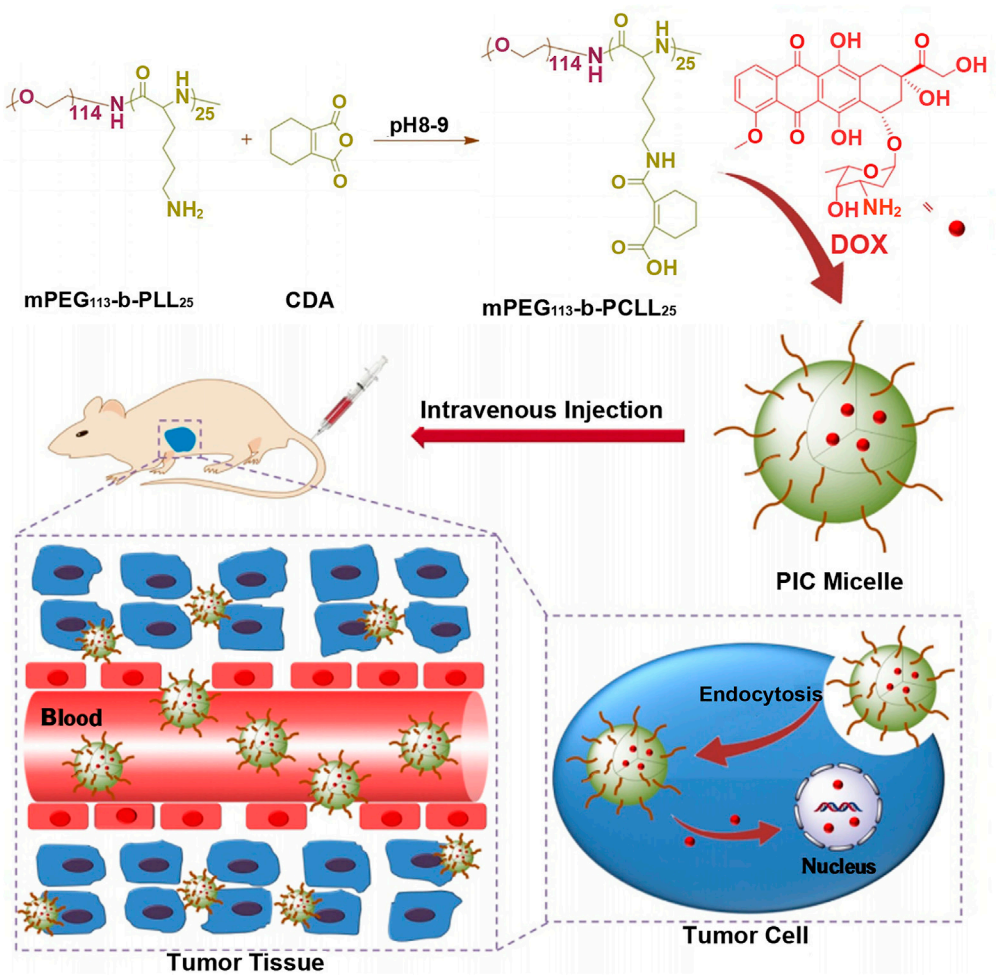

FIGURE 5 | Schematic illustration of the preparation of pH-responsive PIC micelle, and its circulation *in vivo*, accumulation in tumor tissue, and finally, pH-triggered intracellular DOX release after intravenous injection (Wang J. et al., 2015). Abbreviation: PEG, poly(ethylene glycol); PLL, poly(L-lysine); CDA, cis-cyclohexene-1,2-dicarboxylic anhydride; PCLL, poly(N(ε)-((1-carboxy-cis-cyclohexene)-2-carbonyl)-L-lysine; DOX, doxorubicin; PIC micelle, polyion complex micelle.

presence of cellular nucleophiles or nitroreductases. As a consequence, the formed amine groups continued to induce the degradation of the N-(4-aminobenzyloxycarbonyl)-based derivative into small molecular compounds. Owing to the loss of hydrophobic NBCF groups in the polylysine segment of micelle, the micellar core disintegrated and drug was rapidly released (**Figure 6B**).

Polylysine as Micellar Shell

When polylysine is connected to hydrophobic block, polylysine will act as the shell of micelle so that the surface of micelle is positively charged. However, it is generally known that cationic nanocarriers interact strongly with serum components, causing severe aggregation and rapid clearance by the reticuloendothelial system (RES) (Oupicky et al., 2002; Zhang et al., 2020), which results in their short half-life in the blood circulation.

Researchers have made some efforts to address the above issues. A good strategy is to shield positive charge of micelles by occupying amino groups of polylysine. Song et al. (2013) cross-linked polylysine chains in the micellar shell by introducing cisplatin (IV) prodrug as a bi-functional cross-linker to reduce the number of free amino groups. As a result, the amount of positive charge on the surface of micelles was reduced. As shown in **Figure 7**, monomethoxyl poly(ethylene glycol)-b-poly(ε-caprolactone)-*b*-poly(L-lysine) (MPEG-*b*-PCL-*b*-PLL) block copolymer self-assembled into micelle, whose shell was composed of MPEG and PLL segments. Thereafter, PLL segment was cross-linked by cisplatin (IV) prodrug, and amino groups of PLL segment were occupied, which reduced the surface positive charge of micelles. Moreover, the larger the proportion of cross-linked amino groups was, the lower the positive charge of micelles was. The most important thing to note from **Figure 7** was the triggered release of cisplatin (IV) prodrug from the cross-linked micellar shell under acidic condition or in the presence of mild reducing agents. At pH 5.0, the release rate of platinum was significantly higher than that at pH 7.4. Under the condition of 5 mM sodium ascorbate, cisplatin (II) was directly released. The released cisplatin (II)

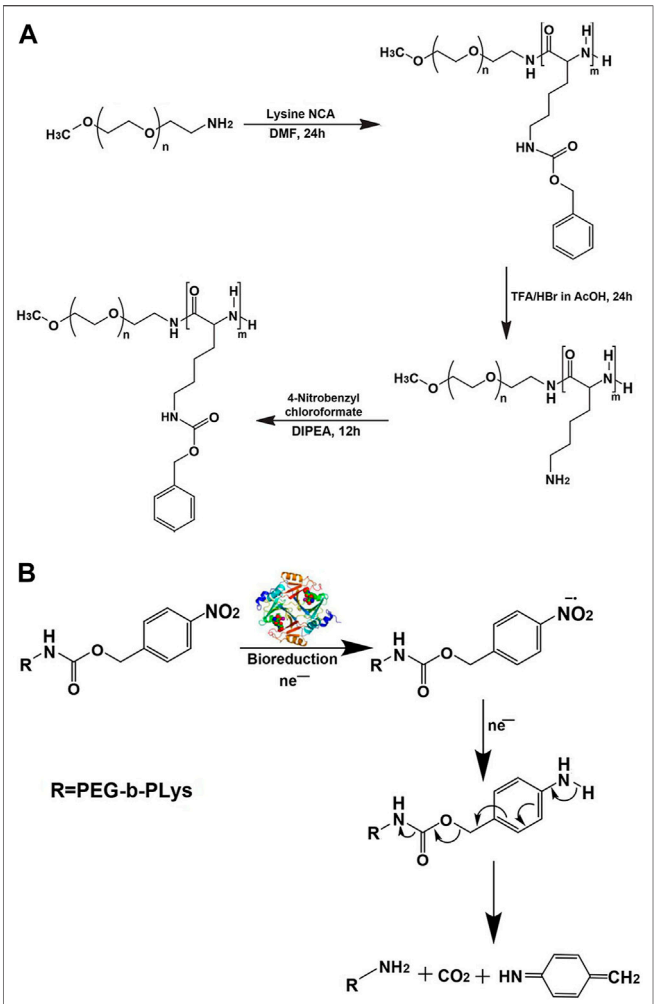

FIGURE 6 | Synthetic route for preparation **(A)** and mechanism of hypoxic reduction under the nitroreductase of the hypoxia-sensitive copolymer **(B)** (Thambi et al., 2016). Abbreviation: PEG, poly(ethylene glycol); PLys, poly(L-lysine); DIPEA, N,N-diisopropylethylamine.

could be chelated by DNA nucleobases of tumor cells, which led to the cross-linking between adjacent nucleobases, along with preventing DNA replication, transcription, and cell division (Boulikas et al., 2007; Khoury et al., 2020).

Another example was shown in **Figure 8** (Ohya et al., 2010). Anionic hyaluronic acid (HA) was coated on the outer layer of poly(L-lysine)-*b*-poly(L-lactide) (PLys-*b*-PLLA) block copolymer micelles by electrostatic interactions. Because amino groups of polylysine were covered by HA, the HA-coated polylysine micelles possessed extremely high resistance to dilution and colloidal stability, whose apparent CMC was 2.1×10^{-11} mg/ml and hydration particle size remained stable in PBS solution containing 10% FBS for 24 h. In the follow-up study (Ohya et al., 2011), the polyanion micelle was used for drug delivery. HA not only improved the stability of micelles and prolonged circulation time in the blood but also controlled drug release rate and reduced the cytotoxicity of HA-coated polylysine micelles.

"Constructing charge-reversal polylysine segment" is another strategy to solve the problem of cationic micelles-based polylysine. The micelles based on charge-reversal polylysine are negatively charged in the blood circulation and will complete positive-surface conversion after reaching tumor tissue or cells (Du et al., 2010; Zhang et al., 2020), which is beneficial to improve the phagocytosis of tumor cells (Du et al., 2010; Pittella et al., 2011). Guan et al. (2017) synthesized folate-poly(L-lysine)-poly(lactic acid) (FA-PLL-PLA), and then, citric acid (CA) was introduced into the side chain amino groups of polylysine by amide bond to complete the construction of a target copolymer, FA-PLL(CA)-PLA. FA-PLL(CA)-PLA could self-assemble to form micelles, whose surface charge was −19.1 mV at pH 7.4. Under the acid environment (pH = 6.5), the micelles were positive in charge (+15.5 mV). Furthermore, the positive charge rapidly increased as the pH value decreased (**Figure 9**). The negative-to-positive charge reversal of micelles is due to break of the amide bond between CA and the side chain amino groups of polylysine segment under the acidic condition. The design of charge-reversal polylysine segment could mask the positive charge of micelles in the blood circulation and expose the positive charge in the tumor tissue or cells, which is beneficial to keep the micellar stability under physiological pH and increase the binding opportunities of the micelles with negatively charged tumor cell membrane in the acidic tumor microenvironment.

HISTIDINE-BASED MICELLES

Extracellular pH of most solid tumors is about 5.8–7.2 (Lee et al., 2008), which is mainly due to lactic acid derived from anaerobic glycolysis and carbonic acid formed from carbon dioxide and water by carbonic anhydrase over-expressed in tumor (Fukumura and Jain, 2007; Lee et al., 2008). Materials protonated in this pH range are suitable for building pH-sensitive drug-delivery systems to target tumor. Histidine is an excellent candidate, whose pK_a value is about 6.0. Moreover, histidine is the only amino acid containing imidazole ring among 20 natural amino acids, which has an electron lone pair on the unsaturated nitrogen, resulting in the amphoteric formation of histidine by protonationdeprotonation (Wu et al., 2013). In the weak acid environment, the imidazole ring undergoes protonation, which making transform of histidine from hydrophobic to hydrophilic, resulting in the increasing solubility of histidine (Liu et al., 2012b). Thus, it is a good method for constructing pH-sensitive micelles to introduce single histidine or polyhistidine into micelles.

Construction of pH-Sensitive Micelles Using Single Histidine

The simplest way to develop micelles containing histidine is to attach hydrophobic histidine to hydrophilic macromolecules, such as hyaluronic acid (Wu et al., 2016), dextran (Yin et al., 2020), and auricularia auricular polysaccharide (AAP) (Wang et al., 2017). In the above micelles, histidine is usually used as a micellar core. Taking histidine-modified AAP (His-AAP) as an example, histidine was

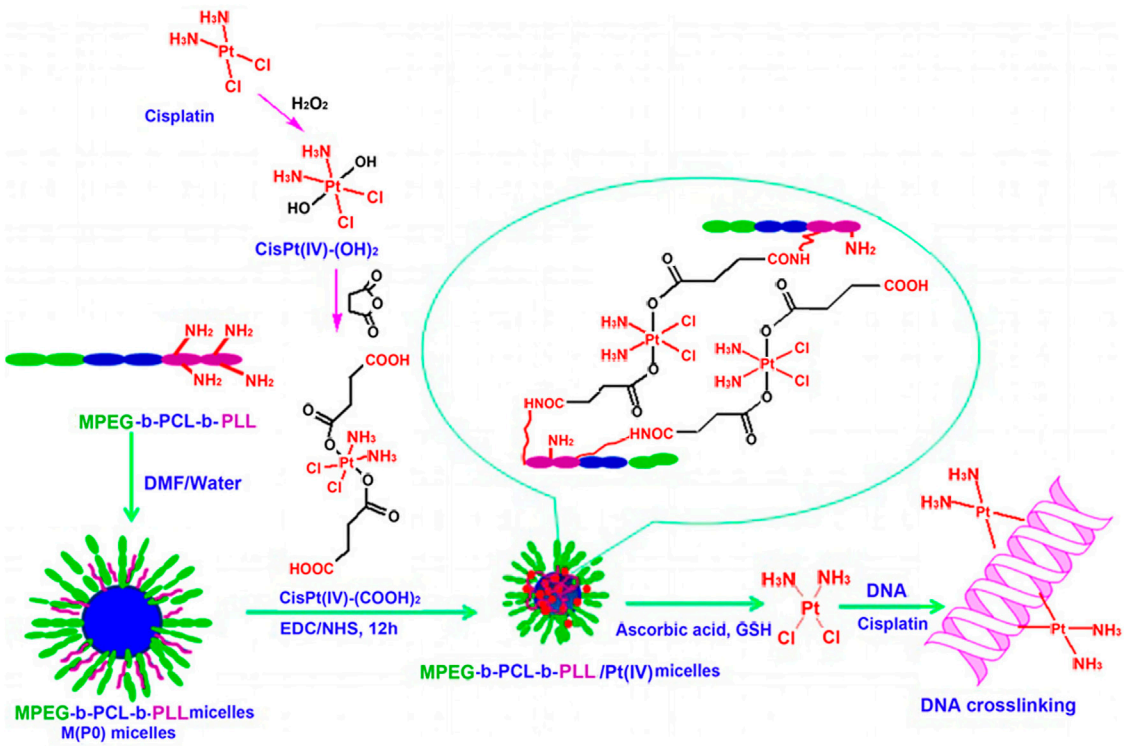

FIGURE 7 | Preparation of MPEG-b-PCL-b-PLL/cisPt (IV) micelles and the proposed pathway of action (Song et al., 2013). Abbreviation: PLys, poly(L-lysine); PLLA, poly(L-lactide); PIC, polyion complex.

linked to AAP by an ester bond. In a neutral medium, His-AAP self-assembled into micelles. Histidine and AAP acted as hydrophobic core and hydrophilic shell, respectively. Next, paclitaxel was loaded into His-AAP micelles. Compared to that at pH 7.4, the paclitaxel accumulated release rate was increased by about 18% for 12 h at pH 5.0 (Wang et al., 2017). Research by Chang et al. (2010) also confirmed that micelles based on histidine had the characteristic of pH-sensitive drug release. N-Boc-histidine was made use of capping PLGA-PEG-PLGA triblock copolymer to prepare histidine-PLGA-PEG-PLGA-histidine. Then, capping triblock polymer self-assembled into micelles. The drug cumulative release rate of DOX-loaded micelles was approximately 20% higher in pH 6.2 medium than that in pH 7.4 medium at 12 h. The elevated accumulative release rate was mainly associated with instability of micellar core, which was caused by ionization of imidazole ring in histidine-PLGA-PEG-PLGA-histidine triblock polymer. In addition, the cumulative release rate of drug-loaded micelles based on PLGA-PEG-PLGA without histidine modification did not differ significantly at pH 6.2 or 7.4, confirming that histidine played a key role in pH-sensitive capacity of micelles.

Construction of pH-Sensitive Micelles With Polyhistidine

Different from histidine, polyhistidine can construct both pH-sensitive middle layer and core of micelles. Furthermore, how to regulate pH-responsiveness of micelles is an important factor needed to be focused on. Although polyhistidine was used as either an intermediate layer or core of micelles, factors affecting pH-responsiveness differed, which would be introduced separately below.

Factors Affecting pH Response of Micelle When Polyhistidine is Adopted as the Intermediate Layer of Micelles

pH-sensitive capability for polyhistidine as a middle layer of micelles is related to the length of polyhistidine block, namely the number of repeat units of histidine. When the number of repeat units of histidine is relatively small such as 5 and 10, polyhistidine micelles have good capability in pH-sensitive drug release. Therefore, the number of repeat units of histidine is a key factor, which should be considered in the process of designing micelles. In a report, block copolymers $Histidine_xLysine_{10}$ (His_xLys_{10}, x = 0, 5, and 10) conjugated with docosahexaenoic acid (DHA) was designed and prepared to self-assemble into micelles (Wang Y. et al., 2015), in which DHA acted as hydrophobic inner core for DOX loading, polyhistidine served as an intermediate pH-sensitive layer, and polylysine block played as hydrophilic shell. *In vitro* drug release experiments were performed in three PBS solutions of pH 7.4, 6.0, and 5.0. As shown in **Figure 10**, at pH 7.4, all three micelles, DHA-Lys_{10}, DHA-His_5Lys_{10}, and DHA-$His_{10}Lys_{10}$, released slowly, and the accumulative DOX release ratio was less than 40% in 100 h. At pH 6.0, DOX release accelerated from both DHA-His_5Lys_{10} and

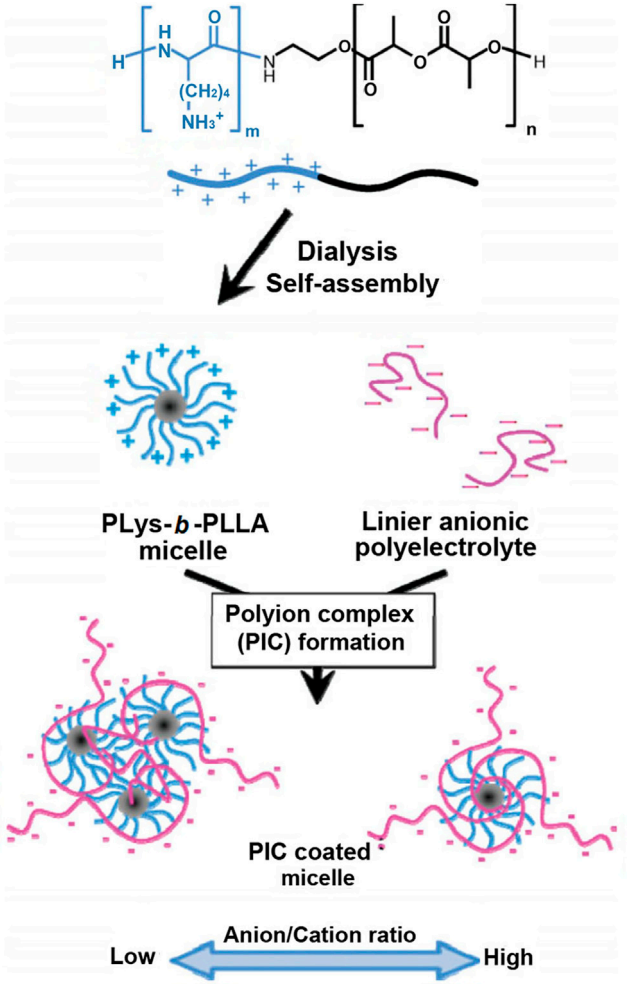

FIGURE 8 | Schematic illustration for the preparation of HA-coated micelles (Ohya et al., 2010). Abbreviation: HA, hyaluronic acid; PLys, poly(L-lysine); PLLA, poly(L-lactide).

DHA-$His_{10}Lys_{10}$ micelles, which was attributed to protonation of imidazole groups of some histidine residues in micelles, whereas the rate of DOX release from DHA-His_5Lys_{10} and DHA-$His_{10}Lys_{10}$ micelles was further speeded up at pH 5.0, especially in the first 10 h. Those results were most likely because the lower pH made more imidazole rings protonate, resulting in the expansion of micellar structure. Furthermore, the longer the histidine block is, the faster the DOX release rate is. In both pH 6.0 and 5.0 media, DOX release from DHA-$His_{10}Lys_{10}$ micelles was faster than that of DHA-His_5Lys_{10} micelles, and the former micelles had a more complete DOX release within 100 h.

However, with increasing the number of repeat units of histidine in micelles, hydrogen-bonding interactions between histidines are probably enhanced, thereby changing the behavior of pH-sensitive drug release. For example, Liu et al. (2012a) used methyl poly(ethylene glycol)-poly(L-histidine)-poly(L-lactide) (mPEG-PH-PLLA) triple block copolymers to investigate the effect of the length of polyhistidine segment on DOX release. At pH 5.0, the cumulative DOX release of $mPEG_{45}$-PH_{15}-$PLLA_{82}$ micelles is close to 80% at 24 h, while for $mPEG_{45}$-PH_{30}-PLA_{82}, the release rate of DOX was 55% at 24 h, and it could not reach 80% until 76 h. It was possible that stronger hydrogen bond interactions existed in polyhistidine of $mPEG_{45}$-PH_{30}-PLA_{82}, leading to retarded DOX release, compared with $mPEG_{45}$-PH_{15}-$PLLA_{82}$. Therefore, when selected as an intermediate layer of micelles, polyhistidine with appropriate chain length can effectively respond to tumor acidic pH microenvironment.

Factors Affecting pH Response of Micelles When Polyhistidine Acts as Micellar Core

There are two methods to regulate pH-responsiveness of micelles when polyhistidine acts as a micellar core. The first method is to connect hydrophilic polymer block to polyhistidine. pK_b value of the whole block copolymer is increased due to the introduction of hydrophilic block segments (Mccurdie and Belfiore, 1999). For example, polyhistidine with a molecular weight of 5,000 had a pK_b value of about 6.5 (Lee E. S. et al., 2003). After introducing PEG with a molecular weight of 2,000, a PH (M_n 5,000)/PEG (M_n 2,000) block copolymer is formed with a pK_b value of about 7.0. As pH is below 7.0, the hydrophilicity of poly(L-histidine) chain segment increased for ionization of histidine imidazole groups, leading to instability of micellar core (Jin et al., 2014). This pH-responsive property is good for drug release outside tumor cells. Jin et al. (2014) adopted pH-responsive PH-*b*-PEG micelles and non-pH-responsive PLLA-*b*-PEG ones to investigate DOX release capability for pH-sensitive micelles based on polyhistidine. In nude mice xenografted by MDA-MB-231 breast cancer, DOX release from micelles was observed by intravital fluorescence microscopy. For PH-*b*-PEG micelles, DOX diffused from tumor blood vessels at a faster rate than that of PLLA-*b*-PEG ones. It was suggested that pH-sensitive PH-*b*-PEG micelles had a rapid dissociation in tumor acidic pH microenvironment, which might reduce the barrier in tumor blood vessels. Moreover, rapid release of DOX made local drug concentration high within the tumor, thus improving bioavailability of drug. After DOX-loaded PH-*b*-PEG and PLLA-*b*-PEG micelles were separately administered *via* tail vein to nude mice three times at 3-day intervals at a dose of 10 mg/kg, the fluorescence intensity of cells was detected *via* flow cytometry, which was extracted from tumor tissues. The result showed that the intensity of cellular uptake of DOX supplied from PH-*b*-PEG micelles was approximately 3.3 times higher than that in PLLA-*b*-PEG micelles. PH-*b*-PEG micelles rapidly released in tumor extracellular pH, which not only promoted endocytosis for drug penetration into tumor cells but also led to more effective inhibition of tumor growth. The tumor volume of PLLA-*b*-PEG micelles treated group was 4.3 times higher than that of PH-*b*-PEG micelles treated group after 21 d of administration, and the latter group significantly suppressed the growth of tumor volume ($p < 0.01$) (**Figure 11**). Above results fully demonstrated that compared with pH-insensitive micelles, it was able for pH-sensitive PH-*b*-PEG micelles to rapidly disintegrate and trigger drug release in the acidic tumor interstitium.

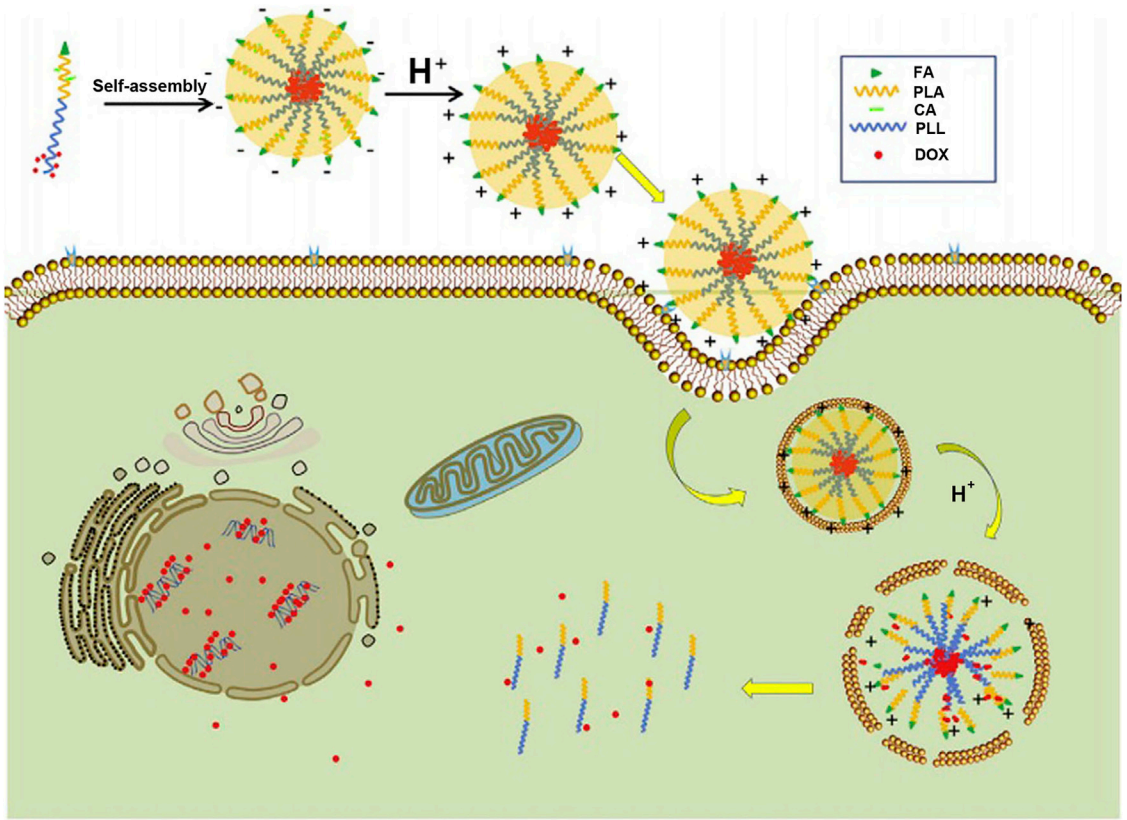

FIGURE 9 | Illustration of the folate-conjugated pH-responsive polymeric micelles based on FA–PLL(CA)–PLA for receptor-mediated endocytosis and pH-triggered release (Guan et al., 2017). Abbreviation: FA, folate; PLL, poly(L-lysine); CA, citric acid; PLA, poly(lactc acid); DOX, doxorubicin.

The second approach is that hydrophobic material is introduced into polyhistidine block by blending or copolymerization. It is known that a hydrophobic environment will reduce the local dielectric constant, thereby weakening the ionization tendency of ionizable groups (Benns et al., 2000; Putnam et al., 2001). Thus, hydrophobic material has an inhibitory effect on the ionization of imidazole group in polyhistidine block, which affects the pH value of triggering release of drugs from micelles and modulates the pH-responsiveness of micelles. Moreover, with increasing the content of hydrophobic material, pK_b of imidazole groups in polyhistidine block shifts to a lower pH. For example, mixed micelles were prepared by PH (M_n 5,000)/PEG (M_n 2,000) (PH-*b*-PEG) and PLLA (M_n 3,000)/PEG (M_n 2,000) (PLLA-*b*-PEG) block copolymers (Lee E. et al., 2003). By adjusting the mixing amount of PLLA-*b*-PEG block copolymer, micelles with different pH-sensitivity could be obtained. When 10 wt.% PLLA-*b*-PEG was added into PH-*b*-PEG micelles, it did not change significantly in destabilizing pH, and the destabilization of micelles occurred below pH 8.0. However, 25 wt.% addition of PLLA-*b*-PEG significantly improved micellar stability, and destabilizing pH was below pH 7.0. Compared to 25 wt.% addition, the destabilizing pH of mixed micelles with 40 wt.% PLLA-*b*-PEG blend was shifted a bit further downward, which occurred below pH 6.8. It was suggested that the destabilizing pH gradually decreased as the content of PLLA-*b*-PEG block copolymer increased. Additionally, the results for cumulative release of DOX-loaded mixed micelles for 24 h at different pH were presented in **Figure 12**. At pH 7.0, mixed micelles containing 10 wt.% PLLA-*b*-PEG displayed the highest cumulative release amount (more than 60%). And about 32% of DOX was released from mixed micelles with 25 wt.% or 40 wt.% of PLLA-*b*-PEG. At pH 6.8, three mixed micelles with 10, 25, and 40 wt.% PLLA-*b*-PEG released approximately 75, 70, and 35%, respectively. At pH 5.0, 10 and 25 wt.% PLLA-*b*-PEG mixed micelles both achieved a release of more than 80%, and for 40 wt.% PLLA-b-PEG micelle, the drug release was more than 70%. It is probable that at low pH, the imidazole group is ionized on the polyhistidine chain, accompanied by an increase in the hydrophilicity of the polyhistidine chain. As a result, the hydrophobic environment of mixed micelle was disrupted, and PLLA-*b*-PEG was separated from micelles, leading to micelles disintegration. The added amount of PLLA-*b*-PEG block copolymer had an effect on the pH value of micellar dissociation. These results suggested that appropriate proportion of PLLA-*b*-PEG polymer could improve the discrimination and sensitivity of the mixed micelles to the acidic extracellular pH of the tumoral microenvironment.

In another example, poly(histidine-*co*-phenylalanine) (PHP) was synthesized via the ring-opening polymerization of the benzyl-protected L-histidine NCA and L-phenylalanine NCA

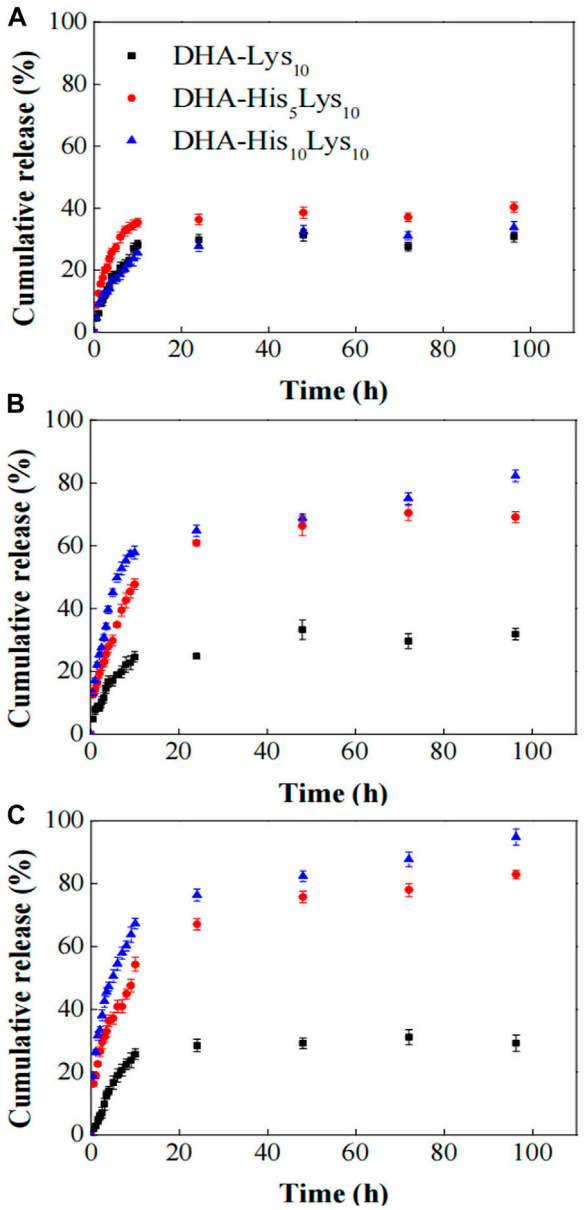

FIGURE 10 | *In vitro* DOX release from DHA-His_xLys_{10} (x = 0, 5, 10) micelles at pH 7.4 **(A)**, 6.0 **(B)**, and 5.0 **(C)** PBS solutions (Wang Y. et al., 2015). Abbreviation: DOX, doxorubicin; DHA, docosahexaenoic acid; His, histidine; Lys, lysine.

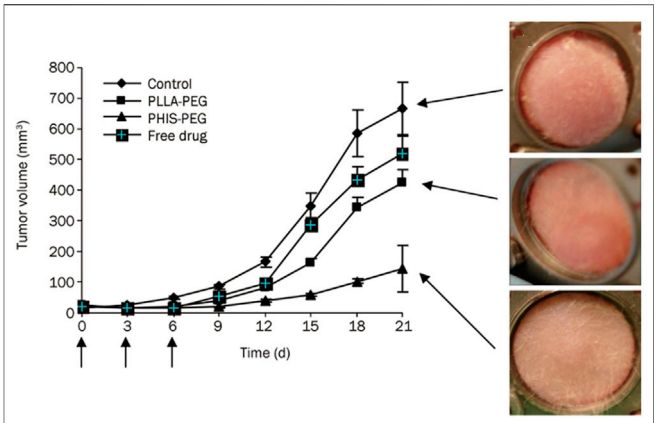

FIGURE 11 | Effects of DOX-loaded pH-sensitive PH-b-PEG micelles and pH-insensitive PLLA-b-PEG micelles on the growth of MDA 231 breast carcinoma in the window chamber model (Jin et al., 2014). Each formulation was administered three times at 3-day intervals (arrows) at a dose of 10 mg/kg for tumor growth inhibition study. Abbreviation: PEG, poly (ethylene glycol); PH, poly(L-histidine); PLLA, poly(L-lactic acid).

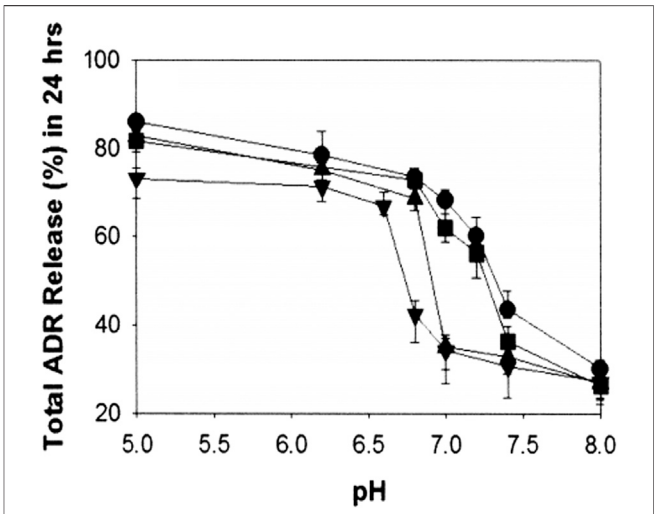

FIGURE 12 | pH-dependent cumulative adriamycin (ADR) release from the mixed micelles composed of polyHis/PEG and PLLA/PEG [PLLA/PEG content in the mixed micelles: 0 wt.% (●), 10 wt.% (■), 25 wt.% (▲), and 40 wt.% (▼)] (Lee E. et al., 2003).

(Kim et al., 2008). As the proportion of phenylalanine increased from 10 to 27%, the apparent pK_b value of PHP decreased from 6.7 to 4.8. In addition, PHP could be coupled with activated monocarboxylated PEG2000 to form a diblock polymer (PHP-*b*-PEG). Various PHP-*b*-PEG polymers were designed by adjusting the molar percentage of phenylalanine in PHP, including PHP(10)-*b*-PEG, PHP(16)-*b*-PEG, PHP(22)-*b*-PEG, and PHP(27)-*b*-PEG. Above four-block polymers self-assembled to form micelles, which were named as PHSM(10), PHSM(16), PHSM(22), and PHSM(27), respectively. pH-responsiveness of polymeric micelles was evaluated by critical micelle concentration (CMC), particle size, and the light transmittance. In the aspect of CMC, at pH 6.0, CMCs of PHSM(10) and PHSM(16) were above 90 μg ml^{-1}. However, when pH was greater than or equal to 6.5, they significantly increased. The elevated CMC of PHSM(10) and PHSM(16) indicated that both micelles were unstable at low pH. CMCs of PHSM(22) and PHSM(27) were lower than 20 μg ml^{-1} at pH 6.0 and 6.5, suggesting that they have good stability. In terms of the change of particle size, PHSM(10) and PHSM(16) showed a great difference. The former decreased rapidly, and the latter exhibited a gradual decrease in the range of pH 6.0 ~ 7.4.

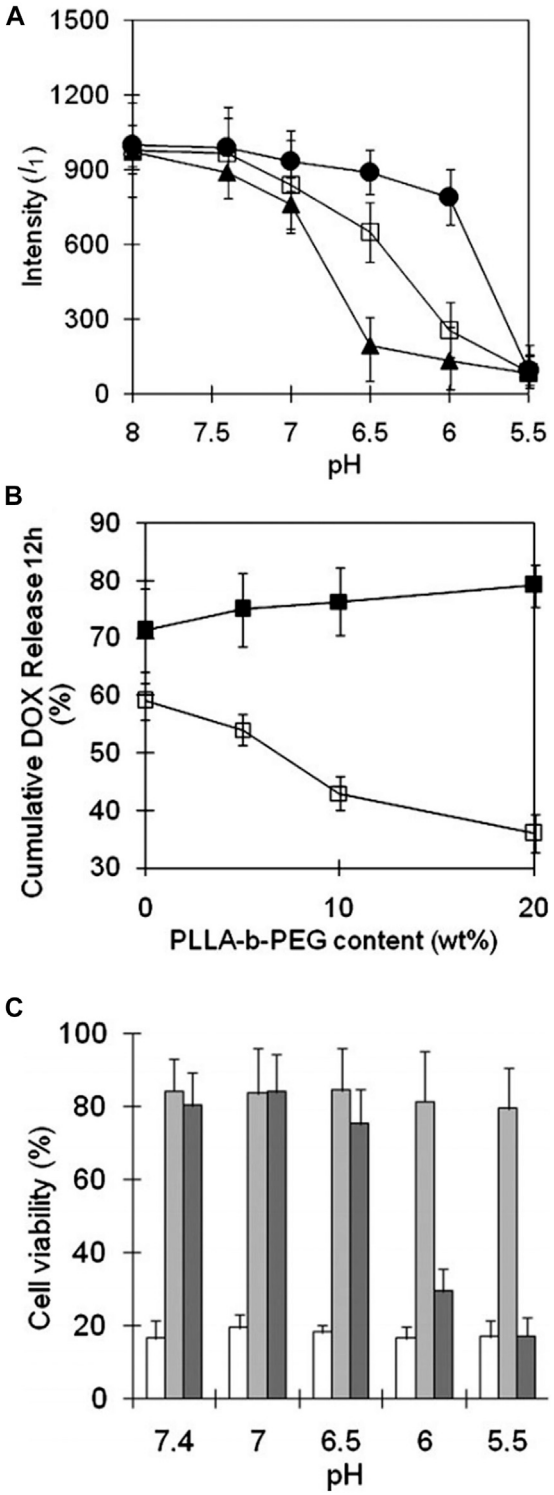

FIGURE 13 | (A) The change of pyrene fluorescence intensity (I_1) with pH at a constant micelle concentration (0.05 g L^{-1}). m-PHSM constructed with the different amounts of PLLA-b-PEG (5%, ▲; 10%, □; 20%, ●) was monitored in NaOH (or HCl)-$Na_2B_4O_7$ buffer solution (pH 8.0) with exposure to each pH for 24 h. **(B)** Cumulative amount of DOX for 12 h released from various m-PHSM at pH 6.5 (□) and pH 6.0 (■). **(C)** Cell viabilities

(*Continued*)

Nevertheless, the particle size of PHSM(22) and PHSM(27) had an insignificant change at pH 5.5 and 6.5. The transmissivity of micellar solution was correlated with change in particle size. The transmittance transition points of PHSM(10), PHSM(16), PHSM(22), and PHSM(27) decreased successively at pH 7.0, 6.5, 5.8, and 5.2, respectively. These observations indicated that the introduction of hydrophobic comonomers could adjust pH-sensitivity of micellar core based on polyhistidine.

In the same report, Kim et al. (2008) mixed PHP-*b*-PEG with PLLA(M_n 3,000)-*b*-PEG(M_n 2,000) to design new pH-sensitive micelles with responsiveness to specific pH, which was possible to achieve accurate targeting of tumor organelles. As mentioned above, the destabilizing pH of PHSM(16) was approximately 6.5. When PLLA-*b*-PEG was introduced into PHP(16)-*b*-PEG to form mixed micelles, micellar triggering pH could be modulated by the added ratio of PLLA-*b*-PEG. pH-sensitivity of mixed micelles was determined by the fluorescence intensity of pyrene under different pH conditions, which was shown in **Figure 13A**. The mixed micelles containing 5, 10, and 20% of PLLA-*b*-PEG were named as m-PHSM (5%), m-PHSM (10%), and m-PHSM (20%), respectively. For m-PHSM (5%) and m-PHSM (10%), the main change in fluorescence intensity occurred at pH > 6.0. The fluorescence intensity of m-PHSM (20%) altered primarily in the range of 5.5 ~ 6.0, which was closer to that of early endosomes. Obviously, the sensitivity of m-PHSM to low pH increased with increasing proportion of blended PLLA-*b*-PEG. This was also confirmed by the release capacity of DOX-loaded m-PHSM (DOX/m-PHSM) at different pH conditions. The 12-h cumulative DOX release from DOX/m-PHSM at pH 6.0 and 6.5 manifested that release of DOX at pH 6.5 decreased with increasing PLLA-*b*-PEG ratio in micelles and an opposite trend happened at pH 6.0 (**Figure 13B**). Compared with DOX/m-PHSM (5%) and DOX/m-PHSM (10%), the amount of drug release from DOX/m-PHSM (20%) was the least at pH 6.5, but it was the most at pH 6.0. The rapid release of DOX at pH 6.0 significantly improved the efficacy. In the *in-vitro* cytotoxicity study, DOX/m-PHSM (20%) was incubated with wild-type human ovarian A2780 for 48 h. The cell viability decreased from ~75% under pH 6.5 to less than 40% under pH 6.0 (**Figure 13C**). The above results indicated that m-PHSM (20%) was likely to achieve the targeting of early endosome.

ARGININE-BASED MICELLES

Arginine possessed some special functions, which were used to fabricate micelles, including cell-membrane-penetrating function and arginine-derived nitric oxide.

FIGURE 13 | determined by MTT assay of ovarian A2780 wild-type carcinoma cells treated with micelles: free DOX (white), DOX/PHIM (gray), and DOX/m-PHSM(20%) (dark gray). DOX dose was equivalent to 1,000 ng ml^{-1} in each formulation (Kim et al., 2008). Abbreviation: m-PHSM, pH-sensitive mixed micelles containing poly(histidine (His)-co-phenylalanine (Phe))-b-poly(ethylene glycol) (PEG) and poly(L-lactic acid) (PLLA)-b-PEG; PHIM, pH-insensitive PLLA-b-PEG micelles.

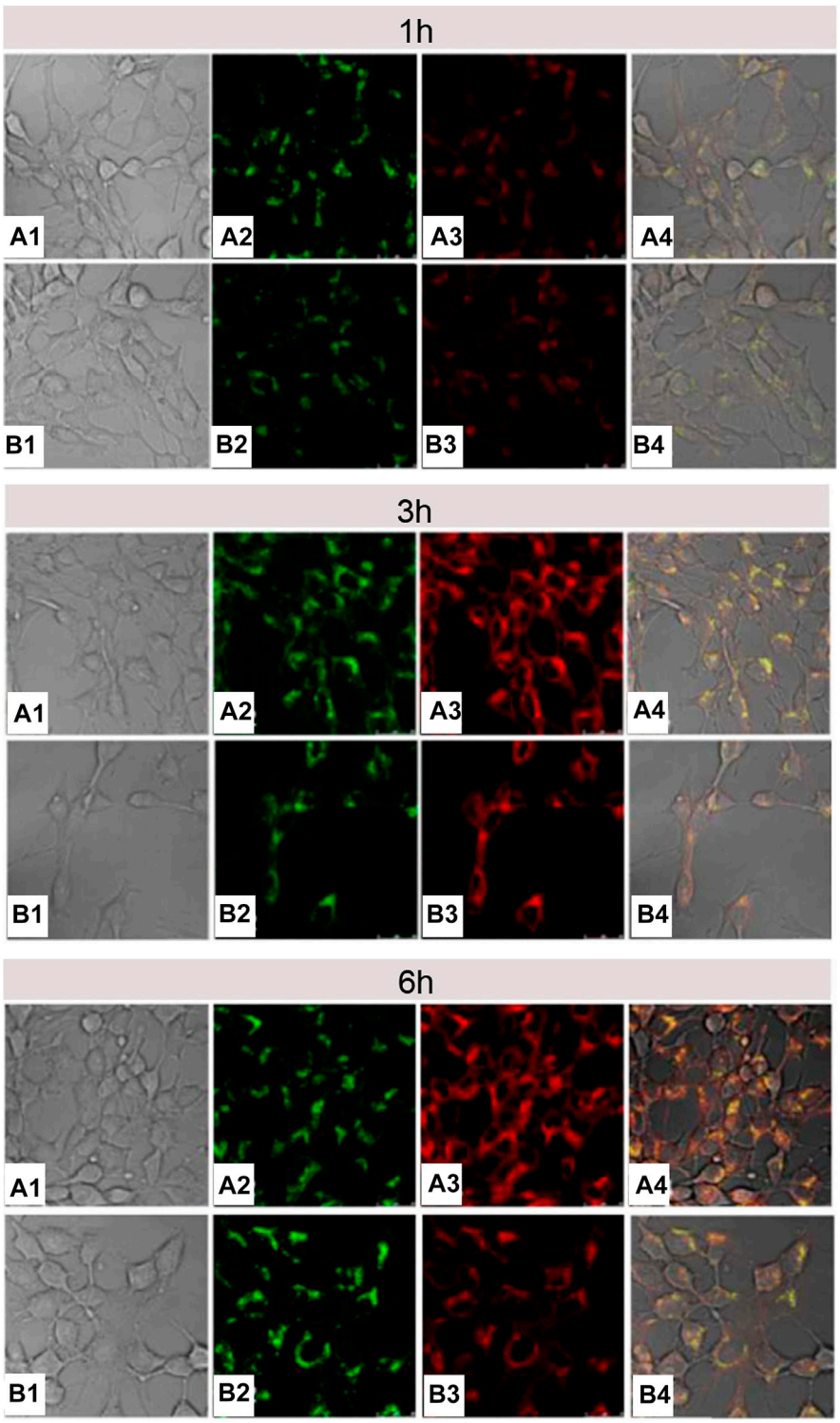

FIGURE 14 | The CLSM images of 4T1 cells treated with DOX/Arg-PEG-PCL-Py **(A)** and DOX/Ac-PEG-PCL-Py micelles **(B)** for 1, 3, and 6 h. The numbers 1, 2, 3, and 4 indicated the bright field, LysoTracker Green fluorescence, DOX fluorescence, and the overlay images, respectively. The concentration of DOX was 10 μg ml^{-1} (Luo et al., 2016). Abbreviation: Arg-PEG-PCL, arginine-modified poly(ethylene glycol)-b-poly(ε-caprolactone); Ac-PEG-PCL, acetic acid-modified PEG-PCL; Py, pyrene.

Construction of Micelles Utilizing Membrane-Penetrating Function of Arginine

Arginine is a primary component of most cell-penetrating peptides (CPPs), whose guanidine group has a key role in the transmembrane transport of peptides (Schröder et al., 2008; Wender et al., 2008).

Cell-membrane-penetrating ability of arginine is related to the quantity of arginine and the density of guanidine groups. Oligoarginine with more than six repeating units of arginine exhibited perfect membrane-penetration effect (Wang P. et al., 2019; Zhai et al., 2019), and vice versa (Mitchell et al., 2000; Wender et al., 2000). In another example, Macewan and Chilkoti (2012) connected five arginines with hydrophobic segment of amphiphilic elastin-like polypeptides (ELP_{BC}s) to build Arg_5-ELP_{BC} with characteristic of temperature sensitivity (Wright and Conticello, 2002; Dreher et al., 2008). Slightly high temperature (e.g. 42°C) could trigger Arg_5-ELP_{BC} to self-assemble into micelles, thus resulting in the increase of local arginine density. Confocal microscopy displayed that at 37°C, there was no obvious uptake by Hela cells incubated with Arg_5-ELP_{BC} for 1 h, whereas, at 42°C, the self-assembled Arg_5-ELP_{BC} micelles showed significantly increased cellular uptake. Moreover, flow cytometry manifested that there was approximately 8-fold difference in cellular uptake for Arg_5-ELP_{BC} at 37 and 42°C. It could be inferred that it was an opportunity for polymer containing less than six arginines to realize cell-membrane penetration if only the surface of micelles was covered with high density of arginine guanidine groups by some way. Song Luo's research (Luo et al., 2016) was consistent with above inference. Specifically, single arginine and pyrene (py) were separately attached to the end of PEG and PCL segment in PEG-*b*-PCL to construct Arg-PEG-*b*-PCL-Py copolymer. Next, Arg-PEG-*b*-PCL-Py copolymer self-assembled into micelles, and guanidine groups of arginine were exposed on the surface of them. In comparison with micelles without modifying arginine, arginine-modified micelles had a more efficient endocytosis and more rapid endo-lysosomal escape (**Figure 14**), indicating that guanidine-functionalized micelles have a stronger capability to pass through the cell membrane. It was important to note that if it was sufficient for local arginine density on micellar surface, even single arginine-decorated micelles could promote tumor cell internalization.

Construction of Micelles Based on Antitumor Ability of Nitric Oxide Derived From Arginine

As early as the 1980s, the immune function of organisms could be regulated by L-arginine (Hibbs et al., 1987). Later, the inhibitory effect of L-arginine on tumor and its mechanism of action were also gradually revealed. Briefly, L-arginine is the substrate of nitric oxide synthase (NOS) (Iyengar et al., 1987). At the early stage of cancer, M1 macrophages infiltrating into tumor tissues overexpress inducible NO synthase (iNOS), which converted L-arginine to NO. The gaseous and lipophilic NO rapidly permeates tumor tissue from M1 macrophages (Thomas et al., 2008). High concentration of NO is cytotoxic and can cause tumor cell apoptosis or induce tumor cell necrosis (Singh et al., 1996; Ambs et al., 1998; Kudo and Nagasaki, 2015).

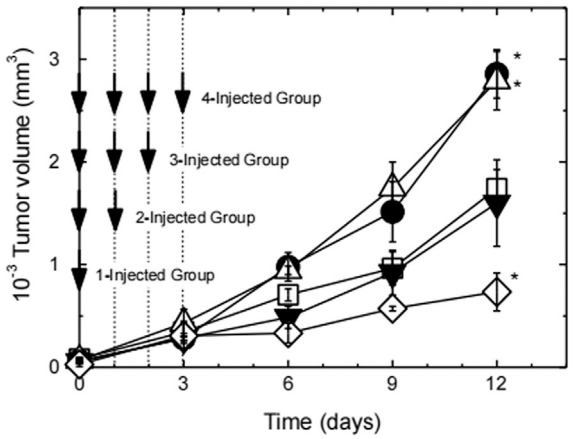

FIGURE 15 | Tumor growth curve of tumor-bearing mice after the first injection of PEG-b-P(L-Arg)/m (Kudo and Nagasaki, 2015). The number of injections was changed from 1 up to 4 times on days 0–3 at a dose of 16 mg/kg on an arginine basis. Injection times are 1 (closed circles), 2 (open triangles), 3 (closed triangles), and 4 (open lozenges). Tumor volume change of PBS-treated mice was also shown as open squares. (n = 4, expressed as mean ± S.E., $^*p < 0.05$). Abbreviation: P(L-Arg), poly(L-Arginine); m, micelles.

It has been reported that the increase of L-arginine outside M1 macrophages will upregulate NO (Tsikas et al., 2000). However, systemic administration of free L-arginine is not a good idea, and it is because that there are a lot of problems such as rapid systemic metabolism or excretion, making L-arginine difficult to accumulate at the tumor site (Lind, 2004). But these issues can be solved *via* the "introducing arginine into nano-micelles" strategy. Owing to the enhanced permeability and retention (EPR) effect of tumor, arginine-rich nano-micelles enabled improved arginine accumulation at the tumor site by passive targeting strategy and generated site-specific high concentration of NO to prevent tumor progression. For instance, Kudo and Nagasaki (2015) synthesized cationic poly((ethylene glycol)-*block*-poly (L-arginine) (PEG-*b*-P(L-Arg)) block copolymers with 62 arginine repeating units, which were electrostatically coupled with polyanion chondroitin sulfate (CS) to form a polyionic complex (PIC) micelle with a particle size of about 50 nm and a near-neutral surface charge (average zeta potential: ~0.09 mV). RAW264.7 macrophages were activated by lipopolysaccharide, which induced the expression of iNOS. The results of *in vivo* distribution of carriers in tumor-bearing mice confirmed that PIC micelles tended to accumulate in the tumor site, which realized the effective delivery of arginine. Subsequently, to investigate *in vivo* antitumor activity of PIC micelles (**Figure 15**), tumor-bearing mice were divided into four groups, which were named as 1-injected group, 2-injected group, 3-injected group, and 4-injected group, respectively. In 1-injected group, tumor-bearing mice received a 16 mg/kg dose of L-arginine by tail vein injection for one time (on day 0), which existed in the PIC micelles. In 2-injected group, the PIC micelles were administered at 16 mg/kg on L-arginine basis for two times (on days 0 and 1, at a total dose

of 32 mg/kg). According to the above-mentioned prescription rules, tumor-bearing mice of 3-injected and 4-injected groups were given a corresponding dose of L-arginine. After 12 d in comparison with the control group, there were significant differences in tumor size for four groups. Tumor volume of 1-injected and 2-injected groups was significantly higher than that of the PBS control group ($p < 0.05$), whereas tumor volume of 3-injected group was close to that of the control group. It was noteworthy that suppression of tumor growth was obviously observed in 4-injected group. These results were also confirmed by Thomas et al. (Hofseth et al., 2003; Thomas et al., 2004). These results showed that the antitumor effect of NO depended on its concentration. Low-dose NO promoted tumor growth, whereas high-dose one inhibited tumor growth. The one possible reason is that low concentration of NO could enhance angiogenesis, thus promoting tumor growth. In contrast, high concentration of NO could lead to tumor cell apoptosis, along with inhibiting tumor growth. Therefore, it is helpful for designing arginine-rich micelles to enhance the therapeutic effect of tumor.

CONCLUSION

Material safety is one of the main problems that affect the development of micelles from basic research to clinical application. Raw materials for building micelles were derived from various natural and synthetic materials. Compared to synthetic materials, natural materials have almost no side effect on human body, which become the first choice for micelles. In natural materials, basic amino acids have been paid much attention for non-toxicity and good biocompatibility.

This review shows design ideas for the construction of micelles by using basic amino acids and their derivatives. It can be summarized as follows:

1) Lysine and its derivatives can build the linker, core, and shell of micelles. As linker, lysine, lysine-based dendrimer, and polylysine provide the rich active groups to connect hydrophilic or hydrophobic materials. Additionally, the surplus amino groups of polylysine as linker can load drug by electrostatic interaction or are covalently cross-linked by introducing disulfide bond, thus improving the stability of drug-loaded micelles. In the construction of micellar core, polylysine can be physically combined with negatively charged polymer by electrostatic interaction, or chemically modified in the side chain amino groups to form micellar core. Modification methods for side-chain amino group of polylysine include charge reversal of polylysine by introducing carboxyl groups, cross-linking of polylysine by introducing sulfhydryl groups, and hydrophobic modification of polylysine by introducing hydrophobic molecules. When acting as the shell of micelles, the positive charge of polylysine is shielded by introducing drug, anionic substances, or polymers to temporarily occupy the amino groups, thereby reducing or reversing the charge of drug-loaded micelles, improving their stability in the blood circulation, and enhancing their efficiency of endocytosis by target cells.
2) Both histidine and polyhistidine can act as the core of micelles to load drug and trigger drug release by acidic pH. When introducing hydrophobic material into the micellar core based on polyhistidine, either by mixing hydrophobic polymer blocks or by introducing other hydrophobic components into the polyhistidine blocks, the ability of micelles to recognize small differences in pH is improved thus achieving accurate targeting of tumor organelles. In addition, polyhistidine as an intermediate layer of triblock polymer micelles can control drug release rate by responding to acidic pH. There is a correlation between the chain length of polyhistidine as the middle layer of micelles and pH-dependent drug release rate.
3) The micelles modified by both single arginine and oligoarginine have high membrane-penetrating ability due to covering the outside of micelles with high density of arginine guanidine groups. Moreover, the high concentration of arginine-rich micelles in tumor site can generate high concentration of NO to enhance antitumor effect.

Considerable progress has been made in the construction of drug-loaded micelles based on lysine, histidine, and arginine, and efficient drug delivery at the target site has been achieved. In addition, cytotoxicity and intracellular delivery processes have been widely studied in many researches. Nevertheless, there are still the following problems to be solved: 1) micelles based on basic amino acids are still produced on a laboratory scale, and issues related to low yield and high cost need to be resolved; 2) most of the researches in drug delivery are only at the basic research stage of cell and animal models. Information was limited on biodistribution, metabolism, and degradation mechanisms of amino acid-based micelles. In order to obtain better biomedical applications, the further corresponding studies related to the above unsolved issues are necessary.

DATA AVAILABILITY STATEMENT

The original contributions presented in the study are included in the article/supplementary material; further inquiries can be directed to the corresponding author.

AUTHOR CONTRIBUTIONS

RL directed the completion of this article. LX wrote the main content of this article. XC, MH, YZ, and SC collected the information for this article. All authors contributed to the article and approved the submitted version.

FUNDING

This work was supported by the National Natural Science Foundation of China (No: 51203157); Antibiotics Research and Re-evaluation Key Laboratory Foundation of Sichuan Province (No: ARRLKF15-04); and Project of Education Department in Sichuan Province (No: 16ZB0421).

REFERENCES

Adityan, S., Tran, M., Bhavsar, C., and Wu, S. Y. (2020). Nano-therapeutics for Modulating the Tumour Microenvironment: Design, Development, and Clinical Translation. *J. Controlled Release* 327, 512–532. doi:10.1016/j.jconrel.2020.08.016

Ambs, S., Merriam, W. G., Ogunfusika, M. O., Bennett, W. P., Ishibe, N., Hussain, S. P., et al. (1998). p53 and Vascular Endothelial Growth Factor Regulate Tumor Growth of NOS2-Expressing Human Carcinoma Cells. *Nat. Med.* 4, 1371–1376. doi:10.1038/3957

Augustine, R., Kim, D.-K., Kalva, N., Eom, K. H., Kim, J. H., and Kim, I. (2020a). Multi-stimuli-responsive Nanomicelles Fabricated Using Synthetic Polymer Polylysine Conjugates for Tumor Microenvironment Dependent Drug Delivery. *J. Mater. Chem. B* 8, 5745–5755. doi:10.1039/D0TB00721H

Augustine, R., Kim, D.-K., Kim, H. A., Kim, J. H., and Kim, I. (2020b). Poly(N-isopropylacrylamide)-b-Poly(L-lysine)-b-Poly(L-histidine) Triblock Amphiphilic Copolymer Nanomicelles for Dual-Responsive Anticancer Drug Delivery. *j nanosci nanotechnol* 20, 6959–6967. doi:10.1166/jnn.2020.18822

Aw, M. S., Simovic, S., Addai-Mensah, J., and Losic, D. (2011). Polymeric Micelles in Porous and Nanotubular Implants as a New System for Extended Delivery of Poorly Soluble Drugs. *J. Mater. Chem.* 21, 7082–7089. doi:10.1039/C0JM04307A

Benns, J. M., Choi, J.-S., Mahato, R. I., Park, J.-S., and Kim, S. W. (2000). pH-Sensitive Cationic Polymer Gene Delivery Vehicle: N-Ac-Poly(l-Histidine)-Graft-Poly(l-Lysine) Comb Shaped Polymer. *Bioconjug. Chem.* 11, 637–645. doi:10.1021/bc0000177

Beyermann, J., and Kukula, H. (2000). Poly(ethylene Oxide)-B-Poly(l-Lysine) Complexes with Retinoic Acid. *Macromolecules* 33, 5906–5911. doi:10.1021/ma000629m

Boudier, A., Aubert-Pouëssel, A., Gérardin, C., Devoisselle, J.-M., and Bégu, S. (2009). pH-sensitive Double-Hydrophilic Block Copolymer Micelles for Biological Applications. *Int. J. Pharmaceutics* 379, 212–217. doi:10.1016/j.ijpharm.2009.05.032

Boudier, A., Aubert-Pouëssel, A., Mebarek, N., Chavanieu, A., Quentin, J., Martire, D., et al. (2011). Development of Tripartite Polyion Micelles for Efficient Peptide Delivery into Dendritic Cells without Altering Their Plasticity. *J. Controlled Release* 154, 156–163. doi:10.1016/j.jconrel.2011.05.016

Boulikas, T., Pantos, T., Bellis, E., and Christofis, P. (2007). Designing Platinum Compounds in Cancer: Structures and Mechanisms. *Cancer Ther.* 5, 537–583.

Brunato, S., Mastrotto, F., Bellato, F., Bastiancich, C., Travanut, A., Garofalo, M., et al. (2021). PEG-polyaminoacid Based Micelles for Controlled Release of Doxorubicin: Rational Design, Safety and Efficacy Study. *J. Controlled Release* 335, 21–37. doi:10.1016/j.jconrel.2021.05.010

Cabral, H., and Kataoka, K. (2014). Progress of Drug-Loaded Polymeric Micelles into Clinical Studies. *J. Controlled Release* 190, 465–476. doi:10.1016/j.jconrel.2014.06.042

Canfield, C.-A., and Bradshaw, P. C. (2019). Amino Acids in the Regulation of Aging and Aging-Related Diseases. *Translational Med. Aging* 3, 70–89. doi:10.1016/j.tma.2019.09.001

Chang, C., Liang, P., Chen, L., Liu, J., Chen, S., Zheng, G., et al. (2017). pH-responsive Nanoparticle Assembly from Peptide Amphiphiles for Tumor Targeting Drug Delivery. *J. Biomater. Sci. Polym. Edition* 28, 1338–1350. doi:10.1080/09205063.2017.1325095

Chang, G., Li, C., Lu, W., and Ding, J. (2010). N-Boc-Histidine-Capped PLGA-PEG-PLGA as a Smart Polymer for Drug Delivery Sensitive to Tumor Extracellular pH. *Macromol. Biosci.* 10, 1248–1256. doi:10.1002/mabi.201000117

Chen, J., Ding, J., Zhang, Y., Xiao, C., Zhuang, X., and Chen, X. (2015). Polyion Complex Micelles with Gradient pH-Sensitivity for Adjustable Intracellular Drug Delivery. *Polym. Chem.* 6, 397–405. doi:10.1039/C4PY01149J

Cheng, F., Pan, Q., Gao, W., Pu, Y., Luo, K., and He, B. (2021). Reversing Chemotherapy Resistance by a Synergy between Lysosomal pH-Activated Mitochondrial Drug Delivery and Erlotinib-Mediated Drug Efflux Inhibition. *ACS Appl. Mater. Interfaces* 13, 29257–29268. doi:10.1021/acsami.1c03196

Deng, C., Jiang, Y., Cheng, R., Meng, F., and Zhong, Z. (2012). Biodegradable Polymeric Micelles for Targeted and Controlled Anticancer Drug Delivery: Promises, Progress and Prospects. *Nano Today* 7, 467–480. doi:10.1016/j.nantod.2012.08.005

Deshmukh, A. S., Chauhan, P. N., Noolvi, M. N., Chaturvedi, K., Ganguly, K., Shukla, S. S., et al. (2017). Polymeric Micelles: Basic Research to Clinical Practice. *Int. J. Pharmaceutics* 532, 249–268. doi:10.1016/j.ijpharm.2017.09.005

Ding, J., Chen, J., Li, D., Xiao, C., Zhang, J., He, C., et al. (2013). Biocompatible Reduction-Responsive Polypeptide Micelles as Nanocarriers for Enhanced Chemotherapy Efficacy *In Vitro*. *J. Mater. Chem. B* 1, 69–81. doi:10.1039/C2TB00063F

Dirisala, A., Osada, K., Chen, Q., Tockary, T. A., Machitani, K., Osawa, S., et al. (2014). Optimized Rod Length of Polyplex Micelles for Maximizing Transfection Efficiency and Their Performance in Systemic Gene Therapy against Stroma-Rich Pancreatic Tumors. *Biomaterials* 35, 5359–5368. doi:10.1016/j.biomaterials.2014.03.037

Dreher, M. R., Simnick, A. J., Fischer, K., Smith, R. J., Patel, A., Schmidt, M., et al. (2008). Temperature Triggered Self-Assembly of Polypeptides into Multivalent Spherical Micelles. *J. Am. Chem. Soc.* 130, 687–694. doi:10.1021/ja0764862

Du, J.-Z., Sun, T.-M., Song, W.-J., Wu, J., and Wang, J. (2010). A Tumor-Acidity-Activated Charge-Conversional Nanogel as an Intelligent Vehicle for Promoted Tumoral-Cell Uptake and Drug Delivery. *Angew. Chem. Int. Edition* 49, 3621–3626. doi:10.1002/anie.200907210

Fukumura, D., and Jain, R. K. (2007). Tumor Microvasculature and Microenvironment: Targets for Anti-angiogenesis and Normalization. *Microvasc. Res.* 74, 72–84. doi:10.1016/j.mvr.2007.05.003

Geihe, E. I., Cooley, C. B., Simon, J. R., Kiesewetter, M. K., Edward, J. A., Hickerson, R. P., et al. (2012). Designed Guanidinium-Rich Amphipathic Oligocarbonate Molecular Transporters Complex, Deliver and Release siRNA in Cells. *Proc. Natl. Acad. Sci.* 109, 13171–13176. doi:10.1073/pnas.1211361109

George, A., Shah, P. A., and Shrivastav, P. S. (2019). Natural Biodegradable Polymers Based Nano-Formulations for Drug Delivery: A Review. *Int. J. Pharmaceutics* 561, 244–264. doi:10.1016/j.ijpharm.2019.03.011

Grossen, P., Witzigmann, D., Sieber, S., and Huwyler, J. (2017). PEG-PCL-based Nanomedicines: A Biodegradable Drug Delivery System and its Application. *J. Controlled Release* 260, 46–60. doi:10.1016/j.jconrel.2017.05.028

Guan, J., Zhou, Z.-Q., Chen, M.-H., Li, H.-Y., Tong, D.-N., Yang, J., et al. (2017). Folate-conjugated and pH-Responsive Polymeric Micelles for Target-cell-specific Anticancer Drug Delivery. *Acta Biomater.* 60, 244–255. doi:10.1016/j.actbio.2017.07.018

Guan, S., Zhang, Q., Bao, J., Duan, T., Hu, R., Czech, T., et al. (2020). Phosphatidylserine Targeting Peptide-Functionalized pH Sensitive Mixed Micelles for Enhanced Anti-tumor Drug Delivery. *Eur. J. Pharmaceutics Biopharmaceutics* 147, 87–101. doi:10.1016/j.ejpb.2019.12.012

Guo, D., Shi, C., Wang, L., Ji, X., Zhang, S., and Luo, J. (2020). Rationally Designed Micellar Nanocarriers for the Delivery of Hydrophilic Methotrexate in Psoriasis Treatment. *ACS Appl. Bio Mater.* 3, 4832–4846. doi:10.1021/acsabm.0c00342

Gupta, R., Shea, J., Scaife, C., Shurlygina, A., and Rapoport, N. (2015). Polymeric Micelles and Nanoemulsions as Drug Carriers: Therapeutic Efficacy, Toxicity, and Drug Resistance. *J. Controlled Release* 212, 70–77. doi:10.1016/j.jconrel.2015.06.019

Harada-Shiba, M., Yamauchi, K., Harada, A., Takamisawa, I., Shimokado, K., and Kataoka, K. (2002). Polyion Complex Micelles as Vectors in Gene Therapy - Pharmacokinetics and *In Vivo* Gene Transfer. *Gene Ther.* 9, 407–414. doi:10.1038/sj.gt.3301665

He, B., Liu, B., He, B., Li, Y., Lai, J., Tang, J. Z., et al. (2012a). Effects of pH-Sensitive Chain Length on Release of Doxorubicin from mPEG-B-PH-B-PLLA Nanoparticles. *Ijn* 7, 4433. doi:10.2147/IJN.S32053

Hibbs, J., Taintor, R., and Vavrin, Z. (1987). Macrophage Cytotoxicity: Role for L-Arginine Deiminase and Imino Nitrogen Oxidation to Nitrite. *Science* 235, 473–476. doi:10.1126/science.2432665

Hofseth, L. J., Saito, S., Hussain, S. P., Espey, M. G., Miranda, K. M., Araki, Y., et al. (2003). Nitric Oxide-Induced Cellular Stress and P53 Activation in Chronic Inflammation. *Proc. Natl. Acad. Sci.* 100, 143–148. doi:10.1073/pnas.0237083100

Hu, X., Liu, G., Li, Y., Wang, X., and Liu, S. (2015). Cell-Penetrating Hyperbranched Polyprodrug Amphiphiles for Synergistic Reductive Milieu-Triggered Drug Release and Enhanced Magnetic Resonance Signals. *J. Am. Chem. Soc.* 137, 362–368. doi:10.1021/ja5105848

Itaka, K., Yamauchi, K., Harada, A., Nakamura, K., Kawaguchi, H., and Kataoka, K. (2003). Polyion Complex Micelles from Plasmid DNA and Poly(ethylene Glycol)-Poly(l-Lysine) Block Copolymer as Serum-Tolerable Polyplex System: Physicochemical Properties of Micelles Relevant to Gene Transfection Efficiency. *Biomaterials* 24, 4495–4506. doi:10.1016/S0142-9612(03)00347-8

Iyengar, R., Stuehr, D. J., and Marletta, M. A. (1987). Macrophage Synthesis of Nitrite, Nitrate, and N-Nitrosamines: Precursors and Role of the Respiratory Burst. *Proc. Natl. Acad. Sci.* 84, 6369–6373. doi:10.1073/pnas.84.18.6369

Jang, W.-D., Nakagishi, Y., Nishiyama, N., Kawauchi, S., Morimoto, Y., Kikuchi, M., et al. (2006). Polyion Complex Micelles for Photodynamic Therapy: Incorporation of Dendritic Photosensitizer Excitable at Long Wavelength Relevant to Improved Tissue-Penetrating Property. *J. Controlled Release* 113, 73–79. doi:10.1016/j.jconrel.2006.03.009

Jiao, X., Yu, Y., Meng, J., He, M., Zhang, C. J., Geng, W., et al. (2019). Dual-targeting and Microenvironment-Responsive Micelles as a Gene Delivery System to Improve the Sensitivity of Glioma to Radiotherapy. *Acta Pharmaceutica Sinica B* 9, 381–396. doi:10.1016/j.apsb.2018.12.001

Jin, Z.-h., Jin, M.-j., Jiang, C.-g., Yin, X.-z., Jin, S.-x., Quan, X.-q., et al. (2014). Evaluation of Doxorubicin-Loaded pH-Sensitive Polymeric Micelle Release from Tumor Blood Vessels and Anticancer Efficacy Using a Dorsal Skin-fold Window Chamber Model. *Acta Pharmacol. Sin.* 35, 839–845. doi:10.1038/aps.2014.12

Jones, D. P., Carlson, J. L., Samiec, P. S., Sternberg, P., Mody, V. C., Reed, R. L., et al. (1998). Glutathione Measurement in Human Plasma. *Clinica Chim. Acta* 275, 175–184. doi:10.1016/S0009-8981(98)00089-8

Kang, Y., Lu, L., Lan, J., Ding, Y., Yang, J., Zhang, Y., et al. (2018). Redox-responsive Polymeric Micelles Formed by Conjugating Gambogic Acid with Bioreducible Poly(amido Amine)s for the Co-delivery of Docetaxel and MMP-9 shRNA. *Acta Biomater.* 68, 137–153. doi:10.1016/j.actbio.2017.12.028

Kanto, R., Yonenuma, R., Yamamoto, M., Furusawa, H., Yano, S., Haruki, M., et al. (2021). Mixed Polyplex Micelles with Thermoresponsive and Lysine-Based Zwitterionic Shells Derived from Two Poly(vinyl Amine)-Based Block Copolymers. *Langmuir* 37, 3001–3014. doi:10.1021/acs.langmuir.0c02197

Kelly, B., and Pearce, E. L. (2020). Amino Assets: How Amino Acids Support Immunity. *Cel Metab.* 32, 154–175. doi:10.1016/j.cmet.2020.06.010

Khoury, A., Deo, K. M., and Aldrich-Wright, J. R. (2020). Recent Advances in Platinum-Based Chemotherapeutics that Exhibit Inhibitory and Targeted Mechanisms of Action. *J. Inorg. Biochem.* 207, 111070. doi:10.1016/j.jinorgbio.2020.111070

Kim, D., Lee, E. S., Oh, K. T., Gao, Z. G., and Bae, Y. H. (2008). Doxorubicin-Loaded Polymeric Micelle Overcomes Multidrug Resistance of Cancer by Double-Targeting Folate Receptor and Early Endosomal pH. *Small* 4, 2043–2050. doi:10.1002/smll.200701275

Kim, S. G., Robby, A. I., Lee, B. C., Lee, G., and Park, S. Y. (2021). Mitochondria-targeted ROS- and GSH-Responsive Diselenide-Crosslinked Polymer Dots for Programmable Paclitaxel Release. *J. Ind. Eng. Chem.* 99, 98–106. doi:10.1016/j.jiec.2021.04.016

Knudsen, K. B., Northeved, H., Kumar Ek, P. P., Permin, A., Gjetting, T., Andresen, T. L., et al. (2015). *In Vivo* toxicity of Cationic Micelles and Liposomes. *Nanomedicine: Nanotechnology, Biol. Med.* 11, 467–477. doi:10.1016/j.nano.2014.08.004

Koo, A. N., Lee, H. J., Kim, S. E., Chang, J. H., Park, C., Kim, C., et al. (2008). Disulfide-cross-linked PEG-Poly(amino Acid)s Copolymer Micelles for Glutathione-Mediated Intracellular Drug Delivery. *Chem. Commun.*, 6570–6572. doi:10.1039/B815918A

Koo, A. N., Min, K. H., Lee, H. J., Lee, S.-U., Kim, K., Chan Kwon, I., et al. (2012). Tumor Accumulation and Antitumor Efficacy of Docetaxel-Loaded Core-Shell-corona Micelles with Shell-specific Redox-Responsive Cross-Links. *Biomaterials* 33, 1489–1499. doi:10.1016/j.biomaterials.2011.11.013

Krivitsky, A., Polyak, D., Scomparin, A., Eliyahu, S., Ofek, P., Tiram, G., et al. (2018). Amphiphilic Poly(α)glutamate Polymeric Micelles for Systemic Administration of siRNA to Tumors. *Nanomedicine: Nanotechnology, Biol. Med.* 14, 303–315. doi:10.1016/j.nano.2017.10.012

Kudo, S., and Nagasaki, Y. (2015). A Novel Nitric Oxide-Based Anticancer Therapeutics by Macrophage-Targeted Poly(l-Arginine)-Based Nanoparticles. *J. Controlled Release* 217, 256–262. doi:10.1016/j.jconrel.2015.09.019

Lee, E., Na, K., and Bae, Y. H. (2003). Polymeric Micelle for Tumor pH and Folate-Mediated Targeting. *J. Controlled Release* 91, 103–113. doi:10.1016/S0168-3659(03)00239-6

Lee, E. S., Gao, Z., and Bae, Y. H. (2008). Recent Progress in Tumor pH Targeting Nanotechnology. *J. Controlled Release* 132, 164–170. doi:10.1016/j.jconrel.2008.05.003

Lee, E. S., Shin, H. J., Na, K., and Bae, Y. H. (2003). Poly(l-histidine)-PEG Block Copolymer Micelles and pH-Induced Destabilization. *J. Controlled Release* 90, 363–374. doi:10.1016/S0168-3659(03)00205-0

Li, Y., Gao, F., Guo, J., Ren, P., Tian, Z., Bai, J., et al. (2020). Polymeric Micelles with Aggregation-Induced Emission Based on Microbial ε-polylysine for Doxorubicin Delivery. *Eur. Polym. J.* 122, 109355. doi:10.1016/j.eurpolymj.2019.109355

Li, Y., Xiao, K., Luo, J., Xiao, W., Lee, J. S., Gonik, A. M., et al. (2011). Well-defined, Reversible Disulfide Cross-Linked Micelles for On-Demand Paclitaxel Delivery. *Biomaterials* 32, 6633–6645. doi:10.1016/j.biomaterials.2011.05.050

Lin, J.-T., Zou, Y., Wang, C., Zhong, Y.-C., Zhao, Y., Zhu, H.-E., et al. (2014). Cationic Micellar Nanoparticles for DNA and Doxorubicin Co-delivery. *Mater. Sci. Eng. C* 44, 430–439. doi:10.1016/j.msec.2014.07.049

Lind, D. S. (2004). Arginine and Cancer. *J. Nutr.* 134, 2837S–2841S. doi:10.1093/jn/134.10.2837S

Liu, R., He, B., Li, D., Lai, Y., Tang, J. Z., and Gu, Z. (2012b). Stabilization of pH-Sensitive mPEG-PH-PLA Nanoparticles by Stereocomplexation between Enantiomeric Polylactides. *Macromol. Rapid Commun.* 33, 1061–1066. doi:10.1002/marc.201100854

Liu, S.-T., Tuan-Mu, H.-Y., Hu, J.-J., and Jan, J.-S. (2015). Genipin Cross-Linked PEG-Block-poly(L-Lysine)/disulfide-Based Polymer Complex Micelles as Fluorescent Probes and pH-/redox-Responsive Drug Vehicles. *RSC Adv.* 5, 87098–87107. doi:10.1039/C5RA18802D

Lu, C., Wen, T., Zheng, M., Liu, D., Quan, G., Pan, X., et al. (2020). Poly(Ethylene Glycol) Crosslinked Multi-Armed Poly(l-Lysine) with Encapsulating Capacity and Antimicrobial Activity for the Potential Treatment of Infection-Involved Multifactorial Diseases. *Pharmaceutics* 12, 47. doi:10.3390/pharmaceutics12010047

Luo, S., Zhang, Y., Cao, J., He, B., and Li, S. (2016). Arginine Modified Polymeric Micelles as a Novel Drug Delivery System with Enhanced Endocytosis Efficiency. *Colloids Surf. B: Biointerfaces* 148, 181–192. doi:10.1016/j.colsurfb.2016.07.023

Luo, Z., Li, P., Deng, J., Gao, N., Zhang, Y., Pan, H., et al. (2013). Cationic Polypeptide Micelle-Based Antigen Delivery System: A Simple and Robust Adjuvant to Improve Vaccine Efficacy. *J. Controlled Release* 170, 259–267. doi:10.1016/j.jconrel.2013.05.027

Lv, S., Song, W., Tang, Z., Li, M., Yu, H., Hong, H., et al. (2014). Charge-Conversional PEG-Polypeptide Polyionic Complex Nanoparticles from Simple Blending of a Pair of Oppositely Charged Block Copolymers as an Intelligent Vehicle for Efficient Antitumor Drug Delivery. *Mol. Pharmaceutics* 11, 1562–1574. doi:10.1021/mp4007387

Ma, J., Zhang, J., Chi, L., Liu, C., Li, Y., and Tian, H. (2020). Preparation of Poly(glutamic Acid) Shielding Micelles Self-Assembled from Polylysine-B-Polyphenylalanine for Gene and Drug Codelivery. *Chin. Chem. Lett.* 31, 1427–1431. doi:10.1016/j.cclet.2020.02.034

Macewan, S. R., and Chilkoti, A. (2012). Digital Switching of Local Arginine Density in a Genetically Encoded Self-Assembled Polypeptide Nanoparticle Controls Cellular Uptake. *Nano Lett.* 12, 3322–3328. doi:10.1021/nl301529p

Mccurdie, M. P., and Belfiore, L. A. (1999). Solid-state Complexes of poly(L-Histidine) with Metal Chlorides from the First Row of Thed-Block. *J. Polym. Sci. B Polym. Phys.* 37, 301–309. doi:10.1002/(SICI)1099-0488(19990215)37:4<301::AID-POLB4>3.0.CO;2-H

Mebarek, N., Aubert-Pouëssel, A., Gérardin, C., Vicente, R., Devoisselle, J.-M., and Bégu, S. (2013). Polymeric Micelles Based on Poly(methacrylic Acid) Block-Containing Copolymers with Different Membrane Destabilizing Properties for Cellular Drug Delivery. *Int. J. Pharmaceutics* 454, 611–620. doi:10.1016/j.ijpharm.2013.06.014

Mitchell, D. J., Steinman, L., Kim, D. T., Fathman, C. G., and Rothbard, J. B. (2000). Polyarginine Enters Cells More Efficiently Than Other Polycationic Homopolymers. *J. Pept. Res.* 56, 318–325. doi:10.1034/j.1399-3011.2000.00723.x

Miyata, K., Kakizawa, Y., Nishiyama, N., Harada, A., Yamasaki, Y., Koyama, H., et al. (2004). Block Catiomer Polyplexes with Regulated Densities of Charge and Disulfide Cross-Linking Directed to Enhance Gene Expression. *J. Am. Chem. Soc.* 126, 2355–2361. doi:10.1021/ja0379666

Nishiyama, N., Nakagishi, Y., Morimoto, Y., Lai, P.-S., Miyazaki, K., Urano, K., et al. (2009). Enhanced Photodynamic Cancer Treatment by Supramolecular Nanocarriers Charged with Dendrimer Phthalocyanine. *J. Controlled Release* 133, 245–251. doi:10.1016/j.jconrel.2008.10.010

Oe, Y., Christie, R. J., Naito, M., Low, S. A., Fukushima, S., Toh, K., et al. (2014). Actively-targeted Polyion Complex Micelles Stabilized by Cholesterol and Disulfide Cross-Linking for Systemic Delivery of siRNA to Solid Tumors. *Biomaterials* 35, 7887–7895. doi:10.1016/j.biomaterials.2014.05.041

Ohya, Y., Takeda, S., Shibata, Y., Ouchi, T., Kano, A., Iwata, T., et al. (2011). Evaluation of Polyanion-Coated Biodegradable Polymeric Micelles as Drug Delivery Vehicles. *J. Controlled Release* 155, 104–110. doi:10.1016/j.jconrel.2010.11.008

Ohya, Y., Takeda, S., Shibata, Y., Ouchi, T., and Maruyama, A. (2010). Preparation of Highly Stable Biodegradable Polymer Micelles by Coating with Polyion Complex. *Macromol. Chem. Phys.* 211, 1750–1756. doi:10.1002/macp.201000167

Osada, K., Oshima, H., Kobayashi, D., Doi, M., Enoki, M., Yamasaki, Y., et al. (2010). Quantized Folding of Plasmid DNA Condensed with Block Catiomer into Characteristic Rod Structures Promoting Transgene Efficacy. *J. Am. Chem. Soc.* 132, 12343–12348. doi:10.1021/ja102739b

Osada, K., Shiotani, T., Tockary, T. A., Kobayashi, D., Oshima, H., Ikeda, S., et al. (2012). Enhanced Gene Expression Promoted by the Quantized Folding of pDNA within Polyplex Micelles. *Biomaterials* 33, 325–332. doi:10.1016/j.biomaterials.2011.09.046

Oupicky, D., Ogris, M., Howard, K. A., Dash, P. R., Ulbrich, K., and Seymour, L. W. (2002). Importance of Lateral and Steric Stabilization of Polyelectrolyte Gene Delivery Vectors for Extended Systemic Circulation. *Mol. Ther.* 5, 463–472. doi:10.1006/mthe.2002.0568

Pittella, F., Zhang, M., Lee, Y., Kim, H. J., Tockary, T., Osada, K., et al. (2011). Enhanced Endosomal Escape of siRNA-Incorporating Hybrid Nanoparticles from Calcium Phosphate and PEG-Block Charge-Conversional Polymer for Efficient Gene Knockdown with Negligible Cytotoxicity. *Biomaterials* 32, 3106–3114. doi:10.1016/j.biomaterials.2010.12.057

Putnam, D., Gentry, C. A., Pack, D. W., and Langer, R. (2001). Polymer-based Gene Delivery with Low Cytotoxicity by a Unique Balance of Side-Chain Termini. *Proc. Natl. Acad. Sci.* 98, 1200–1205. doi:10.1073/pnas.98.3.1200

Schröder, T., Niemeier, N., Afonin, S., Ulrich, A. S., Krug, H. F., and Bräse, S. (2008). Peptoidic Amino- and Guanidinium-Carrier Systems: Targeted Drug Delivery into the Cell Cytosol or the Nucleus. *J. Med. Chem.* 51, 376–379. doi:10.1021/jm070603m

Singh, S. P., Wishnok, J. S., Keshive, M., Deen, W. M., and Tannenbaum, S. R. (1996). The Chemistry of the S-Nitrosoglutathione/glutathione System. *Proc. Natl. Acad. Sci.* 93, 14428–14433. doi:10.1073/pnas.93.25.14428

Song, H., Wang, R., Xiao, H., Cai, H., Zhang, W., Xie, Z., et al. (2013). A Cross-Linked Polymeric Micellar Delivery System for Cisplatin(IV) Complex. *Eur. J. Pharmaceutics Biopharmaceutics* 83, 63–75. doi:10.1016/j.ejpb.2012.09.004

Sugisaki, K., Usui, T., Nishiyama, N., Jang, W.-D., Yanagi, Y., Yamagami, S., et al. (2008). Photodynamic Therapy for Corneal Neovascularization Using Polymeric Micelles Encapsulating Dendrimer Porphyrins. *Invest. Ophthalmol. Vis. Sci.* 49, 894–899. doi:10.1167/iovs.07-0389

Sun, H., Guo, B., Cheng, R., Meng, F., Liu, H., and Zhong, Z. (2009). Biodegradable Micelles with Sheddable Poly(ethylene Glycol) Shells for Triggered Intracellular Release of Doxorubicin. *Biomaterials* 30, 6358–6366. doi:10.1016/j.biomaterials.2009.07.051

Takeda, K. M., Yamasaki, Y., Dirisala, A., Ikeda, S., Tockary, T. A., Toh, K., et al. (2017). Effect of Shear Stress on Structure and Function of Polyplex Micelles from Poly(ethylene Glycol)-Poly(L -lysine) Block Copolymers as Systemic Gene Delivery Carrier. *Biomaterials* 126, 31–38. doi:10.1016/j.biomaterials.2017.02.012

Teng, F., Deng, P., Song, Z., Zhou, F., Feng, R., and Liu, N. (2017). *In Vitro* characterization of pH-Sensitive Azithromycin-Loaded Methoxy Poly (Ethylene Glycol)-Block-Poly (Aspartic Acid-Graft-Imidazole) Micelles. *J. Colloid Interf. Sci.* 496, 16–25. doi:10.1016/j.jcis.2017.02.011

Thambi, T., Son, S., Lee, D. S., and Park, J. H. (2016). Poly(ethylene Glycol)-B-Poly(lysine) Copolymer Bearing Nitroaromatics for Hypoxia-Sensitive Drug Delivery. *Acta Biomater.* 29, 261–270. doi:10.1016/j.actbio.2015.10.011

Thomas, D. D., Espey, M. G., Ridnour, L. A., Hofseth, L. J., Mancardi, D., Harris, C. C., et al. (2004). Hypoxic Inducible Factor 1α, Extracellular Signal-Regulated Kinase, and P53 Are Regulated by Distinct Threshold Concentrations of Nitric Oxide. *Pnas* 101, 8894–8899. doi:10.1073/pnas.0400453101

Thomas, D. D., Ridnour, L. A., Isenberg, J. S., Flores-Santana, W., Switzer, C. H., Donzelli, S., et al. (2008). The Chemical Biology of Nitric Oxide: Implications in Cellular Signaling. *Free Radic. Biol. Med.* 45, 18–31. doi:10.1016/j.freeradbiomed.2008.03.020

Tsikas, D., Böger, R. H., Sandmann, J., Bode-Böger, S. M., and Frölich, J. C. (2000). Endogenous Nitric Oxide Synthase Inhibitors Are Responsible for theL-Arginine Paradox. *FEBS Lett.* 478, 1–3. doi:10.1016/S0014-5793(00)01686-0

Vachutinsky, Y., Oba, M., Miyata, K., Hiki, S., Kano, M. R., Nishiyama, N., et al. (2011). Antiangiogenic Gene Therapy of Experimental Pancreatic Tumor by sFlt-1 Plasmid DNA Carried by RGD-Modified Crosslinked Polyplex Micelles. *J. Controlled Release* 149, 51–57. doi:10.1016/j.jconrel.2010.02.002

Wang, J., Sun, J., Chen, Q., Gao, Y., Li, L., Li, H., et al. (2012). Star-shape Copolymer of Lysine-Linked Di-tocopherol Polyethylene Glycol 2000 Succinate for Doxorubicin Delivery with Reversal of Multidrug Resistance. *Biomaterials* 33, 6877–6888. doi:10.1016/j.biomaterials.2012.06.019

Wang, J., Xu, W., Guo, H., Ding, J., Chen, J., Guan, J., et al. (2015a). Selective Intracellular Drug Delivery from pH-Responsive Polyion Complex Micelle for Enhanced Malignancy Suppression *In Vivo*. *Colloids Surf. B: Biointerfaces* 135, 283–290. doi:10.1016/j.colsurfb.2015.07.065

Wang, P., Liu, W., Liu, S., Yang, R., Pu, Y., Zhang, W., et al. (2019). pH-responsive Nanomicelles of Poly(ethylene Glycol)-Poly(ε-Caprolactone)-poly(L-Histidine) for Targeted Drug Delivery. *J. Biomater. Sci. Polym. Edition* 31, 277–292. doi:10.1080/09205063.2019.1687132

Wang, Y., Li, P., Chen, F., Jia, L., Xu, Q., Gai, X., et al. (2017). A Novel pH-Sensitive Carrier for the Delivery of Antitumor Drugs: Histidine-Modified Auricularia Auricular Polysaccharide Nano-Micelles. *Sci. Rep.* 7, 4751. doi:10.1038/s41598-017-04428-8

Wang, Y., Li, Q. Y., Liu, X. B., Zhang, C. Y., Wu, Z. M., and Guo, X. D. (2015b). Mesoscale Simulations and Experimental Studies of pH-Sensitive Micelles for Controlled Drug Delivery. *ACS Appl. Mater. Inter.* 7, 25592–25600. doi:10.1021/acsami.5b08366

Wang, Y., Yang, T., Wang, X., Dai, W., Wang, J., Zhang, X., et al. (2011). Materializing Sequential Killing of Tumor Vasculature and Tumor Cells via Targeted Polymeric Micelle System. *J. Controlled Release* 149, 299–306. doi:10.1016/j.jconrel.2010.10.027

Wang, Z., Zhang, Y., Cao, B., Ji, Z., Luo, W., Zhai, S., et al. (2019). Explosible Nanocapsules Excited by Pulsed Microwaves for Efficient Thermoacoustic-Chemo Combination Therapy. *Nanoscale* 11, 1710–1719. doi:10.1039/C8NR08498J

Wen, H.-Y., Dong, H.-Q., Xie, W.-j., Li, Y.-Y., Wang, K., Pauletti, G. M., et al. (2011). Rapidly Disassembling Nanomicelles with Disulfide-Linked PEG Shells for Glutathione-Mediated Intracellular Drug Delivery. *Chem. Commun.* 47, 3550–3552. doi:10.1039/C0CC04983B

Wender, P. A., Galliher, W. C., Goun, E. A., Jones, L. R., and Pillow, T. H. (2008). The Design of Guanidinium-Rich Transporters and Their Internalization Mechanisms. *Adv. Drug Deliv. Rev.* 60, 452–472. doi:10.1016/j.addr.2007.10.016

Wender, P. A., Mitchell, D. J., Pattabiraman, K., Pelkey, E. T., Steinman, L., and Rothbard, J. B. (2000). The Design, Synthesis, and Evaluation of Molecules that Enable or Enhance Cellular Uptake: Peptoid Molecular Transporters. *Proc. Natl. Acad. Sci.* 97, 13003–13008. doi:10.1073/pnas.97.24.13003

Wright, E. R., and Conticello, V. P. (2002). Self-assembly of Block Copolymers Derived from Elastin-Mimetic Polypeptide Sequences. *Adv. Drug Deliv. Rev.* 54, 1057–1073. doi:10.1016/S0169-409X(02)00059-5

Wu, H., Zhu, L., and Torchilin, V. P. (2013). pH-sensitive Poly(histidine)-PEG/DSPE-PEG Co-polymer Micelles for Cytosolic Drug Delivery. *Biomaterials* 34, 1213–1222. doi:10.1016/j.biomaterials.2012.08.072

Wu, J.-L., Tian, G.-X., Yu, W.-J., Jia, G.-T., Sun, T.-Y., and Gao, Z.-Q. (2016). pH-Responsive Hyaluronic Acid-Based Mixed Micelles for the Hepatoma-Targeting Delivery of Doxorubicin. *Ijms* 17, 364. doi:10.3390/ijms17040364

Xiao, K., Luo, J., Fowler, W. L., Li, Y., Lee, J. S., Xing, L., et al. (2009). A Self-Assembling Nanoparticle for Paclitaxel Delivery in Ovarian Cancer. *Biomaterials* 30, 6006–6016. doi:10.1016/j.biomaterials.2009.07.015

Xu, H., Yao, Q., Cai, C., Gou, J., Zhang, Y., Zhong, H., et al. (2015a). Amphiphilic Poly(amino Acid) Based Micelles Applied to Drug Delivery: The *In Vitro* and *In Vivo* Challenges and the Corresponding Potential Strategies. *J. Controlled Release* 199, 84–97. doi:10.1016/j.jconrel.2014.12.012

Xu, W., Fan, X., Zhao, Y., and Li, L. (2015b). Cysteine Modified and Bile Salt Based Micelles: Preparation and Application as an Oral Delivery System for Paclitaxel. *Colloids Surf. B: Biointerfaces* 128, 165–171. doi:10.1016/j.colsurfb.2015.02.031

Yao, C., Liu, J., Wu, X., Tai, Z., Gao, Y., Zhu, Q., et al. (2016). Reducible Self-Assembling Cationic Polypeptide-Based Micelles Mediate Co-delivery of Doxorubicin and microRNA-34a for Androgen-independent Prostate Cancer Therapy. *J. Controlled Release* 232, 203–214. doi:10.1016/j.jconrel.2016.04.034

Yeh, J.-C., Yang, H.-H., Hsu, Y.-T., Su, C.-M., Lee, T.-H., and Lou, S.-L. (2013). Synthesis and Characteristics of Biodegradable and Temperature Responsive Polymeric Micelles Based on Poly(aspartic Acid)-G-poly(N-Isopropylacrylamide-Co-N,n-Dimethylacrylamide). *Colloids Surf. A: Physicochemical Eng. Aspects* 421, 1–8. doi:10.1016/j.colsurfa.2012.12.014

Yin, L., Bao, Y., Liu, L., Wang, J., and Chen, L. (2020). Acid-sensitive Reactive Oxygen Species Triggered Dual-drug Delivery Systems for Chemo-photodynamic Therapy to Overcome Multidrug Resistance. *Polym. Int.* 69, 619–626. doi:10.1002/pi.5997

Zhai, S., Hu, X., Ji, Z., Qin, H., Wang, Z., Hu, Y., et al. (2019). Pulsed Microwave-Pumped Drug-free Thermoacoustic Therapy by Highly Biocompatible and Safe Metabolic Polyarginine Probes. *Nano Lett.* 19, 1728–1735. doi:10.1021/acs.nanolett.8b04723

Zhang, H., Wang, K., Zhang, P., He, W., Song, A., and Luan, Y. (2016). Redox-Sensitive Micelles Assembled From Amphiphilic mPEG-PCL-SS-DTX Conjugates for the Delivery of Docetaxel. *Colloids Surf. B. Biointerfaces* 142, 89–97. doi:10.1016/j.colsurfb.2016.02.045

Zhang, M., Chen, X., Li, C., and Shen, X. (2020). Charge-reversal Nanocarriers: An Emerging Paradigm for Smart Cancer Nanomedicine. *J. Controlled Release* 319, 46–62. doi:10.1016/j.jconrel.2019.12.024

Zheng, C., Zheng, M., Gong, P., Deng, J., Yi, H., Zhang, P., et al. (2013). Polypeptide Cationic Micelles Mediated Co-delivery of Docetaxel and siRNA for Synergistic Tumor Therapy. *Biomaterials* 34, 3431–3438. doi:10.1016/j.biomaterials.2013.01.053

Zheng, P., Liu, Y., Chen, J., Xu, W., Li, G., and Ding, J. (2020). Targeted pH-Responsive Polyion Complex Micelle for Controlled Intracellular Drug Delivery. *Chin. Chem. Lett.* 31, 1178–1182. doi:10.1016/j.cclet.2019.12.001

Conflict of Interest: The authors declare that the research was conducted in the absence of any commercial or financial relationships that could be construed as a potential conflict of interest.

Publisher's Note: All claims expressed in this article are solely those of the authors and do not necessarily represent those of their affiliated organizations, or those of the publisher, the editors and the reviewers. Any product that may be evaluated in this article, or claim that may be made by its manufacturer, is not guaranteed or endorsed by the publisher.

frontiers in Bioengineering and Biotechnology

ORIGINAL RESEARCH
published: 15 October 2021
doi: 10.3389/fbioe.2021.751757

An NIR-II Responsive Nanoplatform for Cancer Photothermal and Oxidative Stress Therapy

Bin Huang[1†], Yuanpeng Huang[2†], Han Han[3], Qiuyue Ge[3], Dongliang Yang[3], Yanling Hu[3], Meng Ding[4]*, Yanqing Su[5], Yanbin He[1,6], Jinjun Shao[2] and Jianfeng Chu[1,6]**

[1]Academy of Integrative Medicine of Fujian University of Traditional Chinese Medicine, Fuzhou, China, [2]Xiamen Hospital of Traditional Chinese Medicine, Xiamen, China, [3]School of Physical and Mathematical Sciences, Nanjing Tech University (NanjingTech), Nanjing, China, [4]Nanjing Stomatological Hospital, Medical School of Nanjing University, Nanjing, China, [5]Department of Pharmacy, Xiamen Children's Hospital, Xiamen, China, [6]Fujian Key Laboratory of Integrative Medicine on Geriatrics, Fujian University of Traditional Chinese Medicine, Fuzhou, China

OPEN ACCESS

Edited by:
Bin He,
Sichuan University, China

Reviewed by:
Xianglong Hu,
South China Normal University, China
Xu Zhen,
Nanjing University, China

***Correspondence:**
Dongliang Yang
yangdl1023@njtech.edu.cn
Meng Ding
xzdingmeng@163.com
Jianfeng Chu
jianfengchu@126.com

[†]These authors have contributed equally to this work

Specialty section:
This article was submitted to Biomaterials, a section of the journal Frontiers in Bioengineering and Biotechnology

Received: 02 August 2021
Accepted: 13 September 2021
Published: 15 October 2021

Citation:
Huang B, Huang Y, Han H, Ge Q, Yang D, Hu Y, Ding M, Su Y, He Y, Shao J and Chu J (2021) An NIR-II Responsive Nanoplatform for Cancer Photothermal and Oxidative Stress Therapy. Front. Bioeng. Biotechnol. 9:751757. doi: 10.3389/fbioe.2021.751757

Chemodynamic therapy as an emerging therapeutic strategy has been implemented for oncotherapy. However, the reactive oxygen species can be counteracted by the exorbitant glutathione (GSH) produced by the tumor cells before exerting the antitumor effect. Herein, borneol (NB) serving as a monoterpenoid sensitizer, and copper sulfide (CuS NPs) as an NIR-II photothermal agent were loaded in a thermo-responsive vehicle (NB/CuS@PCM NPs). Under 1,060-nm laser irradiation, the hyperthermia produced by CuS NPs can be used for photothermal therapy and melt the phase change material for drug delivery. In the acidity microenvironment, the CuS NPs released from NB/CuS@PCM NPs could degrade to Cu^{2+}, then Cu^{2+} was reduced to Cu^{+} during the depletion of GSH. As Fenton-like catalyst, the copper ion could convert hydrogen peroxide into hydroxyl radicals for chemodynamic therapy. Moreover, the NB originated from NB/CuS@PCM NPs could increase the intracellular ROS content to improve the treatment outcome of chemodynamic therapy. The animal experimental results indicated that the NB/CuS@PCM NPs could accumulate at the tumor site and exhibit an excellent antitumor effect. This work confirmed that the combination of oxidative stress–induced damage and photothermal therapy is a potential therapeutic strategy for cancer treatment.

Keywords: photothermal ablation therapy, chemodynamic therapy, phase change material, drug delivery, responsive nanomaterial

INTRODUCTION

Due to the hypoxic tumor microenvironment, tumor cells undergo hypoxic metabolism and inhabit in an elevated level of redox homeostasis circumstance (Yang et al., 2020). As an adaptive response, tumor cells will improve their antioxidant capacity, for example, the increased glutathione (GSH) levels in tumor cells further endow the tumor cells with anti-apoptosis and drug-resistant performance (Bansal and Simon, 2018; Liu Z. et al., 2020). Even worse, the exorbitant GSH in tumor cells as a reactive oxygen species (ROS) scavenger not only dramatically reduces the therapeutic efficacy of ROS-medicated therapy but also facilitates tumor metastasis, which makes cancer with high mortality and more difficult to be treated (McCarty et al., 2010; Lin X. et al., 2019; Liu M. D. et al., 2020; Zhu et al., 2021).

Borneol (NB) is a bicyclic monoterpenoid that can be extracted from a variety of Chinese herbal plants, such as valerian, lavender, and chamomile (Su et al., 2013). NB possesses analgesic,

antibacterial, and anti-inflammatory effects, which has been approved by the Food and Drug Administration and widely used in the fields of cosmetics, food, and pharmaceuticals (Bhatia et al., 2008; Cherneva et al., 2012). NB, which serves as a chemosensitizer, can potentiate the therapeutic effect of anticancer drugs (such as cisplatin, paclitaxel, and doxorubicin) through cellular redox homeostasis interference by activating ROS-mediated oxidative damage (Horváthová et al., 2009; Su et al., 2013; Cao et al., 2020). Unfortunately, the overexpressed glutathione (GSH) in the malignant tumor generally attenuates the therapeutic effect of ROS-medicated therapy. Therefore, the synergistic therapy with tumor microenvironment remodeling property is critical for the eradication of the malignant tumor (Liang et al., 2020).

Recently, many chemodynamic agents based on variable metal ions (such as Mo^{5+}/Mo^{6+}, Mn^{2+}/Mn^{4+}, Fe^{2+}/Fe^{3+}, and Cu^{+}/Cu^{2+}) have been widely implemented in tumor microenvironment reconstruction (Liu et al., 2019; Ashok et al., 2020; Sun et al., 2020; Yang et al., 2020; Li Y. et al., 2021; Sun et al., 2021). Using this strategy, a satisfactory outcome is shown in the improvement of the treatment effect. For example, Yang et al. reported $PtCu_3$ nanocages with horseradish peroxidase–like and GSH peroxidase–like catalytic activity, which could consume GSH for boosting the therapeutic effect of chemodynamic therapy (CDT)/sonodynamic therapy (Zhong et al., 2020; Yang H. et al., 2021). The Zhao group fabricated a hydrogen peroxide (H_2O_2)–responsive tin ferrite ($SnFe_2O_4$) nanoparticle with GSH peroxidase–like, Fenton-like, and catalase-like performance for GSH depletion and NIR-I photothermal-CDT (Feng et al., 2021). However, NIR-I light with limited tissue penetration depth and the maximum permissible exposure is 0.33 W cm^{-2}, which is worse than NIR-II light (Shi et al., 2020; Dai et al., 2021; Wang et al., 2021; Zhang et al., 2021). To overcome this predicament, Sun et al. prepared copper sulfide (CuS) with NIR-II photothermal ability functionalized manganese dioxide nanoparticles for GSH elimination and NIR-II photothermal augmented CDT because Cu^{2+} can be reduced to Cu^{+} by the intratumoral GSH and then the H_2O_2 in the tumor can be catalyzed into the hydroxyl radical for CDT (Ma et al., 2019). Therefore, the ingenious design of nanomaterials with GSH consumption and intracellular oxidation homeostasis interference is critical for improving the therapeutic effect of ROS-medicated therapy.

Herein, the phase change material (PCM) was used to encapsulate CuS NPs and NB for disrupting intracellular redox homeostasis and thermal deactivation tumor cells. The NB serving as a chemosensitizer to enhance ROS generation and the CuS NPs working as NIR-II photothermal agent with GSH elimination and Fenton-like catalytic performance were encapsulated into the PCM vehicle to prepare the NB/CuS@PCM NPs for disturbing intracellular redox homeostasis after the PCM was melted by the heat produced by CuS NPs. Subsequently, H_2O_2 in the tumor cells was catalyzed by copper ions to generate hydroxyl radicals for CDT *via* Fenton-like reaction (Ma et al., 2019). Furthermore, the NB could improve intracellular ROS content to boost the CDT performance (**Scheme 1**). Combined with the oxidative stress–induced damage and photothermal therapy, NB/CuS@PCM NPs showed a pronounced antitumor effect *in vitro* and *in vivo*, demonstrating that NB/CuS@PCM NPs would be a potential candidate for oncotherapy.

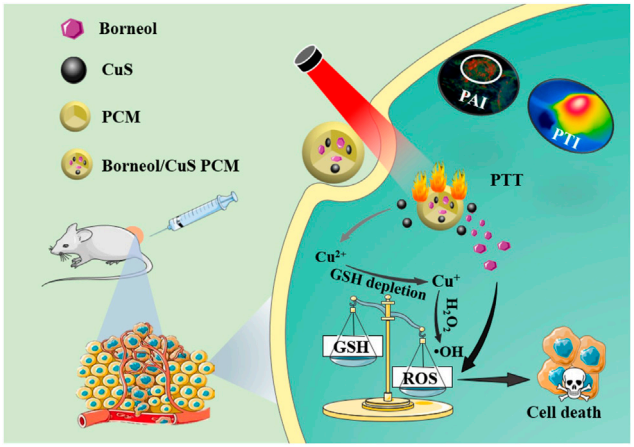

SCHEME 1 | NB/CuS@PCM NPs for tumor photothermal and oxidative stress therapy.

MATERIALS AND METHODS

Materials

Crude borneol was provided by Fujian Green Pine CO., Ltd. and further purified (purity ≥97%) by Fujian Nanping Green Pine Chemical Co., Ltd. Copper chloride ($CuCl_2$), sodium sulfide, and gallic acid were offered by Sinopharm Chemical Reagent Co., Ltd. (Shanghai, China). Dichlorofluorescein diacetate (DCFH-DA), thiazolyl blue tetrazolium bromide (MTT), and propidium iodide (PI) were provided by Beyotime Biotechnology Co., Ltd., Shanghai, China). Glutathione, polyvinylpyrrolidone (K30), and 5,5′-dithiobis-(2-nitrobenzoic acid) (DTNB) were available from Shenggong Biotech Co., Ltd. (China). Murine mammary carcinoma 4T1 cells and the cell culture medium were obtained from Keygen Biotech Co., Ltd. (China).

Synthesis of CuS NPs

100 mg of polyvinylpyrrolidone, 20 mg of gallic acid, and 86 mg of $CuCl_2$ were dissolved in 10 ml of Milli-Q water. After stirring for 1 h, 200 mg of sodium sulfide was added. The solution color would change to black within seconds. After stirring for 4 h, the resulting product was dialyzed with a 10,000 Da-molecular weight cutoff dialysis bag and filtered using a 0.22-μm syringe filter.

Preparation of NB/CuS@PCM NPs

The phase change material (PCM) consisting of 1-hexadecanol and oleic acid (3.5:1) was prepared as previously described (Ewulonu et al., 2019; Zhang et al., 2020; Yang D. et al., 2021; Xu et al., 2021). To construct the NB/CuS@PCM NPs, 20 mg of ovolecithin, 10 mg of DSPE-PEG, and 10 mg of CuS NPs were

dissolved in 10 ml of water and warmed up to 50°C. The ethanol mixture of PCM (10 mg) and NB (10 mg) was quickly injected into the aforementioned solution under sonication conditions. Then the resulting solution was cooled in an ice bath. After purification by dialysis and filtration, NB/CuS@PCM NPs were harvested. The loaded content of NB in CuS/NB@PCM NPs was measured using a UV-vis spectrometer through the chromogenic reaction (Li et al., 2008).

Characterization

The size distribution and morphology of NPs were analyzed *via* a dynamic light scatterer, scanning electron microscope, and transmission electron microscope. The powder X-ray diffraction (XRD) pattern was implemented *via* a D8 Advance X-ray diffractometer. A UV-3600 UV-vis-NIR spectrometer was used for the collection of absorbance spectra. An E50 infrared camera was adopted to measure the sample temperature change.

The release behavior of NB was monitored using vanillin as a chromogenic reagent, as in the method Li described previously (Li et al., 2008). In brief, a certain amount of the concentrated sulfuric acid solution containing 10 mg ml^{-1} vanillin was added to 250 μL of the sample or NB standard solution. The resulting solution was placed at room temperature for 10 min. Finally, the resulting solution was diluted (1:1) with water before monitoring the absorbance spectrum change.

Photothermal Measurement

Different concentrations (0, 25, 50, and 100 μg ml^{-1}) of NB/CuS@PCM NPs were exposed to a 1,060-nm laser (1 W cm^{-2}). And the temperature variation of the sample was determined using a FLIR infrared camera. To investigate the effect of laser power density, NB/CuS@PCM NPs (100 μg ml^{-1}) were exposed to the 1,060-nm laser (0.4, 0.6, 0.8, and 1 W cm^{-2}). To evaluate the photothermal stability, the temperature variation of NB/CuS@PCM NPs (100 μg ml^{-1}) was monitored during five laser (1 W cm^{-2}) on–off cycles.

GSH Depletion

The depletion of GSH was performed as our work previously described (Liu et al., 2019; Shi et al., 2020). In brief, different concentrations of NB/CuS@PCM NP solution (pH = 6.5) were mixed with GSH and DTNB probe (solvent, dimethyl sulfoxide/water, 1:1). The concentrations of GSH and DTNB probe were 10 and 10 mM, respectively. Then the absorbance spectra of samples were collected by using a UV-vis-NIR spectrometer.

Chemodynamic Activity Assay

The methylene blue (MB) probe can react with the hydroxyl radical and then the blue color disappeared, which can confirm the emergence of the hydroxyl radical (Li Q. et al., 2021). To verify the catalytic performance of NB/CuS@PCM NPs, the NB/CuS@PCM NP solution treated with the 1,060-nm laser (1 mg ml^{-1}) was incubated with different solutions (pH = 6.5), for example, NB/CuS@PCM NPs + MB, NB/CuS@PCM NPs + MB + H_2O_2. The concentration of MB and H_2O_2 was 10 μg ml^{-1} and 10 mM, respectively. After incubation for 3 h, the samples were characterized with a UV-vis spectrometer.

Cell Viability Test

The MTT assay was used to evaluate the cytotoxicity of NB/CuS@PCM NPs (Yang et al., 2016; Cheng et al., 2021; Menaga et al., 2021; Yu et al., 2021). First, 150 μL of 4T1 cells (5×10^5 cells ml^{-1}) were added to each well (96-wells plate) and incubated for 16 h. Then the cells were treated with NB/CuS@PCM NPs and CuS@PCM NPs. To assess the photothermal therapeutic performance of nanoparticles, the cells were irradiated with the 1,060-nm laser. To assess the dark toxicity of nanoparticles, the cells were cultured without laser treatment. After cultivation for another 12 h, a routine cytotoxicity assay was implemented. Besides, after the cells were treated with NPs (100 μg ml^{-1}) and laser, the photothermal therapeutic efficiency was also confirmed by calcein AM and PI fluorescent staining.

Intracellular ROS Detection

The intracellular ROS generation was analyzed using a reactive oxygen fluorescent probe (DCFH-DA). First, NB/CuS@PCM and CuS@PCM NPs were treated with the 1,060-nm laser. And the resulting dispersion solutions (pH = 6.5, H_2O_2 = 50 μM) were co-cultivated with 4T1 cells for 1 day. Then the cell was stained with the DCFH-DA probe before fluorescent images were recorded using an X71 inverted fluorescence microscope (Olympus, Japan).

In vivo Antitumor Assay

All animal studies were carried out according to the ethical principles of Guide For the Care and Use of Laboratory Animals of Nanjing Tech University. To probe the therapeutic effect of NB/CuS@PCM NPs *in vivo*, BALB/c mice (female, 4–5 weeks) bearing 4T1 cell xenografts were stochastically assigned to four groups and received different treatments: 1) PBS, 2) NB/CuS@PCM NPs (2 mg ml^{-1}, 100 μL), 3) NB/CuS@PCM NPs (2 mg ml^{-1}, 100 μL) + laser. Four hours after intravenous injection, the tumor was irradiated with the 1,060-nm laser. Afterward, the tumor size was determined using a vernier caliper, and the body weights were monitored simultaneously. After treatment for 14 days, the mice were euthanized and then the organs were collected, fixed in 4% formaldehyde, and embedded in paraffin for histopathological analysis.

RESULTS AND DISCUSSION

First, the CuS NPs were prepared according to the previously reported literature with minor modification (Yang et al., 2014). The sodium sulfide solution was added to the $CuCl_2$ solution supplement with gallic acid to form the CuS NPs. The TEM image in **Supplementary Figure S1A** revealed that the diameter of CuS NPs was about 36 nm, which was consistent with the DLS result (**Supplementary Figure S1B**). As depicted in **Supplementary Figure S1C**, the XRD pattern of CuS NPs was consistent with the standard card (PDF#06–0,464). And the peaks located at 27.4, 29.2, 31.7, 48.0, 52.5, and 59.3° can be ascribed to the lattice planes of (101), (102), (103), (110), (108), and (116), respectively (Shen et al., 2019). The absorbance spectrum of CuS NPs exhibited that gallic acid modified CuS NPs possess a strong NIR-II absorbance

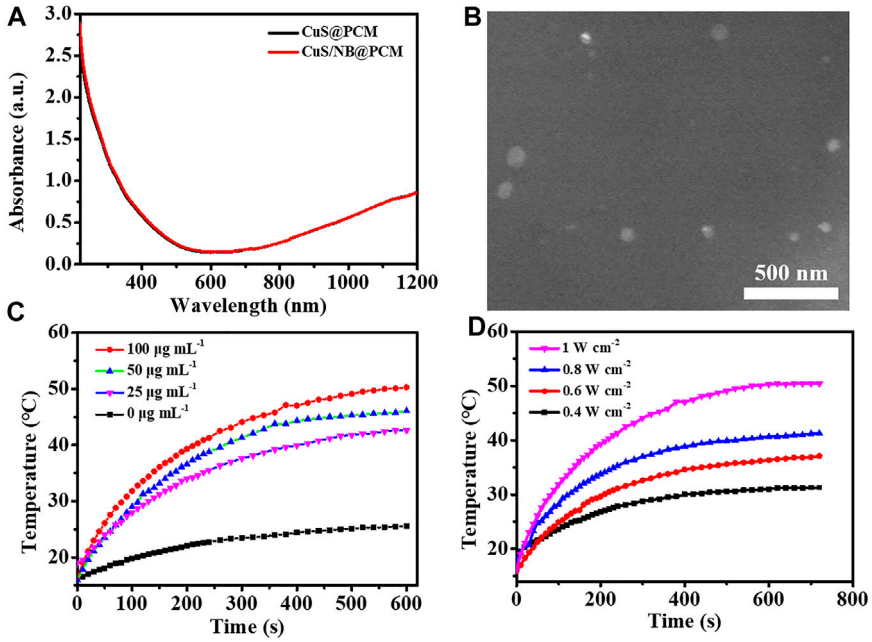

FIGURE 1 | (A) Absorption spectra of CuS@PCM NPs and NB/CuS@PCM NPs. **(B)** TEM image of NB/CuS@PCM NPs. **(C)** Elevated temperature profile of different concentrations of NB/CuS@PCM NPs under 1,064-nm laser (1 W cm^{-2}) exposure. **(D)** The elevated temperature profile of NB/CuS@PCM NPs (100 μg ml^{-1}) under different densities of 1,064-nm laser exposure.

(**Supplementary Figure S1D**). These results confirmed that the CuS NPs were successfully synthesized.

NB is a hydrophobic medical molecule, which sublimates easily and can be rapidly metabolized (Zhang et al., 2008). To realize the controllable delivery of NB and increase its medical effectiveness, NB was loaded to different vehicles (Cao et al., 2020; Li et al., 2015; Tang et al., 2015). To fabricate the on-demand therapeutic platform, the PCM carrier with temperature responsiveness was further used to load NB and NIR-II photothermal agent CuS NPs. The PCM consisting of 1-hexadecanol and oleic acid (mass ratio = 3.5: 1) has a suitable melting point of about 46°C (Zhang et al., 2020). After the PCM containing NB was dropped into the CuS NPs suspension solution, the NB/CuS@PCM NPs could be prepared when the solution was cooled in the ice water bath. As presented in **Figure 1A**, the absorption spectrum of NB/CuS@PCM NPs had no significant difference compare with CuS@PCM NPs. The SEM image indicated that the NB/CuS@PCM NPs held a spherical morphology with a mean diameter of 52.9 nm (**Figure 1B**, **Supplementary Figure S2A**). After treated with the 1,060-nm laser, the mean diameter of NB/CuS@PCM NPs decreased from 52.9 to 47.3 nm because PCM was melted by the heat produced by the CuS NPs (**Supplementary Figure S2B**). The loading efficiency of NB was measured to be 6.28%. Previous studies confirmed that the CuS NPs, which serves as a photothermal agent, have been widely used in biomedical application owing to their high photothermal conversion efficiency and high extinction coefficients in the NIR region (Yang N. et al., 2021). Then the photothermal performance of the NB/CuS@PCM NPs was confirmed under 1,060-nm laser illumination. As exhibited in **Figures 1C,D**, the temperature change of the NB/CuS@PCM NP dispersion revealed a dose and laser power dependence. In detail, the temperature of CuS/NB@PCM NPs (50 μg ml^{-1}) could increase to 42.6°C after 1,060-nm laser irradiation (1 W cm^{-2}) for 10 min. The eventual temperature of NB/CuS@PCM NPs (100 μg ml^{-1}) increased from 31.3°C to 50.4°C as the laser power density increases from 0.4 W cm^{-2} to 1 W cm^{-2}. The photothermal stability analysis indicated that the NB/CuS@PCM NPs possessed high stability even after four cycles of laser irradiation (**Figure 2A**). These results indicated that the CuS NPs encapsulated in the NB/CuS@PCM NPs could produce hyperthermia to melt the thermal-sensitive delivery system.

As we know, there is an acidic environment at the site of solid tumor (Lv et al., 2020). Under the NIR treatment, the CuS NPs released from the PCM were degraded to Cu^{2+}. Then the Cu^{2+} can be transformed into Cu^{+} for Fenton-like chemodynamic therapy (CDT) under the reduction of the exorbitant GSH in the tumor (Wang et al., 2020). As shown in **Figure 2B**, in the acidic environments, the NB/CuS@PCM NPs could deplete GSH in a dose-dependent relationship. The hydroxyl radical generation ability of the NB/CuS@PCM NPs was performed under different conditions (Lin L.-S. et al., 2019). As displayed in **Figure 2C**, under heat conditions, the solution mixed with NB/CuS@PCM NPs, MB, and H_2O_2 exhibited weak absorbance intensity at 665 nm, confirming that heat can promote the generation of hydroxyl radicals. Next, the photo-activated drug release behavior of the NB/CuS@PCM NPs was investigated under 1,060-nm laser irradiation (**Supplementary Figure S3**). As exhibited in **Figure 2D**, under laser irradiation, a plentiful supply of NB was released, demonstrating the NB/CuS@PCM NPs could achieve on-demand NB release. In contrast, without NIR

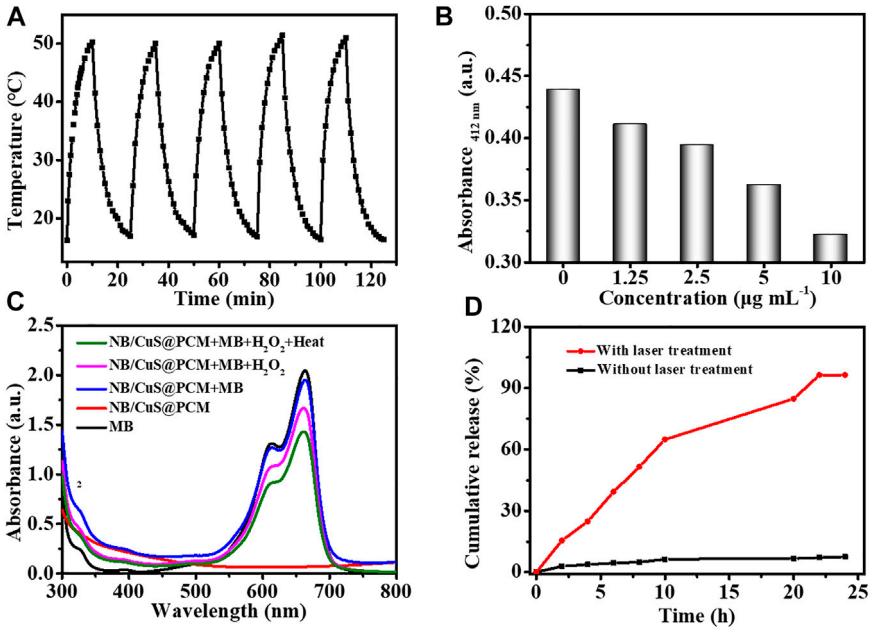

FIGURE 2 | (A) Photothermal stability assay of NB/CuS@PCM NPs. **(B)** GSH-depleting performance of NB/CuS@PCM NPs. **(C)** Generation ability of the hydroxyl radical under different conditions. **(D)** NB release behavior under different conditions.

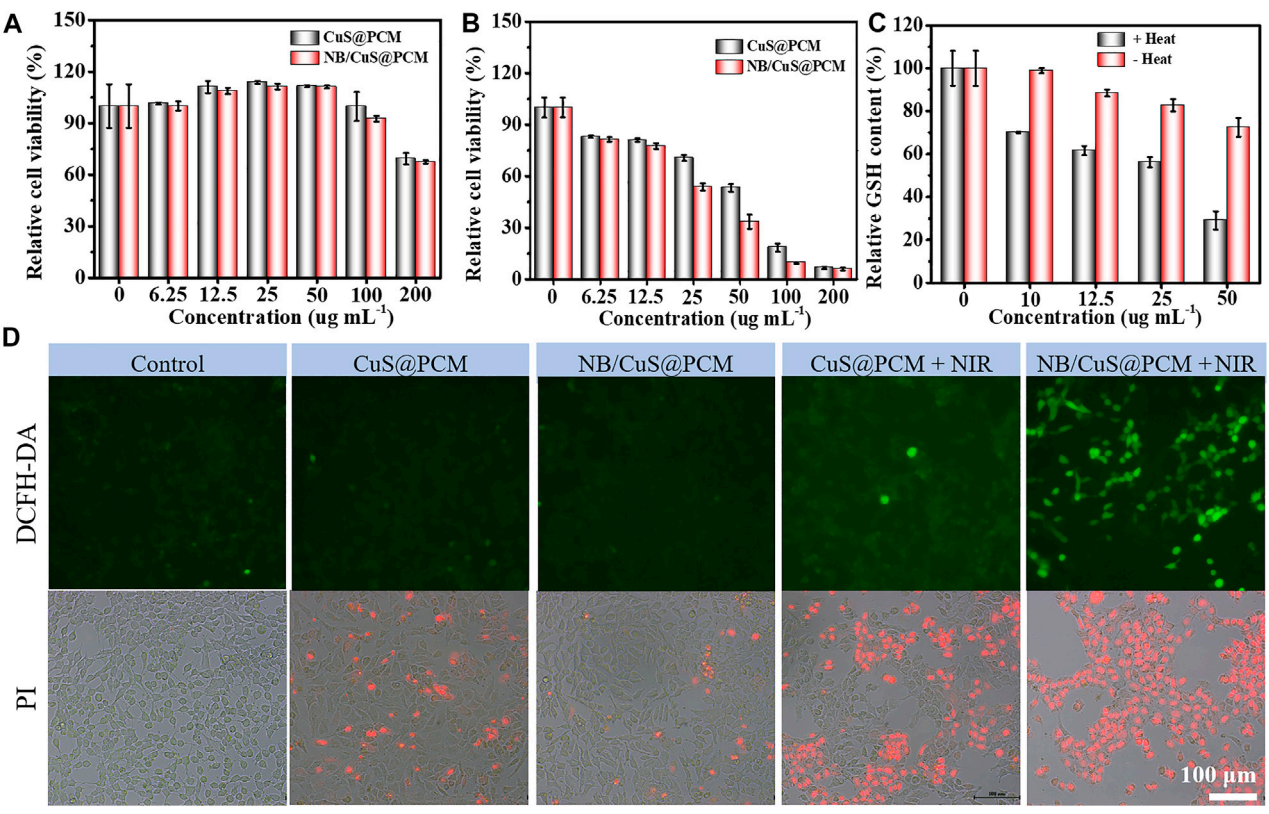

FIGURE 3 | (A) Cytocompatibility assay. **(B)** Cytotoxicity assay of NPs under laser exposure. **(C)** Intracellular GSH-depleting capability of NB/CuS@PCM NPs. **(D)** Intracellular ROS content assay using DCFH-DA probe (green fluorescence). Cell death staining analysis using PI probe (red fluorescence).

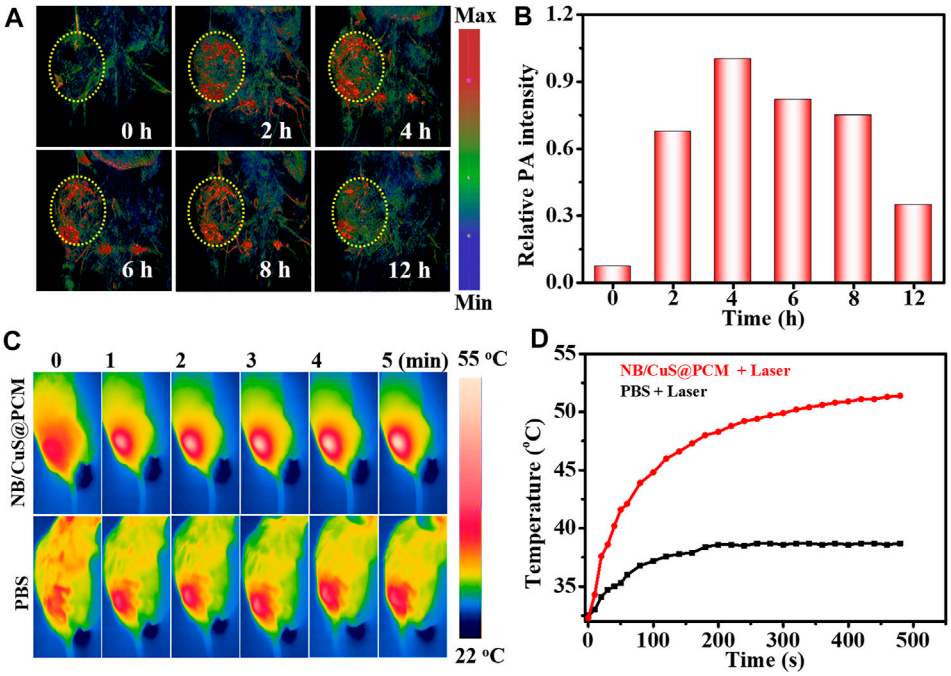

FIGURE 4 | (A,C) NIR-II photoacoustic imaging photo and thermal imaging photo of tumor after the intravenous injection of NB/CuS@PCM NPs. **(B,D)** Photoacoustic signal and temperature change profile after the administration of NB/CuS@PCM NPs.

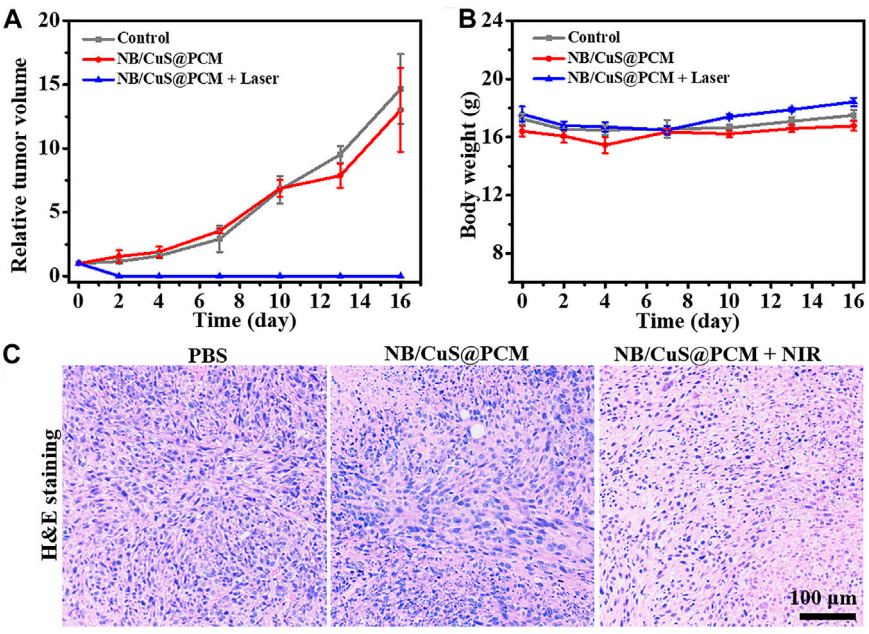

FIGURE 5 | (A) Change of tumor volume after intravenous injection of NPs or PBS with and without NIR light exposure. **(B)** Weight fluctuation of mice during the treatment. **(C)** Histopathological analysis of tumor tissue by H&E staining after 1 day of treatment.

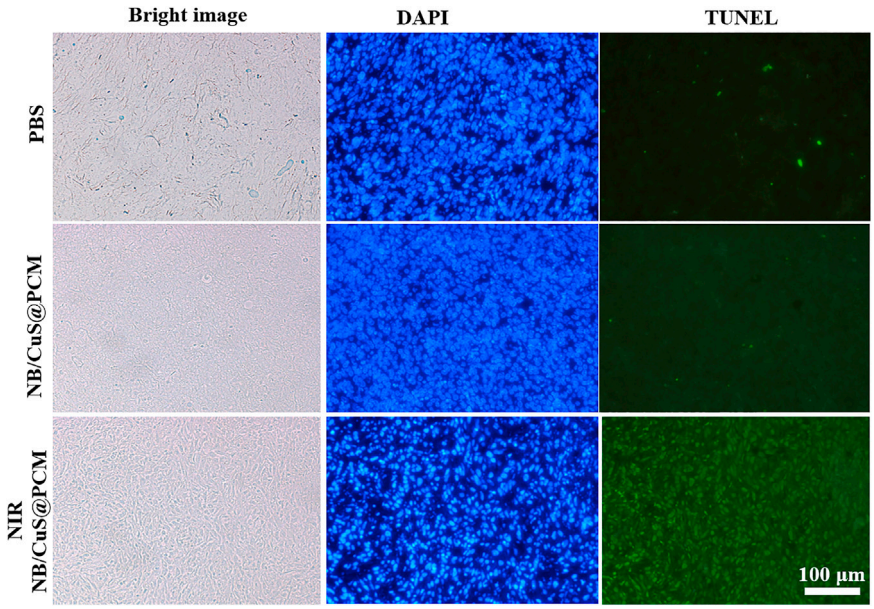

FIGURE 6 | TUNEL assay of tumor tissue after 1 day of treatment. Nucleus was labeled by DAPI with blue fluorescence. The DNA nick was labeled by FITC modified dUTP with green fluorescence.

treatment, a small amount of NB was released from NB/CuS@PCM NPs. More importantly, the uptake of NB/CuS@PCM NPs was enhanced upon exposure to the 1,060-nm laser (**Supplementary Figure S4**).

After validating the catalytic and photothermal properties of NB/CuS@PCM NPs, the antitumor activities of NB/CuS@PCM NPs were evaluated *in vitro*. First of all, the cytotoxicity of NB/CuS@PCM NPs toward 4T1 cells was carried out. As shown in **Figure 3A**, in the dark environment, the cell viability of 4T1 cells was greater than 78% even NB/CuS@PCM NPs was concentration up to 100 μg ml^{-1}. Upon exposure to 1,060-nm laser and NPs at 50 μg ml^{-1}, the cell viability decreased sharply to 53.1% (for CuS@PCM) and 33.4% (for NB/CuS@PCM) (**Figure 3B**). Previous results indicated NB can improve the uptake of anticancer drugs and enhance its therapeutic effect by the increment of ROS content (Cao et al., 2020; Horváthová et al., 2009). The cells treated with NB/CuS@PCM NPs and laser produced a large amount of ROS (**Figure 3D**, DCFH-DA staining, **Supplementary Figure S5**). Moreover, the GSH content in the cells treated with NB/CuS@PCM NPs reduced significantly (**Figure 3C**). These results confirmed that the NB can enhance the therapeutic effect of CDT by the cellular redox homeostasis interference because of the NB with good biocompatibility when the concentration is lesser than 500 μg ml^{-1} (**Supplementary Figure S6**). Finally, the antitumor effect of NB/CuS@PCM NPs is also verified by PI staining (Yan et al., 2021). And the result was consistent with the MTT assay (**Figure 3D**, PI staining).

To further confirm the feasibility of tumor therapy *in vivo*, the photoacoustic imaging (PAI) performance and antitumor effect of NB/CuS@PCM NPs were investigated by using 4T1 tumor-bearing BALB/c mice. After intravenous medication, the accumulation of NB/CuS@PCM NPs in the tumor was monitored. As shown in **Figures 4A,B**, the photoacoustic signal intensity of the tumor reached a maximum 4 h after injection . Thus, 4 h after injection was chosen for photo-triggered drug release and photothermal therapy. Previous studies confirmed that the tumor produces exorbitant GSH and H_2O_2 (Yang et al., 2020). After the PCM was melted, the Cu^{2+} release from the CuS NPs in the acidic tumor environment was reduced to Cu^{+} by the exorbitant GSH (Chen et al., 2019). Thereafter, the Cu^{+} can react with the intratumoral H_2O_2 to produce a highly poisonous hydroxyl radical (·OH) by the Fenton-like process (Wang et al., 2020). As expected, in the NB/CuS@PCM NPs + laser group, the temperature at the tumor site raised rapidly and increased from 32.5 to 52.0°C in 5 min, which confirmed that the hyperthermally produced NB/CuS@PCM NPs were feasible to ablate the tumor cells and trigger the NB and CuS NPs release for enhanced chemodynamic therapy (**Figures 4C,D**). On the contrary, in the control group, the temperature elevated insignificantly, indicating that there was not a photothermal effect when the mice were only treated with the 1,060-nm laser. During treatment, the growth of the tumor was traced. As displayed in **Figure 5A**, in the groups treated with the 1,060-nm laser or NB/CuS@PCM NPs, the growth of tumor was not inhibited. After some time, the tumor volume increased 14.6-fold (for laser treatment) and 13-fold (for NB/CuS@PCM NPs treatment) after 16 days of treatment, while the tumor receiving NB/CuS@PCM NPs and 1,060 nm laser treatment was eliminated (**Figure 5A**; **Supplementary Figure S7**), which fully confirmed the antitumor effect of the NB/CuS@PCM NPs.

To evaluate the antitumor effect of NB/CuS@PCM NPs, the tumors were extracted for histopathological analysis. As shown in

Figure 5C, an insignificant change was observed in the control group or the NB/CuS@PCM NP treatment group. On the contrary, in the treatment group of NB/CuS@PCM NPs + laser, a remarkable deformation could be seen, which indicated that the tumor cells might undergo apoptosis or necrosis, confirming that the NB/CuS@PCM NPs possess a strong antitumor effect with the assistance of laser (**Figure 5C**). To observe apoptotic cells in tissue sections, the terminal transferase–mediated dUTP nick end-labeling (TUNEL) was carried out (Li et al., 2017; Wu et al., 2018; Yang et al., 2019). As expected, after the tumor was treated with NB/CuS@PCM NPs and laser, substantial tumor cells were labeled with green fluorescence (**Figure 6**). This result was consistent with HE staining results.

Finally, the potential biotoxicity of the NB/CuS@PCM NPs was assessed by body weight change analysis, blood routine examination, and pathomorphology analysis. During the treatment, the body weight of the three groups had insignificant change, implying that the NB/CuS@PCM NPs possessed low physiological toxicity. In blood routine examination, various indicators in the blood, such as hemoglobin (HGB), red blood cells (RBC), white blood cells (WBC), and so on, exhibited no obvious fluctuations after the mice received treatment (**Supplementary Figure S8**). Besides, the major organs of mice were collected for histopathological analysis when the treatment was complete. As presented in **Supplementary Figure S9**, there were no prominent morphological changes, indicating NB/CuS@PCM NPs had excellent biocompatibility.

CONCLUSION

In summary, we fabricated an NIR-II–activated nanoplatform (NB/CuS@PCM NPs) for photothermal therapy and intracellular oxidation homeostasis disturbance. The PCM could be melted by the hyperthermia under 1,060-nm laser irradiation to realize the thermo-responsive release of NB and CuS NPs. Under the acidic tumor environment, the copper ion dissociated from the CuS NPs was reduced into Cu^{+} *via* the consumption of GSH. Furthermore, intratumoral H_2O_2 was converted into highly poisonous ·OH to disrupt the intracellular oxidation hemostasis *via* Fenton-like reaction. Besides, the NB could increase the intracellular content of ROS for enhancing the therapeutic effect of chemodynamic therapy. *In vivo*, with the assistance of photoacoustic imaging, NB/CuS@PCM NPs exhibited a satisfactory therapeutic effect in cancer therapy.

DATA AVAILABILITY STATEMENT

The original contributions presented in the study are included in the article/**Supplementary Material**; further inquiries can be directed to the corresponding authors.

ETHICS STATEMENT

The animal study was reviewed and approved by the School of Pharmaceutical Science of Nanjing Tech University.

AUTHOR CONTRIBUTIONS

BH and DY conceived the project; BH and YPH performed the experiments; HH, MD, QG, JS, YL, and JC were involved in data analysis; and BH, MD, and DY wrote the manuscript. All authors read and revised the manuscript before publication.

FUNDING

This work was supported by the Fujian Nature Science Foundation (Grant No. 2020J01748) and Fujian Green Pine Co., Ltd (Grant No. HX2018011).

ACKNOWLEDGMENTS

We would like to thank Fujian Green Pine Co., Ltd. and Fujian Nanping Qingsong Chemical Co., Ltd. for the raw materials and technical support, We are also grateful to the High Performance Computing Center in Nanjing Tech University for supporting the computational resources.

SUPPLEMENTARY MATERIAL

The Supplementary Material for this article can be found online at: https://www.frontiersin.org/articles/10.3389/fbioe.2021.751757/full#supplementary-material

REFERENCES

Ashok, B., Hariram, N., Siengchin, S., and Rajulu, A. V. (2020). Modification of Tamarind Fruit Shell Powder with *In Situ* Generated Copper Nanoparticles by Single Step Hydrothermal Method. *J. Bioresources Bioproducts* 5, 180–185. doi:10.1016/j.jobab.2020.07.003

Bansal, A., and Simon, M. C. (2018). Glutathione Metabolism in Cancer Progression and Treatment Resistance. *J. Cel Biol.* 217, 2291–2298. doi:10.1083/jcb.201804161

Bhatia, S. P., Letizia, C. S., and Api, A. M. (2008). Fragrance Material Review on Borneol. *Food Chem. Toxicol.* 46, S77–S80. doi:10.1016/j.fct.2008.06.031

Cao, W.-q., Zhai, X.-q., Ma, J.-w., Fu, X.-q., Zhao, B.-s., Zhang, P., et al. (2020). Natural Borneol Sensitizes Human Glioma Cells to Cisplatin-Induced Apoptosis by Triggering ROS-Mediated Oxidative Damage and Regulation of MAPKs and PI3K/AKT Pathway. *Pharm. Biol.* 58, 72–79. doi:10.1080/13880209.2019.1703756

Chen, D., Tang, Y., Zhu, J., Zhang, J., Song, X., Wang, W., et al. (2019). Photothermal-pH-hypoxia Responsive Multifunctional Nanoplatform for

Cancer Photo-Chemo Therapy with Negligible Skin Phototoxicity. *Biomaterials* 221, 119422. doi:10.1016/j.biomaterials.2019.119422

Cheng, Z., Zhang, T., Wang, W., Shen, Q., Hong, Y., Shao, J., et al. (2021). D-A-D Structured Selenadiazolesbenzothiadiazole-Based Near-Infrared Dye for Enhanced Photoacoustic Imaging and Photothermal Cancer Therapy. *Chin. Chem. Lett.* 32, 1580–1585. doi:10.1016/j.cclet.2021.02.017

Cherneva, E., Pavlovic, V., Smelcerovic, A., and Yancheva, D. (2012). The Effect of Camphor and Borneol on Rat Thymocyte Viability and Oxidative Stress. *Molecules* 17, 10258–10266. doi:10.3390/molecules170910258

Dai, H., Shen, Q., Shao, J., Wang, W., Gao, F., and Dong, X. (2021). Small Molecular NIR-II Fluorophores for Cancer Phototheranostics. *Innovation* 2, 100082. doi:10.1016/j.xinn.2021.100082

Ewulonu, C. M., Liu, X., Wu, M., and Yong, H. (2019). Lignin-containing Cellulose Nanomaterials: a Promising New Nanomaterial for Numerous Applications. *J. Bioresources Bioproducts* 4, 3–10. doi:10.21967/jbb.v4i1.186

Feng, L., Liu, B., Xie, R., Wang, D., Qian, C., Zhou, W., et al. (2021). An Ultrasmall SnFe 2 O 4 Nanozyme with Endogenous Oxygen Generation and Glutathione Depletion for Synergistic Cancer Therapy. *Adv. Funct. Mater.* 31, 2006216. doi:10.1002/adfm.202006216

Horváthová, E., Slameňová, D., Maršálková, L., Šramková, M., and Wsólová, L. (2009). Effects of Borneol on the Level of DNA Damage Induced in Primary Rat Hepatocytes and Testicular Cells by Hydrogen Peroxide. *Food Chem. Toxicol.* 47, 1318–1323. doi:10.1016/j.fct.2009.03.002

Li, G., Sun, Y., and Yao, H. (2008). Assay of Borneol by the Color Reaction with Vanilin. *Phys. Test. Chem. Anal. B Chemical Anal.* 11, 1083–1084.

Li, L., Luo, X., Leung, P. H., and Law, H. K. (2015). Controlled Release of Borneol from Nano-Fibrous poly(L-Lactic Acid)/Cellulose Acetate Butyrate Membrane. *Textile Res. J.* 86, 1202–1209. doi:10.1177/0040517515603812

Li, N., Cai, H., Jiang, L., Hu, J., Bains, A., Hu, J., et al. (2017). Enzyme-Sensitive and Amphiphilic PEGylated Dendrimer-Paclitaxel Prodrug-Based Nanoparticles for Enhanced Stability and Anticancer Efficacy. *ACS Appl. Mater. Inter.* 9, 6865–6877. doi:10.1021/acsami.6b15505

Li, Q., Zhang, Y., Huang, X., Yang, D., Weng, L., Ou, C., et al. (2021a). An NIR-II Light Responsive Antibacterial Gelation for Repetitious Photothermal/thermodynamic Synergistic Therapy. *Chem. Eng. J.* 407, 127200. doi:10.1016/j.cej.2020.127200

Li, Y., Xiu, W., Yang, K., Wen, Q., Yuwen, L., Luo, Z., et al. (2021b). A Multifunctional Fenton Nanoagent for Microenvironment-Selective Anti-biofilm and Anti-inflammatory Therapy. *Mater. Horiz.* 8, 1264–1271. doi:10.1039/d0mh01921f

Liang, C., Zhang, X., Yang, M., Wang, W., Chen, P., and Dong, X. (2020). Remodeling Tumor Microenvironment by Multifunctional Nanoassemblies for Enhanced Photodynamic Cancer Therapy. *ACS Mater. Lett.* 2, 1268–1286. doi:10.1021/acsmaterialslett.0c00259

Lin, L.-S., Huang, T., Song, J., Ou, X.-Y., Wang, Z., Deng, H., et al. (2019a). Synthesis of Copper Peroxide Nanodots for H2O2 Self-Supplying Chemodynamic Therapy. *J. Am. Chem. Soc.* 141, 9937–9945. doi:10.1021/jacs.9b03457

Lin, X., Hu, Y., Yang, D., and Chen, B. (2019b). Cyanine-coumarin Composite NIR Dye Based Instantaneous-Response Probe for Biothiols Detection and Oxidative Stress Assessment of Mitochondria. *Dyes Pigm.* 174, 107956. doi:10.1016/j.dyepig.2019.107956

Liu, G., Zhu, J., Guo, H., Sun, A., Chen, P., Xi, L., et al. (2019). Mo 2 C-Derived Polyoxometalate for NIR-II Photoacoustic Imaging-Guided Chemodynamic/Photothermal Synergistic Therapy. *Angew. Chem. Int. Ed.* 58, 18641–18646. doi:10.1002/anie.201910815

Liu, M. D., Guo, D. K., Zeng, R. Y., Ye, J. J., Wang, S. B., Li, C. X., et al. (2020a). Yolk-Shell Structured Nanoflowers Induced Intracellular Oxidative/Thermal Stress Damage for Cancer Treatment. *Adv. Funct. Mater.* 30, 2006098. doi:10.1002/adfm.202006098

Liu, Z., Wan, P., Liu, Z., Yang, M., Li, S., Wang, Y., et al. (2020b). Photothermal Generation of Oxygen-Irrelevant Free Radicals with Simultaneous Suppression of Glutathione Synthesis for an Enhanced Photonic Thermodynamic Cancer Therapy. *ACS Biomater. Sci. Eng.* 6, 6186–6194. doi:10.1021/acsbiomaterials.0c00889

Lv, X., Zhang, J., yang, D., Shao, J., Wang, W., Zhang, Q., et al. (2020). Recent Advances in pH-Responsive Nanomaterials for Anti-infective Therapy. *J. Mater. Chem. B* 8, 10700–10711. doi:10.1039/d0tb02177f

Ma, B., Wang, S., Liu, F., Zhang, S., Duan, J., Li, Z., et al. (2019). Self-Assembled Copper-Amino Acid Nanoparticles for *In Situ* Glutathione "AND" H2O2 Sequentially Triggered Chemodynamic Therapy. *J. Am. Chem. Soc.* 141, 849–857. doi:10.1021/jacs.8b08714

McCarty, M. F., Barroso-Aranda, J., and Contreras, F. (2010). Oxidative Stress Therapy for Solid Tumors - A Proposal. *Med. Hypotheses* 74, 1052–1054. doi:10.1016/j.mehy.2009.12.029

Menaga, D., Rahman, P. K. S. M., Rajakumar, S., and Ayyasamy, P. M. (2021). Antioxidant and Cytotoxic Activities of a Novel Isomeric Molecule (PF5) Obtained from Methanolic Extract of Pleurotus florida Mushroom. *J. Bioresources Bioproducts*. doi:10.1016/j.jobab.2021.04.008

Shen, J., Zhang, Y., Chen, D., Li, X., Chen, Z., Cao, S.-a., et al. (2019). A Hollow CuS Nanocube Cathode for Rechargeable Mg Batteries: Effect of the Structure on the Performance. *J. Mater. Chem. A.* 7, 21410–21420. doi:10.1039/c9ta07470h

Shi, Y., Yin, J., Peng, Q., Lv, X., Li, Q., Yang, D., et al. (2020). An Acidity-Responsive Polyoxometalate with Inflammatory Retention for NIR-II Photothermal-Enhanced Chemodynamic Antibacterial Therapy. *Biomater. Sci.* 8, 6093–6099. doi:10.1039/d0bm01165g

Su, J., Lai, H., Chen, J., Li, L., Wong, Y.-S., Chen, T., et al. (2013). Natural Borneol, a Monoterpenoid Compound, Potentiates Selenocystine-Induced Apoptosis in Human Hepatocellular Carcinoma Cells by Enhancement of Cellular Uptake and Activation of ROS-Mediated DNA Damage. *PLoS One* 8, e63502. doi:10.1371/journal.pone.0063502

Sun, H., Zhang, Y., Chen, S., Wang, R., Chen, Q., Li, J., et al. (2020). Photothermal fenton Nanocatalysts for Synergetic Cancer Therapy in the Second Near-Infrared Window. *ACS Appl. Mater. Inter.* 12, 30145–30154. doi:10.1021/acsami.0c07013

Sun, L., Wang, J., Liu, J., Li, L., and Xu, Z. P. (2021). Creating Structural Defects of Drug-Free Copper-Containing Layered Double Hydroxide Nanoparticles to Synergize Photothermal/Photodynamic/Chemodynamic Cancer Therapy. *Small Structures* 2, 2000112. doi:10.1002/sstr.202000112

Tang, B., Fang, G., Gao, Y., Liu, Y., Liu, J., Zou, M., et al. (2015). Lipid-albumin Nanoassemblies Co-loaded with Borneol and Paclitaxel for Intracellular Drug Delivery to C6 Glioma Cells with P-Gp Inhibition and its Tumor Targeting. *Asian J. Pharm. Sci.* 10, 363–371. doi:10.1016/j.ajps.2015.04.004

Wang, Z., Liu, B., Sun, Q., Dong, S., Kuang, Y., Dong, Y., et al. (2020). Fusiform-like Copper(II)-based Metal-Organic Framework through Relief Hypoxia and GSH-Depletion Co-enhanced Starvation and Chemodynamic Synergetic Cancer Therapy. *ACS Appl. Mater. Inter.* 12, 17254–17267. doi:10.1021/acsami.0c01539

Wang, Z., Zhan, M., Li, W., Chu, C., Xing, D., Lu, S., et al. (2021). Photoacoustic Cavitation-Ignited Reactive Oxygen Species to Amplify Peroxynitrite Burst by Photosensitization-Free Polymeric Nanocapsules. *Angew. Chem. Int. Ed.* 60, 4720–4731. doi:10.1002/anie.202013301

Wu, L., Cai, X., Zhu, H., Li, J., Shi, D., Su, D., et al. (2018). PDT-driven Highly Efficient Intracellular Delivery and Controlled Release of Co in Combination with Sufficient Singlet Oxygen Production for Synergistic Anticancer Therapy. *Adv. Funct. Mater.* 28, 1804324. doi:10.1002/adfm.201804324

Xu, Y., Zhao, M., Zhou, Y., Wang, J., Li, M., Li, F., et al. (2021). Rational Design of Near-Infrared Aza-Platinum-Dipyrromethene-Based Nanophototherapy Agent with Multistage Enhancement for Synergistic Antitumor Therapeutics. *Small Structures*, 2100094. doi:10.1002/sstr.202100094

Yan, J., Zhang, Z., Zhan, X., Chen, K., Pu, Y., Liang, Y., et al. (2021). *In Situ* injection of Dual-Delivery PEG Based MMP-2 Sensitive Hydrogels for Enhanced Tumor Penetration and Chemo-Immune Combination Therapy. *Nanoscale* 13, 9577–9589. doi:10.1039/d1nr01155c

Yang, K., Zhu, L., Nie, L., Sun, X., Cheng, L., Wu, C., et al. (2014). Visualization of Protease Activity *In Vivo* Using an Activatable Photo-Acoustic Imaging Probe Based on CuS Nanoparticles. *Theranostics* 4, 134–141. doi:10.7150/thno.7217

Yang, D., Zhang, S., Hu, Y., Chen, J., Bao, B., Yuwen, L., et al. (2016). AIE-active Conjugated Polymer Nanoparticles with Red-Emission for *In Vitro* and *In Vivo* Imaging. *RSC Adv.* 6, 114580–114586. doi:10.1039/c6ra18678e

Yang, D., Chen, F., He, S., Shen, H., Hu, Y., Feng, N., et al. (2019). One-pot Growth of Triangular SnS Nanopyramids for Photoacoustic Imaging and Photothermal Ablation of Tumors. *New J. Chem.* 43, 13256–13262. doi:10.1039/c9nj03045j

Yang, N., Xiao, W., Song, X., Wang, W., and Dong, X. (2020). Recent Advances in Tumor Microenvironment Hydrogen Peroxide-Responsive Materials for Cancer Photodynamic Therapy. *Nano-Micro Lett.* 12, 1–27. doi:10.1007/s40820-019-0347-0

Yang, D., Tu, Y., Wang, X., Cao, C., Hu, Y., Shao, J., et al. (2021a). A Photo-Triggered Antifungal Nanoplatform with Efflux Pump and Heat Shock Protein Reversal Activity for Enhanced Chemo-Photothermal Synergistic Therapy. *Biomater. Sci.* 9, 3293–3299. doi:10.1039/d1bm00457c

Yang, H., Shi, R., Shang, L., and Zhang, T. (2021b). Recent Advancements of Porphyrin-Like Single-Atom Catalysts: Synthesis and Applications. *Small Structures* 2, 2100007. doi:10.1002/sstr.202100007

Yang, N., Guo, H., Cao, C., Wang, X., Song, X., Wang, W., et al. (2021c). Infection Microenvironment-Activated Nanoparticles for Nir-Ii Photoacoustic Imaging-Guided Photothermal/chemodynamic Synergistic Anti-infective Therapy. *Biomaterials* 275, 120918. doi:10.1016/j.biomaterials.2021.120918

Yu, Q., Huang, X., Zhang, T., Wang, W., Yang, D., Shao, J., et al. (2021). Near-infrared Aza-Bodipy Dyes through Molecular Surgery for Enhanced Photothermal and Photodynamic Antibacterial Therapy. *Chem. Res. Chin. Univ.* 37, 951–959. doi:10.1007/s40242-021-1190-7

Zhang, R., Liu, C.-h., Huang, T.-l., Wang, N.-s., and Mi, S.-q. (2008). *In Vitro* Characterization of Borneol Metabolites by GC--MS upon Incubation with Rat Liver Microsomes. *J. Chromatogr. Sci.* 46, 419–423. doi:10.1093/chromsci/46.5.419

Zhang, S., Li, Q., Yang, N., Shi, Y., Ge, W., Wang, W., et al. (2020). Phase-change Materials Based Nanoparticles for Controlled Hypoxia Modulation and Enhanced Phototherapy. *Adv. Funct. Mater.* 29, 1906805. doi:10.1002/adfm.201906805

Zhang, Y., He, X., Zhang, Y., Zhao, Y., Lu, S., Peng, Y., et al. (2021). Native Mitochondria-Targeting Polymeric Nanoparticles for Mild Photothermal Therapy Rationally Potentiated with Immune Checkpoints Blockade to Inhibit Tumor Recurrence and Metastasis. *Chem. Eng. J.* 424, 130171. doi:10.1016/j.cej.2021.130171

Zhong, X., Wang, X., Cheng, L., Tang, Y. a., Zhan, G., Gong, F., et al. (2020). GSH-Depleted PtCu 3 Nanocages for Chemodynamic- Enhanced Sonodynamic Cancer Therapy. *Adv. Funct. Mater.* 30, 1907954. doi:10.1002/adfm.201907954

Zhu, D., Zhang, H., Huang, Y., Lian, B., Ma, C., Han, L., et al. (2021). A Self-Assembling Amphiphilic Peptide Dendrimer-Based Drug Delivery System for Cancer Therapy. *Pharmaceutics* 13, 1092. doi:10.3390/pharmaceutics13071092

Conflict of Interest: The authors declare that the research was conducted in the absence of any commercial or financial relationships that could be construed as a potential conflict of interest.

Publisher's Note: All claims expressed in this article are solely those of the authors and do not necessarily represent those of their affiliated organizations, or those of the publisher, the editors, and the reviewers. Any product that may be evaluated in this article, or claim that may be made by its manufacturer, is not guaranteed or endorsed by the publisher.

frontiers in Bioengineering and Biotechnology

REVIEW
published: 22 October 2021
doi: 10.3389/fbioe.2021.771851

Design and Applications of Tumor Microenvironment-Responsive Nanogels as Drug Carriers

Xinjing Du[1], *Yuting Gao*[1], *Qi Kang*[2]* *and Jinfeng Xing*[1]*

[1]School of Chemical Engineering and Technology, Tianjin University, Tianjin, China, [2]Department of Cardiology, Tianjin Medical University General Hospital, Tianjin, China

In recent years, the exploration of tumor microenvironment has provided a new approach for tumor treatment. More and more researches are devoted to designing tumor microenvironment-responsive nanogels loaded with therapeutic drugs. Compared with other drug carriers, nanogel has shown great potential in improving the effect of chemotherapy, which is attributed to its stable size, superior hydrophilicity, excellent biocompatibility, and responsiveness to specific environment. This review primarily summarizes the common preparation techniques of nanogels (such as free radical polymerization, covalent cross-linking, and physical self-assembly) and loading ways of drug in nanogels (including physical encapsulation and chemical coupling) as well as the controlled drug release behaviors. Furthermore, the difficulties and prospects of nanogels as drug carriers are also briefly described.

Keywords: nanogels, stimuli-responsive, controlled release, drug delivery, tumor microenvironment

OPEN ACCESS

Edited by:
Wenzhong Li,
Freie Universität Berlin, Germany

Reviewed by:
Peng Xue,
Southwest University, China
Xubo Zhao,
Zhengzhou University, China

***Correspondence:**
Qi Kang
kqangel@126.com
Jinfeng Xing
jinfengxing@tju.edu.cn

Specialty section:
This article was submitted to Biomaterials, a section of the journal Frontiers in Bioengineering and Biotechnology

Received: *07 September 2021*
Accepted: *08 October 2021*
Published: *22 October 2021*

Citation:
Du X, Gao Y, Kang Q and Xing J (2021) Design and Applications of Tumor Microenvironment-Responsive Nanogels as Drug Carriers. Front. Bioeng. Biotechnol. 9:771851. doi: 10.3389/fbioe.2021.771851

INTRODUCTION

The use of nanogels as carriers for drugs and other molecules has been extensively studied over the past 2 decades (Raemdonck et al., 2009; Li Y. et al., 2015; Mohammadi et al., 2020; Zhao et al., 2021). Generally, nanogels are defined as 3D sub-micron sized hydrophilic polymer networks formed through physical or chemical cross-linking, exhibiting the comprehensive properties of hydrogels and nanoparticles simultaneously. Physical cross-linking mainly includes hydrophobic interactions, electrostatic interactions, hydrogen bonds, and ionic interactions. Chemical method is to produce covalent bonds during the preparation of nanogels (Neamtu et al., 2017). Researchers define the acceptable nanogel size as 10–1,000 nm, while others have reported the optimal size of nanogel for biomedical applications is less than 200 nm (Akiyama et al., 2007). Nanogels are able to absorb a large quantity of water. The cross-linking network of nanogels is considered as a matrix to hold the inner liquid medium, while the absorbed water can be regarded as a filter medium for the diffusion of cargoes. Nanogels with negative Zeta potential are beneficial to avoid phagocytosis of the immune system and can resist the adsorption of negatively charged proteins (Xiao et al., 2011; Cuggino et al., 2019). Moreover, the swelling and shrinking behavior of nanogels is considered as an indispensable feature, which promotes the diffusion of loaded drug (Clegg et al., 2020).

With the exploration of controlled drug delivery, many kinds of drug carriers have attracted wide attention, such as liposomes, polymer vesicles, micelles, and microemulsions due to their good performances in prolonging blood circulation and improving therapeutic efficiency (Zhu et al., 2017; Iqbal et al., 2020; Large et al., 2021). As an emerging drug carrier, nanogel shows unique and promising prospects in biomedical field because of its good biocompatibility, high drug loading capacity, stimuli-responsiveness, low toxicity, and biodegradability (Pinelli et al., 2020; Shah et al.,

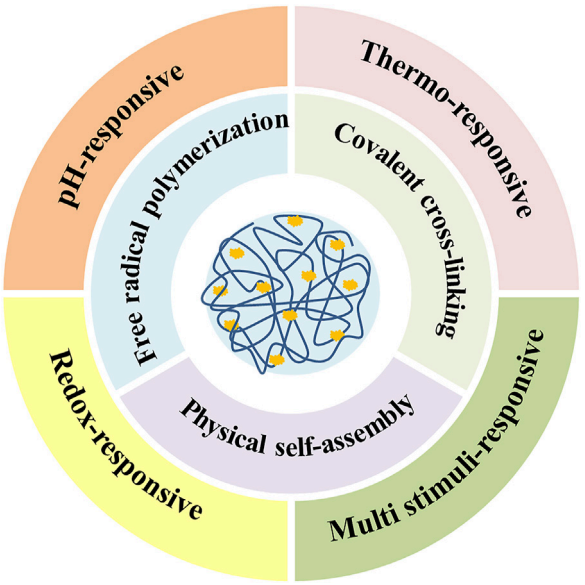

SCHEME 1 | General preparation methods and responsive-release types of drug-loaded nanogels.

2020). In general, an ideal nanogel drug delivery system (NG-DDS) should meet the requirements of the entire drug delivery process. Firstly, nanogels are required to effectively load therapeutic drugs and protect them from phagocytosis, elimination, and burst release. Secondly, nanogels should target to the diseased tissues to reduce damage to normal cells. Afterwards, under corresponding stimulus (temperature, pH, magnetic field, light, redox potential, enzymes, etc.), the structures of nanogels are triggered to collapse, swell, or contract to achieve controlled drug release. Finally, the remaining nanogels should be degradable and eliminated from the body with circulation (Xu et al., 2013; Ahmed et al., 2020). Therefore, the design strategies of nanogels as drug carriers include high drug loading content, good biocompatibility, long circulation time, specific ligands recognized by targeted cells, and stimulus-sensitive degradation characteristics.

In recent years, researchers have developed various nanogels with abundant performances. Most nanogels are designed to load therapeutic drugs such as doxorubicin (DOX), curcumin (CUR), methotrexate (MTX), and cisplatin (CDDP), and the others are utilized to deliver nucleic acids, proteins, and genes (Li et al., 2017; Luckanagul et al., 2018a; Lakkakula et al., 2021). So far, the instability of carriers and the presence of various biological barriers are still the main challenges to drug delivery efficiency (Oh et al., 2008; Sharma et al., 2016; Mauri et al., 2018; Hajebi et al., 2019b; Dreiss, 2020). In order to further explore NG-DDS comprehensively and systematically, this review primarily summarizes the synthetic strategies of nanogels (chemical crosslinking and physical crosslinking), methods of drug loading (physical encapsulation and chemical coupling) as well as stimuli-responsive drug release behaviors (pH, temperature, redox; single, dual, and multi). In addition, according to the development of NG-DDS, major challenges and future prospects of NG-DDS are also depicted (**Scheme 1**).

GENERAL SYNTHETIC METHODS

The preparation of nanogels is divided into chemical methods and physical approaches. Chemical methods involve the formation of covalent bonds and the most common technology is the heterogeneous free radical polymerization (Li Z. et al., 2019; Mackiewicz et al., 2019; Gurnani and Perrier, 2020). Compared with traditional free radical polymerization, controlled living polymerization could synthesize polymers with specific structures and properties (Gurnani and Perrier, 2020). In order to control the molecular weight, particle size, and particular three-dimensional structure of the polymer, atom transfer radical polymerization (ATRP), reversible addition-fragmentation chain transfer (RAFT), and nitroxide radical polymerization (NMRP) have been widely developed. Besides, the introduction of special cross-linkers into the polymerization system also tends to construct covalently cross-linked nanogels. The decomposition of cross-linkers is beneficial to the degradation of nanogels and controlled drug release in the later stage (Pei et al., 2018). Physical cross-linking means the self-assembly of polymers through weaker interactions, including hydrophobic interactions, supramolecular host-guest assembly, electrostatic interactions, and hydrogen bonds (Wei et al., 2013; Ding et al., 2019b). Comparing these two procedures, the chemical cross-linking shows more permanent and stable connections for the polymer network, whereas physically cross-linked structure is more likely to be destroyed. It is notable that the different cross-linked structures also influence the subsequent ways of drug release. A list of cross-linking mechanisms and corresponding release behaviors of drug-loaded nanogels is shown in **Table 1**.

Free Radical Polymerization

Most nanogels are prepared by free radical polymerization, which have the advantages of fast reaction speed, high molecular weight of the products, and the increasing of conversion rate with the extension of reaction time (Noordergraaf et al., 2018; Gao et al., 2020). The structures and properties can be adjusted by changing monomer, crosslinking agent, initiator, reaction medium, reaction time, and reaction temperature to achieve optimal drug delivery effect (Ahmed, 2015). Precipitation polymerization, (micro) emulsion polymerization, and dispersion polymerization are common polymerization techniques. Utilizing N-isopropylacrylamide as the monomer, acrylic dendritic polyglycerol as the crosslinking agent, sodium lauryl sulfate as the stabilizer, temperature-sensitive nanogels loading coumarin six were prepared by precipitation polymerization. The results showed that the drug release was thermo-dependent with a remarkable increase above the volume phase transition temperature of 32–37°C (Sahle et al., 2017). Sengel prepared a drug carrier with N-(2-mercaptoethyl) acrylamide as a monomer and ethylene glycol dimethacrylate as a cross-linker through dispersion polymerization (Sengel and Sahiner, 2019). Emulsion polymerization means monomers are dispersed in water with the help of emulsifiers and mechanical stirring, and micelles are formed above the critical micelle concentration, where polymer chains keep sustained growth. On this basis, micro (mini) emulsion polymerization and

TABLE 1 | The preparation mechanisms and relevant drug release behaviors of NG-DDS.

Network structure	Cross-linking mechanism	The nanogel size	The loaded molecule	Stimuli-responsive drug release	References
Chemical cross-linking	Traditional free radical polymerization	90–230 nm	Doxorubicin	pH/thermo	Wang et al. (2015)
	Controllable/living free radical polymerization	82–153 nm	Coumarin 102	UV light	Xin et al. (2020)
	Disulfide, imine cross-linking	250 nm	Doxorubicin	pH/redox	Pei et al. (2018)
	Click reaction	236 nm	Labeled insulin	Glucose/H_2O_2	Li et al. (2019a)
Physical cross-linking	Hydrophilic and hydrophobic interactions	55.7–259.2 nm	Nile Red	pH	Wang et al. (2018)
	Supramolecular host-guest assembly	108.1–121.4 nm	Doxorubicin and indocyanine green	NIR light	Zan et al. (2015)
	Hydrophobic/electrostatic interactions	140–230 nm	Curcumin	pH/oxidation	Dong et al. (2020)
	Hydrogen bonds	230 nm	DAPI, fluorescein, Nile red	Thermo	Zavgorodnya et al. (2017)
Both	Disulfide cross-linking/hydrophobic interactions	66.95 ± 1.93 nm	Purpurin 18 and 10-hydroxycamplothecin	Redox	Ma et al. (2021)
	Free radical polymerization/hydrogen bonds	18 nm	Curcumin	Thermo/NIR light	Wang et al. (2014)
	Free radical polymerization/disulfide cross-linking/ electrostatic interactions	70 nm	Doxorubicin	pH/thermo/photo	Chen et al. (2017)

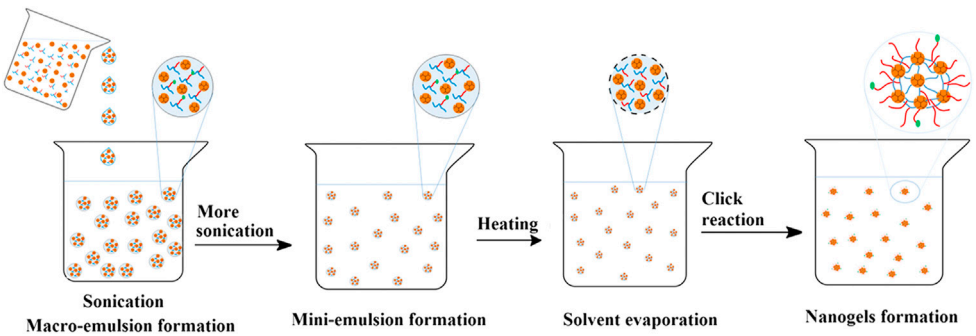

FIGURE 1 | Schematic illustration of the mini-emulsion technique (Abandansari et al., 2014). Copyright (2014) Elsevier.

reverse (micro) emulsion polymerization have been developed (Lovell and Schork, 2020; Pereira et al., 2020). The pH-sensitive H40-based nanogels with new structures were synthesized through mini-emulsion polymerization and click reaction (Abandansari et al., 2014). Firstly, the synthesized reactants were added dropwise to the aqueous phase with sonication to obtain the milky macroemulsion. Then the formed macroemulsion was constantly ultrasonicated under ice cooling to form a stable milky miniemulsion. Subsequently, the miniemulsion was heated and catalysts were added to induce the azide-alkyne click reaction and the pure nanogels were collected through dialysis (**Figure 1**).

With the development of free radical polymerization and controlled drug delivery systems, controllable/living free radical polymerization has attracted much attention (Matyjaszewski and Xia, 2001; Kim et al., 2016; Lou et al., 2017). These prepared polymers have the characteristics of narrow molecular weight distribution and uniform particle size distribution, which facilitate the construction of homogeneous polymer networks and drug loading. ATRP relies on external catalysts (usually transition metal complexes) to reversibly deactivate the free radicals to a dormant state (Matyjaszewski and Xia, 2001). Most of the biodegradable, well-defined and water-dispersed nanogels prepared by ATRP technology occur in reversed micro (mini) emulsions (Siegwart et al., 2009; Averick et al., 2011). The disulfide crosslinked biodegradable nanogels were designed and synthesized employing inverse miniemulsion ATRP (Oh et al., 2007). The releases of encapsulated molecules such as the fluorescent dye rhodamine and the anticancer drug Dox were triggered by the biodegradation of nanogels, demonstrating that these nanogels can be developed as targeted drug delivery carriers for biomedical applications. Compared with ATRP, RAFT with simpler procedures usually uses chain transfer agent (thiocarbonyl compound) rather than poisonous catalysts (Xin et al., 2020). The poly (methyl methacrylate) hair nanoparticles with core-shell structures were prepared through RAFT method. The carriers had high passive drug loading capacity for DOX, exhibiting fast and adjustable drug release behavior at intracellular pH (Qu et al., 2017). It is noticeable that although there are lots of merits of controlled living free radical polymerization, these preparations are rarely studied *in vivo*, and there is little information about biodistribution, clearance and long-term tolerance.

At present, photo-initiated polymerization has become an effective preparation method due to the short reaction time, mild reaction conditions, and controllable time and space (Fu et al., 2015). Messager reported a synthetic method for hyaluronic acid-based nanogels with controllable structures (Messager et al., 2013). Under UV light irradiation, the methacryloyl hyaluronic acid precursor started crosslinking in the droplets of water-in-oil emulsion, which obtained nanoparticles with homogeneous sizes. However, UV radiation may cause potential cell damage, and UV light tends to be scattered by large monomer droplets. Therefore, visible light-induced photopolymerization has been developed because they have longer wavelengths, less scattered by larger objects and better penetration (Matsui et al., 2017; Le Quemener et al., 2018). For example, Bakó prepared nanogels using methacrylic acid poly-γ-glutamic nanoparticles loading antibiotic drug ampicillin by visible (blue) light-initiated photopolymerization, and the release kinetics showed the controlled and efficient release behaviors (Bakó et al., 2016). Notably, our lab has also developed some strategies on the preparation of nanogels through laser photopolymerization, which is related with the investigation of the initiating system, polymerization mechanism and biomedical applications (Li J. et al., 2021; Liu et al., 2021; Peng et al., 2021; Wang et al., 2021). Specifically, Wang chose biocompatible polyethylene glycol diacrylate (PEGDA) as a monomer and ultrasmall nanogels with around 30 nm in size were prepared successfully through surfactant-free photopolymerization at 532 nm. Subsequently, Li in our lab introduced the third component DPI into the EY/TEOA initiating system, which significantly increased the polymerization rate and conversion ratio, and multifunctional PEGDA hydrogels through a beam expansion device were investigated. Liu's work concentrated on rapid preparation of nanogels through laser beam expansion under low monomer concentration. And the role of triethanolamine in the effect on the cross-linking degree of PEGDA nanogels was investigated by Peng, indicating that triethanolamine could adjust the double-bond conversion.

Covalent Cross-Linking

The networks of the nanogels can be obtained not only by the polymerization of C = C bonds, but also by coupling between other groups. Compounds containing disulfide bonds are one of the most commonly used cross-linking agents, because the disulfide bonds are easily broke by high concentrations of glutathione in tumor tissues and cells to achieve redox-responsive drug release. For instance, Tian and his coworkers prepared self-assembled hyaluronic acid and polyethylene glycol diglycidyl ether nanogels, then added with cystamine for the second cross-linking and loaded with DOX into the dense networks (Tian et al., 2019). Double cross-linking structures increased the tightness and decreased the burst release of drugs. Besides, the nanogels containing imine bonds formed by aldamine condensation are extensively utilized to deliver drugs due to their good biological activity and acid-sensitivity (Su et al., 2016; Zhao et al., 2017). The modified alginate was coupled with cystamine *via* disulfide bonds and coupled with DOX *via* imine bonds, achieving folate receptor-mediated targeting and pH/reduction dual-responsive drug release (Pei et al., 2018). The cleavage of unstable disulfide bonds and imine triggered the collapse of nanogels, promoting the DOX release and accumulation in the nucleus. In particular, these nanogels exhibited strong fluorescence in acidic media such as the microenvironment of tumor cells, and could be used for real-time, non-invasive positioning and tracking of cancer cells.

In recent years, click chemistry has become a promising strategy for designing nanogels due to its high reactivity, good selectivity, and mild reaction conditions. The thiol-ene click reaction is common in the addition of thiol to the double bonds under photo-initiation, which is efficient, high-yield, and can tolerate different functional groups (Tasdelen et al., 2016; Le et al., 2018; Phan et al., 2020; Mondal et al., 2021). The PEG and polycyclic phenylborate nanogels loaded with insulin and glucose oxidase (Gox) were developed through a one-pot thiol-ene click chemistry method by using tetrathiol compound QT as a coupling agent (Li C. et al., 2019). Since the H_2O_2 produced during the oxidation of glucose could cause cytotoxicity, the *in-situ* consumption of H_2O_2 effectively alleviated the side effects of Gox. Compared with nanogels without Gox, nanogels loaded with Gox presented better glucose-responsive abilities and stronger insulin release. These novel glucose/H_2O_2 dual-sensitive nanogels for insulin delivery will be a promising candidate material in the treatment of diabetes in the future. Zhang reported the self-assembly of modified PEG with hydrophobic segments through hydrophilic and hydrophobic interactions and cross-linked with thiols as shown in **Figure 2** (Zhang et al., 2019). The loading capacity of nanogels for DOX, gemcitabine, and methotrexate was investigated, showing that all three drugs could be successfully encapsulated inside the nanogels, and delivered to the 3D pancreatic spheroid tumor model. In summary, many researches have demonstrated that click nanogels with good biocompatibility are very suitable for targeted intracellular drug delivery. However, the current research is still in the preliminary stage. In-depth exploration and reasonable design are necessary to realize true clinical applications.

Physical Self-Assembly

Compared with chemical cross-linked nanogels, nanogels prepared by physical cross-linking show new functions and have the potential to process, recycle and self-repair due to the nature of dynamic and reversible non-covalent interactions. Usual preparation techniques are to couple hydrophobic segments to hydrophilic polymers, forming amphiphilic macromolecules, and then nanogels will be obtained *via* self-assembly in aqueous solutions (Chattopadhyay et al., 2016; Thelu et al., 2018; Wang et al., 2018; Wu et al., 2018; Wang et al., 2020). The self-assembled nanogels of ethylene glycol chitosan modified with deoxycholic acid were synthesized, and the diabetic drug palmitoylated exendin-4 (Ex4-C16) was adsorbed on the deoxycholic acid of the chitosan nanogels by hydrophobic interactions (Lee et al., 2012). This kind of drugs could combine with serum albumin to avoid the filtering effect of kidneys and prolong the half-life in the blood. Compared with

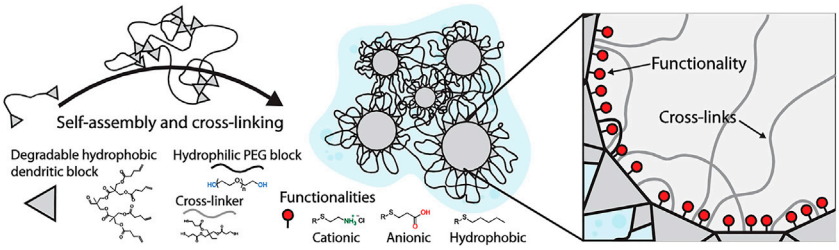

FIGURE 2 | Purposed structure of dendritic nanogels (DNGs) (Zhang et al., 2019). Copyright (2019) John Wiley and Sons.

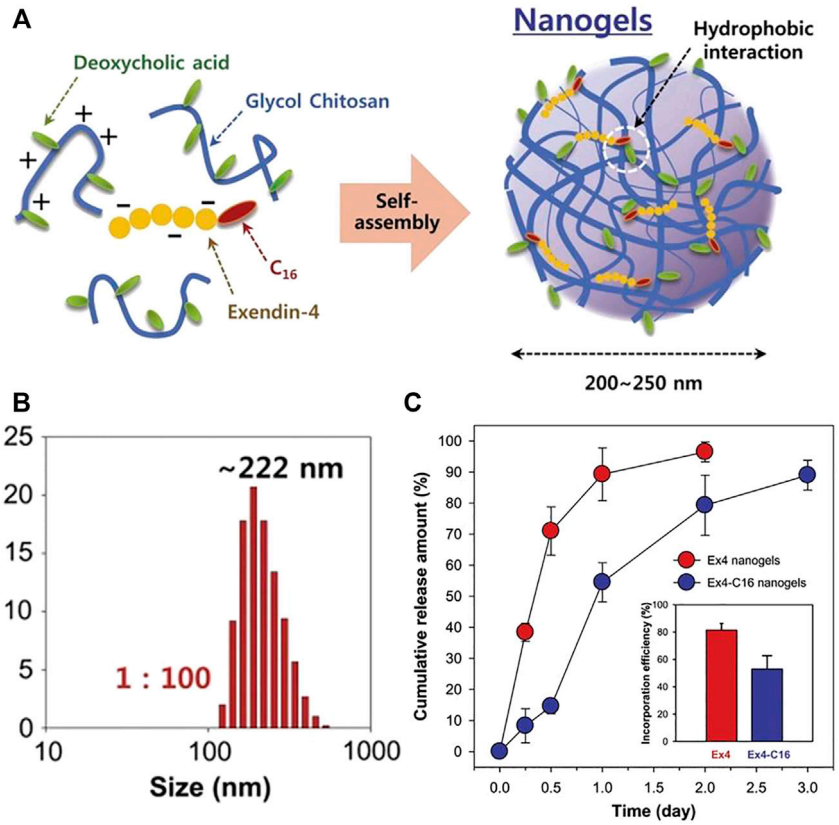

FIGURE 3 | Preparation illustration of nanogels and drug release behaviors. **(A)** An illustration of self-assembled nanogels; **(B)** The nanogel particle size distribution with ratio 1:100; **(C)** Release characteristics of Ex4 and Ex4-C16 from nanogels (Lee et al., 2012). Copyright (2012) Elsevier.

natural Ex4, palmitoylated Ex4 nanogels had lower penetration rate, but the drug release was slower with longer hypoglycemic effects. These nanogels produced hypoglycemia for 2 days in diabetic mice at a relatively low dose (100 nmol/kg), indicating that the nanogels had long-term hypoglycemic abilities as displayed in **Figure 3**. In a word, these drug carriers synthesized by hydrophobic interaction are beneficial to the adsorption of hydrophobic drugs, and the interactions between the drugs and carriers can also delay the drug release.

Supramolecular chemistry refers to the chemistry of molecular aggregates based on non-covalent bond interactions between molecules, which primarily studies weak interactions and the assembly, structure, and performance of molecular aggregates (Zan et al., 2015; Qin et al., 2020). Compared with traditional covalently cross-linked nanogels, supramolecular nanogels are easier to adjust their chemical and physical properties by changing the ratio of different components or introducing different stimulus-responsive groups. Common supramolecular host molecules include cyclodextrin, calixarene, crown ether, and hyperbranched polymer (Webber et al., 2016). According to Ding, the phenylalanine grafted chitosan and DOX were wrapped in the cavity of cucurbit(8)urea [CB(8)] to prepare chitosan nanogels with

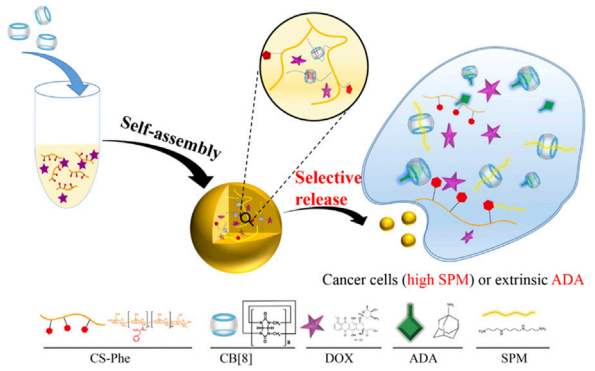

FIGURE 4 | Scheme showing the preparation of host-guest interaction-initiated supramolecular CNGs and their stimuli-responsive payload release in cancer cells (Ding et al., 2019b). Copyright (2019) American Chemical Society.

high drug loading efficiency, good biocompatibility, and selective cytotoxicity against therapeutic targets (Ding et al., 2019a). The CB cavity here functioned as a cross-linking agent, and the self-assembly of macromolecules was realized by wrapping phenylalanine in the cavity. Over-expressed spermine or exogenous stimulus amantadine in tumor cells would replace phenylalanine, because the binding affinity of phenylalanine to CB (8) was much weaker than that of amantadine or spermine to CB (8), leading to decrosslinking of nanogels. This kind of drug carriers could respond to specific endogenous or exogenous stimuli to achieve controlled drug release (**Figure 4**).

Particularly, ionically cross-linked nanogels are provided with better stability than self-assembled nanogels with micellar structures (Perez-Alvarez et al., 2016; Dong et al., 2020). Ionic polysaccharides are commonly used natural macromolecules for the synthesis of nanogels, including chitosan, hyaluronic acid, alginate, etc. (Liang et al., 2015). Nanogels loaded with antitumor drug methotrexate (MTX) were synthesized through ion gel methods using chitosan and sodium tripolyphosphate (TPP) with the small average particle size of 53.34 ± 7.23 nm, which helped nanogels extend blood circulation time and crossed the blood-brain barriers. After coating the nanogels with polysorbate 80, the MTX-loaded nanogels showed sustained drug release behaviors (about 65–70% within 48 h). These surface-modified nanogels might be candidates for drug delivery to the central nervous system (Azadi et al., 2012). Besides, alginate could be mixed with cationic poly [(2-dimethylamino) ethyl methacrylate] in water through electrostatic attraction, forming nanogels with size of 150 nm. When loading DOX, the nanogels exhibited acid-accelerated release behaviors as a result of the protonation of DOX and nanogels in an acidic medium, facilitating drug release due to electrostatic repulsion. This preparation method was simple in operation, and had low cost, no organic solvent or additives, good biocompatibility, and controllable drug release, which is beneficial to the drug delivery (Cai et al., 2012).

Microfluidic Technology

Unlike traditional methods, microfluidic technology has precise fluid control and rapid micro-scale mixing, which has aroused widespread interest in the preparation and engineering of nano-drug delivery materials. Compared with the traditional batch method, the drug-loaded nanomaterials prepared by the microfluidics have better monodispersity and their microstructures could be controlled by changing the flow rate and time (Amrani and Tabrizian, 2018; Nie et al., 2019; Zhang et al., 2020). To solve the issues of nanogels as carriers with large size, poor cell uptake rate, and endoplasmic embedding, Huang reported the preparation of HA-based nanogels with particle size of 80–160 nm *via* microfluidic technology and tetrazole-olefin light click cross-linking (Huang et al., 2019). The microfluidic chip was made of soda lime glass and nano-droplets formed at the intersection of the three water inlets. Within a certain range, the particle size decreased as the flow rate increasing and the concentration of HA reducing. These carriers could load various therapeutic proteins, such as cytochrome C, herceptin, and BSA with reduction-sensitivity because of the broken of disulfide bonds in the presence of glutathione.

Besides, microfluidic synthesized nanogels could show superior performance in the encapsulation and release of loaded cargoes (Rhee et al., 2011; Feng et al., 2015). For example, the alginate-based and growth factor-loaded nanogels were prepared through ionic gelation using the microfluidic technology (Mahmoudi et al., 2020). An alginate solution mixed TGF-β3 as core flow was injected into the microchip, while $CaCl_2$ as the sheath flow was injected into the side channels' inlets of microchip, resulting in the interaction and rapid ionical cross-linking between alginate polymer chains and Ca^{2+} ions. According to the dynamic light scattering analysis, the microfluidic synthesized nanogels had a smaller diameter and a better polydispersity index (43 ± 4 nm, PDI ≤ 0.2) than those of the bulk prepared nanogels (137 ± 22 nm, PDI ≥ 0.5). And the sizes of nanogels would increase with the enhancement of the flow rate ratio, showing a good correlation. Based on the small diameters and compact characteristics of nanogels, the high encapsulation efficiency and slow drug release could be achieved, while the large sizes of the bulk synthesized nanogels caused the low encapsulation efficiency and burst release. Therefore, the nanogels prepared through the microfluidic approach have shown good potential in cargo loading and sustained release.

LOADING WAYS OF DRUG IN NANOGELS

Loading content refers to the amount of drug loaded per unit weight or unit volume of nanogel, and the amount of drug that can be released is the effective drug loading. An efficient nanocarrier system is required to have high drug loading content, because the drug loading capacity directly affects the clinical application (Sun et al., 2017). The loading methods of carriers include non-covalent and covalent means, namely physical packaging and chemical conjugation. A list of drug-loading ways, the encapsulation techniques and corresponding release behaviors of drug-loaded nanogels is shown in **Table 2**.

Physical Encapsulation

Most drugs are loaded in nanogels by non-covalent interactions, including hydrophilic and hydrophobic interactions, hydrogen bonding interactions, and electrostatic interactions, because this method is simple and effective, and does not change the activity of drug molecules (Feng et al., 2010). Among them, the hydrophobic

TABLE 2 | The drug-loading ways and relevant drug release behaviors of NG-DDS.

The drug-loading way	The loaded drug	The encapsulation technique	The encapsulation efficiency (%)	Stimuli-responsive drug release	References
Physical encapsulation	Chlorin e6	The dialysis method	61.9 ± 0.15	Hyaluronidase	Yoon et al. (2012)
	Curcumin	The sonication method	With 114% loading of curcumin over the solution	Temperature	Luckanagul et al. (2018b)
	Doxorubicin	Hydrogen-bonded complexes	82 ± 4	Glutathione	Senthilkumar et al. (2019)
Chemical coupling	Chlorin e6	Amidation reaction	96.23 ± 4.8	—	Lee et al. (2011)
	Doxorubicin	Schiff base formation	32.66	pH	Su et al. (2018)
	Camptothecin	Esterification reaction	95.4 ± 0.9 (grafting rate)	pH/redox	Qu et al. (2019)

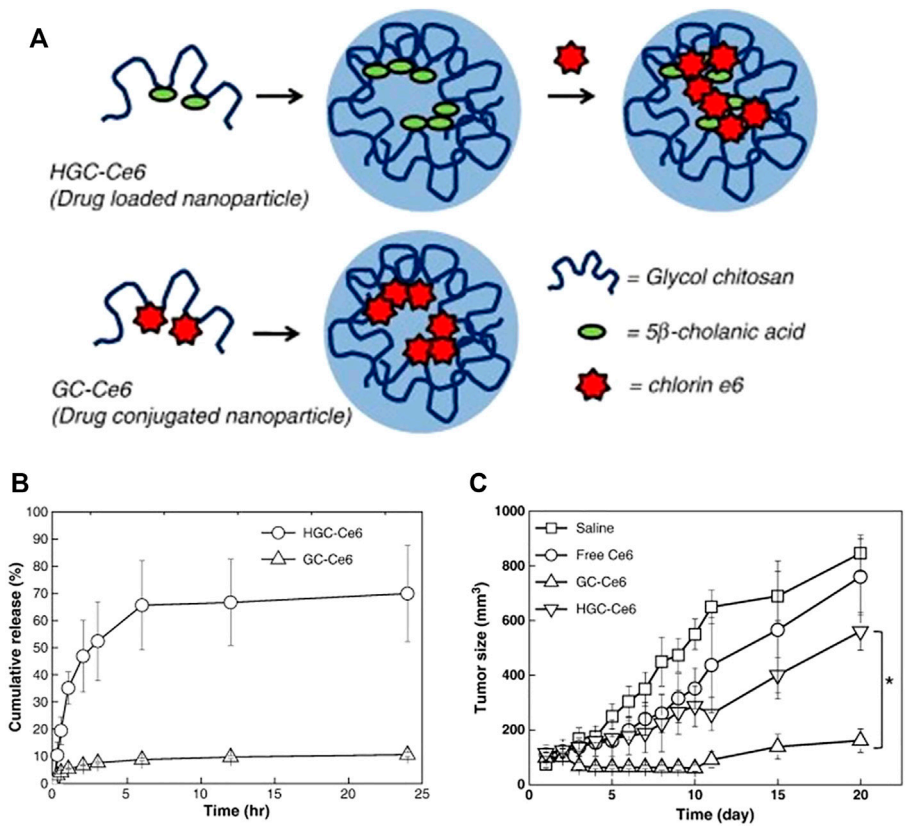

FIGURE 5 | Preparation of HGC-Ce6 and GC-Ce6 and release profiles and *in vivo* therapeutic efficacy. **(A)** Schematic illustration of HGC-Ce6 (drug-loaded nanoparticle) and GC-Ce6 (drug-conjugated nanoparticle); **(B)** *In vitro* release profiles of HGC-Ce6 and GC-Ce6; **(C)** Tumor growth data after photodynamic therapy with free Ce6, HGC-Ce6, or GC-Ce6 (5 mg/kg of Ce6) in HT-29 tumor-bearing mice (Lee et al., 2011). Copyright (2011) Elsevier.

interaction is widely applied, because many therapeutic drugs are hydrophobic that can be adsorbed to the hydrophobic center (mainly in the core) of the nanogels. For instance, Yoon prepared hyaluronic acid nanogels coupled with a hydrophobic segment of 5β-cholanic acid through self-assembly and loaded with chlorin e6 (Ce6) as a hydrophobic photosensitizer with great drug loading content of 80% (Yoon et al., 2012). At the same time, hydrogen bond-based drug loading is also promising due to directionality, selectivity, and relatively strong interaction, providing drug carriers with stronger drug loading capacity and high physical stability (Li et al., 2018). A novel preparation method of three-hydrogen bonds drug conjugated nanogels was developed (Senthilkumar et al., 2019). The hydrogen bond connection achieved a high drug loading ratio (82 ± 4%), while this number was merely 59 ± 3% when drug was loaded through hydrophobic interaction. Importantly, the uniform connection of the hydrogen-bonded conjugates in the network assisted the drug to stay in the gel matrix for long time during the circulation. These nanogels had strong stability, good biocompatibility and achieved sustainable drug release for several days. This new strategy of three-point hydrogen

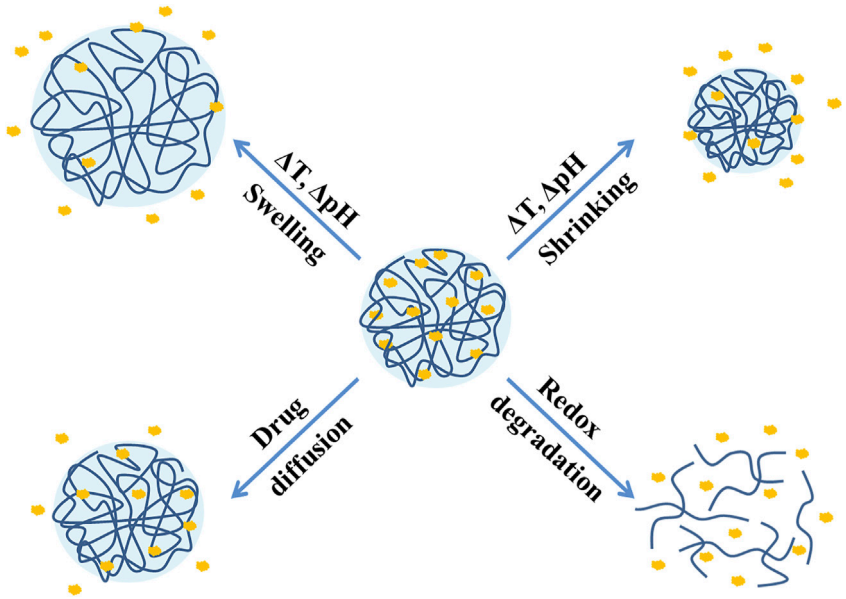

FIGURE 6 | Stimuli-responsive drug release mechanisms of nanogels.

bonds drug coupling could be extended to other carrier systems and various amphiphilic conjugated polymers.

Chemical Coupling

Physical encapsulation usually leads to inevitable burst release, which reduces the therapeutic effect of drugs (Seidi et al., 2018). To overcome this shortcoming and improve the blood circulation time and accumulation of drugs, covalent coupling has been developed. Lee studied the difference between physical loading and chemical coupling of photosensitizers of tumor-targeted glycol chitosan nanogels as shown in **Figure 5** (Lee et al., 2011). On the one hand, the hydrophobic photosensitizer Ce6 was physically loaded into hydrophobically modified carriers. On the other hand, Ce6 was chemically coupled with ethylene glycol chitosan and then nanocarriers were synthesized through self-assembly in aqueous solution. Both nanogels had similar particle sizes and singlet oxygen generation efficiency, but the physical loading exhibited sudden drug release under buffer conditions, where 65% of drugs were released rapidly within 6.5 h, while the chemical coupling presented longer circulation time and more effective tumor accumulation. When two drug carriers and free Ce6 were injected into tumor-bearing mice, only the chemically coupled carriers showed good phototoxicity, and the tumor volume in mice exhibited sharper reduction than others. The high-efficiency therapeutic effect was probably related to the chemical bond between the drugs and nanogels, indicating that this kind of NG-DDS was an effective and promising Ce6 delivery system. In addition, the DOX with active amino groups in the molecules is often coupled to nanogels through Schiff base bond. The pH-sensitive drug-loaded nanogels were obtained through coupling hydroformylated dextran nanogels and DOX (Su et al., 2018). At pH 2.0, 5.0, and 7.4, the drug release amount within 72 h were about 66, 28, and 9%, while the physically loaded nanogels did not demonstrate acid-accelerated release behaviors. In general, although chemical methods slightly solve the problem of drug burst release, some chemical reactions may also affect the activity and efficacy of drugs. It can be observed that these two drug loading methods have respective advantages and disadvantages.

STIMULI-RESPONSIVE DRUG RELEASE BEHAVIORS

As mentioned in the first section, an ideal NG-DDS needs to achieve effective drug release at the target site, and the most common release mechanism is drug diffusion (Clegg et al., 2020). In fact, the developments in recent years have shown that regardless of physical embedding or covalent coupling, the current release mechanism tends to be stimuli-responsive release (such as pH, temperature, redox, light, enzymes, etc.), which mainly divides into drug diffusion and swelling, shrinkage, and degradation of nanogels as described in **Figure 6**. Several stimuli-responsive release systems will be introduced in the following.

pH-Responsive Nanogels

Designing pH-responsive NG-DDS is one of the most commonly used strategies in tumor treatment, because the weakly acidic pH (~6.5) of tumor cells caused by the excessive lactic acid produced by hypoxia is slightly lower than that (~7.4) of normal tissues. Furthermore, the acidic lysosomes in cells (pH 5.0–5.5) are also beneficial to the acid-responsive drug release (Li Z. et al., 2021). To obtain acid-sensitive drug carriers, the modification of pH-sensitive molecules and introduction of pH-sensitive bonds (such as acetal bonds, ketal bonds, and imine bonds) into the nanogels are widely used.

Manchun used glyoxal as a crosslinking agent to synthesize dextrin-based nanogels with acid-sensitive bonds (acetal bond) through emulsion polymerization, loaded with DOX as a model drug, and the drug release behaviors of nanogels with different crosslinking agent content in different pH were investigated (Manchun et al., 2014). When the molar ratio of dextrin and glyoxal was 20:1, the cumulative release amount was about 40, 94, and 100% within 72 h at pH 7.4, 6.8, and 5.0, which presented obvious acid-accelerated release behaviors. Under the same pH conditions, as the increase of molar ratio of dextrin and glyoxal, the release amount was accordingly enhanced, because the content of the crosslinking agent was relevant to the crosslinking density of the nanogels. Afterwards, the author replaced glyoxal with formaldehyde as a crosslinking agent, and exhibited similar acid-responsive drug release (Manchun et al., 2015). Moreover, 2,2-dimethylacryloyloxy-1-ethoxypropane (DMAEP) containing ketal bonds was also employed as a pH-labile crosslinking agent. Acid-responsive DOX-loaded nanogels were formed through free radical copolymerization, using acylated HA as a monomer and DMAEP as a cross-linker, which accelerated the DOX release under acidic conditions (Luan et al., 2017). Borate also has unique acid sensitivity, making borate bonds attractive as driving force for integrated assembly. For example, Zhu reported the self-assembly of dextran and phenylboronic acid-modified cholesterol to synthesize DOX-loaded lysosome-acid targeting drug carriers. At the cellular level, it was clearly demonstrated that lysosomes had a strong influence on the uptake efficiency of nuclear drugs, indicating that lysosomal acidity was the main factor affecting drug efficacy (Zhu et al., 2015).

Currently, nanogels with carboxyl or/and amino groups in the molecular structure are commonly used as pH-responsive drug delivery vehicles. The pH and thermo sensitive nanogels with DOX loading composed of poly (N-isopropylacrylamide-co-acrylicacid) core, a polydopamine layer and an outer folic acid layer were designed and developed (Pu et al., 2021). With the decrease of pH from 7.4 to 5.5, the cumulative DOX release amount improved from 17.6 to 56.5%. The enhancement of drug release at pH 5.5 was attributed to the reduction of carboxyl ionization, which induced electrostatic interaction between carboxyl groups as well as the shrinkage of nangels. Moreover, poly (N,N-dimethylaminoethyl methacrylate) (PDMAEMA) is also a pH-sensitive cationic polymer because of protonation of the amino groups when the pH is lower than pKa of PDMAEMA (approximately 7.5) (Brannigan and Khutoryanskiy, 2017; Li Z. et al., 2021). Injectable PDMAEMA nanogels were developed through facile precipitation polymerization with *in situ* thermogelling behaviors and pH-triggered switching activity (Maiti et al., 2018). According to the release profile, the DOX release was acidic dependent from merely 43% at physiological pH to around 80% at pH 5.8 after 96 h of incubation. On the one hand, the protonation of the amino group resulted in increased electrostatic repulsion, causing the swelling of PDMAEMA nanogels. On the other hand, it might originate from enhanced electrostatic repulsion between quaternized PDMAEMA and positively charged DOX drug molecules, facilitating the DOX release.

Temperature-Sensitive Nanogels

Another feature of tumors and inflammatory areas is that the temperature (40–45°C) is slightly higher than that (37°C) of body fluids, which makes it valuable to design thermo-sensitive nanogels (Seo et al., 2012). Changes in temperature can reverse the segment-segment interaction or the segment-solvent molecule interaction, resulting in swelling or shrinkage of nanogels to achieve responsive drug release with corresponding temperature of the lower and higher critical solution temperature (LCST/UCST) (Yu et al., 2021).

Poly (N-isopropylacrylamide) (PNIPAAm) is one of the most attractive thermo-sensitive polymers with a low LCST of approximately 32°C (Wang et al., 2014). For example, Luckanagul reported the synthesis of chitosan-based nanogels with modification by thermo-sensitive PNIPAM and CUR was successfully loaded through a simple sonication method in aqueous media, showing temperature-responsive drug release behaviors (Luckanagul et al., 2018b). In order to study the influence of the degree of crosslinking and the existence of holes in the nanogels on the drug loading and release characteristics, Hajebi synthesized temperature-responsive hybrid core-shell nanogels using NIPAM and vinyl-modified silica nanoparticles *via* precipitation polymerization, and hollow PNIPAM nanogels were obtained by hydrolysis of silicic acid (Hajebi et al., 2020). All results demonstrated that the hollow nanogels had higher DOX loading content and higher toxicity, whereas hybrid nanogels showed faster drug release. Both nanogels presented thermo-sensitive drug release behaviors. The above results show that PNIPAM NG-DDS is promising for cancer treatment due to heat-sensitive, non-toxic, and biocompatible. However, their clinical applications are restricted due to hard degradation of PNIPAM in the body.

Other molecules like acrylamide (AAm) and N-vinylcaprolactam (NVCL) are similar with NIPAM, which exhibit temperature sensitive behaviors. The NVCL-based nanogels through self-assembly with poly (N-vinylpyrrolidone) were successfully prepared, loaded with the non-steroidal anti-inflammatory drug diclofenac sodium (Zavgorodnya et al., 2017). The cumulative transporting amount of drug at 32°C was 12 times than that at 22°C, showing excellent temperature-controlled drug release. Theune developed thermo-sensitive polypyrrole nanogels with spherical shape (200 nm of hydrodynamic size) using semi-interpenetrating *in-situ* polymerization and the obtained nanogels maintained good temperature responsive behaviors in the near-infrared region (Theune et al., 2019). When the MTX was loaded, temperature did not have much effect on the release with the cumulative release amount of 10–15%. However, the release increased significantly with near-infrared radiation, mainly due to that the local heating of the polypyrrole chains weakened the interactions between the drugs and nanogels, causing collapse of nanogels to promote the drug release. Compared with PNIPAM-based nanogels, polypyrrole-based nanogels can be accumulated in multiple intravenous injections without structural collapse at higher temperatures (such as 37°C). Besides, polymers with thermo-sensitivity, such as polyethylene glycol, polyethylene oxide-polypropylene oxide copolymers, poly (ε-caprolactone), and poly (propylene glycol)

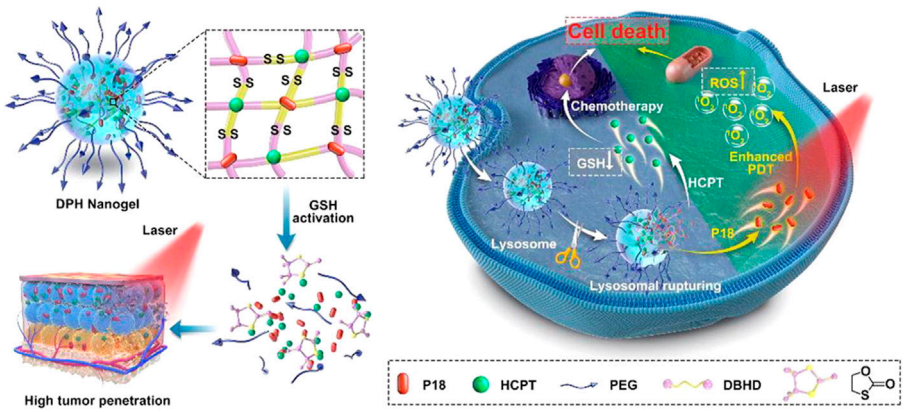

FIGURE 7 | Schematic illustration of redox-responsive prodrug nanogels for combining photodynamic therapy and chemotherapy (Ma et al., 2021). Copyright (2021) Elsevier.

are also expected to be applied to design temperature-dependent nanogels for drug delivery (Yu et al., 2021).

Redox-Sensitive Nanogels

Due to the high proliferation characteristics of tumor cells, high levels of reactive oxygen species (ROS) are overexpressed in tumor tissues and cells, resulting into high levels of reduced glutathione (GSH) in order to maintain redox homeostasis (Wu, 2006). According to research data, the concentration of GSH in tumor cells reaches 2–10 mM, while the concentration in normal tissues is merely around 2–20 μM (Yuan et al., 2018; Kumar et al., 2019). Based on this, Lu developed a two-in-one cross-linking strategy to prepare GSH-responsive prodrug nanogels by coupling DOX and CPT using disulfide compound as cross-linker agent (Lu et al., 2021). Under the high concentration of GSH in tumor, both DOX and CPT released about 75% within 48 h in physiological pH 7.4. Moreover, compared with the single drug, the toxicity of the prodrug nanogels showed significant superiority, indicating the high-performance drug synergetic capacity of this strategy. Similarly, as illustrated in **Figure 7**, a redox-responsive cross-linker was introduced to synthetize prodrug nanogels based CPT and purpurin 18 (P18) with suitable size (~67 nm), high drug loading content, controlled drug release, and deep tumor penetration (Ma et al., 2021). According to the release profile, nearly 90% of CPT released in 10 mM GSH, whereas the cumulative release amount was merely 10% without GSH in the pH 7.4 PBS solution. Simultaneously, the released P18 could be activated by NIR of 700–900 nm as a fluorescence imaging agent, demonstrating that nanogels achieved combined photodynamic and chemotherapy as potential drug carrier and diagnostic agent.

Besides disulfide bonds, Se-Se bonds also show stimulus-responsive to redox conditions due to their lower bond energy. More importantly, selenium is an essential trace element for the human body and its anti-cancer activity has been confirmed by anti-cancer mechanisms and clinical experimental studies (Lanfear et al., 1994; Zhu et al., 1996; Moses et al., 2019). For instance, Li and his coworkers chose sodium diselenide as a crosslinking agent to synthesize nanogels with polyphosphate core and hydrophilic PEG shell (Li C. et al., 2015). The nanogels behaved strong inhibitory effects on the proliferation of the tumor cells, which might be attributed to the cleavage of diselenide bonds in the presence of the over-expressed ROS and GSH in the cancer cell. These nanogels were little toxicity to normal cells, and seemed to be promising and highly effective self-release anticancer drug carriers. In addition, the nanogels containing diselenide bonds could also be loaded with other anticancer drugs to achieve combined therapy. For example, the diselenide cross-linked PEG-based nanogels were simply synthesized through physical self-assembly with 32.7% DOX loading content (Hailemeskel et al., 2018). Experiments showed that the initial release was relatively fast in the first few hours with the presence of GSH and H_2O_2, reaching 52.5 and 54% at 24 and 48 h, respectively. In the absence of GSH and H_2O_2, the 72 h release amount was relatively low at 35.6%. Another important feature of Se is that hydrophobic selenide group can be oxidized to hydrophilic selenoxide/selenone groups with the presence of oxidant. The selenium-containing polyphosphoester nanogels as stable and efficient drug carriers were developed by ring-opening polymerization (Zhang et al., 2018). Under the condition of overproduced ROS in cancer cells (0.05–0.1 mM), the average hydrodynamic diameter of nanogels increased from 164 to 400 nm due to the oxidation of selenide group, which accelerated the efficient intracellular drug release owing to the rapid swelling of nanogels.

External-Stimulus Responsive Nanogels

The above three stimuli belong to the endogenous stimuli of the tumor microenvironment. In addition, some external stimuli, such as light and magnetic field, are also often used in nanogel drug delivery systems. The UV-light responsive crosslinker 5-(acryloyloxy)-2-nitrobenzyl acrylate was introduced into the methoxy polyethylene glycol methacrylate-based nanogels with higher drug loading and encapsulation efficiency, showing good photo-responsive release capability at the 365 nm ultraviolet light (Xin et al., 2020). Zan developed a near-infrared light-triggered nanogel drug release system based on the advantages of high tissue penetration and low damage. The nanogels loaded with indocyanine green and DOX exhibited superior photo-thermal performance and controlled drug

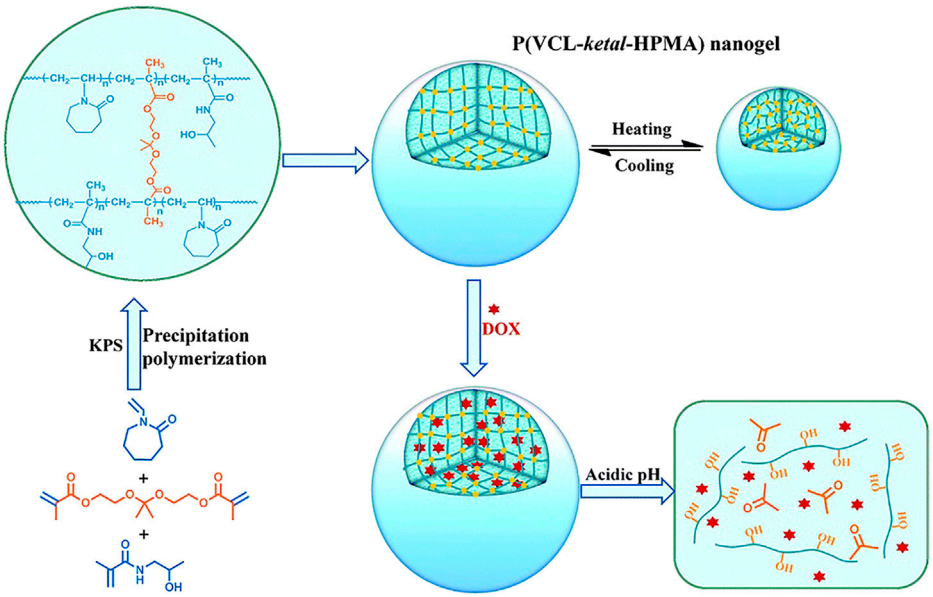

FIGURE 8 | Illustration of the preparation, stimuli-responsive behavior and acid-triggered drug release of the P(VCL-*ketal*-HPMA) nanogel (Wang et al., 2015). Copyright (2015) Royal Society of Chemistry.

release under NIR laser irradiation (Zan et al., 2015). Besides, the magnetic field-responsive hybrid nanogels have been widely developed recently, which can be attributed to the generation of external heat to kill tumor cells when exposed to a magnetic field. The magnetic/NIR-thermally responsive core-shell hybrid nanogels loaded curcumin were prepared, using bifunctional nanoparticles composed of carbon dot and superparamagnetic nanocrystals cluster as the core and the poly (NIPAM-AAm) as the shell. Both alternating magnetic field and the NIR light irradiation produced local heat, resulting in the shrinkage of poly (NIPAM-AAm) shell and the accelerated release of curcumin. Therefore, the multifunctional hybrid nanogel can be considered as an external stimulus-responsive drug carrier.

Dual/Multi-Stimuli Responsive Nanogels

At present, the development trend of nanogels as drug carriers is more and more intelligent. Compared with single stimulus-responsive nanogels, the sensitivity and specificity for dual and multiple responsive nanogels to target tumors might be improved (Hajebi et al., 2019a). The physical or chemical properties of these nanogels can be adjusted in response to a stimuli combination of temperature, pH, redox, light, and enzyme to release their cargoes. In this section, we will discuss dual-stimuli and tri-stimuli responsive nanogels and their release behaviors.

Among various dual-stimuli sensitive nanocarriers, the combination of temperature and pH is currently the most widely used. In order to reduce the release of cisplatin in pH-responsive nanogels, NIPAM was introduced into nanogels as the thermo-sensitive unit (Peng et al., 2013). The release of cisplatin in nanogels containing NIPAM was facilitated by H^+ attack and decreased as the temperature increasing. The results showed that the pH/temperature dual-responsive nanogels are effective intracellular delivery systems for cisplatin drugs. As mentioned above, ketal and PNVCL are common acid and temperature-sensitive compounds. The pH/thermo responsive nanogels loaded with DOX were designed through precipitation polymerization using N-(2-hydroxypropyl) methacrylamide and NVCL as copolymer monomers and the ketal as a cross-linking agent as seen in **Figure 8**. The release of DOX could be accelerated by lowering the pH and increasing the temperature. Compared with nanogels without ketal agent, the nanogels containing ketal showed obvious acid-dependent release behavior, with a release amount of 13% (pH 7.4) and 96% (pH 5.0) at 48 h, and higher cytotoxicity and efficiency to kill HeLa cells (Wang et al., 2015).

Due to the presence of high concentrations of GSH in tumor cells and the acidic environment of the lysosome, pH/GSH dual-sensitive nanogels provide an effective strategy for delivery and intracellular release of anti-cancer drugs (Chen et al., 2014; Li and Liu, 2018). The pH/redox dual-responsive nanogels based on NIPAM and acrylic acid with disulfide bonds as the crosslinking agent were prepared by Yang et al. (2016). As shown in **Figure 9**, when the DOX-loaded nanogels were internalized into the lysosome of tumor cells, they would shrank to partially release DOX, and then disintegrated under the trigger of high intracellular GSH, causing the complete DOX release. Camptothecin (CPT) belongs to plant anticancer drugs, and has good effects on gastrointestinal, head and neck cancers, but its poor water solubility and serious side effects hinder its clinical application (Ulukan and Swaan, 2002; Tai et al., 2014). To solve these, researchers try to modify the prodrug to improve the performance of CPT. For instance, Qu utilized functionalized CPT, methacrylic acid, and N,N'-methylenebisacrylamide as raw materials, where CPT was chemically coupled to nanogels through disulfide bonds (Qu et al., 2019). The drug release was pH and redox dependent, and it accelerated with the increase of GSH level and the decrease of pH value. At physiological pH 7.4, the cumulative release amount for 48 h was less than 8.6%.

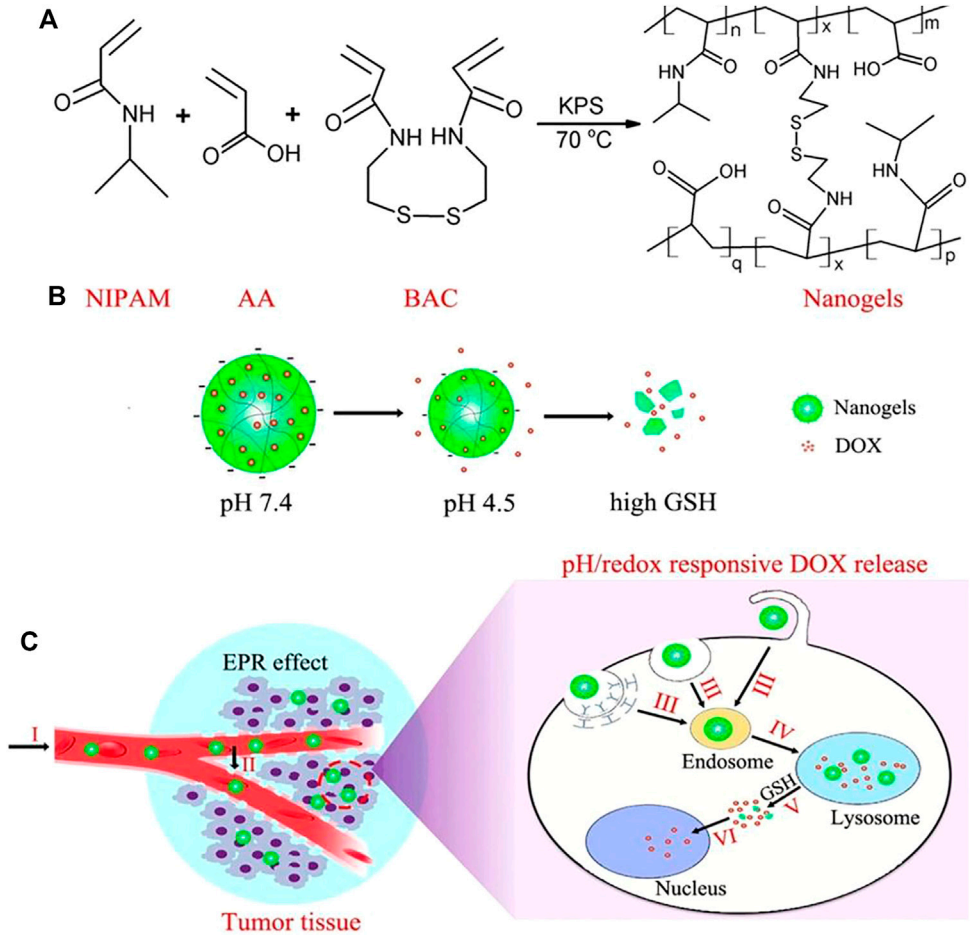

FIGURE 9 | Schematic illustration of P (NIPAM-*ss*-AA) nanogels for anticancer drug delivery. **(A)** Construction of P(NIPAM-*ss*-AA) nanogels; **(B)** Characterization of P(NIPAM-ss-AA) nanogels in response to intracellular microenvironment; **(C)** Site-directed DOX release delivered (Yang et al., 2016). Copyright (2016) American Chemical Society.

However, when the GSH concentration was 2 and 10 mM, the 48 h release amount was 50.9 and 87.7% under the condition of pH 5.0, respectively. It is beneficial to achievie "on-demand" drug release in the microenvironment of tumor cells and tumor tissues for these nanogels.

Compared with single-responsiveness and double-responsiveness, multi-responsiveness are hopeful to improve the versatility of carriers to meet more practical needs. According to Lou, a pH/thermo/redox three-stimuli responsive targeted-liver cancer NG-DDS was developed by using functionalized galactose, NVCL, and methacrylic acid as monomers and disulfide bonds compound as a cross-linking agent to encapsulate DOX (Lou et al., 2015). After entering the cancer cells, GSH triggered the cleavage of disulfide bonds and disintegration of nanogels, leading to the release of drugs. PNIPAM was added to the alginate emulsion and cross-linked with cystamine to prepare nanogels with triple-stimuli properties (temperature, pH and redox sensitivity) (Ji et al., 2017). Under the synergistic effects, the release of DOX was more complete than the release of one or two stimuli, which promoted the tumor-targeting and intracellular delivery characteristics of anticancer drug release.

Besides the above three stimuli system, light stimulation has also attracted much attention due to the rapid development of photodynamic therapy (PDT) and photothermo therapy (PTT). For example, a new type of disulfide cross-linked polyacrylic acid-methyl spiropyran light/pH/redox responsive drug carrier was designed and synthesized, which tended to be isomerization under ultraviolet light or at low pH, and the addition of the reducing agent dithiothreitol caused collapse of nanogels (Chen et al., 2017). The combined stimulation showed synergistic effect on the DOX cumulative release. Multi-responsive PVCL-based nanogels with core/shell structure were synthesized using precipitation polymerization as exhibited in **Figure 10** (Li X. et al., 2021). The nanogels could be employed to modify or/and load with various functional agents to construct multi-stimuli responsive nanoplatforms. DOX-loaded nanogels exhibited pH/NIR/redox triggered drug release, which achieved DOX release of 59.2% under pH 5.5 and NIR laser, and the final DOX cumulative release amount reached 79.2% under pH 5.5 and GSH condition. Remarkably, the combinational therapies are beneficial to the controlled drug release and deeper tissue tumor penetration,

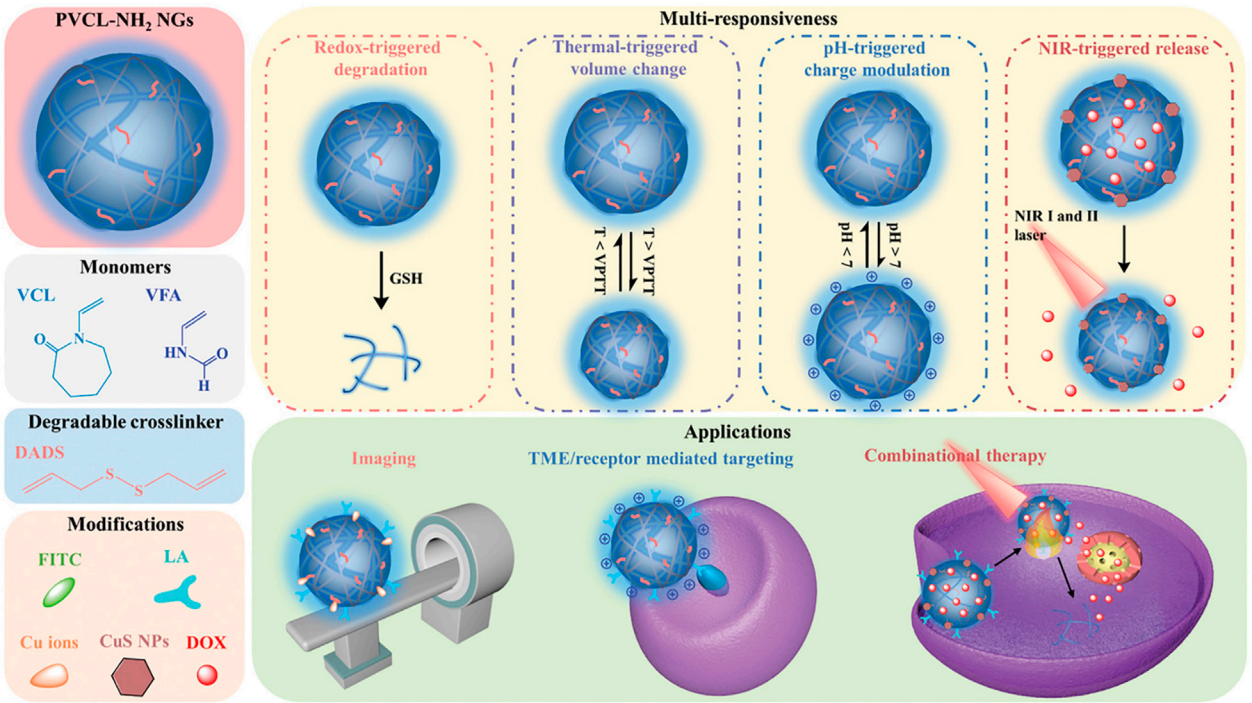

FIGURE 10 | Overview of multi-responsive PVCL-based nanoplatforms (Li X. et al., 2021). Copyright (2021) John Wiley and Sons.

achieving enhanced anticancer efficacy compared with single photothermo therapy and chemotherapy.

MAJOR CHALLENGES AND CONCLUSION

Although there have been lots of research of NG-DDS, there are still problems and challenges in the actual clinical applications. Firstly, the drug loading content of most nanogels is not always high, leading to the low release amount. Therefore, the structures of carriers are required to be further optimized to load more drugs. Secondly, after the carriers entering the blood circulation, the problem of burst release still exists, resulting in significant reduction of drugs that actually target tissues and cells, which requires the deeper exploration of more intelligent stimulus-responsive nanogels to improve the targeting performance and responsiveness. Thirdly, it is currently recognized that the main factor for the enrichment of nanogels in tumor sites is the EPR effect, namely, the high permeability and retention effect due to the rich blood vessels of tumor tissues and the wide vascular wall gap. However, the research on the EPR effect is currently only at the stage of animal experiments and has not been verified in humans. Fourthly, after administration, nanogels are required to overcome lots of biological barriers, such as mucus, skin, tumor microenvironment, blood-brain barrier, etc. Therefore, it is essential to flexibly change the physical and chemical properties of nanogels or modify the surface of nanogels to overcome different biological barriers.

In general, nanogels have shown promising prospects as drug carriers, and provided great potential for intelligent drug delivery. The strategies for designing nanogels as ideal drug carriers should have high drug loading, long circulation time, specific ligands recognized by target cells, and stimulus-sensitive degradation characteristics. There is no doubt that drug carriers are beneficial in tumor treatment, such as reducing drug toxicity, improving efficacy, and enhancing patient tolerance. However, nanogel drug delivery systems can truly achieve clinical applications after solving problems mentioned above.

AUTHOR CONTRIBUTIONS

XD and YG: conceptualization, investigation and writing—original draft. QK and JX: supervision, writing—reviewing and editing. All authors contributed to the article and approved the submitted version.

FUNDING

The National Natural Science Foundation of China (31771094).

ACKNOWLEDGMENTS

Authors thank the support of National Natural Science Foundation of China (31771094) and Tianjin Science and Technology Innovation Platform Program (14TXGCCX00017).

REFERENCES

Abandansari, H. S., Nabid, M. R., Rezaei, S. J. T., and Niknejad, H. (2014). pH-sensitive nanogels based on Boltorn H40 and poly(vinylpyridine) using mini-emulsion polymerization for delivery of hydrophobic anticancer drugs. *Polymer* 55, 3579–3590. doi:10.1016/j.polymer.2014.06.037

Adetunji Moses, O., Khan, M. I., Fang, Q., Qin, L., Rehman, Z. U., Zhang, Y., et al. (2019). PVP intercalated metallic WSe2 as NIR photothermal agents for efficient tumor ablation. *Nanotechnology* 30, 065102. doi:10.1088/1361-6528/aaf151

Ahmed, E. M. (2015). Hydrogel: Preparation, characterization, and applications: A review. *J. Adv. Res.* 6, 105–121. doi:10.1016/j.jare.2013.07.006

Ahmed, S., Alhareth, K., and Mignet, N. (2020). Advancement in nanogel formulations provides controlled drug release. *Int. J. Pharmaceutics* 584, 119435. doi:10.1016/j.ijpharm.2020.119435

Akiyama, E., Morimoto, N., Kujawa, P., Ozawa, Y., Winnik, F. M., and Akiyoshi, K. (2007). Self-Assembled Nanogels of Cholesteryl-Modified Polysaccharides: Effect of the Polysaccharide Structure on Their Association Characteristics in the Dilute and Semidilute Regimes. *Biomacromolecules* 8, 2366–2373. doi:10.1021/bm070136q

Amrani, S., and Tabrizian, M. (2018). Characterization of Nanoscale Loaded Liposomes Produced by 2D Hydrodynamic Flow Focusing. *ACS Biomater. Sci. Eng.* 4, 502–513. doi:10.1021/acsbiomaterials.7b00572

Averick, S. E., Magenau, A. J. D., Simakova, A., Woodman, B. F., Seong, A., Mehl, R. A., et al. (2011). Covalently incorporated protein-nanogels using AGET ATRP in an inverse miniemulsion. *Polym. Chem.* 2, 1476–1478. doi:10.1039/C1PY00050K

Azadi, A., Hamidi, M., Khoshayand, M.-R., Amini, M., and Rouini, M.-R. (2012). Preparation and optimization of surface-treated methotrexate-loaded nanogels intended for brain delivery. *Carbohydr. Polym.* 90, 462–471. doi:10.1016/j.carbpol.2012.05.066

Bakó, J., Kerényi, F., Hrubi, E., Varga, I., Daróczi, L., Dienes, B., et al. (2016). Poly-γ-Glutamic Acid Nanoparticles Based Visible Light-Curable Hydrogel for Biomedical Application. *J. Nanomater.* 2016, 1–10. doi:10.1155/2016/7350516

Brannigan, R. P., and Khutoryanskiy, V. V. (2017). Synthesis and evaluation of mucoadhesive acryloyl-quaternized PDMAEMA nanogels for ocular drug delivery. *Colloids Surf. B: Biointerfaces* 155, 538–543. doi:10.1016/j.colsurfb.2017.04.050

Cai, H., Ni, C., and Zhang, L. (2012). Preparation of complex nano-particles based on alginic acid/poly[(2-dimethylamino) ethyl methacrylate] and a drug vehicle for doxorubicin release controlled by ionic strength. *Eur. J. Pharm. Sci.* 45, 43–49. doi:10.1016/j.ejps.2011.10.020

Chattopadhyay, S., Heine, E., Mourran, A., Richtering, W., Keul, H., and Möller, M. (2016). Waterborne physically crosslinked antimicrobial nanogels. *Polym. Chem.* 7, 364–369. doi:10.1039/C5PY01566A

Chen, S., Bian, Q., Wang, P., Zheng, X., Lv, L., Dang, Z., et al. (2017). Photo, pH and redox multi-responsive nanogels for drug delivery and fluorescence cell imaging. *Polym. Chem.* 8, 6150–6157. doi:10.1039/c7py01424d

Chen, X., Chen, L., Yao, X., Zhang, Z., He, C., Zhang, J., et al. (2014). Dual responsive supramolecular nanogels for intracellular drug delivery. *Chem. Commun.* 50, 3789–3791. doi:10.1039/c4cc00016a

Clegg, J. R., Ludolph, C. M., and Peppas, N. A. (2020). QCM-D assay for quantifying the swelling, biodegradation, and protein adsorption of intelligent nanogels. *J. Appl. Polym. Sci.* 137, 48655. doi:10.1002/app.48655

Cuggino, J. C., Blanco, E. R. O., Gugliotta, L. M., Alvarez Igarzabal, C. I., and Calderón, M. (2019). Crossing biological barriers with nanogels to improve drug delivery performance. *J. Controlled Release* 307, 221–246. doi:10.1016/j.jconrel.2019.06.005

Ding, Y.-F., Wei, J., Li, S., Pan, Y.-T., Wang, L.-H., and Wang, R. (2019a). Host-Guest Interactions Initiated Supramolecular Chitosan Nanogels for Selective Intracellular Drug Delivery. *ACS Appl. Mater. Inter.* 11, 28665–28670. doi:10.1021/acsami.9b09059

Ding, Y.-F., Wei, J., Li, S., Pan, Y.-T., Wang, L.-H., and Wang, R. (2019b). Host-Guest Interactions Initiated Supramolecular Chitosan Nanogels for Selective Intracellular Drug Delivery. *ACS Appl. Mater. Inter.* 11, 28665–28670. doi:10.1021/acsami.9b09059

Dong, S., Jiang, Y., Qin, G., Liu, L., and Zhao, H. (2020). Methionine-Based pH and Oxidation Dual-Responsive Block Copolymer: Synthesis and Fabrication of Protein Nanogels. *Biomacromolecules* 21, 4063–4075. doi:10.1021/acs.biomac.0c00879

Dreiss, C. A. (2020). Hydrogel design strategies for drug delivery. *Curr. Opin. Colloid Interf. Sci.* 48, 1–17. doi:10.1016/j.cocis.2020.02.001

Feng, Q., Zhang, L., Liu, C., Li, X., Hu, G., Sun, J., et al. (2015). Microfluidic based high throughput synthesis of lipid-polymer hybrid nanoparticles with tunable diameters. *Biomicrofluidics* 9, 052604. doi:10.1063/1.4922957

Feng, X., Lv, F., Liu, L., Tang, H., Xing, C., Yang, Q., et al. (2010). Conjugated Polymer Nanoparticles for Drug Delivery and Imaging. *ACS Appl. Mater. Inter.* 2, 2429–2435. doi:10.1021/am100435k

Fu, A., Gwon, K., Kim, M., Tae, G., and Kornfield, J. A. (2015). Visible-light-initiated thiol-acrylate photopolymerization of heparin-based hydrogels. *Biomacromolecules* 16, 497–506. doi:10.1021/bm501543a

Gao, Y., Zhou, D., Lyu, J., Matyjaszewski, K., Tai, H., Newland, B., et al. (2020). Complex polymer architectures through free-radical polymerization of multivinyl monomers. *Nat. Rev. Chem.* 4, 194–212. doi:10.1038/s41570-020-0170-7

Gurnani, P., and Perrier, S. (2020). Controlled radical polymerization in dispersed systems for biological applications. *Prog. Polym. Sci.* 102, 101209. doi:10.1016/j.progpolymsci.2020.101209

Hailemeskel, B. Z., Addisu, K. D., Prasannan, A., Mekuria, S. L., Kao, C.-Y., and Tsai, H.-C. (2018). Synthesis and characterization of diselenide linked poly(ethylene glycol) nanogel as multi-responsive drug carrier. *Appl. Surf. Sci.* 449, 15–22. doi:10.1016/j.apsusc.2017.12.058

Hajebi, S., Abdollahi, A., Roghani-Mamaqani, H., and Salami-Kalajahi, M. (2020). Temperature-Responsive Poly(N-Isopropylacrylamide) Nanogels: The Role of Hollow Cavities and Different Shell Cross-Linking Densities on Doxorubicin Loading and Release. *Langmuir* 36, 2683–2694. doi:10.1021/acs.langmuir.9b03892

Hajebi, S., Rabiee, N., Bagherzadeh, M., Ahmadi, S., Rabiee, M., Roghani-Mamaqani, H., et al. (2019a). Stimulus-responsive polymeric nanogels as smart drug delivery systems. *Acta Biomater.* 92, 1–18. doi:10.1016/j.actbio.2019.05.018

Hajebi, S., Rabiee, N., Bagherzadeh, M., Ahmadi, S., Rabiee, M., Roghani-Mamaqani, H., et al. (2019b). Stimulus-responsive polymeric nanogels as smart drug delivery systems. *Acta Biomater.* 92, 1–18. doi:10.1016/j.actbio.2019.05.018

Huang, K., He, Y., Zhu, Z., Guo, J., Wang, G., Deng, C., et al. (2019). Small, Traceable, Endosome-Disrupting, and Bioresponsive Click Nanogels Fabricated via Microfluidics for CD44-Targeted Cytoplasmic Delivery of Therapeutic Proteins. *ACS Appl. Mater. Inter.* 11, 22171–22180. doi:10.1021/acsami.9b05827

Iqbal, S., Blenner, M., Alexander-Bryant, A., and Larsen, J. (2020). Polymersomes for Therapeutic Delivery of Protein and Nucleic Acid Macromolecules: From Design to Therapeutic Applications. *Biomacromolecules* 21, 1327–1350. doi:10.1021/acs.biomac.9b01754

Ji, P., Zhou, B., Zhan, Y., Wang, Y., Zhang, Y., Li, Y., et al. (2017). Multistimulative Nanogels with Enhanced Thermosensitivity for Intracellular Therapeutic Delivery. *ACS Appl. Mater. Inter.* 9, 39143–39151. doi:10.1021/acsami.7b08209

Kim, H., Kim, B., Lee, C., Ryu, J. L., Hong, S.-J., Kim, J., et al. (2016). Redox-responsive biodegradable nanogels for photodynamic therapy using Chlorin e6. *J. Mater. Sci.* 51, 8442–8451. doi:10.1007/s10853-016-0104-4

Kumar, P., Liu, B., and Behl, G. (2019). A Comprehensive Outlook of Synthetic Strategies and Applications of Redox-Responsive Nanogels in Drug Delivery. *Macromol. Biosci.* 19, 1900071. doi:10.1002/mabi.201900071

Lakkakula, J. R., Gujarathi, P., Pansare, P., and Tripathi, S. (2021). A comprehensive review on alginate-based delivery systems for the delivery of chemotherapeutic agent: Doxorubicin. *Carbohydr. Polym.* 259, 117696. doi:10.1016/j.carbpol.2021.117696

Lanfear, J., Fleming, J., Wu, L., Webster, G., and Harrison, P. R. (1994). The selenium metabolite selenodiglutathione induces p53 and apoptosis: relevance to the chemopreventive effects of selenium. *Carcinogenesis* 15, 1387–1392. doi:10.1093/carcin/15.7.1387

Large, D. E., Abdelmessih, R. G., Fink, E. A., and Auguste, D. T. (2021). Liposome composition in drug delivery design, synthesis, characterization, and clinical application. *Adv. Drug Deliv. Rev.* 176, 113851. doi:10.1016/j.addr.2021.113851

Le, C. M. Q., Cao, X. T., Tu, T. T. K., Gal, Y.-S., and Lim, K. T. (2018). Facile approach to prepare pH and redox-responsive nanogels via Diels-Alder click reaction. *Express Polym. Lett.* 12, 688–698. doi:10.3144/expresspolymlett.2018.59

Lee, J., Lee, C., Kim, T. H., Lee, E. S., Shin, B. S., Chi, S.-C., et al. (2012). Self-assembled glycol chitosan nanogels containing palmityl-acylated exendin-4 peptide as a long-acting anti-diabetic inhalation system. *J. Controlled Release* 161, 728–734. doi:10.1016/j.jconrel.2012.05.029

Lee, S. J., Koo, H., Jeong, H., Huh, M. S., Choi, Y., Jeong, S. Y., et al. (2011). Comparative study of photosensitizer loaded and conjugated glycol chitosan nanoparticles for cancer therapy. *J. Controlled Release* 152, 21–29. doi:10.1016/j.jconrel.2011.03.027

Le Quéméner, F., Subervie, D., Morlet-Savary, F., Lalevée, J., Lansalot, M., Bourgeat-Lami, E., et al. (2018). Visible-Light Emulsion Photopolymerization of Styrene. *Angew. Chem. Int. Ed.* 57, 957–961. doi:10.1002/anie.201710488

Li, C., Huang, W., Zhou, L., Huang, P., Pang, Y., Zhu, X., et al. (2015a). PEGylated poly(diselenide-phosphate) nanogel as efficient self-delivery nanomedicine for cancer therapy. *Polym. Chem.* 6, 6498–6508. doi:10.1039/c5py00995b

Li, C., Liu, X., Liu, Y., Huang, F., Wu, G., Liu, Y., et al. (2019a). Glucose and H2O2 dual-sensitive nanogels for enhanced glucose-responsive insulin delivery. *Nanoscale* 11, 9163–9175. doi:10.1039/c9nr01554j

Li, D., van Nostrum, C. F., Mastrobattista, E., Vermonden, T., and Hennink, W. E. (2017). Nanogels for intracellular delivery of biotherapeutics. *J. Controlled Release* 259, 16–28. doi:10.1016/j.jconrel.2016.12.020

Li, J., and Liu, P. (2018). One-pot fabrication of pH/reduction dual-stimuli responsive chitosan-based supramolecular nanogels for leakage-free tumor-specific DOX delivery with enhanced anti-cancer efficacy. *Carbohydr. Polym.* 201, 583–590. doi:10.1016/j.carbpol.2018.08.102

Li, J., Peng, Y., Peña, J., and Xing, J. (2021a). An initiating system with high efficiency for PEGDA photopolymerization at 532 nm. *J. Photochem. Photobiol. A: Chem.* 411, 113216. doi:10.1016/j.jphotochem.2021.113216

Li, X., Sun, H., Li, H., Hu, C., Luo, Y., Shi, X., et al. (2021b). Multi-Responsive Biodegradable Cationic Nanogels for Highly Efficient Treatment of Tumors. *Adv. Funct. Mater.* 31, 2100227. doi:10.1002/adfm.202100227

Li, Y., Ding, J., Zhu, J., Tian, H., and Chen, X. (2018). Photothermal Effect-Triggered Drug Release from Hydrogen Bonding-Enhanced Polymeric Micelles. *Biomacromolecules* 19, 1950–1958. doi:10.1021/acs.biomac.7b01702

Li, Y., Maciel, D., Rodrigues, J., Shi, X., and Tomás, H. (2015b). Biodegradable Polymer Nanogels for Drug/Nucleic Acid Delivery. *Chem. Rev.* 115, 8564–8608. doi:10.1021/cr500131f

Li, Z., Huang, J., and Wu, J. (2021c). pH-Sensitive nanogels for drug delivery in cancer therapy. *Biomater. Sci.* 9, 574–589. doi:10.1039/d0bm01729a

Li, Z., Van Zee, N. J., Bates, F. S., and Lodge, T. P. (2019b). Polymer Nanogels as Reservoirs To Inhibit Hydrophobic Drug Crystallization. *Acs Nano* 13, 1232–1243. doi:10.1021/acsnano.8b06393

Liang, J., Ma, Y., Sims, S., and Wu, L. (2015). A patterned porous polymer film for localized capture of insulin and glucose-responsive release. *J. Mater. Chem. B* 3, 1281–1288. doi:10.1039/C4TB01537A

Liu, Q., Peña, J., and Xing, J. (2021). Rapid preparation of nanogels by photopolymerization at 532 nm. *Colloids Surf. B: Biointerfaces* 206, 111943. doi:10.1016/j.colsurfb.2021.111943

Lou, S., Gao, S., Wang, W., Zhang, M., Zhang, J., Wang, C., et al. (2015). Galactose-functionalized multi-responsive nanogels for hepatoma-targeted drug delivery. *Nanoscale* 7, 3137–3146. doi:10.1039/c4nr06714b

Lou, S., Zhang, X., Zhang, M., Ji, S., Wang, W., Zhang, J., et al. (2017). Preparation of a dual cored hepatoma-specific star glycopolymer nanogel via arm-first ATRP approach. *Ijn* Vol. 12, 3653–3664. doi:10.2147/ijn.S134367

Lovell, P. A., and Schork, F. J. (2020). Fundamentals of Emulsion Polymerization. *Biomacromolecules* 21, 4396–4441. doi:10.1021/acs.biomac.0c00769

Lu, Y., Jia, D., Ma, X., Liang, M., Hou, S., Qiu, W., et al. (2021). Reduction-Responsive Chemo-Capsule-Based Prodrug Nanogel for Synergistic Treatment of Tumor Chemotherapy. *ACS Appl. Mater. Inter.* 13, 8940–8951. doi:10.1021/acsami.0c21710

Luan, S., Zhu, Y., Wu, X., Wang, Y., Liang, F., and Song, S. (2017). Hyaluronic-Acid-Based pH-Sensitive Nanogels for Tumor-Targeted Drug Delivery. *ACS Biomater. Sci. Eng.* 3, 2410–2419. doi:10.1021/acsbiomaterials.7b00444

Luckanagul, J. A., Pitakchatwong, C., Ratnatilaka Na Bhuket, P., Muangnoi, C., Rojsitthisak, P., Chirachanchai, S., et al. (2018a). Chitosan-based polymer hybrids for thermo-responsive nanogel delivery of curcumin. *Carbohydr. Polym.* 181, 1119–1127. doi:10.1016/j.carbpol.2017.11.027

Luckanagul, J. A., Pitakchatwong, C., Ratnatilaka Na Bhuket, P., Muangnoi, C., Rojsitthisak, P., Chirachanchai, S., et al. (2018b). Chitosan-based polymer hybrids for thermo-responsive nanogel delivery of curcumin. *Carbohydr. Polym.* 181, 1119–1127. doi:10.1016/j.carbpol.2017.11.027

Ma, X., Zhang, T., Qiu, W., Liang, M., Gao, Y., Xue, P., et al. (2021). Bioresponsive prodrug nanogel-based polycondensate strategy deepens tumor penetration and potentiates oxidative stress. *Chem. Eng. J.* 420, 127657. doi:10.1016/j.cej.2020.127657

Mackiewicz, M., Romanski, J., Krug, P., Mazur, M., Stojek, Z., and Karbarz, M. (2019). Tunable environmental sensitivity and degradability of nanogels based on derivatives of cystine and poly(ethylene glycols) of various length for biocompatible drug carrier. *Eur. Polym. J.* 118, 606–613. doi:10.1016/j.eurpolymj.2019.06.031

Mahmoudi, Z., Mohammadnejad, J., Razavi Bazaz, S., Abouei Mehrizi, A., Saidijam, M., Dinarvand, R., et al. (2020). Promoted chondrogenesis of hMCSs with controlled release of TGF-β3 via microfluidics synthesized alginate nanogels. *Carbohydr. Polym.* 229, 115551. doi:10.1016/j.carbpol.2019.115551

Maiti, D., Chao, Y., Dong, Z., Yi, X., He, J., Liu, Z., et al. (2018). Development of a thermosensitive protein conjugated nanogel for enhanced radio-chemotherapy of cancer. *Nanoscale* 10, 13976–13985. doi:10.1039/c8nr03986k

Manchun, S., Cheewatanakornkool, K., Dass, C. R., and Sriamornsak, P. (2014). Novel pH-responsive dextrin nanogels for doxorubicin delivery to cancer cells with reduced cytotoxicity to cardiomyocytes and stem cells. *Carbohydr. Polym.* 114, 78–86. doi:10.1016/j.carbpol.2014.08.002

Manchun, S., Dass, C. R., Cheewatanakornkool, K., and Sriamornsak, P. (2015). Enhanced anti-tumor effect of pH-responsive dextrin nanogels delivering doxorubicin on colorectal cancer. *Carbohydr. Polym.* 126, 222–230. doi:10.1016/j.carbpol.2015.03.018

Matsui, J. K., Lang, S. B., Heitz, D. R., and Molander, G. A. (2017). Photoredox-Mediated Routes to Radicals: The Value of Catalytic Radical Generation in Synthetic Methods Development. *ACS Catal.* 7, 2563–2575. doi:10.1021/acscatal.7b00094

Matyjaszewski, K., and Xia, J. (2001). Atom Transfer Radical Polymerization. *Chem. Rev.* 101, 2921–2990. doi:10.1021/cr940534g

Mauri, E., Perale, G., and Rossi, F. (2018). Nanogel Functionalization: A Versatile Approach To Meet the Challenges of Drug and Gene Delivery. *ACS Appl. Nano Mater.* 1, 6525–6541. doi:10.1021/acsanm.8b01686

Messager, L., Portecop, N., Hachet, E., Lapeyre, V., Pignot-Paintrand, I., Catargi, B., et al. (2013). Photochemical crosslinking of hyaluronic acid confined in nanoemulsions: towards nanogels with a controlled structure. *J. Mater. Chem. B* 1, 3369–3379. doi:10.1039/c3tb20300j

Mohammadi, M., Arabi, L., and Alibolandi, M. (2020). Doxorubicin-loaded composite nanogels for cancer treatment. *J. Controlled Release* 328, 171–191. doi:10.1016/j.jconrel.2020.08.033

Mondal, P., Behera, P. K., and Singha, N. K. (2021). Macromolecular engineering in functional polymers via 'click chemistry' using triazolinedione derivatives. *Prog. Polym. Sci.* 113, 101343. doi:10.1016/j.progpolymsci.2020.101343

Neamtu, I., Rusu, A. G., Diaconu, A., Nita, L. E., and Chiriac, A. P. (2017). Basic concepts and recent advances in nanogels as carriers for medical applications. *Drug Deliv.* 24, 539–557. doi:10.1080/10717544.2016.1276232

Nie, M., Zheng, M., Li, C., Shen, F., Liu, M., Luo, H., et al. (2019). Assembled Step Emulsification Device for Multiplex Droplet Digital Polymerase Chain Reaction. *Anal. Chem.* 91, 1779–1784. doi:10.1021/acs.analchem.8b04313

Noordergraaf, I.-W., Fourie, T., and Raffa, P. (2018). Free-Radical Graft Polymerization onto Starch as a Tool to Tune Properties in Relation to Potential Applications. A Review. *A ReviewProcesses* 6, 31. doi:10.3390/pr6040031

Oh, J. K., Drumright, R., Siegwart, D. J., and Matyjaszewski, K. (2008). The development of microgels/nanogels for drug delivery applications. *Prog. Polym. Sci.* 33, 448–477. doi:10.1016/j.progpolymsci.2008.01.002

Oh, J. K., Siegwart, D. J., Lee, H.-i., Sherwood, G., Peteanu, L., Hollinger, J. O., et al. (2007). Biodegradable Nanogels Prepared by Atom Transfer Radical Polymerization as Potential Drug Delivery Carriers: Synthesis, Biodegradation, *in Vitro* Release, and Bioconjugation. *J. Am. Chem. Soc.* 129, 5939–5945. doi:10.1021/ja069150l

Pei, M., Jia, X., Zhao, X., Li, J., and Liu, P. (2018). Alginate-based cancer-associated, stimuli-driven and turn-on theranostic prodrug nanogel for cancer detection and treatment. *Carbohydr. Polym.* 183, 131–139. doi:10.1016/j.carbpol.2017.12.013

Peng, J., Qi, T., Liao, J., Chu, B., Yang, Q., Li, W., et al. (2013). Controlled release of cisplatin from pH-thermal dual responsive nanogels. *Biomaterials* 34, 8726–8740. doi:10.1016/j.biomaterials.2013.07.092

Peng, Y., Wang, Z., Peña, J., Guo, Z., and Xing, J. (2021). Effect of TEOA on the Process of Photopolymerization at 532 nm and Properties of Nanogels. *Photochem. Photobiol.* doi:10.1111/php.13505

Pereira, S. O., Trindade, T., and Barros-Timmons, A. (2020). Biofunctional Polymer Coated Au Nanoparticles Prepared via RAFT-Assisted Encapsulating Emulsion Polymerization and Click Chemistry. *Polymers* 12, 1442. doi:10.3390/polym12071442

Pérez-Álvarez, L., Manuel Laza, J., and Álvarez-Bautista, A. (2016). Covalently and Ionically Crosslinked Chitosan Nanogels for Drug Delivery. *Cpd* 22, 3380–3398. doi:10.2174/1381612822666160216152008

Phan, Q. T., Patil, M. P., Tu, T. T. K., Kim, G.-D., and Lim, K. T. (2020). Synthesis of zwitterionic redox-responsive nanogels by one-pot amine-thiol-ene reaction for anticancer drug release application. *Reactive Funct. Polym.* 147, 104463. doi:10.1016/j.reactfunctpolym.2019.104463

Pinelli, F., Ortolà, Ó. F., Makvandi, P., Perale, G., and Rossi, F. (2020). *In vivo* drug delivery applications of nanogels: a review. *Nanomedicine* 15, 2707–2727. doi:10.2217/nnm-2020-0274

Pu, X.-Q., Ju, X.-J., Zhang, L., Cai, Q.-W., Liu, Y.-Q., Peng, H.-Y., et al. (2021). Novel Multifunctional Stimuli-Responsive Nanoparticles for Synergetic Chemo-Photothermal Therapy of Tumors. *ACS Appl. Mater. Inter.* 13, 28802–28817. doi:10.1021/acsami.1c05330

Qin, B., Yin, Z., Tang, X., Zhang, S., Wu, Y., Xu, J.-F., et al. (2020). Supramolecular polymer chemistry: From structural control to functional assembly. *Prog. Polym. Sci.* 100, 101167. doi:10.1016/j.progpolymsci.2019.101167

Qu, J.-B., Chapman, R., Chen, F., Lu, H., and Stenzel, M. H. (2017). Swollen Micelles for the Preparation of Gated, Squeezable, pH-Responsive Drug Carriers. *ACS Appl. Mater. Inter.* 9, 13865–13874. doi:10.1021/acsami.7b01120

Qu, Y., Chu, B., Wei, X., Lei, M., Hu, D., Zha, R., et al. (2019). Redox/pH dual-stimuli responsive camptothecin prodrug nanogels for "on-demand" drug delivery. *J. Controlled Release* 296, 93–106. doi:10.1016/j.jconrel.2019.01.016

Raemdonck, K., Demeester, J., and De Smedt, S. (2009). Advanced nanogel engineering for drug delivery. *Soft Matter* 5, 707–715. doi:10.1039/b811923f

Rhee, M., Valencia, P. M., Rodriguez, M. I., Langer, R., Farokhzad, O. C., and Karnik, R. (2011). Synthesis of Size-Tunable Polymeric Nanoparticles Enabled by 3D Hydrodynamic Flow Focusing in Single-Layer Microchannels. *Adv. Mater.* 23, H79–H83. doi:10.1002/adma.201004333

Sahle, F. F., Giulbudagian, M., Bergueiro, J., Lademann, J., and Calderón, M. (2017). Dendritic polyglycerol and N-isopropylacrylamide based thermoresponsive nanogels as smart carriers for controlled delivery of drugs through the hair follicle. *Nanoscale* 9, 172–182. doi:10.1039/c6nr06435c

Seidi, F., Jenjob, R., and Crespy, D. (2018). Designing Smart Polymer Conjugates for Controlled Release of Payloads. *Chem. Rev.* 118, 3965–4036. doi:10.1021/acs.chemrev.8b00006

Sengel, S. B., and Sahiner, N. (2019). Synthesis and characterization of poly(N-(2-mercaptoethyl) acrylamide) microgel for biomedical applications. *Polym. Adv. Technol.* 30, 2109–2121. doi:10.1002/pat.4644

Senthilkumar, T., Lv, F., Zhao, H., Liu, L., and Wang, S. (2019). Conjugated Polymer Nanogel Binding Anticancer Drug through Hydrogen Bonds for Sustainable Drug Delivery. *ACS Appl. Bio Mater.* 2, 6012–6020. doi:10.1021/acsabm.9b00941

Seo, S., Lee, C.-S., Jung, Y.-S., and Na, K. (2012). Thermo-sensitivity and triggered drug release of polysaccharide nanogels derived from pullulan-g-poly(l-lactide) copolymers. *Carbohydr. Polym.* 87, 1105–1111. doi:10.1016/j.carbpol.2011.08.061

Shah, S., Rangaraj, N., Laxmikeshav, K., and Sampathi, S. (2020). "Nanogels as drug carriers - Introduction, chemical aspects, release mechanisms and potential applications". *Int. J. Pharmaceutics* 581, 119268. doi:10.1016/j.ijpharm.2020.119268

Sharma, A., Garg, T., Aman, A., Panchal, K., Sharma, R., Kumar, S., et al. (2016). Nanogel-an advanced drug delivery tool: Current and future. *Artif. Cell Nanomedicine, Biotechnol.* 44, 165–177. doi:10.3109/21691401.2014.930745

Siegwart, D. J., Srinivasan, A., Bencherif, S. A., Karunanidhi, A., Oh, J. K., Vaidya, S., et al. (2009). Cellular Uptake of Functional Nanogels Prepared by Inverse Miniemulsion ATRP with Encapsulated Proteins, Carbohydrates, and Gold Nanoparticles. *Biomacromolecules* 10, 2300–2309. doi:10.1021/bm9004904

Su, H., Jia, Q., and Shan, S. (2016). Synthesis and characterization of Schiff base contained dextran microgels in water-in-oil inverse microemulsion. *Carbohydr. Polym.* 152, 156–162. doi:10.1016/j.carbpol.2016.06.091

Su, H., Zhang, W., Wu, Y., Han, X., Liu, G., Jia, Q., et al. (2018). Schiff base-containing dextran nanogel as pH-sensitive drug delivery system of doxorubicin: Synthesis and characterization. *J. Biomater. Appl.* 33, 170–181. doi:10.1177/0885328218783969

Sun, Z., Yi, Z., Zhang, H., Ma, X., Su, W., Sun, X., et al. (2017). Bio-responsive alginate-keratin composite nanogels with enhanced drug loading efficiency for cancer therapy. *Carbohydr. Polym.* 175, 159–169. doi:10.1016/j.carbpol.2017.07.078

Tai, W., Mo, R., Lu, Y., Jiang, T., and Gu, Z. (2014). Folding graft copolymer with pendant drug segments for co-delivery of anticancer drugs. *Biomaterials* 35, 7194–7203. doi:10.1016/j.biomaterials.2014.05.004

Tasdelen, M. A., Kiskan, B., and Yagci, Y. (2016). Externally stimulated click reactions for macromolecular syntheses. *Prog. Polym. Sci.* 52, 19–78. doi:10.1016/j.progpolymsci.2015.09.003

Thelu, H. V. P., Albert, S. K., Golla, M., Krishnan, N., Ram, D., Srinivasula, S. M., et al. (2018). Size controllable DNA nanogels from the self-assembly of DNA nanostructures through multivalent host-guest interactions. *Nanoscale* 10, 222–230. doi:10.1039/c7nr06985e

Theune, L. E., Buchmann, J., Wedepohl, S., Molina, M., Laufer, J., and Calderón, M. (2019). NIR- and thermo-responsive semi-interpenetrated polypyrrole nanogels for imaging guided combinational photothermal and chemotherapy. *J. Controlled Release* 311-312, 147–161. doi:10.1016/j.jconrel.2019.08.035

Tian, Y., Tian, R., Chen, L., Jin, R., Feng, Y., Bai, Y., et al. (2019). Redox-Responsive Nanogel with Intracellular Reconstruction and Programmable Drug Release for Targeted Tumor Therapy. *Macromol. Rapid Commun.* 40, 1800824. doi:10.1002/marc.201800824

Ulukan, H., and Swaan, P. W. (2002). Camptothecins. *Drugs* 62, 2039–2057. doi:10.2165/00003495-200262140-00004

Wang, H., Ke, F., Mararenko, A., Wei, Z., Banerjee, P., and Zhou, S. (2014). Responsive polymer-fluorescent carbon nanoparticle hybrid nanogels for optical temperature sensing, near-infrared light-responsive drug release, and tumor cell imaging. *Nanoscale* 6, 7443–7452. doi:10.1039/c4nr01030b

Wang, S., Ha, Y., Huang, X., Chin, B., Sim, W., and Chen, R. (2018). A New Strategy for Intestinal Drug Delivery via pH-Responsive and Membrane-Active Nanogels. *ACS Appl. Mater. Inter.* 10, 36622–36627. doi:10.1021/acsami.8b15661

Wang, X., Peng, Y., Peña, J., and Xing, J. (2021). Preparation of ultrasmall nanogels by facile emulsion-free photopolymerization at 532 nm. *J. Colloid Interf. Sci.* 582, 711–719. doi:10.1016/j.jcis.2020.08.056

Wang, Y., Zheng, J., Tian, Y., and Yang, W. (2015). Acid degradable poly(vinylcaprolactam)-based nanogels with ketal linkages for drug delivery. *J. Mater. Chem. B* 3, 5824–5832. doi:10.1039/c5tb00703h

Wang, Y., Zu, M., Ma, X., Jia, D., Lu, Y., Zhang, T., et al. (2020). Glutathione-Responsive Multifunctional "Trojan Horse" Nanogel as a Nanotheranostic for Combined Chemotherapy and Photodynamic Anticancer Therapy. *ACS Appl. Mater. Inter.* 12, 50896–50908. doi:10.1021/acsami.0c15781

Webber, M. J., Appel, E. A., Meijer, E. W., and Langer, R. (2016). Supramolecular biomaterials. *Nat. Mater* 15, 13–26. doi:10.1038/nmat4474

Wei, X., Senanayake, T. H., Warren, G., and Vinogradov, S. V. (2013). Hyaluronic acid-based nanogel-drug conjugates with enhanced anticancer activity designed for the targeting of CD44-positive and drug-resistant tumors. *Bioconjug. Chem.* 24, 658–668. doi:10.1021/bc300632w

Wu, C., Hu, W., Wei, Q., Qiao, L., Gao, Y., Lv, Y., et al. (2018). Controllable Growth of Core-Shell Nanogels via Esterase-Induced Self-Assembly of Peptides for Drug Delivery. *J Biomed. Nanotechnol* 14, 354–361. doi:10.1166/jbn.2018.2492

Wu, W.-S. (2006). The signaling mechanism of ROS in tumor progression. *Cancer Metastasis Rev.* 25, 695–705. doi:10.1007/s10555-006-9037-8

Xiao, K., Li, Y., Luo, J., Lee, J. S., Xiao, W., Gonik, A. M., et al. (2011). The effect of surface charge on *in vivo* biodistribution of PEG-oligocholic acid based micellar nanoparticles. *Biomaterials* 32, 3435–3446. doi:10.1016/j.biomaterials.2011.01.021

Xin, F., Wei, M., Jiang, S., Gao, Y., Nie, J., Wu, Y., et al. (2020). Design of hydrophilic photocleavage o-nitrobenzyl acrylate-modified nanogels with outstanding biocompatibility prepared by RAFT polymerization for drug carrier. *Eur. Polym. J.* 122, 109364. doi:10.1016/j.eurpolymj.2019.109364

Xu, S., Olenyuk, B. Z., Okamoto, C. T., and Hamm-Alvarez, S. F. (2013). Targeting receptor-mediated endocytotic pathways with nanoparticles: Rationale and advances. *Adv. Drug Deliv. Rev.* 65, 121–138. doi:10.1016/j.addr.2012.09.041

Yang, H., Wang, Q., Huang, S., Xiao, A., Li, F., Gan, L., et al. (2016). Smart pH/Redox Dual-Responsive Nanogels for On-Demand Intracellular Anticancer Drug Release. *ACS Appl. Mater. Inter.* 8, 7729–7738. doi:10.1021/acsami.6b01602

Yoon, H. Y., Koo, H., Choi, K. Y., Lee, S. J., Kim, K., Kwon, I. C., et al. (2012). Tumor-targeting hyaluronic acid nanoparticles for photodynamic imaging and therapy. *Biomaterials* 33, 3980–3989. doi:10.1016/j.biomaterials.2012.02.016

Yu, Y., Cheng, Y., Tong, J., Zhang, L., Wei, Y., and Tian, M. (2021). Recent advances in thermo-sensitive hydrogels for drug delivery. *J. Mater. Chem. B* 9, 2979–2992. doi:10.1039/d0tb02877k

Yuan, D., Ding, L., Sun, Z., and Li, X. (2018). MRI/Fluorescence bimodal amplification system for cellular GSH detection and tumor cell imaging based on manganese dioxide nanosheet. *Sci. Rep.* 8, 1747. doi:10.1038/s41598-018-20110-z

Zan, M., Li, J., Huang, M., Lin, S., Luo, D., Luo, S., et al. (2015). Near-infrared light-triggered drug release nanogels for combined photothermal-chemotherapy of cancer. *Biomater. Sci.* 3, 1147–1156. doi:10.1039/c5bm00048c

Zavgorodnya, O., Carmona-Moran, C. A., Kozlovskaya, V., Liu, F., Wick, T. M., and Kharlampieva, E. (2017). Temperature-responsive nanogel multilayers of poly(N-vinylcaprolactam) for topical drug delivery. *J. Colloid Interf. Sci.* 506, 589–602. doi:10.1016/j.jcis.2017.07.084

Zhang, L., Chen, Q., Ma, Y., and Sun, J. (2020). Microfluidic Methods for Fabrication and Engineering of Nanoparticle Drug Delivery Systems. *ACS Appl. Bio Mater.* 3, 107–120. doi:10.1021/acsabm.9b00853

Zhang, Y., Andrén, O. C. J., Nordström, R., Fan, Y., Malmsten, M., Mongkhontreerat, S., et al. (2019). Off-Stoichiometric Thiol-Ene Chemistry to Dendritic Nanogel Therapeutics. *Adv. Funct. Mater.* 29, 1806693. doi:10.1002/adfm.201806693

Zhang, Y., Ma, C., Zhang, S., Wei, C., Xu, Y., and Lu, W. (2018). ROS-responsive selenium-containing polyphosphoester nanogels for activated anticancer drug release. *Mater. Today Chem.* 9, 34–42. doi:10.1016/j.mtchem.2018.04.002

Zhao, G., Long, L., Zhang, L., Peng, M., Cui, T., Wen, X., et al. (2017). Smart pH-sensitive nanoassemblies with cleavable PEGylation for tumor targeted drug delivery. *Sci. Rep.* 7, 3383. doi:10.1038/s41598-017-03111-2

Zhao, Q., Zhang, S., Wu, F., Li, D., Zhang, X., Chen, W., et al. (2021). Rational Design of Nanogels for Overcoming the Biological Barriers in Various Administration Routes. *Angew. Chem. Int. Ed.* 60, 14760–14778. doi:10.1002/anie.201911048

Zhu, J.-Y., Lei, Q., Yang, B., Jia, H.-Z., Qiu, W.-X., Wang, X., et al. (2015). Efficient nuclear drug translocation and improved drug efficacy mediated by acidity-responsive boronate-linked dextran/cholesterol nanoassembly. *Biomaterials* 52, 281–290. doi:10.1016/j.biomaterials.2015.02.048

Zhu, Y., Yang, B., Chen, S., and Du, J. (2017). Polymer vesicles: Mechanism, preparation, application, and responsive behavior. *Prog. Polym. Sci.* 64, 1–22. doi:10.1016/j.progpolymsci.2015.05.001

Zhu, Z., Kimura, M., Itokawa, Y., Aoki, T., Takahashi, J. A., Nakatsu, S., et al. (1996). Apoptosis induced by selenium in human glioma cell lines. *Biol. Trace Elem. Res.* 54, 123–134. doi:10.1007/BF02786259

Conflict of Interest: The authors declare that the research was conducted in the absence of any commercial or financial relationships that could be construed as a potential conflict of interest.

Publisher's Note: All claims expressed in this article are solely those of the authors and do not necessarily represent those of their affiliated organizations, or those of the publisher, the editors and the reviewers. Any product that may be evaluated in this article, or claim that may be made by its manufacturer, is not guaranteed or endorsed by the publisher.

frontiers in Bioengineering and Biotechnology

ORIGINAL RESEARCH
published: 26 October 2021
doi: 10.3389/fbioe.2021.753879

Ocular Wnt/β-Catenin Pathway Inhibitor XAV939-Loaded Liposomes for Treating Alkali-Burned Corneal Wound and Neovascularization

Yueyang Zhong[1,2†], Kai Wang[1,2†], Yin Zhang[1,2], Qichuan Yin[1,2], Su Li[1,2], Jiaming Wang[3], Xiaobo Zhang[1,2], Haijie Han[1,2] and Ke Yao[1,2*]*

[1]Eye Center, The Second Affiliated Hospital, School of Medicine, Zhejiang University, Hangzhou, China, [2]Zhejiang Provincial Key Lab of Ophthalmology, The Second Affiliated Hospital, School of Medicine, Zhejiang University, Hangzhou, China, [3]The First Affiliated Hospital, School of Public Health, Institute of Translational Medicine, State Key Laboratory of Experimental Hematology, School of Medicine, Zhejiang University, Hangzhou, China

OPEN ACCESS

Edited by:
Yakai Feng,
Tianjin University, China

Reviewed by:
Ashley Carson Brown,
North Carolina State University, United States
Qian Li,
Texas A&M University, United States
Xuefang Hao,
Inner Mongolia University for Nationalities, China

***Correspondence:**
Ke Yao
xlren@zju.edu.cn
Haijie Han
hanhj90@zju.edu.cn

[†]These authors have contributed equally to this work

Specialty section:
This article was submitted to Biomaterials, a section of the journal Frontiers in Bioengineering and Biotechnology

Received: 05 August 2021
Accepted: 20 September 2021
Published: 26 October 2021

Citation:
Zhong Y, Wang K, Zhang Y, Yin Q, Li S, Wang J, Zhang X, Han H and Yao K (2021) Ocular Wnt/β-Catenin Pathway Inhibitor XAV939-Loaded Liposomes for Treating Alkali-Burned Corneal Wound and Neovascularization. Front. Bioeng. Biotechnol. 9:753879. doi: 10.3389/fbioe.2021.753879

Corneal wound involves a series of complex and coordinated physiological processes, leading to persistent epithelial defects and opacification. An obstacle in the treatment of ocular diseases is poor drug delivery and maintenance. In this study, we constructed a Wnt/β-catenin pathway inhibitor, XAV939-loaded liposome (XAV939 NPs), and revealed its anti-inflammatory and antiangiogenic effects. The XAV939 NPs possessed excellent biocompatibility in corneal epithelial cells and mouse corneas. *In vitro* corneal wound healing assays demonstrated their antiangiogenic effect, and LPS-induced expressions of pro-inflammatory genes of IL-1β, IL-6, and IL-17α were significantly suppressed by XAV939 NPs. In addition, the XAV939 NPs significantly ameliorated alkali-burned corneas with slight corneal opacity, reduced neovascularization, and faster recovery, which were attributed to the decreased gene expressions of angiogenic and inflammatory cytokines. The findings supported the potential of XAV939 NPs in ameliorating corneal wound and suppressing neovascularization, providing evidence for their clinical application in ocular vascular diseases.

Keywords: liposomes, Wnt/β-catenin pathway, XAV939, corneal wound, corneal neovascularization

INTRODUCTION

As one of the most vulnerable parts of the eye that is exposed to the external environment, the cornea is consistently susceptible to potential infectious and traumatic damages (Mobaraki et al., 2019; Chen F. et al., 2020; Han et al., 2020a). In addition, the constantly increasing number of refractive surgeries has prompted corneal wound healing an important clinical problem. Corneal wound involves a series of complex and dynamic pathological processes, including cell death, inflammatory and immune response, corneal neovascularization (CNV), and limbal stem cell deficiency, which compromise corneal transparency and lead to decreased vision (Roshandel et al., 2018; Ziaei et al., 2018). Previous studies have illustrated the effectiveness of inhibiting inflammatory responses and blocking angiogenic signaling pathways in accelerating corneal wound healing, providing potential therapeutic options that target multiple processes in treating corneal wounds (Ellenberg et al., 2010; Chandler et al., 2019; Yang J. et al., 2020, Yang et al., 2020 S.; Rebibo et al., 2021).

The evolutionarily highly conserved Wnt signaling pathway regulates various processes, including proliferation, polarization, migration, apoptosis, and stem cell maintenance and differentiation, which are related to systemic development and various congenital and developmental diseases (Reya and Clevers, 2005; Klaus and Birchmeier, 2008; Clevers and Nusse, 2012; Feng et al., 2020). In addition, previous studies have implicated the indispensable role of the Wnt pathway in developmental and pathological ocular angiogenesis (Ouyang et al., 2014; Wang Z. et al., 2019). In the canonical Wnt signaling pathway, Wnt ligands bind to the receptor complex of frizzled receptors and low-density lipoprotein receptor–related protein 5/6, which results in the stabilization of β-catenin and the degradation of Axin (Huang et al., 2009; Clevers and Nusse, 2012). Without phosphorylation, β-catenin is translocated into the nucleus and binds to the transcription factors to activate Wnt target genes (Huang et al., 2009; Clevers and Nusse, 2012). Consequently, various inhibitors along the Wnt signaling pathway have been identified to regulate abnormal gene activation, among which XAV939, a small molecule that stabilizes Axin and stimulates β-catenin degradation, exhibits therapeutic promise in treating Wnt pathway–dependent diseases (Huang et al., 2009). Further studies have identified the anti-inflammatory and antitumor activities of XAV939, yet its potential in treating ocular vascular diseases has not been reported (Li et al., 2018; Almasoud et al., 2020; Zhang et al., 2020).

One obstacle to the treatment of ocular diseases is poor drug delivery and maintenance (Fan et al., 2021; Zhang et al., 2021). The topical eye drop solution, which is one of the most common and preferred methods of drug administration to the eye, is readily excreted through tear drainage and peribulbar blood flow. For instance, it is estimated that 60% of the drug is eliminated within 2 min and is completely discharged within 15 min, resulting in low drug absorption (Jumelle et al., 2020). Moreover, eye drops are unlikely to deliver drugs with insoluble properties. As such, the liposome delivery system, one of the first polymeric nanoparticles approved by the FDA, allows the delivery of hydrophobic and hydrophilic compounds with varying sizes and properties (Kompella et al., 2013; Anselmo and Mitragotri, 2019; Chen X. et al., 2020; Chang et al., 2021; Shi et al., 2021). As biodegradable and biocompatible lipid assemblies, liposomes can achieve sustained drug release to the ocular surface and high penetration into the inner structure (Kompella et al., 2013; Peng et al., 2020; Tavakoli et al., 2020; Yuba, 2020). Various studies have reported prolonged release, improved efficacy, and reduced toxicity of liposome-capsulated drugs, thereby providing substantial potentials for clinical applications (Eriksen et al., 2018; Jin et al., 2019; Ma et al., 2020).

In this study, we constructed a Wnt/β-catenin pathway inhibitor, XAV939-loaded liposomes (XAV939 NPs), and investigated its anti-inflammatory and antiangiogenic effects. The effects of corneal wound healing and CNV suppression were investigated in an alkali-burned mouse model to explore its therapeutic potential in treating ocular vascular diseases.

MATERIALS AND METHODS

Preparation of XAV939 NPs

The liposomes loaded with XAV939 were prepared using a thin-film hydration method as described in previous studies (Alfaifi et al., 2020; Ye et al., 2020). In brief, 3 mg of XAV939 (MedChemExpress, China), 8 mg of L-α-phosphatidylcholine (soybean lecithin, J&K Scientific, China), 3 mg of 1,2-distearoyl-sn-glycero-3-phosphoethanolamine-N-[methoxy (polyethylene glycol)-2000] [DSPE-PEG (2000), AVT Pharmaceutical Technology Co., Ltd, China], and 2 mg of cholesterol (J&K Scientific, China) were dissolved in 10.0 ml chloroform in a round-bottom flask. The mixture was evaporated under reduced pressure in a rotary evaporator for 3 h, and a homogeneous phospholipid film was formed. Then, 10 ml of double-distilled water was added into the round-bottom flask to hydrate the phospholipid film for 1 h, and the liposomes were ultrasonicated for 1 min to form a uniform suspension. The final concentration of XAV939 in the liposomes was 1 mM.

Characterization of XAV939 NPs

The hydrodynamic size and polydispersity index of the XAV939 NPs were measured by dynamic light scattering (DLS, Zetasizer Nano ZS90, Malvern, United Kingdom). The samples were filtered through a 0.22-μm Millipore filter before taking the measurements, and their morphologies were characterized by cryo-electron microscopy (Cryo-EM) on a 200 kV Talos F200C microscope (FEI, Holland).

Cell Culture

Human corneal epithelial cells (HCEs) were purchased from the American Type Culture Collection (United States). Human umbilical vein endothelial cells (HUVECs) were purchased from Beyotime Biotechnology (China). The HCEs were cultured with DMEM/F12 (Corning, United States) with 10% fetal bovine serum (FBS) and 1% penicillin–streptomycin. The HUVECs were cultured with DMEM (Corning, United States) with 10% FBS and 1% penicillin–streptomycin. All cells were incubated in a 37°C/5% CO_2 humidified chamber.

Cytotoxicity Assays

Cell Counting Kit-8 Assay

Cytotoxicity was measured with a cell counting kit-8 (CCK-8) assay (Dojindo, Japan) (Han et al., 2017; Han et al., 2020b). Briefly, the HCE cells were seeded in a 96-well plate to reach the density of 1×10^4 per well. The cells were incubated with a 100 μl DMEM/F12 medium and treated with 10% phosphate buffered saline (PBS) or XAV939 NPs of different XAV939 equivalent concentrations: 0, 0.1, 1, 10, 25, and 50 μM. After 24 h of incubation, 10 μl CCK-8 solution was added to each well and maintained for 2 h at 37°C according to the manufacturer's instructions. The optical density at 450 nm (OD_{450nm}) was measured using an absorbance microplate reader (Bio-rad iMark, United States).

Calcein-AM/Propidium Iodide Assay

For Calcein-AM/propidium iodide (PI) assay (Yeasen, China), the HCE cells were seeded in a 12-well plate with a density of 1×10^5 cells per well. The cells were incubated with 1 ml DMEM/F12 medium and treated with 10% PBS or XAV939 NPs of different XAV939 equivalent concentrations: 0, 0.1, 1, 10, 25, and 50 μM. After 24 h of incubation, the medium was removed, and the cells were rinsed with PBS three times. Subsequently, the cells were treated with 0.67 μM Calcein AM and 1.5 μM PI and were incubated for 15 min at 37°C. The cells were then observed under a fluorescence microscope (Leica, Germany), and images of live (green) and dead (red) cells were obtained.

Quantitative Reverse Transcription-Polymerase Chain Reaction

The HCEs were seeded in a 12-well plate until they reached a density of 1×10^5 cells per well. The cells were first incubated with a fresh DMEM/F12 medium containing 1% FBS, and 10% PBS, XAV939 (10 μM), or XAV939 NPs (10 μM XAV939 equivalent) for 24 h. To induce an inflammatory response, the cells were treated with 1 μg/ml lipopolysaccharides (LPS, Sigma Aldrich, United States) for 2 h. The total RNA of the HCEs was extracted using TRIzol reagent (Invitrogen, Carlsbad, United States) and reverse-transcribed using the PrimeScript™ RT Master Mix (Takara Bio Inc., Japan). Reverse transcription–polymerase chain reaction (RT-PCR) was performed using the ChamQTM SYBR Color qPCR Master Mix (Vazyme Biotech Co., Ltd., China) on a 7500 Fast Real-Time PCR System (Thermo Scientific, United States). The relative gene expressions of inflammatory cytokines, including interleukin (IL)-1β, IL-6, and IL-17α, were analyzed and normalized to the GAPDH level. The relative quantitation was calculated with the comparative cycle threshold Ct ($\Delta\Delta Ct$) method.

Cell Migration Assay

Vascular endothelial cells proliferation has been validated as an initial step in angiogenesis, followed by migration, adhesion, and differentiation (Lamalice et al., 2007). Therefore, for the cell migration assay, we adopted HUVECs, which have been abundantly used (Lamalice et al., 2007; Wang M. et al., 2019). These cells were seeded in a 6-well plate until they reached a density of 2×10^5 cells per well. After a confluent monolayer was formed, a wound was generated in each well by a sterilized 200 μl peptide tip, and the cells were washed three times with PBS. The cells were then treated with 1 μg/ml recombinant human vascular endothelial growth factor-165 ($rhVEGF_{165}$, PeproTech Inc., United States) and combined with 10% PBS, XAV939 (10 μM) or XAV939 NPs (10 μM XAV939 equivalent) and incubated with a fresh DMEM medium containing 1% FBS. Cell migration and wound closure were observed at 0, 12, and 24 h with an Olympus inverted light microscope, and microphotographs were taken at 10× magnification with an Oplenic digital camera. The scratch widths and the percentage of wound closure were quantified using ImageJ software (National Institutes of Health, Bethesda, United States).

Immunoblotting

The HUVECs were seeded in a 6-well plate with a density of 2×10^5 cells per well. These cells were then treated with 1 μg/ml $rhVEGF_{165}$ and combined with the previously indicated treatments. After 24 h of incubation, the cells were rinsed three times with PBS. The cell lysates were harvested with a lysis buffer with protease and phosphatase inhibitors (Sangon Biotech, China). After lysing on ice for 30 min, the cell lysates were centrifuged at 14,000 × g for 15 min at 4°C. The protein concentration was calculated using a bicinchoninic acid protein assay kit (Thermo Scientific, United States) and normalized. Thirty micrograms of protein were resolved with 6–10% sodium dodecyl sulfate-polyacrylamide gel electrophoresis and electro-transferred to polyvinylidene fluoride membranes. The membranes were then blocked with a protein-free rapid blocking buffer (Epizyme, China) and immunoblotted with the following antibodies: rabbit monoclonal anti–β-catenin (Cell Signaling Technology, United States, 1:1000), rabbit monoclonal anti-Axin 1 (Cell Signaling Technology, United States, 1:1000), and rabbit monoclonal anti–β-actin (Cell Signaling Technology, United States, 1:1000). All quantitative data were normalized to β-actin as an endogenous control. ImageJ software was used to analyze the band intensity.

Animals

Female C57BL/6 mice aged 6–8 weeks were purchased from Shanghai SLAC Laboratory Animal Co., Ltd, China. All animal experiments strictly abided by the Association for Research in Vision and Ophthalmology Statement for the Use of Animals in Ophthalmic and Vision Research and the guidelines of Zhejiang University Administration on Laboratory Animal Care.

In Vivo Biocompatibility Assessment

To assess the biocompatibility of the liposomes, 10 μl of XAV939 NPs (10 μM XAV939 equivalent) was topically administered to the eyes of the healthy mice in the experimental group. The control group received 10 μl of saline solution. On days 3, 7, and 14, the mice were anesthetized, and the ocular surface was observed with a slit lamp microscope. After 14 days of treatment, the mice were sacrificed, and the eyeballs and major visceral organs, including the heart, liver, spleen, lung, and kidney, were fixed to perform hematoxylin and eosin (H&E) staining for histological observation.

Alkali-Burned Injury Mouse Model

The alkali-burned injury mouse model was developed to generate corneal wound and CNV, as previously described (Anderson et al., 2014). A mouse was first anesthetized through a peritoneal injection of sodium pentobarbital (100 mg/kg) and topical administration of 0.5% proparacaine solution to the corneal surface of the right eye. Then, a 2-mm-diameter filter paper was soaked in 1 N sodium hydroxide (NaOH) solution and tapped on a dry filter paper for 5 s to absorb the excess alkali.

The NaOH-soaked filter paper was placed on the center of the mouse's right cornea for 30 s and then rinsed with 10 ml of PBS for 60 s. All alkali-burned injury procedures were performed by the same investigators to minimize variability, and the mice were randomly divided into three groups: saline, XAV939 (10 μM, dissolved in 0.1% v/v DMSO/saline), and XAV939 NPs (10 μM XAV939 equivalent). All alkali-burned eyes were treated with 10 μl of the abovementioned eye drop solution twice daily for 14 consecutive days.

Clinical Examination

On days 3, 7, and 14, all mice were weighed and observed with a slit lamp microscope, and representative images were taken. Two examiners independently performed clinical evaluations and reported a final score according to the established methods (Anderson et al., 2014):

1) Corneal opacity (0–4): 0 = completely clear; 1 = slightly hazy, iris and pupil easily visible; 2 = slightly opaque, iris and pupil detectable; 3 = opaque, pupils hardly detectable; and 4 = completely opaque, pupil undetectable.
2) CNV (0–3): 0 = no CNV, 1 = CNV at the corneal limbus, 2 = CNV spanning over the corneal limbus to the corneal center, and 3 = CNV invading the corneal center.
3) Neovessels (0–3): 0 = no neovessels; 1 = neovessels detectable under a surgical microscope; 2 = neovessels easily visible under a surgical microscope; and 3 = neovessels visible to the naked eye.

CNV was calculated based on the range of clock hours of corneal neovessels. The CNV size was calculated as follows:

$$S = \frac{C}{12} * 3.1416 * \left[r^2 - (r - l)^2\right],$$

where S = CNV size, C = clock hours of CNV, r = radius of the mouse cornea, and l = length of the longest neovessel from the limbus.

Immunohistochemistry

After 14 days of treatment, the mice were sacrificed, and the right eyes were enucleated under a stereomicroscope (Leica, Germany), followed by fixation with 4% paraformaldehyde (PFA, Biosharp, China) overnight. The eyeballs were then embedded in paraffin, sectioned, and stained with H&E. The sections were then observed under a microscope (Leica, Germany), and representative photographs were taken. The central corneal thickness was measured and analyzed independently by two examiners using ImageJ software. To assess the biosafety and toxicity of XAV939 and XAV939 NPs, the alkali-burned mice were sacrificed and major visceral organs were enucleated to perform H&E staining.

Immunofluorescence

On day 15, the mice were sacrificed, and the eyeballs were harvested for corneal flat mount staining. After being fixed in 4% PFA overnight, the corneas with the limbal area were carefully dissected under a stereomicroscope. To make the cornea lie flat, four incisions were made from the periphery toward the center cornea. After being rinsed with PBS with Tween-20 (PBST) three times, the corneas were blocked with 1% bovine serum albumin, 2% goat serum, and 0.2% Triton X-100 in PBS for 2 h and incubated with rabbit anti–mouse CD31 antibody (Abcam, United Kingdom, 1:50) prepared in a blocking buffer at 4°C overnight. The corneas were then rinsed with PBST six times and incubated with Alexa-Fluor 555-conjugated goat anti-rabbit secondary antibody (Invitrogen Life Technologies, United States, 1:1000) for 2 h at room temperature, followed by rinsing with PBST six times. Immunofluorescent images of the corneas were obtained using a fluorescence microscope. The neovessels length and the ratio between the CNV area and whole cornea area were calculated with ImageJ software.

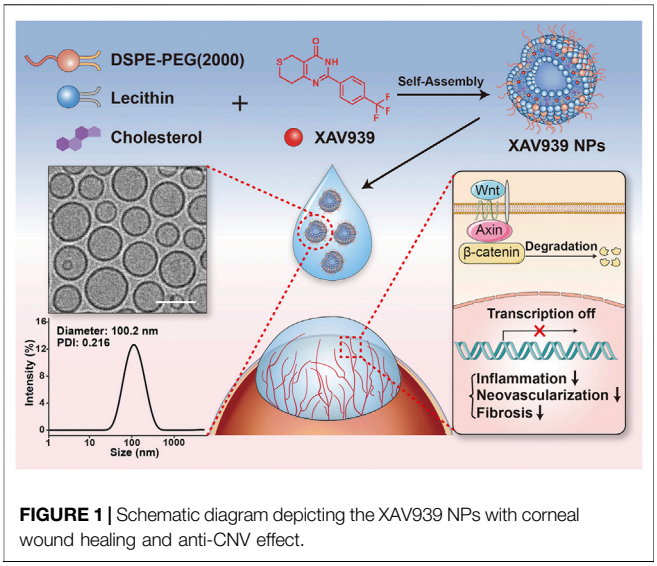

FIGURE 1 | Schematic diagram depicting the XAV939 NPs with corneal wound healing and anti-CNV effect.

qRT-PCR

After 14 days of treatment, the mice were sacrificed, and the right corneas were excised. The total RNA of the corneas was extracted using TRIzol reagent. Two corneas were pooled as one biological replica, and three samples were conducted for each group. The methods used for qRT-PCR have been described in the previous section. The relative gene expression quantification included the following: *Vegfs*, *Vegfrs*, *Mmps*, *α-Sma*, *Cd31*, and *Il-6*. The gene expressions were normalized to the GAPDH level, and the relative quantitation was calculated with the $\Delta\Delta Ct$ method.

Statistical Analyses

All statistical analyses were performed using SPSS 26.0 (IBM Corp., United States). The data were presented as the mean with its standard error of mean (SEM). Comparisons among three or more groups were performed for statistical significance using one-way analysis of variance (ANOVA). The statistical significance was defined as $p < 0.05$.

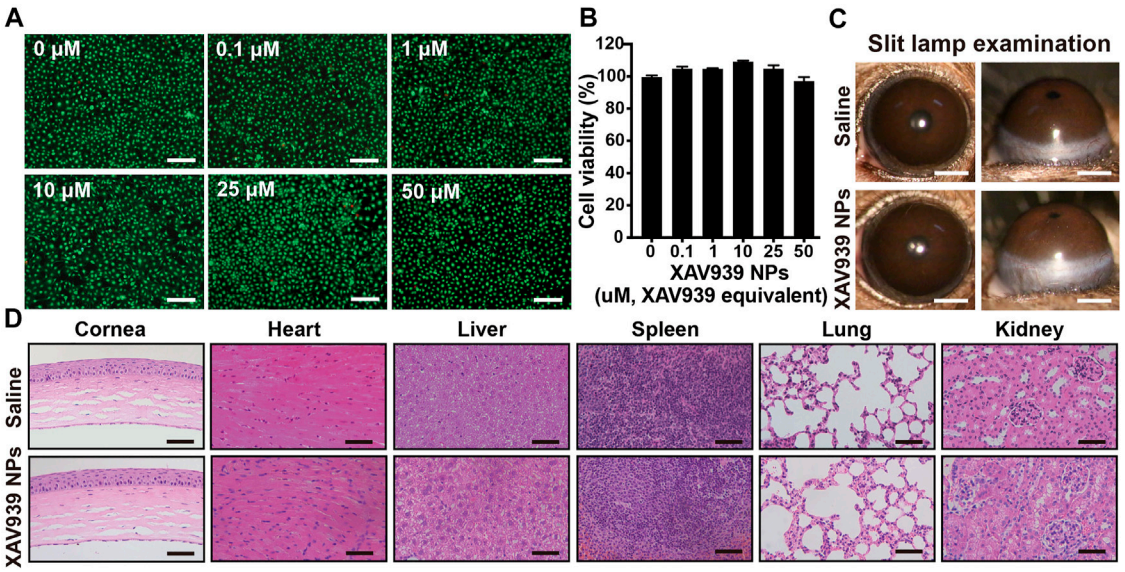

FIGURE 2 | *In vitro* and *in vivo* biocompatibility assessments. Calcein-AM/PI assay **(A)** and CCK-8 assay **(B)** of HCEs following exposure of different concentrations of XAV939 NPs. Results are presented as the mean ± SEM. $n = 5$. Scale bar: 200 μm. **(C)** Representative images of slit lamp examination following 14 days treatment of saline and XAV939 NPs (10 μM XAV939 equivalent). Scale bar: 1 mm. **(D)** Representative images of H&E staining of the cornea, heart, liver, spleen, lung, and kidney following 14 days treatment of saline and XAV939 NPs (10 μM XAV939 equivalent) in healthy mice. Scale bar: 100 μm.

RESULTS AND DISCUSSION

Preparation and Characterization of XAV939 NPs

As illustrated in **Figure 1**, the hydrophobic drug XAV939 was loaded into liposomes formed of L-α-phosphatidylcholine, DSPE-PEG (2000), and cholesterol to obtain biocompatible XAV939 NPs. The encapsulation efficiency of the XAV939 NPs was calculated to be 91.2%. The XAV939 NPs exhibited a low polydispersity index (PDI = 0.216) with a hydrodynamic diameter of approximately 100.2 nm using DLS measurements (**Figure 1**). The cryo-EM images show that XAV939 NPs are spherical and well-dispersed round-shaped vesicles and are predominantly unilamellar (**Figure 1**), similar to the previously reported liposomes (Cong et al., 2021).

In Vitro Cytotoxicity Assessment

To assess the cytotoxicity of XAV939 NPs, HCE cells incubated with different concentrations of XAV939 NPs were evaluated by the CCK-8 assay and Calcein-AM/PI assay. After incubation for 24 h, cytotoxicity was assessed with the Calcein-AM/PI assay, where green fluorescence represents live cells and red fluorescence represents dead cells. As shown in **Figure 2A**, few red cells were observed over the concentrations ranging from 0.1 to 50 μM. The results were confirmed by the CCK-8 assay, which indicated the relatively low cytotoxicity of XAV939 NPs with equivalent drug concentrations (**Figure 2B**). The cell viability treated with XAV939 NPs over a range of concentrations was not significantly different. Even at the highest equivalent concentration of 50 μM, the cell viability treated with XAV939 NPs was 96.9%. Taken together, the *in vitro* cytotoxicity assays confirmed good cytocompatibility of the XAV939 NPs, and the equivalent concentration of 10 μM XAV939 was chosen for further experiments.

In Vivo Biocompatibility Assessment in Healthy Mice

The *in vivo* biocompatibility evaluation of XAV939 NPs was assessed with a corneal stimulation test conducted on healthy mice eyes. As shown in **Figure 2C**, topical XAV939 NPs (10 μM XAV939 equivalent) or saline were administered to healthy mouse eyes twice daily and observed consecutively for 14 days. Clinical examination exhibited no visible signs of corneal opacity, inflammation, conjunctival congestion, CNV, or hemalopia in the mice's eyes in both groups. After 14 days of examination, the mice were sacrificed to conduct corneal and systemic anatomical morphology assessments by H&E staining. Anatomical segments of the cornea and major visceral organs of the XAV939 NPs group showed a comparable morphology to the control group (**Figure 2D**). No signs of inflammatory infiltration, cellular lesions, or acute or chronic physiological toxicity were observed in either group, indicating good biocompatibility of XAV939 NPs *in vivo*. Previous studies have reported the *in vivo* biocompatibility of 10 μM of XAV939 in mouse models of dermal fibrosis and cutaneous and cartilage injury (Distler et al., 2013; Bastakoty et al., 2015). Based on these preliminary results, it can be hypothesized that XAV939 NPs embrace satisfactory ocular tolerance and can act as secure theranostic agents for further ocular drug delivery applications.

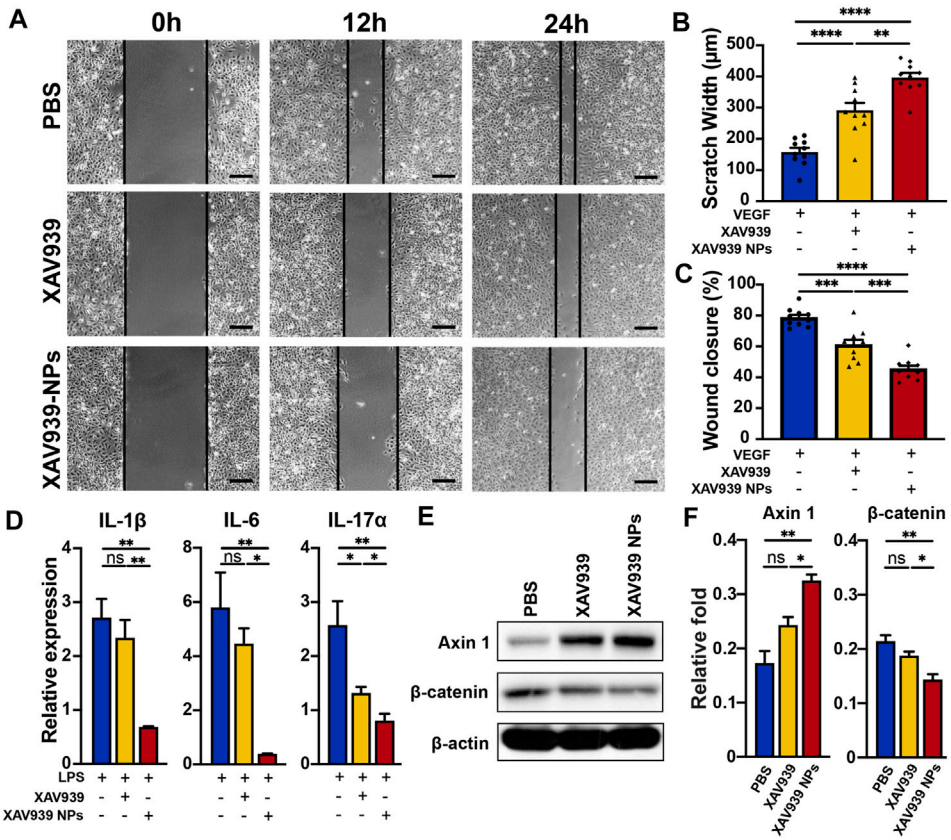

FIGURE 3 | *In vitro* antiangiogenesis and anti-inflammatory effects through Wnt/β-catenin signaling pathway regulation. **(A)** Scratch wound migration assay of HUVECs stimulated with rhVEGF$_{165}$ (1 μg/ml) following exposure of PBS, XAV939 (10 μM), and XAV939 NPs (10 μM XAV939 equivalent). Scale bar: 200 μm. Quantification of the scratch widths **(B)** and the percentage of wound closure **(C)**. Results are presented as the mean ± SEM. $n = 10$. **(D)** Relative expression of mRNA levels of IL-1β, IL-6, and IL-17α of HCEs stimulated with LPS (1 μg/ml) following exposure of PBS, XAV939 (10 μM), and XAV939 NPs (10 μM XAV939 equivalent). Results are presented as the mean ± SEM. $n = 3$. Western blot analysis **(E)** and quantification of the relative protein levels **(F)** of Wnt pathway components Axin 1 and β-catenin following pretreatment of PBS, XAV939 (10 μM), and XAV939 NPs (10 μM XAV939 equivalent). Results are presented as the mean ± SEM. $n = 3$. (One-way ANOVA, $^{*}p < 0.05$, $^{**}p < 0.01$, $^{***}p < 0.001$, $^{****}p < 0.0001$, ns, not significant).

In Vitro Antiangiogenesis Effect

Previous studies have verified the vital roles of the vascular endothelium in wound healing and angiogenesis, which are indicated by excessive cellular proliferation and migration (Wilson et al., 2001; Dorrell et al., 2007). Here, the antiangiogenesis effect of XAV939 NPs (10 μM XAV939 equivalent) was assessed with a HUVEC cell migration assay. The average scratch width and percentage of wound closure observed after 24 h of indicated incubation at each time point are presented in **Figure 3A**. The average initial scratch wound of the HUVECs was 736 μm in each group. Following induction by 1 μg/ml rhVEGF$_{165}$, significantly increased proliferation and migration of the HUVECs were observed in the control group, with 320 μm scratch width at 12 h and 157 μm scratch width at 24 h (**Figure 3B**). Nevertheless, pretreatment with XAV939 and XAV939 NPs remarkably attenuated the stimulation of rhVEGF$_{165}$. Previous evidence has also suggested that XAV939 significantly inhibited the proliferation and migration of vascular smooth muscle cells after stimulation with platelet-derived growth factor-BB, which is attributable to the regulatory role of XAV939 in the Wnt signaling pathway (Chen et al., 2016). In particular, HUVECs pretreated with XAV939 NPs presented significantly wider scratch wounds (396 vs. 291 μm, $p < 0.01$) and delayed wound closure (45 vs. 61%, $p < 0.001$) than the XAV939 group, suggesting an enhanced antimigration effect of XAV939 NPs (**Figures 3B,C**). This is attributable to the high affinity and similarity of the liposomes delivery system with the cell membrane, which in turn facilitates an effective internalization and cellular uptake of the nanoparticles (Skotland et al., 2017; Patel et al., 2020).

In Vitro Anti-Inflammatory Effect

As one of the initial pathological processes of corneal injury, inflammation can be ascribed as a precursor to the development and deterioration of CNV (Lee et al., 2014; Huang et al., 2017). To evaluate the potential anti-inflammatory effect of XAV939 NPs, HCEs were stimulated with 1 μg/ml of LPS for 2 h, and the expressions of the pro-inflammatory genes, including IL-1β, IL-6, and IL-17α, were examined. A significantly upregulated pro-inflammatory gene expression was found in the control

group. For instance, the relative expression of IL-6 achieved more than a five-fold elevation after LPS stimulation. However, cells pretreated with 10 μM of XAV939 and XAV939 NPs exhibited significantly suppressed pro-inflammatory gene expressions (**Figure 3D**). The XAV939 NPs group showed the lowest levels of IL-1β ($p < 0.01$ vs. control and $p < 0.01$ vs. XAV939), IL-6 ($p < 0.01$ vs. control and $p < 0.05$ vs. XAV939), and IL-17α ($p < 0.01$ vs. control and $p < 0.05$ vs. XAV939). Our results are in accord with those obtained in a previous study that identified the anti-inflammatory activity of XAV939 in both human bronchial epithelial cells and HUVECs (Jang et al., 2019). During the inflammatory process, the Wnt signaling pathway was activated, and XAV939 was found to dose-dependently suppress LPS-induced pro-inflammatory signaling (Koopmans et al., 2017). Therefore, with the liposome delivery system, XAV939 NPs mediated substantial and sustained drug release and exhibited a greater anti-inflammatory effect.

In Vitro Wnt/β-Catenin Signaling Pathway Regulation

The Wnt/β-catenin signaling pathway controls various biological processes, and abnormal activation of the Wnt pathway has been observed in various ocular congenital and developmental vascular diseases (Huang et al., 2009; Chen et al., 2011; Lee et al., 2012; Wang et al., 2015). Previous studies have identified that XAV939 can stimulate β-catenin degradation by stabilizing Axin and selectively inhibiting abnormal β-catenin–mediated transcription (Huang et al., 2009). To evaluate the mechanism of XAV939 NPs and the modulation of the Wnt/β-catenin signaling pathway, the protein levels of the key modulators of the pathway were investigated (**Figure 3E**). The pretreatment of 10 μM of XAV939 significantly increased the protein levels of Axin 1 and that of XAV939 NPs exhibited the effect to a greater extent ($p < 0.01$ vs. control and $p < 0.05$ vs. XAV939). Additionally, XAV939 and XAV939 NPs decreased the abundance of β-catenin ($p < 0.01$ vs. control and $p < 0.05$ vs. XAV939), which is the key regulator of the transcription of Wnt pathway-responsive genes (**Figure 3F**). Our results showed that XAV939 displayed a significant inhibitory effect on the abnormally activated Wnt signaling pathway, and the XAV939 NPs group exhibited better performance. Consistent with previous evidence, the inhibitors of the Wnt signaling pathway exhibit therapeutic potential for ocular neovascularization diseases (Chen et al., 2007; Hu et al., 2013).

In Vivo Anti-CNV and Corneal Wound Healing Effects

As one of the most severe causes of corneal wound, alkali-burned corneas suffer from immediate epithelial defects, followed by opacification, CNV, and fibrosis in the later stage (Kubota et al., 2011). Based on the above findings, the efficacy of XAV939 NPs in promoting corneal wound healing and inhibiting CNV was further assessed using an alkali-burned injury mouse model. Briefly, alkali-burned mice were topically administered with the indicated treatments twice daily for 14 days, and clinical

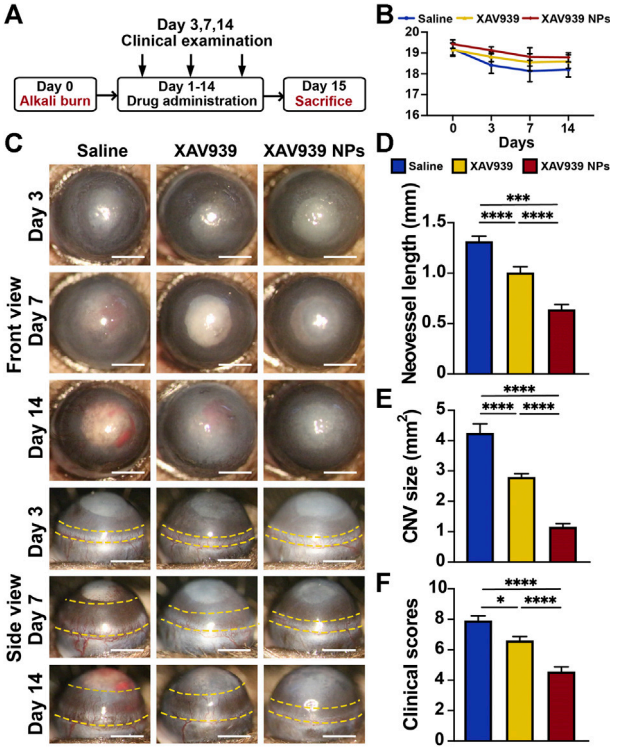

FIGURE 4 | *In vivo* anti-CNV and corneal wound healing effects. **(A)** Schematic timeline of the experimental process. **(B)** Representative front and side images of slit lamp examination on day 3, day 7, and day 14 of the indicated treatments. Yellow dot lines indicate the range of CNV. Scale bar: 1 mm. **(C)** Mice's weights during the clinical observation of 14 days treatment. Results are presented as the mean ± SEM. $n = 6$. Quantification of the neovessel length **(D)**, CNV size **(E),** and clinical scores **(F)** on day 14 with indicated treatments. Results are presented as the mean ± SEM. $n = 6$. (One-way ANOVA, $^{*}p < 0.05$, $^{***}p < 0.001$, $^{****}p < 0.0001$).

examination was conducted with a slit lamp microscope, after which the mice were sacrificed for histological assessments (**Figure 4A**). During the 14 days of observation, the body weights of the mice in each group were steady and comparable (**Figure 4B**). **Figure 4C** presents the representative front and side photographs of morphological differences induced by different treatments. Generally, corneal opacity and edema were observed on day 3 after the alkali burn, reached their peak on day 7, and gradually weakened afterward in all treatment groups. After the injury, the corneas underwent rapid and dynamic regeneration and repairment (Chandler et al., 2019). Specifically, mice treated with XAV939 NPs had significantly reduced opacification and edema compared to that of the XAV939 group and the saline group during the observation, suggesting an ameliorated inflammatory response.

With respect to CNV, the neovessels were found to expand over the limbal vascular plexus on day 7 and reached the peak on day 14 in all groups. The mice treated with saline presented with the most apparent neovessels, which expanded over the corneal limbus on day 7 and gradually invaded the corneal center. During the corneal healing process, mice treated with XAV939 NPs

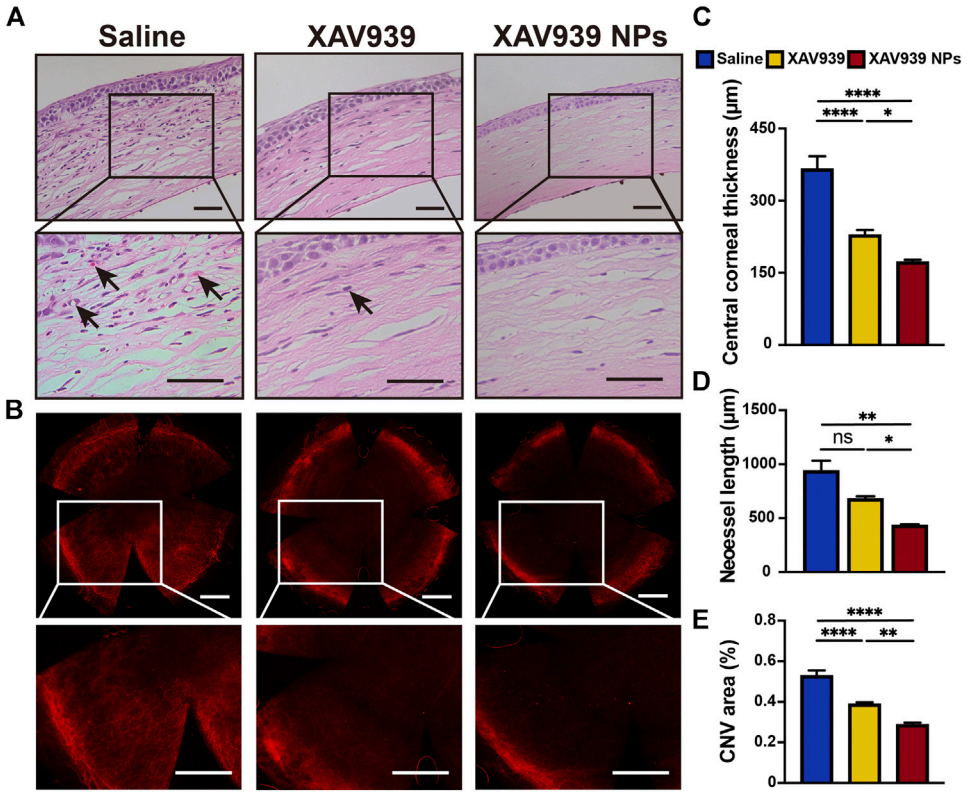

FIGURE 5 | Immunohistochemistry and immunofluorescence assessments of the corneal sections. **(A)** H&E staining of the corneal sections following 14 days of the indicated treatment. The black arrows mark the CNV sites. Scale bar: 50 μm. **(B)** CD31 corneal flat mount staining of the corneal sections following 14 days of the indicated treatment. Scale bar: 500 μm. Quantification of the central corneal thickness **(C)**, neovessel length **(D)**, and CNV area (%) **(E)**. Results are presented as the mean ± SEM. $n = 3$. (One-way ANOVA, $^{*}p < 0.05$, $^{**}p < 0.01$, $^{****}p < 0.0001$, ns, not significant).

consistently showed slower development and growth of neovessels than the XAV939 group and the saline group. Notably, a slight intraocular lens opacity was observed in all treatment groups, which indicated the development of cataract. According to previous studies, such phenomena are attributable to repeated anesthetization, the stimulus of strong light from the slit lamp, low body temperature, and eye dryness after an alkali burn (Ridder et al., 2002; Lee et al., 2020). Therefore, avoiding unnecessary anesthetics use and light exposure, keeping the ocular surface moisturized, and maintaining body temperature may prevent the formation of lens opacity.

Additional quantifications of CNV size, neovessel length, and clinical scores were calculated and compared among the groups on day 14 (**Figures 4D–F**). In the control group, the CNV size was 4.25 mm^2 with a neovessel length of 1.32 mm. The XAV939 group had an average CNV size of 2.81 mm^2 and a neovessel length of 1.03 mm. Mice treated with XAV939 NPs presented with a significantly smaller CNV size of 1.25 mm^2 and neovessel length of 0.66 mm ($p < 0.001$ for the control group; $p < 0.001$ for the XAV939 group). Furthermore, the evaluation of the clinical scores indicated significantly better corneal wound healing in the XAV939 NPs group (4.57 points) than in the XAV939 group (6.60 points, $p < 0.001$) and the control group (7.91 points, $p < 0.001$). As expected, XAV939 NPs treatment had better suppression of the ocular inflammatory response and CNV than XAV939 alone. It is speculated that hydrophobic XAV939 was relatively insoluble in the mice's eyes and was therefore readily cleared away, which may hamper the treatment effect. On the other hand, the XAV939 NPs with a liposomal delivery system achieved better bioavailability and longer retention on the ocular surface, thereby providing better therapeutic efficacy. With further consideration on the price, consecutive administration of the XAV939 NPs (10 μM XAV939 equivalent) for 14 consecutive days is estimated to cost $ 0.86, which is fairly affordable compared to $ 1.3 of 0.1% sodium hyaluronate eye drops.

Histological and Immunofluorescent Analyses *In Vivo*

Histological morphology of healthy and alkali-burned mice eyes in all treatment groups was observed with H&E staining (**Figure 5A**). After the alkali burn, the corneas became generally loosened and frangible. Consistent with the clinical examination, the control group was marked with severely destroyed and exfoliated laminal squamous epithelium,

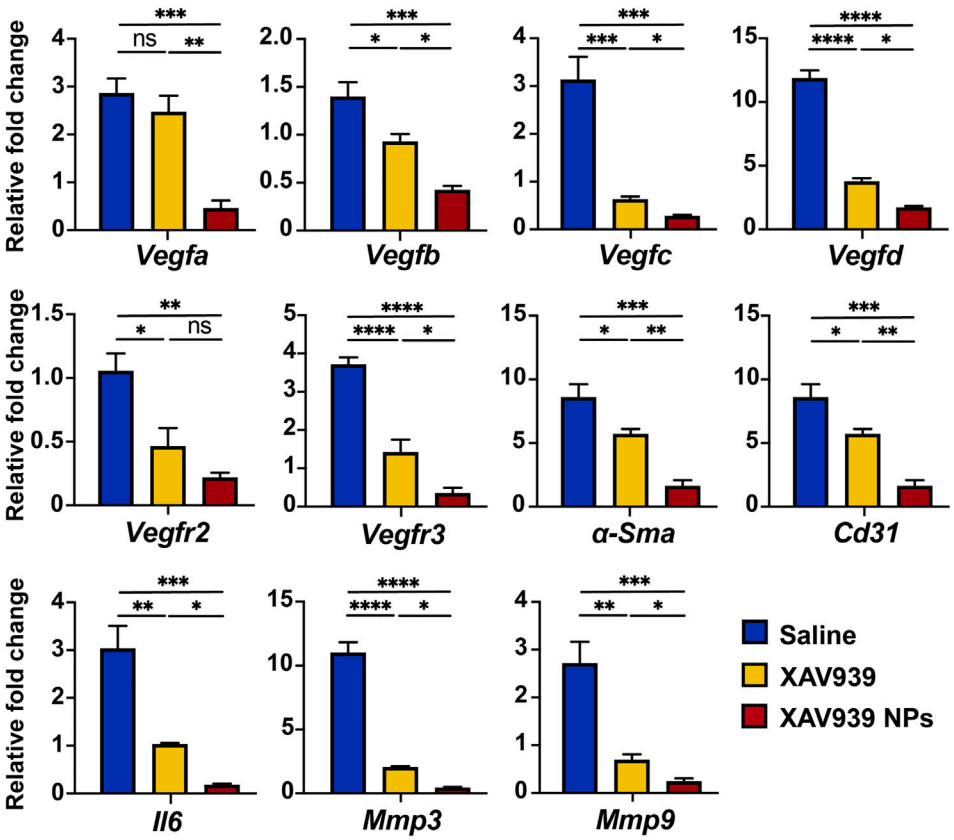

FIGURE 6 | Relative gene expression analyses of *Vegfa, Vegfb, Vegfc, Vegfd, Vegfr2, Vegfr3, α-Sma, Cd31, IL-6, Mmp3,* and *Mmp9* for each group following 14 days of the indicated treatment. Results are presented as the mean ± SEM. $n = 3$ (two corneas served as one biological replica). (One-way ANOVA, $^{*}p < 0.05$, $^{**}p < 0.01$, $^{****}p < 0.0001$, ns, not significant).

edematous stromal layers, disordered collagen fibers, and more CNV. In addition, more inflammatory infiltration, edema, and epithelial layer detachment were observed. The average central corneal thickness in the control group was 368.3 μm, compared to the values of 231.1 μm noted for the XAV939 group ($p < 0.001$) and 174.5 μm for the XAV939 NPs group ($p < 0.001$) (**Figure 5C**). The corneal thickness was thinner and more regularly arranged in the XAV939 and XAV939 NPs groups. In the XAV939 group, better morphology and less edema were found, but still presented with slight CNV. In contrast, owing to prolonged retention on the cornea surface, XAV939 NPs-treated corneas showed apparent repairment and inhibition of CNV compared to the other groups.

To better visualize the CNV of the cornea in all groups, corneal flat mount immunofluorescent staining of the vascular endothelial cell marker CD31 was conducted. The CD31 molecule not only facilitated the formation of intercellular junctions between endothelial cells but also signaled the leukocytes to the vasculature (Mansouri et al., 2006). As displayed in **Figure 5B**, excessive growth of neovessels was found to expand to the cornea center in the saline group. Significant suppression of CNV was observed in the XAV939 and XAV939 NPs groups. CNV areas and neovessel lengths were quantified and compared between the groups. In the saline group, the neovessels expanded over half of the whole corneas with an area percentage of 54% and a length of 924.5 μm (**Figures 5D,E**). CNV in mice treated with XAV939 was slightly ameliorated, with the CNV size observed to be 38% ($p < 0.0001$ vs. saline group) and a neovessel length of 680.7 μm (ns. vs. saline). The XAV939 NPs group almost recovered from injury, with a CNV area of 29% ($p < 0.0001$ vs. saline; $p < 0.01$ vs. XAV939) and a length of 435.5 μm ($p < 0.01$ vs. saline; $p < 0.05$ vs. XAV939). Therefore, the corneal wound healing and therapeutic efficacy of XAV939 NPs might be related to the downregulation of CD31. Taken together, these results indicate that the XAV939 NPs demonstrated a significant advantage over free XAV939 in attenuating corneal wound and CNV after alkali burns.

Angiogenic and Inflammatory Gene Expression Assessment

Alkali-burn injury to the cornea involves a complex and dynamic inflammatory and immune response which consequently leads to inevitable CNV and fibrosis in the later stage (Sakimoto et al., 2012; Huang et al., 2017; Sun et al., 2018). In the angiogenesis cascade, VEGFs and their receptors have been identified as the main critical regulating factors (Ellenberg et al., 2010; Apte et al., 2019). According to previous evidence, the Wnt signaling pathway is an upstream pathway regulating VEGFs, and its inhibitors have displayed satisfactory efficacy in inhibiting

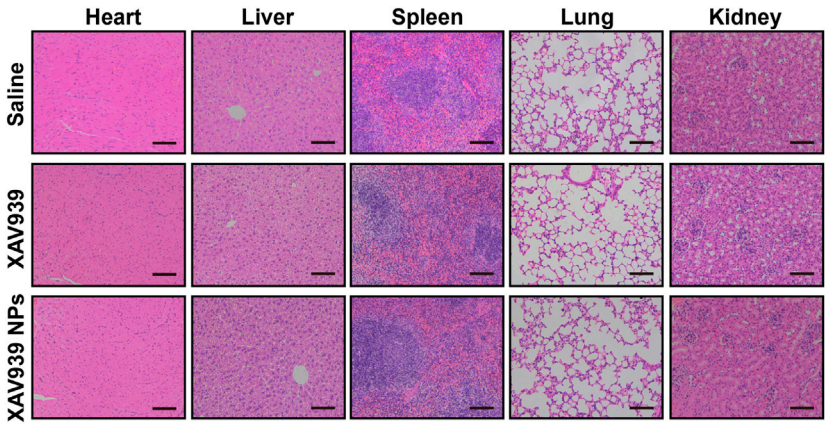

FIGURE 7 | Main visceral organs biosafety assessments in alkali-burned mice. Representative images of H&E staining of the heart, liver, spleen, lung, and kidney following 14 days treatment of saline, 10 μM XAV939, and XAV939 NPs (10 μM XAV939 equivalent). Scale bar: 200 μm.

retinal neovascularization formation (Lee et al., 2012; Hu et al., 2013; Yu et al., 2019). To assess the potential effect of XAV939 NPs on the pathogenesis of CNV, the relative gene expression levels of mice corneas were measured for angiogenic factors (**Figure 6**). In our study, the relative expressions of angiogenic genes were significantly reduced following the XAV939 NPs treatment. The XAV939 NPs group displayed significantly lower levels of *Vegfa* ($p < 0.001$ vs. saline; $p < 0.01$ vs. XAV939), *Vegfb* ($p < 0.001$ vs. saline; $p < 0.05$ vs. XAV939), *Vegfc* ($p < 0.001$ vs. saline; $p < 0.05$ vs. XAV939), and *Vegfd* ($p < 0.0001$ vs. saline; $p < 0.05$ vs. XAV939). Significantly decreased expressions of *Vegfr2* and *Vegfr3* were also found in the XAV939 NPs group. Treatment with XAV939 also significantly reduced the elevation of *Vegfs* and *Vegfrs* compared to that of the saline group, but was not comparable to the effect of XAV939 NPs.

During the process of corneal wound healing and CNV, the keratocytes in the corneal stroma begin with the transition to fibroblast and myofibroblast to repair the corneal wound edge, which indicates corneal scarring and fibrosis (Maltseva et al., 2001; Ziaei et al., 2018). Therefore, the relative gene expressions of *α-Sma*, a typical marker for myofibroblasts, and *Cd31*, a typical marker for endothelial cells, were further analyzed. As shown in **Figure 6**, *α-Sma* was significantly suppressed by XAV939 NPs treatment ($p < 0.001$ vs. saline; $p < 0.01$ vs. XAV939). The expression of *Cd31* was also inhibited in the XAV939 NPs group ($p < 0.001$ vs. saline; $p < 0.01$ vs. XAV939). The results also implied inhibited fibrosis and CNV in mice treated with XAV939 NPs.

During the progress of chemical burn–induced corneal injury, inflammatory signaling has been identified as an initial response. Previous studies have deduced the vital role of *Il-6* trans-signaling in ocular surface inflammation after the alkali burn (Sakimoto et al., 2012; Han et al., 2020c). In addition, overexpressed inflammation-associated target genes, such as Mmps, have also been reported, and the inhibition of inflammatory signaling pathways could alleviate the corneal wound and accelerate the healing process (Vandooren et al., 2013; Lee et al., 2014). Further analyses were conducted for inflammatory-related genes. Up to 10-fold upregulated expressions of *Il-6*, *Mmp3*, and *Mmp9* were observed for the control group. Mice treated with XAV939 and XAV939 NPs showed suppressed expressions of the pro-inflammatory genes. However, better efficacy was observed for the XAV939 NPs group, with inhibited genes of *Il-6* ($p < 0.001$ vs. saline; $p < 0.05$ vs. XAV939), *Mmp3* ($p < 0.0001$ vs. saline; $p < 0.05$ vs. XAV939), and *Mmp9* ($p < 0.001$ vs. saline; $p < 0.05$ vs. XAV939). Altogether, these results reconfirm the therapeutic effect of XAV939 NPs through the regulation of angiogenic, inflammatory-related, and fibrotic-related gene expressions.

Biosafety Assessments of Alkali-Burned Mice

Further biosafety assessments were conducted to investigate the toxicity of XAV939 and XAV939 NPs by H&E staining of major visceral organs, including the heart, liver, spleen, lung, and kidney, in the alkali-burned mice. As presented in **Figure 7**, treatment with XAV939 and XAV939 NPs did not exhibit significant morphological or histological differences from the control group. The results indicated the reliable systemic biosafety of topical treatment of XAV939 and XAV939 NPs, thus further proving the superiority and biocompatibility of XAV939 NPs in treating alkali-burned corneal wounds.

CONCLUSION

In this study, the therapeutic potential of the Wnt/β-catenin pathway inhibitor XAV939 in treating ocular vascular disease was reported for the first time. In addition, biocompatible liposomes were used to enhance the water solubility and bioavailability of hydrophobic XAV939, enabling ocular application. *In vitro* studies indicated XAV939 NPs' anti-inflammatory and antiangiogenic efficacy through the regulation of the Wnt signaling pathway, which exhibited an advantage over XAV939 treatment. When topically administered to alkali-burned corneas, XAV939 NPs demonstrated enhanced corneal wound healing and suppressed CNV, and the expressions of

angiogenic and inflammatory-related genes were inhibited by XAV939 NPs, further confirming their anti-inflammatory and antiangiogenic effects. Taken together, our results illustrate the therapeutic potential of the ocular liposomes of XAV939, thus providing a promising alternative therapy for corneal wound repair and CNV inhibition.

DATA AVAILABILITY STATEMENT

The raw data supporting the conclusions of this article will be made available by the authors, without undue reservation, to any qualified researcher.

ETHICS STATEMENT

The animal study was reviewed and approved by The Association for Research in Vision and Ophthalmology Statement for the Use of Animals in Ophthalmic and Vision Research.

AUTHOR CONTRIBUTIONS

YuZ, HH, and KY conceived and designed the research process; YuZ and KW performed the experiments; YuZ, YiZ, and QY performed data curation; YuZ, SL, JW, and XZ performed analyses; YuZ and KW drafted the manuscript; and HH and KY revised the manuscript and had primary responsibility for the final content. All authors approved the final version to be published and agreed to be accountable for all aspects of the work.

FUNDING

This research was supported by the National Natural Science Foundation of China (Grant Nos. 82070939 and 81870641), the National Key R&D Program of China (No. 2018YFC1106104), the Key Research and Development Project of Zhejiang Province (No. 2020C03035), and the Natural Science Foundation of Zhejiang Province of China (No. LQ20E030011).

REFERENCES

Alfaifi, A. A., Heyder, R. S., Bielski, E. R., Almuqbil, R. M., Kavdia, M., Gerk, P. M., et al. (2020). Megalin-targeting Liposomes for Placental Drug Delivery. *J. Controlled Release* 324, 366–378. doi:10.1016/j.jconrel.2020.05.033

Almasoud, N., Binhamdan, S., Younis, G., Alaskar, H., Alotaibi, A., Manikandan, M., et al. (2020). Tankyrase Inhibitor XAV-939 Enhances Osteoblastogenesis and Mineralization of Human Skeletal (Mesenchymal) Stem Cells. *Sci. Rep.* 10, 16746. doi:10.1038/s41598-020-73439-9

Anderson, C., Zhou, Q., and Wang, S. (2014). An Alkali-Burn Injury Model of Corneal Neovascularization in the Mouse. *JoVE* 86, 51159. doi:10.3791/51159

Anselmo, A. C., and Mitragotri, S. (2019). Nanoparticles in the Clinic: An Update. *Bioeng. Transl Med.* 4, e10143. doi:10.1002/btm2.10143

Apte, R. S., Chen, D. S., and Ferrara, N. (2019). VEGF in Signaling and Disease: Beyond Discovery and Development. *Cell* 176, 1248–1264. doi:10.1016/j.cell.2019.01.021

Bastakoty, D., Saraswati, S., Cates, J., Lee, E., Nanney, L. B., and Young, P. P. (2015). Inhibition of Wnt/β-catenin Pathway Promotes Regenerative Repair of Cutaneous and Cartilage Injury. *FASEB j.* 29, 4881–4892. doi:10.1096/fj.15-275941

Chandler, H. L., Tan, T., Yang, C., Gemensky-Metzler, A. J., Wehrman, R. F., Jiang, Q., et al. (2019). MG53 Promotes Corneal Wound Healing and Mitigates Fibrotic Remodeling in Rodents. *Commun. Biol.* 2, 71. doi:10.1038/s42003-019-0316-7

Chang, D., Ma, Y., Xu, X., Xie, J., and Ju, S. (2021). Stimuli-Responsive Polymeric Nanoplatforms for Cancer Therapy. *Front. Bioeng. Biotechnol.* 9, 707319. doi:10.3389/fbioe.2021.707319

Chen, Y., Hu, Y., Lu, K., Flannery, J. G., and Ma, J.-X. (2007). Very Low Density Lipoprotein Receptor, a Negative Regulator of the Wnt Signaling Pathway and Choroidal Neovascularization. *J. Biol. Chem.* 282, 34420–34428. doi:10.1074/jbc.M611289200

Chen, J., Stahl, A., Krah, N. M., Seaward, M. R., Dennison, R. J., Sapieha, P., et al. (2011). Wnt Signaling Mediates Pathological Vascular Growth in Proliferative Retinopathy. *Circulation* 124, 1871–1881. doi:10.1161/CIRCULATIONAHA.111.040337

Chen, L., Zhuang, J., Singh, S., Wang, K., Xiong, M., Xu, D., et al. (2016). XAV939 Inhibits Intima Formation by Decreasing Vascular Smooth Muscle Cell Proliferation and Migration through Blocking Wnt Signaling. *J. Cardiovasc. Pharmacol.* 68, 414–424. doi:10.1097/FJC.0000000000000427

Chen, F., Le, P., Fernandes-Cunha, G. M., Heilshorn, S. C., and Myung, D. (2020a). Bio-orthogonally Crosslinked Hyaluronate-Collagen Hydrogel for Suture-free Corneal Defect Repair. *Biomaterials* 255, 120176. doi:10.1016/j.biomaterials.2020.120176

Chen, X., Jia, F., Li, Y., Deng, Y., Huang, Y., Liu, W., et al. (2020b). Nitric Oxide-Induced Stromal Depletion for Improved Nanoparticle Penetration in Pancreatic Cancer Treatment. *Biomaterials* 246, 119999. doi:10.1016/j.biomaterials.2020.119999

Clevers, H., and Nusse, R. (2012). Wnt/β-Catenin Signaling and Disease. *Cell* 149, 1192–1205. doi:10.1016/j.cell.2012.05.012

Cong, X., Chen, J., and Xu, R. (2021). Tumor-Acidity Responsive Polymeric Nanoparticles for Targeting Delivery of Angiogenesis Inhibitor for Enhanced Antitumor Efficacy with Decreased Toxicity. *Front. Bioeng. Biotechnol.* 9, 664051. doi:10.3389/fbioe.2021.664051

Distler, A., Deloch, L., Huang, J., Dees, C., Lin, N.-Y., Palumbo-Zerr, K., et al. (2013). Inactivation of Tankyrases Reduces Experimental Fibrosis by Inhibiting Canonical Wnt Signalling. *Ann. Rheum. Dis.* 72, 1575–1580. doi:10.1136/annrheumdis-2012-202275

Dorrell, M., Uusitalo-Jarvinen, H., Aguilar, E., and Friedlander, M. (2007). Ocular Neovascularization: Basic Mechanisms and Therapeutic Advances. *Surv. Ophthalmol.* 52, S3–S19. doi:10.1016/j.survophthal.2006.10.017

Ellenberg, D., Azar, D. T., Hallak, J. A., Tobaigy, F., Han, K. Y., Jain, S., et al. (2010). Novel Aspects of Corneal Angiogenic and Lymphangiogenic Privilege. *Prog. Retin. Eye Res.* 29, 208–248. doi:10.1016/j.preteyeres.2010.01.002

Eriksen, A. Z., Eliasen, R., Oswald, J., Kempen, P. J., Melander, F., Andresen, T. L., et al. (2018). Multifarious Biologic Loaded Liposomes that Stimulate the Mammalian Target of Rapamycin Signaling Pathway Show Retina Neuroprotection after Retina Damage. *ACS Nano* 12, 7497–7508. doi:10.1021/acsnano.8b00596

Fan, W., Han, H., Chen, Y., Zhang, X., Gao, Y., Li, S., et al. (2021). Antimicrobial Nanomedicine for Ocular Bacterial and Fungal Infection. *Drug Deliv. Transl. Res.* 11, 1352–1375. doi:10.1007/s13346-021-00966-x

Feng, T., Zhou, L., Wang, Z., Li, C., Zhang, Y., Lin, J., et al. (2020). Dual-stimuli Responsive Nanotheranostics for Mild Hyperthermia Enhanced Inhibition of Wnt/β-Catenin Signaling. *Biomaterials* 232, 119709. doi:10.1016/j.biomaterials.2019.119709

Han, H., Valdepérez, D., Jin, Q., Yang, B., Li, Z., Wu, Y., et al. (2017). Dual Enzymatic Reaction-Assisted Gemcitabine Delivery Systems for Programmed Pancreatic Cancer Therapy. *ACS Nano* 11, 1281–1291. doi:10.1021/acsnano.6b05541

Han, H., Gao, Y., Chai, M., Zhang, X., Liu, S., Huang, Y., et al. (2020a). Biofilm Microenvironment Activated Supramolecular Nanoparticles for Enhanced Photodynamic Therapy of Bacterial Keratitis. *J. Controlled Release* 327, 676–687. doi:10.1016/j.jconrel.2020.09.014

Han, H., Hou, Y., Chen, X., Zhang, P., Kang, M., Jin, Q., et al. (2020b). Metformin-Induced Stromal Depletion to Enhance the Penetration of Gemcitabine-Loaded Magnetic Nanoparticles for Pancreatic Cancer Targeted Therapy. *J. Am. Chem. Soc.* 142, 4944–4954. doi:10.1021/jacs.0c00650

Han, H., Yin, Q., Tang, X., Yu, X., Gao, Q., Tang, Y., et al. (2020c). Development of Mucoadhesive Cationic Polypeptide Micelles for Sustained Cabozantinib Release and Inhibition of Corneal Neovascularization. *J. Mater. Chem. B* 8, 5143–5154. doi:10.1039/D0TB00874E

Hu, Y., Chen, Y., Lin, M., Lee, K., Mott, R. A., and Ma, J.-x. (2013). Pathogenic Role of the Wnt Signaling Pathway Activation in Laser-Induced Choroidal Neovascularization. *Invest. Ophthalmol. Vis. Sci.* 54, 141–154. doi:10.1167/iovs.12-10281

Huang, S.-M. A., Mishina, Y. M., Liu, S., Cheung, A., Stegmeier, F., Michaud, G. A., et al. (2009). Tankyrase Inhibition Stabilizes Axin and Antagonizes Wnt Signalling. *Nature* 461, 614–620. doi:10.1038/nature08356

Huang, J., Wang, W., Yu, J., Yu, X., Zheng, Q., Peng, F., et al. (2017). Combination of Dexamethasone and Avastin by Supramolecular Hydrogel Attenuates the Inflammatory Corneal Neovascularization in Rat Alkali Burn Model. *Colloids Surf. B: Biointerf.* 159, 241–250. doi:10.1016/j.colsurfb.2017.07.057

Jang, J., Jung, Y., Chae, S., Bae, T., Kim, S.-M., Shim, Y. J., et al. (2019). XAV939, a Wnt/β-Catenin Pathway Modulator, Has Inhibitory Effects on LPS-Induced Inflammatory Response. *Immunopharmacol. Immunotoxicol.* 41, 394–402. doi:10.1080/08923973.2018.1536984

Jin, Q., Deng, Y., Chen, X., and Ji, J. (2019). Rational Design of Cancer Nanomedicine for Simultaneous Stealth Surface and Enhanced Cellular Uptake. *ACS Nano* 13, 954–977. doi:10.1021/acsnano.8b07746

Jumelle, C., Gholizadeh, S., Annabi, N., and Dana, R. (2020). Advances and Limitations of Drug Delivery Systems Formulated as Eye Drops. *J. Controlled Release* 321, 1–22. doi:10.1016/j.jconrel.2020.01.057

Klaus, A., and Birchmeier, W. (2008). Wnt Signalling and its Impact on Development and Cancer. *Nat. Rev. Cancer* 8, 387–398. doi:10.1038/nrc2389

Kompella, U. B., Amrite, A. C., Pacha Ravi, R., and Durazo, S. A. (2013). Nanomedicines for Back of the Eye Drug Delivery, Gene Delivery, and Imaging. *Prog. Retin. Eye Res.* 36, 172–198. doi:10.1016/j.preteyeres.2013.04.001

Koopmans, T., Eilers, R., Menzen, M., Halayko, A., and Gosens, R. (2017). β-Catenin Directs Nuclear Factor-κB P65 Output via CREB-Binding Protein/p300 in Human Airway Smooth Muscle. *Front. Immunol.* 8, 1086. doi:10.3389/fimmu.2017.01086

Kubota, M., Shimmura, S., Kubota, S., Miyashita, H., Kato, N., Noda, K., et al. (2011). Hydrogen andN-Acetyl-L-Cysteine Rescue Oxidative Stress-Induced Angiogenesis in a Mouse CornealAlkali-Burn Model. *Invest. Ophthalmol. Vis. Sci.* 52, 427–433. doi:10.1167/iovs.10-6167

Lamalice, L., Le Boeuf, F., and Huot, J. (2007). Endothelial Cell Migration during Angiogenesis. *Circ. Res.* 100, 782–794. doi:10.1161/01.RES.0000259593.07661.1e

Lee, K., Hu, Y., Ding, L., Chen, Y., Takahashi, Y., Mott, R., et al. (2012). Therapeutic Potential of a Monoclonal Antibody Blocking the Wnt Pathway in Diabetic Retinopathy. *Diabetes* 61, 2948–2957. doi:10.2337/db11-0300

Lee, H., Jun, J.-H., Jung, E.-H., Koo, B., and Kim, Y. (2014). Epigalloccatechin-3-gallate Inhibits Ocular Neovascularization and Vascular Permeability in Human Retinal Pigment Epithelial and Human Retinal Microvascular Endothelial Cells via Suppression of MMP-9 and VEGF Activation. *Molecules* 19, 12150–12172. doi:10.3390/molecules190812150

Lee, H., Kim, H. K., Shin, H. S., Han, S. J., Yoon, S., Seong, J. K., et al. (2020). Evaluation of Factors Related to Anaesthesia-Induced Lens Opacity in Experimental Mice. *Lab. Anim. Res.* 36, 1. doi:10.1186/s42826-019-0031-z

Li, C., Zheng, X., Han, Y., Lv, Y., Lan, F., and Zhao, J. (2018). XAV939 Inhibits the Proliferation and Migration of Lung Adenocarcinoma A549 Cells through the WNT Pathway. *Oncol. Lett.* 15, 8973–8982. doi:10.3892/ol.2018.8491

Ma, Y., Cai, F., Li, Y., Chen, J., Han, F., and Lin, W. (2020). A Review of the Application of Nanoparticles in the Diagnosis and Treatment of Chronic Kidney Disease. *Bioact. Mater.* 5, 732–743. doi:10.1016/j.bioactmat.2020.05.002

Maltseva, O., Folger, P., Zekaria, D., Petridou, S., and Masur, S. K. (2001). Fibroblast Growth Factor Reversal of the Corneal Myofibroblast Phenotype. *Invest. Ophthalmol. Vis. Sci.* 42, 2490–2495.

Mansouri, M., Douglas, J., Rose, P. P., Gouveia, K., Thomas, G., Means, R. E., et al. (2006). Kaposi Sarcoma Herpesvirus K5 Removes CD31/PECAM from Endothelial Cells. *Blood* 108, 1932–1940. doi:10.1182/blood-2005-11-4404

Mobaraki, M., Abbasi, R., Omidian Vandchali, S., Ghaffari, M., Moztarzadeh, F., and Mozafari, M. (2019). Corneal Repair and Regeneration: Current Concepts and Future Directions. *Front. Bioeng. Biotechnol.* 7, 135. doi:10.3389/fbioe.2019.00135

Ouyang, H., Xue, Y., Lin, Y., Zhang, X., Xi, L., Patel, S., et al. (2014). WNT7A and PAX6 Define Corneal Epithelium Homeostasis and Pathogenesis. *Nature* 511, 358–361. doi:10.1038/nature13465

Patel, G., Thakur, N. S., Kushwah, V., Patil, M. D., Nile, S. H., Jain, S., et al. (2020). Liposomal Delivery of Mycophenolic Acid with Quercetin for Improved Breast Cancer Therapy in SD Rats. *Front. Bioeng. Biotechnol.* 8, 631. doi:10.3389/fbioe.2020.00631

Peng, Y., Chen, L., Ye, S., Kang, Y., Liu, J., Zeng, S., et al. (2020). Research and Development of Drug Delivery Systems Based on Drug Transporter and Nano-Formulation. *Asian J. Pharm. Sci.* 15, 220–236. doi:10.1016/j.ajps.2020.02.004

Rebibo, L., Tam, C., Sun, Y., Shoshani, E., Badihi, A., Nassar, T., et al. (2021). Topical Tacrolimus Nanocapsules Eye Drops for Therapeutic Effect Enhancement in Both Anterior and Posterior Ocular Inflammation Models. *J. Controlled Release* 333, 283–297. doi:10.1016/j.jconrel.2021.03.035

Reya, T., and Clevers, H. (2005). Wnt Signalling in Stem Cells and Cancer. *Nature* 434, 843–850. doi:10.1038/nature03319

Ridder III, W. H., Nusinowitz, S., and Heckenlively, J. R. (2002). Causes of Cataract Development in Anesthetized Mice. *Exp. Eye Res.* 75, 365–370. doi:10.1006/exer.2002.2007

Roshandel, D., Eslani, M., Baradaran-Rafii, A., Cheung, A. Y., Kurji, K., Jabbehdari, S., et al. (2018). Current and Emerging Therapies for Corneal Neovascularization. *Ocul. Surf.* 16, 398–414. doi:10.1016/j.jtos.2018.06.004

Sakimoto, T., Sugaya, S., Ishimori, A., and Sawa, M. (2012). Anti-inflammatory Effect of IL-6 Receptor Blockade in Corneal Alkali Burn. *Exp. Eye Res.* 97, 98–104. doi:10.1016/j.exer.2012.02.015

Shi, Y., Feng, X., Lin, L., Wang, J., Chi, J., Wu, B., et al. (2021). Virus-inspired Surface-Nanoengineered Antimicrobial Liposome: A Potential System to Simultaneously Achieve High Activity and Selectivity. *Bioactive Mater.* 6, 3207–3217. doi:10.1016/j.bioactmat.2021.02.038

Skotland, T., Sandvig, K., and Llorente, A. (2017). Lipids in Exosomes: Current Knowledge and the Way Forward. *Prog. Lipid Res.* 66, 30–41. doi:10.1016/j.plipres.2017.03.001

Sun, J., Huang, W., Yang, S.-F., Zhang, X.-P., Yu, Q., Zhang, Z.-Q., et al. (2018). Gαi1 and Gαi3mediate VEGF-Induced VEGFR2 Endocytosis, Signaling and Angiogenesis. *Theranostics* 8, 4695–4709. doi:10.7150/thno.26203

Tavakoli, S., Peynshaert, K., Lajunen, T., Devoldere, J., del Amo, E. M., Ruponen, M., et al. (2020). Ocular Barriers to Retinal Delivery of Intravitreal Liposomes: Impact of Vitreoretinal Interface. *J. Controlled Release* 328, 952–961. doi:10.1016/j.jconrel.2020.10.028

Vandooren, J., Van den Steen, P. E., and Opdenakker, G. (2013). Biochemistry and Molecular Biology of Gelatinase B or Matrix Metalloproteinase-9 (MMP-9): The Next Decade. *Crit. Rev. Biochem. Mol. Biol.* 48, 222–272. doi:10.3109/10409238.2013.770819

Wang, Z., Cheng, R., Lee, K., Tyagi, P., Ding, L., Kompella, U. B., et al. (2015). Nanoparticle-Mediated Expression of a Wnt Pathway Inhibitor Ameliorates Ocular Neovascularization. *Arterioscler Thromb. Vasc. Biol.* 35, 855–864. doi:10.1161/ATVBAHA.114.304627

Wang, Z., Liu, C.-H., Huang, S., and Chen, J. (2019a). Wnt Signaling in Vascular Eye Diseases. *Prog. Retin. Eye Res.* 70, 110–133. doi:10.1016/j.preteyeres.2018.11.008

Wang, M., Wang, C., Chen, M., Xi, Y., Cheng, W., Mao, C., et al. (2019b). Efficient Angiogenesis-Based Diabetic Wound Healing/Skin Reconstruction through Bioactive Antibacterial Adhesive Ultraviolet Shielding Nanodressing with Exosome Release. *ACS Nano* 13, 10279–10293. doi:10.1021/acsnano.9b03656

Wilson, S. E., Mohan, R. R., Mohan, R. R., Ambrósio, R., Hong, J., and Lee, J. (2001). The Corneal Wound Healing Response:. *Prog. Retin. Eye Res.* 20, 625–637. doi:10.1016/S1350-9462(01)00008-8

Yang, J., Luo, L., Oh, Y., Meng, T., Chai, G., Xia, S., et al. (2020a). Sunitinib Malate-Loaded Biodegradable Microspheres for the Prevention of Corneal Neovascularization in Rats. *J. Controlled Release* 327, 456–466. doi:10.1016/j.jconrel.2020.08.019

Yang, S., Zhang, Y., Zhang, Z., Dan, J., Zhou, Q., Wang, X., et al. (2020b). Insulin Promotes Corneal Nerve Repair and Wound Healing in Type 1 Diabetic Mice

by Enhancing Wnt/β-Catenin Signaling. *Am. J. Pathol.* 190 (11), 2237–2250. doi:10.1016/j.ajpath.2020.08.006

Ye, J., Yang, Y., Jin, J., Ji, M., Gao, Y., Feng, Y., et al. (2020). Targeted Delivery of Chlorogenic Acid by Mannosylated Liposomes to Effectively Promote the Polarization of TAMs for the Treatment of Glioblastoma. *Bioact. Mater.* 5, 694–708. doi:10.1016/j.bioactmat.2020.05.001

Yu, Y., Lin, X., Wang, Q., He, M., and Chau, Y. (2019). Long-term Therapeutic Effect in Nonhuman Primate Eye from a Single Injection of anti-VEGF Controlled Release Hydrogel. *Bioeng. Transl. Med.* 4, e10128. doi:10.1002/btm2.10128

Yuba, E. (2020). Development of Functional Liposomes by Modification of Stimuli-Responsive Materials and Their Biomedical Applications. *J. Mater. Chem. B* 8, 1093–1107. doi:10.1039/c9tb02470k

Zhang, J., Si, J., Gan, L., Guo, M., Yan, J., Chen, Y., et al. (2020). Inhibition of Wnt Signalling Pathway by XAV939 Enhances Radiosensitivity in Human Cervical Cancer HeLa Cells. *Artif. Cell Nanomed. Biotechnol.* 48, 479–487. doi:10.1080/21691401.2020.1716779

Zhang, X., Lai, K., Li, S., Wang, J., Li, J., Wang, W., et al. (2021). Drug-eluting Intraocular Lens with Sustained Bromfenac Release for Conquering Posterior Capsular Opacification. *Bioact. Mater.* doi:10.1016/j.bioactmat.2021.07.015

Ziaei, M., Greene, C., and Green, C. R. (2018). Wound Healing in the Eye: Therapeutic Prospects. *Adv. Drug Deliv. Rev.* 126, 162–176. doi:10.1016/j.addr.2018.01.006

Conflict of Interest: The authors declare that the research study was conducted in the absence of any commercial or financial relationships that could be construed as a potential conflict of interest.

Publisher's Note: All claims expressed in this article are solely those of the authors and do not necessarily represent those of their affiliated organizations, or those of the publisher, the editors, and the reviewers. Any product that may be evaluated in this article or claim that may be made by its manufacturer is not guaranteed or endorsed by the publisher.

frontiers in Bioengineering and Biotechnology

REVIEW
published: 04 November 2021
doi: 10.3389/fbioe.2021.783354

Smart Polymeric Delivery System for Antitumor and Antimicrobial Photodynamic Therapy

*Zhijia Wang, Fu-Jian Xu and Bingran Yu**

Laboratory of Biomedical Materials and Key Lab of Biomedical Materials of Natural Macromolecules Beijing University of Chemical Technology, Ministry of Education, Beijing University of Chemical Technology, Beijing, China

Photodynamic therapy (PDT) has attracted tremendous attention in the antitumor and antimicrobial areas. To enhance the water solubility of photosensitizers and facilitate their accumulation in the tumor/infection site, polymeric materials are frequently explored as delivery systems, which are expected to show target and controllable activation of photosensitizers. This review introduces the smart polymeric delivery systems for the PDT of tumor and bacterial infections. In particular, strategies that are tumor/bacteria targeted or activatable by the tumor/bacteria microenvironment such as enzyme/pH/reactive oxygen species (ROS) are summarized. The similarities and differences of polymeric delivery systems in antitumor and antimicrobial PDT are compared. Finally, the potential challenges and perspectives of those polymeric delivery systems are discussed.

Keywords: polymer, target, activatable, photodynamic therapy, antibacterial

OPEN ACCESS

Edited by:
Yakai Feng,
Tianjin University, China

Reviewed by:
Wuli Yang,
Fudan University, China
Dong Wang,
Shenzhen University, China

****Correspondence:***
Bingran Yu
yubr@mail.buct.edu.cn

Specialty section:
This article was submitted to Biomaterials, a section of the journal Frontiers in Bioengineering and Biotechnology

Received: *26 September 2021*
Accepted: *14 October 2021*
Published: *04 November 2021*

Citation:
Wang Z, Xu F-J and Yu B (2021) Smart Polymeric Delivery System for Antitumor and Antimicrobial Photodynamic Therapy. Front. Bioeng. Biotechnol. 9:783354. doi: 10.3389/fbioe.2021.783354

INTRODUCTION

Photodynamic therapy (PDT) has attracted intensive attention for the treatment of tumor and bacteria during recent years(Celli et al., 2010; Bugaj, 2011; Kamkaew et al., 2013; Lincoln et al., 2013; Tian et al., 2013). For instance, for traditional cancer therapy strategies such as chemotherapy and radiotherapy, patients often suffer from severe side effects, limited tumor suppression, and unavoidable regrowth of metastatic tumor. In comparison, PDT has high spatiotemporal selectivity in triggering tumor cell death and can generate immune response (Wang et al., 2020), showing advantages over the traditional cancer therapies. On the other hand, concerning antibacterial therapy, antibiotic resistance problems become increasingly prominent (Maisch et al., 2004). PDT is expected to be a promising alternative to antibiotic therapy for combating bacterial infections (Klausen et al., 2020). PDT therapeutics such as Porfimer sodium, ALA, and Verteporfin have been approved worldwide to be used in clinics (Agostinis et al., 2011). PDT has been approved to treat some diseases in clinical trials, such as premalignant tumors, cutaneous malignant tumors, tumors of the head, neck, and oral cavity, lung, gastrointestinal, and other tumors (Brown et al., 2004), viral lesions, acne, gastric infection by *Helicobacter pylori,* and brain abcesses (Hamblin and Hasan, 2004).

The mechanism of PDT is described in **Figure 1**. With light irradiation, the photosensitizer is promoted to its singlet excited state, followed by intersystem crossing to its triplet state. As the transition from triplet excited state (T_1) to ground state is spin forbidden, this T_1 state is relatively long-lived and can react with molecular oxygen. Concerning the reaction type between the T_1 state and molecular oxygen, there are two possibilities. Electron transfer between the T_1 state and molecular oxygen will initially produce a superoxide anion ($O_2^{\bullet-}$), and subsequently produce other

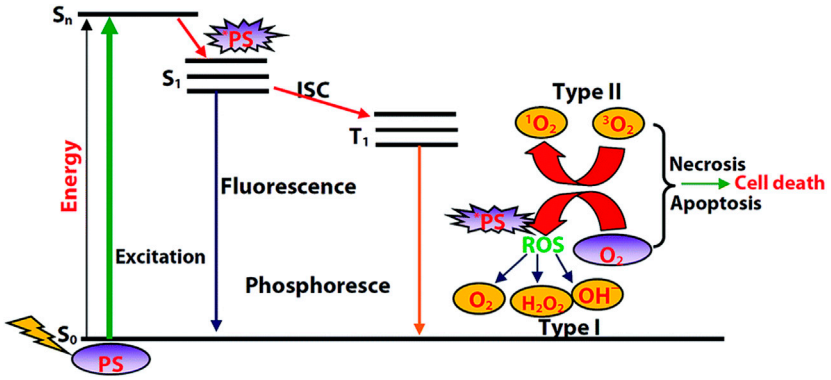

FIGURE 1 | Diagram illustrating the process of PDT. Reprinted with permission from Majumdar et al. (2014).

ROS such as hydroxyl radical or hydrogen peroxide that is toxic to cells or bacteria, which is the so-called Type I PDT. Energy transfer between the T_1 state and molecular oxygen will produce toxic singlet oxygen ($^1O_2$) to kill tumor cells or bacteria, which is Type II PDT.

It is obvious that triplet photosensitizer, light, and oxygen are three key factors of PDT. Among these, triplet photosensitizer plays a leading role (Majumdar et al., 2014). Although a variety of conventional photosensitizers such as porphyrin derivatives (e.g., chlorin e6, PpIX), phthalocyanine derivatives (e.g., ZnPc), and some newly developed triplet photosensitizers such as Bodipy derivatives have PDT ability (Detty et al., 2004), their water solubility is unsatisfactory. The delivery of those photosensitizers to tumor or infected site is a critical issue.

Polymers consist of many structural units or monomers that are connected with a covalent bond; hence, they have a super high molecular weight. Some polymers play the role of triplet photosensitizers as they can produce ROS (Blacha-Grzechnik, 2021). Some reports found that polymers may have enhanced ROS production ability than monomers, which might be due to the increased number of vibrational energy levels and broader energy bands of polymers as compared with monomers (Wu et al., 2018c; Liu et al., 2021). More commonly, polymers functioned as carries of organic triplet photosensitizer, which increases its water solubility and its accumulation in the tumor or infected site (Regehly et al., 2007; Lee et al., 2009; Park S. Y. et al., 2011; Huang et al., 2016; Cui et al., 2019). In addition, small molecules tend to be cleaned up quickly from the body; hence, the polymers are expected to extend the circulation time. Polymers can also serve as a gene delivery vector, e.g., the delivery of a genetically encoded photosensitizer (such as killerred, miniSOG) for PDT cancer treatment (Sarkisyan et al., 2015; Tseng et al., 2015). Polymers have versatile functions and can combine with other therapy strategies, achieving multimodal therapy (Li and Pu, 2020). For instance, polymers can act as prodrugs for PDT and chemotherapy (Xu et al., 2016; Wang et al., 2019; Lu L. et al., 2020), the combination of polymer and cytotoxic enzymes shows outstanding tumor treatment efficacy (Li et al., 2019c); it can also function as a blockader to intervene in the protein biosynthesis to depress the tumor (Li et al., 2019b); the polymers become stimulants in the combination of PDT and immunotherapy (Li et al., 2019a)

Smart polymers that can target tumor/infected tissues or be activatable by the tumor/bacterial microenvironment are highly desired. Although the PDT has relatively high spatial selectivity, there is still great concern about the skin phototoxicity. For instance, patients treated with porphyrin derivatives have to stay in the dark for at least 72 h, which is a great psychological challenge to patients. An activatable delivery system is beneficial to reduce the skin phototoxicity. Small organic molecules tend to be cleared out from the body, and an activatable polymeric delivery system can protect the small photosensitizer and achieve on site release of photosensitizer. Moreover, the nonspecifically distribution of the triplet photosensitizer in the whole body requires a higher dose of photosensitizer, which is more likely to lead to organ damage; a specific accumulation of the photosensitizer to the lesion site is beneficial to reduce administration dosage, elevate the therapeutic efficacy, and play down the side effects. Hence, developing smart polymeric delivery systems that can target the tumor/bacterial site or activate by the tumor/bacterial microenvironment is urgent. In recent years, elegant works have been conducted in these areas (Hoffman, 2008; Li and Huh, 2014; Kamaly et al., 2016; Chen et al., 2017; Wu L. et al., 2018; Wu et al., 2018b; Li and Yan, 2018; Li et al., 2020; Zheng et al., 2020; Han et al., 2021). This review will give a brief summary on the smart polymeric delivery system for antitumor and antimicrobial photodynamic therapy. Note that due to the limitation of the space, we only selected part of typical articles as examples to introduce in detail. The authors apologize for omitting some important and elegant works in advance.

SMART POLYMERIC DELIVERY SYSTEM FOR ANTITUMOR PHOTODYNAMIC THERAPY

Cancer has been a leading cause of death all over the world (Ferlay et al., 2010). Data from the World Health Organization (WHO)

shows that nearly 10 million deaths from cancer occurred in 2020. Traditional cancer therapy strategies such as chemotherapy and radiotherapy have severe side effects (Mitsunaga et al., 2011; Wang and Guo, 2013; Lucky et al., 2015) Moreover, there are great concerns on the drug resistance and radioactivity for chemotherapy and radiotherapy, respectively (Mitsunaga et al., 2011; Wang and Guo, 2013; Lucky et al., 2015).

PDT has attracted tremendous attention since its birth in the early 1900s, when Tappeiner conducted the first therapy to himself by topical eosin and sunlight. Later, Figger et al. and Lipson et al. discovered the photosensitizer hematoporphyrin and forwarded the PDT of the tumor to clinical applications, respectively (Figge et al., 1948). Compared with conventional approaches of cancer therapy such as surgical excision, chemotherapy, and radiotherapy, PDT shows great advantages such as higher spatial/temporal resolution and the anti-drug resistance.

As the photosensitizers may distributed over the whole body, a smart polymeric delivery system is beneficial for precise therapy. The delivery system is expected to protect the photosensitizers from systemic clearance, and carry the photosensitizer to the tumor site. In some cases, the delivery system releases the photosensitizers, either with a slow sustained release or a burst of release. Hence, the sustained release and biodegradable polymeric delivery systems are introduced. Smart polymeric delivery systems that can target the tumor and be activatable by the tumor microenvironment are highlighted.

Sustained Release and Biodegradable Polymeric Delivery System

One of the most crucial functions of a polymeric delivery system is to enhance the water solubility of hydrophobic photosensitizers. For instance, polyethylene glycol (PEG) is one of the most frequently used polymers to increase the water solubility. PEG provides stealth to photosensitizers, making them invisible to microorganisms and cells. Hence the protection by PEG resisted protein adsorption and prolonged the circulatory half-life of photosensitizer (Keerthiga et al., 2020), which is beneficial to achieve long-term antitumor effects.

Polymers with high molecular weight may raise great concern about their toxicity. Hence, it is highly desired that the polymer can be degraded into small nontoxic fragments such as water and carbon dioxide, which is easy to be metabolized from the body (Kamaly et al., 2016). Concerning this aspect, biodegradable polymers such as polylactide (PLA), poly (glycolic acid) (PGA), poly (lactic-co-glycolic acid) (PLGA), and poly-β-benzyl-L-aspartate (PBLA) have been developed, which can be degraded slowly by the hydrolysis of the ester bond (Vert et al., 1992; Hoffman, 2008; Kim et al., 2009; Keerthiga et al., 2020) Hence the encapsulated photosensitizers can be sustained released.

Tumor-Target Polymeric Delivery System

Passive Targeting

The passive targeting of those polymeric nanoparticles is referred to the enhanced permeation and retention (EPR) effect proposed by Hiroshi Maeda in Kumamoto, Japan, with the theory based on the high permeability of blood vessels at tumor sites, due to the leakage of the tumor vasculature as a consequence of growing fast (Hoffman, 2008). There are plenty of systems that enhance the accumulation efficacy to tumor *via* EPR effect (Regehly et al., 2007; Lee et al., 2009). However, this targeting strategy may release a considerable quantity of drugs before substantial uptake by tumor cells. Moreover, recently the EPR effect is becoming a controversial topic as researchers found that human bodies do not have obvious leakage of tumor vasculature and EPR effect. Hence, the general applicability of this EPR effect is challenged and still an open question.

Active Targeting

Active targeting includes the use of targeting moieties such as ligands, antibodies, and aptamers that can recognize specific receptors on tumor vasculature, tumor cells, and even tumor subcellular organelles for enhanced delivery of photosensitizers (Li and Yan, 2018; Zhang et al., 2020; Zheng et al., 2020)

The tumor vasculature targeting is an efficient way to combat cancer as a result of cutting off the supply of oxygen and nutrients. In addition, by interrupting the tumor vessel integrity, an increased accumulation of the materials to the tumor tissue is expected to improve the PDT efficacy. Vascular endothelial growth factor (VEGF) and its receptor are hallmarks of tumor cells, which can be utilized as main antiangiogenic targets (Tirand et al., 2006; Prasad et al., 2014). Vascular cell adhesion molecule-1 (VCAM-1) is involved in tumor cell adhesion and metastasis (Yin et al., 2017), and matrix metalloproteinases (MMPs) are responsible for the angiogenesis and metastasis (Danhier et al., 2010; Liu T. W. et al., 2016), RGD ligands are another frequently used target and the recognition is *via* $\alpha_v\beta_3$ integrin (Yuan et al., 2014). All of them are crucial tumor vasculature targets.

Target tumor cells are a straightforward targeting strategy that accelerate the phagocytosis/endocytosis of nanocarriers (Hanahan and Weinberg, 2011; Liu L. et al., 2016; Liu et al., 2017). The representative receptors are CD44 receptor (Jiang et al., 2017), folate (FA) receptor (Li et al., 2018d), transferrin receptor (Kaspler et al., 2016), epidermal growth factor (EGF) receptor (del Carmen et al., 2005), etc.

Subcellular targeting, such as mitochondria, lysosome, nucleus, and endoplasmic reticulum, is another type of targeting. Among these, mitochondria targeting is of great importance as mitochondria is the energy factory of tumor cells (Chakrabortty et al., 2017). The triphenylphosphonium (TPP) cation is a typical mitochondria targeting moiety. Due to the limited diffusion distance of singlet oxygen, the subcellular targeting of different organelles may lead to varying degrees of destruction of tumor cells.

With a large amount of targeting candidates mentioned above, herein we only choose one example for the demonstration of the importance of targeting function in PDT. Target function is especially crucial to cross the blood-brain-barrier (BBB) in the treatment of brain tumor. The treatment of brain disease is not a trivial task as the delivery of the drugs to the brain area is very difficult due to the BBB. An iRGD-conjugated prodrug micelle

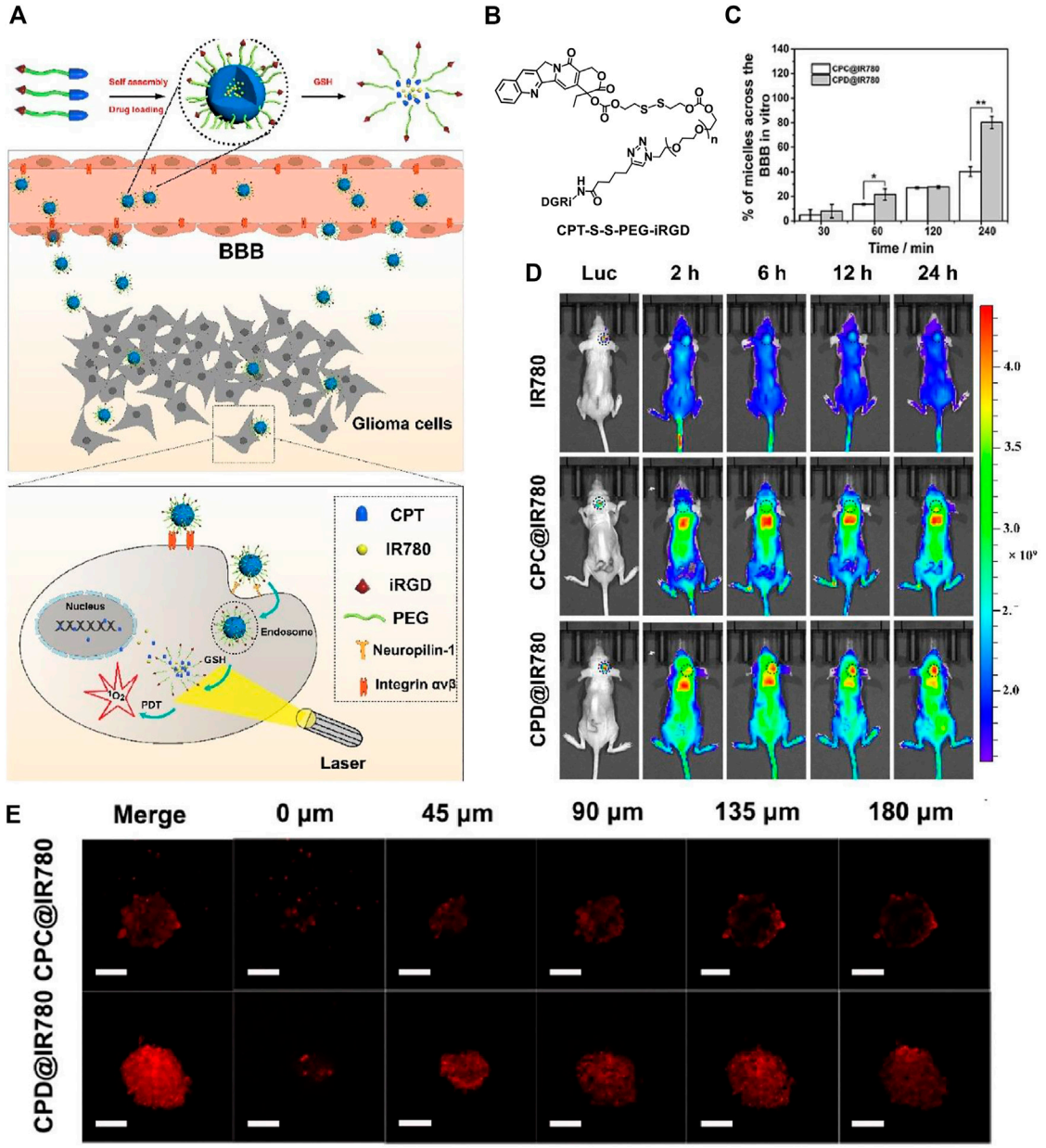

FIGURE 2 | (A) Preparation of self-assembled micelles, BBB penetrating, and glioma cell targeting by the iRGD peptide and GSH-induced disassembly for the combination of chemotherapy and photodynamic therapy; **(B)** molecular structure of CPT-S-S-PEG-iRGD; **(C)** the quantitative analysis of absorption spectra in the lower chamber after CPC@IR780 micelles and CPD@IR780 micelles were cultured in the upper chamber for different times; **(D)** whole body fluorescence imaging of U87 orthotopic glioma mice at different time intervals. Dashed line indicates the glioma site; **(E)** intratumoral penetration characterization using U87 tumor spheroids treated with micelles in 45 μm interval between consecutive slides. Reprinted with permission from Lu L. et al. (2020).

with BBB penetrability was used to enhance the anti-glioma therapy (Lu L. et al., 2020) As shown in **Figure 2**, the structure of the polymer CPT-S-S-PEG-iRGD consists of a prodrug camptothecin (CPT) for chemotherapy, a disulfide linker responsive to glutathione (GSH), and the internalizing RGD peptide (iRGD) as targeting moiety. The ability to cross the BBB and target glioma cells is expected to be enhanced *via* αvβ integrin and neuropilin-1 mediated ligand transportation. The polymer is self-assembled into micelle with a diameter of approximately 100 nm. A photosensitizer IR780 is loaded into the micelle for PDT.

Hence, the micelle is functionalized as the CPT and photosensitizer IR780 carrier, which is responsive to the high concentration of GSH in glioma tumor and triggers the release of the therapeutics CPT and IR780. The iRGD peptide bonded at the surface of the micelles is responsible for the cross of the BBB and glioma tumor targeting. The penetration ability of the micelles is examined *in vitro* BBB model, which is established by co-culture

of bEnd.3 cells and U87 cells in the upper and lower chamber, respectively. The bEnd.3 simulates the BBB. By examination of the uptake efficiency of the micelles by U87 cells in the lower chamber, the penetration ability of the materials is found to be significantly improved (**Figure 2C**). The results show that 89.92 ± 1% of iRGD modified CPD@IR780 micelles cross the simulated BBB into the lower chamber, while for the unmodified CPC@IR780 micelles the value is only 41.78 ± 0.22%.

The authors further constructed U87 tumor spheroids *in vitro* to examine the penetration ability (**Figure 2E**). For the CPD@IR780 micelles, the fluorescence is stronger and uniformly distributed in the glioma spheroids. While for the CPC@IR780 micelles, the fluorescence is mainly distributed in the periphery of the glioma spheroids. These results demonstrated the enhanced penetration ability to the glioma spheroids of **CPD@IR780** micelles due to iRGD modification. The biodistribution of micelles *in vivo* was studied (**Figure 2D**). The iRGD modified CPD@IR780 micelles show enhanced accumulation in the brain, as compared to the unmodified CPC@IR780 micelles and IR780. Confocal images of brain sections of U87 orthotopic glioma mice were studied. The iRGD modified CPD@IR780 micelles show preferably distribution in glioma tumor cells instead of healthy cells. All those results confirmed the target ability of CPD@IR780 micelles to glioma cells. The combination of activatable chemotherapy and PDT with target function to enhance penetration to BBB successfully extended the survival time of mice bearing glioma tumor.

Tumor-Activatable Polymeric Delivery System

Abnormal expression of proteins usually has a close relationship with diseases. Enzymes are especially crucial biomarkers, and a variety of enzymes are overexpressed by tumor cells or tumor associated macrophages. For instance, hyaluronidase, matrixmetalloproteinases, and cathepsin B are overexpressed in tumor cells. The enzyme-activated polymeric delivery systems have been developed, which have high specificity as compared with other activation strategies such as pH and GSH activation (Bae and Na, 2010; Park W. et al., 2011; Li H. et al., 2017; Huo et al., 2019).

The increased glycolysis and proton-pump activities on plasma membranes of cancer cells produce a large amount of lactic acid, resulting in a slightly acidic extracellular microenvironment of tumor. The pH value of tumor sites is in the range of 6.0–7.0, which is lower than that of normal tissues (pH = 7.4) (Pan et al., 2013). Taking advantage of the difference in pH, an acid activatable system can be designed (Du et al., 2010; Du et al., 2011; Yuan et al., 2012; Tseng et al., 2015; Li F. et al., 2018; Dong et al., 2018; Lin et al., 2019; Lu Y. et al., 2020) mainly based on the protonation of the amine group or acid cleavage of acidic-labile linkers such as hydrazone linkers (Braslawsky et al., 1990), Schiff base linkers (-RC = N-) (Ke et al., 2014), *cis*-acotinyl linkers (Zhu et al., 2010), acetal linkers (Gu et al., 2013), etc. (**Figure 3A**).

Reactive oxygen species (ROS) and GSH are of great importance for maintaining the redox stability. Tumor cells have higher levels of ROS due to the oncogenic stimulation, mitochondrial malfunction, and increased metabolic activity(Li X. et al., 2017). For instance, the concentration of hydrogen peroxide in tumor cells is reported to be approximately 10 μM, which is higher than normal cells. Boronic acid esters are typical hydrogen peroxide-responsive moieties (Saravanakumar et al., 2017; Zeng et al., 2020). In addition, GSH is abundant in a tumor intracellular environment (2–10 mM) (Li and Yan, 2018). Disulfides and sulfonyl group are frequently utilized to construct GSH-responsive polymeric delivery systems (Kim et al., 2014; Li et al., 2014; Liu X. et al., 2016). The representative ROS and GSH responsive organic moieties are summarized in **Figure 3A**.

Due to the consumption of oxygen within about 100 μm of the inadequate tumor vasculatures by quickly proliferating cancer cells, the oxygen concentration of tumors is only about 4%, which is very distinct from normal tissues. Based on this, hypoxia-responsive polymeric systems have been developed and three representative hypoxia-responsive moieties have been summarized in **Figure 3A**.

Based on the different microenvironments of tumor and normal tissues, a variety of activatable polymeric delivery systems are emerging (Park et al., 2016; Sun et al., 2017; Wei et al., 2018; Li et al., 2019c; Yan et al., 2020; Zeng et al., 2020; Yang et al., 2021). Despite the different structures and constituents of thousands of reports, they mainly achieve the activation *via* the following three strategies: (1) self-quenching and dequenching of photosensitizers due to aggregation and disintegration; (2) utilize another quencher to quench the triplet state of photosensitizer and dequenching upon cleavage of sensitive bonds; and (3) the change of size and surface charge to induce an enhanced internalization by tumor cells. These three strategies are summarized in **Figure 3B**.

Herein we introduce some typical polymeric delivery systems for PDT, as an illustration of the above-mentioned activations and strategies.

Enzyme

Choi et al. reported a protease biodegradable poly-L-lysine, grafted with PEG and photosensitizer Ce6 (L-SR15). As shown in **Figure 4**, the quenched fluorescence and singlet oxygen production ability is recovered due to the degradation of the poly-L-lysine by tumor-associated protease cathepsin B. A poly-D-lysine backbone (D-SR16) that is uncleavable by proteases was synthesized for comparison. *In vitro* results are shown in **Figures 4B,C**, both the fluorescence/singlet oxygen generation ability of L-SR15 and D-SR16 are significantly decreased as compared with the free Ce6. The fluorescence intensity/singlet oxygen generation ability of L-SR15 is recovered by the addition of cathepsin B, while there is no change for D-SR16. The fluorescence/singlet oxygen generation ability enhancement can be inhibited by the addition of cathepsin B inhibitor CA-074. *In vivo* results show that the tumor can be imaged by the L-SR15 (**Figure 4D**), due to the selectively activation by the cathepsin B in the tumor site. The tumor volume is significantly depressed for the L-SR15 group as compared with D-SR16 group or L-SR15 + inhibitor CA-074 group. These results demonstrated that the tumor-specific

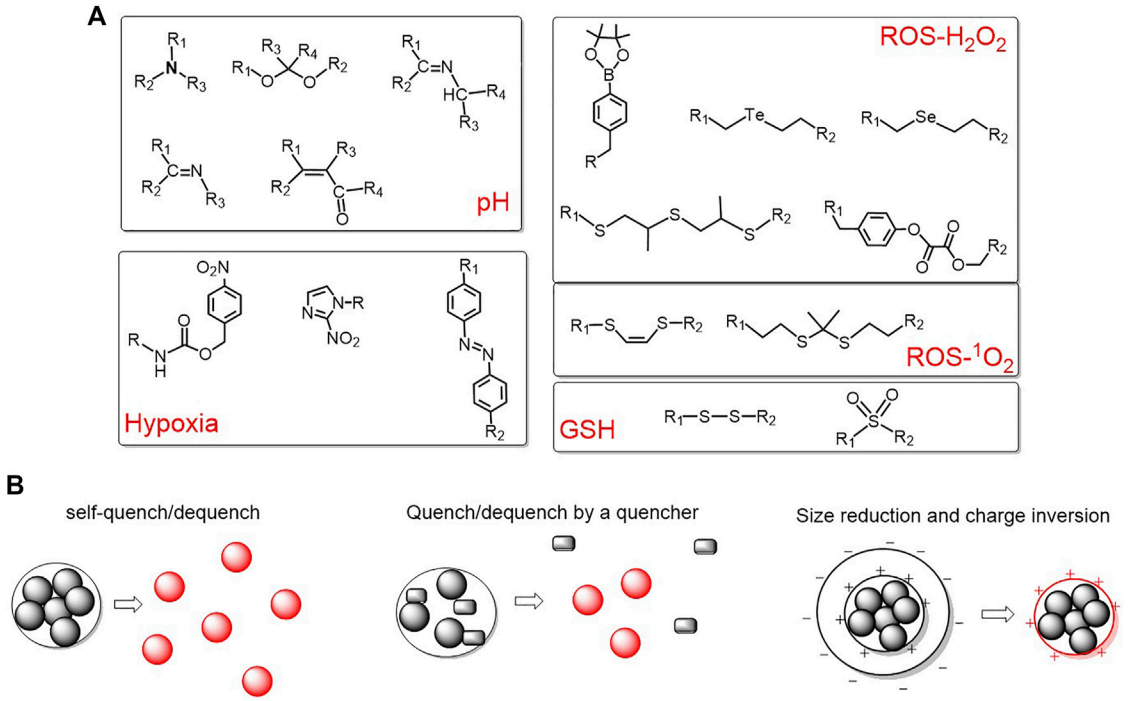

FIGURE 3 | (A) Representative pH/ROS/GSH/hypoxia-responsive linkers for activatable polymeric delivery system; **(B)** three commonly used activation strategies.

protease cleaved the poly-L-lysine backbone, restoring the self-quenched fluorescence/singlet oxygen production ability of Ce6 and achieving selective imaging and PDT of the tumor.

A similar strategy was reported by Kun Na et al., who is also one of the pioneer researchers in this area. For instance, photosensitizer Pheophorbide (Pba) was dangled onto hyaluronic acid (HA), which leads to self-quenching of the photosensitizer. The polymer can be easily internalized by HA receptor-mediated endocytosis and then degraded by intracellular microenvironment enzymes, releasing free Pba with recovered PDT efficacy (Li et al., 2010). However, those reports by Choi et al. and Kun Na et al. are based on the self-quenching of photosensitizers. Both the quenching and activation efficiency are highly dependent on the substitution degree of the photosensitizers to the polymer backbone. A higher degree of substitution will lead to higher quenching efficiency but maybe lower activation efficiency because it decreases the recognition site of the biomarker.

Zheng et al. reported a molecular beacon system based on intramolecular quenching (Zheng et al., 2007). As shown in **Figure 5A**, triplet photosensitizer (pyropheophorbide, Pyro) is connected with a quencher (BHQ3) by a peptide linker, which is activatable by tumor-associated protease MM7. Both the fluorescence and the singlet oxygen production ability of Pyro can be quenched by BHQ3, while it restored upon cleavage of the peptide linker by the MM7. This is confirmed with fluorescence emission and the direct detection of singlet oxygen (**Figure 5C** and **Figure 5E**). The molecular beacon is specifically cleavable by MM7 peptide ($PP_{MMP7}B$ + MMP7 in **Figure 5C**), while uncleavable by MM2 peptide ($PP_{MMP7}B$ + MMP2 in **Figure 5C**). Moreover, the addition of MM7 inhibitor ($PP_{MMP7}B$ + MMP7+inhibitor in **Figure 5C**) cannot restore the fluorescence and singlet oxygen production ability. All these results demonstrate the selectivity of the peptide linker to MM7. The cleavage of the peptide linker was further evidenced by high performance liquid chromatography (HPLC) in **Figure 5D**. The $PP_{MMP7}B$ has a retention time of approximately 26.1 min. The cleavage of $PP_{MMP7}B$ by MM7 resulted in two fragments peaked at 14.1 and 36.0 min, corresponding to the BHQ3 moiety and Pyro moiety, respectively, which is confirmed by the UV-vis absorption spectroscopy and MALDI-TOF mass spectroscopy. The $PP_{MMP7}B$ shows significant photodynamic cytotoxicity (**Figure 5F**) in KB cells (MMP7 overexpressed cell line) compared with the BT20 cells (MMP7 less expressed cell line). The KB tumors are found to be greatly depressed by the enzyme cleavable molecular beacon $PP_{MMP7}B$.

pH

Liu et al. constructed an imaging-guided pH sensitive PDT platform by using charge reversible up-conversion nanoparticles (Wang et al., 2013). As shown in **Figure 6A**, the pH-sensitive polymer PAH-DMMA-PEG (negatively charged) was grafted onto the positive surface of the Mn^{2+}-doped, Ce6 layered up-conversion nanoparticles (UCNPs) *via* electrostatic interactions (UCNP@2XCe6-DMMA-PEG). At pH = 6.8, the nanoparticle zeta potential increasing from approximately −18 mV to +10 mV, confirming the acid-responsive detaching of the PEG coating from the UCNPs. UCNP@2XCe6-SA-PEG that is not responsive to acid is used as a reference. As expected,

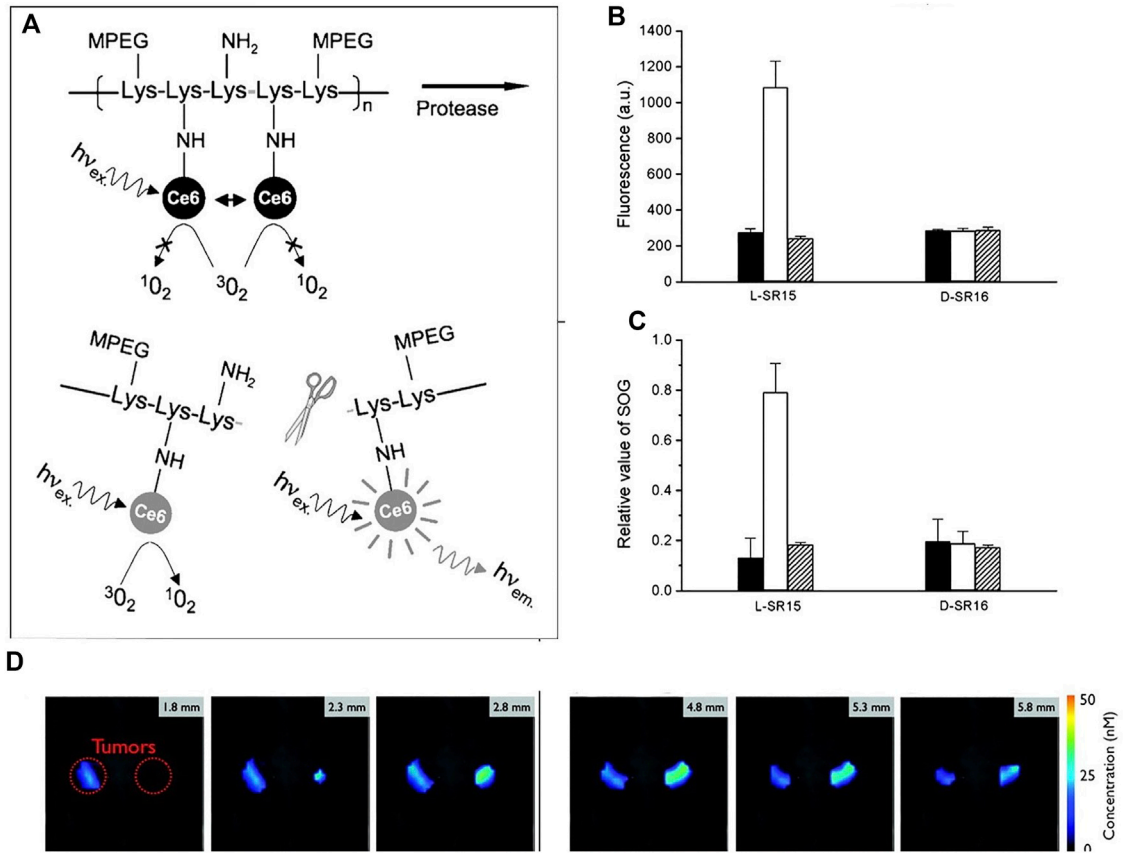

FIGURE 4 | (A) Schematic diagram of PM-PDT strategy; **(B)** activation of fluorescence intensity and **(C)** singlet oxygen generation of L-SR15 and D-SR16 with phosphate buffer (black columns), cathepsin B (white columns), and CA-074 inhibitor-pretreated cathepsin B (striped columns); **(D)** six consecutive slices from a three-dimensional fluorescence-mediated tomographic scan (Choi et al., 2006).

the zeta potential remained the same in pH = 7.4 and pH = 6.8. The ability of the internalization by cancer cells at different pH was studied by confocal laser scanning microscopy imaging. The UCNP@2XCe6-DMMA-PEG at pH = 6.8 shows increased internalization ability than at pH = 7.4, hence enhanced phototoxicity to HeLa cells was observed (**Figure 6D**). Owing to the doping of the Mn^{2+} to the UCNPs, the materials can be used for dual-modal imaging, i.e., up-conversion luminescence imaging and magnetic resonance imaging (**Figure 6B** and **Figure 6C**). Both materials show good accumulation in tumor sites. UCNP@2XCe6-DMMA-PEG has a longer retention in tumor than the reference UCNP@2XCe6-SA-PEG. This is due to the acid-responsive detaching of the PEG coating resulting in a strong positive surface of UCNPs, which enhanced the stickiness of the material to the negatively charged cancer cell membranes and tumor tissues. The longer retention time of UCNP@2XCe6-DMMA-PEG contributes to the better PDT efficacy *in vivo* than UCNP@2XCe6-SA-PEG (**Figure 6E**).

ROS

An ROS responsive self-degrading polymer was constructed for enhanced chemotherapy and PDT (Wang et al., 2019). As shown in **Figure 7A**, the therapeutic prodrug DOX was conjugated to the polymer with a pendant thioketal bond, which is responsive to ROS such as singlet oxygen or hydrogen peroxide. The triplet photosensitizer Ce6 with a planar aromatic structure interacted with the DOX *via* π-π stacking, constituting a self-assembled nanoparticle PEG-PBC-TKDOX(Ce6). In the tumor microenvironment or upon light irradiation, the abundant hydrogen peroxide in the tumor microenvironment or the singlet oxygen produced from irradiated Ce6 leads to the cleavage of the pendant thioketal bond, followed by the cascade reaction of self-destructive polymer. Accordingly, the Ce6 and DOX are actively released (**Figure 7A**). The degradation of the polymer was confirmed by ^{1}H-NMR characterization and the decrease of the molecular weight in the presence of hydrogen peroxide. The release of DOX was confirmed by confocal laser scanning microscopy imaging. Free DOX has fluorescence and accumulates in nuclear. As compared with those without light irradiation, KB cells incubated with PEG-PBC-TKDOX(Ce6) upon light irradiation show enhanced accumulation in nuclear, indicating the release of DOX from polymer backbone. Biodistribution of DOX and Ce6 was studied (**Figures 7B,C**). The light irradiation enhanced the accumulation of the PEG-PBC-TKDOX(Ce6) in tumor sites. This may be attributed to the ROS induced destruction of the polymer, as smaller molecular

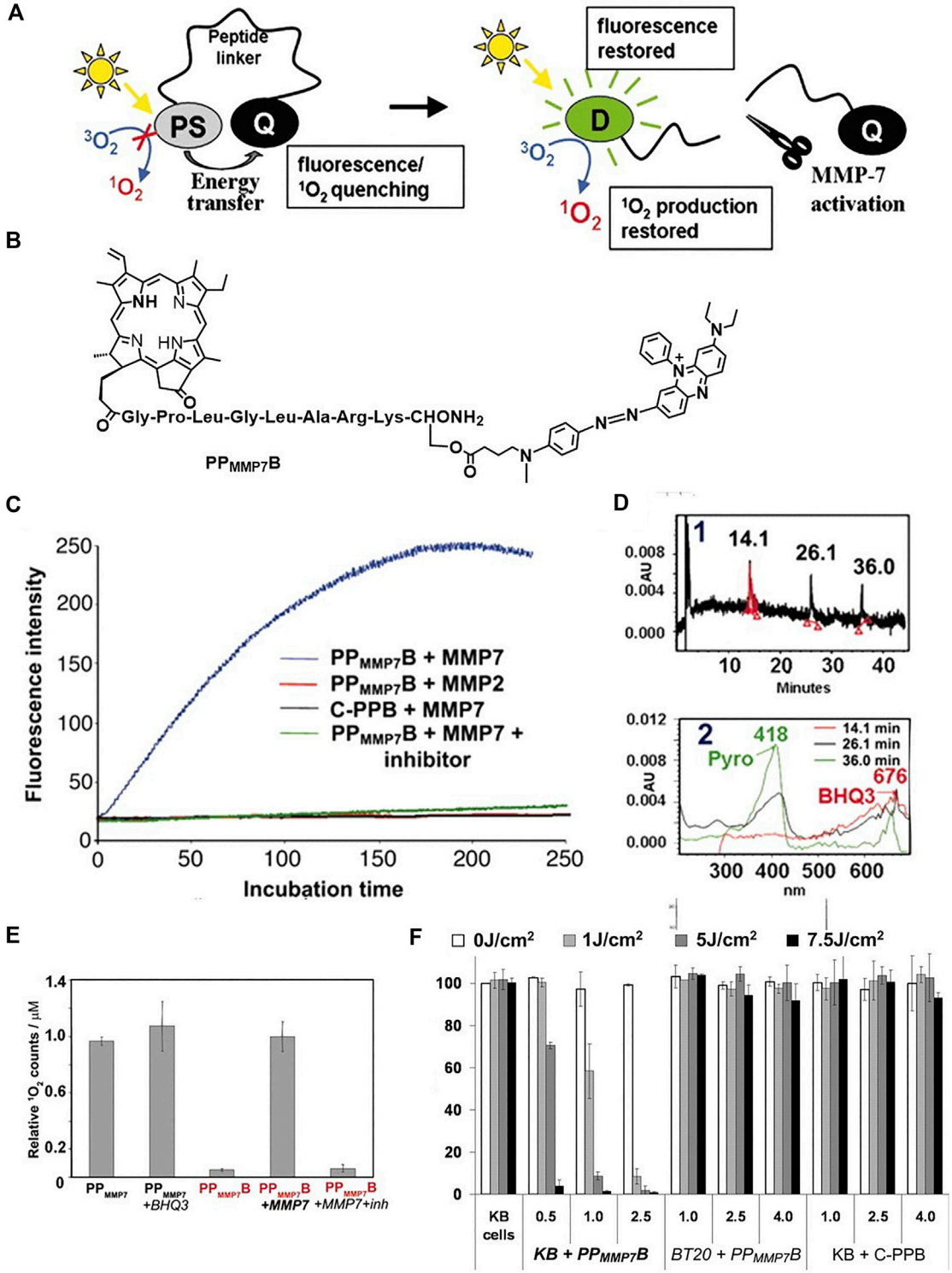

FIGURE 5 | (A) The concept of photodynamic molecular beacons. **(B)** Molecular structure of $PP_{MMP7}B$. **(C)** Fluorescence kinetics of different groups. **(D)** HPLC spectrum of **$PP_{MMP7}B$** + MMP7 incubated at 37°C for 2 h and corresponding UV-vis spectra. **(E)** The relative $^1O_2$ counts of different groups. **(F)** Photodynamic cytotoxicity determined by MTT assay as a function of PS and light doses, compared with untreated cells. Copyright (2007) National Academy of Sciences (Zheng et al., 2007).

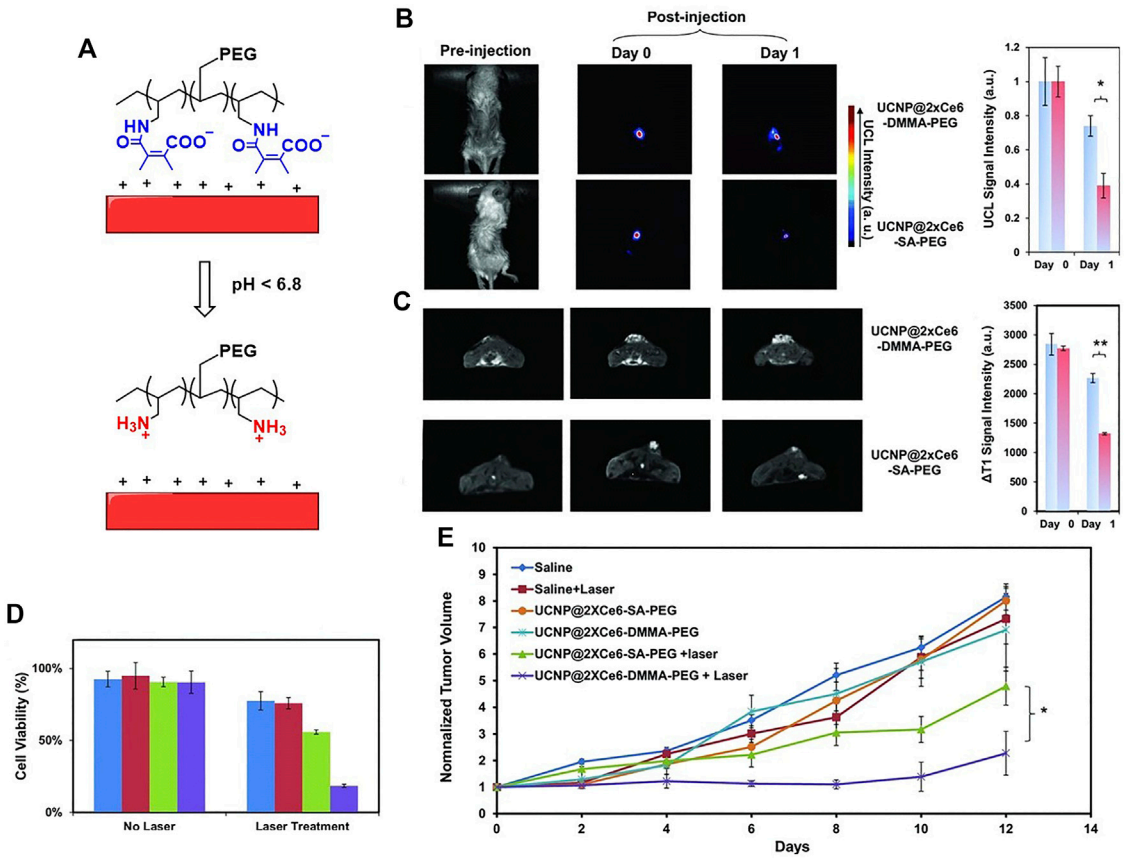

FIGURE 6 | (A) Schematic illustration of pH-responsive smart theranostic UCNPs, showing the detachment of PAH-DMMA-PEG from the positively charged nanoparticle surface under pH 6.8; **(B)** *in vivo* UCL images and **(C)** T_1 MR images of mice after intratumoral injection with UCNP@2xCe6-DMMA-PEG or UCNP@2xCe6-SA-PEG. The images were taken at different times post-injection; **(D)** cell viability data of HeLa cells after various treatments indicated with and without the 980 nm laser irradiation as evaluated by the standard MTT assay; **(E)** tumor growth curves of different groups of mice after various treatments. Reprinted with permission from Wang et al. (2013).

size is known to have better tumor accumulation ability (Wang et al., 2019). The PEG-PBC-TKDOX(Ce6) upon light irradiation shows outstanding therapeutic efficacy (**Figure 7D**) and decreased free DOX-related side effects such as decrease of body weight (**Figure 7E**).

GSH

Natural polysaccharides have been popularly used for the development of self-quenchable nanoparticles due to their good water solubility, biodegradability, biocompatibility, and tumor targeting ability (Bae et al., 2010; Bae and Na, 2010; Li et al., 2011; Yoon et al., 2012) Kang Moo Huh et al. constructed a GSH responsive pheophorbide a-glycol chitosan system for PDT. As shown in **Figure 8C**, the photosensitizer pheophorbide a (PheoA) was dangled onto the glycol chitosan *via* a reducible disulfide bond (PheoA-ss-GC in **Figure 8A**), which is sensitive to the GSH that is abundant in the tumor microenvironment. The conjugate tends to aggregate into nanoparticles and the fluorescence/singlet oxygen production ability of PheoA is diminished due to self-quenching. The cleavage of the disulfide bond by GSH recovered both the fluorescence and singlet oxygen production ability, achieving the on-site release of the photosensitizer and selectively killing tumor cells. A reference compound (PheoA-GC in **Figure 8B**) that has no disulfide bond linker was also synthesized for comparison. The recovery of fluorescence and singlet oxygen production ability of PheoA-ss-GC were evidenced both in cuvette and *in vitro*. As shown in **Figure 8D**, the fluorescence of PheoA is obvious in the KB cells treated with PheoA-ss-GC, while it was completely quenched in the cells treated with PheoA-GC. Moreover, the PheoA-ss-GC shows significantly higher phototoxicity to KB cells than PheoA-GC (**Figure 8E**) as the self-quenching effect of the photosensitizer is greatly alleviated upon the activation of high concentration of GSH in tumor cells. Consequently, outstanding PDT efficacy of PheoA-ss-GC is achieved (**Figure 8F**).

Hypoxia

Tumor tissues are known to be hypoxic. Taking advantage of this characteristic, Zhao et al. designed multifunctional micelles that are dually responsive to hypoxia and singlet oxygen (Li et al., 2018c). The molecular structure is consisted of azobenzene and imidazole. The hypoxic atmosphere of the tumor tissues induces the collapse of azobenzene and consequently provoked PEG shedding (dePEGylation); the singlet oxygen produced by Ce6

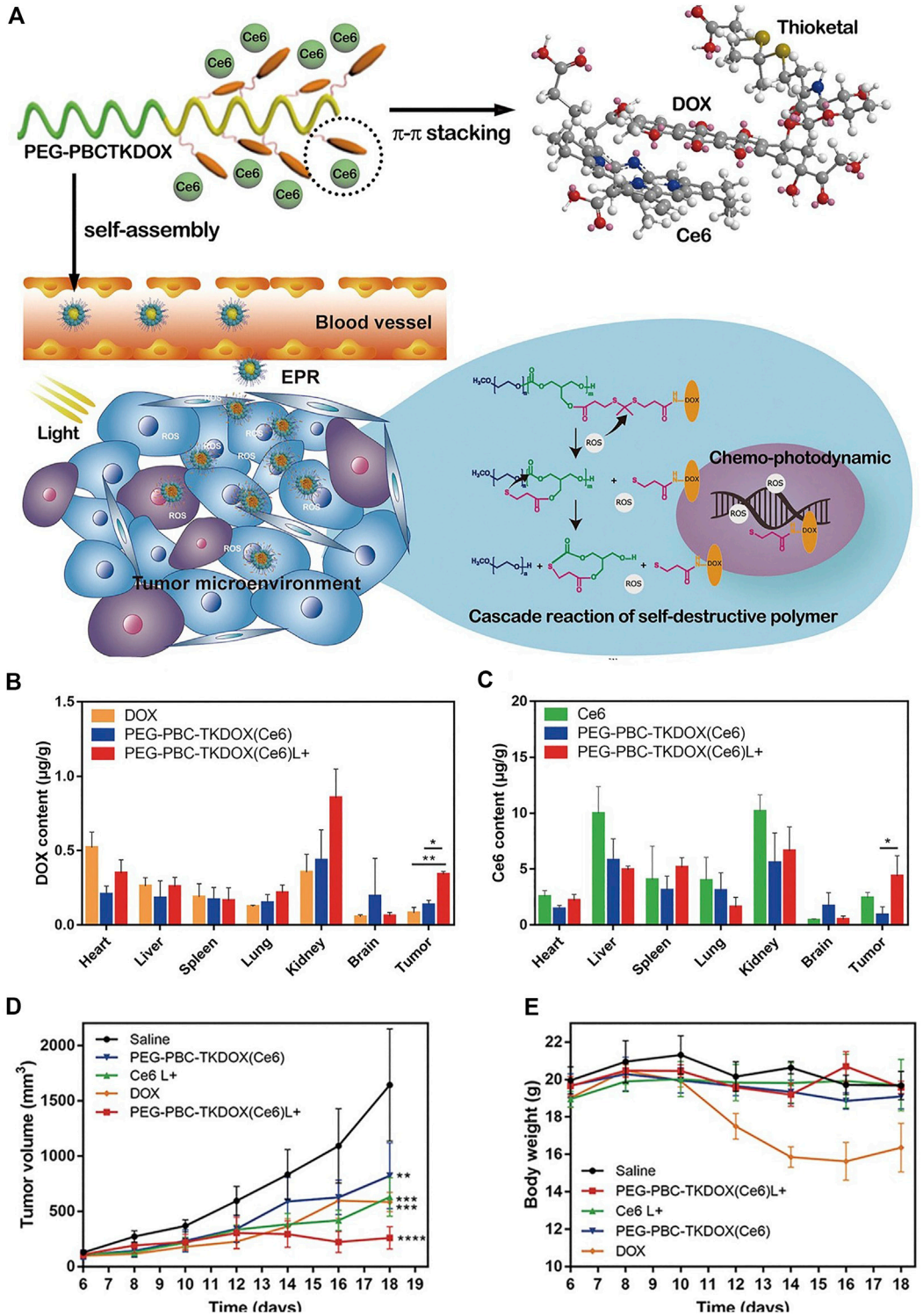

FIGURE 7 | (A) Schematic drawing of the cascade reaction of self-destructive polymeric nanomicelles; **(B)** biodistribution of DOX solution and PEG-PBC-TKDOX (Ce6) micelles at 12 h with or without light irradiation; **(C)** biodistribution of Ce6 solution and PEG-PBC-TKDOX (Ce6) micelles at 12 h with or without light irradiation; **(D)** growth curves of subcutaneously inoculated KB tumors. Intravenous injections were given to mice at day 7, day 9, and day 11. The 660 nm laser irradiation followed at 12 h after each injection; **(E)** body weight changes (n = 5, **, $p < 0.01$, ***, $p < 0.001$, ****, $p < 0.0001$). Reprinted with permission from Wang et al. (2019).

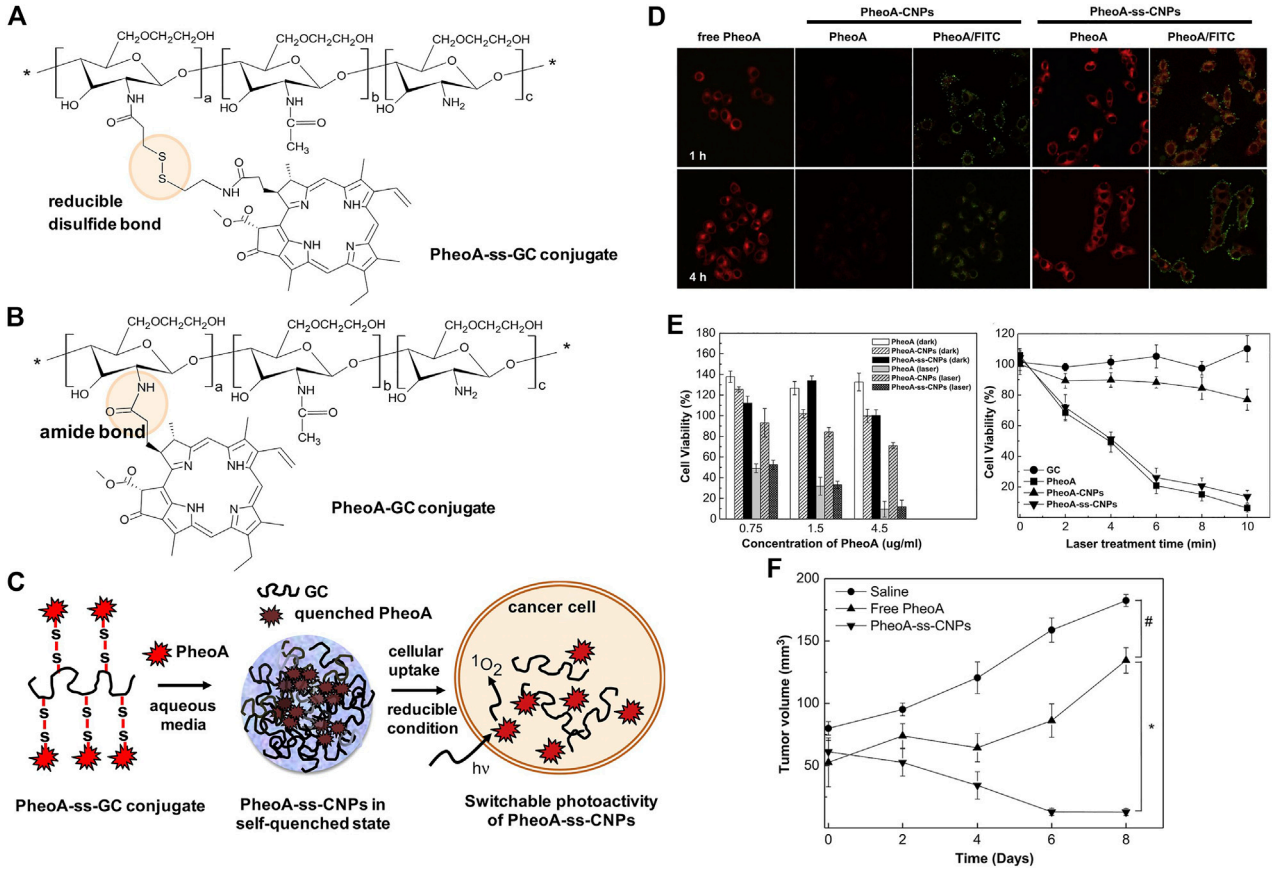

FIGURE 8 | Chemical structures of **(A)** PheoA-ss-GC and **(B)** PheoAeGC conjugates and **(C)** illustration of bioreducible PheoA-ss-CNPs for switchable photoactivity of PheoA; **(D)** CLMS images of KB cells treated with free PheoA, PheoAeCNPs, and PheoA-ss-CNPs; **(E)** phototoxicity and dark toxicity of free PheoA, PheoAeCNPs, and PheoA-ss-CNPs; **(F)** tumor growth of HT-29 tumor-bearing mice after various treatments. Reprinted with permission from Oh et al. (2013).

upon light irradiation leads to an oxidation of hydrophobic imidazole to hydrophilic urea, followed by a rapid release of Ce6. Enhanced internalization of micelles by LLC cells and improved PDT efficacy is observed.

Temperature

Besides the internal triggers such as pH, enzyme, GSH, and hypoxia, external triggers such as temperature can also activate the PDT. Poly (N-isopropylacrylamide) (PNIPAM) is a frequently used thermo-sensitive polymer (Liu et al., 2009; Lv et al., 2015). It can go through the phase transition from hydrophilic to hydrophobic state when the temperature is above the lower critical solution temperature (LCST) (Stöber et al., 1968; Pelton and Chibante, 1986; Pelton, 2000). The LCST of PNIPAM in water is approximately 32–33°C. Molecular structure modification to the PNIPAM (co-polymerization with other monomers) or adjusting the pH value can affect this LCST value (Hoare and Pelton, 2004; Rijcken et al., 2007; Dai et al., 2012; Zhang et al., 2013; Jiang et al., 2014). Hence it is possible to adjust this LCST to suitable values such as body temperature (ca. 37°C). In addition, tumor tissues are reported to have a higher temperature than normal tissues due to inflammation and cancer cell immortalization (Wang et al., 2013; Lv et al., 2015)

A nanoplatform based on the pH-temperature sensitive polymer was constructed for cancer therapy (Xu et al., 2016). As shown in **Figure 9**, the up-conversion nanoparticles (UCNP) are decorated with carbon dots and chemotherapeutic reagent DOX and PDT reagent zinc(II)-phthalocyanine (ZnPc). The up-converted fluorescence excited the ZnPc to its triplet state and produce singlet oxygen, and the decorated carbon dots generate photothermal effect upon near infrared laser irradiation. This thermal effect at tumor acidic tissues induces the shrinkage of P(NIPAm-MAA) polymer, leading to the controlled drug release. As shown in **Figure 9F**, the nanoplatform shows significant drug release at 50°C (pH = 7.4). Moreover, the drug can be efficiently released at acidic conditions (pH = 4.0, **Figure 9G**) at 37°C. These results show that the drug release can be controlled by pH and temperature. The thermal effect of the nanoplatform upon NIR laser irradiation was shown in **Figure 9D**. The NIR laser irradiation to the material accumulated in tumor site increased the local temperature, hence the drug release

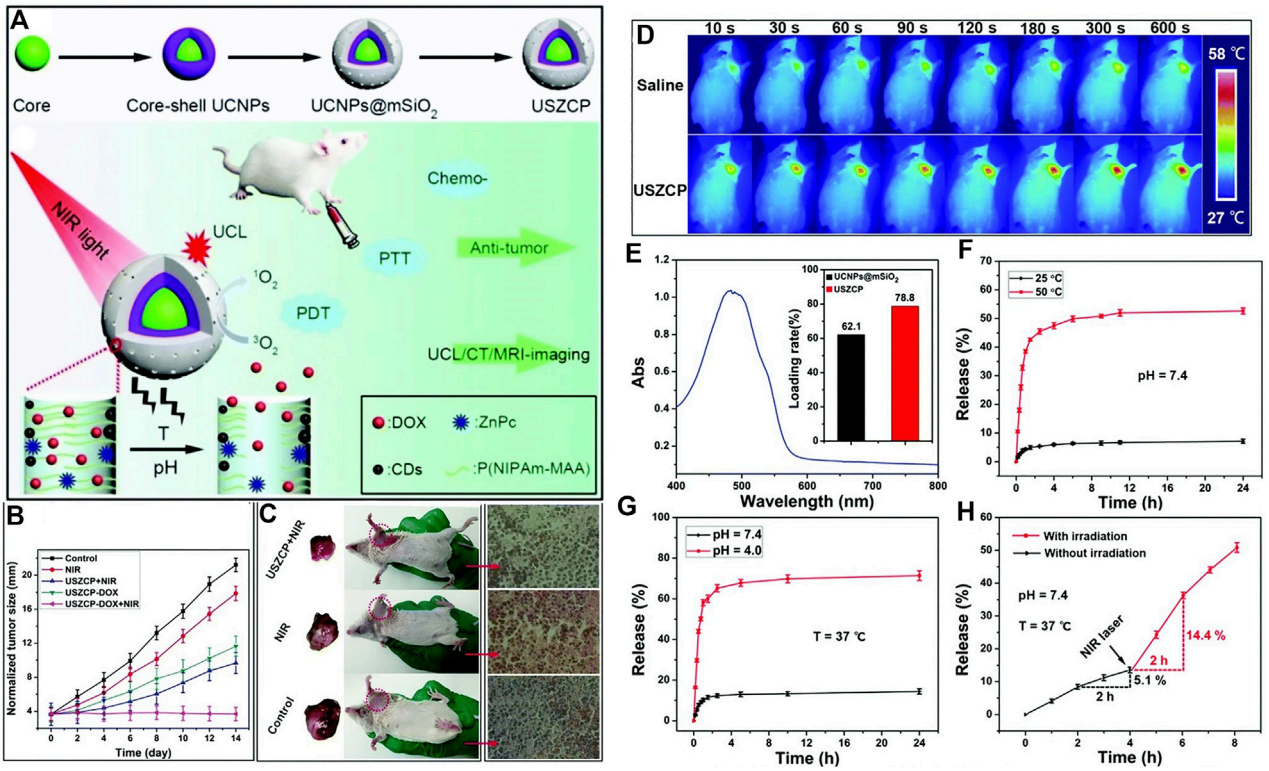

FIGURE 9 | (A) Schematic illustration of pH-temperature sensitive polymer for cancer therapy. **(B)** Changes in the tumor size of the H22 tumor obtained from mice after different treatments; **(C)** Picture of tumor and H&E staining; **(D)** *in vivo* infrared thermal images of a tumor-bearing mouse after injection of USZCP under NIR irradiation with different times; **(E)** UV-vis absorption spectrum of DOX (inset shows the DOX loading content of UCNPs@mSiO2 and USZCP); the release efficiency of USZCP–DOX at different **(F)** temperatures and **(G)** pH values; **(H)** the release efficiency of USZCP–DOX triggered by a NIR laser. Reprinted with permission from Xu et al. (2016).

upon NIR laser irradiation can be expected (**Figure 9H**). The combination of the PDT and chemotherapy shows an outstanding therapeutic efficacy (**Figure 9B** and **Figure 9C**).

SMART POLYMERIC DELIVERY SYSTEM FOR ANTIMICROBIAL PHOTODYNAMIC THERAPY

Antibiotics have been the most effective strategies to fight against bacterial infections. However, the abuse of antibiotics has led to severe antimicrobial resistance (Bush et al., 2011). There are approximately 700,000 deaths per year due to antimicrobial resistance all over the world (Klausen et al., 2020). Developing other anti-bacterial strategies such as PDT that are alternatives to antibiotics is of great urgency (Demidova and Hamblin, 2004; Hamblin and Hasan, 2004; Pagonis et al., 2010; Huang et al., 2012).

The delivery of the photosensitizer to the bacteria (especially Gram-negative bacteria) is not a trial task due to its structural features. As shown in **Figure 10**, the cell wall of Gram-positive bacteria consists of thick, porous layers of peptidoglycan embedded with proteins and lipoteichoic acid. The porous layers are relatively easy to go through for photosensitizers. Moreover, the lipoteichoic acids on the outside are negatively charged, which tends to bind with cationic agents (Minnock et al., 2000; Lambert, 2002). As a comparison, the cell wall of Gram-negative bacteria is thicker, being composed of a peptidoglycan layer, the inner cytoplasmatic membrane, and the outer membrane. This additional outer membrane of Gram-negative bacteria is composed of phospholipids and lipopolysaccharides, which is an effective barrier that limits the penetration of photosensitizers (Minnock et al., 2000). Hence, a smart polymeric delivery system that can target the bacteria and selectively kill the bacteria is necessary for optimal antimicrobial PDT.

Bacterial-Target Polymeric Delivery System

Structure-Inherent Targeting

As it has been mentioned that the structures of the tumor cells and the bacteria are different, photosensitizers that are commonly used in PDT of tumors cannot always be fit for the PDT of bacteria, especially Gram-negative bacteria (Malik et al., 1992). For instance, the cell wall of Gram-negative bacteria is thick and it has been a tough issue to deliver the photosensitizer into the Gram-negative bacteria. Hence, the Gram-negative bacteria are notoriously difficult to deal with (Malik et al., 1992).

As the bacteria are heavily negatively charged, the cationic photosensitizers are beneficial for their penetration and targeting to bacteria *via* electrostatic interactions (Minnock et al., 1996;

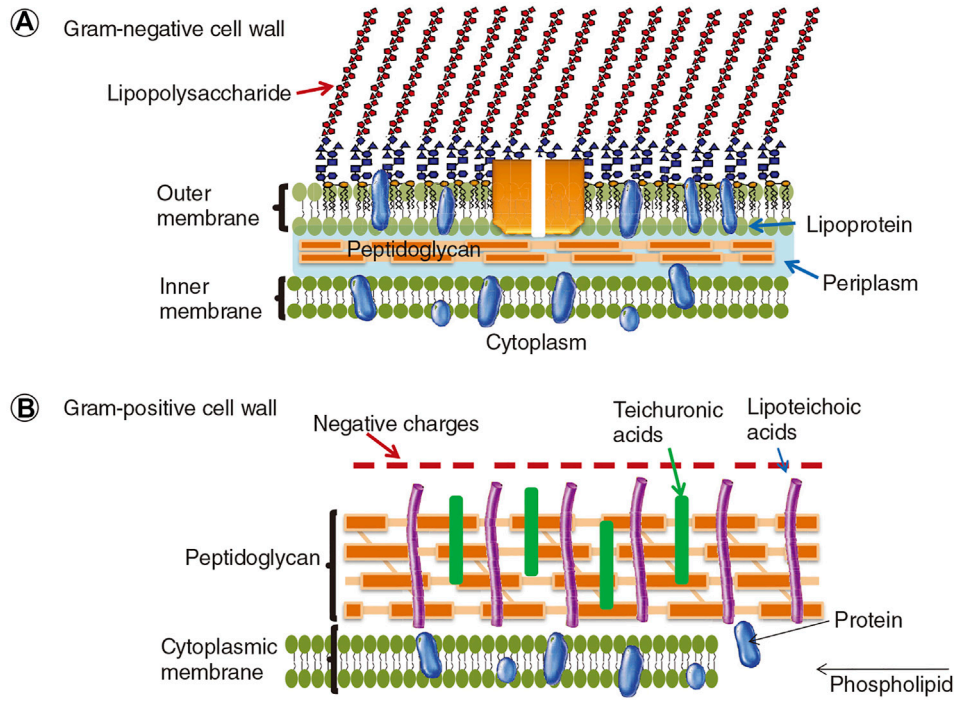

FIGURE 10 | The cell walls of Gram-negative and Gram-positive bacteria. Reprinted with permission from Yin et al. (2015).

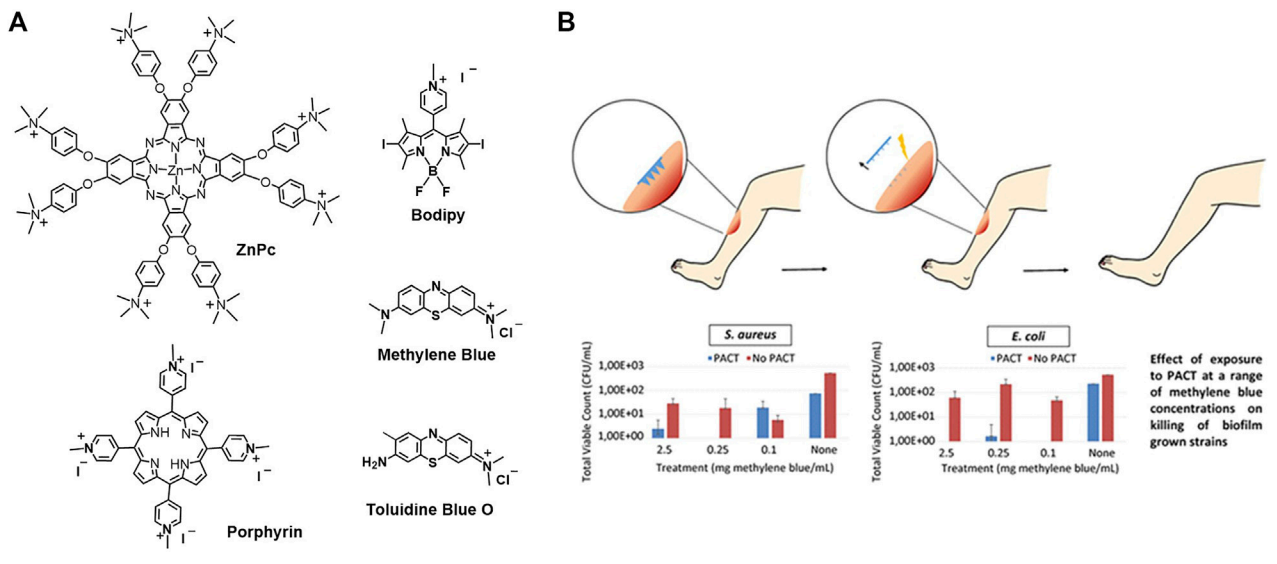

FIGURE 11 | (A) Molecular structure of cationic photosensitizers; **(B)** methylene blue-loaded microneedle for photodynamic antimicrobial chemotherapy at a range of methylene blue concentrations on killing of biofilm grown strains *S. aureus* and *E. coli* (Caffarel-Salvador et al., 2015).

Chen et al., 2020). This is a kind of structure-inherent targeting. Cationic photosensitizers such as methylene blue, cationic porphyrins, cationic Bodipy, and cationic phenoxyphthalocyaninato zinc (II) are shown as examples in **Figure 11A**.

Active Targeting

Similar to the anti-tumor therapy, there is also active targeting strategy to achieve better PDT efficacy. As the structures of tumor cells and bacteria are different, the target point also varies. For instance, the anti-tumor therapy targets the tumor vasculature,

tumor cells, and tumor subcellular organelles such as mitochondria, lysosome, nucleus, and endoplasmic reticulum. While the anti-bacterial therapy targets the bacteria membranes, bacterial exopolysaccharides (EPS), fimbriae, etc. For instance, various EPS are produced by bacteria to create a binding network between pathogens. Hence, bacterial EPS extracted from *Lactobacillus plantarum* can be utilized as targeting moiety (Li C. et al., 2018; Klausen et al., 2020). In addition, glycan is a commonly used targeting moiety with specific binding to lectins. Concerning to this aspect, different sugars such as mannose, sialic acid, and galactose have been utilized to target different pathogens. For instance, D-mannose has been used to bind to FimA protein of *Escherichia coli* (*E. coli*) (Krogfelt et al., 1990). As a deeper investigation and understanding to the bacteria, more and more target moieties are emerging.

Physical Penetration Targeting

As it has been introduced that the bacteria, especially Gram-negative bacteria, have thick cell walls, it makes them very difficult to deal with. Physical penetration by microneedles is an attractive strategy to go across the barriers and target the bacteria (Henry et al., 1998; Lee et al., 2008; Tuan-Mahmood et al., 2013; Donnelly et al., 2014; Kearney et al., 2014; Park et al., 2014). Methylene blue-loaded dissolving microneedles were constructed for antimicrobial PDT (Caffarel-Salvador et al., 2015). The microneedles were fabricated with aqueous blends of Gantrez® AN-139 co-polymer loading with different percentages of methylene blue. As presented in **Figure 11B**, the microneedles are in the micron range and are arranged in arrays. Loading high percentages of methylene blue (5% w/w) resulted in a decrease of needle height and microneedle strength. Loading suitable percentages of methylene blue (0.5% w/w) shows good mechanical strength that enables the insertion of the microneedles into the wound. The insertion distance is in the range of 378–504 μm, which is measured with a human tissue mimicker Parafilm™. The microneedles are expected to dissolve, followed by the release of the methylene blue. Upon photoirradiation, efficient bactericidal activity against *Staphylococcus aureus* (*S. aureus*) and *E. coli* biofilms was observed (**Figure 11B**).

Bacterial-Activatable Polymeric Delivery System

Due to the encapsulation of EPS, the biofilm microenvironment is lack of oxygen, which leads to anaerobic glycolysis (Flemming et al., 2016). Recalling from the tumor-activatable polymeric delivery system section, the tumor tissues are also hypoxic. The anaerobic glycolysis or the anaerobic respiration contributes to the acidic and highly reductive microenvironment of both bacterial biofilms and tumor tissues (Gales et al., 2008; Chen et al., 2013; Koo et al., 2017). For instance, the pH in the methicillin resistant *Staphylococcus aureus* (MRSA) biofilm microenvironment is less than 5.5, and the concentration of GSH in *E. coli* biofilm is up to 10 mM (Fux et al., 2005; Gales et al., 2008; Chen et al., 2013; Klare et al., 2016). Hence, the microenvironment of bacteria is similar to that of tumor, which is hypoxic, acidic, highly reductive, and has abundant ROS. Taking advantage of the differences between bacteria and normal tissues, the activatable polymeric delivery system can be developed, achieving selectively killing of the bacteria while keeping the host normal tissue unaffected. Hence, decreased side effect is expected. Herein we presented some typical examples of activatable polymeric delivery systems for anti-bacteria PDT (Radovic-Moreno et al., 2012; Li F. et al., 2018; Zhao et al., 2019; Broenstrup et al., 2021; Wu et al., 2021; Ye et al., 2021).

Enzyme

Hypocrellin A-loaded lipase sensitive polymer system was reported. The Hypocrellin A is a perylenequinoid pigment that is isolated from the tradition Chinese medicine and it is reported to have singlet oxygen production ability, hence it functioned as a photosensitizer. The lipase sensitive polymer methoxy poly (ethylene glycol)-blockpoly (ε-caprolactone) (mPEG-PCL) self-assembled to micelles, which is used to encapsulate the photosensitizer Hypocrellin A and enhance its water solubility. As shown in **Figure 12A**, this Hypocrellin A-loaded polymer micelles can be degraded by the bacterial lipase, along with the release of the photosensitizer. The release of Hypocrellin A in the presence of lipase in PBS was confirmed and presented in **Figure 12C**. An *in vitro* antibacterial study shows that the light irradiation significantly reduced the minimum inhibitory concentration (MIC) and minimum bactericidal concentration (MBC) values (0.69 and 1.38 mg/L, respectively), as compared with that in the dark (250 and 500 mg/L, respectively). This result demonstrated that the antibacterial activity is mainly attributed to PDT. An *in vivo* antibacterial study shows that the *MRSA* in spleen and blood is cleared up and the bacteria in liver is significantly reduced upon PDT (**Figure 12D**). Compared with the free Hypocrellin A, the polymeric micelles show slightly higher MIC and MBC values, which might be due to the incomplete release of Hypocrellin A. However, the lipase sensitive polymeric micelles achieve significantly increased survival rate, indicating that the lipase sensitive polymeric micelles are a potent polymeric system for combating MRSA infection.

pH

A pH-sensitive, surface charge switchable supramolecular polymeric system was constructed (Hu et al., 2019). As shown in **Figure 13A**, the pH-sensitive poly (ethylene glycol) (PEG) block polypeptide copolymer [PEG-(KLAKLAK)2-DA] interacted with the α-CD prodrugs (PDT therapeutics α-CD-Ce6 and NO therapeutics α-CD-NO) *via* host-guest interaction, forming a negatively charged supramolecular nanocarrier at physiological pH. The negative charge is in favor of the long-term blood circulation. While in acidic conditions (pH = 5.5), the amide bond tends to be cleaved, leading to a switch of the surface charge of the nanocarrier. The obtained positive charge is beneficial for the penetration into biofilms due to the stronger interaction and adhesion to the negatively charged bacterial membrane. As compared with the surface charge unswitchable nanocarrier α-CD-Ce6-NO-SA, the surface charge switchable

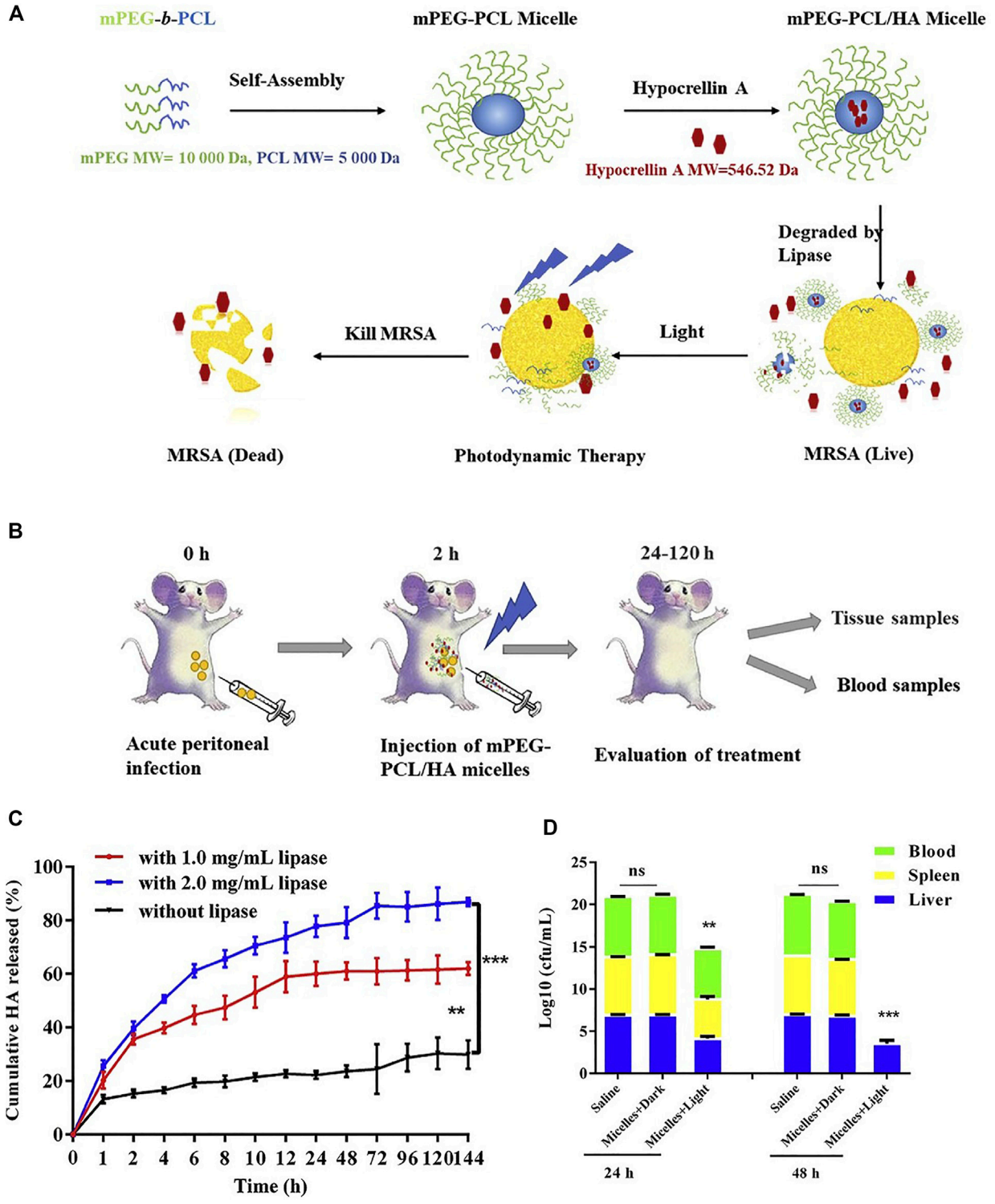

FIGURE 12 | (A) Schematic illustration of the mPEG-PCL/HA micelles for enhanced photodynamic antibacterial activity; **(B)** schematic illustration of the mPEG-PCL/HA micelles for the *in vivo* treatment; **(C)** cumulative release of HA from micelles without or with lipase (1.0, 2.0 mg/ml); **(D)** total bacterial counts in the liver, spleen, and blood of mice after being treated with mPEG-PCL/HA micelles (HA dose: 5 mg/kg) in dark or light irradiation for 24 and 48 h. Reprinted with permission from Guo et al. (2020).

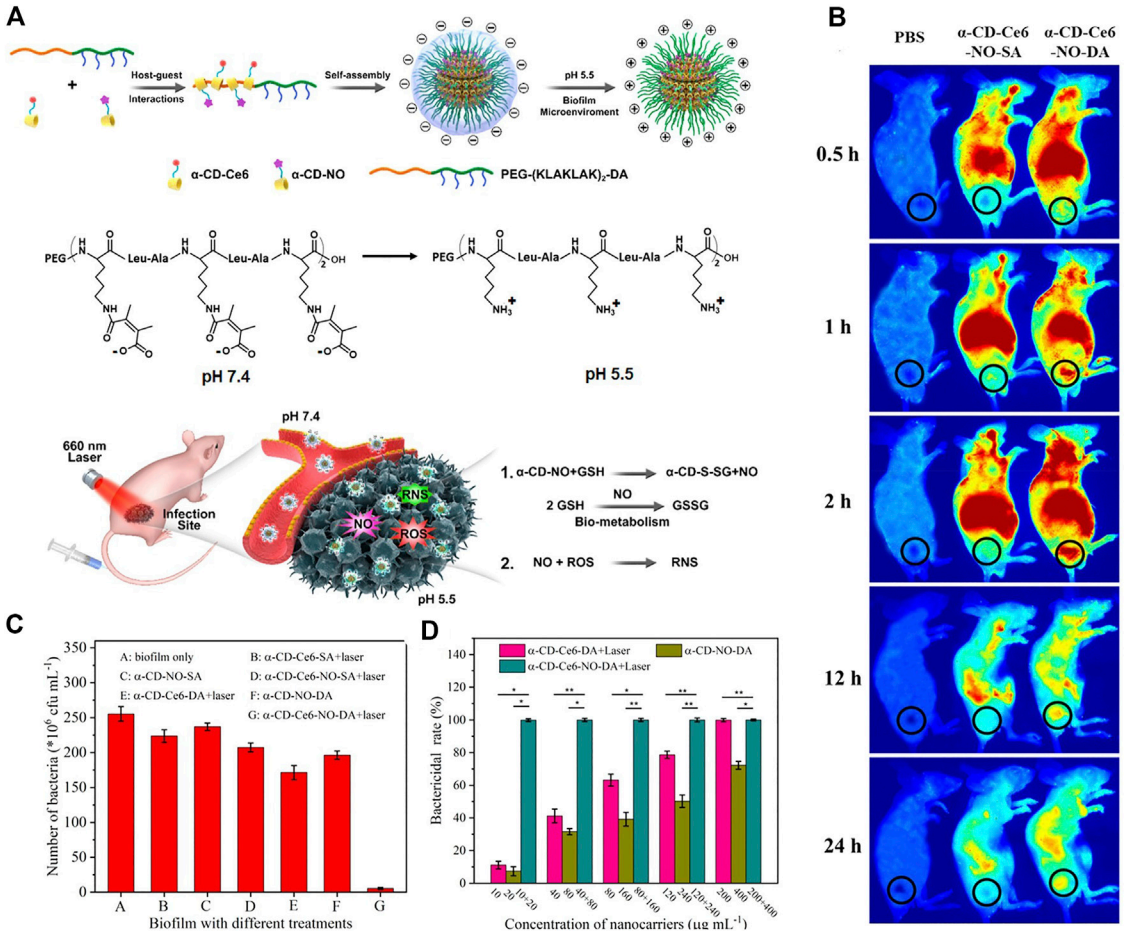

FIGURE 13 | (A) Schematic diagram of the acid-activated charge reversal of PEG-(KLAKLAK)2-DA at pH 5.5 and the mechanisms of the MRSA biofilm associated infection eradication by synergistic effects between ROS and NO produced by α-CD-Ce6-NO-DA nanocarriers; **(B)** *in vivo* time-dependent body fluorescence imaging of the MRSA biofilm infected mice after various treatments; **(C)** related bactericidal results of different nanocarriers with the same Ce6 concentration under laser irradiation, characterized by the standard plate counting assay. **(D)** *In vivo* bactericidal rates of various treatments. Reprinted with permission from Hu et al. (2019).

nanocarrier α-CD-Ce6-NO-DA shows enhanced penetration to biofilms and accumulation in MRSA biofilm infected area (**Figure 13B**). Hence, it is reasonable that upon light irradiation, enhanced bactericidal rate was observed for α-CD-Ce6-NO-DA as compared with α-CD-Ce6-NO-SA (**Figure 13C** and **Figure 13D**).

Another pH-sensitive charge reversible nanoparticle system was constructed for enhanced penetration and antibacterial PDT efficiency (Wu et al., 2021). As shown in **Figure 14A**, the photosensitizer Rose Bengal is dangled with dopamine, and then decorated with polymyxin B (PMB) and gluconic acid (GA) layer-by-layer. Resembling the isoelectric point of protein, the resulted nanoparticles (RB@PMB@GA) are negatively charged at physiological pH while they switched to positive charged when the pH is below 5.5, due to the presence of an amino group and a carboxyl group. Consequently, the antibacterial efficiency is greatly improved at pH = 5.0 (**Figure 14B**), due to the pH-sensitive charge inversion. To be specific, as presented in **Figure 14C**, only Gram-positive bacteria *S. aureus* were effectively killed upon light irradiation at pH = 7.4, while the Gram-negative bacteria *E. coli* were not affected unless in acidic condition (pH = 5.0). This indicates that the charge inversion in acidic condition enhanced the penetration and adhesion to bacteria. As the positively charged polymers are expected to quickly infiltrate biofilms *via* electrostatic interactions, the nanoparticles show outstanding biofilm penetration and eradication ability (**Figures 14D–F**).

ROS

A pH/H_2O_2 dual responsive polymeric system to combat the *S. aureus* and its biofilm is presented in **Figure 15A**(Zhao et al., 2021) The polymer POEGMA-b-PBMA is assembled with a surface charge-switchable photosensitizer, 5,10,15,20-tetra-{4-[3-(N,N-dimethyl-ammonio) propoxy]phenyl} porphyrin (TAPP) into nanoparticles with an average diameter of 180 nm. The large amount of H_2O_2 in *S. aureus* reacts with the arylboronic ester moiety and induces the disintegration of the nanoparticles, followed by the release of TAPP. The TAPP is further protonated in an acidic bacterial microenvironment, which increases its hydrophilicity and reduces its self-

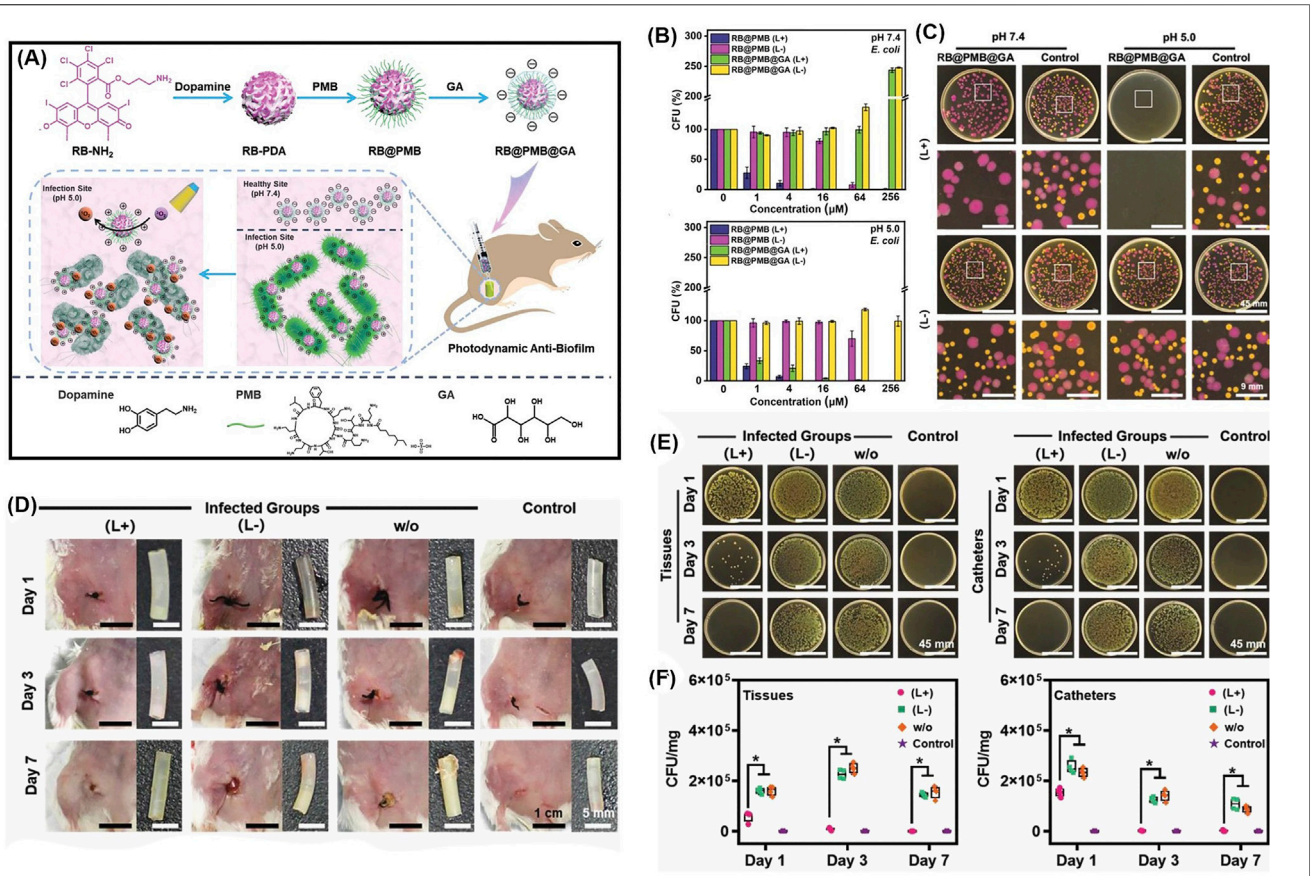

FIGURE 14 | (A) Schematic illustration of the preparation process of photodynamic NPs for enhanced penetration and antibacterial efficiency in biofilms; **(B)** antibacterial activities against *E. coli* at pH 7.4 and pH 5.0, with or without irradiation; **(C)** photographs of *E. coli* labeled with the red protein and *S. aureus* colonies incubated together with the different treatments; **(D)** typical photographs of the incision areas and implanted catheters from mice under different treatments on Days 1, 3, and 7; **(E)** photographs of *P. aeruginosa* bacterial colonies, and **(F)** quantitative analysis of bacterial colony-forming units obtained from the tissues and catheters in each group. Reprinted with permission from Wu et al. (2021).

quenching effect. As a result, enhanced fluorescence emission and singlet oxygen production ability of TAPP were observed in the presence of H_2O_2 at pH = 5.5. The *in vitro* antibacterial effect was examined (**Figure 15B** and **Figure 15C**). The zeta potential of the bacteria is increased from −10 to +2 mV when incubated with the nanoparticles, indicating the adherence ability of nanoparticles to bacteria. There was 80% of *S. aureus* killed by nanoparticles in the presence of H_2O_2 upon light irradiation (**Figure 15B** and **Figure 15C**). *In vivo* anti-biofilm activity of nanoparticles was quantified, and an obvious depression of biofilm was observed for the PDT treatment group.

GSH

Disulfide bond is frequently used as the GSH responsive linker to construct smart polymeric delivery systems for antibacterial PDT (Lu et al., 2018; Ye et al., 2020). For instance, the hyperbranched PEG was loaded with (Zinc)Porphyrins *via* disulfide and benzacetal linkers, which are sensitive to reductive (GSH) and acidic microenvironment of bacteria, respectively (Staegemann et al., 2018). The release of photosensitizer (Zinc)Porphyrins is confirmed *via* thin layer chromatography (TLC), size exclusion chromatography (SEC), dialysis and extraction, etc. The polymeric material shows significant phototoxicity against *S. aureus*. The benzacetal linker containing polymeric material was also applied for the PDT of tumor, which shows a less efficient depression of the tumor. This might be due to the more reductive and acidic microenvironment of bacteria than tumor, leading to more complete release of photosensitizers in bacteria and hence a better PDT efficacy. This result indicates that the treatments of cancer and bacteria are different.

SUMMARY AND OUTLOOK

Photodynamic therapy (PDT) has attracted great attention in the antitumor and antimicrobial area. This review introduces the smart polymeric delivery system for the PDT of tumor and bacterial infections. In particular, targeted and activatable polymeric delivery systems are highlighted. Due to the different structure of tumor and bacterial cells, the target point is different to some extent. For instance, the anti-tumor therapy targets the tumor vasculature, tumor cells, and tumor subcellular

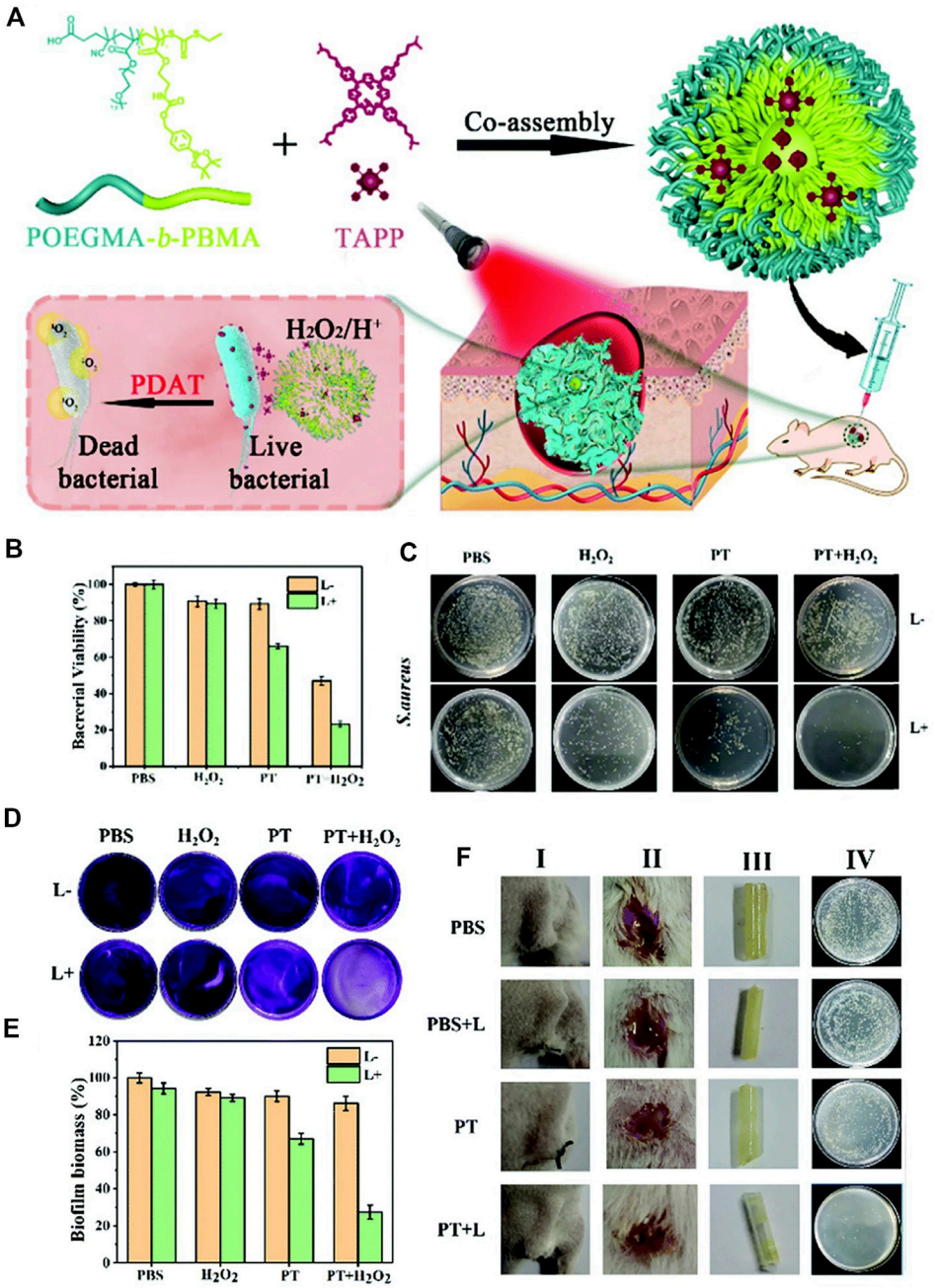

FIGURE 15 | (A) Schematic diagram of a pH/H_2O_2 dual-responsive nanoplatform and its photodynamic antimicrobial therapy process; **(B)** bacterial viability of *S. aureus* treated with different conditions at pH = 5.5; **(C)** the corresponding *S. aureus* on agar plates after different treatments. Reprinted with permission from Zhao et al. (2021).

organelles such as mitochondria, lysosome, nucleus, and endoplasmic reticulum. While the anti-bacterial therapy targets the bacteria membranes, bacterial exopolysaccharides (EPS), and fimbriae, etc. On the other hand, the microenvironment of tumor and bacteria shares plenty of similarities such as hypoxic, acidic, highly reductive and have abundant ROS, etc. Hence, activatable polymeric delivery systems for both tumor and bacteria treatment have been developed. The activation is mainly *via* the following three strategies: (1) self-quenching and dequenching of photosensitizers due to aggregation and disintegration; (2) utilize another quencher to quench the triplet state of photosensitizer and dequenching upon cleavage of sensitive bonds; and (3) the change of size and surface charge to induce an enhanced internalization and penetration of tumor cells or bacterial cells.

Despite of the vigorous development of smart polymeric delivery system for PDT of tumor and bacteria, there are still some problems. First, there is great concern to the uncertainty of

the molecular structure of polymers, which leads to the problem of reproducibility. Without a stable production and stable property, it is difficult for polymers to be applied in the clinic.

Second, concerning the passive targeting, recently the EPR effect is becoming a controversial topic and the general applicability of this EPR effect is challenged and still an open question.

Third, concerning the activatable polymeric delivery system, although the microenvironment of tumor/bacteria is different from that of normal tissues, there are still risks of inefficient specificity. For instance, ROS is not only abundant in tumor/bacteria cells, but also active in inflamed tissues. In addition, normal cells also have acidic subcellular compartments such as endosome and lysosome that are similar to those of cancer cells, which limits the pH-activatable theranostics to some extent.

Last but not the least, the reported polymeric delivery systems are usually complicated, and there is great concern to their toxicities. Developing non-toxic and simple polymeric delivery systems and forward their application from bench to bedside is highly desired.

AUTHOR CONTRIBUTIONS

ZW conceptualized and wrote the manuscript and BY and FX revised the manuscript. All authors approved the final version of the manuscript.

FUNDING

ZW thanks the China Postdoctoral Science Foundation (2020M670108) for financial support. FX thanks the Beijing Outstanding Young Scientist Program (Project No. BJJWZYJH01201910010024).

REFERENCES

Agostinis, P., Berg, K., Cengel, K. A., Foster, T. H., Girotti, A. W., Gollnick, S. O., et al. (2011). Photodynamic Therapy of Cancer: an Update. *CA: A Cancer J. Clinicians* 61 (4), 250–281. doi:10.3322/caac.20114

Bae, B.-C., Li, F., Ling, D., and Na, K. (2010). Self-organized Nanogel from Pullulan/pheophorbide-A Conjugate as a Macromolecular Photodynamic Agent. *J. Porphyrins Phthalocyanines* 14 (10), 851–858. doi:10.1142/s1088424610002707

Bae, B.-C., and Na, K. (2010). Self-quenching Polysaccharide-Based Nanogels of Pullulan/folate-Photosensitizer Conjugates for Photodynamic Therapy. *Biomaterials* 31 (24), 6325–6335. doi:10.1016/j.biomaterials.2010.04.030

Blacha-Grzechnik, A. (2021). New Approach in the Application of Conjugated Polymers: The Light-Activated Source of Versatile Singlet Oxygen Molecule. *Materials* 14 (5), 1098. doi:10.3390/ma14051098

Braslawsky, G. R., Edson, M. A., Pearce, W., Kaneko, T., and Greenfield, R. S. (1990). Antitumor Activity of Adriamycin (Hydrazone-linked) Immunoconjugates Compared with Free Adriamycin and Specificity of Tumor Cell Killing. *Cancer Res.* 50 (20), 6608–6614.

Broenstrup, M., Tegge, W., Guerra, G., Höltke, A., Schiller, L., Beutling, U., et al. (2021). Selective Bacterial Targeting and Infection-triggered Release of Antibiotic Colistin Conjugates. *Angew. Chem.* 60, 17989–17997. doi:10.1002/anie.202104921

Brown, S. B., Brown, E. A., and Walker, I. (2004). The Present and Future Role of Photodynamic Therapy in Cancer Treatment. *Lancet Oncol.* 5 (8), 497–508. doi:10.1016/s1470-2045(04)01529-3

Bugaj, A. M. (2011). Targeted Photodynamic Therapy - a Promising Strategy of Tumor Treatment. *Photochem. Photobiol. Sci.* 10 (7), 1097–1109. doi:10.1039/c0pp00147c

Bush, K., Courvalin, P., Dantas, G., Davies, J., Eisenstein, B., Huovinen, P., et al. (2011). Tackling Antibiotic Resistance. *Nat. Rev. Microbiol.* 9 (12), 894–896. doi:10.1038/nrmicro2693

Caffarel-Salvador, E., Kearney, M.-C., Mairs, R., Gallo, L., Stewart, S., Brady, A., et al. (2015). Methylene Blue-Loaded Dissolving Microneedles: Potential Use in Photodynamic Antimicrobial Chemotherapy of Infected Wounds. *Pharmaceutics* 7 (4), 397–412. doi:10.3390/pharmaceutics7040397

Celli, J. P., Spring, B. Q., Rizvi, I., Evans, C. L., Samkoe, K. S., Verma, S., et al. (2010). Imaging and Photodynamic Therapy: Mechanisms, Monitoring, and Optimization. *Chem. Rev.* 110 (5), 2795–2838. doi:10.1021/cr900300p

Chakrabortty, S., Agrawalla, B. K., Stumper, A., Vegi, N. M., Fischer, S., Reichardt, C., et al. (2017). Mitochondria Targeted Protein-Ruthenium Photosensitizer for Efficient Photodynamic Applications. *J. Am. Chem. Soc.* 139 (6), 2512–2519. doi:10.1021/jacs.6b13399

Chen, H., Li, S., Wu, M., Kenry, Z., Huang, Z., Lee, C. S., et al. (2020). Membrane-Anchoring Photosensitizer with Aggregation-Induced Emission Characteristics for Combating Multidrug-Resistant Bacteria. *Angew. Chem.* 132 (2), 642–646. doi:10.1002/ange.201907343

Chen, J., Ding, J., Wang, Y., Cheng, J., Ji, S., Zhuang, X., et al. (2017). Sequentially Responsive Shell-Stacked Nanoparticles for Deep Penetration into Solid Tumors. *Adv. Mater.* 29 (32), 1701170. doi:10.1002/adma.201701170

Chen, N. H., Couñago, R. M., Djoko, K. Y., Jennings, M. P., Apicella, M. A., Kobe, B., et al. (2013). A Glutathione-dependent Detoxification System Is Required for Formaldehyde Resistance and Optimal Survival ofNeisseria Meningitidisin Biofilms. *Antioxid. Redox Signaling* 18 (7), 743–755. doi:10.1089/ars.2012.4749

Choi, Y., Weissleder, R., and Tung, C.-H. (2006). Selective Antitumor Effect of Novel Protease-Mediated Photodynamic Agent. *Cancer Res.* 66 (14), 7225–7229. doi:10.1158/0008-5472.can-06-0448

Cui, D., Huang, J., Zhen, X., Li, J., Jiang, Y., and Pu, K. (2019). A Semiconducting Polymer Nano-prodrug for Hypoxia-Activated Photodynamic Cancer Therapy. *Angew. Chem.* 131 (18), 5981–5985. doi:10.1002/ange.201814730

Dai, Y., Ma, P. a., Cheng, Z., Kang, X., Zhang, X., Hou, Z., et al. (2012). Up-Conversion Cell Imaging and pH-Induced Thermally Controlled Drug Release from $NaYF_4$:Yb^{3+}/Er^{3+}@Hydrogel Core-Shell Hybrid Microspheres. *ACS Nano* 6 (4), 3327–3338. doi:10.1021/nn300303q

Danhier, F., Feron, O., and Préat, V. (2010). To Exploit the Tumor Microenvironment: Passive and Active Tumor Targeting of Nanocarriers for Anti-cancer Drug Delivery. *J. Controlled Release* 148 (2), 135–146. doi:10.1016/j.jconrel.2010.08.027

del Carmen, M. G., Rizvi, I., Chang, Y., Moor, A. C. E., Oliva, E., Sherwood, M., et al. (2005). Synergism of Epidermal Growth Factor Receptor-Targeted Immunotherapy with Photodynamic Treatment of Ovarian Cancer *In Vivo*. *J. Natl. Cancer* 97 (20), 1516–1524. doi:10.1093/jnci/dji314

Demidova, T. N., and Hamblin, M. R. (2004). Photodynamic Therapy Targeted to Pathogens. *Int. J. Immunopathol Pharmacol.* 17 (3), 245–254. doi:10.1177/039463200401700304

Detty, M. R., Gibson, S. L., and Wagner, S. J. (2004). Current Clinical and Preclinical Photosensitizers for Use in Photodynamic Therapy. *J. Med. Chem.* 47 (16), 3897–3915. doi:10.1021/jm040074b

Dong, Z., Feng, L., Hao, Y., Chen, M., Gao, M., Chao, Y., et al. (2018). Synthesis of Hollow Biomineralized CaCO3-Polydopamine Nanoparticles for Multimodal Imaging-Guided Cancer Photodynamic Therapy with Reduced Skin Photosensitivity. *J. Am. Chem. Soc.* 140 (6), 2165–2178. doi:10.1021/jacs.7b11036

Donnelly, R. F., Morrow, D. I. J., McCrudden, M. T. C., Alkilani, A. Z., Vicente-Pérez, E. M., O'Mahony, C., et al. (2014). Hydrogel-Forming and Dissolving Microneedles for Enhanced Delivery of Photosensitizers and Precursors. *Photochem. Photobiol.* 90 (3), 641–647. doi:10.1111/php.12209

Du, J.-Z., Du, X.-J., Mao, C.-Q., and Wang, J. (2011). Tailor-Made Dual pH-Sensitive Polymer-Doxorubicin Nanoparticles for Efficient Anticancer Drug Delivery. *J. Am. Chem. Soc.* 133 (44), 17560–17563. doi:10.1021/ja207150n

Du, J.-Z., Sun, T.-M., Song, W.-J., Wu, J., and Wang, J. (2010). A Tumor-Acidity-Activated Charge-Conversional Nanogel as an Intelligent Vehicle for Promoted Tumoral-Cell Uptake and Drug Delivery. *Angew. Chem.* 122 (21), 3703–3708. doi:10.1002/ange.200907210

Ferlay, J., Shin, H.-R., Bray, F., Forman, D., Mathers, C., and Parkin, D. M. (2010). Estimates of Worldwide burden of Cancer in 2008: GLOBOCAN 2008. *Int. J. Cancer* 127 (12), 2893–2917. doi:10.1002/ijc.25516

Figge, F. H. J., Weiland, G. S., and Manganiello, L. O. J. (1948). Cancer Detection and Therapy. Affinity of Neoplastic, Embryonic, and Traumatized Tissues for Porphyrins and Metalloporphyrins. *Exp. Biol. Med.* 68 (3), 640–641. doi:10.3181/00379727-68-16580

Flemming, H.-C., Wingender, J., Szewzyk, U., Steinberg, P., Rice, S. A., and Kjelleberg, S. (2016). Biofilms: an Emergent Form of Bacterial Life. *Nat. Rev. Microbiol.* 14 (9), 563–575. doi:10.1038/nrmicro.2016.94

Fux, C. A., Costerton, J. W., Stewart, P. S., and Stoodley, P. (2005). Survival Strategies of Infectious Biofilms. *Trends Microbiol.* 13 (1), 34–40. doi:10.1016/j.tim.2004.11.010

Gales, G. g., Penninckx, M., Block, J.-C., and Leroy, P. (2008). Role of Glutathione Metabolism Status in the Definition of Some Cellular Parameters and Oxidative Stress Tolerance ofSaccharomyces Cerevisiaecells Growing as Biofilms. *FEMS Yeast Res.* 8 (5), 667–675. doi:10.1111/j.1567-1364.2008.00401.x

Gu, Y., Zhong, Y., Meng, F., Cheng, R., Deng, C., and Zhong, Z. (2013). Acetal-linked Paclitaxel Prodrug Micellar Nanoparticles as a Versatile and Potent Platform for Cancer Therapy. *Biomacromolecules* 14 (8), 2772–2780. doi:10.1021/bm400615n

Guo, L.-Y., Yan, S.-Z., Tao, X., Yang, Q., Li, Q., Wang, T.-S., et al. (2020). Evaluation of Hypocrellin A-Loaded Lipase Sensitive Polymer Micelles for Intervening Methicillin-Resistant *Staphylococcus Aureus* Antibiotic-Resistant Bacterial Infection. *Mater. Sci. Eng. C* 106, 110230. doi:10.1016/j.msec.2019.110230

Hamblin, M. R., and Hasan, T. (2004). Photodynamic Therapy: a New Antimicrobial Approach to Infectious Disease? *Photochem. Photobiol. Sci.* 3 (5), 436–450. doi:10.1039/b311900a

Han, T., Wang, X., Wang, D., and Tang, B. Z. (2021). Functional Polymer Systems with Aggregation-Induced Emission and Stimuli Responses. *Top. Curr. Chem. (Cham)* 379 (1), 7–47. doi:10.1007/s41061-020-00321-7

Hanahan, D., and Weinberg, R. A. (2011). Hallmarks of Cancer: the Next Generation. *Cell* 144 (5), 646–674. doi:10.1016/j.cell.2011.02.013

Henry, S., McAllister, D. V., Allen, M. G., and Prausnitz, M. R. (1998). Microfabricated Microneedles: a Novel Approach to Transdermal Drug Delivery. *J. Pharm. Sci.* 87 (8), 922–925. doi:10.1021/js980042+

Hoare, T., and Pelton, R. (2004). Highly pH and Temperature Responsive Microgels Functionalized with Vinylacetic Acid. *Macromolecules* 37 (7), 2544–2550. doi:10.1021/ma035658m

Hoffman, A. S. (2008). The Origins and Evolution of "Controlled" Drug Delivery Systems. *J. Controlled Release* 132 (3), 153–163. doi:10.1016/j.jconrel.2008.08.012

Hu, D., Deng, Y., Jia, F., Jin, Q., and Ji, J. (2019). Surface Charge Switchable Supramolecular Nanocarriers for Nitric Oxide Synergistic Photodynamic Eradication of Biofilms. *ACS Nano* 14 (1), 347–359. doi:10.1021/acsnano.9b05493

Huang, L., Li, Z., Zhao, Y., Zhang, Y., Wu, S., Zhao, J., et al. (2016). Ultralow-power Near Infrared Lamp Light Operable Targeted Organic Nanoparticle Photodynamic Therapy. *J. Am. Chem. Soc.* 138 (44), 14586–14591. doi:10.1021/jacs.6b05390

Huang, Y.-Y., Sharma, S. K., Dai, T., Chung, H., Yaroslavsky, A., Garcia-Diaz, M., et al. (2012). Can Nanotechnology Potentiate Photodynamic Therapy? *Nanotechnol. Rev.* 1 (2), 111–146. doi:10.1515/ntrev-2011-0005

Huo, D., Zhu, J., Chen, G., Chen, Q., Zhang, C., Luo, X., et al. (2019). Eradication of Unresectable Liver Metastasis through Induction of Tumour Specific Energy Depletion. *Nat. Commun.* 10 (1). doi:10.1038/s41467-019-11082-3

Jiang, B.-P., Zhang, L., Guo, X.-L., Shen, X.-C., Wang, Y., Zhu, Y., et al. (2017). Poly(N-phenylglycine)-Based Nanoparticles as Highly Effective and Targeted Near-Infrared Photothermal Therapy/Photodynamic Therapeutic Agents for Malignant Melanoma. *Small* 13 (8), 1602496. doi:10.1002/smll.201602496

Jiang, Y., Yang, X., Ma, C., Wang, C., Chen, Y., Dong, F., et al. (2014). Interfacing a Tetraphenylethene Derivative and a Smart Hydrogel for Temperature-dependent Photoluminescence with Sensitive Thermoresponse. *ACS Appl. Mater. Inter.* 6 (7), 4650–4657. doi:10.1021/am501106x

Kamaly, N., Yameen, B., Wu, J., and Farokhzad, O. C. (2016). Degradable Controlled-Release Polymers and Polymeric Nanoparticles: Mechanisms of Controlling Drug Release. *Chem. Rev.* 116 (4), 2602–2663. doi:10.1021/acs.chemrev.5b00346

Kamkaew, A., Lim, S. H., Lee, H. B., Kiew, L. V., Chung, L. Y., and Burgess, K. (2013). BODIPY Dyes in Photodynamic Therapy. *Chem. Soc. Rev.* 42 (1), 77–88. doi:10.1039/c2cs35216h

Kaspler, P., Lazic, S., Forward, S., Arenas, Y., Mandel, A., and Lilge, L. (2016). A Ruthenium(ii) Based Photosensitizer and Transferrin Complexes Enhance Photo-Physical Properties, Cell Uptake, and Photodynamic Therapy Safety and Efficacy. *Photochem. Photobiol. Sci.* 15 (4), 481–495. doi:10.1039/c5pp00450k

Ke, X., Coady, D. J., Yang, C., Engler, A. C., Hedrick, J. L., and Yang, Y. Y. (2014). pH-sensitive Polycarbonate Micelles for Enhanced Intracellular Release of Anticancer Drugs: a Strategy to Circumvent Multidrug Resistance. *Polym. Chem.* 5 (7), 2621–2628. doi:10.1039/c3py01784b

Kearney, M.-C., Brown, S., McCrudden, M. T. C., Brady, A. J., and Donnelly, R. F. (2014). Potential of Microneedles in Enhancing Delivery of Photosensitising Agents for Photodynamic Therapy. *Photodiagnosis Photodynamic Ther.* 11 (4), 459–466. doi:10.1016/j.pdpdt.2014.09.003

Keerthiga, R., Zhao, Z., Pei, D., and Fu, A. (2020). Photodynamic Nanophotosensitizers: Promising Materials for Tumor Theranostics. *ACS Biomater. Sci. Eng.* 6 (10), 5474–5485. doi:10.1021/acsbiomaterials.0c01058

Kim, J., Yoon, H.-J., Kim, S., Wang, K., Ishii, T., Kim, Y.-R., et al. (2009). Polymer-metal Complex Micelles for the Combination of Sustained Drug Releasing and Photodynamic Therapy. *J. Mater. Chem.* 19 (26), 4627–4631. doi:10.1039/b904224e

Kim, W. L., Cho, H., Li, L., Kang, H. C., and Huh, K. M. (2014). Biarmed Poly(ethylene Glycol)-(pheophorbide A)2 Conjugate as a Bioactivatable Delivery Carrier for Photodynamic Therapy. *Biomacromolecules* 15 (6), 2224–2234. doi:10.1021/bm5003619

Klare, W., Das, T., Ibugo, A., Buckle, E., Manefield, M., and Manos, J. (2016). Glutathione-disrupted Biofilms of Clinical *Pseudomonas aeruginosa* Strains Exhibit an Enhanced Antibiotic Effect and a Novel Biofilm Transcriptome. *Antimicrob. Agents Chemother.* 60 (8), 4539–4551. doi:10.1128/aac.02919-15

Klausen, M., Ucuncu, M., and Bradley, M. (2020). Design of Photosensitizing Agents for Targeted Antimicrobial Photodynamic Therapy. *Molecules* 25 (22), 5239. doi:10.3390/molecules25225239

Koo, H., Allan, R. N., Howlin, R. P., Stoodley, P., and Hall-Stoodley, L. (2017). Targeting Microbial Biofilms: Current and Prospective Therapeutic Strategies. *Nat. Rev. Microbiol.* 15 (12), 740–755. doi:10.1038/nrmicro.2017.99

Krogfelt, K. A., Bergmans, H., and Klemm, P. (1990). Direct Evidence that the FimH Protein Is the Mannose-specific Adhesin of *Escherichia coli* Type 1 Fimbriae. *Infect. Immun.* 58 (6), 1995–1998. doi:10.1128/iai.58.6.1995-1998.1990

Lambert, P. A. (2002). Cellular Impermeability and Uptake of Biocides and Antibiotics in Gram-Positive Bacteria and Mycobacteria. *J. Appl. Microbiol.* 92, 46S–54S. doi:10.1046/j.1365-2672.92.5s1.7.x

Lee, J. W., Park, J.-H., and Prausnitz, M. R. (2008). Dissolving Microneedles for Transdermal Drug Delivery. *Biomaterials* 29 (13), 2113–2124. doi:10.1016/j.biomaterials.2007.12.048

Lee, S. J., Park, K., Oh, Y.-K., Kwon, S.-H., Her, S., Kim, I.-S., et al. (2009). Tumor Specificity and Therapeutic Efficacy of Photosensitizer-Encapsulated Glycol Chitosan-Based Nanoparticles in Tumor-Bearing Mice. *Biomaterials* 30 (15), 2929–2939. doi:10.1016/j.biomaterials.2009.01.058

Li, C., Lin, F., Sun, W., Wu, F.-G., Yang, H., Lv, R., et al. (2018a). Self-assembled Rose Bengal-Exopolysaccharide Nanoparticles for Improved Photodynamic Inactivation of Bacteria by Enhancing Singlet Oxygen Generation Directly in the Solution. *ACS Appl. Mater. Inter.* 10 (19), 16715–16722. doi:10.1021/acsami.8b01545

Li, F., Bae, B.-c., and Na, K. (2010). Acetylated Hyaluronic Acid/Photosensitizer Conjugate for the Preparation of Nanogels with Controllable Phototoxicity: Synthesis, Characterization, Autophotoquenching Properties, Andin vitroPhototoxicity against HeLa Cells. *Bioconjug. Chem.* 21 (7), 1312–1320. doi:10.1021/bc100116v

Li, F., Chen, C., Yang, X., He, X., Zhao, Z., Li, J., et al. (2018b). Acetal-linked hyperbranched polyphosphoester nanocarriers loaded with chlorin e6 for pH-

activatable photodynamic therapy. *ACS Appl. Mater. Inter.* 10 (25), 21198–21205. doi:10.1021/acsami.8b06758

Li, H., Wang, P., Deng, Y., Zeng, M., Tang, Y., Zhu, W.-H., et al. (2017a). Combination of Active Targeting, Enzyme-Triggered Release and Fluorescent Dye into Gold Nanoclusters for Endomicroscopy-Guided Photothermal/photodynamic Therapy to Pancreatic Ductal Adenocarcinoma. *Biomaterials* 139, 30–38. doi:10.1016/j.biomaterials.2017.05.030

Li, J., Cui, D., Huang, J., He, S., Yang, Z., Zhang, Y., et al. (2019a). Organic Semiconducting Pro-nanostimulants for Near-Infrared Photoactivatable Cancer Immunotherapy. *Angew. Chem.* 131 (36), 12810–12817. doi:10.1002/ange.201906288

Li, J., Cui, D., Jiang, Y., Huang, J., Cheng, P., and Pu, K. (2019b). Near-Infrared Photoactivatable Semiconducting Polymer Nanoblockaders for Metastasis-Inhibited Combination Cancer Therapy. *Adv. Mater.* 31 (46), 1905091. doi:10.1002/adma.201905091

Li, J., Huang, J., Lyu, Y., Huang, J., Jiang, Y., Xie, C., et al. (2019c). Photoactivatable Organic Semiconducting Pro-nanoenzymes. *J. Am. Chem. Soc.* 141 (9), 4073–4079. doi:10.1021/jacs.8b13507

Li, J., Meng, X., Deng, J., Lu, D., Zhang, X., Chen, Y., et al. (2018c). Multifunctional Micelles Dually Responsive to Hypoxia and Singlet Oxygen: Enhanced Photodynamic Therapy *via* Interactively Triggered Photosensitizer Delivery. *ACS Appl. Mater. Inter.* 10 (20), 17117–17128. doi:10.1021/acsami.8b06299

Li, J., and Pu, K. (2020). Semiconducting Polymer Nanomaterials as Near-Infrared Photoactivatable Protherapeutics for Cancer. *Acc. Chem. Res.* 53 (4), 752–762. doi:10.1021/acs.accounts.9b00569

Li, J., Yao, S., Wang, K., Lu, Z., Su, X., Li, L., et al. (2018d). Hypocrellin B-Loaded, Folate-Conjugated Polymeric Micelle for Intraperitoneal Targeting of Ovarian Cancer *In Vitro* and *In Vivo*. *Cancer Sci.* 109 (6), 1958–1969. doi:10.1111/cas.13605

Li, L., and Huh, K. M. (2014). Polymeric Nanocarrier Systems for Photodynamic Therapy. *Biomater. Res.* 18 (1), 19–14. doi:10.1186/2055-7124-18-19

Li, L., Bae, B.-c., Tran, T. H., Yoon, K. H., Na, K., and Huh, K. M. (2011). Self-quenchable Biofunctional Nanoparticles of Heparin-Folate-Photosensitizer Conjugates for Photodynamic Therapy. *Carbohydr. Polym.* 86 (2), 708–715. doi:10.1016/j.carbpol.2011.05.011

Li, L., Nurunnabi, M., Nafiujjaman, M., Jeong, Y. Y., Lee, Y.-k., and Huh, K. M. (2014). A Photosensitizer-Conjugated Magnetic Iron Oxide/gold Hybrid Nanoparticle as an Activatable Platform for Photodynamic Cancer Therapy. *J. Mater. Chem. B* 2 (19), 2929–2937. doi:10.1039/c4tb00181h

Li, T., and Yan, L. (2018). Functional Polymer Nanocarriers for Photodynamic Therapy. *Pharmaceuticals* 11 (4), 133. doi:10.3390/ph11040133

Li, X., Kim, J., Yoon, J., and Chen, X. (2017b). Cancer-Associated, Stimuli-Driven, Turn on Theranostics for Multimodality Imaging and Therapy. *Adv. Mater.* 29 (23), 1606857. doi:10.1002/adma.201606857

Li, Y., Wu, Q., Kang, M., Song, N., Wang, D., and Tang, B. Z. (2020). Boosting the Photodynamic Therapy Efficiency by Using Stimuli-Responsive and AIE-Featured Nanoparticles. *Biomaterials* 232, 119749. doi:10.1016/j.biomaterials.2019.119749

Lin, A.-L., Li, S.-Z., Xu, C.-H., Li, X.-S., Zheng, B.-Y., Gu, J.-J., et al. (2019). A pH-Responsive Stellate Mesoporous Silica Based Nanophotosensitizer for *In Vivo* Cancer Diagnosis and Targeted Photodynamic Therapy. *Biomater. Sci.* 7 (1), 211–219. doi:10.1039/c8bm00386f

Lincoln, R., Kohler, L., Monro, S., Yin, H., Stephenson, M., Zong, R., et al. (2013). Exploitation of Long-Lived 3IL Excited States for Metal-Organic Photodynamic Therapy: Verification in a Metastatic Melanoma Model. *J. Am. Chem. Soc.* 135 (45), 17161–17175. doi:10.1021/ja408426z

Liu, C., Guo, J., Yang, W., Hu, J., Wang, C., and Fu, S. (2009). Magnetic Mesoporous Silica Microspheres with Thermo-Sensitive Polymer Shell for Controlled Drug Release. *J. Mater. Chem.* 19 (27), 4764–4770. doi:10.1039/b902985k

Liu, L.-H., Qiu, W.-X., Zhang, Y.-H., Li, B., Zhang, C., Gao, F., et al. (2017). A Charge Reversible Self-Delivery Chimeric Peptide with Cell Membrane-Targeting Properties for Enhanced Photodynamic Therapy. *Adv. Funct. Mater.* 27 (25), 1700220. doi:10.1002/adfm.201700220

Liu, L., Ruan, Z., Li, T., Yuan, P., and Yan, L. (2016a). Near Infrared Imaging-Guided Photodynamic Therapy under an Extremely Low Energy of Light by Galactose Targeted Amphiphilic Polypeptide Micelle Encapsulating BODIPY-Br2. *Biomater. Sci.* 4 (11), 1638–1645. doi:10.1039/c6bm00581k

Liu, S., Feng, G., Tang, B. Z., and Liu, B. (2021). Recent Advances of AIE Light-Up Probes for Photodynamic Therapy. *Chem. Sci.* 12 (19), 6488–6506. doi:10.1039/d1sc00045d

Liu, T. W., Akens, M. K., Chen, J., Wilson, B. C., and Zheng, G. (2016b). Matrix Metalloproteinase-Based Photodynamic Molecular Beacons for Targeted Destruction of Bone Metastases *In Vivo*. *Photochem. Photobiol. Sci.* 15 (3), 375–381. doi:10.1039/c5pp00414d

Liu, X., Wu, M., Hu, Q., Bai, H., Zhang, S., Shen, Y., et al. (2016c). Redox-activated Light-Up Nanomicelle for Precise Imaging-Guided Cancer Therapy and Real-Time Pharmacokinetic Monitoring. *ACS Nano* 10 (12), 11385–11396. doi:10.1021/acsnano.6b06688

Lu, L., Zhao, X., Fu, T., Li, K., He, Y., Luo, Z., et al. (2020a). An iRGD-Conjugated Prodrug Micelle with Blood-Brain-Barrier Penetrability for Anti-glioma Therapy. *Biomaterials* 230, 119666. doi:10.1016/j.biomaterials.2019.119666

Lu, M.-m., Ge, Y., Qiu, J., Shao, D., Zhang, Y., Bai, J., et al. (2018). Redox/pH Dual-Controlled Release of Chlorhexidine and Silver Ions from Biodegradable Mesoporous Silica Nanoparticles against Oral Biofilms. *Ijn* 13, 7697–7709. doi:10.2147/ijn.s181168

Lu, Y., Song, G., He, B., Zhang, H., Wang, X., Zhou, D., et al. (2020b). Strengthened Tumor Photodynamic Therapy Based on a Visible Nanoscale Covalent Organic Polymer Engineered by Microwave Assisted Synthesis. *Adv. Funct. Mater.* 30 (45), 2004834. doi:10.1002/adfm.202004834

Lucky, S. S., Soo, K. C., and Zhang, Y. (2015). Nanoparticles in Photodynamic Therapy. *Chem. Rev.* 115 (4), 1990–2042. doi:10.1021/cr5004198

Lv, R., Yang, P., He, F., Gai, S., Yang, G., Dai, Y., et al. (2015). An Imaging-Guided Platform for Synergistic Photodynamic/photothermal/chemo-Therapy with pH/temperature-Responsive Drug Release. *Biomaterials* 63, 115–127. doi:10.1016/j.biomaterials.2015.05.016

Maisch, T., Szeimies, R.-M., Jori, G., and Abels, C. (2004). Antibacterial Photodynamic Therapy in Dermatology. *Photochem. Photobiol. Sci.* 3 (10), 907–917. doi:10.1039/b407622b

Majumdar, P., Nomula, R., and Zhao, J. (2014). Activatable Triplet Photosensitizers: Magic Bullets for Targeted Photodynamic Therapy. *J. Mater. Chem. C* 2 (30), 5982–5997. doi:10.1039/c4tc00659c

Malik, Z., Ladan, H., and Nitzan, Y. (1992). Photodynamic Inactivation of Gram-Negative Bacteria: Problems and Possible Solutions. *J. Photochem. Photobiol. B: Biol.* 14 (3), 262–266. doi:10.1016/1011-1344(92)85104-3

Minnock, A., Vernon, D. I., Schofield, J., Griffiths, J., Howard Parish, J., and Brown, S. B. (1996). Photoinactivation of Bacteria. Use of a Cationic Water-Soluble Zinc Phthalocyanine to Photoinactivate Both Gram-Negative and Gram-Positive Bacteria. *J. Photochem. Photobiol. B: Biol.* 32 (3), 159–164. doi:10.1016/1011-1344(95)07148-2

Minnock, A., Vernon, D. I., Schofield, J., Griffiths, J., Parish, J. H., and Brown, S. B. (2000). Mechanism of Uptake of a Cationic Water-Soluble Pyridinium Zinc Phthalocyanine across the Outer Membrane of *Escherichia coli*. *Antimicrob. Agents Chemother.* 44 (3), 522–527. doi:10.1128/aac.44.3.522-527.2000

Mitsunaga, M., Ogawa, M., Kosaka, N., Rosenblum, L. T., Choyke, P. L., and Kobayashi, H. (2011). Cancer Cell-Selective *In Vivo* Near Infrared Photoimmunotherapy Targeting Specific Membrane Molecules. *Nat. Med.* 17 (12), 1685–1691. doi:10.1038/nm.2554

Oh, I.-h., Min, H. S., Li, L., Tran, T. H., Lee, Y.-k., Kwon, I. C., et al. (2013). Cancer Cell-specific Photoactivity of Pheophorbide A-Glycol Chitosan Nanoparticles for Photodynamic Therapy in Tumor-Bearing Mice. *Biomaterials* 34 (27), 6454–6463. doi:10.1016/j.biomaterials.2013.05.017

Pagonis, T. C., Chen, J., Fontana, C. R., Devalapally, H., Ruggiero, K., Song, X., et al. (2010). Nanoparticle-based Endodontic Antimicrobial Photodynamic Therapy. *J. Endodontics* 36 (2), 322–328. doi:10.1016/j.joen.2009.10.011

Pan, L., Liu, J., He, Q., Wang, L., and Shi, J. (2013). Overcoming Multidrug Resistance of Cancer Cells by Direct Intranuclear Drug Delivery Using TAT-Conjugated Mesoporous Silica Nanoparticles. *Biomaterials* 34 (11), 2719–2730. doi:10.1016/j.biomaterials.2012.12.040

Park, S. Y., Baik, H. J., Oh, Y. T., Oh, K. T., Youn, Y. S., and Lee, E. S. (2011a). A Smart Polysaccharide/drug Conjugate for Photodynamic Therapy. *Angew. Chem. Int. Ed.* 50 (7), 1644–1647. doi:10.1002/anie.201006038

Park, S. Y., Lee, H. U., Lee, Y.-C., Kim, G. H., Park, E. C., Han, S. H., et al. (2014). Wound Healing Potential of Antibacterial Microneedles Loaded

with green tea Extracts. *Mater. Sci. Eng. C* 42, 757–762. doi:10.1016/j.msec.2014.06.021

Park, W., Bae, B.-c., and Na, K. (2016). A Highly Tumor-specific Light-Triggerable Drug Carrier Responds to Hypoxic Tumor Conditions for Effective Tumor Treatment. *Biomaterials* 77, 227–234. doi:10.1016/j.biomaterials.2015.11.014

Park, W., Park, S.-j., and Na, K. (2011b). The Controlled Photoactivity of Nanoparticles Derived from Ionic Interactions between a Water Soluble Polymeric Photosensitizer and Polysaccharide Quencher. *Biomaterials* 32 (32), 8261–8270. doi:10.1016/j.biomaterials.2011.07.023

Pelton, R. H., and Chibante, P. (1986). Preparation of Aqueous Latices with N-Isopropylacrylamide. *Colloids Surf.* 20 (3), 247–256. doi:10.1016/0166-6622(86)80274-8

Pelton, R. (2000). Temperature-sensitive Aqueous Microgels. *Adv. Colloid Interf. Sci.* 85 (1), 1–33. doi:10.1016/s0001-8686(99)00023-8

Prasad, P., Gordijo, C. R., Abbasi, A. Z., Maeda, A., Ip, A., Rauth, A. M., et al. (2014). Multifunctional Albumin-MnO2 Nanoparticles Modulate Solid Tumor Microenvironment by Attenuating Hypoxia, Acidosis, Vascular Endothelial Growth Factor and Enhance Radiation Response. *ACS Nano* 8 (4), 3202–3212. doi:10.1021/nn405773r

Radovic-Moreno, A. F., Lu, T. K., Puscasu, V. A., Yoon, C. J., Langer, R., and Farokhzad, O. C. (2012). Surface Charge-Switching Polymeric Nanoparticles for Bacterial Cell wall-targeted Delivery of Antibiotics. *ACS Nano* 6 (5), 4279–4287. doi:10.1021/nn3008383

Regehly, M., Greish, K., Rancan, F., Maeda, H., Böhm, F., and Röder, B. (2007). Water-soluble Polymer Conjugates of ZnPP for Photodynamic Tumor Therapy. *Bioconjug. Chem.* 18 (2), 494–499. doi:10.1021/bc060158u

Rijcken, C. J. F., Hofman, J.-W., van Zeeland, F., Hennink, W. E., and van Nostrum, C. F. (2007). Photosensitiser-loaded Biodegradable Polymeric Micelles: Preparation, Characterisation and *In Vitro* PDT Efficacy. *J. Controlled Release* 124 (3), 144–153. doi:10.1016/j.jconrel.2007.09.002

Saravanakumar, G., Kim, J., and Kim, W. J. (2017). Reactive-Oxygen-Species-Responsive Drug Delivery Systems: Promises and Challenges. *Adv. Sci.* 4 (1), 1600124. doi:10.1002/advs.201600124

Sarkisyan, K. S., Zlobovskaya, O. A., Gorbachev, D. A., Bozhanova, N. G., Sharonov, G. V., Staroverov, D. B., et al. (2015). KillerOrange, a Genetically Encoded Photosensitizer Activated by Blue and green Light. *PLoS One* 10 (12), e0145287. doi:10.1371/journal.pone.0145287

Staegemann, M. H., Gräfe, S., Gitter, B., Achazi, K., Quaas, E., Haag, R., et al. (2018). Hyperbranched Polyglycerol Loaded with (Zinc-)Porphyrins: Photosensitizer Release under Reductive and Acidic Conditions for Improved Photodynamic Therapy. *Biomacromolecules* 19 (1), 222–238. doi:10.1021/acs.biomac.7b01485

Stöber, W., Fink, A., and Bohn, E. (1968). Controlled Growth of Monodisperse Silica Spheres in the Micron Size Range. *J. Colloid Interf. Sci.* 26 (1), 62–69. doi:10.1016/0021-9797(68)90272-5

Sun, C., Ji, S., Li, F., and Xu, H. (2017). Diselenide-containing Hyperbranched Polymer with Light-Induced Cytotoxicity. *ACS Appl. Mater. Inter.* 9 (15), 12924–12929. doi:10.1021/acsami.7b02367

Tian, J., Ding, L., Xu, H.-J., Shen, Z., Ju, H., Jia, L., et al. (2013). Cell-specific and pH-Activatable Rubyrin-Loaded Nanoparticles for Highly Selective Near-Infrared Photodynamic Therapy against Cancer. *J. Am. Chem. Soc.* 135 (50), 18850–18858. doi:10.1021/ja408286k

Tirand, L., Frochot, C., Vanderesse, R., Thomas, N., Trinquet, E., Pinel, S., et al. (2006). A Peptide Competing with VEGF165 Binding on Neuropilin-1 Mediates Targeting of a Chlorin-type Photosensitizer and Potentiates its Photodynamic Activity in Human Endothelial Cells. *J. Control Release* 111 (1-2), 153–164. doi:10.1016/j.jconrel.2005.11.017

Tseng, S. J., Liao, Z. X., Kao, S. H., Zeng, Y. F., Huang, K. Y., Li, H. J., et al. (2015). Highly Specific *In Vivo* Gene Delivery for P53-Mediated Apoptosis and Genetic Photodynamic Therapies of Tumour. *Nat. Commun.* 6 (1). doi:10.1038/ncomms7456

Tuan-Mahmood, T.-M., McCrudden, M. T. C., Torrisi, B. M., McAlister, E., Garland, M. J., Singh, T. R. R., et al. (2013). Microneedles for Intradermal and Transdermal Drug Delivery. *Eur. J. Pharm. Sci.* 50 (5), 623–637. doi:10.1016/j.ejps.2013.05.005

Vert, M., Li, S. M., Spenlehauer, G., and Guérin, P. (1992). Bioresorbability and Biocompatibility of Aliphatic Polyesters. *J. Mater. Sci. Mater. Med.* 3 (6), 432–446. doi:10.1007/bf00701240

Wang, C., Cheng, L., Liu, Y., Wang, X., Ma, X., Deng, Z., et al. (2013). Imaging-Guided pH-Sensitive Photodynamic Therapy Using Charge Reversible Upconversion Nanoparticles under Near-Infrared Light. *Adv. Funct. Mater.* 23 (24), 3077–3086. doi:10.1002/adfm.201202992

Wang, M., Zhai, Y., Ye, H., Lv, Q., Sun, B., Luo, C., et al. (2019). High Co-loading Capacity and Stimuli-Responsive Release Based on cascade Reaction of Self-Destructive Polymer for Improved Chemo-Photodynamic Therapy. *ACS Nano* 13 (6), 7010–7023. doi:10.1021/acsnano.9b02096

Wang, X., and Guo, Z. (2013). Targeting and Delivery of Platinum-Based Anticancer Drugs. *Chem. Soc. Rev.* 42 (1), 202–224. doi:10.1039/c2cs35259a

Wang, Z., Huang, L., Yan, Y., El-Zohry, A. M., Toffoletti, A., Zhao, J., et al. (2020). Elucidation of the Intersystem Crossing Mechanism in a Helical BODIPY for Low-Dose Photodynamic Therapy. *Angew. Chem.* 132 (37), 16248–16255. doi:10.1002/ange.202005269

Wei, X., Liu, L., Guo, X., Wang, Y., Zhao, J., and Zhou, S. (2018). Light-activated ROS-Responsive Nanoplatform Codelivering Apatinib and Doxorubicin for Enhanced Chemo-Photodynamic Therapy of Multidrug-Resistant Tumors. *ACS Appl. Mater. Inter.* 10 (21), 17672–17684. doi:10.1021/acsami.8b04163

Wu, L., Sun, Y., Sugimoto, K., Luo, Z., Ishigaki, Y., Pu, K., et al. (2018a). Engineering of Electrochromic Materials as Activatable Probes for Molecular Imaging and Photodynamic Therapy. *J. Am. Chem. Soc.* 140 (47), 16340–16352. doi:10.1021/jacs.8b10176

Wu, S., Xu, C., Zhu, Y., Zheng, L., Zhang, L., Hu, Y., et al. (2021). Biofilm-Sensitive Photodynamic Nanoparticles for Enhanced Penetration and Antibacterial Efficiency. *Adv. Funct. Mater.* 31, 2103591. doi:10.1002/adfm.202103591

Wu, W., Mao, D., Cai, X., Duan, Y., Hu, F., Kong, D., et al. (2018b). ONOO- and ClO- Responsive Organic Nanoparticles for Specific *In Vivo* Image-Guided Photodynamic Bacterial Ablation. *Chem. Mater.* 30 (11), 3867–3873. doi:10.1021/acs.chemmater.8b01320

Wu, W., Mao, D., Xu, S., Kenry, F., Hu, F., Li, X., et al. (2018c). Polymerization-enhanced Photosensitization. *Chem* 4 (8), 1937–1951. doi:10.1016/j.chempr.2018.06.003

Xu, J., Yang, D., Lv, R., Liu, B., Gai, S., He, F., et al. (2016). Design, Fabrication, Luminescence and Biomedical Applications of UCNPs@mSiO2-ZnPc-CDs-P(NIPAm-MAA) Nanocomposites. *J. Mater. Chem. B* 4 (35), 5883–5894. doi:10.1039/c6tb01677d

Yan, J., Wu, Q., Zhao, Z., Wu, J., Ye, H., Liang, Q., et al. (2020). Light-assisted Hierarchical Intratumoral Penetration and Programmed Antitumor Therapy Based on Tumor Microenvironment (TME)-amendatory and Self-Adaptive Polymeric Nanoclusters. *Biomaterials* 255, 120166. doi:10.1016/j.biomaterials.2020.120166

Yang, J., Pan, S., Gao, S., Li, T., and Xu, H. (2021). CO/chemosensitization/antiangiogenesis Synergistic Therapy with H2O2-Responsive Diselenide-Containing Polymer. *Biomaterials* 271, 120721. doi:10.1016/j.biomaterials.2021.120721

Ye, M., Zhao, Y., Wang, Y., Yodsanit, N., Xie, R., and Gong, S. (2020). pH-Responsive Polymer-Drug Conjugate: An Effective Strategy to Combat the Antimicrobial Resistance. *Adv. Funct. Mater.* 30 (39), 2002655. doi:10.1002/adfm.202002655

Ye, M., Zhao, Y., Wang, Y., Zhao, M., Yodsanit, N., Xie, R., et al. (2021). A Dual-Responsive Antibiotic-Loaded Nanoparticle Specifically Binds Pathogens and Overcomes Antimicrobial-Resistant Infections. *Adv. Mater.* 33 (9), 2006772. doi:10.1002/adma.202006772

Yin, H., Shi, X., Wang, H., Jin, W., Li, Y., and Fu, Y. (2017). Photodynamic Therapy Targeting VCAM-1-Expressing Human Umbilical Vein Endothelial Cells Using a PpIX-VCAM-1 Binding Peptide-Quantum Dot Conjugate. *RSC Adv.* 7 (80), 50562–50570. doi:10.1039/c7ra10648c

Yin, R., Agrawal, T., Khan, U., Gupta, G. K., Rai, V., Huang, Y.-Y., et al. (2015). Antimicrobial Photodynamic Inactivation in Nanomedicine: Small Light Strides against Bad Bugs. *Nanomedicine* 10 (15), 2379–2404. doi:10.2217/nnm.15.67

Yoon, H. Y., Koo, H., Choi, K. Y., Lee, S. J., Kim, K., Kwon, I. C., et al. (2012). Tumor-targeting Hyaluronic Acid Nanoparticles for Photodynamic Imaging and Therapy. *Biomaterials* 33 (15), 3980–3989. doi:10.1016/j.biomaterials.2012.02.016

Yuan, Y.-Y., Mao, C.-Q., Du, X.-J., Du, J.-Z., Wang, F., and Wang, J. (2012). Surface Charge Switchable Nanoparticles Based on Zwitterionic Polymer for Enhanced

Drug Delivery to Tumor. *Adv. Mater.* 24 (40), 5476–5480. doi:10.1002/adma.201202296

Yuan, Y., Liu, J., and Liu, B. (2014). Conjugated-Polyelectrolyte-Based Polyprodrug: Targeted and Image-Guided Photodynamic and Chemotherapy with On-Demand Drug Release upon Irradiation with a Single Light Source. *Angew. Chem. Int. Ed.* 53 (28), 7163–7168. doi:10.1002/anie.201402189

Zeng, L., Cheng, H., Dai, Y., Su, Z., Wang, C., Lei, L., et al. (2020). *In Vivo* Regenerable Cerium Oxide Nanozyme-Loaded pH/H2O2-Responsive Nanovesicle for Tumor-Targeted Photothermal and Photodynamic Therapies. *ACS Appl. Mater. Inter.* 13 (1), 233–244. doi:10.1021/acsami.0c19074

Zhang, C., Chen, W., Zhang, T., Jiang, X., and Hu, Y. (2020). Hybrid Nanoparticle Composites Applied to Photodynamic Therapy: Strategies and Applications. *J. Mater. Chem. B* 8 (22), 4726–4737. doi:10.1039/d0tb00093k

Zhang, X., Yang, P., Dai, Y., Ma, P. a., Li, X., Cheng, Z., et al. (2013). Multifunctional Up-Converting Nanocomposites with Smart Polymer Brushes Gated Mesopores for Cell Imaging and Thermo/pH Dual-Responsive Drug Controlled Release. *Adv. Funct. Mater.* 23 (33), 4067–4078. doi:10.1002/adfm.201300136

Zhao, Y., Yu, C., Yu, Y., Wei, X., Duan, X., Dai, X., et al. (2019). Bioinspired Heteromultivalent Ligand-Decorated Nanotherapeutic for Enhanced Photothermal and Photodynamic Therapy of Antibiotic-Resistant Bacterial Pneumonia. *ACS Appl. Mater. Inter.* 11 (43), 39648–39661. doi:10.1021/acsami.9b15118

Zhao, Y., Zhu, Y., Yang, G., Xia, L., Yu, F., Chen, C., et al. (2021). A pH/H2O2 Dual Triggered Nanoplatform for Enhanced Photodynamic Antibacterial Efficiency. *J. Mater. Chem. B* 9, 5076–5082. doi:10.1039/d1tb00441g

Zheng, G., Chen, J., Stefflova, K., Jarvi, M., Li, H., and Wilson, B. C. (2007). Photodynamic Molecular beacon as an Activatable Photosensitizer Based on Protease-Controlled Singlet Oxygen Quenching and Activation. *Proc. Natl. Acad. Sci.* 104 (21), 8989–8994. doi:10.1073/pnas.0611142104

Zheng, Y., Li, Z., Chen, H., and Gao, Y. (2020). Nanoparticle-based Drug Delivery Systems for Controllable Photodynamic Cancer Therapy. *Eur. J. Pharm. Sci.* 144, 105213. doi:10.1016/j.ejps.2020.105213

Zhu, S., Hong, M., Tang, G., Qian, L., Lin, J., Jiang, Y., et al. (2010). Partly PEGylated Polyamidoamine Dendrimer for Tumor-Selective Targeting of Doxorubicin: the Effects of PEGylation Degree and Drug Conjugation Style. *Biomaterials* 31 (6), 1360–1371. doi:10.1016/j.biomaterials.2009.10.044

Conflict of Interest: The authors declare that the research was conducted in the absence of any commercial or financial relationships that could be construed as a potential conflict of interest.

Publisher's Note: All claims expressed in this article are solely those of the authors and do not necessarily represent those of their affiliated organizations, or those of the publisher, the editors, and the reviewers. Any product that may be evaluated in this article, or claim that may be made by its manufacturer, is not guaranteed or endorsed by the publisher.

frontiers in Bioengineering and Biotechnology

ORIGINAL RESEARCH
published: 29 November 2021
doi: 10.3389/fbioe.2021.787320

Mitochondrial Targeting and pH-Responsive Nanogels for Co-Delivery of Lonidamine and Paclitaxel to Conquer Drug Resistance

Enping Chen[1†], Ting Wang[1†], Junmei Zhang[1], Xiang Zhou[1], Yafan Niu[1], Fu Liu[1], Yinan Zhong[1], Dechun Huang[1,2] and Wei Chen[1,2]**

[1]Department of Pharmaceutical Engineering, School of Engineering, China Pharmaceutical University, Nanjing, China, [2]Engineering Research Center for Smart Pharmaceutical Manufacturing Technologies, Ministry of Education, School of Engineering, China Pharmaceutical University, Nanjing, China

OPEN ACCESS

Edited by:
Bin He,
Sichuan University, China

Reviewed by:
Yiran Zheng,
Soochow University, China
Xiaohui Pu,
Henan University, China

***Correspondence:**
Yinan Zhong
ynzhong@cpu.edu.cn
Wei Chen
w.chen@cpu.edu.cn

[†]These authors have contributed equally to this work

Specialty section:
This article was submitted to Biomaterials, a section of the journal Frontiers in Bioengineering and Biotechnology

Received: 30 September 2021
Accepted: 29 October 2021
Published: 29 November 2021

Citation:
Chen E, Wang T, Zhang J, Zhou X, Niu Y, Liu F, Zhong Y, Huang D and Chen W (2021) Mitochondrial Targeting and pH-Responsive Nanogels for Co-Delivery of Lonidamine and Paclitaxel to Conquer Drug Resistance. Front. Bioeng. Biotechnol. 9:787320. doi: 10.3389/fbioe.2021.787320

Multidrug resistance (MDR) is one of the leading causes of the failure of cancer chemotherapy and mainly attributed to the overexpression of drug efflux transporters in cancer cells, which is dependent on adenosine triphosphate (ATP). To overcome this phenomenon, herein, a mitochondrial-directed pH-sensitive polyvinyl alcohol (PVA) nanogel incorporating the hexokinase inhibitor lonidamine (LND) and the chemotherapeutic drug paclitaxel (PTX) was developed to restore the activity of PTX and synergistically treat drug-resistant tumors. The introduction of 2-dimethylaminoethanethiol (DMA) moiety into the nanogels not only promoted the drug loading capacity but also enabled the lysosomal escape of the nanogels. The subsequent mitochondrial targeting facilitated the accumulation and acid-triggered payload release in the mitochondria. The released LND can destroy the mitochondria by exhausting the mitochondrial membrane potential (MMP), generating reactive oxygen species (ROS) and restraining the energy supply, resulting in apoptosis and susceptibility of the MCF-7/MDR cells to PTX. Hence, the nanogel-enabled combination regimen of LND and PTX showed a boosted anti-tumor efficacy in MCF-7/MDR cells. These mitochondrial-directed pH-sensitive PVA nanogels incorporating both PTX and LND represent a new nanoplatform for MDR reversal and enhanced therapeutic efficacy.

Keywords: multidrug resistance reversal, mitochondrial targeting, pH responsive, nanogel, combination therapy

INTRODUCTION

Chemotherapy remains one of the major means for treating tumors; however, the therapeutic efficacy is perplexed by many reasons including the multidrug resistance (MDR) (Lage 2008; Holohan et al., 2013; Rebucci and Michiels, 2013). The underlying mechanisms are complex and can be mainly summed up in the increased drug efflux from the cytoplasm to the extracellular compartment *via* the adenosine triphosphate (ATP)-binding cassette (ABC) transporters in the cells such as P-glycoprotein (P-gp) and multidrug resistance-associated protein 1 (MRP1) driven by the energy supply of ATP (Cole 2014; Kartal-Yandim et al., 2016; Assaraf et al., 2019). In order to reverse MDR, many strategies have been dedicated to the MDR inhibition by interfering the energy supply, re-sensitizing the tumor cells to the chemotherapeutic drugs (Abdallah et al., 2015; Assanhou et al., 2015; Li et al., 2016; Tu et al., 2018; Gao et al., 2019; Cheng et al., 2021; Liu et al., 2021).

Lonidamine (LND), which is a hexokinase inhibitor, blocks the energy supply and mitochondrial respiration, leading to mitochondrial dysfunction (Floridi et al., 1981; Price et al., 1996; Nath et al., 2016). In addition, LND triggers cell apoptosis by dissipating mitochondrial membrane potential (MMP) and generating reactive oxygen species (ROS). The combination of LND as a chemosensitizer with chemotherapeutic drugs provides an effective strategy for treating drug-resistant tumors (Li et al., 2002; Nath et al., 2013; Nath et al., 2015; Huang et al., 2020). Nevertheless, the poor water solubility and the lack of targetability of the drugs compromised their efficacy and limited their applications. Nanomedicine by virtue of its unique properties, such as the solubilization of the hydrophobic drugs and the delivery of the payload to the tumor sites *via* the enhanced permeability and retention (EPR) effect, has received widespread attention (Golombek et al., 2018; Majumder et al., 2019; Cao et al., 2020; Qiao et al., 2021). Nowadays, multifunctional nanomedicine integrating various modules of targeting (Qiao et al., 2019), lysosomal escaping, stimuli sensitivity, etc. (Pu et al., 2019; Zong et al., 2020; Zhong et al., 2021; Zong et al., 2021) could further improve the drug delivery efficacy, maximizing the therapeutic outcomes (Chen et al., 2017; Shahriari et al., 2019; Yang et al., 2019; He et al., 2021; Peng et al., 2021). It should be noted that the mitochondrial-targeting strategy plays an essential role in fully taking advantage of LND (Li et al., 2013; Zhang et al., 2015; Liu et al., 2017; Guo et al., 2021). Additionally, the biosafety of nanomedicine is a big concern.

In this study, we have constructed a triphenylphosphine (TPP)-installed pH-sensitive biocompatible polyvinyl alcohol (PVA) nanogel containing 2-dimethylaminoethanethiol (DMA) moiety for mitochondrial-directed co-delivery of LND and the chemotherapeutic drug paclitaxel (PTX) in drug-resistant tumors. The nanogels (T-D-NGs@LND and PTX) were fabricated by *in situ* crosslinking of the acrylate in PVA derivative under UV light and the concurrent co-loading of LND and PTX *via* hydrophobic and/or electrostatic interactions. After the internalization in the drug-resistant tumor cells, T-D-NGs@LND and PTX escaped from the lysosome due to the proton sponge effect of DMA moiety, effectively accumulated in the mitochondria with the orientation of TPP module, and rapidly released the payload resulting from the acid-triggered cleavage of the acetal linker within the network of nanogels (**Scheme 1**). The unleashed LND acted on the mitochondria and de-energized the cancer cells, resulting in cell apoptosis and making the cells more susceptible to the released PTX. The nanogel-mediated drug resistance alleviation and synergistic effect significantly boosted the anti-tumor activity in MCF-7/MDR cells, holding a great potential for conquering MDR.

EXPERIMENTAL SECTION

Preparation of DMA-Modified Vinyl Ether Acrylate-Functionalized PVA

Vinyl ether acrylate (VEA) and VEA-functionalized PVA (PVA-*g*-VEA) were prepared based on the previous reports (Chen et al., 2017). For the synthesis of DMA-functionalized PVA-*g*-VEA (PVA-*g*-VEA-DMA), DMA and Et_3N (20 μl) were added to a 10-ml solution of PVA-*g*-VEA (0.413 g, 0.024 mmol) in methanol under stirring, and the reaction was continued for 12 h. Afterwards, the above mixture solution was condensed by rotary evaporation. Finally, PVA-*g*-VEA-DMA was purified using the precipitant of ice-cold diethyl ether and then dried using the vacuum drier.

Preparation of TPP-Functionalized PVA-*g*-VEA-DMA

To synthesize TPP-modified PVA-*g*-VEA-DMA, a mixture of TPP (70.5 mg, 0.16 mmol), DCC (49.1 mg, 0.24 mmol), and DMAP (20.3 mg, 0.17 mmol) was dissolved in dimethyl sulfoxide (DMSO) (10 ml), and the obtained solution was vigorously stirred for 1 h for activation of the carboxyl group in TPP. Subsequently, a solution of PVA-*g*-VEA-DMA (100 mg) in DMSO (5 ml) was slowly added for a 24-h reaction under stirring. After that, PVA-*g*-VEA-DMA/TPP was purified *via* extensive dialysis [molecular weight cut off (MWCO): 3.5 kDa] against methanol for 24 h, concentrated through rotary evaporation, precipitated in ice-cold diethyl ether, as well as vacuum dried.

Preparation and Characterization of Nanogels

Acid-responsive nanogels were prepared using the UV-crosslinking method. Briefly, the nanogels were obtained by dissolving the polymer of PVA-*g*-VEA-DMA/TPP in water (1 mg/ml) with the addition of a photoinitiator (I2959, 5 wt% of polymer), adjusting solution pH to 6.8, and stirring under UV exposure for 10 min. To prepare drug-loaded nanogels, a solution of PTX and LND in DMSO (10 mg/ml) was added in the aqueous polymer solution with a feeding ratio of 10%. Through adjusting the solution pH to 6.8 and *in situ* crosslinking of acrylate in the polymers under UV light for 10 min, PTX and LND co-loaded nanogels were obtained. A Millipore ultrafiltration centrifugal tube with a MWCO of 10,000 was used to remove the free drugs.

pH-Induced Degradation of Nanogels and *In Vitro* Release Profile of LND and PTX

pH-induced degradation of nanogels was studied by detecting the nanogel size change *via* dynamic light scattering (DLS) in different conditions (pH 7.4 and 5.0) for different periods (0, 6, and 24 h). The unleash behavior of LND and PTX-loaded nanogels was explored in different conditions (pH 7.4 and 5.0) through the dialysis procedure. In brief, a dialysis bag (MWCO: 3,500) containing 1 ml of PTX and LND co-loaded nanogel suspension was placed into a large-volume tube with 20 ml of the corresponding medium under a continuous shaking at 100 rpm at 37°C. At various time intervals (0, 2, 4, 6, 8, 10, 24, 52, 56, and 72 h), 5 ml of the medium in the tube of each group was extracted and supplemented by the newly prepared medium. The collected media of each group were concentrated and subjected to HPLC for quantification of the released PTX and LND.

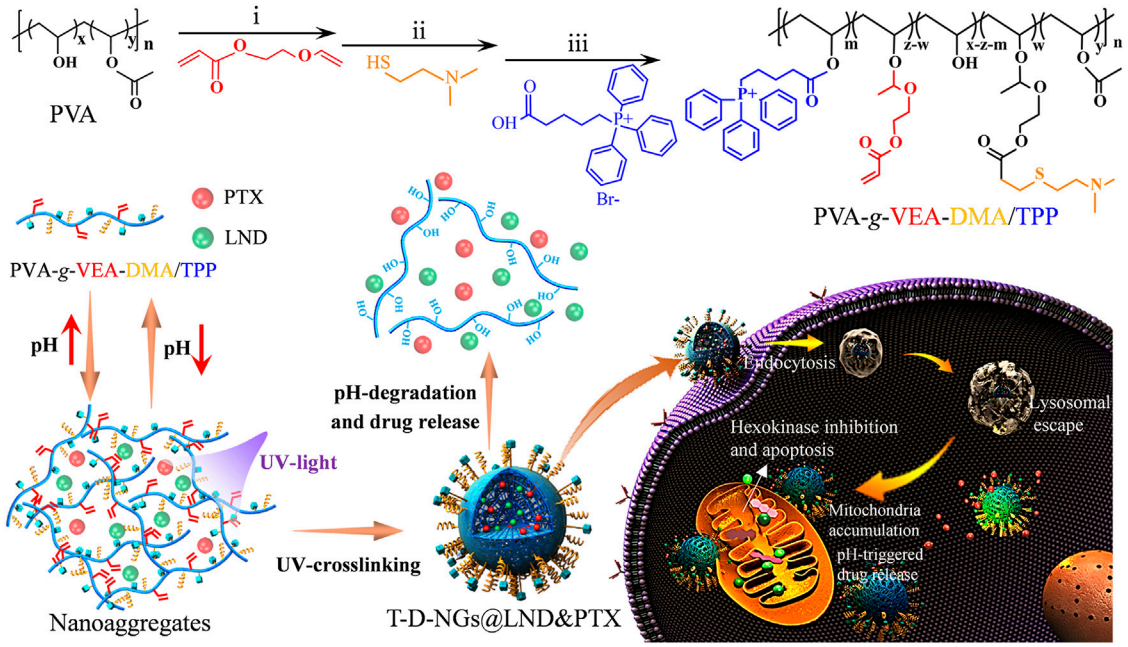

SCHEME 1 | Schematic illustrations for the constituent, fabrication, and destruction of T-D-NGs@LND and PTX and its endocytosis, lysosomal escape, mitochondrial orientation, and acid-triggered drug release within drug-resistant tumor cells for synergistic effect including LND-induced apoptosis, drug resistance alleviation, and restored chemotherapeutics of PTX.

Lysosomal Escape and Co-Localization Into the Mitochondria

MCF-7/MDR cells (1×10^5 cell/well) were seeded into a 24-well plate containing a rounded coverslip in each well. After 24 h, fluorescein isothiocyanate (FITC)-labeled NGs, D-NGs, and T-D-NGs were added and incubated with the cells for 8 h. Then, the medium was removed, and the cells were incubated with 500 μl of serum-free media containing 200 nM MitoTracker® Red CM-H2XRos probes at 37°C for 20 min or 500 μl of serum-free media containing 50 nM LysoTracker® Red DND-99 probes at 37°C for 30 min. After washing thrice in phosphate-buffered saline (PBS) and fixation of the cells using 4% paraformaldehyde for 20 min, 4′,6-diamidino-2-phenylindole (DAPI) was added for 10-min staining of the cell nucleus, and the excess DAPI was removed by washing thrice in PBS. Finally, the fluorescence images of each group were obtained by confocal laser microscope (CLSM, LSM700, Zeiss, Germany) and processed using the ZEN imaging software.

Mitochondrial Membrane Potential (Δψm) Depolarization

To measure the mitochondrial depolarization, the cationic fluorochrome JC-1 was employed to detect mitochondrial membrane potential change. Briefly, MCF-7/MDR cells were seeded in a 12-well plate (1×10^5 cells/well) and incubated for 24 h. Then, free LND, NGs@LND, D-NGs@LND, and T-D-NGs@LND at a LND dosage of 50 μg/ml were severally added and incubated with the cells for 12 h. Thereafter, the cells were washed with PBS followed by incubation with 0.0125 M JC-1 at 37°C for 20 min. After washing thrice in PBS, the cells were observed using a fluorescence microscope (IX73, Olympus, Japan).

ROS Level Detection

A ROS assay kit (Beyotime, China) was utilized for the detection of the intracellular ROS level. Briefly, MCF-7/MDR cells were cultured in a 12-well plate (1×10^5 cells/well) and incubated for 24 h. Then, free LND, NGs@LND, D-NGs@LND, and T-D-NGs@LND at a LND dosage of 50 μg/ml were respectively added and incubated with the cells for 12 h. Afterwards, the cells were washed with PBS for two times and stained with dichlorodihydro-fluorescein diacetate (DCFH-DA) for 20 min. After washing thrice in PBS and fixation of the cells using 4% paraformaldehyde for 20 min, DAPI was added for a 10-min staining of the cell nucleus, and the excess DAPI was removed by washing thrice in PBS. Finally, the cells were observed using a fluorescence microscope (IX73, Olympus, Japan).

ATP Content Detection

An ATP assay kit (Beyotime, China) was utilized for the detection of the intracellular ATP levels. MCF-7/MDR cells were cultured in a six-well plate (1×10^5 cell/well) for 24 h. After that, free LND, NGs@LND, D-NGs@LND, and T-D-NGs@LND at a LND dosage of 50 μg/ml were respectively added and incubated with the cells for 12 h. The intracellular ATP level was measured according to the manufacturer's protocol.

In Vitro Anti-Tumor Activity

To evaluate the apoptosis-inducing effect of different LND formulations, MCF-7/MDR cells were seeded into 12-well

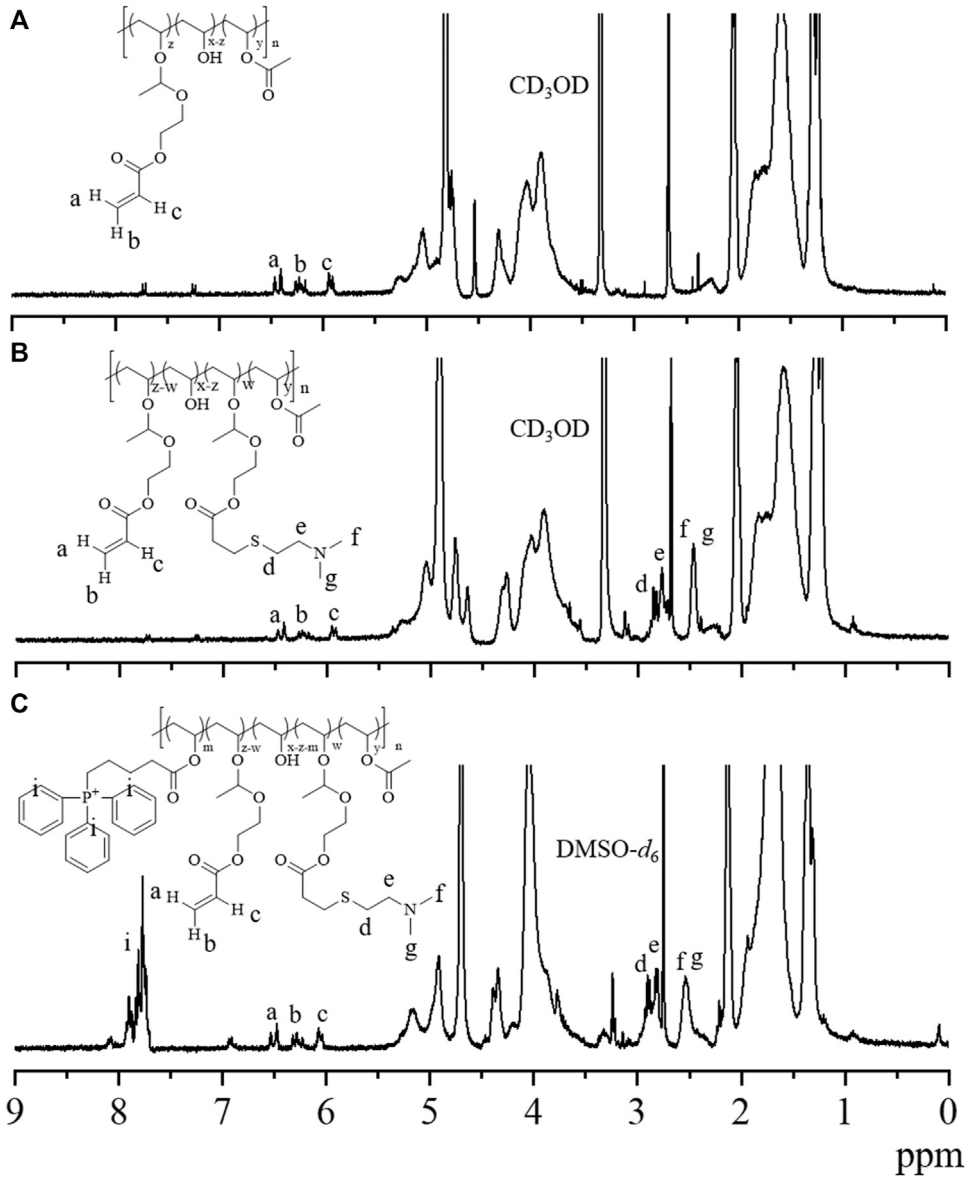

FIGURE 1 | ^{1}H NMR spectra of **(A)** PVA-*g*-VEA (300 MHz, CD_3OD), **(B)** PVA-*g*-VEA-DMA (300 MHz, CD_3OD), and **(C)** PVA-*g*-VEA-DMA/TPP (300 MHz, DMSO-d_6). VEA, vinyl ether acrylate; PVA-*g*-VEA, VEA-functionalized PVA; PVA-*g*-VEA-DMA, DMA-functionalized PVA-*g*-VEA; TPP, triphenylphosphine.

plates (1×10^5 cell/well) and cultured for 24 h at 37°C. Then, different LND formulations (50 μg/ml LND) were added and incubated with the cells for 12 h. After that, the cells were digested and collected for Annexin V-FITC/propidium iodide (PI) staining based on the manufacturer's instructions and analyzed by flow cytometry.

MTT assay was utilized to study the cytotoxicity of MCF-7/MDR cells receiving various formulations. The cells were cultured in 96-well plates for 24 h and then incubated with various formulations or free drug. After 48-h incubation, MTT solution was added for 4-h incubation. Then, the culture medium was replaced by DMSO for detection under a microplate reader with the absorbance at 490 nm.

Statistical Analysis

Data were expressed as mean ± standard deviation. Differences between groups were assessed by a two-tailed unpaired Student's *t*-test or one-way ANOVA with Tukey's *post hoc* test. The level of significance was set at probabilities of $^{*}p < 0.05$, $^{**}p < 0.01$, and $^{***}p < 0.001$.

RESULTS AND DISCUSSION

Synthesis and Characterization of TPP-Modified PVA Nanogels

We started with the synthesis of PVA-*g*-VEA/VEA-DMA/TPP polymer, in which the pendent VEA, positively charged DMA,

and mitochondria-recognizable TPP were successively conjugated onto the water-soluble PVA backbone (**Scheme 1**). The VEA was firstly grafted onto PVA polymers *via* an acetalization reaction between vinyl ether and hydroxyl group in the presence of PTSA. The signals at δ 6.6 and δ 5.85–6.45 attributable to the vinyl protons of VEA and newly formed acetal methine proton, respectively, revealed the successful conjugation of VEA to the polymers, and the VEA grafting ratio was determined to be about 6.1% by comparing the integral of the peaks at δ 1.3 and at δ 6.6 (**Figure 1A**). DMA was further conjugated with acrylate in PVA-VEA, yielding a DMA functionality of about 2.66% with 3.44% acrylate left for UV-mediated crosslinking according to the ^{1}H NMR spectra (**Figure 1B**). Lastly, the obtained polymeric conjugates were coupled with TPP on the backbone using DCC and DMAP *via* esterification, and the content of the TPP moiety on PVA-VEA-DMA-TPP was about 1.3 wt% as revealed from the integrals of the peaks at δ 7.68 of benzene protons and at δ 1.3 (**Figure 1C**).

T-D-NGs were then obtained by dissolving the polymer of PVA-*g*-VEA/VEA-DMA/TPP in water, adjusting pH to 7.8, crosslinking acrylate in the presence of I2959 under UV light. D-NGs and NGs were prepared in a similar way. As displayed in **Figure 2A–C**, T-D-NGs, D-NGs, and NGs presented a typical spherical shape with uniform sizes of about 170 nm. pH-responsive T-D-NGs were explored by detecting the size change of T-D-NGs in acetate buffer (pH 5.0) for different times *via* DLS measurement. T-D-NGs displayed a swelled structure with a size of about several hundred nanometers after 6 h and later a small-sized particle with a size of about 17 nm after 24 h, whereas the size of T-D-NGs maintained almost the same at pH 7.4 after 24-h incubation (**Figure 2D**). These results revealed that T-D-NGs possessed a good colloidal stability in the physiological condition while suffered from the destruction at pH 5.0 that mimicked intracellular acidic condition. It should be noted that the swelled structure of T-D-NGs in response to acidic condition in their initial stage was ascribed to their partial cleavage of the acetal linkers in the network of T-D-NGs, which ultimately led to complete disassociation and small-sized conjugates in the acidic condition.

Preparation and Characterization of Drug-Loaded Nanogels

LND, which is a small-molecule hexokinase inhibitor, and chemotherapeutic PTX were co-loaded into the T-D-NGs *via* hydrophobic and/or electrostatic interactions. LND and PTX-loaded nanogels showed increased sizes in comparison to the blank nanogels as determined by DLS (**Table 1**). The introduction of DMA and TPP moieties in the nanogels dramatically improved drug loading content (DLC) from 2 wt% to about 5 wt% at a theoretical DLC of 10 wt%, which was probably due to their increased hydrophobicity and electropositivity.

The *in vitro* LND and PTX release profiles from T-D-NGs were studied at various pH, i.e., pH 5.0 and pH 7.4. As displayed in **Figure 2E, F**, a small amount of LND (31.7%) and PTX (34.5%) was leaked from T-D-NGs at pH 7.4 after 72 h, respectively, whereas more than 70% of LND and PTX were released at pH 5.0 after 72 h, further confirming pH-triggered disassociation of the nanogels and the subsequent payload release.

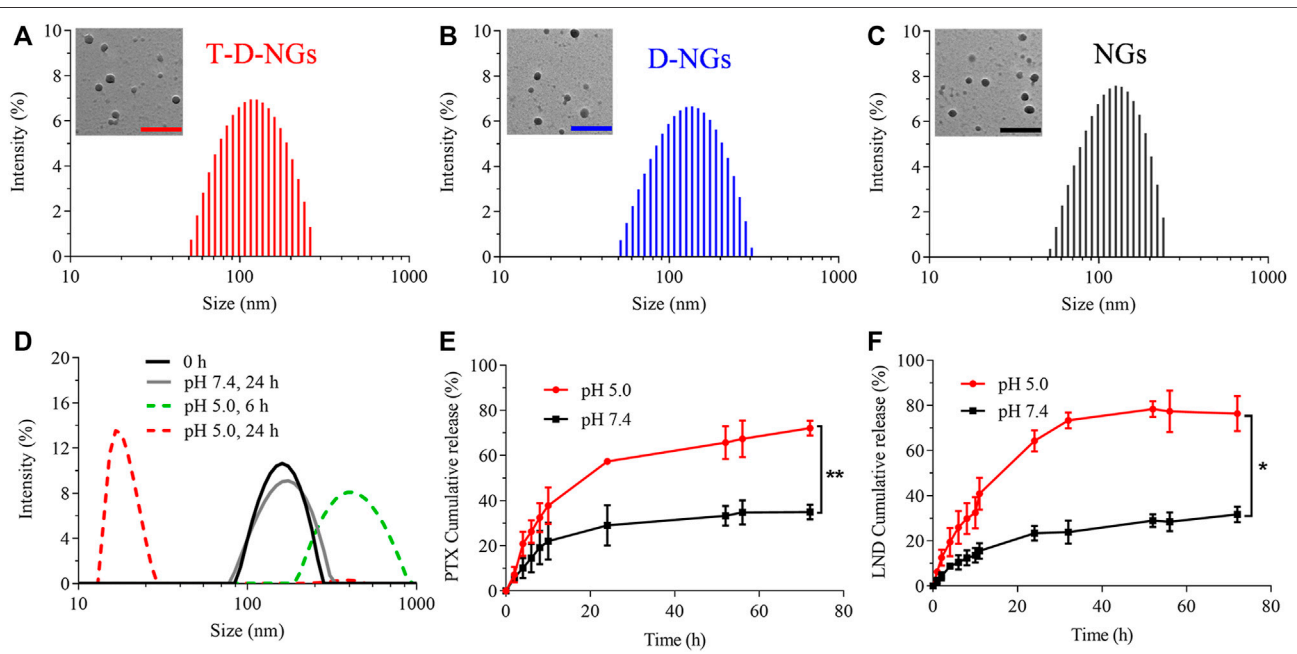

FIGURE 2 | Size distribution of **(A)** T-D-NGs, **(B)** D-NGs, and **(C)** NGs determined by DLS and TEM (inset). Scale bars: 500 nm. **(D)** pH-triggered size variation of T-D-NGs for different times (0, 6, and 24 h) determined by DLS. *In vitro* **(E)** PTX and **(F)** LND release from T-D-NGs (2 mg/ml) at 37°C ($n = 3$, $^{*}p < 0.05$, $^{**}p < 0.01$). DLS, dynamic light scattering; TEM, transmission electron microscopy; PTX, paclitaxel; LND, lonidamine.

TABLE 1 | Characteristics of different drug-loaded nanogels[a]

Nanogels	DLE (%)[b]		DLC (%)[b]		Size[c]	PDI[c]
	PTX	LND	PTX	LND		
NGs	23.01 ± 1.0	20.74 ± 0.2	2.25 ± 0.1	2.03 ± 0.1	165.6 ± 0.6	0.22
D-NGs	46.70 ± 5.5	57.69 ± 6.7	4.46 ± 0.5	5.45 ± 0.6	211.7 ± 3.2	0.15
T-D-NG	53.21 ± 0.9	74.92 ± 0.4	5.05 ± 0.1	5.05 ± 0.1	182.3 ± 6.1	0.21

[a]*The concentration of nanogels was set at 1.0 mg/ml.*
[b]*Determined by HPLC.*
[c]*Determined by DLS.*

Escape From Lysosomes and Mitochondrial Targeting

The cellular behaviors of T-D-NGs were investigated by using CLSM in MCF-7/MDR cells. T-D-NGs, D-NGs, and NGs were labeled with FITC for CLSM imaging, and the results showed that FITC-labeled NGs (FITC-NGs, green signal) were captured by lysosomes (red signal) with colocalized orange signal within cells for 8-h incubation, while most of the green signal of FITC-labeled T-D-NGs (FITC-T-D-NGs) and FITC-labeled D-NGs (FITC-D-NGs) were separated from the red signal of lysosomes after 8 h, indicating the successful escape of FITC-T-D-NGs and FITC-D-NGs from lysosomes with the aid of DMA module in the nanogels (**Figure 3**). In the following, we evaluated the mitochondrial-targeting ability of FITC-T-D-NGs, FITC-D-NGs, and FITC-NGs by staining the mitochondria with MitoTracker (red). After 12 h, a large area of FITC-T-D-NGs were overlapped with the mitochondria, resulting in intense orange fluorescence in the merged image (**Figure 4**). In contrast, FITC-D-NGs presented separated green and red fluorescence, and hardly any green signal was observed in the FITC-NG group with only red fluorescence in the merged image. All the above results demonstrated that FITC-T-D-NGs could efficiently escape from the lysosomes and target the mitochondria for facilitating LND delivery, while FITC-NGs and FITC-D-NGs either got trapped in the lysosomes or lacked mitochondrial orientation.

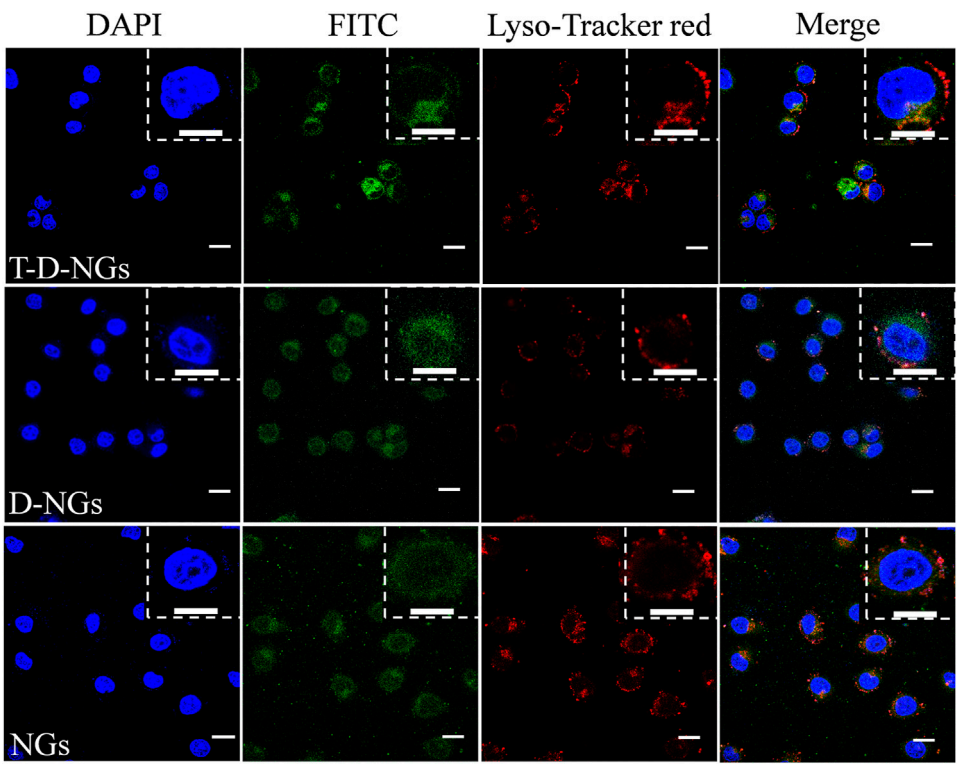

FIGURE 3 | CLSM images of MCF-7/MDR cells treated with different FITC-labeled nanogels (500 μg/ml) following 8-h incubation. The lysosomes were stained with LysoTracker Red, and the cell nuclei were stained with DAPI (blue signal). Scale bar: 20 μm. CLSM, confocal laser microscope; FITC, fluorescein isothiocyanate; DAPI, 4′,6-diamidino-2-phenylindole.

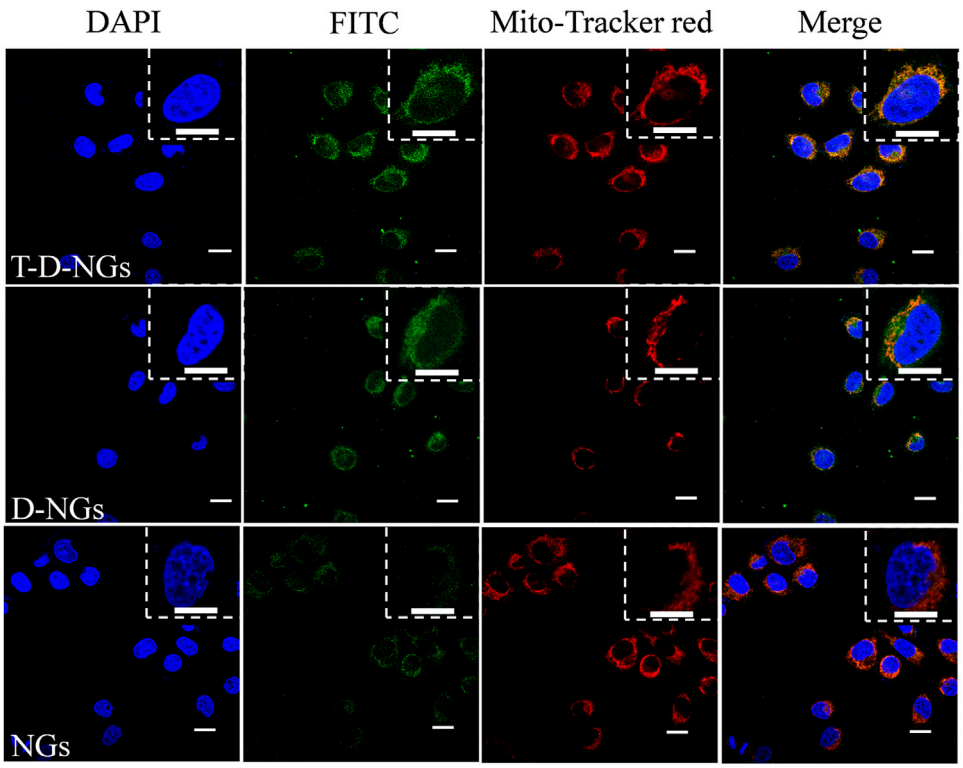

FIGURE 4 | CLSM images of MCF-7/MDR cells treated with different FITC-labeled nanogels (500 μg/ml) following 12-h incubation. The mitochondria were stained with MitoTracker Red, and the cell nuclei were stained with DAPI (blue signal). Scale bars: 20 μm.

Dysfunction of the Mitochondria

To explore the underlying mechanism of LND-loaded T-D-NGs (T-D-NGs@LND) in interfering mitochondrial functions, the measurements of MMP, ROS production, and ATP secretion in MCF-7/MDR cells were performed. JC-1 staining was firstly employed, which served as a fluorescence probe to detect MMP. JC-1 forms aggregates with red fluorescence at a high MMP, while remains monomers with green fluorescence at a low potential level, which is indicative of early apoptosis. After 12-h incubation, free LND displayed minimal green signal and intense red signal level comparable to the PBS group in MCF-7/MDR cells due to its slow diffusion and poor mitochondrial targeting (**Figure 5A**; **Supplementary Figure S1**). NGs@LND slightly increased the green fluorescence to some extent and maintained the strong red fluorescence, revealing an insufficient dissipation of MMP because of being trapped in lysosomes and limited accumulation in the mitochondria as demonstrated above. D-NGs@LND ameliorated this phenomena because of its lysosomal escape aided by DMA moieties in the nanogels. T-D-NGs@LND was the most effective in dissipating MMP with the strongest green fluorescence concomitant with the weakest red fluorescence, which was ascribed to its lysosomal escape, mitochondrial accumulation, and effective LND release triggered by acid within cells.

ROS production causes oxidative cell damage at a high level, which was another mechanism involved in cancer cell apoptosis *via* the mitochondrial pathway. ROS production level was detected by a fluorescence probe of DCFH-DA *via* CLSM imaging. The trend of the intracellular ROS production level was similar with the results of the dissipation of MMP (**Figure 6**; **Supplementary Figure S2**), verifying that T-D-NGs@LND induced a large amount of intracellular ROS production in the mitochondria, potentially for anti-tumor applications.

Cumulative evidences demonstrated that LND had the potential to inhibit hexokinase enzyme that was implicated in ATP generation and mitochondrial respiration. ATP secretion from the MCF-7/MDR cells receiving various LND formulations was estimated through the ATP assay kit. As expected, T-D-NGs@LND significantly decreased ATP secretion from the cells with a decline of about 60.9% versus 43.48%, 30.44%, and 15.95% for D-NGs@LND, NGs@LND, and free LND severally after 12-h incubation (**Supplementary Figure S3**). Such a pronounced inhibition of ATP secretion in MCF-7/MDR cell induced by T-D-NGs@LND further confirmed the precise and efficient delivery of LND into the mitochondria and also laid a solid foundation for MDR reversal by suppressing P-gp that was dependent on ATP.

Anti-Tumor Activity

The cell apoptosis with the treatments of various LND formulations *via* the mitochondrial pathway was explored *via* Annexin V-FITC/PI staining through flow cytometry. LND

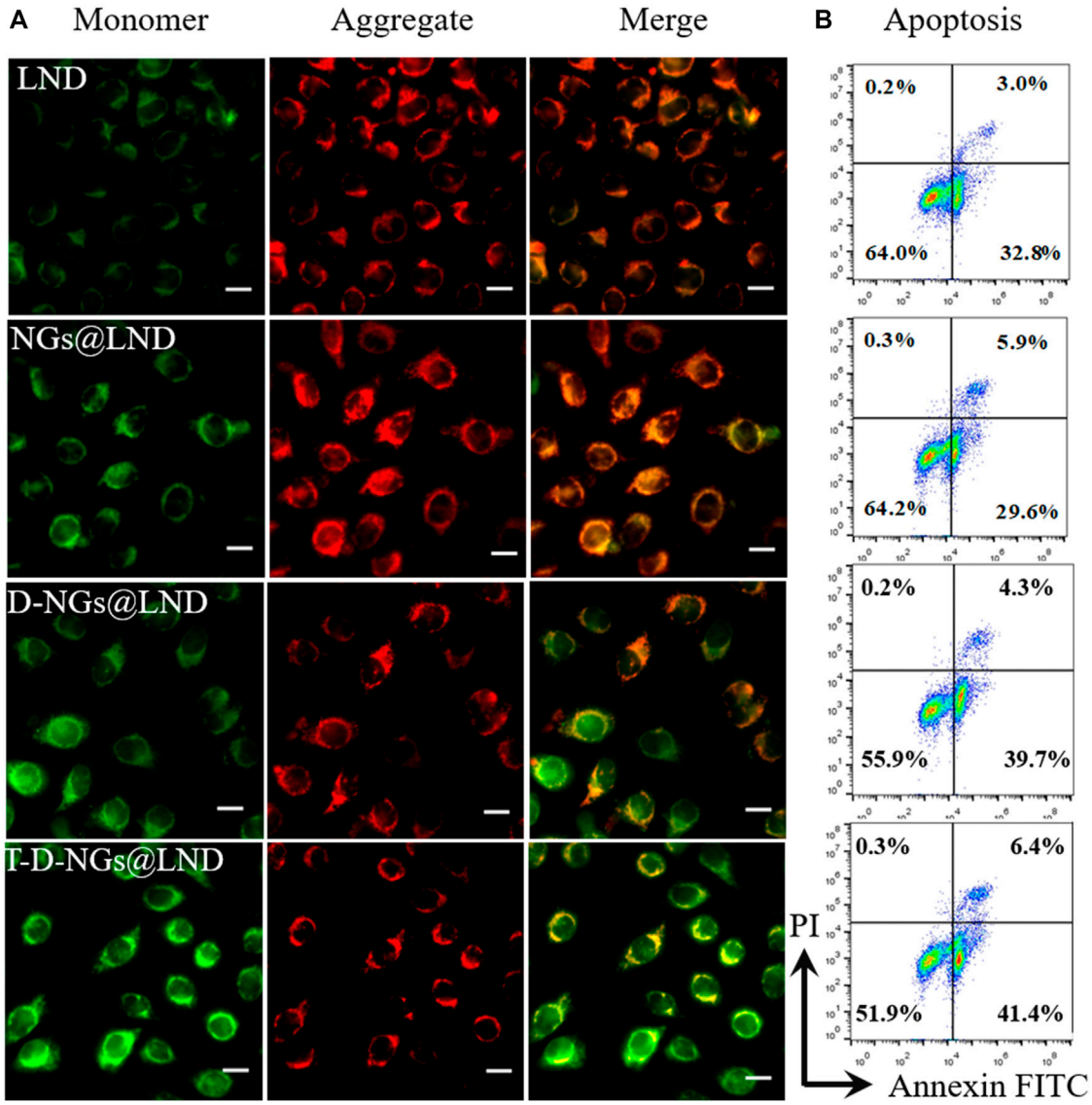

FIGURE 5 | (A) The MMP depolarization level of MCF-7/MDR cells incubated with LND, NGs@LND, D-NGs@LND, and T-D-NGs@LND for 12 h. The mitochondrial channel was stained with JC-1. Scale bars: 20 μm. **(B)** Cell apoptosis studies with treatments of various LND-loaded nanogels for 12 h. MMP, mitochondrial membrane potential.

could induce cell apoptosis *via* several mechanisms like destruction of MMP and oxidative stress of overproduced ROS in the mitochondria as noted above. Total apoptotic rates of about 47.8% was found in T-D-NGs@LND-treated cells, which was higher than the D-NGs@LND (44%), NGs@LND (35.5%), and free LND (35.8%) groups (**Figure 5B**). Moreover, T-D-NGs@LND caused both higher early (41.4%) and late (6.4%) apoptosis than other treatments. MTT assay was also carried out and showed that all of the LND formulations led to a dose-dependent cytotoxicity toward MCF-7/MDR cells, among which T-D-NGs@LND displayed the most potent anti-tumor activity with a cell viability of about 33.47% at a LND concentration of 100 μg/ml for 48 h (**Figure 7A**). Taken together, T-D-NGs@LND was demonstrated to exert direct tumor cell-killing ability of LND by overcoming lysosomal trap, navigating into the mitochondria and efficiently releasing LND.

Furthermore, the potential role of LND for drug resistance reversal and chemo-sensitization was utilized to reactivate the treatment ability of PTX in MCF-7/MDR cells. Thus, the combination of LND and PTX in T-D-NGs could bring about a synergistic anti-tumor activity by fully exerting tumor cell killing of both LND and PTX. To verify the above assumption, MTT assay was performed in MCF-7/MDR cells receiving PTX- and/or LND-loaded nanogels for 48 h. As displayed in **Figure 7B**, all the PTX formulations and free PTX revealed mild cytotoxicity toward the cells with cell viabilities more than 40% even at a high PTX

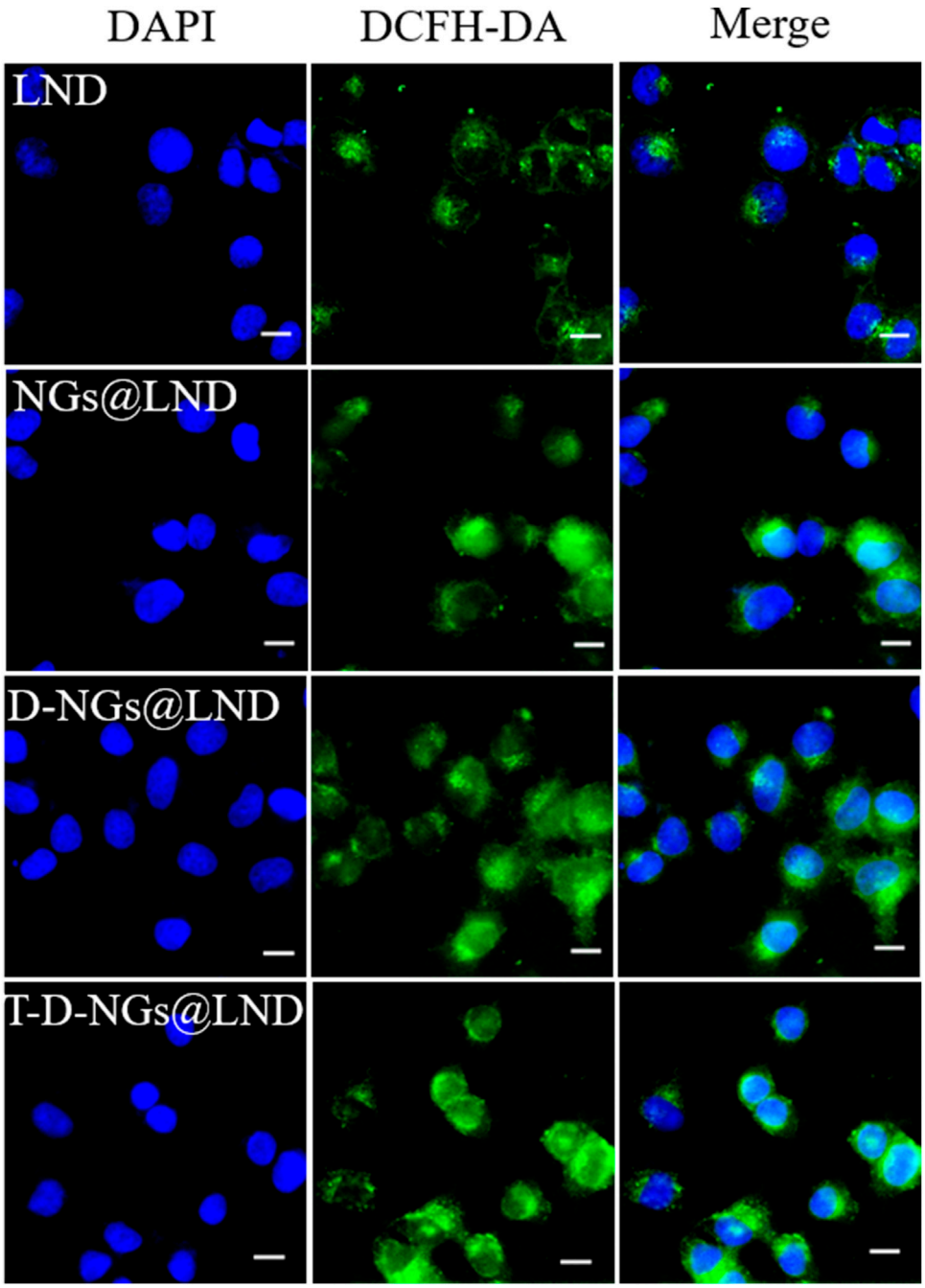

FIGURE 6 | Intracellular ROS level in MCF-7/MDR cells receiving LND, NGs@LND, D-NGs@LND, and T-D-NGs@LND for 12 h using a probe of DCFH-DA. Scale bars: 20 μm. ROS, reactive oxygen species; DCFH-DA, dichlorodihydro-fluorescein diacetate.

concentration of 20 μg/ml, reflecting drug resistance of the cells and inactivation of PTX formulations. The combination of LND and PTX in various formulations showed cytotoxicity toward the cells in a PTX dose-dependent fashion at a fixed LND concentration of 50 μg/ml (**Figure 7C**). As predicted, T-D-NGs@LND and PTX remarkably boosted the tumor cell-killing activity with a cell viability of about 18.59% at LND and PTX concentrations of 50 and 20 μg/ml for 48 h, which was much lower than T-D-NG-enabled monotherapy (T-D-NGs@LND and T-D-NGs@PTX), revealing the reversal of drug resistance and the synergistic therapeutic efficacy of unleashed LND and PTX. The half maximal inhibitory PTX concentration (IC_{50}) of T-D-NGs@LND and PTX (LND: 50 μg/ml) was also calculated, which was determined to be 7.44 μg/ml. T-D-NGs@LND and PTX also displayed a much higher anti-tumor activity as compared with D-NGs@LND and PTX (IC_{50}: 10.70 μg/ml), NGs@LND and PTX

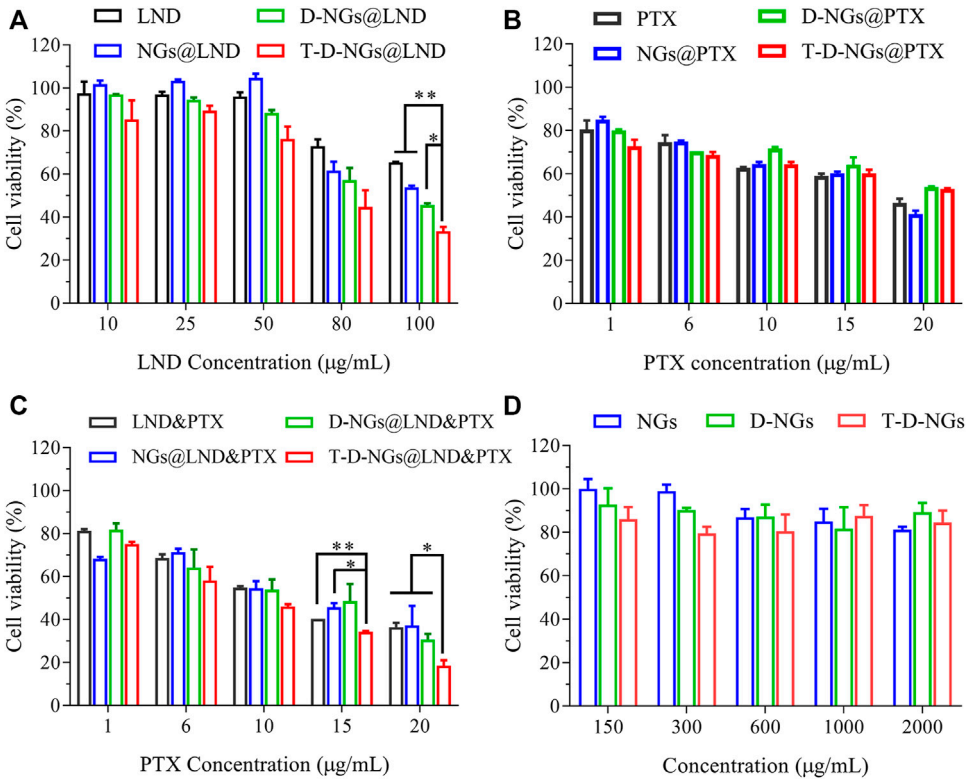

FIGURE 7 | Cytotoxicity of MCF-7/MDR cells after 48-h treatments of **(A)** LND-loaded nanogels, **(B)** PTX-loaded nanogels, **(C)** LND and PTX-loaded nanogels (LND: 50 μg/ml), and **(D)** drug-free nanogels (n = 3, $^*p < 0.05$, $^{**}p < 0.01$).

(IC_{50}: 11.96 μg/ml), and LND and PTX (IC_{50}: 11.49 μg/ml), further verifying T-D-NG-mediated lysosomal escape, mitochondrial accumulation, and acid-triggered payload release for fully exerting the efficacy of both drugs. In the meanwhile, the cytotoxicities of drug-free nanogels toward the cells were also assessed, and the results showed cell viabilities of 80%–100% at nanogel concentrations ranging from 0.15 to 2 mg/ml (**Figure 7D**), confirming the superior biocompatibility of the nanogels, which was mainly made up of FDA-approved biocompatible PVA backbone.

CONCLUSION

In conclusion, we have developed mitochondrial-directed pH-sensitive nanogels incorporating LND and PTX (T-D-NGs@LND and PTX) for drug resistance reversal and synergistic therapy against drug-resistant tumors. After internalization into MCF-7/MDR cells, T-D-NGs@LND and PTX efficiently escaped from the lysosomes with the aid of DMA moiety in the nanogels, accumulated into the mitochondria, and rapidly released the payload in the acidic conditions. The released LND, on one hand, directly induced cell apoptosis *via* dampening the mitochondrial membrane potential, promoting oxidative stress from the ROS production; on the other hand, it facilitated drug resistance reversal and sensitization of PTX activity by blocking the energy source and thus inhibiting drug resistance-related P-gp expression. As a result, T-D-NGs@LND and PTX demonstrated a significantly potent anti-tumor activity against MCF-7/MDR cells with an extremely low IC_{50} of 7.44 μg/ml PTX (LND: 50 μg/ml) after 48-h treatment and a synergistic effect of LND and PTX. Our work provides a promising and synergistic strategy to conquer tumor MDR.

DATA AVAILABILITY STATEMENT

The original contributions presented in the study are included in the article/**Supplementary Material**; further inquiries can be directed to the corresponding authors.

AUTHOR CONTRIBUTIONS

EC conducted the investigation, formal analysis, and original draft preparation. TW conducted the data curation, methodology, and formal analysis and reviewed and edited the manuscript. JZ conducted the data curation and reviewed and edited the manuscript. XZ conducted the data curation, investigation, and software processing. YN and FL conducted the investigation. YZ supervised the study, acquired funding, served as project administrator, and reviewed and edited the manuscript. DH contributed resources and acquired funding.

WC supervised and conceptualized the study, served as project administrator, acquired funding, and reviewed and edited the manuscript. All authors contributed to the article and approved the submitted version.

FUNDING

This work was funded by the National Natural Science Foundation of China (NSFC 51803238, 51973233, and 21878337), the Jiangsu Specially-Appointed Professor Program, and the Nanjing Scientific and Technological Innovation Program for Overseas Talents to WC.

SUPPLEMENTARY MATERIAL

The Supplementary Material for this article can be found online at: https://www.frontiersin.org/articles/10.3389/fbioe.2021.787320/full#supplementary-material.

REFERENCES

Abdallah, H. M., Al-Abd, A. M., El-Dine, R. S., and El-Halawany, A. M. (2015). P-glycoprotein Inhibitors of Natural Origin as Potential Tumor Chemo-Sensitizers: A Review. *J. Adv. Res.* 6, 45–62. doi:10.1016/j.jare.2014.11.008

Assanhou, A. G., Li, W., Zhang, L., Xue, L., Kong, L., Sun, H., et al. (2015). Reversal of Multidrug Resistance by Co-delivery of Paclitaxel and Lonidamine Using a Tpgs and Hyaluronic Acid Dual-Functionalized Liposome for Cancer Treatment. *Biomaterials* 73, 284–295. doi:10.1016/j.biomaterials.2015.09.022

Assaraf, Y. G., Brozovic, A., Gonçalves, A. C., Jurkovicova, D., Linē, A., Machuqueiro, M., et al. (2019). The Multi-Factorial Nature of Clinical Multidrug Resistance in Cancer. *Drug Resist. Updates* 46, 100645. doi:10.1016/j.drup.2019.100645

Cao, J., Huang, D., and Peppas, N. A. (2020). Advanced Engineered Nanoparticulate Platforms to Address Key Biological Barriers for Delivering Chemotherapeutic Agents to Target Sites. *Adv. Drug Deliv. Rev.* 167, 170–188. doi:10.1016/j.addr.2020.06.030

Chen, W., Hou, Y., Tu, Z., Gao, L., and Haag, R. (2017). Ph-degradable Pva-Based Nanogels via Photo-Crosslinking of Thermo-Preinduced Nanoaggregates for Controlled Drug Delivery. *J. Controlled Release* 259, 160–167. doi:10.1016/j.jconrel.2016.10.032

Cheng, F., Pan, Q., Gao, W., Pu, Y., Luo, K., and He, B. (2021). Reversing Chemotherapy Resistance by a Synergy between Lysosomal Ph-Activated Mitochondrial Drug Delivery and Erlotinib-Mediated Drug Efflux Inhibition. *ACS Appl. Mater. Inter.* 13, 29257–29268. doi:10.1021/acsami.1c03196

Cole, S. P. C. (2014). Multidrug Resistance Protein 1 (Mrp1, Abcc1), a "multitasking" Atp-Binding Cassette (Abc) Transporter. *J. Biol. Chem.* 289, 30880–30888. doi:10.1074/jbc.R114.609248

Floridi, A., Paggi, M. G., Marcante, M. L., Silvestrini, B., Caputo, A., and De Martino, C. (1981). Lonidamine, a Selective Inhibitor of Aerobic Glycolysis of Murine Tumor Cells. *J. Natl. Cancer Inst.* 66, 497–499. doi:10.1093/jnci/66.3.497

Gao, L., Dong, B., Zhang, J., Chen, Y., Qiao, H., Liu, Z., et al. (2019). Functional Biodegradable Nitric Oxide Donor-Containing Polycarbonate-Based Micelles for Reduction-Triggered Drug Release and Overcoming Multidrug Resistance. *ACS Macro Lett.* 8, 1552–1558. doi:10.1021/acsmacrolett.9b00758

Golombek, S. K., May, J.-N., Theek, B., Appold, L., Drude, N., Kiessling, F., et al. (2018). Tumor Targeting via Epr: Strategies to Enhance Patient Responses. *Adv. Drug Deliv. Rev.* 130, 17–38. doi:10.1016/j.addr.2018.07.007

Guo, X., Yang, N., Ji, W., Zhang, H., Dong, X., Zhou, Z., et al. (2021). Mito-Bomb: Targeting Mitochondria for Cancer Therapy. *Adv. Mater.* 33, 2007778. doi:10.1002/adma.202007778

He, Y., Lei, L., Cao, J., Yang, X., Cai, S., Tong, F., et al. (2021). A Combinational Chemo-Immune Therapy Using an Enzyme-Sensitive Nanoplatform for Dual-Drug Delivery to Specific Sites by cascade Targeting. *Sci. Adv.* 7, 1. doi:10.1126/sciadv.aba0776

Holohan, C., Van Schaeybroeck, S., Longley, D. B., and Johnston, P. G. (2013). Cancer Drug Resistance: An Evolving Paradigm. *Nat. Rev. Cancer* 13, 714–726. doi:10.1038/nrc3599

Huang, Y., Sun, G., Sun, X., Li, F., Zhao, L., Zhong, R., et al. (2020). The Potential of Lonidamine in Combination with Chemotherapy and Physical Therapy in Cancer Treatment. *Cancers* 12, 3332. doi:10.3390/cancers12113332

Kartal-Yandim, M., Adan-Gokbulut, A., and Baran, Y. (2016). Molecular Mechanisms of Drug Resistance and its Reversal in Cancer. *Crit. Rev. Biotechnol.* 36, 716–726. doi:10.3109/07388551.2015.1015957

Lage, H. (2008). An Overview of Cancer Multidrug Resistance: A Still Unsolved Problem. *Cell. Mol. Life Sci.* 65, 3145–3167. doi:10.1007/s00018-008-8111-5

Li, N., Zhang, C.-X., Wang, X.-X., Zhang, L., Ma, X., Zhou, J., et al. (2013). Development of Targeting Lonidamine Liposomes that Circumvent Drug-Resistant Cancer by Acting on Mitochondrial Signaling Pathways. *Biomaterials* 34, 3366–3380. doi:10.1016/j.biomaterials.2013.01.055

Li, W., Zhang, H., Assaraf, Y. G., Zhao, K., Xu, X., Xie, J., et al. (2016). Overcoming Abc Transporter-Mediated Multidrug Resistance: Molecular Mechanisms and Novel Therapeutic Drug Strategies. *Drug Resist. Updates* 27, 14–29. doi:10.1016/j.drup.2016.05.001

Li, Y. C., Fung, K. P., Kwok, T. T., Lee, C. Y., Suen, Y. K., and Kong, S. K. (2002). Mitochondrial Targeting Drug Lonidamine Triggered Apoptosis in Doxorubicin-Resistant Hepg2 Cells. *Life Sci.* 71, 2729–2740. doi:10.1016/s0024-3205(02)02103-3

Liu, Y., Zhang, X., Zhou, M., Nan, X., Chen, X., and Zhang, X. (2017). Mitochondrial-targeting Lonidamine-Doxorubicin Nanoparticles for Synergistic Chemotherapy to Conquer Drug Resistance. *ACS Appl. Mater. Inter.* 9, 43498–43507. doi:10.1021/acsami.7b14577

Liu, Z., Zhong, Y., Zhou, X., Huang, X., Zhou, J., Huang, D., et al. (2021). Inherently Nitric Oxide Containing Polymersomes Remotely Regulated by Nir for Improving Multi-Modal Therapy on Drug Resistant Cancer. *Biomaterials* 277, 121118. doi:10.1016/j.biomaterials.2021.121118

Majumder, J., Taratula, O., and Minko, T. (2019). Nanocarrier-based Systems for Targeted and Site Specific Therapeutic Delivery. *Adv. Drug Deliv. Rev.* 144, 57–77. doi:10.1016/j.addr.2019.07.010

Nath, K., Guo, L., Nancolas, B., Nelson, D. S., Shestov, A. A., Lee, S.-C., et al. (2016). Mechanism of Antineoplastic Activity of Lonidamine. *Biochim. Biophys. Acta (Bba) - Rev. Cancer* 1866, 151–162. doi:10.1016/j.bbcan.2016.08.001

Nath, K., Nelson, D. S., Heitjan, D. F., Leeper, D. B., Zhou, R., and Glickson, J. D. (2015). Lonidamine Induces Intracellular Tumor Acidification and ATP Depletion in Breast, Prostate and Ovarian Cancer Xenografts and Potentiates Response to Doxorubicin. *NMR Biomed.* 28, 281–290. doi:10.1002/nbm.3240

Nath, K., Nelson, D. S., Ho, A. M., Lee, S.-C., Darpolor, M. M., Pickup, S., et al. (2013). 31P and1H MRS of DB-1 Melanoma Xenografts: Lonidamine Selectively Decreases Tumor Intracellular pH and Energy Status and Sensitizes Tumors to Melphalan. *NMR Biomed.* 26, 98–105. doi:10.1002/nbm.2824

Peng, Y., Lu, J., Li, R., Zhao, Y., Hai, L., Guo, L., et al. (2021). Glucose and Triphenylphosphonium Co-modified Redox-Sensitive Liposomes to Synergistically Treat Glioma with Doxorubicin and Lonidamine. *ACS Appl. Mater. Inter.* 13, 26682–26693. doi:10.1021/acsami.1c02404

Price, G. S., Page, R. L., Riviere, J. E., Cline, J. M., and Thrall, D. E. (1996). Pharmacokinetics and Toxicity of Oral and Intravenous Lonidamine in Dogs. *Cancer Chemother. Pharmacol.* 38, 129–135. doi:10.1007/s002800050460

Pu, X., Zhao, L., Li, J., Song, R., Wang, Y., Yu, K., et al. (2019). A Polymeric Micelle with an Endosomal Ph-Sensitivity for Intracellular Delivery and Enhanced Antitumor Efficacy of Hydroxycamptothecin. *Acta Biomater.* 88, 357–369. doi:10.1016/j.actbio.2019.02.039

Qiao, H., Chen, X., Chen, E., Zhang, J., Huang, D., Yang, D., et al. (2019). Folated Ph-Degradable Nanogels for the Simultaneous Delivery of Docetaxel and an Ido1-inhibitor in Enhancing Cancer Chemo-Immunotherapy. *Biomater. Sci.* 7, 2749–2758. doi:10.1039/c9bm00324j

Qiao, Y., Wei, Z., Qin, T., Song, R., Yu, Z., Yuan, Q., et al. (2021). Combined Nanosuspensions from Two Natural Active Ingredients for Cancer Therapy with Reduced Side Effects. *Chin. Chem. Lett.* 32, 2877–2881. doi:10.1016/j.cclet.2021.03.049

Rebucci, M., and Michiels, C. (2013). Molecular Aspects of Cancer Cell Resistance to Chemotherapy. *Biochem. Pharmacol.* 85, 1219–1226. doi:10.1016/j.bcp.2013.02.017

Shahriari, M., Zahiri, M., Abnous, K., Taghdisi, S. M., Ramezani, M., and Alibolandi, M. (2019). Enzyme Responsive Drug Delivery Systems in Cancer Treatment. *J. Controlled Release* 308, 172–189. doi:10.1016/j.jconrel.2019.07.004

Tu, Z., Qiao, H., Yan, Y., Guday, G., Chen, W., Adeli, M., et al. (2018). Directed Graphene-Based Nanoplatforms for Hyperthermia: Overcoming Multiple Drug Resistance. *Angew. Chem. Int. Ed.* 57, 11198–11202. doi:10.1002/anie.201804291

Yang, X., Hu, C., Tong, F., Liu, R., Zhou, Y., Qin, L., et al. (2019). Tumor Microenvironment-Responsive Dual Drug Dimer-Loaded PEGylated Bilirubin Nanoparticles for Improved Drug Delivery and Enhanced Immune-Chemotherapy of Breast Cancer. *Adv. Funct. Mater.* 29, 1901896. doi:10.1002/adfm.201901896

Zhang, B.-F., Xing, L., Cui, P.-F., Wang, F.-Z., Xie, R.-L., Zhang, J.-L., et al. (2015). Mitochondria Apoptosis Pathway Synergistically Activated by Hierarchical Targeted Nanoparticles Co-delivering Sirna and Lonidamine. *Biomaterials* 61, 178–189. doi:10.1016/j.biomaterials.2015.05.027

Zhong, Y., Zhang, J., Zhang, J., Hou, Y., Chen, E., Huang, D., et al. (2021). Tumor Microenvironment-Activatable Nanoenzymes for Mechanical Remodeling of Extracellular Matrix and Enhanced Tumor Chemotherapy. *Adv. Funct. Mater.* 31, 2007544. doi:10.1002/adfm.202007544

Zong, L., Wang, H., Hou, X., Fu, L., Wang, P., Xu, H., et al. (2021). A Novel Gsh-Triggered Polymeric Nanomicelles for Reversing Mdr and Enhancing Antitumor Efficiency of Hydroxycamptothecin. *Int. J. Pharmaceutics* 600, 120528. doi:10.1016/j.ijpharm.2021.120528

Zong, L., Wang, Y., Qiao, P., Yu, K., Hou, X., Wang, P., et al. (2020). Reduction-sensitive Poly(ethylene Glycol)-Polypeptide Conjugate Micelles for Highly Efficient Intracellular Delivery and Enhanced Antitumor Efficacy of Hydroxycamptothecin. *Nanotechnology* 31, 165102. doi:10.1088/1361-6528/ab6749

Conflict of Interest: The authors declare that the research was conducted in the absence of any commercial or financial relationships that could be construed as a potential conflict of interest.

Publisher's Note: All claims expressed in this article are solely those of the authors and do not necessarily represent those of their affiliated organizations, or those of the publisher, the editors, and the reviewers. Any product that may be evaluated in this article, or claim that may be made by its manufacturer, is not guaranteed or endorsed by the publisher.

frontiers in Bioengineering and Biotechnology

ORIGINAL RESEARCH
published: 30 November 2021
doi: 10.3389/fbioe.2021.770121

Nitrate-Functionalized poly(ε-Caprolactone) Small-Diameter Vascular Grafts Enhance Vascular Regeneration *via* Sustained Release of Nitric Oxide

Sen Yang[1,2], Xueni Zheng[3,4], Meng Qian[3,4], He Wang[3,4], Fei Wang[3,4], Yongzhen Wei[3,4], Adam C. Midgley[3,4], Ju He[2], Hongyan Tian[1]* and Qiang Zhao[3,4,5]**

[1]Department of Peripheral Vascular Disease, First Affiliated Hospital of Xi'an Jiaotong University, Xi'an, China, [2]Department of Vascular Surgery, Tianjin First Central Hospital, Nankai University, Tianjin, China, [3]State Key Laboratory of Medicinal Chemical Biology, College of Life Sciences, Nankai University, Tianjin, China, [4]Key Laboratory of Bioactive Materials (Ministry of Education), College of Life Sciences, Nankai University, Tianjin, China, [5]Zhengzhou Cardiovascular Hospital and 7th People's Hospital of Zhengzhou, Zhengzhou, China

Artificial small-diameter vascular grafts (SDVG) fabricated from synthetic biodegradable polymers, such as poly(ε-caprolactone) (PCL), exhibit beneficial mechanical properties but are often faced with issues impacting their long-term graft success. Nitric oxide (NO) is an important physiological gasotransmitter with multiple roles in orchestrating vascular tissue function and regeneration. We fabricated a functional vascular graft by electrospinning of nitrate-functionalized poly(ε-caprolactone) that could release NO in a sustained manner via stepwise biotransformation *in vivo*. Nitrate-functionalized SDVG (PCL/NO) maintained patency following abdominal arterial replacement in rats. PCL/NO promoted cell infiltration at 3-months post-transplantation. In contrast, unmodified PCL SDVG showed slow cell in-growth and increased incidence of neointima formation. PCL/NO demonstrated improved endothelial cell (EC) alignment and luminal coverage, and more defined vascular smooth muscle cell (VSMC) layer, compared to unmodified PCL SDVG. In addition, release of NO stimulated Sca-1$^+$ vascular progenitor cells (VPCs) to differentiate and contribute to rapid luminal endothelialization. Furthermore, PCL/NO inhibited the differentiation of VPCs into osteopontin-positive cells, thereby preventing vascular calcification. Overall, PCL/NO demonstrated enhanced cell ingrowth, EC monolayer formation and VSMC layer regeneration; whilst inhibiting calcified plaque formation. Our results suggested that PCL/NO could serve as promising candidates for improved and long-term success of SDVG implants.

Keywords: small-diameter vascular grafts, nitric oxide, vascular regeneration, vascular progenitor cells (VPCs), vascular calcification

OPEN ACCESS

Edited by:
Yakai Feng,
Tianjin University, China

Reviewed by:
Katsuhiro Hosoyama,
Iwate Prefectural Central Hospital, Japan
Xin Jing,
Hunan University of Technology, China
Haifeng Liu,
Beihang University, China

****Correspondence:***
Adam C. Midgley
midgleyac@nankai.edu.cn
Hongyan Tian
tianhhyy@mail.xjtu.edu.cn
Qiang Zhao
qiangzhao@nankai.edu.cn

Specialty section:
This article was submitted to Biomaterials, a section of the journal Frontiers in Bioengineering and Biotechnology

Received: *03 September 2021*
Accepted: *04 November 2021*
Published: *30 November 2021*

Citation:
Yang S, Zheng X, Qian M, Wang H, Wang F, Wei Y, Midgley AC, He J, Tian H and Zhao Q (2021) Nitrate-Functionalized poly(ε-Caprolactone) Small-Diameter Vascular Grafts Enhance Vascular Regeneration via Sustained Release of Nitric Oxide. Front. Bioeng. Biotechnol. 9:770121. doi: 10.3389/fbioe.2021.770121

INTRODUCTION

Cardiovascular disease (CVD) is the leading cause of global mortality (Roth et al., 2015; Virani et al., 2021). CVDs are frequently associated with damaged vasculature, functional inadequacies of blood vessels, and peripheral arterial diseases. Surgical replacement of the dysfunctional blood vessels with autologous vessels, such as saphenous veins and radial internal mammary arteries, are considered the gold-standard option for intervention. However, limited availability of suitable donor vessels, donor site co-morbidities, infection risk, and prevalence of long-term graft complications necessitate the development of alternative options. Synthetic polymer vascular grafts, including expanded polytetrafluoroethylene (ePTFE; Teflon/GORE-TEX) and polyethylene terephthalate (PET; Dacron) tubular prosthetics, are clinically employed as large diameter vascular grafts, but fail to perform adequately when used as small diameter vascular grafts (SDVG; $\leq$ 6 mm). Explanations for high failure rates are largely related to immunogenicity, poor hemocompatibility of the materials, and lack of bioactivity; often resulting in thrombosis, intimal hyperplasia, atherosclerosis, calcification, infection, and subpar long-term patency (Greenwald and Berry, 2000; Zilla et al., 2007; Hadinata et al., 2009). Thus, progression in the bioengineering of artificial alternatives for SDVGs is driven by urgent necessity.

The use of polycaprolactone (PCL) to manufacture "off-the-shelf" vascular grafts yields biocompatible artificial SDVGs that exhibit patency and mechanical properties capable of withstanding arterial blood flow pressure (de Valence et al., 2012). In combination with the versatile technique of electrospinning, PCL can be processed into fibrous extracellular matrix (ECM)-like materials with fiber and pore diameters ranging from the micrometer to nanometer scale, which enables the tuning of structural scaffold mechanical properties and to facilitate cell attachment, migration, and bioactive factor or nutrient exchange (Park et al., 2019). However, PCL vascular grafts have slow degradation rates, poor hydrophilicity, and low bioactivity (Pektok et al., 2008; Valence et al., 2013; Yang et al., 2019). Therefore, cell ingrowth, vascularization, and ECM deposition is hampered in long-term implantation. The timely regeneration of a functional endothelium provides an antithrombotic interface (Ren et al., 2015) and regulates the formation of organized vascular smooth muscle cell (VSMC) layers during vessel remodeling (McCallinhart et al., 2020). Functionalization of PCL grafts can help achieve antithrombotic actions (Yao et al., 2014; Wei et al., 2019) until a functional endothelium has formed on the graft lumen. It is the consensus that endothelial cells (ECs) have a limited migration ability from anastomotic sites (Zheng et al., 2012). Thus, augmenting PCL SDVG bioactivity is necessary to achieve rapid re-endothelization and to limit occurrence of vascular complications.

Nitric oxide (NO) is a gasotransmitter and signaling molecule, endogenously produced by the endothelium. NO is essential in maintaining cardiovascular homeostasis (Yang et al., 2018) and dysfunctions in NO signaling is often an associated-complication of CVD pathologies (Erdmann et al., 2013). NO-based interventions were shown to attenuate myocardial infarction (Rassaf et al., 2014; Zhu et al., 2021), thrombus formation (Heusch, 2015; Heusch and Gersh, 2017; Yang et al., 2020a), and convey immunomodulatory and cardioprotective effects (Bogdan, 2001; Chouchani et al., 2013). NO release or generation mechanisms have been incorporated into multiple cardiovascular implants, including stents (Zhang et al., 2019; Yang et al., 2020b) and vascular grafts (Wang et al., 2015), with demonstratable benefits to the promotion of angiogenesis, re-endothelialization, and vascular tissue regeneration (Yang et al., 2015; Li et al., 2018; Kabirian et al., 2019). In addition to the l-arginine derived NO, generation of NO can be achieved from biotransformation of endogenous NO-donors, such as S-nitrosothiols and nitrates present in blood and tissues (Lundberg et al., 2008; Panesar, 2008; Lundberg et al., 2009; Qian et al., 2021). However, the bioavailability of circulating endogenous NO donors at any one time is finite and with the added complications of reactivity, short half-life, labile nature, and instability of NO (Nichols et al., 2012; Midgley et al., 2020), achieving long-term controlled release at efficacious concentrations by NO-generating/NO-donor functionalised vascular grafts remains a major clinical challenge.

Accumulating evidence have implicated NO in diverse regulatory effects on progenitor and stem cells, including impacting paracrine secretion patterns, and the production of growth factors and exosomes. (Bonafè et al., 2015; Midgley et al., 2020). In addition, endothelial nitric oxide synthase (eNOS) was implicated in the mobilization of stem and progenitor cells from cardiovascular niches (Aicher et al., 2003). In murine vessels, stem cell antigen-1 (Sca-1) expressing vascular progenitor cells (VPCs) in the adventitia were shown to migrate to the intima and contribute to vascular remodeling (Hu et al., 2004; Covas et al., 2005; Ingram et al., 2005). Sca-1$^+$ VPCs from the media of mouse abdominal aorta could differentiate into ECs or VSMCs in response to angiogenic growth factors *in vitro* (Sainz et al., 2006). Under stable physiological conditions *in vivo* Sca-1+ VPCs differentiate into a balanced ratio of EC:VSMC, which becomes dysregulated during vascular pathogenesis (Torsney and Xu, 2011). Cardiac resident Sca-1+ progenitor cells were implicated in contributing to cardiac vasculature regeneration, with involvement in EC expansion after myocardial infarction (Vagnozzi et al., 2018). Therefore, resident Sca-1$^+$ VPCs contribution to ECs and VSMCs during vascular tissue repair may be key events important in limiting the occurrence of intimal hyperplasia. Whether the vasoprotective effect of NO during vascular remodeling is associated with the modulation and participation of resident Sca-1$^+$ VPCs, is currently unknown.

In this study, we designed nitrate-functionalized vascular grafts based on a design concept that utilizes a blend of low-molecular weight nitrate-functionalized PCL polymers with high-molecular weight PCL. PCL/NO SDVGs were first tested for mechanical properties. Consistent and controlled long-term release of NO was modelled *in vitro* by incubation of grafts with enzymes to mimic *in vivo* biotransformation cascades. Rat abdominal aorta replacement models were used to assess the performance of implanted PCL/NO SDVG and to demonstrate the beneficial effects of sustained local NO delivery in the regeneration of vascular tissues. The capacity for PCL/NO SDVGs to induce

Sca-1^+ VPC recruitment and direct their differentiation into vascular cells during vascular regeneration was also assessed. The results of this study support the intention to establish NO-functionalized graft fabrication strategies for substantial clinical viability and improvement of long-term SDVG implant success.

MATERIALS AND METHODS

Fabrication of Nitrate-Functionalized Vascular Grafts

Briefly, PCL (M_n 80,000) was mixed with PCL-ONO_2 (M_n 2,000) at blending ratios of 9/1 (w/w), according to our previously published protocol (Zhu et al., 2021). The mixture was dissolved in mixed chloroform/methanol (5:1, v/v) by sufficient stirring to obtain homogeneous solution with a final concentration of 10% (w/v). Microfiber grafts were fabricated by electrospinning using a setup previously described with minor modification (Wei et al., 2019). Briefly, polymer solution was ejected at a continuous rate (2 ml/h) using a syringe pump through a stainless-steel needle (2 mm i.d.) and collected on a rotating stainless-steel mandrel. A high voltage (15 kV) was applied to the needle with a variable high-voltage power supplier. Electrospinning continued until scaffold wall thickness reached approximately 350 μm. The resulting scaffold was then removed from the mandrel and placed into a vacuum overnight to remove the residual solvent. Prior to use in experiments, the grafts were sterilized by immersion in 75% ethanol for 30 min, and then exposed to UV light overnight.

Characterization and Composition

The surface morphology of electrospun mats was observed under a field emission scanning electron microscopy (SEM; Quanta 200, Czech Republic) at an accelerating voltage of 10 KV. The surface was sputter-coated with gold before observation. The surface chemistry was characterized using Fourier transform infrared spectroscopy (FTIR) and at a single attenuated total reflectance (ATR) mode (Bio-Rad FTS 6000 Spectrometer: spectral resolution, 8 cm^{-1}). The PCL mats were subjected to energy dispersive X-ray spectroscopy (EDS) using a Quanta FEI 650 device (Quanta FEI). The quantification of elements (C, N, O) in the region struck by the rapid electron were determined graphically.

Mechanical Tests

The mechanical properties of the scaffolds were assessed by a tensile-testing machine with a load capacity of 1 kN (Instron). Samples with 6.28 mm width, 350 μm thickness, and 2 cm length in each scaffold group (n = 3) were prepared. The inter-clamp distance was set as 1 cm, and then, samples were pulled longitudinally at a rate of 10 mm/min until rupture. The stress-strain curves of the scaffolds were recorded. The Young's modulus was calculated based on the slope of the stress-strain curve in the elastic region. Burst pressure was measured by filling a graft segment (3 cm length) with soft paraffin (Vaseline) whilst clamping one end and hermetically sealing the other with a vascular catheter. A constant filling rate of 0.1 ml/min was applied, and the filling pressure was recorded until the graft wall burst.

NO Release From PCL/NO Grafts

The NO releasing profile was determined by 3-Amino, 4-aminomethyl-2′, 7′-difluorescein, diacetate (DAF-FM) probe (Beyotime, China) according to the manufacturer's protocol. Briefly, 6 mg of nitrate-functionalized materials were put into 2 ml of PBS buffer (pH 7.4) containing DAF-FM (5 μM), and muscular homogenate or peritoneal fluid were added at certain concentration to act as catalyst for the NO generation, respectively. After pre-determined time interval, solution was transferred into 96-well plates, and the fluorescence intensity was measured by a microplate reader (Synergy 4-BioTek, USA).

In vitro Nitrate Release

10 mg nitrate-functionalized materials were incubated in PBS buffer at 37°C. The production of nitrate was evaluated according to the Griess method using the Total Nitric Oxide Assay Kit (Beyotime Biotechnology, S0023). The optical density was measured at 540 nm, and the amount of nitrate was determined using sodium nitrate as a reference standard.

Measurement of NO Generation From Nitrates

$NaNO_3$ was dissolved into 2 ml of PBS, or the muscular homogenate or peritoneal fluid at a final concentration of 200 μM. Samples were placed on a shaker at 37°C and the NO generation was determined by DAF-FM probe. After pre-determined time interval, solution was transferred into 96-well plates, and the fluorescence intensity was measured by a microplate reader (Synergy 4-BioTek, USA).

In vivo Implantation

The use of experimental animals was approved by the Animal Experiments Ethical Committee of Nankai University and carried out in conformity with the Guide for Care and Use of Laboratory Animals. The procedure was carried out as described previously. In brief, rats were anesthetized with chloral hydrate (300 mg/kg) by an intraperitoneal injection. Heparin (100 units/kg) was administered for anticoagulation by tail vein injection before surgery. A midline laparotomy incision was then performed, and the abdominal aorta was isolated, clamped, and transected. The tubular PCL grafts (2.0 mm in inner diameter and 1.0 cm in length) were sewn in an end-to-end fashion with 8–10 interrupted stitches using 9–0 monofilament nylon sutures (Yuan Hong, Shanghai, China). No anticoagulation drug was administered to the rats after surgery. At the predetermined time points (1 and 3 months), the patency and blood velocity of the grafts was visualized by high-resolution ultrasound (Vevo 2100 System, Canada) after the rats were anesthetized with isoflurane.

Histological Analysis

After 3 months, animals were sacrificed by injection of overdose chloral hydrate. Subsequently, grafts were explanted, rinsed with saline, and cut into two parts from the middle. One part was sectioned into suture-site, quartile, and middle segments (1.5 mm) for frozen cross-sectioning. The other half was longitudinally cut into two pieces. One piece was first observed by stereomicroscope,

and then for frozen longitudinal section. The other piece was processed for SEM examination.

Briefly, the samples were fixed with 2.5% glutaraldehyde overnight, and dehydrated in a sequence of ethanol solutions for 5 min each. After air-drying at room temperature, samples were mounted onto aluminium stubs and then sputter-coated with gold for SEM.

After embedded in OCT and snap-frozen in liquid nitrogen, the samples were cryo-sectioned to 6 mm in thickness. Subsequently, sections were stained with H&E (Legend) or von Kossa (Legend) using standard histological methods. Images were observed under an upright microscope using a 4×, 10× or 20× objective lens (Leica, Germany), photographed and then analysed using ImageJ software (1.8.0, NIH, Bethesda, MD, USA).

For immunofluorescent staining, the frozen sections were fixed in cold acetone for 10 min, air-dried, and rinsed once with 0.01 mM PBS. Then slides were incubated in 5% normal goat serum (Zhongshan Golden bridge Biotechnology, China) for 45 min at 4 C. For intracellular antigen staining, 0.1% Triton-PBS was used to permeate the membrane before incubation with serum. Then the sections were incubated with primary antibodies in PBS overnight at 4 C, followed by incubation with secondary antibody in PBS for 2 h at room temperature. The nuclei were counterstained with 4,6-diamidino-2-phenylindole (DAPI) containing mounting solution (DAPI Fluoromount G, Southern Biotech, UK).

Endothelial cell staining was performed using monoclonal mouse anti-CD31 (Abcam, 1:100) primary antibody. The smooth muscle cells were stained using rabbit anti-α-SMA (Abcam, 1:100) and mouse anti-smooth muscle myosin heavy chain (SM-MHC, Santa Cruz, 1:100) primary antibodies. Rabbit anti-Sca-1 (Abcam, 1:100) was used to visualize vascular progenitor cells. Goat anti-mouse IgG (1:200, Invitrogen) and goat anti-rabbit IgG (1:200, Invitrogen) were used as the secondary antibodies. Sections that were not incubated with primary antibodies were used as negative controls to assess and eliminate background staining. Immunohistochemistry images were captured by fluorescence microscope (Zeiss Axio Imager Z1, Germany) and analysed by ImageJ software (1.8.0 NIH). Endothelial coverage rate was calculated according to the following equation:

$$\text{Endothelial coverage}\,(\%) = \frac{\text{Length of CD31 labelled endothelium}\,(\mu\text{m})}{\text{Total length of longitudinal graft section}\,(\mu\text{m})} \times 100$$

Four sections per sample and four samples per group were included to obtain the statistical results.

Statistical Analysis

All quantitative *in vitro* results were obtained from at least three samples for analysis. All qualitative and quantitative *in vivo* results were obtained from at least four animal per experimental group. GraphPad Prism software v5.0 (San Diego, CA, USA) was used for statistical analysis. Student's *t*-tests were used for comparisons of means between two groups. Comparisons of means among three or more groups were done by one-way ANOVA and for grouped data with two or more variables, two-way ANOVA was performed. Differences were considered significant at $^{*}p$ =<0.05 and $^{**}p$ = <0.01.

RESULTS

Characterization of Nitrate-Functionalized PCL Vascular Grafts

Fabricated PCL and PCL/NO SDVGs were successfully prepared by electrospinning (**Figure 1A**) and visualized by SEM (**Figure 1B**). SDVGs exhibited homogenously distributed fibers within the graft. The tubular SDVGs had regular and uniform structure with inner diameters of 2 mm. The SDVGs possessed well-defined fiber morphology, and the average fiber diameter of PCL and PCL/NO SDVGs was 5.62 ± 0.36 μm and 5.36 ± 0.63 μm, respectively (**Figure 1C**). EDS analysis demonstrated an elevated nitrogen peak within the PCL/NO graft group, indicating the increased nitrogen content (-ONO_2) (**Figure 1D**). Furthermore, FTIR verified incorporation of -ONO_2 groups in the PCL/NO grafts, as evidenced by characteristic NO_2 group peak (1,660 cm^{-1}), which was only present in the PCL/NO graft group (**Figure 1E**). The assessed burst pressure of the PCL and PCL/NO grafts showed that there was no significant difference between the PCL and PCL/NO grafts. Both grafts demonstrated burst pressure values above the 1,600 mmHg threshold for withstanding arterial pressure (**Figure 1F**). Mechanical testing indicated that PCL/NO had a non-significant tendency to exhibit lower tensile strength and elongation at break than PCL, whereas calculated Young's moduli of PCL/NO SDVGs also showed no significance difference compared to PCL (**Figure 1G**). The *in vitro* release of NO from nitrate-functionalized SDVGs was first evaluated by NO fluorescent probe (DAF), and generation of NO was detected in the PBS buffer with the addition of peritoneal fluid or muscular homogenate (**Figure 1H**), suggesting that the biotransformation is catalyzed by the relevant enzymes in the abdominal microenvironment where the graft was implanted. To get further insight into the transformation mechanism, the hydrolysis of nitrate-functionalized SDVGs in PBS was investigated. Nitrate ions (NO_3^-) were the main hydrolysis product, and the release of NO_3^- demonstrated a sustained and linear accumulated release profile over 30 days (**Figure 1I**). The released NO_3^- could be further reduced to NO under the catalysis of reductase present in the muscle instead of abdominal fluid (**Figure 1J**). These results suggested that the biotransformation of nitrate-functionalized PCL may proceed through two distinct pathways. First, it could be reduced directly into NO by the reductase in the peritoneal fluid, similar to the transformation of organic nitrates, such as GTN (Ferreira and Mochly-Rosen, 2012). Additionally, as a macromolecular nitrate, PCL-ONO_2 undergoes non-enzymatic hydrolysis to release nitrate anion. Then, the generated nitrate anions are further reduced to release NO via the NO_3→NO2→NO sequential pathway under the catalysis of reductase within muscular tissues (Zhu et al., 2021).

In vivo Implantation and Performance of Nitrate-Functionalized PCL Vascular Grafts

The fabricated SDVGs were assessed for 3-months *in vivo* performance using a rat abdominal artery replacement model (**Figure 2A**). After 3 months of implantation time, the patency

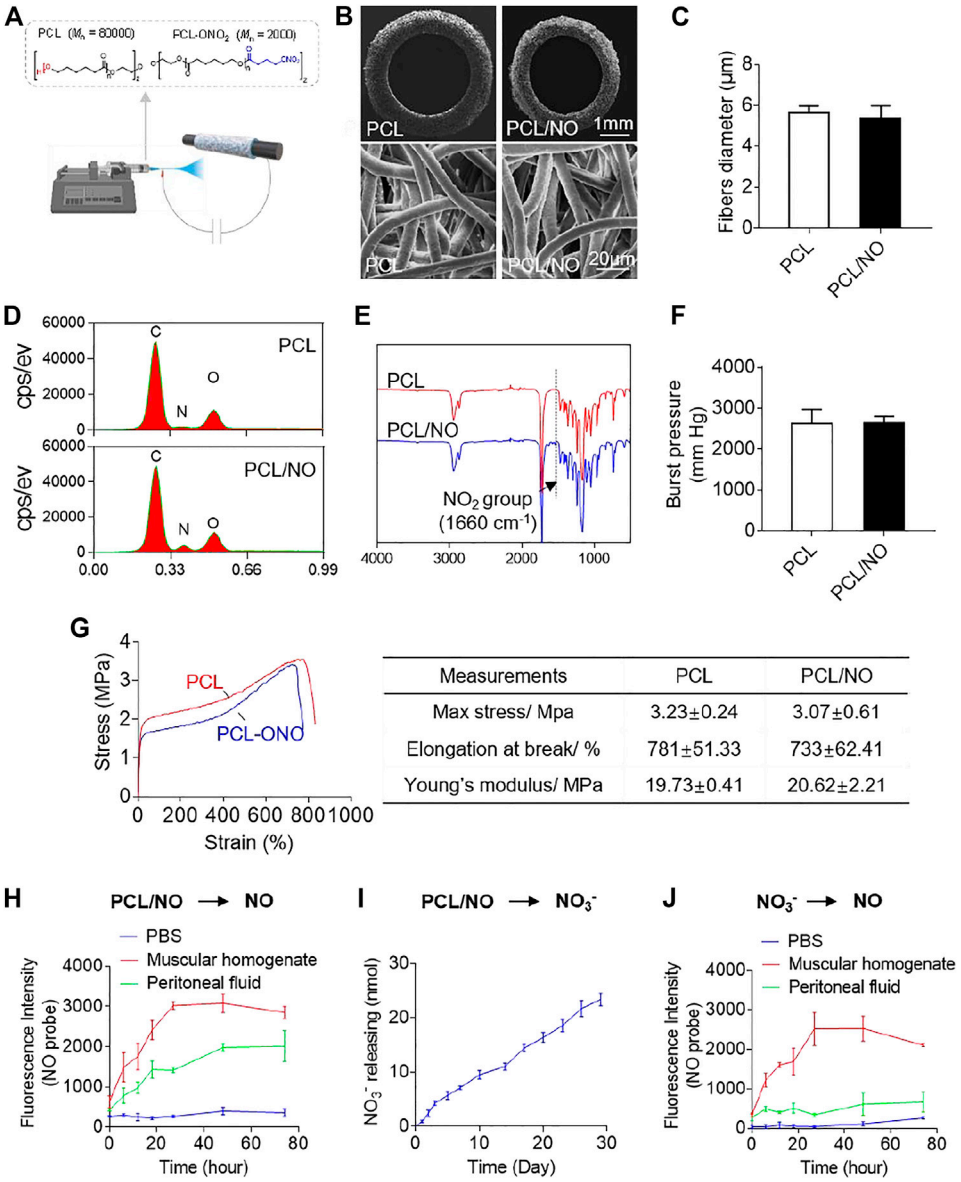

Measurements	PCL	PCL/NO
Max stress/ Mpa	3.23±0.24	3.07±0.61
Elongation at break/ %	781±51.33	733±62.41
Young's modulus/ MPa	19.73±0.41	20.62±2.21

FIGURE 1 | Fabrication and characterization of nitrate-functionalized SDVGs. **(A)** Schematic illustrating the PCL/NO SDVG synthesis by electrospinning of PCL blends. **(B)** SEM images of SDVG enface cross-sections (**top row**; scale bar = 1 mm) and surface networks of PCL microfibers (**bottom row**; scale bar = 20 μm). **(C)** Average PCL microfiber diameter in PCL and PCL/NO SDVGs. (D) EDS analysis of the SDVGs demonstrating an elevated nitrogen-peak in PCL/NO. (E) FTIR analysis of the SDVGs demonstrating the presence of NO2 groups (1,660 cm-1) in PCL/NO grafts. **(F)** The burst pressure of the SDVGs. **(G)** Representative stress-strain curves of the PCL and PCL/NO vascular grafts and the quantitative analysis of mechanical properties shown in the table alongside. Data presented as mean ± S.E.M. **(H)** NO generation from PCL/NO in the presence of muscular homogenate (20 mg/ml) or peritoneal fluid was detected by DAF-FM *in vitro*. **(I)** The long-term and slow accumulative release of nitrate and nitrite ions from SDVGs over 30 days in PBS buffer. **(J)** Reduction of NO3– into NO in the presence of muscular homogenate (20 mg/ml) or peritoneal fluid. Images and data are representative of n = 3 independent experiments.

rates of both SDVGs were 4/4, and excised grafts showed no sign of material rupture, structural deformation, or stenosis after 3 months of implantation time (**Figure 2B**). Immunohistochemistry staining of DAPI in SDVG enface cross-sections (**Figure 2C**) demonstrated a significantly enhanced cellular infiltration at 0–150 μm and 150–300 μm depths from the luminal surface by 1 month in PCL/NO SDVGs compared to PCL SDVGs, and by 3 months post-implantation the cell numbers within grafts were consistent amongst both grafts and at the assessed graft depths (**Figure 2D**). H&E staining showed that PCL SDVGs developed a thin neointimal layer at 1 and 3 months after implantation, whereas a thicker neointimal tissue layer was present in PCL/NO SDVGs at 1 and 3 months after implantation (**Figure 2E**). The average neointimal thickness of PCL/NO was significantly greater than that in the PCL group (**Figure 2F**), whereas luminal diameter (**Figure 2G**) remained unchnaged at 1- and 3-months in both graft groups. The results

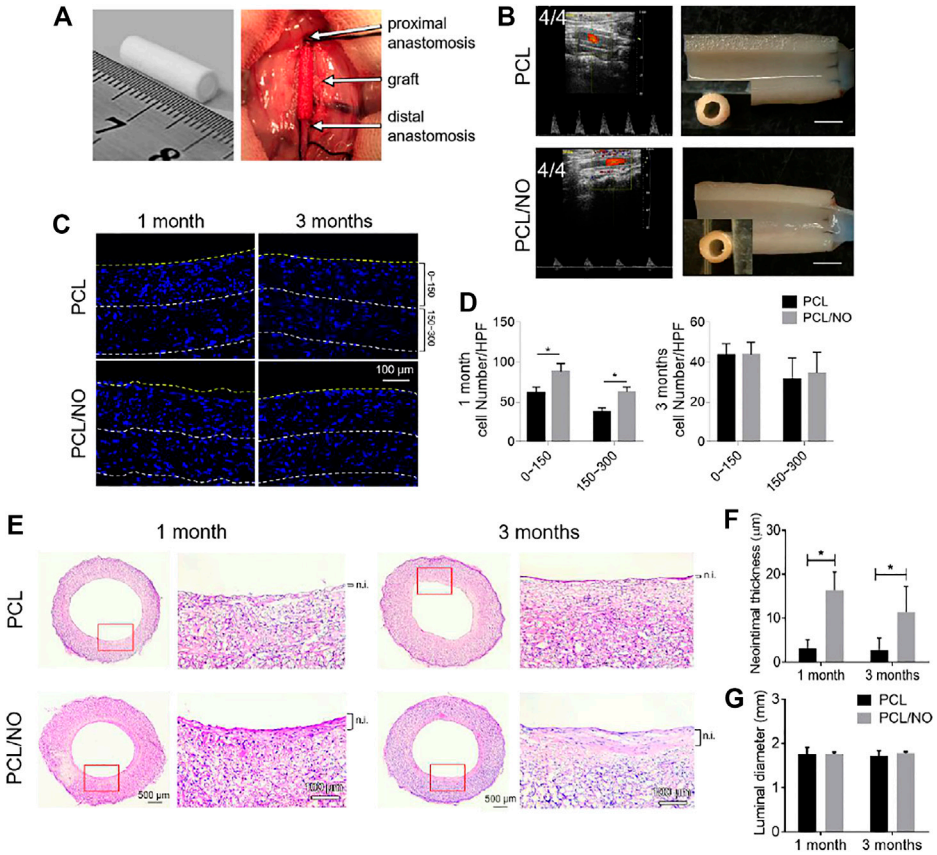

FIGURE 2 | *In vivo* performance of SDVGs in abdominal aorta replacement rat models. **(A)** Photographic representation of fabricated grafts **(left)** and surgical implantation and anastomosis of SDVGs in rat abdominal aortae **(right)**. **(B)** High-resolution ultrasound imaging of implanted SDVGs at 3 months, patency rating inset **(left panels)**. Longitudinally cut transections of SDVGs and observation by stereomicroscope, inset panels are stereomicroscope images of enface cross-sections before transection, scale bars = 2 mm **(right panels)**. **(C)** DAPI stained sections of SDVGs at 1- and 3-months post-implantation to visualize cell infiltration at 0–150 μm and 150–300 μm graft depths. Yellow dashed line indicates the graft lumen surface, white dashed lines indicate 150 and 300 μm depths from the lumen surface. Scale bar = 100 μm. **(D)** The average cell number per high-powered field (HPF) within different SDVG depths at 1 month **(left)** and 3 months **(right)**. **(E)** H&E staining of enface SDVG sections. Scale bars = 500 μm. Red boxes indicate the view shown in zoomed images alongside each panel. Scale bars = 100 μm. The neointima (n.i.) is labeled alongside zoomed panels. Calculated **(F)** average neointimal thickness and **(G)** luminal diameter of PCL and PCL/NO SDVGs at 1- and 3-months post-implantation. Images and data are representative of $n = 4$ independent experiments.

indicated that PCL/NO SDVGs promoted cell infiltration and accelerated neointimal formation whilst maintaining graft structure and performance.

Nitrate-Functionalized Grafts Have Enhanced Endothelium Coverage

To assess the degree of SDVG endothelialization, SEM was used to visualize endothelial coverage on the luminal surface (**Figure 3A**). At 1 month, PCL and PCL/NO demonstrated a degree of cell coverage; at the mid-, quarter-, and suture-sites. PCL microfibers could still be identified, but less so in the suture site segments of the lumens. At 3 months, PCL microfiber structures could be seen at the mid and quarter site of the PCL graft lumen, but EC coverage was evident and was improved at the suture site. The majority of the lumen sections in PCL/NO grafts exhibited ECs with tight cell junctions aligned to the blood flow direction, and individual PCL microfiber structures were difficult to detect. Immunofluorescence staining for the EC marker, CD31 (**Figure 3B**), confirmed the observations made from SEM. Quantification and statistical analysis of EC coverage indicated that PCL/NO SDVGs significantly improved endothelial coverage at 1-month post-implantation, and there were no statistically significant differences detected in EC coverage between the two grafts after 3 months of implantation time (**Figure 3C**). These results suggested that PCL/NO SDVGs promoted the earlier formation of an endothelium in the graft lumen, compared to PCL SDVGs.

Nitrate-Functionalized Grafts Improve the Formation of an Organized VSMC Layer

To evaluate vascular smooth muscle regeneration, fluorescence immunohistochemistry was performed to visualize α-smooth muscle actin (α-SMA) expressing VSMCs (**Figure 4A**). At

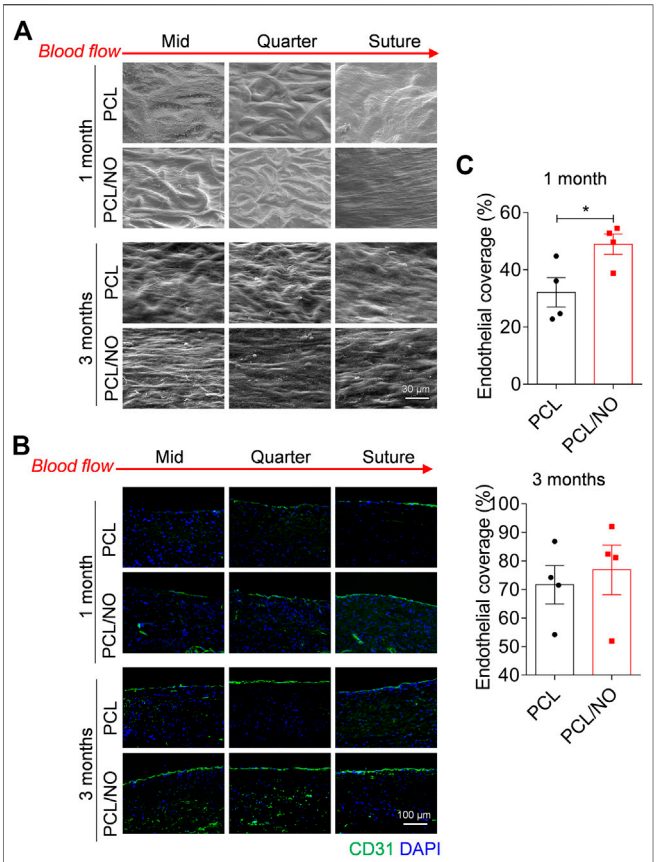

FIGURE 3 | Sustained NO release from nitrate-functionalized SDVGs increases endothelialization. **(A)** SEM images of the luminal surface of the SDVGs at the mid-, quarter- and suture-site segments after 1 month and after 3 months (scale bars = 30 μm). Images orientated to blood flow direction. Red dashed boxes indicate location of zoomed inset images outline in red. **(B)** CD31 staining of endothelial cells within transverse sections of the SDVGs at the mid-, quarter- and suture-site segments after 1 month **(top rows)** and after 3 months **(bottom rows)**. Images orientated to blood flow direction. Scale bars = 100 μm. **(C)** Quantification of the average percentage of endothelial cell monolayer coverage of SDVG lumens at 1 month **(top)** and at 3 months **(bottom)**. Images and data are representative of $n = 4$ independent experiments.

1 month, a layer of uniformly distributed α-SMA$^+$ cells formed in the PCL/NO group, whereas a thin layer of α-SMA$^+$ cells formed in the PCL group. At 3 months, the PCL/NO maintained a compact and uniform α-SMA$^+$ cell layer. In contrast, a thin layer of α-SMA$^+$ cells remained present in the PCL group and an abundance of α-SMA$^+$ cells were present in the SDVG wall. The α-SMA$^+$ cell layer was significantly thicker than in the control group at both time points (**Figure 4B**). The sections were stained to visualize smooth muscle myosin heavy chain (SM-MHC), a marker of mature and contractile VSMCs (**Figure 4C**). The results indicated that in the PCL group, a thin SM-MHC$^+$ layer had formed but a large amount of SM-MHC$^+$ cells were present throughout the SDVG wall at 1-month post-implantation. At 3 months, the PCL group displayed a more uniform layer of SM-MHC$^+$ VSMCs, but the layer remained thin. In contrast, the PCL/NO group exhibited thicker uniform layers of SM-MHC$^+$ cells at both 1- and 3-months post-implantation. The SM-MHC$^+$ VSMCs in the PCL/NO group showed superior thickness to the PCL group (**Figures 4D**) and similarities in thickness and organisation to the α-SMA$^+$ cell layer at 3 months, suggesting that the VSMCs in the neo-tissue possessed the contractile phenotype. These results demonstrated that NO release from PCL SDVGs enhanced the regeneration of contractile VSMC layers.

Nitrate-Functionalized Grafts Promote Sca-1$^+$ VPC Recruitment and Contribution to Vascular Regeneration

The effect of NO release on the recruitment of Sca-1$^+$ VPCs was assessed at 3-months post-implantation by immunohistochemistry (**Figure 5A**). Infiltration of Sca-1$^+$ VPCs into the SDVG walls was detectable in both graft groups. The release of NO enhanced the recruitment of Sca-1$^+$ VPCs into the PCL/NO SDVGs, resulting in a significantly greater number of cells compared to the PCL group. Co-immunostaining for CD31 and Sca-1 demonstrated that a proportion of the Sca-1$^+$ cells differentiated into ECs and contributed to the formation of the endothelium (**Figure 5B**). Sca-1$^+$ cells co-expressing CD31 were most evident in the PCL/NO group, within the SDVG walls and within the endothelium, as evidenced by double-positive staining. Co-immunostaining for α-SMA and Sca-1 showed that a proportion of the Sca-1$^+$ cells differentiated into VSMCs and contributed to the formation of the smooth muscle layer in both SDVG groups (**Figure 5C**). Vascular graft calcification is a common feature of pathogenesis associated with long-term implantation (de Valence et al., 2012; Jiang et al., 2017). Co-immunostaining to visualize Sca-1 and osteogenic marker osteopontin (OPN) revealed that a small proportion of Sca-1$^+$ VPCs has differentiated to OPN$^+$ cells in PCL SDVGs, and that there were significantly greater numbers of Sca-1$^+$/OPN$^+$ cells than in PCL/NO SDVGs, which were largely absent of OPN expressing cells (**Figure 6A**). Quantification of Sca-1$^+$ VPCs co-expressing the different cell markers indicated that there were no statistically significant differences between Sca-1$^+$/α-SMA$^+$ VSMC numbers in PCL and PCL/NO groups. However, there were significantly more Sca-1$^+$/CD31$^+$ EC numbers and significantly fewer Sca-1$^+$/OPN$^+$ osteogenic cells in the PCL/NO group, compared to the PCL group (**Figure 6B**). Von Kossa staining for calcified tissues in SDVGs at 3 months post-implantation indicated that calcification was present in PCL SDVGs sections but largely absent in the majority of PCL/NO SDVGs sections (**Figures 6C,D**). However, quantification of calcified area was variable in the PCL SDVGs, indicating no statistically significant differences between PCL and PCL/NO SDVG groups. These results suggested that NO was vasculoprotective by inducing VPC differentiation into vascular cells and that NO may inhibit VPC differentiation to osteoblastic lineages, thereby enhancing vascular regeneration and limiting calcification.

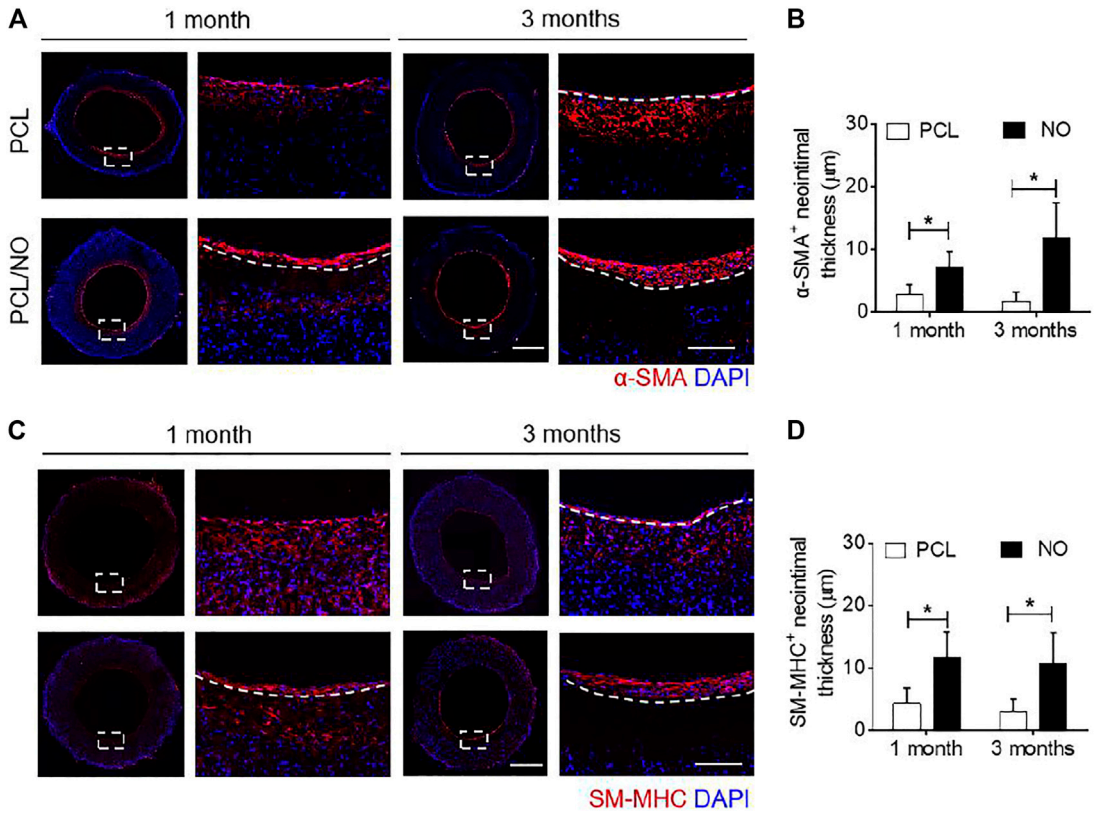

FIGURE 4 | Sustained NO release from nitrate-functionalized SDVGs enhances the formation of an organized VSMC layer. **(A)** Immunohistochemical staining of SDVG enface sections (**left panels**, scale bar = 1 mm; **right panels**, scale bar = 100 μm) for α-SMA expression at 1- and 3-months post-implantation. **(B)** Quantification of average α-SMA$^+$ neointimal thickness. **(C)** Immunohistochemical staining of SDVG enface sections (**left panels**, scale bar = 1 mm; **right panels**, scale bar = 100 μm) for SM-MHC expression at 1- and 3-months post-implantation. **(D)** Quantification of average SM-MHC$^+$ neointimal layer thickness. Images and data are representative of n = 4 independent experiments. White dashed line boxes indicate zoomed area. White dashed line borders indicate the graft wall.

DISCUSSION

Development of functional SDVGs with improved long-term outcomes remains a clinical demand. In physiological tissue microenvironments, NO is a crucial gasotransmitter and signalling molecule, which is continuously produced and released by ECs within the blood vessel lumens (de Mel et al., 2011). Previous studies have focused on developing NO-releasing or NO-generating materials (Enayati et al., 2021). The sustained release of NO was shown to markedly inhibit platelet adhesion and thrombus formation (Gkaliagkousi et al., 2009; Zhao et al., 2013). Our previous work further showed that NO release from vascular grafts improved tissue regeneration, remodelling, and physiological function (Wang et al., 2015). However, challenges associated with exogenous NO delivery include burst release, dose-dependent toxicity, and short half-life and diffusion distance of NO released for donors, which ultimately has restricted the commercialization of NO releasing materials (Panesar, 2008). In the present study, organic nitrates were utilized as NO donor compounds. It has been extensively demonstrated that organic nitrates undergo biotransformation to NO through different enzymatic pathways (Zhu et al., 2021). Therefore, we hypothesized that NO release from nitrate functionalized SDVGs would provide beneficial effects on the promotion of vascular regeneration whilst inhibiting the incidence of graft failure. Results showed that NO improved the regeneration of vascular grafts after 3 months of implantation, consistent with trends observed previously (Kabirian et al., 2019; Enayati et al., 2021). Overall, the prolonged, low-level release of NO achieved by PCL/NO SDVGs provided endothelium-mimicry to the graft lumen, whilst regulating VPC regeneration of the EC and VSMC layers, thus achieving markedly improved vascular regeneration, whilst minimizing the occurrence of pathological tissue remodelling.

Within the past 2 decades, several types of vascular stem cells, in addition to circulating progenitors, have been identified and characterized, with evidence that they are not only involved, but also play pivotal contributory roles in blood vessel remodelling and disease development (Wang et al., 2018; Zhang et al., 2018). Vascular tissue-resident stem cells, or vascular progenitor cells (VPCs), have been discovered to display the capacity to differentiate into vascular cell lineages, which may also contribute to the regenerative process post-graft implantation. Sca-1$^+$ vascular progenitor cells (VPCs) can contribute to EC and VSMC populations during vascular remodelling (Torsney and Xu, 2011) and are important cell source mediating tissue

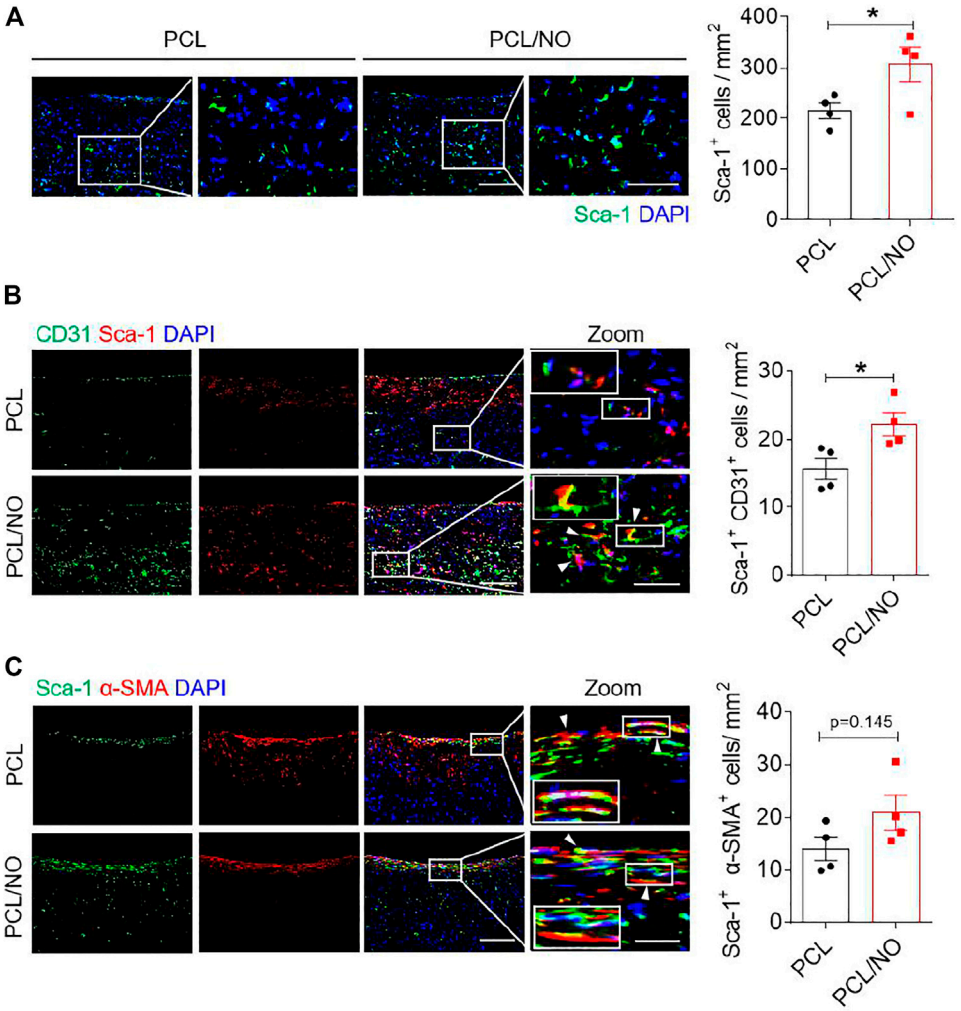

FIGURE 5 | Sustained NO release from nitrate-functionalized SDVGs promotes Sca-1$^+$ VPC differentiation into EC and VSMCs. **(A)** Immunohistochemical staining for Sca-1$^+$ VPCs in SDVGs. Scale bar = 100 μm. The quantification of Sca-1$^+$ VPCs per 1 mm^2 section area is shown alongside. **(B)** Immunohistochemical staining for Sca-1$^+$ (red)/CD31$^+$ (green) ECs in SDVGs after 3 months. Scale bar = 100 μm. The quantification of Sca-1$^+$/CD31$^+$ ECs per 1 mm^2 area at 3 months post-implantation is shown alongside. **(C)** Immunohistochemical staining for Sca-1$^+$ (green)/α-SMA$^+$ (red) VSMCs in SDVGs at 3 months post-implantation. Scale bar = 100 μm. White arrow heads indicate double-positive staining in cells. White boxes indicate the position of the inset zoomed images. The quantification of Sca-1$^+$/α-SMA$^+$ VSMCs per 1 mm^2 area at 3 months post-implantation is shown alongside. Images and data are representative of n = 4 independent experiments.

regeneration of vascular grafts (Issa Bhaloo et al., 2018). In this work, we investigated the fates of Sca-1$^+$ VPCs in the NO-enriched vascular tissue microenvironment. Sca-1$^+$ VPCs are resident to the adventitial layer of the vessel walls with described roles in regeneration of blood vessels following vascular injury, but also to pathological remodelling (Hu et al., 2004). Genetic lineage tracing suggested that Sca-1 expressing VSMCs constituted over 40% of the VSMCs in the vessel wall during recovery of vessel injury. Under homeostasis and after wire injury, pre-existing VSMCs were the major source for VSMC expansion, but after significant loss of local VSMCs, VPCs from the adventitia appear to act as the source of new VSMCs in vascular repair and regeneration (Hu et al., 2004; Roostalu et al., 2018; Tang et al., 2020). Disruption of the elastic lamellae is suggested to be an important requirement that facilitates migration of adventitial VPCs to the media and intima (Psaltis and Simari, 2015; Zhang et al., 2018). This is likely to occur in human vascular pathologies and surgeries, such as transplant vasculopathy, vein graft arteriosclerosis and artificial vascular graft implantation. Our previous work demonstrated that the adventitial resident VPCs played a major role in the vascular graft regeneration (Issa Bhaloo et al., 2018; Pan et al., 2018), via migration toward the vessel graft and differentiation into ECs or VSMCs, respectively. Indeed, in the present study, we showed that following SDVG implantation, a population of Sca-1$^+$ differentiated to ECs in the presence of sustained NO release; VSMCs regardless of NO release; and osteogenic lineages in the absence of NO release. The former is supported by our previous studies that demonstrated that Sca-1$^+$/CD31$^+$ cells migrated from the surrounding tissue to the midportion of the vascular grafts

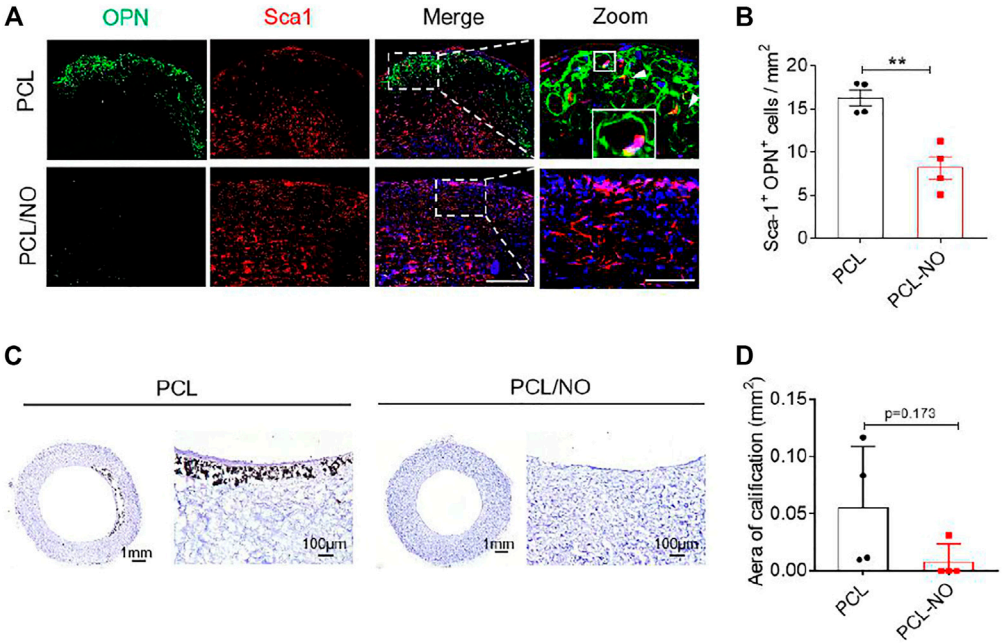

FIGURE 6 | Sustained NO release from nitrate-functionalized SDVGs inhibits vascular calcification. **(A)** Immunohistochemical staining of cross sections (scale bar = 100 μm) for OPN (osteogenic cells, green) and Sca-1 (vascular progenitor cells, red). White boxes indicate area of magnified images (scale bar = 20 μm), white box shows area of inset enlarged image of positive staining around a PCL microfiber. **(B)** Quantification of Sca-1$^+$/OPN$^+$ cells per 1 mm^2 area at 3 months post-implantation. **(C)** Histochemical staining of SDVG (left panels, scale bar = 1 mm; right panels, scale bar = 100 μm) sections with Von Kossa stain to visualize calcified plaque formation. **(D)** Quantification of the area of calcification present in SDVG sections at 3 months post-implantation. Images and data are representative of n = 4 independent experiments.

under favourable conditions (Pan et al., 2018). The latter may be indicative of material influence over cell infiltration and activation. Nonetheless, our study demonstrated that sustained release of NO exhibited a governance over Sca-1$^+$ fate.

NO has been reported to play roles in modifying stem cell behaviours, such as survival, migration, proliferation, differentiation, and apoptosis (Midgley et al., 2020). Previously, it was demonstrated that NO signalling was important in the endothelial differentiation of embryonic stem cells (Nie et al., 2017). The relationship between NO and its influence over Sca-1+ VPC migration and fate has not previously been thoroughly investigated, especially in the context of vascular graft implantation. This study provides evidence that adds to the increasing pool of information suggestive of the importance of NO in directing Sca-1+ VPC differentiation into ECs and VSMCs during vascular regeneration. Indeed, we showed that the facilitation of local NO levels increased the number of CD31$^+$ cells that co-expressed Sca-1$^+$. However, there was a presence of a Sca-1$^+$ VPC population that did not express CD31 or α-SMA, which raises the question about whether these cells contributed to vascular tissue regeneration in different way, whether directly or passively. Additionally, it is still unknown whether the increased recruitment of Sca-1$^+$ specifically to the graft site was dependent on NO across the 3 months of implantation time assessed. Deeper exploration of the full extent of Sca-1$^+$ VPC contribution, recruitment mechanisms, and relation to vascular graft success would form suitable research directions for future investigations.

Vascular calcification is a prominent contributor to cardiovascular morbidity and mortality (Paloian and Giachelli, 2014). Once considered a passive precipitative process, it is now appreciated that vascular calcification is an active cell-mediated process with striking resemblance to osteogenesis (Shroff et al., 2013). Previous studies have shown that Sca-1$^+$ (Sca-1$^+$/PDGFRα$^+$ and Sca-1$^+$/PDGFRα$^-$) stem/progenitor cells exhibit osteoblastic differentiation potential (Cho et al., 2013; Kramann et al., 2016). These findings suggest that a subtype of vessel-resident progenitor cells offer a promising therapeutic target for the prevention of vascular calcification. Indeed, Sca-1$^+$ VPCs were reported to contribute to osteoblastic lineages that drive the formation of calcified plaques (Cho et al., 2013). Here we found that following local generation of NO from grafts, numbers of Sca-1$^+$/OPN$^+$ cells were decreased in the vascular wall, which implied that NO inhibit vascular grafts calcification via a modulation of Sca-1$^+$ VPC behaviour. The detailed molecular mechanisms of this action remained to be elucidated.

Long-term evaluation beyond the point of complete PCL degradation is rarely performed in pre-clinical studies, and this represents a key area of the research field that is lacking strong evidence in the favour of clinical adoption of PCL vascular grafts. Classic approaches to arterial substitutes prefer the use of mechanically strong materials (Niklason et al., 1999). However, biodegradability also offers an advantage for tissue remodelling and regeneration (Wu et al., 2012). Ideally, graft materials should degrade gradually in tandem with the synthesis of new ECM by

the graft-populating cells, eventually resulting in a completely regenerated and polymer-free artery. Electrospun PCL vascular grafts are attractive candidates for off-the-shelf and readily available artificial vascular grafts, especially in terms of maintained patency, mechanical properties, and rapid endothelialization (Pektok et al., 2008), but PCL does have shortcomings, such as widely reported insufficiencies in facilitation of late-stage tissue remodelling and regeneration of the vascular wall, often leading to hyperplasia and calcification (de Valence et al., 2012). Therefore, integration of additional biological cues into the PCL fiber structure have formed a major focus in the development of artificial vascular grafts, and ultimately aims to achieve clinical success through the *in-situ* tissue engineering of arterial tissues. Here, we identified that NO release served as a beneficial cue for tissue regeneration in rats. However, there remains a requirement to perform extended studies in future investigations to address whether PCL/NO grafts regenerate structural and functional arterial tissue with the capability to resist arterial pressure and maintain long-term patency, beyond the point of complete PCL microfiber degradation [estimated to take 18–24 months (de Valence et al., 2012)]. Indeed, larger animal models become a necessity when assessing performance of regenerated vascular tissues after the completion of the PCL biodegradation term.

In summary, nitrate-functionalized SDVGs were successfully developed and achieved localised delivery of NO to the transplant site. In rat abdominal aorta replacement models, transplant of PCL/NO SDVGs demonstrated therapeutic efficacy, including maintenance of vessel patency and enhanced vascular regeneration, characterized by earlier regeneration of endothelium and organised smooth muscle layers, compared to PCL SDVGs. The remarkable enhancement of vascular regeneration was NO-dependent, and the prolonged release of low levels of NO from PCL/NO SDVGs promoted regenerative mechanisms, which were demonstrated to be a result of the rapid induction of Sca-1^+ VPCs to the graft site. Our data suggested that NO plays roles in inhibiting Sca-1^+ cell differentiation into OPN^+ osteogenic cells, and instead promoted Sca-1^+ cell differentiation into ECs. The rapid re-establishment of endothelial and smooth muscle layers inhibited the occurrence of graft failure and incidence of calcified plaque formation. Taken together, our data suggests that PCL/NO SDVGs are suitable artificial alternatives to autologous vessels and strong candidates for used in surgical interventions for small diameter vessel replacement or bypass surgery.

DATA AVAILABILITY STATEMENT

The original contributions presented in the study are included in the article/Supplementary Material, further inquiries can be directed to the corresponding authors.

ETHICS STATEMENT

The animal study was reviewed and approved by the Animal Care and Use Committee of Nankai University.

AUTHOR CONTRIBUTIONS

QZ conceived the original concept and initiated this project. QZ designed the experiment and supervised the entire project. MQ carried out the synthesis of all compounds. HW prepared the vascular grafts. FW and MQ performed NO releasing assay. SY and XZ performed the *in vivo* evaluation and analyzed data under the supervision of QZ. JH helped in data collection. HT provided critical feedback and helped in review of the article. AM, YW, and QZ wrote the paper with input from other authors.

FUNDING

The research was supported and funding by research grants from the National Key R&D Program of China (2018YFE0200503), National Natural Science Foundation of China (Nos. 81925021, 82050410449, and 81871500), and Science and Technology Project of Tianjin of China (No. 18JCJQJC46900).

REFERENCES

Aicher, A., Heeschen, C., Mildner-Rihm, C., Urbich, C., Ihling, C., Technau-Ihling, K., et al. (2003). Essential Role of Endothelial Nitric Oxide Synthase for Mobilization of Stem and Progenitor Cells. *Nat. Med.* 9, 1370–1376. doi:10.1038/nm948

Bogdan, C. (2001). Nitric Oxide and the Immune Response. *Nat. Immunol.* 2, 907–916. doi:10.1038/ni1001-907

Bonafè, F., Guarnieri, C., and Muscari, C. (2015). Nitric Oxide Regulates Multiple Functions and Fate of Adult Progenitor and Stem Cells. *J. Physiol. Biochem.* 71, 141–153. doi:10.1007/s13105-014-0373-9

Cho, H.-J., Cho, H.-J., Lee, H.-J., Song, M.-K., Seo, J.-Y., Bae, Y.-H., et al. (2013). Vascular Calcifying Progenitor Cells Possess Bidirectional Differentiation Potentials. *Plos Biol.* 11, e1001534. doi:10.1371/journal.pbio.1001534

Chouchani, E. T., Methner, C., Nadtochiy, S. M., Logan, A., Pell, V. R., Ding, S., et al. (2013). Cardioprotection by S-Nitrosation of a Cysteine Switch on Mitochondrial Complex I. *Nat. Med.* 19, 753–759. doi:10.1038/nm.3212

Covas, D., Piccinato, C., Orellana, M., Siufi, J., Silvajr, W., Jr., Protosiqueira, R., et al. (2005). Mesenchymal Stem Cells Can Be Obtained from the Human Saphena Vein. *Exp. Cel Res.* 309, 340–344. doi:10.1016/j.yexcr.2005.06.005

de Mel, A., Murad, F., and Seifalian, A. M. (2011). Nitric Oxide: A Guardian for Vascular Grafts? *Chem. Rev.* 111, 5742–5767. doi:10.1021/cr200008n

de Valence, S., Tille, J.-C., Mugnai, D., Mrowczynski, W., Gurny, R., Möller, M., et al. (2012). Long Term Performance of Polycaprolactone Vascular Grafts in a Rat Abdominal Aorta Replacement Model. *Biomaterials* 33, 38–47. doi:10.1016/j.biomaterials.2011.09.024

Enayati, M., Schneider, K. H., Almeria, C., Grasl, C., Kaun, C., Messner, B., et al. (2021). S-Nitroso Human Serum Albumin as a Nitric Oxide Donor in Drug-Eluting Vascular Grafts: Biofunctionality and Preclinical Evaluation. *Acta Biomater.* 134, 276–288. doi:10.1016/j.actbio.2021.07.048

Erdmann, J., Stark, K., Stark, K., Esslinger, U. B., Rumpf, P. M., Koesling, D., et al. (2013). Dysfunctional Nitric Oxide Signalling Increases Risk of Myocardial Infarction. *Nature* 504, 432–436. doi:10.1038/nature12722

Ferreira, J. C. B., and Mochly-Rosen, D. (2012). Nitroglycerin Use in Myocardial Infarction Patients - Risks and Benefits -. *Circ. J.* 76, 15–21. doi:10.1253/circj.cj-11-1133

Gkaliagkousi, E., Corrigall, V., Becker, S., de Winter, P., Shah, A., Zamboulis, C., et al. (2009). Decreased Platelet Nitric Oxide Contributes to Increased Circulating Monocyte-Platelet Aggregates in Hypertension. *Eur. Heart J.* 30, 3048–3054. doi:10.1093/eurheartj/ehp330

Greenwald, S. E., and Berry, C. L. (2000). Improving Vascular Grafts: The Importance of Mechanical and Haemodynamic Properties. *J. Pathol.* 190, 292–299. doi:10.1002/(sici)1096-9896(200002)190:3<292:aid-path528>3.0.co;2-s

Hadinata, I. E., Hayward, P. A. R., Hare, D. L., Matalanis, G. S., Seevanayagam, S., Rosalion, A., et al. (2009). Choice of Conduit for the Right Coronary System: 8-Year Analysis of Radial Artery Patency and Clinical Outcomes Trial. *Ann. Thorac. Surg.* 88, 1404–1409. doi:10.1016/j.athoracsur.2009.06.010

Heusch, G., and Gersh, B. J. (2017). The Pathophysiology of Acute Myocardial Infarction and Strategies of protection beyond Reperfusion: A Continual Challenge. *Eur. Heart J.* 38, 774–784. doi:10.1093/eurheartj/ehw224

Heusch, G. (2015). Molecular Basis of Cardioprotection. *Circ. Res.* 116, 674–699. doi:10.1161/circresaha.116.305348

Hu, Y., Zhang, Z., Torsney, E., Afzal, A. R., Davison, F., Metzler, B., et al. (2004). Abundant Progenitor Cells in the Adventitia Contribute to Atherosclerosis of Vein Grafts in ApoE-Deficient Mice. *J. Clin. Invest.* 113, 1258–1265. doi:10.1172/jci19628

Ingram, D. A., Mead, L. E., Moore, D. B., Woodard, W., Fenoglio, A., and Yoder, M. C. (2005). Vessel Wall-Derived Endothelial Cells Rapidly Proliferate Because They Contain a Complete Hierarchy of Endothelial Progenitor Cells. *Blood* 105, 2783–2786. doi:10.1182/blood-2004-08-3057

Issa Bhaloo, S., Wu, Y., Le Bras, A., Yu, B., Gu, W., Xie, Y., et al. (2018). Binding of Dickkopf-3 to CXCR7 Enhances Vascular Progenitor Cell Migration and Degradable Graft Regeneration. *Circ. Res.* 123, 451–466. doi:10.1161/circresaha.118.312945

Jiang, B., Suen, R., Wang, J.-J., Zhang, Z. J., Wertheim, J. A., and Ameer, G. A. (2017). Vascular Scaffolds with Enhanced Antioxidant Activity Inhibit Graft Calcification. *Biomaterials* 144, 166–175. doi:10.1016/j.biomaterials.2017.08.014

Kabirian, F., Brouki Milan, P., Zamanian, A., Heying, R., and Mozafari, M. (2019). Nitric Oxide-Releasing Vascular Grafts: A Therapeutic Strategy to Promote Angiogenic Activity and Endothelium Regeneration. *Acta Biomater.* 92, 82–91. doi:10.1016/j.actbio.2019.05.002

Kramann, R., Goettsch, C., Wongboonsin, J., Iwata, H., Schneider, R. K., Kuppe, C., et al. (2016). Adventitial MSC-Like Cells Are Progenitors of Vascular Smooth Muscle Cells and Drive Vascular Calcification in Chronic Kidney Disease. *Cell stem cell* 19, 628–642. doi:10.1016/j.stem.2016.08.001

Li, X., Qiu, H., Gao, P., Yang, Y., Yang, Z., and Huang, N. (2018). Synergetic Coordination and Catecholamine Chemistry for Catalytic Generation of Nitric Oxide on Vascular Stents. *NPG Asia Mater.* 10, 482–496. doi:10.1038/s41427-018-0052-3

Lundberg, J. O., Weitzberg, E., and Gladwin, M. T. (2008). The Nitrate-Nitrite-Nitric Oxide Pathway in Physiology and Therapeutics. *Nat. Rev. Drug Discov.* 7, 156–167. doi:10.1038/nrd2466

Lundberg, J. O., Gladwin, M. T., Ahluwalia, A., Benjamin, N., Bryan, N. S., Butler, A., et al. (2009). Nitrate and Nitrite in Biology, Nutrition and Therapeutics. *Nat. Chem. Biol.* 5, 865–869. doi:10.1038/nchembio.260

McCallinhart, P. E., Biwer, L. A., Clark, O. E., Isakson, B. E., Lilly, B., and Trask, A. J. (2020). Myoendothelial Junctions of Mature Coronary Vessels Express Notch Signaling Proteins. *Front. Physiol.* 11, 29. doi:10.3389/fphys.2020.00029

Midgley, A. C., Wei, Y., Li, Z., Kong, D., and Zhao, Q. (2020). Nitric-Oxide-Releasing Biomaterial Regulation of the Stem Cell Microenvironment in Regenerative Medicine. *Adv. Mater.* 32, e1805818. doi:10.1002/adma.201805818

Nichols, S. P., Storm, W. L., Koh, A., and Schoenfisch, M. H. (2012). Local Delivery of Nitric Oxide: Targeted Delivery of Therapeutics to Bone and Connective Tissues. *Adv. Drug Deliv. Rev.* 64, 1177–1188. doi:10.1016/j.addr.2012.03.002

Nie, Y., Zhang, K., Zhang, S., Wang, D., Han, Z., Che, Y., et al. (2017). Nitric Oxide Releasing Hydrogel Promotes Endothelial Differentiation of Mouse Embryonic Stem Cells. *Acta Biomater.* 63, 190–199. doi:10.1016/j.actbio.2017.08.037

Niklason, L. E., Gao, J., Abbott, W. M., Hirschi, K. K., Houser, S., Marini, R., et al. (1999). Functional Arteries Grown *In Vitro*. *Science* 284, 489–493. doi:10.1126/science.284.5413.489

Paloian, N. J., and Giachelli, C. M. (2014). A Current Understanding of Vascular Calcification in CKD. *Am. J. Physiology-Renal Physiol.* 307, F891–F900. doi:10.1152/ajprenal.00163.2014

Pan, Y., Yang, J., Wei, Y., Wang, H., Jiao, R., Moraga, A., et al. (2018). Histone Deacetylase 7-Derived Peptides Play a Vital Role in Vascular Repair and Regeneration. *Adv. Sci.* 5, 1800006. doi:10.1002/advs.201800006

Panesar, N. S. (2008). Downsides to the Nitrate-Nitrite-Nitric Oxide Pathway in Physiology and Therapeutics? *Nat. Rev. Drug Discov.* 7, 710. doi:10.1038/nrd2466-c1

Park, S., Kim, J., Lee, M.-K., Park, C., Jung, H.-D., Kim, H.-E., et al. (2019). Fabrication of strong, Bioactive Vascular Grafts with PCL/Collagen and PCL/Silica Bilayers for Small-Diameter Vascular Applications. *Mater. Des.* 181, 108079. doi:10.1016/j.matdes.2019.108079

Pektok, E., Nottelet, B., Tille, J.-C., Gurny, R., Kalangos, A., Moeller, M., et al. (2008). Degradation and Healing Characteristics of Small-Diameter Poly(ε-Caprolactone) Vascular Grafts in the Rat Systemic Arterial Circulation. *Circulation* 118, 2563–2570. doi:10.1161/circulationaha.108.795732

Psaltis, P. J., and Simari, R. D. (2015). Vascular Wall Progenitor Cells in Health and Disease. *Circ. Res.* 116, 1392–1412. doi:10.1161/circresaha.116.305368

Qian, M., Liu, Q., Wei, Y., Guo, Z., and Zhao, Q. (2021). In-Ssitu Biotransformation of Nitric Oxide by Functionalized Surfaces of Cardiovascular Stents. *Bioactive Mater.* 6, 1464–1467. doi:10.1016/j.bioactmat.2020.10.030

Rassaf, T., Totzeck, M., Hendgen-Cotta, U. B., Shiva, S., Heusch, G., and Kelm, M. (2014). Circulating Nitrite Contributes to Cardioprotection by Remote Ischemic Preconditioning. *Circ. Res.* 114, 1601–1610. doi:10.1161/circresaha.114.303822

Ren, X., Feng, Y., Guo, J., Wang, H., Li, Q., Yang, J., et al. (2015). Surface Modification and Endothelialization of Biomaterials as Potential Scaffolds for Vascular Tissue Engineering Applications. *Chem. Soc. Rev.* 44, 5680–5742. doi:10.1039/c4cs00483c

Roostalu, U., Aldeiri, B., Albertini, A., Humphreys, N., Simonsen-Jackson, M., Wong, J. K. F., et al. (2018). Distinct Cellular Mechanisms Underlie Smooth Muscle Turnover in Vascular Development and Repair. *Circ. Res.* 122, 267–281. doi:10.1161/circresaha.117.312111

Roth, G. A., Forouzanfar, M. H., Moran, A. E., Barber, R., Nguyen, G., Feigin, V. L., et al. (2015). Demographic and Epidemiologic Drivers of Global Cardiovascular Mortality. *N. Engl. J. Med.* 372, 1333–1341. doi:10.1056/nejmoa1406656

Sainz, J., Al Haj Zen, A., Caligiuri, G., Demerens, C., Urbain, D., Lemitre, M., et al. (2006). Isolation of "Side Population" Progenitor Cells from Healthy Arteries of Adult Mice. *Arterioscler Thromb. Vasc. Biol.* 26, 281–286. doi:10.1161/01.atv.0000197793.83391.91

Shroff, R., Long, D. A., and Shanahan, C. (2013). Mechanistic Insights into Vascular Calcification in CKD. *J. Am. Soc. Nephrol.* 24, 179–189. doi:10.1681/asn.2011121191

Tang, J., Wang, H., Huang, X., Li, F., Zhu, H., Li, Y., et al. (2020). Arterial Sca1+ Vascular Stem Cells Generate De Novo Smooth Muscle for Artery Repair and Regeneration. *Cell stem cell* 26, 81–96. doi:10.1016/j.stem.2019.11.010

Torsney, E., and Xu, Q. (2011). Resident Vascular Progenitor Cells. *J. Mol. Cell Cardiol.* 50, 304–311. doi:10.1016/j.yjmcc.2010.09.006

Vagnozzi, R. J., Sargent, M. A., Lin, S.-C. J., Palpant, N. J., Murry, C. E., and Molkentin, J. D. (2018). Genetic Lineage Tracing of Sca-1 + Cells Reveals Endothelial but Not Myogenic Contribution to the Murine Heart. *Circulation* 138, 2931–2939. doi:10.1161/circulationaha.118.035210

Valence, S. D., Tille, J.-C., Chaabane, C., Gurny, R., Bochaton-Piallat, M.-L., Walpoth, B. H., et al. (2013). Plasma Treatment for Improving Cell Biocompatibility of a Biodegradable Polymer Scaffold for Vascular Graft Applications. *Eur. J. Pharmaceutics Biopharmaceutics* 85, 78–86. doi:10.1016/j.ejpb.2013.06.012

Virani, S. S., Alonso, A., Aparicio, H. J., Benjamin, E. J., Bittencourt, M. S., Callaway, C. W., et al. (2021). Heart Disease and Stroke Statistics-2021 Update: A Report from the American Heart Association. *Circulation* 143, e254–e743. doi:10.1161/CIR.0000000000000950

Wang, Z., Lu, Y., Qin, K., Wu, Y., Tian, Y., Wang, J., et al. (2015). Enzyme-Functionalized Vascular Grafts Catalyze Iin-Ssitu Release of Nitric Oxide from Exogenous NO Prodrug. *J. Controlled Release* 210, 179–188. doi:10.1016/j.jconrel.2015.05.283

Wang, D., Li, L. K., Dai, T., Wang, A., and Li, S. (2018). Adult Stem Cells in Vascular Remodeling. *Theranostics* 8, 815–829. doi:10.7150/thno.19577

Wei, Y., Wu, Y., Zhao, R., Zhang, K., Midgley, A. C., Kong, D., et al. (2019). MSC-Derived sEVs Enhance Patency and Inhibit Calcification of Synthetic Vascular Grafts by Immunomodulation in a Rat Model of Hyperlipidemia. *Biomaterials* 204, 13–24. doi:10.1016/j.biomaterials.2019.01.049

Wu, W., Allen, R. A., and Wang, Y. (2012). Fast-Degrading Elastomer Enables Rapid Remodeling of a Cell-Free Synthetic Graft into a Neoartery. *Nat. Med.* 18, 1148–1153. doi:10.1038/nm.2821

Yang, Z., Yang, Y., Xiong, K., Li, X., Qi, P., Tu, Q., et al. (2015). Nitric Oxide Producing Coating Mimicking Endothelium Function for Multifunctional Vascular Stents. *Biomaterials* 63, 80–92. doi:10.1016/j.biomaterials.2015.06.016

Yang, T., Zelikin, A. N., and Chandrawati, R. (2018). Progress and Promise of Nitric Oxide-Releasing Platforms. *Adv. Sci.* 5, 1701043. doi:10.1002/advs.201701043

Yang, Y., Lei, D., Zou, H., Huang, S., Yang, Q., Li, S., et al. (2019). Hybrid Electrospun Rapamycin-Loaded Small-Diameter Decellularized Vascular Grafts Effectively Inhibit Intimal Hyperplasia. *Acta Biomater.* 97, 321–332. doi:10.1016/j.actbio.2019.06.037

Yang, Z., Zhao, X., Hao, R., Tu, Q., Tian, X., Xiao, Y., et al. (2020). Bioclickable and Mussel Adhesive Peptide Mimics for Engineering Vascular Stent Surfaces. *Proc. Natl. Acad. Sci. USA* 117, 16127–16137. doi:10.1073/pnas.2003732117

Yang, Y., Gao, P., Wang, J., Tu, Q., Bai, L., Xiong, K., et al. (2020). Endothelium-Mimicking Multifunctional Coating Modified Cardiovascular Stents via a Stepwise Metal-Catechol-(Amine) Surface Engineering Strategy. *Research (Wash D C)* 2020, 9203906. doi:10.34133/2020/9203906

Yao, Y., Wang, J., Cui, Y., Xu, R., Wang, Z., Zhang, J., et al. (2014). Effect of Sustained Heparin Release from PCL/Chitosan Hybrid Small-Diameter Vascular Grafts on Anti-Thrombogenic Property and Endothelialization. *Acta Biomater.* 10, 2739–2749. doi:10.1016/j.actbio.2014.02.042

Zhang, L., Issa Bhaloo, S., Chen, T., Zhou, B., and Xu, Q. (2018). Role of Resident Stem Cells in Vessel Formation and Arteriosclerosis. *Circ. Res.* 122, 1608–1624. doi:10.1161/circresaha.118.313058

Zhang, F., Zhang, Q., Li, X., Huang, N., Zhao, X., and Yang, Z. (2019). Mussel-Inspired Dopamine-CuII Coatings for Sustained *In Situ* Generation of Nitric Oxide for Prevention of Stent Thrombosis and Restenosis. *Biomaterials* 194, 117–129. doi:10.1016/j.biomaterials.2018.12.020

Zhao, Q., Zhang, J., Song, L., Ji, Q., Yao, Y., Cui, Y., et al. (2013). Polysaccharide-Based Biomaterials with On-Demand Nitric Oxide Releasing Property Regulated by Enzyme Catalysis. *Biomaterials* 34, 8450–8458. doi:10.1016/j.biomaterials.2013.07.045

Zheng, W., Wang, Z., Song, L., Zhao, Q., Zhang, J., Li, D., et al. (2012). Endothelialization and Patency of RGD-Functionalized Vascular Grafts in a Rabbit Carotid Artery Model. *Biomaterials* 33, 2880–2891. doi:10.1016/j.biomaterials.2011.12.047

Zhu, D., Hou, J., Qian, M., Jin, D., Hao, T., Pan, Y., et al. (2021). Nitrate-Functionalized Patch Confers Cardioprotection and Improves Heart Repair after Myocardial Infarction via Local Nitric Oxide Delivery. *Nat. Commun.* 12, 4501. doi:10.1038/s41467-021-24804-3

Zilla, P., Bezuidenhout, D., and Human, P. (2007). Prosthetic Vascular Grafts: Wrong Models, Wrong Questions and No Healing. *Biomaterials* 28, 5009–5027. doi:10.1016/j.biomaterials.2007.07.017

Conflict of Interest: The authors declare that the research was conducted in the absence of any commercial or financial relationships that could be construed as a potential conflict of interest.

Publisher's Note: All claims expressed in this article are solely those of the authors and do not necessarily represent those of their affiliated organizations, or those of the publisher, the editors and the reviewers. Any product that may be evaluated in this article, or claim that may be made by its manufacturer, is not guaranteed or endorsed by the publisher.

frontiers in Bioengineering and Biotechnology

ORIGINAL RESEARCH
published: 07 December 2021
doi: 10.3389/fbioe.2021.791954

Inhibition of Neovascularization and Inflammation in a Mouse Model of Corneal Alkali Burns Using Cationic Liposomal Tacrolimus

Xueqi Lin[1,2], *Xuewen Yu*[1,2], *Xiang Chen*[1,2], *Siting Sheng*[1,2], *Jingwen Wang*[1,2], *Ben Wang*[3,4]* *and Wen Xu*[1,2]*

[1]Eye Center, The Second Affiliated Hospital, Zhejiang University School of Medicine, Hangzhou, China, [2]Zhejiang Provincial Key Lab of Ophthalmology, The Second Affiliated Hospital, School of Medicine, Zhejiang Univerity, Hangzhou, China, [3]Cancer Institute (Key Laboratory of Cancer Prevention and Intervention, China National Ministry of Education), The Second Affiliated Hospital, Zhejiang University School of Medicine, Hangzhou, China, [4]Institute of Translational Medicine, Zhejiang University, Hangzhou, China

OPEN ACCESS

Edited by:
Yakai Feng,
Tianjin University, China

Reviewed by:
Di Huang,
Massachusetts Eye and Ear Infirmary and Harvard Medical School, United States
Liangju Kuang,
Harvard Medical School, United States

***Correspondence:**
Ben Wang
bwang@zju.edu.cn
Wen Xu
xuwen2003@zju.edu.cn

Specialty section:
This article was submitted to Biomaterials, a section of the journal Frontiers in Bioengineering and Biotechnology

Received: 09 October 2021
Accepted: 17 November 2021
Published: 07 December 2021

Citation:
Lin X, Yu X, Chen X, Sheng S, Wang J, Wang B and Xu W (2021) Inhibition of Neovascularization and Inflammation in a Mouse Model of Corneal Alkali Burns Using Cationic Liposomal Tacrolimus. Front. Bioeng. Biotechnol. 9:791954. doi: 10.3389/fbioe.2021.791954

Eye drops account for more than 90% of commercialized ophthalmic drugs. However, eye drops have certain shortcomings, such as short precorneal retention time and weak corneal penetration. The requirement of frequent instillation of eye drops also causes poor patient compliance, which may lead to further aggravation of the disease. We aimed to develop a cationic liposome formulation to increase the bioavailability of the therapeutic agent and solve the aforementioned problems. In the present study, we prepared cationic liposomal tacrolimus (FK506) with a surface potential of approximately +30 mV, which could bind to the negatively charged mucin layer of the ocular surface. Our results showed that the content of FK506 in the cornea was increased by 93.77, 120.30, 14.24, and 20.36 times at 5, 30, 60, and 90 min, respectively, in the FK506 liposome group (0.2 mg/ml) compared with the free drug group (0.2 mg/ml). Moreover, FITC-labeled FK506 liposomes significantly prolonged the ocular surface retention time to 50 min after a single dose. In addition, the results of the Cell Counting Kit-8 assay, live and dead cell assay, sodium fluorescein staining, and hematoxylin and eosin staining all indicated that FK506 liposomes had good biological compatibility in both human corneal epithelial cells and mouse eyeballs. Compared with the free drug at the same concentration, FK506 liposomes effectively inhibited vascular endothelial growth factor-induced green fluorescent protein-transduced human umbilical vein endothelial cell migration and tube formation *in vitro*. In a mouse corneal neovascularization model induced by alkali burns, FK506 liposomes (0.2 mg/ml) enhanced corneal epithelial recovery, inhibited corneal neovascularization, and reduced corneal inflammation, and its therapeutic effect was better than those of the commercial FK506 eye drops (1 mg/ml) and the free drug (0.2 mg/ml). Collectively, these results indicate that cationic FK506 liposomes could increase the efficacy of FK506 in the corneal neovascularization model. Therefore, cationic FK506 liposomes can be considered as a promising ocular drug delivery system.

Keywords: tacrolimus, liposomes, corneal neovascularization, bioavailability, corneal permeability, ocular retention time

1 INTRODUCTION

Corneal neovascularization (CoNV), one of the most common causes for reduced corneal transparency and vision loss, can be induced by inflammation and a variety of angiogenic stimuli (Chuang et al., 2019; Chen et al., 2021). At present, among the many therapeutic agents used for the treatment of CoNV caused by alkali burns, anti-inflammatory drugs and anti-vascular endothelial growth factor (VEGF) drugs are the most commonly used regimens (Roshandel et al., 2018). FK506 is a potent immunosuppressant and an effective drug candidate for CoNV therapy; previous studies have reported the anti-angiogenesis and anti-inflammation effects of FK506 in treating corneal alkali burns in mice (Park et al., 2015; Chen et al., 2018; Wu et al., 2019).

Eye drops remain the most common method of administration for the current treatment of eye diseases, accounting for 90% of commercialized ophthalmic drugs (Alvarez-Trabado et al., 2017; Jumelle et al., 2020). Although eye drops are the most non-invasive and the simplest method of administration, due to the complicated anatomical and physiological characteristics of the eye as well as the rapid clearance mechanisms (e.g., tear dilution, blinking, and nasolacrimal duct drainage) on the ocular surface, 95% of these drugs are drained to the whole body through the nasolacrimal duct, and the bioavailability of common eye drops is extremely low (1–5%) (Lin et al., 2021). To achieve therapeutic effects, high concentrations and frequent use of eye drops are usually required to achieve a locally effective drug concentration, and this can result in serious off-target effects and low patient compliance (Urtti, 2006; Mu et al., 2018; Jumelle et al., 2020). Extending the ocular surface residence time and increasing the corneal permeability are the two most common methods of ameliorating drug bioavailability (Jumelle et al., 2020). Previous studies have reported that some FK506 formulations, such as liposomes (Pleyer et al., 1993; Whitcup et al., 1998; Zhang et al., 2010; Dai et al., 2013), micelles (Lin et al., 2019), and niosomes (Li et al., 2014; Zeng et al., 2016), have effectively enhanced the corneal permeability and have been evaluated in animal models of uveitis, dry eye, and corneal transplantation. In addition, previous extensive studies have also demonstrated that for poorly water-soluble drugs, such as FK506, cationic liposomes show potential for enhancing ocular bioavailability (Gai et al., 2018). However, to the best of our knowledge, no previous research has evaluated the potential of cationic FK506 liposomes in the treatment of corneal alkali burns.

In this study, we developed cationic FK506 liposome eye drops using cationic phospholipids 1,2-dioleoyl-3-trimethylammonium-propane (DOTAP) and 1,2-dioleoyl-sn-glycero-3-phosphoethanolamine (DOPE). This study aimed to demonstrate that in comparison with commercial FK506 eye drops and the free drug, FK506 liposomes showed improved therapeutic effects on CoNV and corneal inflammation in a mouse corneal alkali burn model. Moreover, we evaluated the biocompatibility of cationic FK506 liposomes, their inhibitory effects on angiogenesis *in vitro* and *in vivo*, and the improvement in corneal permeability and ocular retention time.

2 MATERIALS AND METHODS

2.1 Materials

DOTAP was acquired from AVT Pharmaceutical Tech Co., Ltd (Shanghai, China). DOPE was obtained from Sigma. 1,2-distearoyl-sn-glycero-3-phosphoethanolamine-N-[methoxy(polyethyleneglycol)-2000] (DSPE-PEG2000) was provided by Shanghai Yuanye Biological Technology Co., Ltd. FK506 was purchased from Selleck (Shanghai, China). Solvents, such as chloroform, methanol, and acetonitrile, were supplied by the materials and chemicals procurement management platform of Zhejiang University.

2.2 Preparation of FK506 Liposomes

FK506 liposomes were prepared using the membrane hydration method according to the published procedure (Mendez et al., 2014; Wu et al., 2021). Briefly, DOTAP, DOPE, cholesterol, DSPE-PEG2000 (at a ratio of 4:4:4:1) and 2 mg FK506 were dissolved in chloroform, and the solvent was evaporated on a rotary evaporator to form a semi-transparent lipid film. Then, the film was hydrated with PBS, sonicated for 40 min, and filtered through a 0.2-μm polycarbonate membrane extrusion filter to further homogenize the particle size. The DSPE-PEG2000 was replaced with FITC-PEG2000-DSPE for the FITC-labeled liposome synthesis.

2.3 Characterization of FK506 Liposomes

2.3.1 Transmission Electron Microscopy

The liposomes were placed on a copper mesh and then negatively stained with ammonium molybdate. The morphology and structure of the FK506 liposomes were observed using TEM (JEM-1400, JEOL, Japan) at the acceleration voltage of 80 kV.

2.3.2 Size Distribution and Zeta Potential

The particle size, zeta potential, and polydispersity (PDI) of FK506 liposomes and blank liposomes were determined using a Malvern Nano-ZSE laser particle size analyzer. The liposomes were diluted 100 times, followed by gentle vibration before measurement.

2.3.3 *In vitro* Drug Release Profile and Entrapment Efficiency

The release profile of FK506 liposomes was measured as follows. Briefly, an 8-ml volume of FK506 liposomes was transferred to a dialysis bag and then submerged in 30 ml of 1% sodium dodecyl sulfate solution for drug release analysis. At the indicated time points, 1 ml of dialysate was taken out and freeze dried. Later, the freeze-dried powder was re-dissolved in 0.4 ml of methanol, and the drug concentration was measured by HPLC (Agilent 1100, USA, FK506 210 nm).

The HPLC conditions were as follows: C18 column (250 mm × 4.6 mm 4 micron, Phenomenex); the mobile phase included acetonitrile and 0.1% phosphoric acid (80:20, v:v); flow rate: 1 ml/min; and column temperature: 50°C. The EE was calculated as follows: EE (%) = amount of FK506 entrapped/total amount of FK506 × 100%.

2.4 Cells

Green fluorescent protein-transduced human umbilical vein endothelial cells (HUVEC-GFPs) and human corneal epithelial cells (HCECs) were maintained in DMEM medium (Corning, USA) containing 1% penicillin, 1% streptomycin, and 10% fetal bovine serum (FBS) in a 37°C incubator supplied with 5% CO_2.

2.4.1 Cell Counting Kit-8 Assay

Briefly, 5,000 HCECs were inoculated per well in a 96-well plate. After culturing for 24 h, different concentrations of the free drug and FK506 liposomes (0, 3.91, 7.81, 15.63, 31.25, and 62.5 μg/ml) were added into each well for another 24-h incubation. Then, the HCECs were gently washed with PBS and replaced with 100 μL of medium containing 10 μL of CCK-8 liquid (Dojindo, Japan) for CCK-8 analysis. After incubating for another 2 h, the absorbance values were measured at 450 nm on a microplate reader (Molecular Devices Spectramax M5, USA).

2.4.2 Live and Dead Cell Assay

HCECs were inoculated in a 24-well plate at a density of 1×10^4 cells/well and cultured overnight. Then, the free drug and the FK506 liposomes were added at different concentrations (0, 5, 25, and 35 μg/ml) and incubated for 24 h. Subsequently, the drug solution was removed, and the cells were washed 3 times with PBS. After that, the cells were stained using a Calcein-AM/PI double staining kit (Yeason, China) (Calcein-AM, 0.67 μM; PI, 1.5 μM) and incubated at 37°C for 15 min in the dark. Finally, an inverted fluorescence microscope (Zeiss, Germany) was used to record the images.

2.4.3 Cell Model

HUVEC-GFP cells were cultivated according to the conditions mentioned above. *In vitro* angiogenesis assays were carried out by adding a high concentration of recombinant human VEGF-165 (rhVEGF, PeproTech, USA) to the culture medium to simulate the environment of neovascularization.

2.4.4 Wound Healing Assay

HUVEC-GFP cells were seeded in a 12-well plate at a density of 1×10^4 cells/well and were adhered overnight. Subsequently, a 200-μL pipette tip was utilized to produce uniform scratches. Then, serum-free DMEM containing 100 ng/ml VEGF was added with 5 μg/ml of the free drug or FK506 liposomes and incubated with the cells for another 48 h. The migration profile was recorded by an inverted fluorescence microscope at 24 and 48 h, and the widths of the scratches were measured by ImageJ software (NIH, USA).

2.4.5 Transwell Migration Assay

HUVEC-GFP cells (1.5×10^4) were resuspended in serum-free DMEM containing different concentrations of FK506 liposomes and the free drug (0, 5, 15, and 25 μg/ml) and seeded in the upper chamber of Transwell inserts (BD Bioscience, USA). The lower chamber was a medium (600 μL) containing 10% FBS as a chemoattractant. After incubating for 24 h, the cells were dyed with a mixed solution of 4% paraformaldehyde and 0.05% crystal violet for 15 min and then thoroughly washed with PBS solution. Then, the cells in the upper chamber were gently wiped off, and the cells in the lower chamber were counted under a light microscope.

2.4.6 Tube Formation Assay

Briefly, 250 μL of Matrigel (Corning, 356230) was carefully smeared in a pre-cooled 24-well plate and incubated at 37°C to form a gel. Later, 2.3×10^5 HUVEC-GFP cells were suspended in the culture medium, supplemented with 200 ng/ml rhVEGF and different concentrations of FK506 liposomes or the free drug, and seeded on the surface of the Matrigel. At 6 h, tube formation was captured using an inverted fluorescence microscope and analyzed using ImageJ software.

2.5 Animals

All C57BL/6 mice (6–8 weeks, 20–25 g, male) were purchased from Shanghai SLAC Laboratory Animal Co., Ltd. New Zealand rabbits weighing from 2 to 2.5 kg were acquired from the Experimental Animal Center of Zhejiang Academy of Medical Sciences (Hangzhou, China).

2.5.1 Ethics Statement

The animal experiments were carried out following the "Statement on the Use of Animals in Ophthalmology and Vision Research" described by the Association for Research in Vision and Ophthalmology. The research protocols were approved by the Animal Ethics Committee of the Second Affiliated Hospital of Zhejiang University School of Medicine (batch number: [2021] No. [057]).

2.5.2 Ocular Surface Stimulation Test

FK506 liposome eye drops (0.2 mg/ml, 10 μL) were locally administered four times a day for 14 days. Mice treated with normal saline (NS) served as the control group. On day 14, the eye irritation was evaluated using a slit lamp microscope (66 Vision-Tech, China) and corneal sodium fluorescein staining; then, the eyeballs were removed for hematoxylin and eosin (H&E) staining.

2.5.3 Biocompatibility Evaluation of FK506 Liposomes *in vivo*

The mice were sacrificed at the end of the treatment. For each mouse, the blood was collected and centrifuged at 3,000 g for 15 min, and the supernatant was taken for liver and kidney function analysis. In addition, the heart, liver, spleen, lung, and kidney were collected and subjected to H&E staining for the toxicity assessment.

2.5.4 Mouse Model of Corneal Alkali Burns

Mice corneal alkali burn model was established as previously described (Anderson et al., 2014). The mice were generally anesthetized via intraperitoneal injection of 0.3% pentobarbital sodium and locally anesthetized using proparacaine hydrochloride eye drops (Alcon-Couvreur, Belgium). The 2-mm round filter papers were soaked in 1M NaOH solution for 20 s, placed in the center of the mice corneas for 40 s, and then quickly removed. Finally, 20 ml of NS was used to rinse the ocular surface. On the first day after surgery, all animals were randomly

divided into four groups: the NS group (n = 6), the commercial FK506 eye drop group (FK 1 mg/ml, n = 6), the free drug group (0.2 mg/ml) (n = 6), and the FK506 liposome group (0.2 mg/ml) (n = 6). Treatment for each mouse was administered four times a day (10 μL each time) for 14 days.

2.5.5 Clinical Assessment

On days 1, 3, 7, and 14, the corneas of the mice from different groups were observed, photographed, and scored according to the previous scoring system (Han et al., 2020b; Zhong et al., 2021). Briefly, the corneal turbidity was scored from 0 to 4 points, and the CoNV area and the size of the blood vessels were scored from 0 to 3 points. Additionally, each cornea was stained with fluorescein sodium ophthalmic strips for examination of the corneal epithelial defect. ImageJ software was used to quantify the vessel lengths, CoNV areas, and areas of corneal epithelial defect.

2.5.6 H&E Staining and Immunohistochemistry Staining

The mouse eyeballs were enucleated, fixed in 4% paraformaldehyde overnight, embedded in paraffin, and then prepared into 4-μm-thick paraffin sections. H&E staining was carried out, and immunohistochemistry (IHC) staining was conducted using anti-α-smooth muscle actin (Wuhan Sanying Biotechnology; dilution 1:2,000).

2.5.7 Immunofluorescence Staining

After fixing in 4% paraformaldehyde for 1 h, the intact corneas were carefully peeled off and blocked for 2 h. Then, the corneas were incubated with rabbit anti-mouse CD31 antibody (Abcam; dilution 1:50) at 4°C overnight and then incubated with Alexa Fluor 555-conjugated goat anti-rabbit secondary antibodies (Invitrogen; dilution 1:500) for 1 h in the dark. Finally, the corneas were radially cut, flat mounted, and observed under a fluorescence microscope.

2.5.8 Quantitative RT-PCR

The total RNA of the cornea was extracted using TRIzol reagent (Accurate Biotechnology, China). Then, reverse transcription and real-time PCR were carried out according to the operating steps provided in the instructions. The relative expressions of the target genes, such as VEGF-A, VEGF-R3, interleukin (IL)-6, and matrix metalloproteinase (MMP)-9, were determined using the $2^{-\Delta\Delta Ct}$ method, and GAPDH was adopted as the housekeeping gene.

2.5.9 Retention of FK506 Liposomes on the Ocular Surface

Three types of fluorescent eye drops (FITC dye solution, free-drug solution, and FITC-labeled FK506 liposomes, 5 μL) were dripped into the eyes of the mice after they were anesthetized. A Xenogen IVIS Lumina imaging system (Perkin Elmer, Akron, OH, USA) was used to capture images of the eyes every 5 min, and the percentage of residual fluorescence intensity was calculated as the proportion of the fluorescence intensity at the corresponding time point to the initial fluorescence intensity.

2.5.10 FK506 Content in the Cornea/Aqueous Humor

Briefly, 75 μL of three FK506 preparations (0.02% FK506 liposome eye drops, 0.02% free-drug solution, and 0.1% commercial FK506 eye drops) was added to the eyes of the rabbits, respectively. The rabbits were euthanized at 5, 30, 60, and 90 min after administration, the corneas were collected, and 150 μL of aqueous humor was harvested. After cutting into pieces, the cornea was suspended in two volumes of NS containing high-strength ceramic beads and then fully broken. Then, three volumes of acetonitrile were added to extract the drug from the cornea. As for the aqueous humor, one volume of acetonitrile was added to the sample to extract the drug. Finally, the samples were centrifuged at 10,000 rpm for 10 min, and 200 μL of supernatant was used for FK506 concentration measurement using a mass spectrometer (Agilent Technologies, USA).

The HPLC conditions of the LC/MS/MS were as follows: Zorbax SB C18 column (150 mm × 2.1 mm, 3.5 μm); the mobile phases included phase A and phase B (phase A contained 5 mmol sodium acetate and 0.1% formic acid, and phase B was methanol); the precursor was 821.5 m/z; the ion product was 786.4; and the flow rate was 0.3 ml/min.

2.6 Statistical Analysis

All data were expressed as means ± standard deviations (SDs). The statistical differences between groups were determined using two-tailed Student's t test or one-way analysis of variance (ANOVA). A p-value of <0.05 was considered statistically significant.

3 RESULTS AND DISCUSSION

3.1 Characterization of FK506 Liposomes

3.1.1 Morphology, Size Distribution, and Zeta Potential

The TEM image (**Figure 1A**) showed that the liposomes were nearly spherical nanostructures with a particle size of approximately 200 nm. Further dynamic light scattering results (**Figures 1B,C**) indicated that the average hydrodynamic diameter of FK506 liposomes and blank liposomes were 235.23 ± 26.22 nm and 270.17 ± 8.33 nm, respectively. And the particle dispersion index of the two liposomes were 0.30 ± 0.05 and 0.30 ± 0.04, indicating that the particle size of the liposomes was uniformly dispersed. Moreover, the zeta potential of FK506 liposomes and blank liposomes were approximately +24.33 ± 0.81 mV and +27.90 ± 1.13 mV, respectively (**Figure 1C**).

Previous literature has shown that a small particle size can enhance the permeability of the cornea, hence increasing the bioavailability of the therapeutic agent. The small particle size and uniform spherical structure can also ensure low irritation to the ocular tissues when used as an ophthalmic drug delivery system (Gai et al., 2018). Furthermore, the positive charge of the cationic liposomes not only provides an effective repulsive force between the liposomes and the negatively charged mucins on the ocular surface, therefore significantly prolonging the drug retention time

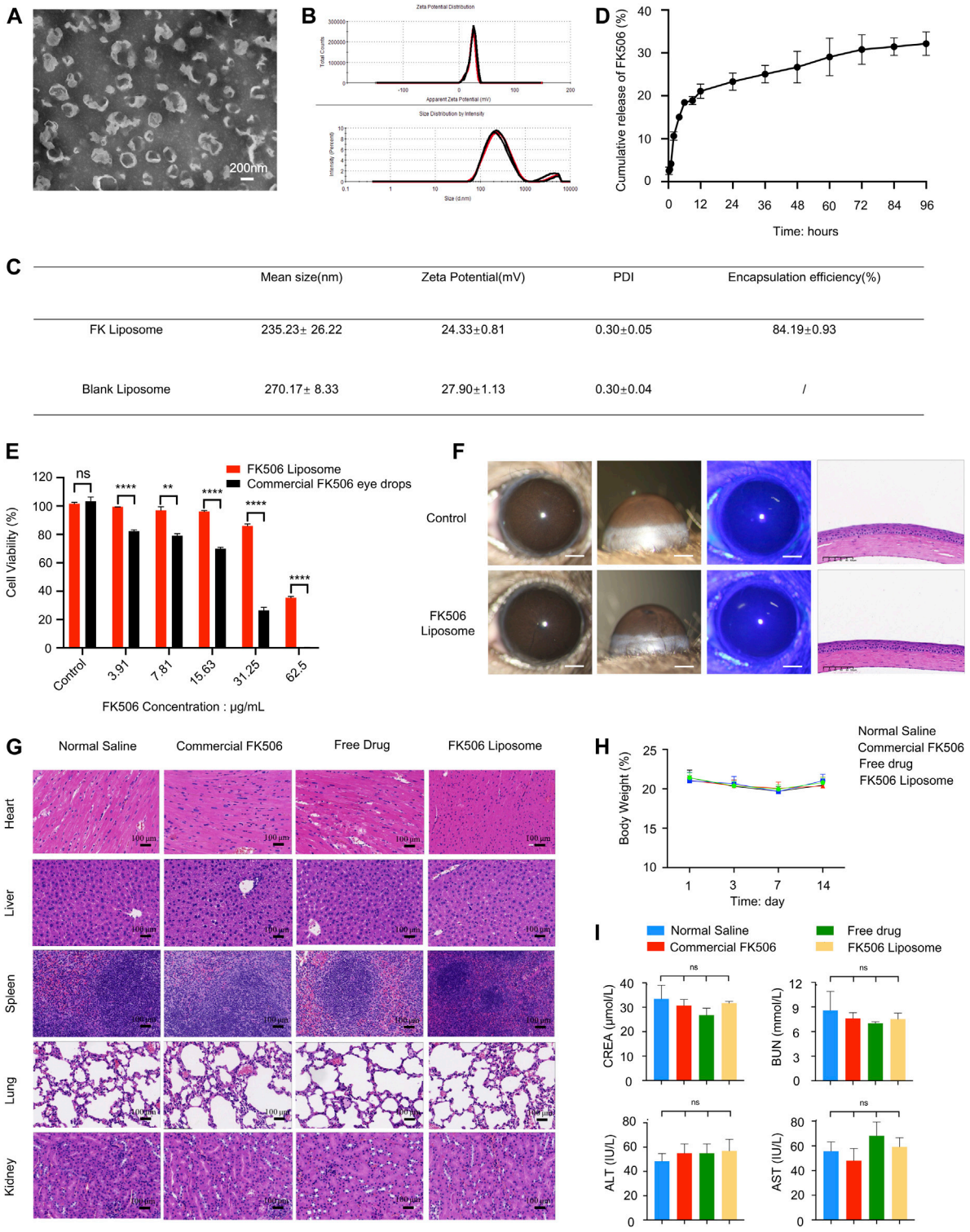

FIGURE 1 | Characterization and biocompatibility evaluation of FK506 liposomes. **(A)** TEM image of FK506 liposomes. Scale bar: 200 nm. **(B)** Zeta potential and size distribution of liposomes revealed by dynamic light scattering. **(C)** Characterization of FK506 liposomes and blank liposomes. **(D)** *In vitro* release profile of FK506 liposomes (n = 4). **(E)** CCK-8 assay of the HCECs exposed to free-drug or FK506 liposomes (n = 3). **(F)** *In vivo* biocompatibility evaluation of FK506 liposomes. The corneas were examined with a slit lamp microscope (scale bar: 1 mm), corneal fluorescein staining (scale bar: 1 mm), and H&E staining (scale bar: 100 μm) after 14 days of treatment with NS or FK506 liposomes (0.2 mg/ml). **(G)** Topical application of FK506 liposomes neither influenced the function of the main organs *in vivo* (scale bar: 100 μm) nor changed the **(H)** body weight of the mice in the four groups during the 14-days treatment period. **(I)** Toxicity studies of liver function (ALT, AST) (*Continued*)

FIGURE 1 | and kidney function (UA, BUN) in mice after receiving commercial FK506 eye drops (1 mg/ml), free drug solution (0.2 mg/ml), or FK506 liposomes (0.2 mg/ml) for 14 consecutive days ($n = 3$). The data was presented as mean ± SD, two-tailed Student's t test and one-way ANOVA, $^{*}p < 0.05$, $^{**}p < 0.01$, $^{***}p < 0.001$, and $^{****}p < 0.0001$; ns denotes no significance.

and facilitating the uptake of liposomes by the ocular surface cells, but also enhances the stability of the liposomes when used as a drug delivery system.

3.1.2 *In vitro* Drug Release Profile and Entrapment Efficiency

Figure 1D shows the 96-h *in vitro* cumulative release curve of FK506 liposomes. FK506 liposomes released approximately 28.14% of the total amount of the drug in 96 h *in vitro*; the drug was released more quickly in the first 6 h (approximately 16.16% was released in the first 6 h). Moreover, the average EE of FK506 liposomes was 84.19 ± 0.93% (**Figure 1C**) (measured through three batches of FK506 liposomes).

The rapid release rate of FK506 liposomes in the early stage provides a sufficient drug dose to inhibit corneal inflammation in the initial stage of CoNV. Meanwhile, the slower, sustained release in the later stage helps to release the drug for a long period of time to inhibit the growth of CoNV. Since FK506 is a hydrophobic drug that is encapsulated in the lipid bilayer of liposomes, the slow release of FK506 can be ascribed to the high affinity of FK506 to the hydrophobic part of the formulation. The *in vitro* sustained-release curve showed that FK506 liposomes possessed sustained-release properties after being encapsulated by liposomes.

3.2 Biocompatibility Evaluation of FK506 Liposomes

3.2.1 Cytotoxicity Evaluation *in vitro*

At all concentrations, the viability of the cells from the FK506 liposome group was significantly higher than that of cells from the free-drug group (**Figure 1E**). Even at an FK506 concentration of 31.25 μg/ml, the cell viability of HCECs in the FK506 liposome group was still more than 80% (86.02 ± 2.52%), while the cell viability of the free-drug group at the same concentration was only 26.48 ± 3.55% ($p < 0.0001$). Similarly, live and dead cell staining was conducted; red and green represented dead cells and live cells, respectively. At the same drug concentration, the number of live cells in the visual field in the FK506 liposome group was markedly higher than that in the free-drug group (**Supplementary Figure 1**).

Since cationic liposomes have certain cytotoxicity, it is necessary to evaluate the biocompatibility of cationic FK506 liposomes beforehand. Both the CCK-8 assay and Calcein-AM/PI staining demonstrated that the cationic FK506 liposomes had good biosafety, and the toxicity of cationic FK506 liposomes to HCECs was much less than that of the free FK506 at the same drug concentration, indicating that the cytotoxicity of FK506 could be significantly reduced after liposomal encapsulation.

3.2.2 Ocular Surface Stimulation Test

After 14 days of topical administration of FK506 liposomes, the results of the slit lamp evaluation indicated that the corneas of the mice were smooth and transparent, and no hyperemia, inflammation, or neovascularization was found. Moreover, the sodium fluorescein images showed no green staining, indicating that there were no defects in the corneal epithelium during the FK506 liposome treatment. In addition, H&E staining indicated that the anatomical structures of the mouse corneas were complete and neatly arranged, and no vascular lumens or inflammatory cells were observed, similarly to the corneas of the normal mice. These results demonstrated that FK506 liposomes had no potential negative effects on mouse corneas, indicating good ocular biocompatibility. These results are shown in **Figure 1F**.

3.2.3 Biocompatibility Evaluation of FK506 Liposomes *in vivo*

The mice treated with NS, commercial FK506 eye drops, the free drug, and FK506 liposomes did not exhibit significant histological differences (**Figure 1G**). In addition, the body weight of the mice remained stable during the 14 days, with no significant differences between the four groups (**Figure 1H**). Further biochemical tests showed that the liver functions (alanine aminotransferase, ALT; aspartate aminotransferase, AST) and kidney functions (creatinine, CREA; blood urea nitrogen, BUN) of the mice were all within the normal ranges after receiving different preparations for 14 days (**Figure 1I**).

Due to the narrow therapeutic window of FK506, long-term use of high-concentration FK506 may cause severe off-target, systemic effects, such as liver and kidney toxicity and neurotoxicity (Liu et al., 2019). Therefore, the aforementioned results all indicate that FK506 liposomes are superior with regard to biosafety.

3.3 The Inhibitory Effects of FK506 Liposomes on Vascular Endothelial Growth Factor-Induced Angiogenesis *in vitro*

3.3.1 Wound Healing Assay and Transwell Migration Assay

A wounding healing assay was performed to assess the influence of the free drug and FK506 liposomes at the same concentration on the migration property of HUVEC-GFPs cells *in vitro*. The VEGF treatment (100 ng/ml) induced the surrounding HUVEC-GFP cells to crawl toward the center of the scratch, almost filling the gap within 48 h, showing the smallest scratch width in all treatment groups (**Figure 2A**). However, both FK506 liposomes and the free drug significantly delayed the migration of HUVEC-GFP cells. Notably, compared with the free drug at 5 μg/ml, FK506 liposomes significantly reduced the migration of HUVEC cells at the same concentration ($p < 0.05$) (**Figure 2B**). The findings of the transwell assay revealed the same tendency (**Figure 2C**). FBS served as a chemical attractant to promote the migration of HUVECs to the lower chamber of transwell inserts. Compared with the NS, VEGF, and free-drug groups, the number of vascular endothelial cells that migrated to the

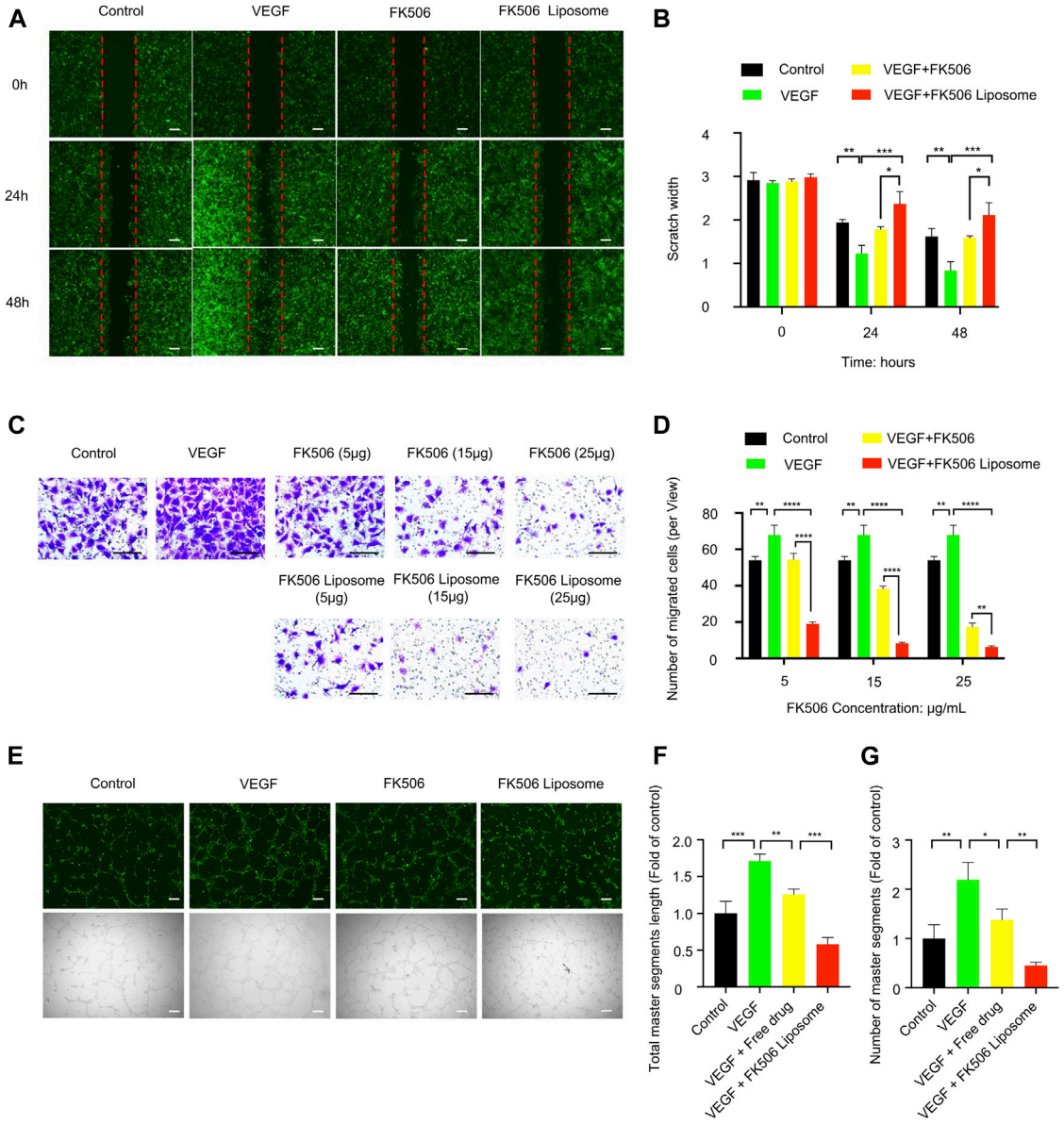

FIGURE 2 | *In vitro* evaluation of FK506 liposomes in the inhibition of angiogenesis. **(A)** FK506 liposomes inhibited the migration of HUVEC-GFP cells by wounding healing assay (scale bar: 200 μm, n = 3). **(B)** Quantitative analysis of the scratch widths. **(C)** Different concentrations of FK506 liposomes inhibited the migration of HUVEC-GFP cells by transwell migration assay (scale bar: 100 μm, n = 3). **(D)** Quantitative analysis of the number of migrated cells in each view. **(E)** Tube formation activity of HUVEC-GFP cells. Representative fluorescence and bright-field images of HUVEC-GFP cells after co-incubation with 15 μg/ml FK506 or FK506 liposomes for 6 h (scale bar: 200 μm, n = 3). Quantitative analysis of **(F)** total master segment length and **(G)** number of master segments.

underside of the transwell membrane was significantly reduced in the FK506 liposome treatment group at all drug concentrations (**Figure 2C**). The migration rates of HUVECs inhibited by FK506 liposomes were 27.94, 12.25, and 9.31% at FK506 concentrations of 5, 15, and 25 μg/ml, respectively (**Figure 2D**).

3.3.2 Tube Formation Assay

The tube formation assay indicated that the formation of capillary networks was more abundant in the 200 ng/ml VEGF induction group and that fewer disconnected network tubes were observed in the free-drug and FK506 liposome treatment groups (**Figure 2E**). In addition, the quantitative analysis found that compared with the free-drug group, at the same concentration, FK506 liposomes were more effective in inhibiting the formation of the capillary networks. After incubation with 15 μg/ml FK506 liposomes for 6 h, tubes showed a shorter total master segment length ($p < 0.001$) and a smaller number of master segments ($p < 0.01$) (**Figures 2F,G**). Additionally, the result of the tube formation assay was consistent with those of the migration assays of vascular endothelial cells *in vitro*.

Blood vessel formation is induced by many factors, such as hypoxia and inflammation, and followed by the recruitment of

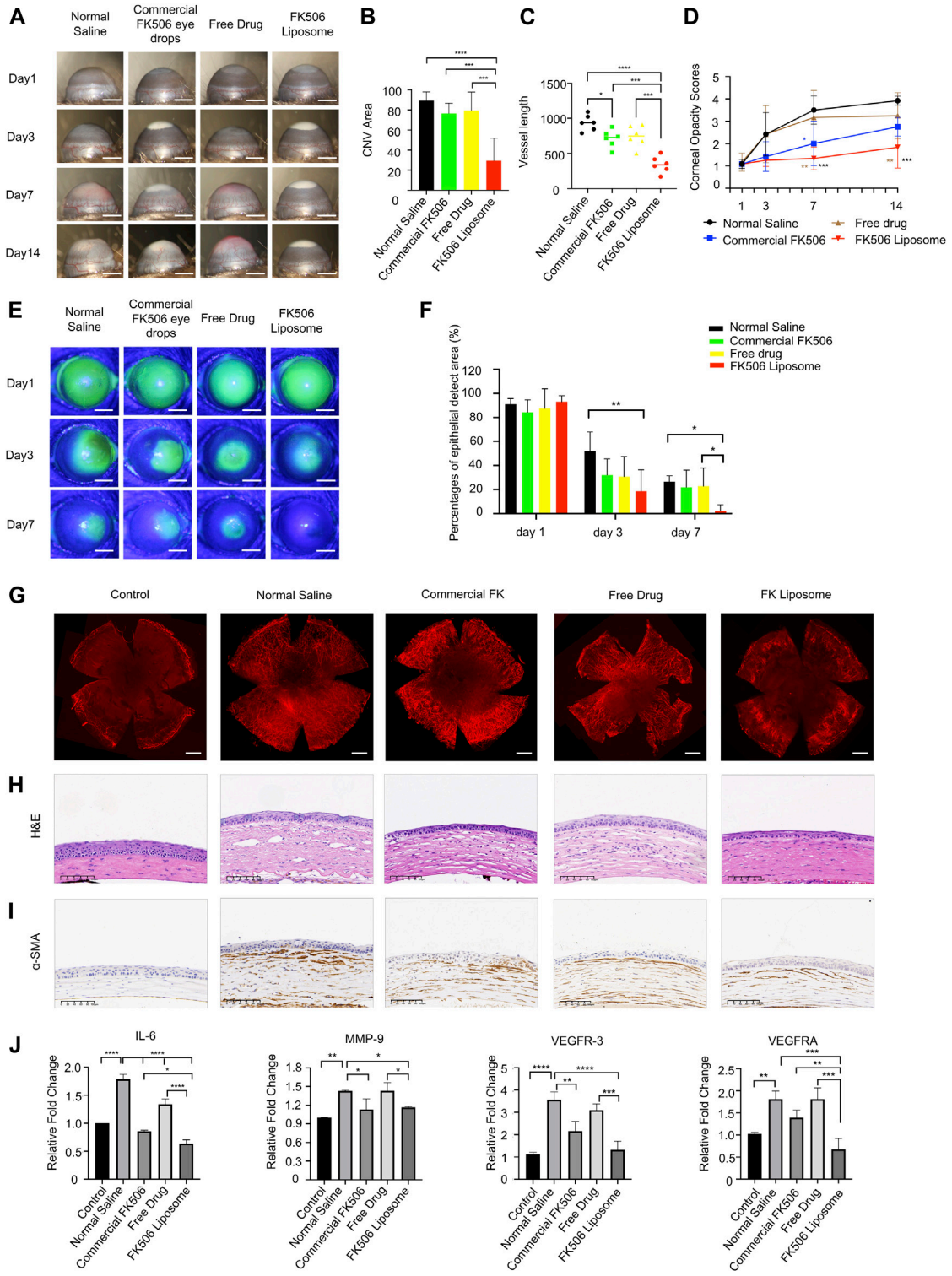

FIGURE 3 | *In vivo* therapeutic effect evaluation of FK506 liposomes in mouse corneal alkali burn model. **(A)** Slit-lamp examination of CoNV on the 1st, 3rd, 7th, and 14th days after corneal alkali burn. Scale bar: 1 mm. **(B)** Quantification of the CoNV area ($n = 6$). **(C)** Quantitative analysis of the corneal vessel length ($n = 6$). **(D)** The corneal opacity score on the 14th day of treatment ($n = 6$). **(E)** The corneal sodium fluorescein staining areas in each treatment group on days 1, 4, and 7 (scale bar: 1 mm) and their **(F)** quantitative analysis ($n = 6$). **(G)** CD31 vascular endothelial marker immunofluorescence staining on day 14. Scale bar: 500 μm. **(H)** H&E staining and **(I)** α-SMA IHC staining of corneal sections after treatment with various formulations for 14 days. Scale bars: 100 μm. **(J)** The expressions of vascular endothelial growth factors (VEGF-A, VEGFR-3) and inflammatory factors (IL-6, MMP-9) in the corneas of each treatment group on the 14th day ($n = 3$). The data was presented as mean ± SD, one-way ANOVA, $^{*}p < 0.05$, $^{**}p < 0.01$, $^{***}p < 0.001$, and $^{****}p < 0.0001$.

inflammatory cells, production of angiogenic factors, basement membrane degradation, and proliferation, migration, and tube formation of vascular endothelial cells, etc. (Nowak-Sliwinska et al., 2018; Chen et al., 2021). FK506 liposomes inhibited the specific stages of angiogenesis induced by $rhVEGF_{165}$, including the migration and tube formation of HUVEC-GFP cells. Among these stages, migration is one of the early steps of angiogenesis (Nowak-Sliwinska et al., 2018), and tube formation indicates the maturation of migrated vascular endothelial cells (Han et al., 2020b). The results mentioned above implied that FK506 liposomes had a stronger inhibitory effect on angiogenesis, which might be attributed to cationic liposomes increasing the intracellular uptake of FK506.

3.4 Anti-Corneal Neovascularization Effect of FK506 Liposomes *in vivo*

3.4.1 Inhibition of Neovascularization

On day 14, neovascularization in the NS group and free-drug group formed and almost invaded the center of the cornea (**Figure 3A**). Dense vessels around the entire eyeball were observed from the limbus, and the CoNV areas of the two groups accounted for 89.41 ± 8.58% and 79.59 ± 18.17% of the entire cornea, respectively (**Figure 3B**). In addition, anterior chamber hemorrhage was also observed in some mice in the NS group. Moreover, the average CoNV area was 76.64 ± 10.03% in the commercial FK506 eye drop group. In contrast, the FK506 liposome group showed only moderate neovascularization, which was mainly confined around the limbus, and the blood vessels were relatively sparse (**Figure 3A**). Compared with the NS group, the commercial FK506 eye drop group, and the free-drug group, the CoNV area was reduced by 59.97% ($p < 0.0001$), 47.2% ($p < 0.001$), and 50.15% ($p < 0.001$) in the FK506 liposome group (**Figure 3B**), respectively. In addition, the lengths of the blood vessels increased significantly with time. On day 14, the vessel lengths in the NS group (937.57 ± 111.66), commercial FK506 eye drop group (711.89 ± 124.48), free-drug group (745.24 ± 152.80), and FK506 liposome group (342.90 ± 116.85) were quantitatively analyzed (**Figure 3C**). The results showed that both the commercial FK506 eye drops and FK506 liposomes effectively reduced the vessel lengths; the effect of FK506 liposomes was better ($p < 0.0001$ vs. NS; $p < 0.001$ vs. free drug; $p < 0.001$ vs. commercial FK506 eye drops). Compared with the NS group, mice treated with FK506 liposomes showed a reduction in vessel length of approximately 63.43% (**Figure 3C**).

Meanwhile, the corneas were also stained with a vascular endothelial cell marker (CD31) to more intuitively study the CoNV area at the end of the 14th day (**Figure 3G**). Similar to the aforementioned results, after administration of FK506 liposomes, the CoNV area and vessel length were significantly reduced compared with the other three groups (**Figure 3G**; **Supplementary Figure 2**), indicating that FK506 liposomes were more effective in delivering drugs and inhibiting the formation of new blood vessels compared with the free drug and commercial FK506 eye drops.

Bakunowicz-Łazarczyk and Urban (2016) showed that in the acute phase of alkali burns, anti-inflammation, anti-angiogenesis, and enhancing epithelial healing are the key aspects in clinical treatments. The new blood vessels gradually grew out on days 3 and 7 and reached the peak on day 14. New vessels can block and diffract the penetration of light through their physical presence and can further damage the structural integrity of the cornea (Sharif and Sharif, 2019). The significant reduction in angiogenesis after FK506 treatment was essential for maintaining optimal vision and protecting the eyes from infection and structural damage. One of the treatment methods for CoNV is to begin anti-angiogenesis at an early stage and stop the formation of neovascularization, while the other is intended to trigger vascular degeneration by inducing the reversal of immature blood vessels. FK506 may act via these two aspects to inhibit the formation of CoNV (Sharif and Sharif, 2019). The therapeutic effect of FK506 liposomes on CoNV was associated with the preocular retention time and the amount of drug entering the cornea. The aforementioned findings further confirmed that FK506 liposomes had a greater effect on reducing CoNV.

3.4.2 Corneal Turbidity Scores

After the mouse model of alkali burns was established, the corneal stroma developed edema, and the corneas lost transparency over time. On days 7 and 14 after treatment, the corneal turbidity score of the cationic FK506 liposome group was markedly lower compared with those of the NS group (day 7, 1.33 ± 0.52 vs. 3.50 ± 0.63, $p < 0.001$; day 14, 1.83 ± 0.93 vs. 3.92 ± 0.20, $p < 0.001$) and the free-drug group (day 7, 1.33 ± 0.52 vs. 3.17 ± 1.21, $p < 0.01$; day 14, 1.83 ± 0.93 vs. 3.25 ± 1.04, $p < 0.01$), indicating that the transparency of the cornea gradually improved after treatment with FK506 liposomes (**Figure 3D**). In contrast, the corneal transparency in the NS group gradually deteriorated over time. The corneal transparency of the commercial FK506 eye drop group was significantly improved on day 7 compared with that of the NS group ($p < 0.05$). However, no significant difference between the two groups was detected on day 14. Similarly, mice treated with the free drug showed no difference in corneal opacity compared with the NS group on day 14, and the internal structure of the anterior chamber was still not clearly visible.

The cornea is an avascular structure, which is an essential element for obtaining optimal vision (Qazi et al., 2010; Kather and Kroll, 2014; Nicholas and Mysore, 2021). In the case of inflammation and hypoxia, the expressions of angiogenesis factors are up-regulated, and CoNV is formed, leading to a vicious circle of corneal opacity and chronic inflammation. Except for small corneal scrapes, the damaged cornea is unable to return to its original transparency. After a corneal injury, when the corneal stromal cells transform into activated fibroblasts, the reflectivity of the corneal stromal cells is increased, thereby enhancing the turbidity of the cornea (Zahir-Jouzdani et al., 2019). In addition to causing severe tissue damage, corneal alkali burns can also cause the production of many growth factors and inflammatory cytokines, which promote corneal opacity after injury. The results of the present study showed that treatment with FK506 liposomes could help restore corneal optical transparency and vision after alkali burns.

3.4.3 Corneal Epithelial Defect Area

Figure 3E illustrates the typical images of corneal epithelial defects on days 1, 3, and 7 of alkali burn treatment. Sodium

fluorescein staining showed that on day 1, corneal surfaces were extensively stained in all groups, indicating that the corneal epithelia in all groups were severely damaged. On day 3, the area of the corneal epithelial defects in the FK506 liposome group (18.67 ± 17.82%) was significantly smaller than that in the NS group (52.00 ± 15.86%) ($p < 0.01$) (**Figure 3F**). However, there was no difference in sodium fluorescein staining areas among the free-drug group (30.83 ± 16.76%), commercial FK506 eye drop group (32.17 ± 13.26%), and NS group. On day 7, the areas of corneal epithelial defects in the free-drug group (22.83 ± 15.15%) and commercial FK506 eye drop group (21.83 ± 14.28%) were similar to that in the NS group (26.67 ± 4.80%) (**Figure 3F**). However, quantification results on day 7 showed that the corneal epithelial defects in the FK506 liposome treatment group (2.17 ± 5.31%) were markedly smaller than those in the NS group and the free-drug group ($p < 0.05$ for both), indicating that FK506 liposomes exhibited the fastest wound healing effect and could significantly improve corneal epithelial healing after alkali burns.

Furthermore, CoNV is also closely related to corneal epithelial defects. When the cornea is injured, the normal differentiation of limbal stem cells is disturbed; metaplasia and keratosis will occur in the corneal epithelium, leading to transparency loss and subepithelial CoNV (Kather and Kroll, 2014). In recent studies, the anti-angiogenic effect of the corneal epithelium and its role in the prevention of CoNV have been widely accepted (Roshandel et al., 2018). After alkali burns, the structure of the cornea is destroyed, thereby promoting the entrance of pathogenic factors into the deeper layers of the cornea. After FK506 treatment, the rapid recovery of the corneal epithelium can help rebuild the corneal structure and prevent further invasion of inflammatory mediators (Chowdhury et al., 2013). Therefore, the acceleration of corneal epithelialization in the FK506 liposome group could strengthen corneal healing after alkali burns.

3.5 H&E Staining and α-smooth Muscle Actin Staining

As shown in **Figure 3H**, the most severe corneal stroma edema was found in the NS group, and this group's corneal thickness was also the thickest among all groups. Additionally, the corneal stromata in the NS group were loosely arranged, and there were many neovascular cavities and inflammatory cells infiltrated. The corneal thickness in the free-drug group was still very high, while the vascular lumens and inflammatory cell infiltration were significantly reduced, indicating that local drug treatment helped restore the normal structure of the cornea. However, the corneas treated with commercial FK506 eye drops and FK506 liposomes only had mild edema, and the central corneal thickness was significantly reduced, showing relatively normal stromata. In addition, the numbers of neovascular lumens and infiltrated inflammatory cells were also lower than in the other two groups. The results of α-SMA IHC staining showed that compared with the other three groups, the FK506 liposome group had a weaker α-SMA staining intensity (**Figure 3I**).

After an alkali burn, the corneal epithelium is severely damaged, and the corneal stroma has edema. The restoration of the normal anatomical structure of the cornea is the optimal result, and it can promote the restoration of vision. The microscopic morphological changes of the cornea after the FK506 liposome treatment indicated that liposomes effectively reduced the degree of inflammation and inhibited the formation of CoNV after alkali burns. Furthermore, α-SMA is a vascular smooth muscle marker produced by fibroblasts that can locate mature blood vessels (Chen et al., 2021). After alkali burns, fibroblasts produce α-SMA in the process of scar formation, leading to corneal fibrosis and severe pathological corneal opacity, which greatly affects a patient's corneal transparency (Joung et al., 2020). Therefore, inhibiting the differentiation of fibroblasts into myofibroblasts after a corneal alkali burn is an important aspect of treatment. The results of both H&E staining and α-SMA staining showed that the administration of FK506 liposomes helped to restore the normal structure of the cornea and reduce the degree of corneal fibrosis.

3.6 Evaluation of Corneal Inflammation and Angiogenesis-Related Factors Using qRT-PCR

To further explore the therapeutic mechanisms of FK506 liposomes in CoNV and corneal inflammation caused by alkali burns, qRT-PCR was used to study the expressions of several inflammatory and angiogenesis-related cytokines at the mRNA level on day 14. The corneas in the NS group expressed high levels of angiogenic factors VEGF-A and VEGFR-3 and inflammation-related cytokines IL-6 and MMP-9 ($p < 0.01$ vs. controls) (**Figure 3J**). Compared with the other three treatment methods, FK506 liposomes significantly reduced the expression of VEGF-A ($p < 0.0001$ vs. NS; $p < 0.001$ vs. the free drug; $p < 0.01$ vs. commercial FK506 eye drops). Moreover, both the commercial FK506 eye drops and the FK506 liposomes effectively reduced the expression of MMP-9 ($p < 0.05$). Furthermore, all treatment groups exhibited reduced expression of IL-6; the reduction was the most significant in the FK506 liposome group ($p < 0.0001$ vs. NS; $p < 0.0001$ vs. the free drug; $p < 0.05$ vs. commercial FK506 eye drops). Similar to VEGF-A and IL-6, the lowest expression of VEGFR-3 was also detected in the corneas treated with FK506 liposomes ($p < 0.0001$ vs. NS; $p < 0.001$ vs. the free drug). The free drug had no significant effect on reducing VEGFR-3 or MMP-9 ($p > 0.05$ vs. NS), while FK506 liposomes significantly reduced the expressions of the four cytokines in the corneas ($p < 0.05$ vs. NS).

CoNV is attributed to the imbalance between the expressions of pro-angiogenic factors and anti-angiogenic factors in the cornea. Among the cytokines that promote the formation of CoNV, VEGF is the most direct and is one of the strongest angiogenesis-promoting cytokines known in current research. Furthermore, VEGF-A plays a critical role in promoting neovascularization in the cornea and retina. Meanwhile, VEGFR-3 could also promote neovascularization by regulating lymphangiogenesis. In addition, angiogenesis requires the degradation of the extracellular matrix surrounding capillaries. MMPs can lyse the vascular basement membrane, promote the movement of vascular endothelial cells to the injured sites, and assist in the formation of blood vessels. MMP-2 and MMP-9, as

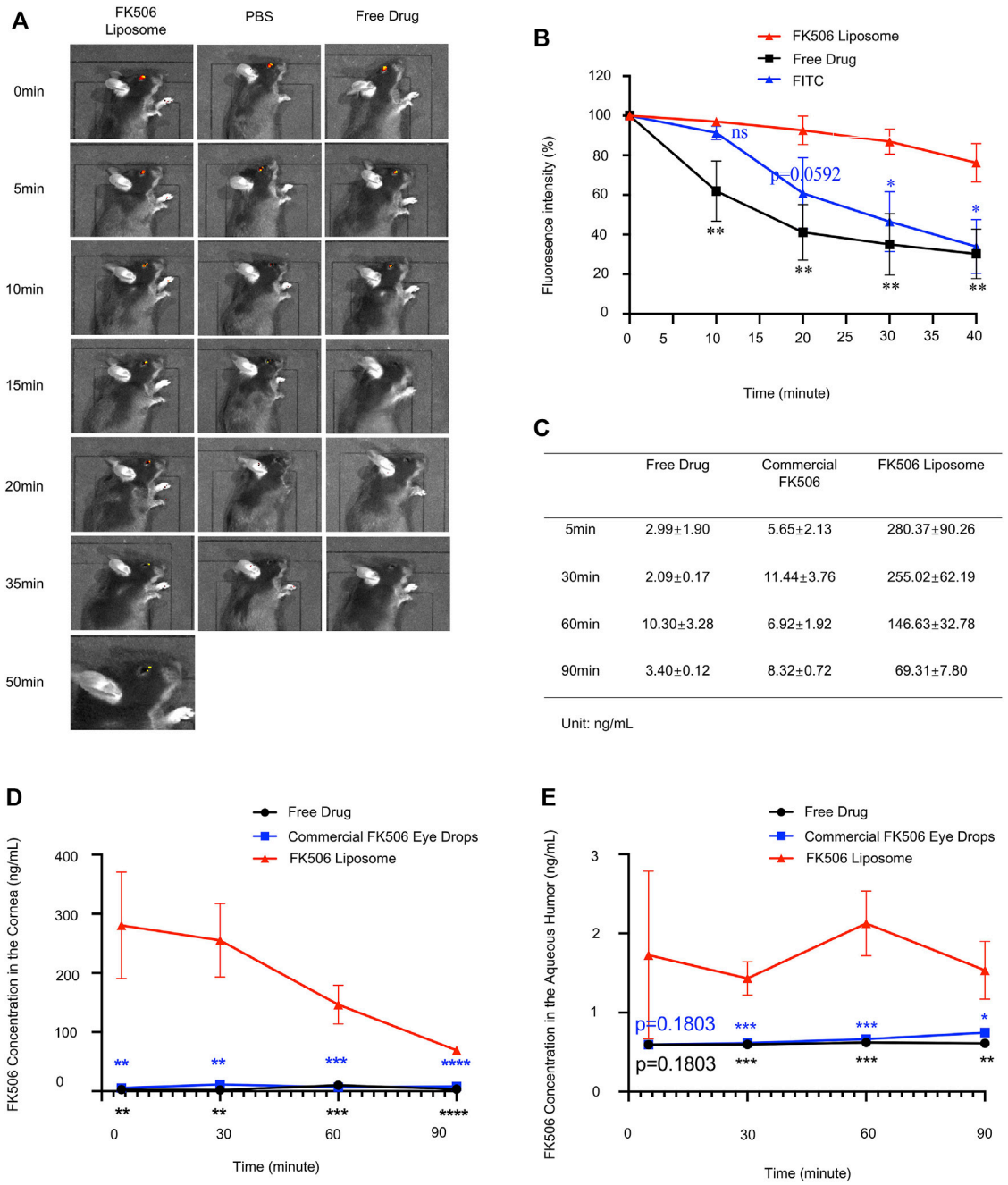

FIGURE 4 | (A) After instilling three different preparations for 0, 5, 10, 15, 20, 35, and 50 min, the fluorescence intensity on the ocular surface. **(B)** Fluorescence intensity variation curve of different treatment groups tracked by IVIS at different time intervals ($n = 3$). **(C)** FK506 concentration in the rabbit corneas after using different FK506 preparations at different time intervals ($n = 3$). **(D)** Corneal FK506 concentration-time curve ($n = 3$); **(E)** FK506 concentration in the aqueous humor of rabbits after using different FK506 preparations at different time intervals ($n = 3$). The data was presented as mean ± SD, one-way ANOVA, $^{*}p < 0.05$, $^{**}p < 0.01$, $^{***}p < 0.001$, and $^{****}p < 0.0001$; ns denotes no significance.

the most effective metalloproteinases, are closely related to CoNV (Nicholas and Mysore, 2021). In addition, inflammation is also a core part of neovascularization (Roshandel et al., 2018). Research has shown that IL-6 is important in VEGF-mediated ocular neovascularization. The expression of IL-6 can be strongly induced in the early stage of corneal alkali burns (Tian et al., 2021). IL-6 can promote the expression of VEGF (Tian et al., 2021), and these two factors lead to the increase in vascular permeability and the formation of new blood vessels. These results indicate that FK506 liposomes may inhibit CoNV and inflammation by blocking the pathways related to VEGF, MMP, and IL-6.

3.7 Retention of FK506 Liposomes on the Ocular Surface

The pre-corneal retention time was expressed as the intensity of the residual fluorescence on the ocular surface. **Figure 4A** shows the residual fluorescence on the ocular surface at different time points after using three different preparations. After using the eye drops for 10 min, the residual fluorescence intensity in the mice treated with FITC-labeled FK506 liposomes (97.02 ± 1.71%) was significantly higher than that in the mice treated with the free-drug solution (61.97 ± 15.3%) ($p < 0.01$). The fluorescence intensities of the free-drug solution and the fluorescent dye solution showed significant attenuation in 10–20 min and completely disappeared at the end of the 20th minute. However, at the end of the 50th minute, fluorescent signals from the mice in the cationic FK506 liposome group were still detectable. **Figure 4B** shows the percentage of the residual fluorescence intensity to the initial fluorescence intensity at different time points.

This finding indicated that compared with the other two preparations, cationic FK506 liposomes were not quickly eliminated from the cornea; this might be attributed to the electrostatic effect between the cationic liposomes and the negatively charged mucin layer, causing the liposomes to remain on the corneas for a longer period of time (Han et al., 2020a). Moreover, the viscosity of the FK506 liposomes was higher than those of the other two formulations; this might also play a role in prolonging the retention time on the ocular surface.

3.8 FK506 Content in the Cornea and the Aqueous Humor

Figures 4C,D show the concentrations of FK506 in the corneas after topical administration of three different preparations. At 5, 30, 60, and 90 min after administration, the corneal drug concentration in the FK506 liposome group was 93.77 ($p < 0.01$), 120.30 ($p < 0.01$), 14.24 ($p < 0.001$), and 20.36 times ($p < 0.0001$) higher, respectively, than in the free-drug group at the same time points. Moreover, the corneal drug level was 49.58 ($p < 0.01$), 21.95 ($p < 0.01$), 21.19 ($p < 0.001$), and 8.33 times ($p < 0.0001$) higher than that of the commercial FK506 eye drops at the time points mentioned above.

We also measured the drug content in the aqueous humor and found that the drug contents in the commercial FK506 eye drop group and the free-drug group were almost negligible at all time points. At 5, 30, 60, and 90 min after administration, the drug concentration in the aqueous humor of the FK506 liposome group was 2.91, 2.40 ($p < 0.001$), 3.43 ($p < 0.001$), and 2.51 times ($p < 0.05$) higher, respectively, than in the free-drug group at the same time points. Moreover, the cornea drug level was 2.91, 2.33 ($p < 0.001$), 3.21 ($p < 0.001$), and 2.05 times ($p < 0.01$) higher, respectively, than in the commercial FK506 eye drop group. **Figure 4E** illustrates the curve of the FK506 concentration in the aqueous humor over time.

The underlying mechanism of the stronger corneal permeability of FK506 liposomes might be attributed to the following aspects. First, FK506 liposomes adhered to the corneal surface and continuously penetrated the aqueous humor due to the electrostatic interaction between the positive liposomes and the negative ocular surface mucins. Second, the positively charged liposome surface assisted in opening the tight junctions between cells and increasing the absorption of the drug. Finally, due to the amphiphilic nature of liposomes and the membrane fusion between the liposomes and the corneal epithelium, hydrophobic FK506 could break through the hydrophilic and lipophilic barriers between different layers of the cornea after being encapsulated by liposomes. Commercial FK506 eye drops are an eye suspension that can retain the drug particles in the precorneal cavity to prolong the contact time between FK506 and the cornea. However, the particle size of the therapeutic agent determines the time required for the drug molecule to enter the corneal tissues, which might be the reason why the bioavailability of commercial FK506 eye drops was affected (Gote et al., 2019). Therefore, both the ocular surface retention time and corneal penetration experiments proved that cationic FK506 liposomes had a longer residence time and better corneal permeability.

4 CONCLUSION

In the present study, we demonstrated the potential of cationic FK506 liposomes in improving the ocular bioavailability and therapeutic effects of hydrophobic FK506. Compared with the free drug (0.2 mg/ml) and commercial FK506 eye drops (1 mg/ml), cationic FK506 liposomes (0.2 mg/ml) exhibited a 2.5-fold prolonged ocular residence time and an approximately 120-fold amount of the drug entering into the cornea. Furthermore, both *in vitro* and *in vivo* experiments proved that cationic FK506 liposomes had good biocompatibility. Additionally, the inhibitory effects of FK506 liposomes on VEGF-induced vascular endothelial cell migration and tube formation were also confirmed *in vitro*. Meanwhile, the present research showed that compared with the free drug and commercial FK506 eye drops, cationic FK506 liposomes could better inhibit the formation of CoNV caused by alkali burns, reduce inflammation, and promote corneal epithelial healing. Collectively, cationic FK506 liposomes might have broad prospects in the treatment of CoNV and corneal inflammation in the future.

DATA AVAILABILITY STATEMENT

The original contributions presented in the study are included in the article/**Supplementary Material**, further inquiries can be directed to the corresponding authors.

ETHICS STATEMENT

The animal study was reviewed and approved by Animal Ethics Committee of the Second Affiliated Hospital of Zhejiang University School of Medicine.

AUTHOR CONTRIBUTIONS

XL, XY, XC, SS, JW, BW, and WX designed and implemented the entire study. XL, XY, and WX analyzed the data and wrote the manuscript.

FUNDING

We thank the financial support from Zhejiang Province Key Research and Development Program (2017C03046).

ACKNOWLEDGMENTS

We thank Zhang Xiaomin of Zhejiang University for her help in the TEM part of this article.

SUPPLEMENTARY MATERIAL

The Supplementary Material for this article can be found online at: https://www.frontiersin.org/articles/10.3389/fbioe.2021.791954/full#supplementary-material

REFERENCES

Alvarez-Trabado, J., Diebold, Y., and Sanchez, A. (2017). Designing Lipid Nanoparticles for Topical Ocular Drug Delivery. *Int. J. Pharmaceutics* 532 (1), 204–217. doi:10.1016/j.ijpharm.2017.09.017

Anderson, C., Zhou, Q., and Wang, S. (2014). An Alkali-Burn Injury Model of Corneal Neovascularization in the Mouse. *J. Vis. Exp.* 86, 51159. doi:10.3791/51159

Chen, L., Zhong, J., Li, S., Li, W., Wang, B., Deng, Y., et al. (2018). The Long-Term Effect of Tacrolimus on Alkali Burn-Induced Corneal Neovascularization and Inflammation Surpasses that of Anti-vascular Endothelial Growth Factor. *Drug Des. Devel Ther.* 12, 2959–2969. doi:10.2147/DDDT.S175297

Chen, Z., Mao, X., Ye, X., Li, S., Wu, T., Wang, Q., et al. (2021). A Novel and Biocompatible Nanofiber of VEGF Peptide for Enhanced Corneal Neovascularization Suppression. *Chem. Eng. J.* 416, 129081. doi:10.1016/j.cej.2021.129081

Chowdhury, S., Guha, R., Trivedi, R., Kompella, U. B., Konar, A., and Hazra, S. (2013). Pirfenidone Nanoparticles Improve Corneal Wound Healing and Prevent Scarring Following Alkali Burn. *PLoS One* 8 (8), e70528. doi:10.1371/journal.pone.0070528

Chuang, Y.-L., Fang, H.-W., Ajitsaria, A., Chen, K.-H., Su, C.-Y., Liu, G.-S., et al. (2019). Development of Kaempferol-Loaded Gelatin Nanoparticles for the Treatment of Corneal Neovascularization in Mice. *Pharmaceutics* 11 (12), 635. doi:10.3390/pharmaceutics11120635

Gai, X., Cheng, L., Li, T., Liu, D., Wang, Y., Wang, T., et al. (2018). *In Vitro* and *In Vivo* Studies on a Novel Bioadhesive Colloidal System: Cationic Liposomes of Ibuprofen. *AAPS PharmSciTech* 19 (2), 700–709. doi:10.1208/s12249-017-0872-4

Gote, V., Sikder, S., Sicotte, J., and Pal, D. (2019). Ocular Drug Delivery: Present Innovations and Future Challenges. *J. Pharmacol. Exp. Ther.* 370 (3), 602–624. doi:10.1124/jpet.119.256933

Han, H., Gao, Y., Chai, M., Zhang, X., Liu, S., Huang, Y., et al. (2020a). Biofilm Microenvironment Activated Supramolecular Nanoparticles for Enhanced Photodynamic Therapy of Bacterial Keratitis. *J. Controlled Release* 327, 676–687. doi:10.1016/j.jconrel.2020.09.014

Han, H., Yin, Q., Tang, X., Yu, X., Gao, Q., Tang, Y., et al. (2020b). Development of Mucoadhesive Cationic Polypeptide Micelles for Sustained Cabozantinib Release and Inhibition of Corneal Neovascularization. *J. Mater. Chem. B* 8 (23), 5143–5154. doi:10.1039/d0tb00874e

Joung, C., Noh, H., Jung, J., Song, H. Y., Bae, H., Pahk, K., et al. (2020). A Novel CD147 Inhibitor, SP-8356, Attenuates Pathological Fibrosis in Alkali-Burned Rat Cornea. *Int. J. Mol. Sci.* 21 (8), 2990. doi:10.3390/ijms21082990

Jumelle, C., Gholizadeh, S., Annabi, N., and Dana, R. (2020). Advances and Limitations of Drug Delivery Systems Formulated as Eye Drops. *J. Controlled Release* 321, 1–22. doi:10.1016/j.jconrel.2020.01.057

Kather, J. N., and Kroll, J. (2014). Transgenic Mouse Models of Corneal Neovascularization: New Perspectives for Angiogenesis Research. *Invest. Ophthalmol. Vis. Sci.* 55 (11), 7637–7651. doi:10.1167/iovs.14-15430

Li, Q., Li, Z., Zeng, W., Ge, S., Lu, H., Wu, C., et al. (2014). Proniosome-derived Niosomes for Tacrolimus Topical Ocular Delivery: *In Vitro* Cornea Permeation, Ocular Irritation, and *In Vivo* Anti-allograft Rejection. *Eur. J. Pharm. Sci.* 62, 115–123. doi:10.1016/j.ejps.2014.05.020

Lin, S., Ge, C., Wang, D., Xie, Q., Wu, B., Wang, J., et al. (2019). Overcoming the Anatomical and Physiological Barriers in Topical Eye Surface Medication Using a Peptide-Decorated Polymeric Micelle. *ACS Appl. Mater. Inter.* 11 (43), 39603–39612. doi:10.1021/acsami.9b13851

Lin, X., Wu, X., Chen, X., Wang, B., and Xu, W. (2021). Intellective and Stimuli-Responsive Drug Delivery Systems in Eyes. *Int. J. Pharmaceutics* 602, 120591. doi:10.1016/j.ijpharm.2021.120591

Liu, D., Wu, Q., Chen, W., Lin, H., Zhu, Y., Liu, Y., et al. (2019). A Novel FK506 Loaded Nanomicelles Consisting of Amino-Terminated Poly(ethylene glycol)-block-poly(D,L)-lactic Acid and Hydroxypropyl Methylcellulose for Ocular Drug Delivery. *Int. J. Pharmaceutics* 562, 1–10. doi:10.1016/j.ijpharm.2019.03.022

Mendez, N., Herrera, V., Zhang, L., Hedjran, F., Feuer, R., Blair, S. L., et al. (2014). Encapsulation of Adenovirus Serotype 5 in Anionic Lecithin Liposomes Using a Bead-Based Immunoprecipitation Technique Enhances Transfection Efficiency. *Biomaterials* 35 (35), 9554–9561. doi:10.1016/j.biomaterials.2014.08.010

Mu, C., Shi, M., Liu, P., Chen, L., and Marriott, G. (2018). Daylight-Mediated, Passive, and Sustained Release of the Glaucoma Drug Timolol from a Contact Lens. *ACS Cent. Sci.* 4 (12), 1677–1687. doi:10.1021/acscentsci.8b00641

Nicholas, M. P., and Mysore, N. (2021). Corneal Neovascularization. *Exp. Eye Res.* 202, 108363. doi:10.1016/j.exer.2020.108363

Nowak-Sliwinska, P., Alitalo, K., Allen, E., Anisimov, A., Aplin, A. C., Auerbach, R., et al. (2018). Consensus Guidelines for the Use and Interpretation of Angiogenesis Assays. *Angiogenesis* 21 (3), 425–532. doi:10.1007/s10456-018-9613-x

Park, J.-H., Joo, C.-K., and Chung, S. K. (2015). Comparative Study of Tacrolimus and Bevacizumab on Corneal Neovascularization in Rabbits. *Cornea* 34, 449–455. doi:10.1097/ico.0000000000000336

Pleyer, U., Lutz, S., Jusko, W. J., Nguyen, K. D., Narawane, M., Rückert, D., et al. (1993). Ocular Absorption of Topically Applied FK506 from Liposomal and Oil Formulations in the Rabbit Eye. *Invest. Ophthalmol. Vis. Sci.* 34 (9), 2737–2742.

Qazi, Y., Wong, G., Monson, B., Stringham, J., and Ambati, B. K. (2010). Corneal Transparency: Genesis, Maintenance and Dysfunction. *Brain Res. Bull.* 81 (2-3), 198–210. doi:10.1016/j.brainresbull.2009.05.019

Qi, J., Dai, R., Zhou, L., Lu, Y., Wu, W., and Liu, W. (2013). Liposomes Containing Bile Salts as Novel Ocular Delivery Systems for Tacrolimus (FK506): *In Vitro* Characterization and Improved Corneal Permeation. *Int. J. Nanomedicine* 8, 1921–1933. doi:10.2147/IJN.S44487

Roshandel, D., Eslani, M., Baradaran-Rafii, A., Cheung, A. Y., Kurji, K., Jabbehdari, S., et al. (2018). Current and Emerging Therapies for Corneal Neovascularization. *Ocul. Surf.* 16 (4), 398–414. doi:10.1016/j.jtos.2018.06.004

Sharif, Z., and Sharif, W. (2019). Corneal Neovascularization: Updates on Pathophysiology, Investigations & Management. *Rom. J. Ophthalmol.* 63 (1), 15–22. doi:10.22336/rjo.2019.4

Tian, Y., Zhang, F., Qiu, Y., Wang, S., Li, F., Zhao, J., et al. (2021). Reduction of Choroidal Neovascularization via Cleavable VEGF Antibodies Conjugated to Exosomes Derived from Regulatory T Cells. *Nat. Biomed. Eng.* 5, 968–982. doi:10.1038/s41551-021-00764-3

Urtti, A. (2006). Challenges and Obstacles of Ocular Pharmacokinetics and Drug Delivery. *Adv. Drug Deliv. Rev.* 58 (11), 1131–1135. doi:10.1016/j.addr.2006.07.027

Whitcup, S. M., Pleyer, U., Lai, J. C., Lutz, S., Mochizuki, M., and Chan, C.-C. (1998). Topical Liposome-Encapsulated FK506 for the Treatment of Endotoxin-Induced Uveitis. *Ocul. Immunol. Inflamm.* 6 (1), 51–56. doi:10.1076/ocii.6.1.51.8079

Wu, D., Zhao, Z., Kim, J., Razmi, A., Wang, L. L. W., Kapate, N., et al. (2021). Gemcitabine and Doxorubicin in Immunostimulatory Monophosphoryl Lipid A Liposomes for Treating Breast Cancer. *Bioeng. Transl Med.* 6 (1), e10188. doi:10.1002/btm2.10188

Wu, Y., Xu, Z., Yang, Y., Qiu, J., Yang, M., Wu, C., et al. (2019). Tetramethylpyrazine (TMP) Ameliorates Corneal Neovascularization via Regulating Cell Infiltration into Cornea after Alkali Burn. *Biomed. Pharmacother.* 109, 1041–1051. doi:10.1016/j.biopha.2018.10.091

Zahir-Jouzdani, F., Khonsari, F., Soleimani, M., Mahbod, M., Arefian, E., Heydari, M., et al. (2019). Nanostructured Lipid Carriers Containing Rapamycin for Prevention of Corneal Fibroblasts Proliferation and Haze Propagation after Burn Injuries: *In Vitro* and *In Vivo*. *J. Cel Physiol* 234 (4), 4702–4712. doi:10.1002/jcp.27243

Zeng, W., Li, Q., Wan, T., Liu, C., Pan, W., Wu, Z., et al. (2016). Hyaluronic Acid-Coated Niosomes Facilitate Tacrolimus Ocular Delivery: Mucoadhesion, Precorneal Retention, Aqueous Humor Pharmacokinetics, and Transcorneal Permeability. *Colloids Surf. B: Biointerfaces* 141, 28–35. doi:10.1016/j.colsurfb.2016.01.014

Zhang, R., He, R., Qian, J., Guo, J., Xue, K., and Yuan, Y.-f. (2010). Treatment of Experimental Autoimmune Uveoretinitis with Intravitreal Injection of Tacrolimus (FK506) Encapsulated in Liposomes. *Invest. Ophthalmol. Vis. Sci.* 51 (7), 3575–3582. doi:10.1167/iovs.09-4373

Zhong, Y., Wang, K., Zhang, Y., Yin, Q., Li, S., Wang, J., et al. (2021). Ocular Wnt/β-Catenin Pathway Inhibitor XAV939-Loaded Liposomes for Treating Alkali-Burned Corneal Wound and Neovascularization. *Front. Bioeng. Biotechnol.* 9, 753879. doi:10.3389/fbioe.2021.753879

Conflict of Interest: The authors declare that the research was conducted in the absence of any commercial or financial relationships that could be construed as a potential conflict of interest.

Publisher's Note: All claims expressed in this article are solely those of the authors and do not necessarily represent those of their affiliated organizations, or those of the publisher, the editors and the reviewers. Any product that may be evaluated in this article, or claim that may be made by its manufacturer, is not guaranteed or endorsed by the publisher.

frontiers in Bioengineering and Biotechnology

ORIGINAL RESEARCH
published: 22 February 2022
doi: 10.3389/fbioe.2022.805996

Efficient Transient Expression of Plasmid DNA Using Poly (2-(*N*,*N*-Dimethylamino) Ethyl Methacrylate) in Plant Cells

Zishuai An[1,2,3], *Bing Cao*[1,2,3], *Junzhe Zhang*[1,2,3], *Baihong Zhang*[1,2,3], *Chengqian Zhou*[4], *Xianglong Hu*[1,2,3]* and *Wenli Chen*[1,2,3]*

[1]MOE Key Laboratory of Laser Life Science and Institute of Laser Life Science, College of Biophotonics, South China Normal University, Guangzhou, China, [2]Guangdong Provincial Key Laboratory of Laser Life Science, College of Biophotonics, South China Normal University, Guangzhou, China, [3]Guangzhou Key Laboratory of Spectral Analysis and Functional Probes, College of Biophotonics, South China Normal University, Guangzhou, China, [4]Neuroscience Laboratory, Hugo Moser Research Institute at Kennedy Krieger, Baltimore, MD, United States

Nanomaterials have been widely studied for their potential to become the new generation of nanocarriers in gene transfection, yet it remains still difficult to apply them efficiently and succinctly to plant cells. Poly (2-(*N*,*N*-dimethylamino) ethyl methacrylate) (PDMAEMA), which possesses temperature and pH dual-sensitivity, has largely been applied in animal cells, but it is rarely involved in plant cells. As a proof of concept, PDMAEMA as a gene carrier is incubated with plasmid GFP (pGFP) to explore its transfection ability in plants, and cationic polymer polyethylenimine (PEI) is used as a control. pGFP was efficiently condensed into the nanostructure by electrostatic interactions at an N/P (amino group from cationic polymers/phosphate group from plasmid DNA (pDNA)) ratio of 15; after complexation into nanocarriers, pGFP was protected from endonuclease degradation according to the DNase I digestion assay. After incubation with protoplasts and leaves, GFP was observed with confocal microscopy in plant cells. Western blot experiments confirmed GFP expression at the protein level. Toxicity assay showed PDMAEMA had a lower toxicity than PEI. These results showed that transient expression of pGFP was readily achieved in *Arabidopsis thaliana* and *Nicotiana benthamiana*. Notably, PDMAEMA showed lower cytotoxicity than PEI upon incubation with *Nicotiana benthamiana* leaves. PDMAEMA exhibited great potency for DNA delivery in plant cells. This work provides us with new ideas of more concise and more effective methods for plant transformation.

Keywords: poly (2-(N, N-dimethylamino) ethyl methacrylate) (PDMAEMA), polyethylenimine (PEI), plant cells, gene delivery, gene transfection

OPEN ACCESS

Edited by:
Wenzhong Li,
Freie Universität Berlin, Germany

Reviewed by:
Hui Gao,
Tiangong University, China
Honghao Hou,
Southern Medical University, China

***Correspondence:**
Wenli Chen
chenwl@scnu.edu.cn
Xianglong Hu
huxlong@mail.ustc.edu.cn

Specialty section:
This article was submitted to Biomaterials, a section of the journal Frontiers in Bioengineering and Biotechnology

Received: *31 October 2021*
Accepted: *19 January 2022*
Published: *22 February 2022*

Citation:
An Z, Cao B, Zhang J, Zhang B, Zhou C, Hu X and Chen W (2022) Efficient Transient Expression of Plasmid DNA Using Poly (2-(N,N-Dimethylamino) Ethyl Methacrylate) in Plant Cells. Front. Bioeng. Biotechnol. 10:805996. doi: 10.3389/fbioe.2022.805996

INTRODUCTION

Great progress has been made in plant biotechnology in the recent years, but it remains still difficult to efficiently perform genetic transformation on plants (Altpeter et al., 2016). Although the agrobacterium-mediated delivery system is the most classic method for plant genetic transformation, it still has defects such as limitation of plant species and low transformation efficiency (Baltes et al., 2017). Biolistic (gene gun) is another plant transformation tool, which can deliver biomolecules into more general plants without species limitation, but it may cause plant tissue

damage under high bombardment pressure and require a large amount of DNA to perform an efficient plant transformation (Altpeter et al., 2016). Plant viral vectors such as tobacco mosaic virus can also be used to perform transient expression of the exogenous gene in plants. Viral vectors are compatible with various plant species. However, due to relatively narrow virus–host specificity, different plant species may require different vectors.

In recent years, increasing interests have been focused in biological and biomedical applications of nanomaterials (Mei et al., 2019). Among them, the application of nanomaterials for gene delivery in animal cells has been widely studied (Gregory et al., 2020; Yan et al., 2020). Various delivery platforms such as mesoporous silica nanoparticles (Ding et al., 2020), carbon nanotubes (Cifuentes-Rius et al., 2017), gold nanoparticles (Huo et al., 2014; Ortega-Munoz et al., 2016), quantum dots (Liu et al., 2019), magnetic nanoparticles (Lo Y.-L. et al., 2015; Huang et al., 2019), DNA origami (Liu et al., 2018), nanodroplets (Zhang et al., 2019; Cao et al., 2020), and polymers (Chu et al., 2020; Guo et al., 2020; Wang et al., 2020; Wang Z. et al., 2021) can load drugs or other active biomolecules and deliver them to target sites due to their relatively small size, special chemical composition, or functionalized surface structure. Among these many nanomaterials, cationic polymers have attracted more and more attention in molecular delivery due to their advantages of easy synthesis, high stability, low toxicity, low immunogenicity, and compatibility with larger molecular payloads (Yin et al., 2013; Lo C.-W. et al., 2015; Ding et al., 2021). Positively charged cationic polymers can interact with negatively charged DNA by electrostatic interactions and condense DNA into a compact complex in nanoscale (Lo C.-W. et al., 2015). The charge of the complex remains positive and makes it easier to internalize into cells based on the interaction with the negatively charged cell membranes (Lo C.-W. et al., 2015; Demirer et al., 2019). Poly (2-(*N,N*-dimethylamino) ethyl methacrylate) (PDMAEMA) and polyethylenimine (PEI) are two typical cationic polymers with a high density of positively charged amine groups, and have both been used for DNA delivery in animal cells (Wu et al., 2011; Yu et al., 2012; Lo C.-W. et al., 2015; Guo et al., 2021; Richter et al., 2021). Yet, their applications in plant cells are rarely investigated. Hence, it is meaningful to interrogate their potency for plants, such as the controlled release of agrochemicals and target-specific delivery of biomolecules (Faraz et al., 2019; Bijali and Acharya, 2020; Wang W. et al., 2021). PEI shows a relatively high toxicity than other cationic polymers including PDMAEMA in animal cells (Lo C.-W. et al., 2015). Compared with human cancer therapy, there are few studies on the application of nanotechnology in plants. In agriculture field, applications of nanomaterials have been found to efficiently resist environmental stress and improve the efficiency of agrochemicals, including fertilizers and pesticides in an environment-friendly way (Khot et al., 2012; Shang et al., 2019; Fincheira et al., 2020). Mesoporous silica nanoparticles have shown great potential to deliver an exogenous gene into intact *Arabidopsis thaliana* roots and protoplasts without any mechanical aids (Torney et al., 2007; Chang et al., 2013). Additionally, carbon nanotubes with high aspect ratios can efficiently deliver plasmid DNAs (35S–GFP–NOS and UBQ10–GFP–NOS) to several mature plants (Demirer et al., 2019; Kwak et al., 2019). However, there is still a need to develop new delivery methods with good transfection efficiency, good biocompatibility, low toxicity, and immunogenicity in plant cells (Keles et al., 2016).

In our previous study, functioned gold nanoparticles were used to carry a small interfering RNA and successfully silenced a target gene (*NPR1*) in *Arabidopsis thaliana* (Lei et al., 2020). To further explore the transfection behavior of PDMAEMA in plant cells, we combine plasmid GFP (pGFP) as a reporter gene with PDMAEMA and incubated them with protoplasts and leaves to transfect plant cells. GFP fluorescence was successfully observed with confocal microscopy in plant cells. GFP expressions were also detected in the protein level. We managed to transiently transfect plant cells using PDMAEMA, which laid the foundation for the genetic transformation of plants.

MATERIALS AND METHODS

Materials

Plasmid DNA (pDNA) pBI221-GFP (**Supplementary Figure S1**) was purified using a HiPure Plasmid EF Maxi Kit (Magen, Guangzhou, China) for all experiments in this study. The concentration and purity of pGFP were determined by the absorbance ratio at OD_{260}/OD_{280} using a Nano Drop 2000 (Thermo Scientific). Cellulase R-10 (MX7352, Yakult Japan) and MacerozymeR-10 (DH188-2, Dingguo, China) were used for protoplast extraction. The following chemicals were purchased from Sigma-Aldrich: 4-cyano-4-(phenylcarbonothioylthio) pentanoate (CPADB), 2-(dimethylamino) ethyl methacrylate (DMAEMA, 99%) sodium chloride, calcium chloride dehydrate, 2-(N-morpholino) ethanesulfonic acid (MES), D-mannitol, potassium chloride, magnesium chloride hexahydrate, polyethylene glycol (4,000), and polyethylenimine (branched, 25 kDa). 2, 2′-Azobis (2-methylpropionitrile) (AIBN) was obtained from Acros chemicals. 1,4-Dioxane was purchased from Sinopharm Chemical Reagent Co. Ltd. Water used in the study was deionized with a Milli-QSP reagent water system (Millipore).

The seeds of *Arabidopsis thaliana* and *Nicotiana benthamiana* were germinated in pots with a mixture of soil and vermiculite at a ratio of 4:1. The two plants were both grown in the growth chamber (16 h light at 23°C/8 h dark at 23°C). The light intensity was approximately 120 μmol photons $m^{-2}s^{-1}$, and the relative humidity was about 82%.

METHODS

Synthesis of PDMAEMA

The synthesis of PDMAEMA was referred to the previous report (Hu et al., 2014; Cao et al., 2020; Xiao et al., 2020). The chain transfer agent, 4-cyano-4-(phenylcarbonothioylthio) pentanoate (CPADB, 73.3 mg, 0.262 mmol), 2-(dimethylamino) ethyl methacrylate (DMAEMA, 1,450 mg, 9.22 mmol), and 2, 2′-azobis

(2-methylpropionitrile) (AIBN, 8.6 mg, 0.052 mmol) were mixed and charged into a glass ampoule containing 1,4-dioxane (1.375 mL). The ampoule was degassed via three freeze–pump–thaw cycles and flame-sealed under vacuum. Then, the glass ampoule was immersed into an oil bath (70°C) to start polymerization. After 12 h, the ampoule was quenched into liquid nitrogen to terminate the polymerization. The mixture was precipitated into an excess of petroleum ether to generate red residues; the residues were dissolved in dichloromethane and precipitated into petroleum ether. After three cycles of dissolution–precipitation, the final product was dried in a vacuum oven overnight at room temperature, yielding a red solid (1,085 mg, yield: 71.2%). The degree of polymerization of DMAEMA was determined to be ~37 based on the ^{1}H NMR analysis (**Supplementary Figure S2**).

Preparation of PDMAEMA + DNA and PEI + DNA Complexes

Gel retardation assay was performed to determine the N/P ratio of the cationic polymer and DNA (Luo et al., 2011). The complexes of pGFP and polymer were freshly prepared before experiments. The N/P ratio of the complex was counted according to the molar ratio of the amino group from the cationic polymer relative to the phosphate group from pDNA. The solution of plasmid was added to the solution of polymer by gradually increasing PDMAEMA or PEI and the same amount of pGFP. N/P ratios were 1:1, 2:1, 5:1, 10:1, and 15:1. The mixtures were then incubated at room temperature for 30 min to form stable complexes and were run electrophoresis on a 1% agarose gel.

Measurements of Particle Size

A total of 5 micrograms of DNA (1,600 ng/μL) were mixed with PDMAEMA (1 mg/mL) or PEI (1 mg/mL) at the fixed N/P ratio of 15. The formed complexes were diluted in 10 mM $MgCl_2$/MES (pH 5.7) to a final volume of 800 μL. The particle sizes of PDMAEMA + DNA and PEI + DNA complexes were evaluated using the Nano-ZS (Malvern, U.K.). The data are calculated as the means of three measurements.

DNase I Protection Assay

DNase I protection assay was performed as described in reference by Luo et al., (2011) with some modifications to investigate the ability of polymers to protect DNA against endonuclease degradation. The samples of PDMAEMA + DNA (N/P 4.38:1) and PEI + DNA (N/P 2.6:1) complexes were freshly prepared. After incubating the complexes for 30 min at room temperature, samples were treated with DNase I at 37 °C for 10 min, followed by denaturation of DNase I at 65 °C for 10 min, and 2 μL of sodium dodecyl sulfate (SDS, 1% w/v, final concentration 0.1%) was added, and the samples were incubated for 2 h at 37 °C to completely dissociate DNA from the complexes. The samples of naked DNA with or without DNase I treatment were used as positive or negative controls, respectively. The DNA dissociated from PDMAEMA or PEI after DNase I treatment was run on a 1% agarose gel.

Protoplast Isolation From *Arabidopsis thaliana* Leaves

Protoplasts were isolated from the leaves of wild-type *Arabidopsis thaliana* as described by Yoo et al., (2007). In brief, epidermis-removed leaves by adhesive tape were immersed in 15 mL of enzyme solution (1.5% cellulase R-10, 0.75% Macerozyme R-10, 0.5 M mannitol, 10 mM MES with pH 5.7, 10 mM $CaCl_2$, and 0.1% BSA), then incubated at 25 °C for 3 h in the dark with stirring gently. The undigested leaf tissue was removed by filtration with a 75-μm nylon mesh, and then 10 mL W5 solution (1.54 mM NaCl, 125 mM $CaCl_2$, 5 mM KCl, 2 mM MES with pH 5.7, and 5 mM glucose) was added, followed by centrifugation at 60 rcf for 5 min at 4 °C. The pelleted protoplasts were resuspended in W5 solution with a pH of 5.7, which has similar osmolality and pH to those of the protoplasts. The isolated protoplasts are viable on ice for over 24 h. Even then, the freshly isolated protoplasts should be used for gene expression.

Protoplast Transformation With PDMAEMA + DNA, PEI + DNA, and PEG/Ca^{2+}

Protoplast transfection was performed as described in reference by Demirer et al., (2019) with some modifications. A volume of 100 μL (about 1×10^4) of isolated protoplasts in W5 solution was added to about 10 μL of PDMAEMA + DNA, PEI + DNA containing 10 μg DNA, or for the control sample containing the same amount of pDNA and mixed well by gently tapping the tube. The mixture was incubated at room temperature for 24 h to ensure sufficient internalization and expression. For PEG/Ca^{2+} transformation, *Arabidopsis* mesophyll protoplasts were added to 110 μL PEG-Ca^{2+} solution (100 mM $CaCl_2$, 0.2 M mannitol, and 40% PEG 4000) for 15 min incubation at room temperature. Then, protoplasts were diluted in 220 μL W5 solution, followed by 440 and 880 μL W5 solution to wash off the PEG, and after which the protoplasts were harvested by centrifugation at 60 *g* for 5 min at 4 °C. The pellet was washed twice with W5 solution, resuspended in 100 μL W5 solution, and incubated for 24 h at room temperature in the dark. Confocal laser scanning microscope (CLSM) imaging was performed to detect GFP expression by imaging the protoplasts.

Infiltration of Leaves With PDMAEMA + DNA, PEI + DNA, or PDMAEMA + FAM-siRNA$_{NPR1}$

Healthy leaves from *Arabidopsis thaliana* (three to four weeks old) and *Nicotiana benthamiana* (3 weeks old) were chosen for experiments. After preparation of PDMAEMA + DNA and PEI + DNA complexes containing 10 μg DNA at a N/P ratio of 15 (total volume 10 μL), it was diluted with 10 mM $MgCl_2$/MES with pH 5.7 to a final volume of 200 μL and then infiltrated on the abaxial surface of the leaves using a 1-mL needleless syringe by applying gentle pressure. FAM-siRNA$_{NPR1}$ (20 μM) (Lei et al., 2020) was mixed with PDMAEMA (1 mg/mL) at the fixed N/P ratio of 15 and incubated at room temperature for 30 min. The formed complexes were diluted 10 times in 10 mM $MgCl_2$/MES (pH 5.7) before infiltration.

Confocal Microscope Imaging

The images of *Arabidopsis thaliana* protoplasts and leaves were captured using a confocal laser scanning microscope (Carl Zeiss LSM 880 META, Germany). The captured images were processed with commercial Zen software (Carl Zeiss, Germany). GFP fluorescence was captured with 488 nm laser excitation and

539 nm emission wavelengths. Chlorophyll autofluorescence was captured with 633 nm laser excitation and 691 nm emission wavelengths.

Protein Extraction and Western Blot

The protoplasts after incubation with PDMAEMA + DNA or PEI + DNA and the cell culture in the dark were added an equal volume of 2× sample buffer directly at 100 °C for 10 min. For protein extraction of plant leaves, 0.4 g of leaf tissue was ground in liquid nitrogen before adding extraction buffer. The extracts were centrifuged, and the supernatant protein was collected to be denatured in the SDS sample buffer at 100 °C for 10 min. The same amount of total protein for each sample was run on 10% SDS-PAGE gels.

After electrophoresis, protein was transferred onto a polyvinylidene difluoride (PVDF) membrane and then blocked for 2 h with 5% (w/v) skim milk powder in TBS plus 0.1% (v/v) Tween 20 (TBST). For GFP detection, the antibody (JL-8, Monoclonal Antibody, A-6455, WB: 1:1,000, Fisher, Invitrogen, Waltham, MA, USA) directly against GFP protein was diluted in TBST at a ratio of 1:1,000 and incubated with the membrane overnight at 4 °C. The membrane was then washed three times with TBST for 10 min. Goat anti-mouse IgG-HRP (Absin, abs 20001) was then incubated with the membrane for 2 hours at room temperature. The membrane was washed twice for 10 minutes and another one time for 30 minutes with TBST. Clarity Western Substrate (BIO-RAD) was used for chemiluminescent detection of the GFP protein. The detection was performed using a LI-COR Odyssey Infrared Imaging System (Tanon, 5,200, China).

Toxicity Assay

To evaluate plant toxicity, the expression of a known gene called *respiratory burst oxidase homolog B* (*NbRboh B*) in *Nicotiana benthamiana* leaves infiltrated with different samples was detected by qPCR analysis (Demirer et al., 2019), and three-week-old leaves of *Nicotiana benthamiana* were infiltrated with buffer (10 mM $MgCl_2$/MES with pH 5.7, as a negative control), 1% SDS (as a positive control), PDMAEMA + DNA (N/P ratio of 15:1), and PEI + DNA (N/P ratio of 15:1). The infiltrated leaves were collected respectively at 1 h, 3 h, 6 h, and 12 h post-infiltration. The total RNA was extracted from the collected leaves using Trizol and reverse transcribed into cDNA using HiScript RT SuperMix (Vazyme). qPCR was performed using Hieff qPCR SYBR Green Master Mix (Yeason Biotech). *Elongation factor 1* (*EF1*) was measured as a reference gene in the experiment.

Primers for *NbRboh B* are as follows:

Forward: 5′-TTTCTCTGAGGTTTGCCAGCCACCACC TAA-3′; Reverse: 5′-GCCTTCATGTTGTTGACAATGTCT TTAACA-3′.

Primers for *EF1* are as follows:

Forward: 5′-TGGTGTCCTCAAGCCTGGTATGGTTGT-3′; Reverse: 5′- ACGCTTGAGATCCTTAACCGCAACATTCTT-3′(Demirer et al., 2019).

qPCR was run at an annealing temperature of 60 °C with 40 cycles. The fold change of *NbRboh B* expression was normalized with respect to EF1 known as a reference gene. qPCR assay was performed for PDMAEMA + DNA, PEI + DNA, and 1% SDS in triplicate-independent experiments. For each sample, three technical replicates and three biological replicates were performed.

Besides the qPCR analysis, the Fv/Fm ratio is also commonly used to indicate the plant toxicity assay (Demirer et al., 2019). The Fv/Fm ratio represents the variable/maximum fluorescence measurement of the photosystem II in plants. The same 3-week-old leaf of *Nicotiana benthamiana* was infiltrated on four different locations at the abaxial surface with the buffer (10 mM $MgCl_2$/MES with pH 5.7) as a negative control and PDMAEMA + DNA (N/P ratio of 15:1), PEI + DNA (N/P ratio of 15:1), or 1% SDS as a positive control. The infiltrated leaves were then incubated for 24 h. Subsequently, the infiltrated leaf was dark-treated for 30 min, and chlorophyll fluorescence-related parameters were measured using the Imaging-PAM Maxi fluorimeter (Walz) to calculate the Fv/Fm ratio.

Data Processing and Statistical Analysis

All experiments were repeated at least three times or three parallel replicate samples, and the results were processed by GraphPad Prism 8, and then the *t*-test (*$p < 0.05$, **$p < 0.01$, ***$p < 0.001$, and ****$p < 0.0001$) was used for statistical analysis. Data were expressed as mean ± SD.

RESULTS AND DISCUSSION

Characterization of PDMAEMA + DNA and PEI + DNA

Gel electrophoresis shift assay was performed to characterize the interaction and stabilities of the DNA complexes with PDMAEMA or PEI. As shown in **Figures 1A,C**, two polymers combined with the same amount of DNA (1 μg) at different N/P ratios showed different migration of DNA across the gel relative to DNA only. All bands of the DNA complexes with PDMAEMA or PEI were present at different positions compared to those of free DNA. The amount of the migrated free DNA was reduced with an increasing N/P ratio. In other words, with a low N/P ratio, DNA has not been completely coated with PDMAEMA or PEI, and DNA bands can be seen. When the N/P ratio increased, all DNAs were gradually wrapped to form a stable complex, and the DNA bands were no longer visible. The optimal N/P ratio of PDMAEMA + DNA was 4.38:1 and that of PEI + DNA was 2.6:1 (**Supplementary Figures S3A, B**). As shown in **Figures 1A,C**, about 100% of the DNA was captured by PDMAEMA at an N/P ratio of 10 and PEI at an N/P ratio of 5, and thus no free-form plasmid DNA remained in the lane of the gel. **Figures 1B,D** show the average sizes for complexes of PDMAEMA + DNA and PEI + DNA formed at a constant DNA concentration of 5 μg and at an N/P ratio of 15. The average hydrodynamic diameters of the complexes PDMAEMA + DNA (N/P ratio 15) and PEI + DNA (N/P ratio 15) dispersed in 10 mM $MgCl_2$/MES (pH 5.7) were both between 80 and 165 nm, respectively. The most distribution of the diameter of PDMAEMA + DNA and PEI + DNA is 105 nm (**Figures 1B,D**). However, the size of complexes at a low N/P ratio

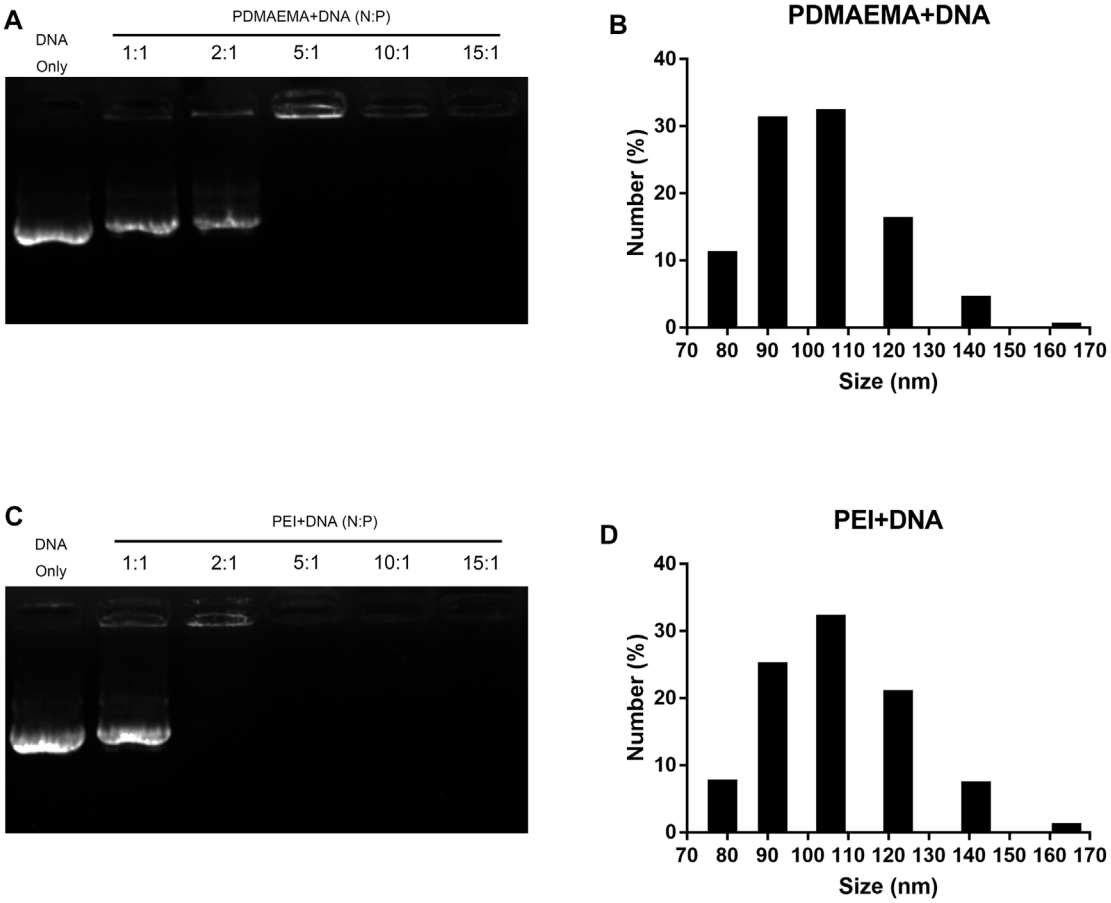

FIGURE 1 | Characterization of PDMAEMA + DNA and PEI + DNA. **(A)** Gel retardation assay of PDMAEMA + DNA (1 μg) at N/P ratios of 1:1, 2:1, 5:1, 10:1, and 15:1. **(B)** Hydrodynamic diameter distributions of PDMAEMA + DNA (5 μg) (N/P ratio 15) determined by dynamic light scattering. **(C)** Gel retardation assay of PEI + DNA (1 μg) at N/P ratios of 1:1, 2:1, 5:1, 10:1, and 15:1. **(D)** Hydrodynamic diameter distributions of PEI + DNA (5 μg) (N/P ratio 15) determined by dynamic light scattering.

(4.38:1 for PDMAEMA + DNA and 2.6:1 for PEI + DNA) is larger than that of complexes at a high ratio of 15 (See **Figures 1B,D** and **Supplementary Figures S1B, D**). Besides, higher N/P ratios are more conducive to transfection efficiencies (Clamme et al., 2003; Maury et al., 2014; Neuberg and Kichler, 2014). Therefore, an N/P ratio of 15 was chosen for all the transfection experiments in this study.

PDMAEMA and PEI Protect DNA From DNase I Degradation

Protection of DNA from nuclease degradation facilitates cell internalization and improves the gene delivery efficiency *in vivo* and *in vitro* (Luo et al., 2011). In consideration of the degradation of nuclease in cells, DNase I was employed to mimic the nuclease in the cell and to test the ability of PDMAEMA and PEI in protecting DNA from nuclease degradation (Lo C.-W. et al., 2015). First, we needed to determine an appropriate concentration of DNase I for this treatment. A decreasing concentration gradient of DNase I was respectively added to the same amount of DNA (1 μg). The different amounts of DNA are shown across the gel with treatment at different concentrations of DNase I (**Figure 2A**). DNA was slightly decomposed after treatment at 37 °C for 10 min (Lane 3, **Figure 2A**) compared to the untreated DNA (Lane 2, **Figure 2A**). A small amount of DNA was degraded after DNase I treatment at concentrations of 0.05 mg/mL and 0.01 mg/mL, but DNA was degraded (Lane 4, **Figure 2A**) after that of 1 mg/mL. Most of the DNA was degraded after DNase I treatment of 1 mg/mL (Lane 5, **Figure 2A**). DNase I treatment of 1 mg/mL is excess for DNA degradation. A lane of 0.1 mg/mL DNase I treatment is more optimal than the lane of DNA and DNA treated. Therefore, the optimal concentration (0.1 mg/mL) of DNase I for DNA degradation was determined. The N/P ratio is important for a compact combination of cationic polymer and DNA. Therefore, the threshold N/P ratios of 4.38:1 for PDMAEMA + DNA and 2.6:1 for PEI + DNA (**Supplementary Figure S3**) were chosen for the DNase I degradation experiments. For DNase I protection assay, DNase I (0.1 mg/mL) was added to the same amount of DNA (1 μg) combined with PDMAEMA or PEI at the threshold N/P ratio. The naked DNA was degraded by DNase I (Lane 4, **Figure 2B**) as the control group and was used to compare to the

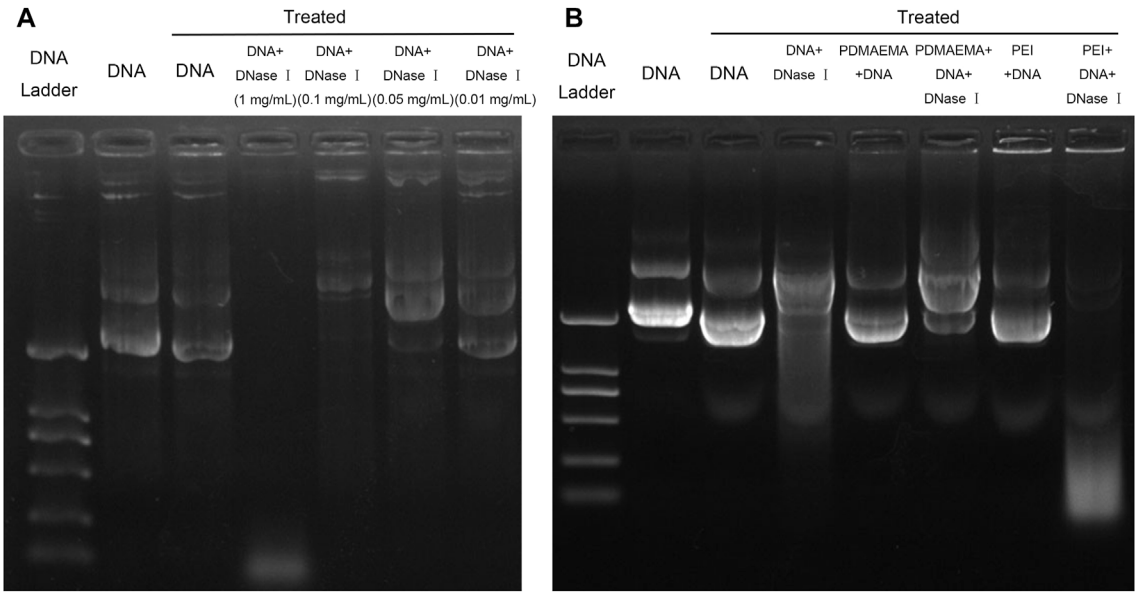

FIGURE 2 | Plasmid DNA protection assay. **(A)** Same amount (1 μg) of pDNA treated by DNase I was run on a 1% agarose gel to determine the optimal DNase I concentration for DNA degradation. **(B)** Agarose gel electrophoresis of DNA, PDMAEMA + DNA (N/P ratio of 4.38:1), and PEI + DNA (N/P ratio of 2.6) incubated with DNase I to evaluate DNA protection against nuclease degradation.

PDMAEMA + DNA and PEI + DNA groups to test the protection of PDMAEMA and PEI. The DNase I protection assay showed that PDMAEMA and PEI were capable of forming compact complexes with DNA, which could largely protect DNA from nuclease degradation (Lane 6 compared with Lane 5, Lane 8 compared with Lane 7, **Figure 2B**). A part of the DNA from PEI + DNA was not shifted but retained in the sample well, and the unclear band at the bottom of the lanes was the degraded DNA (Lane 8, **Figure 2B**). The more amount of degraded DNA means the weaker ability of cationic polymers to protect DNA from degradation. The protective ability of PDMAEMA was even stronger than that of PEI (Lane 6 compared with Lane 8, **Figure 2B**). Similar results about DNase I protection assay of the peptide dendrimers were shown in the previous study (Luo et al., 2011).

Transfection in Isolated *Arabidopsis thaliana* Protoplasts

Generally, the cell wall of plants consists mostly of fibrous structures such as cellulose, pectin, and lignin, which may play a role of barrier against the entry of exogenous substances. Protoplasts are plant cells without cell walls. Therefore, to avoid the cell wall as a barrier, the protoplast isolated from *Arabidopsis thaliana* leaves was employed to perform the transfection experiment. Plasmid DNA (pBI221 vector contains a GFP gene) was used as a report gene in the transfection experiment. The total charges of PDMAEMA + DNA and PEI + DNA complexes maintained a positive value (**Supplementary Figure S4**). Hence, it facilitated the interaction with negatively charged cell membranes and the internalization of complexes into plant protoplasts (Lakshmanan et al., 2013). To evaluate the transfection of PDMAEMA and PEI, DNA complexes of PDMAEMA or PEI were incubated with protoplasts isolated from *Arabidopsis thaliana* leaves as an expression host. Transient GFP expression was detected in protoplasts when protoplasts were incubated with PDMAEMA + DNA or PEI + DNA 24 h later, while there was no GFP fluorescence observed in the protoplasts treated with DNA only (**Figure 3A**, **Supplementary Figure S4**).

Polyethylene glycol 4,000 (PEG 4000) is a polymer fusogenic agent, which is commonly used for plant protoplast transfection. It can facilitate the entry and expression of DNA by changing membrane permeability with the existence of Ca^{2+} (Yoo et al., 2007) and was used as a positive control in this experiment. Western blot was also performed to verify the GFP expression in the protein level in the protoplasts incubated with PDMAEMA + DNA, PEI + DNA, and PEG/Ca^{2+}+DNA (**Figure 3B**). The GFP fluorescence of control PEG/Ca^{2+}+DNA was obviously stronger than that of PDMAEMA + DNA and PEI + DNA, but the Western blot band of the control was weaker than that of PDMAEMA + DNA and PEI + DNA. The transfection way of PEG/Ca^{2+} is different from that of PDMAEMA + DNA and PEI + DNA. Therefore, the incubation time between protoplast and PDMAEMA + DNA or PEI + DNA was 12 h while that of PEG/Ca^{2+} was 15 min. The more fluorescence but less protein level for PEG/Ca^{2+}+DNA treatment may be caused by the protoplast buffer containing PEG 4000, which was not exactly removed in the blocked sample running in one way. Also, we used all

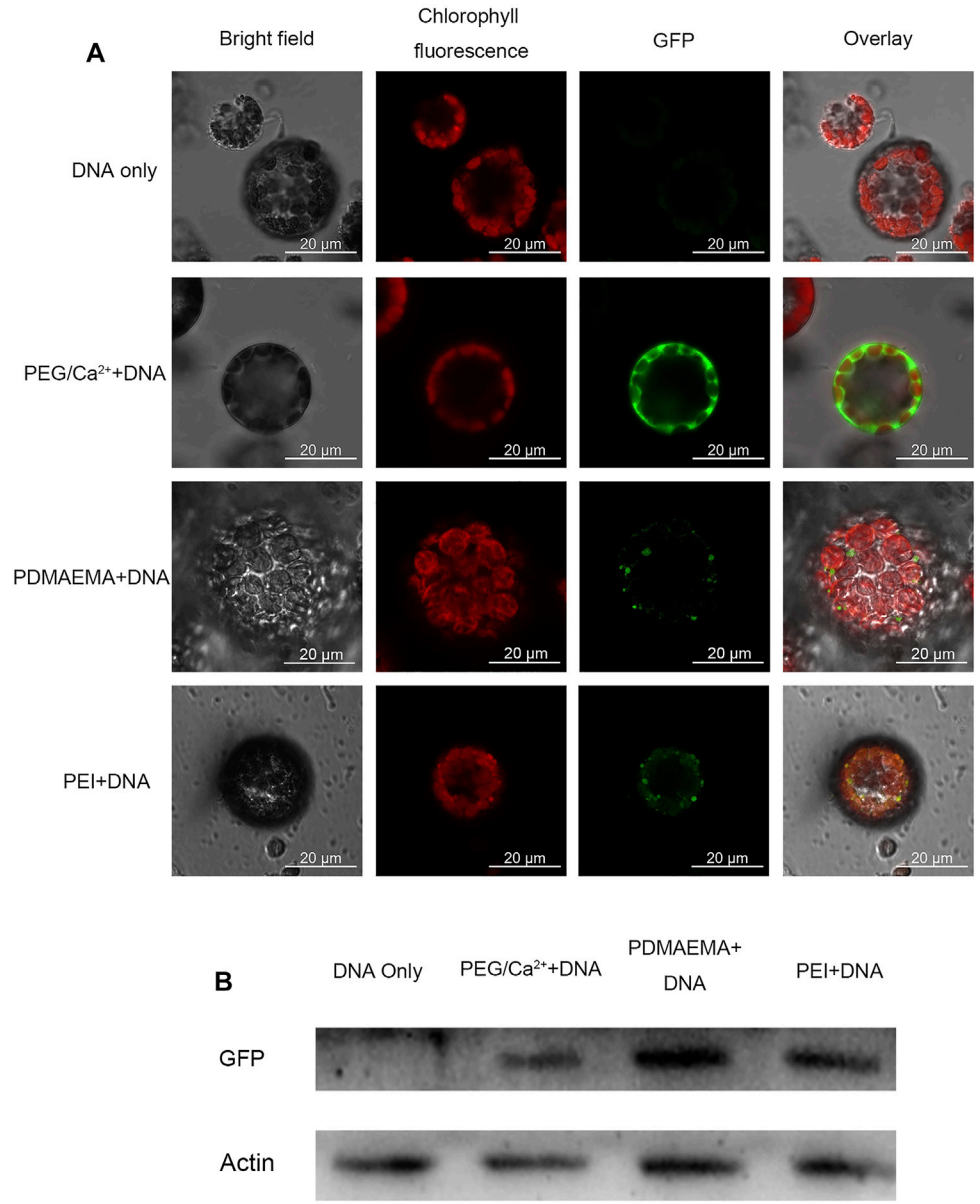

FIGURE 3 | GFP expression imaging in *Arabidopsis thaliana* protoplast. **(A)** Confocal microscope was used to image the *Arabidopsis thaliana* protoplast incubated with DNA only as a negative control, PEG/Ca^{2+} as a positive control, PDMAEMA + DNA (N/P ratio of 15:1), and PEI + DNA (N/P ratio of 15:1). GFP fluorescence images were captured with 488 nm laser excitation and 539 nm emission wavelengths. Chlorophyll autofluorescence images were captured with 633 nm laser excitation and 691 nm emission wavelengths. Scale bar, 20 μm. Protoplasts were incubated with PEG/Ca^{2+} for 15 min and washed with W5 solution to remove PEG. Then, protoplasts were resuspended with W5 solution in a 1.5-mL tube for another 12 h in the dark. The protoplasts were incubated with PDMAEMA + DNA or PEI + DNA directly for 12 h. **(B)** Western blot of the GFP expression level of *Arabidopsis thaliana* protoplasts incubated with DNA only, DNA-PEG/Ca^{2+}, PDMAEMA + DNA, and PEI + DNA.

the protoplast solution to run the Western blot instead of the supernatant. The results demonstrated that the PDMAEMA + DNA and PEI + DNA can serve as delivery systems and cause DNA expression in *Arabidopsis thaliana* protoplasts.

Transfection in *Arabidopsis thaliana* Leaves

Arabidopsis thaliana leaves were used as the experiment material to further study the expression of plasmid DNA delivered by these two polymers. After preparation of PDMAEMA + DNA and PEI + DNA at the N/P ratio of 15, they were infiltrated on the abaxial surface of the three-week-old *Arabidopsis thaliana* leaves lamina using a needleless syringe. DNA only (in 10 mM $MgCl_2$/MES) was used as a control. GFP fluorescence was observed by confocal microscopy in the stoma cells of leaves, 24 h after infiltration with these two complexes. There was no GFP fluorescence

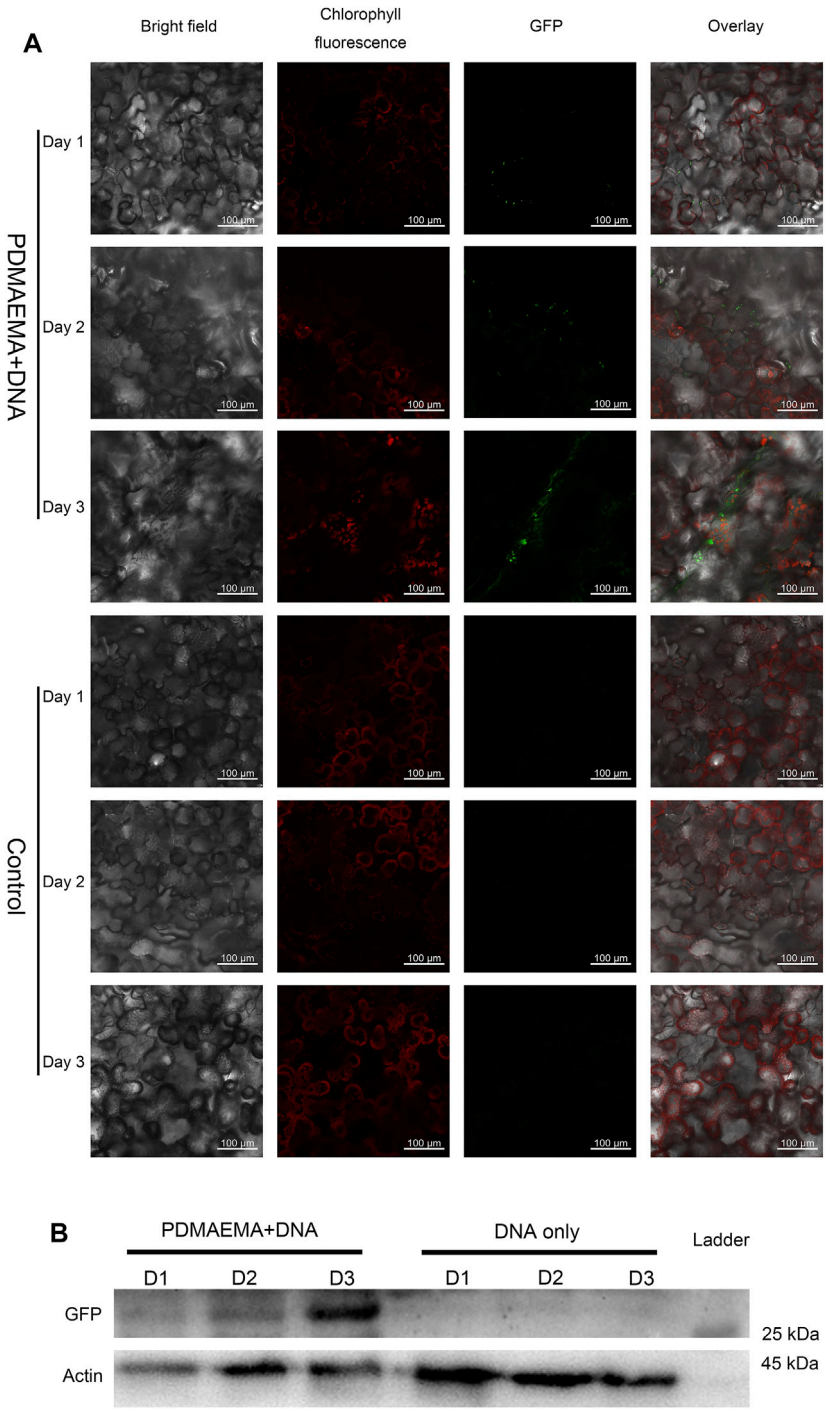

FIGURE 4 | GFP expression in *Nicotiana benthamiana* leaves. **(A)** *Nicotiana benthamiana* leaves infiltrated with DNA only (in 10 mM $MgCl_2$/MES as a control) and PDMAEMA + DNA (N/P ratio of 15:1) are imaged using a confocal microscope to detect GFP expression in the leaf lamina in 1 day, 2 days, and 3 days. Experiments were performed with intact leaves from healthy plants. Scale bar, 100 μm. **(B)** Western blot of GFP expression of *Nicotiana benthamiana* leaves infiltrated with DNA only (in 10 mM $MgCl_2$/MES as control) and PDMAEMA + DNA in 1 day, 2 days, and 3 days.

detected in the leaves infiltrated with DNA only (**Supplementary Figure S5**). These results showed that PDMAEMA + DNA and PEI + DNA traverse the plant cell wall and the plasma membrane to enter the plant cell in some way and have an expression in the stoma cells of leaves within 24 h. But, this transfection effect is not so significant compared to that of protoplasts. One possible reason was that infiltration time is not sufficient for a preferable

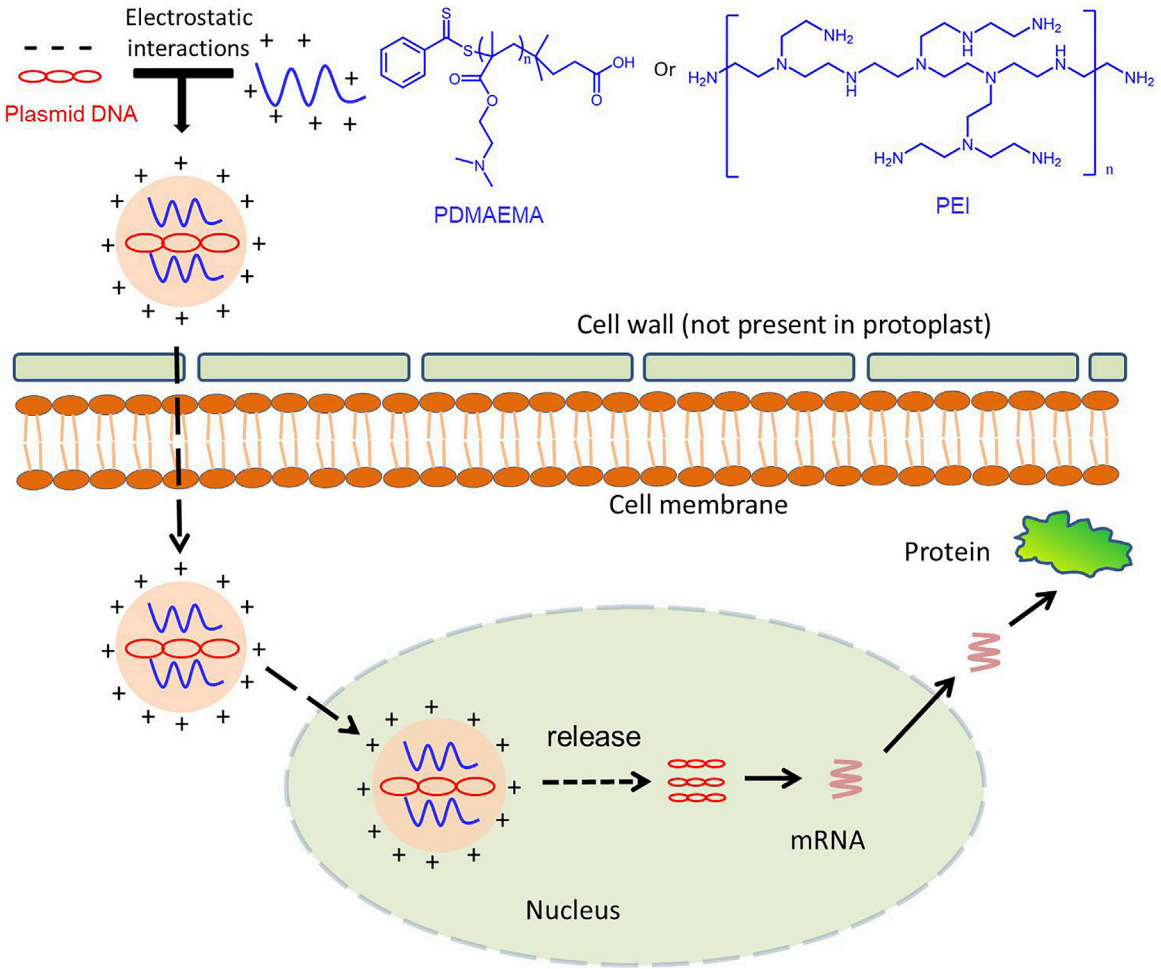

FIGURE 5 | Schematic illustration for the polymer-based gene delivery system in the plant cell.

expression. Therefore, a time-course transformation experiment was performed in a subsequent study.

Transfection in *Nicotiana benthamiana* Leaves

Additionally, gene expression experiments were also performed in *Nicotiana benthamiana* leaves to demonstrate the applicability of cationic polymers in different plant species. *Nicotiana benthamiana* leaves of three weeks old were infiltrated with DNA only (in 10 mM $MgCl_2$/MES with pH 5.7 as control) and PDMAEMA + DNA on three successive days. On the fourth day, one part of leaves of different treatment was collected to perform confocal microscope imaging (GFP expression for 1 day, 2 days, and 3 days was observed at the same time), while the other part of the leaves was collected to perform Western blot to detect GFP expression in the protein level. The cells around the infiltrated area were transfected with PDMAEMA + DNA (**Figure 4A**) or PEI + DNA (**Supplementary Figure S6A**), and GFP fluorescence was observed in both the leaves treated with PDMAEMA and PEI compared to the autofluorescence of chloroplasts (red in **Figure 4A**) as control. Specifically, the DNA complexes of PDMAEMA showed a GFP expression on first day, and the transfection effect was gradually obvious up to the third day (**Figure 4A**). The time-course study showed that the PDMAEMA-based gene delivery system was effective to perform transfection in a short time, and the PEI-based gene delivery system had a similar phenomenon (**Supplementary Figure S6A**). For control experiments, transfection into *Nicotiana benthamiana* leaves was performed using DNA in 10 mM $MgCl_2$/MES, and there was no GFP fluorescence detected in the control group (**Figure 4A**). Western blot was also performed to confirm the GFP expression in the case of time-course treatment (**Figure 4B**, also see **Supplementary Figure S6B**), and it was basically consistent with confocal image results.

Based on the transfection results related to *Nicotiana benthamiana* leaves, the transfection behavior with PDMAEMA

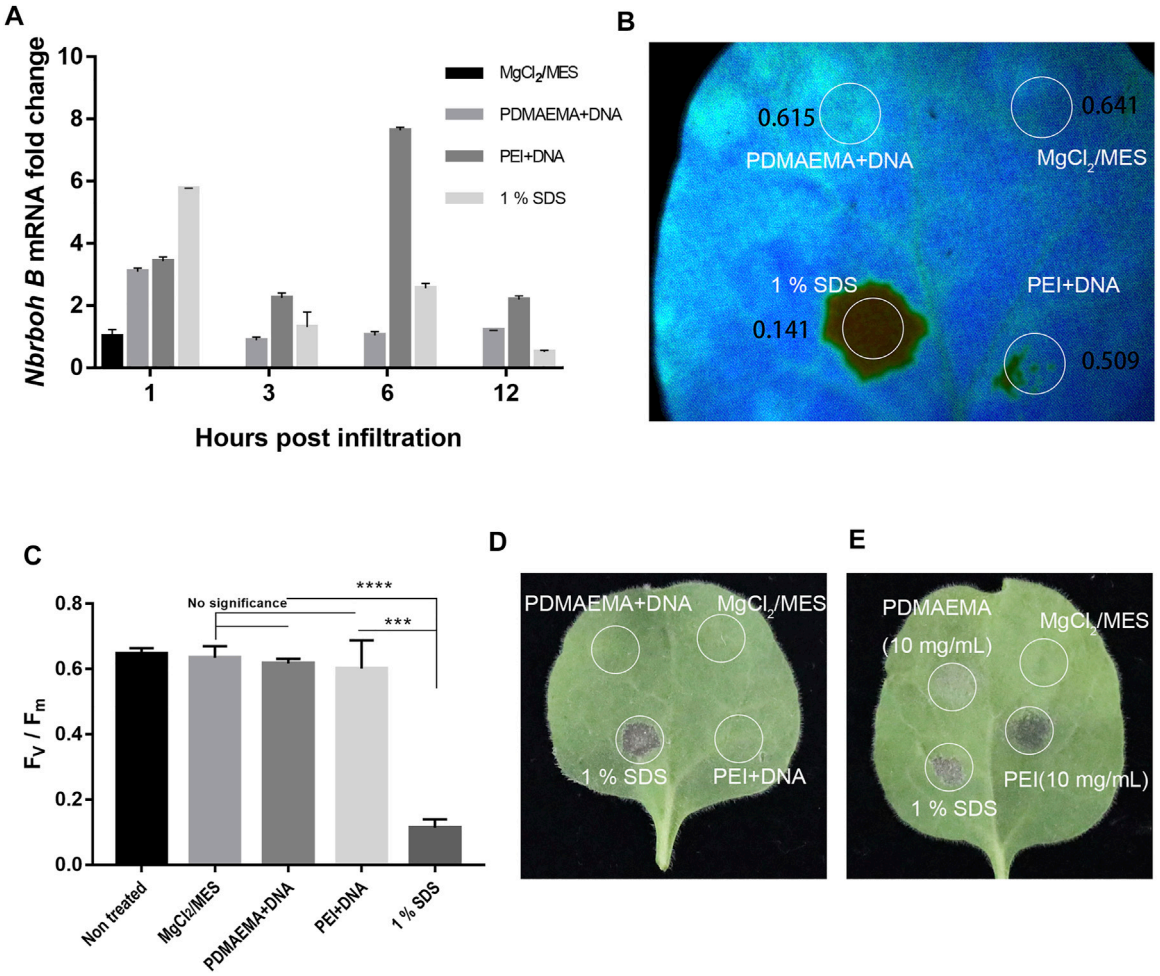

FIGURE 6 | Toxicity assay. **(A)** qPCR analysis of *Nbrboh B* in *Nicotiana benthamiana* leaves with different infiltrations ($MgCl_2$/MES (10 mM) as control, PDMAEMA + DNA (N/P ratio of 15:1), PEI + DNA (N/P ratio of 15:1), and 1% SDS at a time course. **(B)** Photosystem II Fv/Fm of different locations treated with PDMAEMA + DNA (N/P ratio of 15:1), PEI + DNA (N/P ratio of 15:1), 1% SDS, and $MgCl_2$/MES (10 mM) as control on the same *Nicotiana benthamiana* leaf. **(C)** Statistical data of the (B) Fv/Fm ratio represent the variable/maximum fluorescence measurement of the photosystem II quantum efficiency. **(D)** Phenotype of the single *Nicotiana benthamiana* leaf infiltrated with $MgCl_2$/MES (10 mM), PDMAEMA + DNA (N/P ratio of 15:1), PEI + DNA (N/P ratio of 15:1), and 1% SDS on different positions. **(E)** Phenotype of a single *Nicotiana benthamiana* leaf infiltrated with $MgCl_2$/MES (10 mM), 1% SDS, PDMAEMA (10 mg/mL), and PEI (10 mg/mL) on different positions.

was achieved in both *Arabidopsis thaliana* and *Nicotiana benthamiana* leaves. The internalization mechanism of complexes is via endocytosis pathways in animal cells (Midoux et al., 2008). But, the specific internalization mechanism of exogenous complexes remains unknown in plant cells (Xia et al., 2021). The endocytotic pathway in plant cells is different from that in the animal; during the process, the pH of the endosomes does not decrease to a dangerous level. Rather, the vacuole of plant cells possesses the lowest pH and is the final destiny for endocytosis (Xia et al., 2020). Plant cell walls consist of some modifications such as pit, perforation plate, spiral thickening, and wart. Also, the diameter of some pits is more than 1 μm, so a minority of complexes may enter the cell via pits of the cell walls (Lakshmanan et al., 2013). Besides, there is ample evidence for stomatal uptake of nanoparticles, for example, hydrophilic chitosan nanocarriers (86.8 nm in size) entered through stomata in the plant leaves (Nadendla et al., 2018). PEI is a cationic polymer with a proton sponge effect. PEI as a carrier is widely used in the delivery of nucleic acids in animal cells (Godbey et al., 2001), and PDMAEMA may have a similar delivery function.

To verify the delivery function of PDMAEMA, we used the complex of FAM-siRNA$_{NPR1}$ and PDMAEMA to infiltrate *Nicotiana benthamiana* leaves and observed its localization by confocal microscopy. Because PDMAEMA binds stably to FAM-siRNA$_{NPR1}$, the fluorescence of FAM represents the entry of PDMAEMA into cells. Point-like distribution and clustering were observed, but only infiltrating FAM-siRNA$_{NPR1}$ did not have this phenomenon; these results illustrated that PDMAEMA was able to deliver nucleic acid into plant cells (**Figure 5**). According to the article (Midoux et al., 2008) and our results, we proposed a scheme: plasmid DNA interacts with cationic polymers by electrostatic interaction forming positively charged

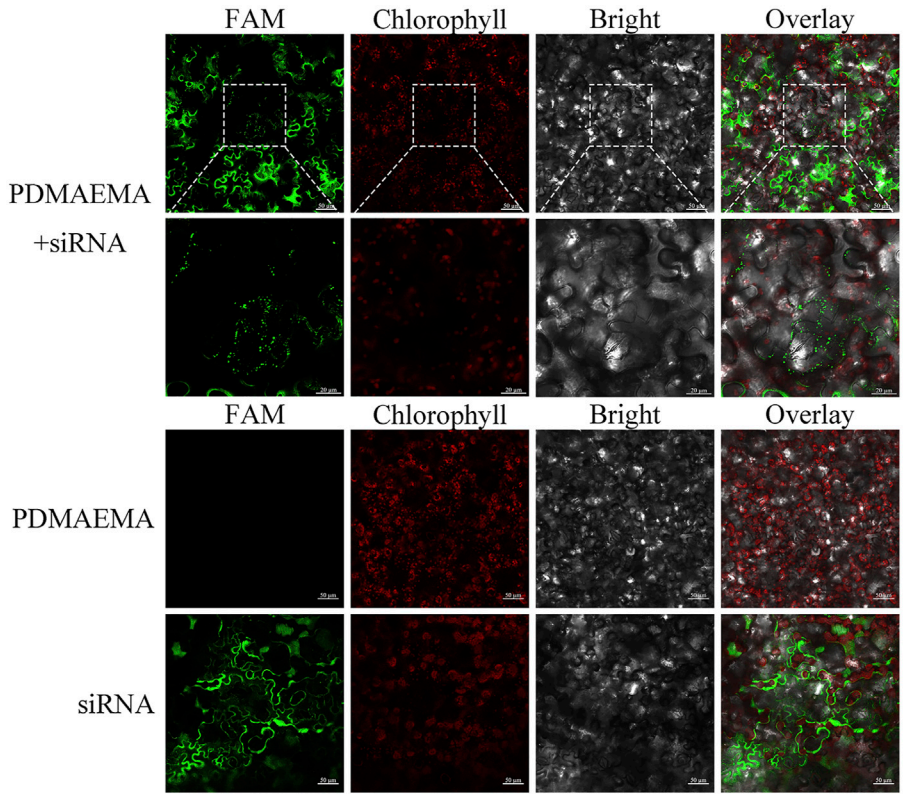

SCHEME 1 | PDMAEMA + FAM-siRNA$_{NPR1}$-infiltrating *Nicotiana benthamiana* leaves. FAM-siRNA$_{NPR1}$ (20 μM) was mixed with PDMAEMA (1 mg/mL) at the fixed N/P ratio of 15 and incubated at room temperature for 30 min. The formed complexes were diluted 10 times in 10 mM $MgCl_2$/MES (pH 5.7) before infiltration, taking only infiltrating PDMAEMA or FAM-siRNA$_{NPR1}$ as a control.

complexes. Then, the positively charged complexes make it easy to traverse the plant cell wall and interact with the membrane to internalize into the plant cell. After entering the plant cell, PDMAEMA and PEI can also protect DNA from degradation. Most of the complexes release plasmid DNA through the proton sponge effect, and it is possible that some DNA enters the nucleus and participates in the transcription and translation. A small part of the complexes enters the nucleus and releases plasmid DNA complexes with an unknown mechanism, participating in the transcription process and translation (**Scheme 1**). The specific mechanism deserves further study.

Toxicity Tests in Plant Leaves

To evaluate biocompatibility of these two polymers, we performed toxicity assays in *Nicotiana benthamiana* leaves. We use the expression of *respiratory burst oxidase homolog B* (*Nbrboh B*), a known gene indicating stress conditions in *Nicotiana benthamiana*, to quantify the toxicity of the polymers as they are directly proportional (Demirer et al., 2019). We used qPCR analysis to determine the toxicity of these two polymers at different time points of the treatment.

As shown in **Figure 6A**, at 1 h, samples treated with PDMAEMA + DNA and PEI + DNA upregulated *Nbrboh B* related to the sample treated with 10 mM $MgCl_2$/MES (as a negative control). However, they did not upregulate *Nbrboh B* too much compared to the sample treated with 1% SDS (as a positive control). These results illustrated that 1% SDS caused the most toxicity; at 3 h, 1% SDS, PDMAEMA + DNA, and PEI + DNA caused the upregulation of *Nbrboh B* to decrease, and the expression of PEI + DNA treatment was the most and showed that the toxicity of PEI may be the largest; *Nbrboh B* was at the highest level at 6 h and 12 h with PEI + DNA treatment, while PDMAEMA + DNA treatment with *Nbrboh B* was a continuous downward process; hence, the toxicity of PDMAEMA might be lower than that of PEI. It was in accordance with the previous study that PDMAEMA had less toxicity than PEI does (Verbaan et al., 2003). There are reports that *RbohB* is a fast responsive gene that can be upregulated within minutes; therefore, the long sampling time points are not quite reasonable for the purpose of the experiment (Xia et al., 2020), so the high expression level for PEI at 6 h could result from a second wounding wave for stressed plants, and 12 h is too long to sample for *RbohB* genes.

Additionally, photosystem II measurements were also performed to determine the toxicity in *Nicotiana benthamiana* leaves (**Figure 6B**). The results showed that PDMAEMA + DNA-infiltrated positions (with an Fv/Fm ratio of 0.615) and PEI +

DNA-infiltrated positions (with an Fv/Fm ratio of 0.641) in *Nicotiana benthamiana* leaves had similar photosynthesis quantum yields. But, position treated with 1% SDS as a positive control showed a significant decrease in the photosystem II quantum yield with an Fv/Fm ratio of 0.141 in *Nicotiana benthamiana* leaves, indicating a strong stress or tissue damage. Also, there was no significant difference between the position treated with 1% SDS and the negative control (**Figure 6C**). The phenotype of positions with different infiltration of leaves showed that PDMAEMA + DNA and PEI + DNA had no obvious toxicity compared with 10 mM $MgCl_2$/MES treatment as a negative control and 1% SDS treatment as a positive control (**Figure 6D**).

Furthermore, in order to compare the toxicity between PDMAEMA and PEI, we used the diluted PDMAEMA (10 mg/mL) and PEI (10 mg/mL) in 10 mM $MgCl_2$/MES and infiltrated the *Nicotiana benthamiana* leaves. PEI showed a higher toxicity than PDMAEMA according to the phenotype of *Nicotiana benthamiana* leaves (**Figure 6E**). The result was consistent with the qPCR analysis (**Figure 6A**) and previous examinations toward animal cells (Verbaan et al., 2003; Xu et al., 2009; Agarwal et al., 2012).

CONCLUSION

The gene delivery system on the basis of cationic polymer PDMAEMA is an original method for transient transformation in plant cells. In this proof-of-concept study, complexes of DNA and cationic polymers (PDMAEMA and PEI) with a small hydrodynamic diameter were formed at the specific N/P ratio. Meanwhile, we confirmed that PDMAEMA and PEI protect DNA from degradation after the formation of complexes (PDMAEMA + DNA and PEI + DNA). The expression of pGFP was detected by confocal microscopy imaging and confirmed by Western blotting analysis. Polymer-mediated delivery is appropriate to transient transfection because of its operability efficiency and low toxicity. In conclusion, PDMAEMA-mediated transient transformation is achieved in plant cells without obvious toxicity or tissue damage. PDMAEMA and PDMAEMA-based gene delivery materials are more promising for gene delivery to plants due to their relatively low cytotoxicity and facile fabrication compared to PEI. Polymer-based plant transfection platforms probably provide promising extra opportunities in plant genetic engineering.

DATA AVAILABILITY STATEMENT

The datasets presented in this study can be found in online repositories. The names of the repository/repositories and accession number(s) can be found in the article/ **Supplementary Material**.

AUTHOR CONTRIBUTIONS

ZA: investigation, methodology, and writing—original draft. BC: methodology and writing—review and editing. JZ and BZ added to the experiment. CZ: language polishing. XH: conceptualization, methodology, resources, writing—review and editing, and supervision. WC: conceptualization, methodology, resources, writing—review and editing, and supervision. All authors contributed to the article and approved the submitted version.

FUNDING

This study was financially supported by the National Natural Science Foundation of China (31570256).

ACKNOWLEDGMENTS

We thank Caiji Gao (School of Life Sciences, South China Normal University, China) for kind support of plasmid DNA pBI221-GFP.

SUPPLEMENTARY MATERIAL

The Supplementary Material for this article can be found online at: https://www.frontiersin.org/articles/10.3389/fbioe.2022.805996/full#supplementary-material

REFERENCES

Agarwal, S., Zhang, Y., Maji, S., and Greiner, A. (2012). PDMAEMA Based Gene Delivery Materials. *Mater. Today* 15 (9), 388–393. doi:10.1016/S1369-7021(12)70165-7

Altpeter, F., Springer, N. M., Bartley, L. E., Blechl, A., Brutnell, T. P., Citovsky, V., et al. (2016). Advancing Crop Transformation in the Era of Genome Editing. *Plant Cell* 28 (7), tpc.00196.2016–1520. doi:10.1105/tpc.16.00196

Baltes, N. J., Gil-Humanes, J., and Voytas, D. F. (2017). Genome Engineering and Agriculture: Opportunities and Challenges. *Gene Editing in Plants* 149, 1–26. doi:10.1016/bs.pmbts.2017.03.011

Bijali, J., and Acharya, K. (2020). Current Trends in Nano-technological Interventions on Plant Growth and Development: a Review. *IET nanobiotechnol.* 14 (2), 113–119. doi:10.1049/iet-nbt.2019.0008

Cao, B., Lyu, X., Wang, C., Lu, S., Xing, D., and Hu, X. (2020). Rational Collaborative Ablation of Bacterial Biofilms Ignited by Physical Cavitation and Concurrent Deep Antibiotic Release. *Biomaterials* 262, 120341. doi:10.1016/j.biomaterials.2020.120341

Chang, F.-P., Kuang, L.-Y., Huang, C.-A., Jane, W.-N., Hung, Y., Hsing, Y.-i. C., et al. (2013). A Simple Plant Gene Delivery System Using Mesoporous Silica Nanoparticles as Carriers. *J. Mater. Chem. B* 1 (39), 5279–5287. doi:10.1039/c3tb20529k

Chu, C., Lyu, X., Wang, Z., Jin, H., Lu, S., Xing, D., et al. (2020). Cocktail Polyprodrug Nanoparticles Concurrently Release Cisplatin and Peroxynitrite-Generating Nitric Oxide in Cisplatin-Resistant Cancers. *Chem. Eng. J.* 402, 126125. doi:10.1016/j.cej.2020.126125

Cifuentes-Rius, A., Boase, N. R. B., Font, I., Coronas, N., Ramos-Perez, V., Thurecht, K. J., et al. (2017). *In Vivo* Fate of Carbon Nanotubes with Different Physicochemical Properties for Gene Delivery Applications. *ACS Appl. Mater. Inter.* 9 (13), 11461–11471. doi:10.1021/acsami.7b00677

Clamme, J. P., Azoulay, J., and Mély, Y. (2003). Monitoring of the Formation and Dissociation of Polyethylenimine/DNA Complexes by Two Photon Fluorescence Correlation Spectroscopy. *Biophysical J.* 84 (3), 1960–1968. doi:10.1016/S0006-3495(03)75004-8

Demirer, G. S., Zhang, H., Matos, J. L., Goh, N. S., Cunningham, F. J., Sung, Y., et al. (2019). High Aspect Ratio Nanomaterials Enable Delivery of Functional Genetic Material without DNA Integration in Mature Plants. *Nat. Nanotechnol.* 14 (5), 456–464. doi:10.1038/s41565-019-0382-5

Ding, P., Liu, W., Guo, X., Cohen Stuart, M. A., and Wang, J. (2021). Optimal Synthesis of Polyelectrolyte Nanogels by Electrostatic Assembly Directed Polymerization for Dye Loading and Release. *Soft Matter* 17 (4), 887–892. doi:10.1039/d0sm01715a

Ding, Z., Wang, D., Shi, W., Yang, X., Duan, S., Mo, F., et al. (2020). *In Vivo* Targeting of Liver Cancer with Tissue- and Nuclei-specific Mesoporous Silica Nanoparticle-Based Nanocarriers in Mice. *Ijn* 15, 8383–8400. doi:10.2147/Ijn.S272495

Faraz, A., Faizan, M., Sami, F., Siddiqui, H., Pichtel, J., and Hayat, S. (2019). Nanoparticles: Biosynthesis, Translocation and Role in Plant Metabolism. *IET nanobiotechnol.* 13 (4), 345–352. doi:10.1049/iet-nbt.2018.5251

Fincheira, P., Tortella, G., Duran, N., Seabra, A. B., and Rubilar, O. (2020). Current Applications of Nanotechnology to Develop Plant Growth Inducer Agents as an Innovation Strategy. *Crit. Rev. Biotechnol.* 40 (1), 15–30. doi:10.1080/07388551.2019.1681931

Gregory, J. V., Kadiyala, P., Doherty, R., Cadena, M., Habeel, S., Ruoslahti, E., et al. (2020). Systemic Brain Tumor Delivery of Synthetic Protein Nanoparticles for Glioblastoma Therapy. *Nat. Commun.* 11 (1), 5687. doi:10.1038/s41467-020-19225-7

Guo, Q., Guo, H., Lan, T., Chen, Y., Chen, X., Feng, Y., et al. (2021). Co-delivery of Antibiotic and Baicalein by Using Different Polymeric Nanoparticle Cargos with Enhanced Synergistic Antibacterial Activity. *Int. J. Pharmaceutics* 599, 120419. doi:10.1016/j.ijpharm.2021.120419

Guo, X., Cao, B., Wang, C., Lu, S., and Hu, X. (2020). In Vivophotothermal Inhibition of Methicillin-resistantStaphylococcus Aureusinfection Byin Situtemplated Formulation of Pathogen-Targeting Phototheranostics. *Nanoscale* 12 (14), 7651–7659. doi:10.1039/d0nr00181c

Hu, X., Li, Y., Liu, T., Zhang, G., and Liu, S. (2014). Photodegradable Neutral-Cationic Brush Block Copolymers for Nonviral Gene Delivery. *Chem. Asian J.* 9 (8), 2148–2155. doi:10.1002/asia.201402171

Huang, R.-Y., Lin, Y.-H., Lin, S.-Y., Li, Y.-N., Chiang, C.-S., and Chang, C.-W. (2019). Magnetic Ternary Nanohybrids for Nonviral Gene Delivery of Stem Cells and Applications on Cancer Therapy. *Theranostics* 9 (8), 2411–2423. doi:10.7150/thno.29326

Huo, S., Jin, S., Ma, X., Xue, X., Yang, K., Kumar, A., et al. (2014). Ultrasmall Gold Nanoparticles as Carriers for Nucleus-Based Gene Therapy Due to Size-dependent Nuclear Entry. *ACS Nano* 8 (6), 5852–5862. doi:10.1021/nn5008572

Khot, L. R., Sankaran, S., Maja, J. M., Ehsani, R., and Schuster, E. W. (2012). Applications of Nanomaterials in Agricultural Production and Crop protection: A Review. *Crop Prot.* 35, 64–70. doi:10.1016/j.cropro.2012.01.007

Kwak, S.-Y., Lew, T. T. S., Sweeney, C. J., Koman, V. B., Wong, M. H., Bohmert-Tatarev, K., et al. (2019). Chloroplast-selective Gene Delivery and Expression in Planta Using Chitosan-Complexed Single-Walled Carbon Nanotube Carriers. *Nat. Nanotechnol.* 14 (5), 447–455. doi:10.1038/s41565-019-0375-4

Lakshmanan, M., Kodama, Y., Yoshizumi, T., Sudesh, K., and Numata, K. (2013). Rapid and Efficient Gene Delivery into Plant Cells Using Designed Peptide Carriers. *Biomacromolecules* 14 (1), 10–16. doi:10.1021/bm301275g

Lei, W.-X., An, Z.-S., Zhang, B.-H., Wu, Q., Gong, W.-J., Li, J.-M., et al. (2020). Construction of Gold-siRNANPR1 Nanoparticles for Effective and Quick Silencing of NPR1 in *Arabidopsis thaliana*. *RSC Adv.* 10 (33), 19300–19308. doi:10.1039/d0ra02156c

Liu, J., Song, L., Liu, S., Jiang, Q., Liu, Q., Li, N., et al. (2018). A DNA-Based Nanocarrier for Efficient Gene Delivery and Combined Cancer Therapy. *Nano Lett.* 18 (6), 3328–3334. doi:10.1021/acs.nanolett.7b04812

Liu, Y., Zhao, N., and Xu, F.-J. (2019). pH-Responsive Degradable Dextran-Quantum Dot Nanohybrids for Enhanced Gene Delivery. *ACS Appl. Mater. Inter.* 11 (38), 34707–34716. doi:10.1021/acsami.9b12198

Lo, C.-W., Liao, W.-H., Wu, C.-H., Lee, J.-L., Sun, M.-K., Yang, H.-S., et al. (2015a). Synergistic Effect of PEI and PDMAEMA on Transgene Expression *In Vitro*. *Langmuir* 31 (22), 6130–6136. doi:10.1021/acs.langmuir.5b00520

Lo, Y.-L., Chou, H.-L., Liao, Z.-X., Huang, S.-J., Ke, J.-H., Liu, Y.-S., et al. (2015b). Chondroitin Sulfate-Polyethylenimine Copolymer-Coated Superparamagnetic Iron Oxide Nanoparticles as an Efficient Magneto-Gene Carrier for microRNA-Encoding Plasmid DNA Delivery. *Nanoscale* 7 (18), 8554–8565. doi:10.1039/c5nr01404b

Luo, K., Li, C., Wang, G., Nie, Y., He, B., Wu, Y., et al. (2011). Peptide Dendrimers as Efficient and Biocompatible Gene Delivery Vectors: Synthesis and *in vitro* Characterization. *J. Controlled Release* 155 (1), 77–87. doi:10.1016/j.jconrel.2010.10.006

Maury, B., Gonçalves, C., Tresset, G., Zeghal, M., Cheradame, H., Guégan, P., et al. (2014). Influence of pDNA Availability on Transfection Efficiency of Polyplexes in Non-proliferative Cells. *Biomaterials* 35 (22), 5977–5985. doi:10.1016/j.biomaterials.2014.04.007

Mei, Y., Wang, R., Jiang, W., Bo, Y., Zhang, T., Yu, J., et al. (2019). Recent Progress in Nanomaterials for Nucleic Acid Delivery in Cancer Immunotherapy. *Biomater. Sci.* 7 (7), 2640–2651. doi:10.1039/c9bm00214f

Midoux, P., Breuzard, G., Gomez, J., and Pichon, C. (2008). Polymer-based Gene Delivery: a Current Review on the Uptake and Intracellular Trafficking of Polyplexes. *Cgt* 8 (5), 335–352. doi:10.2174/156652308786071014

Nadendla, S. R., Rani, T. S., Vaikuntapu, P. R., Maddu, R. R., and Podile, A. R. (2018). Harpin Encapsulation in Chitosan Nanoparticles for Improved Bioavailability and Disease Resistance in Tomato. *Carbohydr. Polym.* 199, 11–19. doi:10.1016/j.carbpol.2018.06.094

Neuberg, P., and Kichler, A. (2014). Recent Developments in Nucleic Acid Delivery with Polyethylenimines. *Adv. Genet.* 88, 263–288. doi:10.1016/B978-0-12-800148-6.00009-2

Ortega-Muñoz, M., Giron-Gonzalez, M. D., Salto-Gonzalez, R., Jodar-Reyes, A. B., De Jesus, S. E., Lopez-Jaramillo, F. J., et al. (2016). Polyethyleneimine-Coated Gold Nanoparticles: Straightforward Preparation of Efficient DNA Delivery Nanocarriers. *Chem. Asian J.* 11 (23), 3365–3375. doi:10.1002/asia.201600951

Richter, F., Mapfumo, P., Martin, L., Solomun, J. I., Hausig, F., Frietsch, J. J., et al. (2021). Improved Gene Delivery to K-562 Leukemia Cells by Lipoic Acid Modified Block Copolymer Micelles. *J. Nanobiotechnol.* 19 (1), 70. doi:10.1186/s12951-021-00801-y

Shang, Y., Hasan, M. K., Ahammed, G. J., Li, M., Yin, H., and Zhou, J. (2019). Applications of Nanotechnology in Plant Growth and Crop Protection: A Review. *Molecules* 24 (14), 2558. doi:10.3390/molecules24142558

Torney, F., Trewyn, B. G., Lin, V. S.-Y., and Wang, K. (2007). Mesoporous Silica Nanoparticles Deliver DNA and Chemicals into Plants. *Nat. Nanotech* 2 (5), 295–300. doi:10.1038/nnano.2007.108

Verbaan, F., van Dam, I., Takakura, Y., Hashida, M., Hennink, W., Storm, G., et al. (2003). Intravenous Fate of Poly(2-(dimethylamino)ethyl Methacrylate)-Based Polyplexes. *Eur. J. Pharm. Sci.* 20 (4-5), 419–427. doi:10.1016/j.ejps.2003.09.005

Wang, C., Zhao, W., Cao, B., Wang, Z., Zhou, Q., Lu, S., et al. (2020). Biofilm-Responsive Polymeric Nanoparticles with Self-Adaptive Deep Penetration for *In Vivo* Photothermal Treatment of Implant Infection. *Chem. Mater.* 32 (18), 7725–7738. doi:10.1021/acs.chemmater.0c02055

Wang, W., Yuan, J., and Jiang, C. (2021a). Applications of Nanobodies in Plant Science and Biotechnology. *Plant Mol. Biol.* 105 (1-2), 43–53. doi:10.1007/s11103-020-01082-z

Wang, Z., Zhan, M., Li, W., Chu, C., Xing, D., Lu, S., et al. (2021b). Photoacoustic Cavitation-Ignited Reactive Oxygen Species to Amplify Peroxynitrite Burst by Photosensitization-Free Polymeric Nanocapsules. *Angew. Chem. Int. Ed.* 60 (9), 4720–4731. doi:10.1002/anie.202013301

Wu, X., He, X., Zhong, L., Lin, S., Wang, D., Zhu, X., et al. (2011). Water-soluble Dendritic-Linear Triblock Copolymer-Modified Magnetic Nanoparticles: Preparation, Characterization and Drug Release Properties. *J. Mater. Chem.* 21 (35), 13611–13620. doi:10.1039/C1JM11613D

Xia, X., Shi, B., Wang, L., Liu, Y., Zou, Y., Zhou, Y., et al. (2021). From Mouse to Mouse-ear Cress: Nanomaterials as Vehicles in Plant Biotechnology. *Exploration* 1 (1), 9–20. doi:10.1002/exp.20210002

Xia, X., Zhang, H.-M., Offler, C. E., and Patrick, J. W. (2020). Enzymes Contributing to the Hydrogen Peroxide Signal Dynamics that Regulate wall Labyrinth Formation in Transfer Cells. *J. Exp. Bot.* 71 (1), 219–233. doi:10.1093/jxb/erz443

Xiao, F., Cao, B., Wen, L., Su, Y., Zhan, M., Lu, L., et al. (2020). Photosensitizer Conjugate-Functionalized Poly(hexamethylene Guanidine) for Potentiated

Broad-Spectrum Bacterial Inhibition and Enhanced Biocompatibility. *Chin. Chem. Lett.* 31 (9), 2516–2519. doi:10.1016/j.cclet.2020.06.038

Xu, F. J., Ping, Y., Ma, J., Tang, G. P., Yang, W. T., Li, J., et al. (2009). Comb-Shaped Copolymers Composed of Hydroxypropyl Cellulose Backbones and Cationic Poly((2-Dimethyl Amino)ethyl Methacrylate) Side Chains for Gene Delivery. *Bioconjug. Chem.* 20 (8), 1449–1458. doi:10.1021/bc900044h

Yan, T., Zhu, S., Hui, W., He, J., Liu, Z., and Cheng, J. (2020). Chitosan Based pH-Responsive Polymeric Prodrug Vector for Enhanced Tumor Targeted Co-delivery of Doxorubicin and siRNA. *Carbohydr. Polym.* 250, 116781. doi:10.1016/j.carbpol.2020.116781

Yin, L., Tang, H., Kim, K. H., Zheng, N., Song, Z., Gabrielson, N. P., et al. (2013). Light-Responsive Helical Polypeptides Capable of Reducing Toxicity and Unpacking DNA: Toward Nonviral Gene Delivery. *Angew. Chem. Int. Ed.* 52 (35), 9182–9186. doi:10.1002/anie.201302820

Yoo, S.-D., Cho, Y.-H., and Sheen, J. (2007). Arabidopsis Mesophyll Protoplasts: a Versatile Cell System for Transient Gene Expression Analysis. *Nat. Protoc.* 2 (7), 1565–1572. doi:10.1038/nprot.2007.199

Yu, S., Chen, J., Dong, R., Su, Y., Ji, B., Zhou, Y., et al. (2012). Enhanced Gene Transfection Efficiency of PDMAEMA by Incorporating Hydrophobic Hyperbranched Polymer Cores: Effect of Degree of Branching. *Polym. Chem.* 3 (12), 3324–3329. doi:10.1039/C2PY20487H

Zhang, G., Lin, S., Leow, C. H., Pang, K. T., Hernández-Gil, J., Long, N. J., et al. (2019). Quantification of Vaporised Targeted Nanodroplets Using High-Frame-Rate Ultrasound and Optics. *Ultrasound Med. Biol.* 45 (5), 1131–1142. doi:10.1016/j.ultrasmedbio.2019.01.009

Conflict of Interest: The authors declare that the research was conducted in the absence of any commercial or financial relationships that could be construed as a potential conflict of interest.

Publisher's Note: All claims expressed in this article are solely those of the authors and do not necessarily represent those of their affiliated organizations, or those of the publisher, the editors, and the reviewers. Any product that may be evaluated in this article, or claim that may be made by its manufacturer, is not guaranteed or endorsed by the publisher.

Advantages of publishing in Frontiers

OPEN ACCESS
Articles are free to read for greatest visibility and readership

FAST PUBLICATION
Around 90 days from submission to decision

HIGH QUALITY PEER-REVIEW
Rigorous, collaborative, and constructive peer-review

TRANSPARENT PEER-REVIEW
Editors and reviewers acknowledged by name on published articles

Frontiers
Avenue du Tribunal-Fédéral 34
1005 Lausanne | Switzerland

Visit us: www.frontiersin.org
Contact us: frontiersin.org/about/contact

REPRODUCIBILITY OF RESEARCH
Support open data and methods to enhance research reproducibility

DIGITAL PUBLISHING
Articles designed for optimal readership across devices

FOLLOW US
@frontiersin

IMPACT METRICS
Advanced article metrics track visibility across digital media

EXTENSIVE PROMOTION
Marketing and promotion of impactful research

LOOP RESEARCH NETWORK
Our network increases your article's readership